**Hugo Daniel Pereira Fernandes**

Mestre em Engenharia Civil

# Strengthening of flat slabs with reinforced concrete overlay – Analysis and development of the solution

Dissertação para obtenção do Grau de Doutor em Engenharia Civil, Especialidade de Estruturas

Orientador: Válter José da Guia Lúcio,
Professor Associado, FCT-UNL
Coorientador: António Manuel Pinho Ramos,
Professor Auxiliar, FCT-UNL

Júri:

Presidente: Prof. Doutor Fernando Manuel Anjos Henriques
Arguentes: Prof. Doutor Sérgio Manuel Rodrigues Lopes
Prof.ª Doutora Carla Alexandre Cruz Marchão

Vogais: Prof. Doutor Válter José da Guia Lúcio
Prof. Doutor Carlos Manuel Chastre Rodrigues
Prof. Doutor Mário Jorge de Seixas Pimentel
Prof.ª Doutora Ana Rita Faria Conceição de Sousa Gião

FACULDADE DE CIÊNCIAS E TECNOLOGIA
UNIVERSIDADE NOVA DE LISBOA

**Março 2019**

**Reforço de lajes fungiformes com lâmina de betão complementar – análise e desenvolvimento da solução**

**Strengthening of flat slabs with reinforced concrete overlay – analysis and development of the solution**

*Aos meus.*

# AGRADECIMENTOS

Esta Tese foi financiada pelo Ministério da Ciência, Tecnologia e Ensino Superior – Fundação para a Ciência e a Tecnologia através da Bolsa de Doutoramento SFRH/BD/89505/2012. Os trabalhos realizados no âmbito desta tese foram desenvolvidos no Departamento de Engenharia Civil da Faculdade de Ciências e Tecnologia da Universidade NOVA de Lisboa, onde foram efetuados também os ensaios experimentais, modelação numérica e caracterização de materiais.

O culminar deste trabalho não seria possível sem um rol de pessoas que contribuíram para a sua conclusão, e que foram um meio essencial para atingir este fim.

Ao Prof. Doutor Válter Lúcio, meu orientador científico, por todo o companheirismo e orientação ao longo deste trabalho, sendo fundamental a sua contribuição através da experiência e destreza no que diz respeito a estruturas de betão armado que permitiram moldar os objetivos desta Tese. Pessoalmente, o meu muito obrigado, professor.

Ao Prof. Doutor António Ramos, meu coorientador científico, por todo o companheirismo e orientação durante os trabalhos desta Tese, tendo as suas sugestões sido preponderantes para os objetivos desta Tese, juntamente com a sua atitude prática que contribuiu deveras para a execução dos trabalhos e produção de peças escritas.

Aos Prof. Doutor Fernando Pinho, Prof. Doutor Carlos Chastre e Prof. Doutor Corneliu Cismasiu, que acompanharam a minha evolução desde o Mestrado até ao Doutoramento. Agradeço pela sua amizade, formação e contribuição para este trabalho, através de sugestões tanto a nível de trabalho experimental no laboratório como de teoria a aplicar aos resultados e enquanto docentes do plano curricular do Doutoramento.

Ao Eng.º Doutor Duarte Faria, cujo companheirismo e conhecimento do tema contribuíram para a prossecução dos trabalhos experimentais, tendo-me acompanhado também desde o início da dissertação de Mestrado.

A todos os professores do Departamento de Engenharia Civil que de uma ou outra forma, contribuíram para a realização deste trabalho. Sim, também a eles o meu muito obrigado.

Aos meus amigos e colegas da investigação, em especial ao André Almeida, ao Micael Inácio, ao Nuno Dinarte, ao Nuno Mamede e ao Noel Franco, com quem tive a oportunidade de trabalhar e aprender imenso, bem como aos restantes amigos, colegas e alunos de Mestrado que me acompanharam ao longo destes anos de investigação, cujo seu companheirismo tornou possível que se atingisse este objetivo. Agradeço ainda a todos os meus amigos que desde o curso sempre me deram força para continuar e aos colegas que de alguma forma contribuíram para este trabalho.

Ao Eng.º Massimo Lapi, que conheci como aluno de Mestrado e que se revelou numa grande ajuda tanto no auxílio com ensaios experimentais, como no tratamento dos resultados, agradeço a sua dedicação e amizade tendo contribuído deveras para o tema desta Tese e para a sua difusão através dos artigos científicos que realizamos em conjunto. Ao seu orientador, Prof. Dr. Maurizio Orlando da Universidade de Florença, o meu obrigado por toda a colaboração no desenvolvimento dos artigos científicos.

Aos técnicos de laboratório que sem eles não teria sido possível a realização dos ensaios experimentais, ao Eng.º Vítor Silva, ao Sr. José Gaspar e ao Jorge Silvério, que foram incansáveis na realização dos ensaios e articulação do espaço no laboratório de estruturas pesadas do DEC. O meu muito obrigado pela amizade, disponibilidade, horas dedicadas a este trabalho e companheirismo que acompanharam todo os trabalhos.

À D.ª Maria da Luz e à Carla Figueiredo, que me acompanham desde o início do curso até ao Doutoramento e que foram incansáveis no tratamento de toda a logística de Secretariado, intercedendo sempre no melhor interesse dos objetivos desta Tese. Além das suas competências, são duas pessoas que tenho na maior consideração e que levo comigo.

Às funcionárias administrativas da Divisão de Apoio à Formação Avançada da FCT-UNL, em especial à Sr.ª Gracinda Caetano, por todo o apoio prestado na resolução de questões relacionadas com esta Tese, o meu muito obrigado porque não seria possível atingir este objetivo sem o seu apoio técnico e contribuição pessoal.

À D.ª Beatriz e família, que fez parte desta instituição e com quem travei uma amizade que se faz longa. Embora se tenha reformado, continua a acompanhar-me, tornando-me visita da casa. O meu muito obrigado pela força e alento.

Às colegas da D.ª Beatriz, em especial à D.ª Marília, pelas palavras de simpatia em todos os dias de trabalho incluído os fins de semana em que precisava trabalhar no laboratório. Por todos os sorrisos de bom dia, o meu muito obrigado.

À Profico Lda., que me acolhe profissionalmente e que apoiou sempre os meus objetivos relativamente ao Doutoramento, muito agradeço cada vez que prescindiu da minha presença para que eu pudesse tratar de assuntos relacionados com os trabalhos desta Tese e bem como concluí-la. Demonstro a minha gratidão em especial ao Eng.º Eduardo Monteiro, Diretor de Projeto do meu departamento e que tornou possível toda esta logística.

Sendo essencial a colaboração de diversas entidades na realização dos modelos experimentais para os objetivos desta Tese, ressalvo a Concremat, S.A. e a Secil Prebetão S.A. a quem agradeço pela disponibilidade do espaço, fornecimento de materiais e auxílio na execução dos ditos modelos. Apesar da grande disponibilidade, companheirismo e apoio tanto nos departamentos técnicos como na produção, agradeço a estas entidades diretamente nas pessoas do Eng.º José Figueiredo e do Eng.º Luís Machado, que articularam e auxiliaram a produção ao destacarem os meios necessários para o efeito, além da sua contribuição pessoal. Muito agradeço.

À HILTI Portugal Lda., que me acompanha desde a minha dissertação de Mestrado, o meu agradecimento pela cedência de resina para os ensaios *pull-off* e ferramentas sempre que foi necessário, agilizando a execução dos mesmos. À SIKA Portugal S.A., pela cedência de material na preparação dos extensómetros e selagem dos varões embebidos nas lajes. À VSL pela cedência do material necessário para o sistema de reação dos ensaios experimentais. À Escola Superior de Tecnologia do Barreiro pela disponibilidade e auxílio na execução de ensaios de caracterização de betão e armaduras. A todos, o meu obrigado.

Quero agradecer à minha família, aos meus amigos e à minha namorada, que têm sido incansáveis no apoio ao meu trabalho e aos objetivos desta Tese.

Aos meus amigos (é-me impossível enumerar-vos a todos), mesmo não podendo estar sempre presente, facto é que os anos vão passando mas a amizade sempre melhora com o vosso apoio, companheirismo e tudo o que temos direito. Obrigado. A vida é melhor assim.

Aos meus pais, cujo apoio incondicional foi pedra basilar na minha formação pessoal e profissional. A vós, o meu muito obrigado pelo amor e apoio que não acabam.

À D.ª Lucinda, a nossa Xinda, que cuidou de mim em criança e foi muito importante para a minha família e para o meu desenvolvimento enquanto pessoa, que esteve presente nas nossas vidas até à minha entrada na faculdade mas que partiu deste mundo antes de me ver formado como Engenheiro. A ela agradeço todas as horas de cuidado e dedicação.

À Sílvia, pelo apoio e carinho incansáveis, que foram essenciais para este objetivo. O teu amor, incentivo e compreensão foram essenciais para atingir os objetivos a que me propus e que sem eles não teria conseguido da mesma forma. A ti, o meu muito obrigado meu amor.

Só espero ter oportunidade para retribuir todo o apoio e incentivo que ao longo destes anos me foram dando alento para continuar, culminando num objetivo que almejei e que partilho com todos vós, porque na realidade, não o conseguiria de outra forma.

A todos, o meu muito obrigado.

# Reforço de lajes fungiformes com lâmina de betão complementar – análise e desenvolvimento da solução


## RESUMO

O reforço de estruturas por aplicação de uma nova camada de betão é uma solução tradicional de encamisamento de pilares, vigas e lajes. Consiste numa solução económica e eficiente para o reforço de estruturas dado que utiliza os mesmos materiais base, aço e betão. Usualmente, é aplicada em zonas de compressão, dado o comportamento reconhecido do betão à compressão, colocando diversos desafios para o controlo da fendilhação quando aplicada em zonas de tração.

O reforço com uma nova camada de betão na face tracionada requer o controlo do descolamento desta camada, em serviço e para os estados limites últimos da estrutura. O dimensionamento desta solução de reforço requer a consideração global dos esforços atuantes na estrutura em questão, bem como da capacidade resistente local da interface como garantia da integridade estrutural. Tal necessidade leva à pormenorização da interface entre as duas camadas de betão para um comportamento melhorado da ligação, nomeadamente através da preparação da superfície e de armadura de ligação entre camadas. O estudo do comportamento desta interface serviu de base na aplicação do reforço aos modelos de laje.

O presente trabalho tem como objetivo caracterizar a solução de reforço aplicada a modelos de laje unidirecionais e bidirecionais. Todos os modelos foram reforçados com uma nova camada de betão na face tracionada. Os modelos unidirecionais foram ensaiados monotonicamente à flexão até à rotura, e os modelos bidirecionais foram carregados localmente e monotonicamente até à rotura. Foram calibrados modelos numéricos com os resultados experimentais através do software de análise não-linear ATENA 3D®.

Os resultados foram então comparados com os códigos atuais e definidos vários parâmetros para auxílio à aplicação do reforço estrutural com uma nova camada de betão.



## Palavras-chave

Reforço de estruturas

Betão armado

Aderência betão-betão

Interface betão-betão

Modelação numérica.

Punçoamento

# Strengthening of flat slabs with reinforced concrete overlay – analysis and development of the solution


## ABSTRACT

Strengthening of concrete structures with a new concrete layer has been commonly used for columns, beams and slabs. This technique is economic and efficient for structural strengthening since it uses the same base materials, steel and concrete. It is usually applied on the compressed face of the concrete element due to concrete's recognized behaviour under compression, posing several challenges to control cracking and resistance when applied on the tensile face.

Strengthening of concrete structures with a new concrete layer applied on the tensile face requires controlling the debonding phenomenon of added concrete for service and ultimate limit states. Designing such strengthening solution requires the consideration for the strength of the global structure and the local interface capacity for maintaining structural integrity throughout the load history. Such requirement leads to the need for interface detailing solutions between the two concrete layers that improve the behaviour of the composite section, namely the roughening of the existing surface and stitching reinforcement. The knowledge from studying such interface was applied to the strengthening of slab specimens.

This work presents the study performed on concrete unidirectional slab specimens and on column-supported slab specimens. All specimens were strengthened with a reinforced concrete overlay on the tensile face. The former consisted on the flexural monotonic loading of the specimens until failure, and the latter consisted on specimens loaded monotonically and concentrically until failure. The calibration of numerical models based on experimental test results was also performed with the nonlinear analysis software ATENA 3D®.

All results were then compared to current codes and regulations, and some guidelines were defined for the correct application of strengthening with a reinforced concrete overlay on existing structures.



## Keywords

Structural strengthening

Reinforced concrete

Concrete-to-concrete bond

Concrete-to-concrete interface

Numerical modelling

Punching

# Contents

# Index of Figures

# Index of Tables

## ABBREVIATIONS AND ACRONYMS

$A3D_L$ numerical model of rectangular specimens with longer overlays

$A3D_S$ numerical model of rectangular specimens with shorter overlays

ACI American Concrete Institute

ANC a strengthened specimen with ANChored flexural reinforcement

AVG average pull-off stress

COV coefficient of variation

CSA Canadian Standardization Association

CSCT critical shear crack theory

DG diamond grinder

EC2 Eurocode 2

EXP refers to experimental results/parameters

FCM fixed crack model

FE finite element

FRC fibre reinforced concrete

FRP fibre reinforced polymer

ICD interface crack dilation

MS maximum strain

MTD mean texture depth

NUM refers to numerical results/parameters

RC reinforced concrete

RCM rotated crack model

RCO reinforced concrete overlay patch

REF a reference strengthened specimen (only roughened, without interface reinforcement)

$Ref_{3D}$ numerical reference specimen strengthened to 3*d*

$Ref_{4D}$ numerical reference specimen strengthened to 4*d*

$R_L$ rectangular specimens with shorter RCO patch

$R_S$ rectangular specimens with shorter RCO patch

$S_{3D}$ square specimens strengthened until 3*d* from the column face

$S_{4D}$ square specimens strengthened until 3*d* from the column face

SBETA numerical modelling material for concrete in ATENA® software

SCC self-compacting concrete

SD standard deviation

SG strain gauges

SMP steel moil point

SPM sand patch method

STANC a strengthened specimen with a combination of the STC and ANC detailings

STC a strengthened specimen with STeel Connectors (steel dowels) as interface reinforcement

SUB a specimen that comprises only the substratum layer

**UNITS**

cm centimetre(s)

$cm^2$ square centimetre(s)

GPa Giga Pascal

kN kilo Newton

kPa kilo Pascal

m meter(s)

$m^2$ square meter(s)

mm millimetre(s)

$mm^2$ square millimetre(s)

MPa Mega Pascal

Mpa/s Mega Pascal per second

mrad milliradian(s)

rad radian(s)

**CAPITAL ROMAN LETTERS**

$A_{dg}$ projected area of maximum aggregate on the interface

$A_{s,i}$ area of interface crossing reinforcement

$A_{s,o}$ area of longitudinal reinforcement for the overlay

$A_{s,s}$ area of longitudinal reinforcement for the substratum

$A_{sl}$ area of flexural shear reinforcement

$A_{spec}$ contact area of pull-off test specimen

$A_{sw}/s$ area of shear reinforcement

$B$ slab dimensions for punching

$C$ compression

Coh cohesion of a concrete-to-concrete interface

$E$ modulus of elasticity of concrete

$E_{cm}$ mean modulus of elasticity of concrete

$E_r$ modulus of elasticity of the strengthening layer's concrete

$E_s$ modulus of elasticity of reinforcement

$F_{anc}$ load at the anchored end of interface reinforcement

$F_S$ load at the substratum reinforcement

$F_{SO}$ load at the overlay reinforcement

$F_v$ shear load at reinforcement

$F_{0,max}$ shear load at reinforcement when $S_{max}$ is reached

$G$ shear modulus

$G_F$ fracture energy of concrete

$G_{F0}$ tabled value for the fracture energy of concrete

$G_{F,i}$ fracture energy of the interface

$G_{F,soft}$ softening fracture energy of the interface

$G_{F,wconc}$ fracture energy of the weakest concrete of a composite cross-section

I moment of inertia of the cross-section

$I_0$ moment of inertia of the uncracked cross-section

$I_1$ moment of inertia of the cracked cross-section

$K_{NN}$ interface normal stiffness

$K_{TT}$ interface tangential stiffness

$L_{RCO}$ size of the strengthening reinforced concrete overlay

$M_{cr}$ cracking moment of the cross-section

$P_{MS}$ load at midspan for the maximum strain of reinforcement

$P_{max}$ load at midspan for the maximum strain of reinforcement

$R_a$ average roughness of the surface profile

$R_{max}$ maximum peak-to-valley height

$R_p$ peak-to-mean roughness of the surface profile

$R_{p,inf}$ peak-to-mean roughness of the lower effective depth surface profile

$R_{p,sup}$ peak-to-mean roughness of the higher effective depth surface profile

$R_t$ total roughness of the surface profile

$R_{t,SPM}$ total roughness assessed through the sand patch method

$R_v$ maximum valley depth

$R_y$ total roughness height

$R_{z(DIN)}$ peak-to-valley height of the surface profile

$S_r$ reinforcement spacing

$S_{max}$ the slip when $F_{0,max}$ is reached

$T$ tension

V volume

$V_{exp}$ experimentally assessed punching capacity of the slab

$V_{F,max}$ maximum dowel action force

$V_{flex}$ flexural punching capacity of the slab

$V_{norm}$ normalised punching capacity of the slab

$V_{num}$ numerically assessed punching capacity of the slab

$V_R$ punching capacity of the slab

$V_{Rd,s}$ punching capacity of the slab with specific punching reinforcement

$V_S$ acting punching load of the slab

$V_{spec}$ specimens' punching capacity of the slab

**LOWER CASE ROMAN LETTERS**

b width of the specimen

$b_0$ punching control perimeter

$b_1$ punching basic control perimeter

$c$ cohesion (coefficient)

$c_a$ coefficient that accounts for adhesion of a rigid interface

$c_r$ coefficient that accounts for adhesion of a ductile interface

$d$ is the effective depth of reinforcement

$d_g$ aggregate size

$d_{g,o}$ aggregate size of the overlaid concrete

$d_{g,s}$ aggregate size of the substratum

$d_{g_0}$ tabled reference aggregate size

$d_{eq}$ equivalent effective depth

$d_{s,o}$ is the effective depth of the overlay reinforcement

$d_{s,s}$ is the effective depth of the substratum reinforcement

| | |
|---|---|
| e | eccentricity |
| $f_{b,c}$ | bond stress of the grout-concrete interface |
| $f_{b,s}$ | bond stress of the steel-grout interface |
| $f_{cd}$ | concrete design compressive strength |
| $f_{c,eq}$ | equivalent compressive strength of concrete |
| $f_{c,ol}$ | compressive strength of the overlay concrete |
| $f_{c,ref}$ | reference compressive strength of concrete |
| $f_{c,spec}$ | specimen compressive strength of concrete |
| $f_{c,sub}$ | compressive strength of the substratum concrete |
| $f_{ccm}$ | mean value of concrete compressive strength in cubic specimens |
| $f_{ck}$ | characteristic compressive strength of concrete |
| $f_{cm}$ | mean value of concrete compressive strength in cylinder specimens |
| $f_{cm,0}$ | scaling value for concrete compressive strength ($f_{cm,0}$=10MPa) |
| $f_{ct}$ | axial tensile strength of concrete |
| $f_{ct,sp}$ | tensile splitting strength of concrete |
| $f_{ctm}$ | mean value of axial tensile strength of concrete |
| $f_{t,i}$ | concrete tensile strength of specimen $i$ |
| $f_{ctk,0.05}$ | concrete characteristic tensile strength for the 5% percentile |
| $f_{syd}$ | design yielding stress of steel reinforcement |
| $f_y$ | yielding stress of steel |
| h | height of the cross-section |
| $h_r$ | thickness of the strengthening layer |
| $h_{RCO}$ | height of the overlaid concrete |
| $h_s$ | thickness of the substratum |
| $h_{sc}$ | height of the strengthened cross-section |
| $k$ | size effect factor; coefficient for flexural resistance at slip |

$k_{d_g}$ coefficient that accounts for the roughness of the critical shear crack

$k_1$ reduction factor of interface crossing reinforcement

$k_2$ interaction coefficient for flexural resistance of the rebar

$k_{-F}$ coefficient that accounts for shear of reinforcement crossing the interface

$k_e$ factor that accounts for eccentricity of loads

$k_y$ ratio between the maximum stress and yield stress of rebar

$k_\psi$ coefficient that accounts for the rotation of the slab

$l_{RCO}$ length of the overlaid concrete

$l_{anc}$ anchorage length of post installed reinforcement

$l_{anc,calc}$ calculated anchorage length of post installed reinforcement

$l_{anc,req}$ required anchorage length of post installed reinforcement

$l_{ch}$ concrete fractal parameter

$m_{Rd}$ resisting bending moment

$m_{Sd}$ acting bending moment

$p_i$ peak measurements of a surface profile

s relative slip

$s_{max}$ limit for relative slip

$r_0$ control perimeter that accounts for the angle of the critical shear crack

$r_c$ radius of the column

$r_q$ loaded radius of the slab

$r_s$ radius of the slab

$r_s$ radius of the slab

t thickness

$u_0$ column perimeter

$u_1$ basic control perimeter

$u$ control perimeter of the slab

v distance to the highest stressed fibre

w crack opening

$w_t$ waviness of the surface profile

$\overline{z}$ average of measured heights of the surface profile

$z_i$ measured height of a point on the surface profile

**GREEK LETTERS**

α angle of interface crossing reinforcement; tabled factor for dowel action of interface crossing reinforcement

$\beta_c$ tabled coefficient regarding the angle of the concrete strut

$\gamma_c$ minoring factor for concrete

$\Delta v_1$ horizontal relative displacement of direction 1

$\Delta v_2$ horizontal relative displacement of direction 2

$\Delta F_{SO}$ increment of load at the overlay reinforcement

$\Delta l$ infinitesimal concrete block

$\Delta u$ vertical relative displacement

ε coefficient that accounts for the eccentricity of the shear load

$\varepsilon_{sh}$ strain due to shrinkage of the strengthening layer

$\varepsilon_{s,o}$ strain of the overlay reinforcement

$\varepsilon_{s,s}$ strain of the substratum reinforcement

ζ coefficient that accounts for stress at the rebar

θ angle of the resulting force

$\lambda$ coefficient related to friction

μ coefficient of friction of a concrete-to-concrete interface

$\nu$ reduction factor for concrete strength

| | |
|---|---|
| $\xi$ | coefficient that accounts for concrete fractal parameters; size effect factor |
| $\rho$ | steel reinforcement ratio |
| $\rho_i$ | ratio of reinforcement crossing the interface |
| $\rho_o$ | ratio of reinforcement at the overlay |
| $\rho_s$ | ratio of reinforcement at the substratum |
| $\sigma$ | normal stress |
| $\sigma_c$ | concrete compressive stress |
| $\sigma_{eq}$ | equivalent stress |
| $\sigma_N$ | interface normal stresses |
| $\sigma_{pull\text{-}off}$ | specimen pull-off strength of the interface |
| $\sigma_s$ | steel stress |
| $\sigma_u$ | rebar maximum stress |
| $\sigma_y$ | rebar yield stress |
| $\sigma_{y,med}$ | average rebar yield stress |
| $\tau$ | shear stress |
| $\tau_0$ | maximum shear stress (for $\sigma_c$) in the Mohr-Coulomb failure criterion |
| $\tau_{anc}$ | shear capacity of the bonding agent |
| $\tau_c$ | shear capacity by adhesion of the concrete-to-concrete interface |
| $\tau_R$ | shear strength of the interface |
| $\tau_{xz}$ | interface tangential stresses on the xx direction |
| $\tau_{yz}$ | interface tangential stresses on the yy direction |
| $\upsilon$ | Poisson coefficient |
| $\phi$ | angle of friction |
| $\psi$ | slab rotation |
| $\psi_{res}$ | residual rotation of the slab after unloading |
| $\omega$ | width of the critical shear crack |

**OTHER SYMBOLS**

$0d$ zero times the effective depth of reinforcement (column face)

$2d$ two times the effective depth of reinforcement

$3d$ three times the effective depth of reinforcement (size of $S_{3D}$ specimens' RCO)

$4d$ four times the effective depth of reinforcement (size of $S_{4D}$ specimens' RCO)

Ø diameter

$Ø_b$ diameter of bored hole

$Ø_s$ nominal diameter of reinforcement

# 1. INTRODUCTION

## 1.1. Background

With concrete being one of the main materials in construction of the twentieth century, the need for structural strengthening or retrofitting of existing structures leads to the development of solutions that aim to improve the stiffness or strength of existing structures. Research and development of composite materials and the environmental impact when compared to basic materials (steel and concrete), led to strengthening solutions that make use of such materials. The biggest requirements when using composite materials are the skill and logistics needed for applying on site, since they require fixing to the existing structure and fully depend on proper bonding to the existing structure. Such requirements make traditional materials more widely applicable on practical situations due to the broad knowledge acquired over the years on new and existing structures. Other than economic reasons, the state of the existing structure also weighs on the choice for strengthening. By allowing the removal of degraded concrete, jacketing or overlaying concrete covers more aspects of a structural intervention by using a duality of purpose when strengthening existing structures.

Strengthening techniques for flat slabs have existed ever since this structural system was applied. Depending on the scope of the strengthening solution adopted, it may vary from the simplest enlargement of the column that supports the slab to the more elaborate solutions that require composite materials. Cracking is usually related to tensile stress phenomena and spalling due to compressive stresses. Flexural stresses combine both the aforementioned stress fields and require that the strengthening techniques become more elaborate to account for both. Shear is then the flow of stresses crossing the element, with shear failure being an undesired mechanism of structural collapse due to its brittle nature.

The state of cracking and deformation are the main aspects that affect shrinkage of the newly added RC layer, which may lead to poor bonding of such layer and the inefficiency of strengthening. To minimize such effects, the existing structure should be relieved of existing loads by a supporting system that directly transfers such loads to the foundations and allows for a residual resilience of the existing structure. When all conditions have been ensured, surface preparation, placing of formwork and reinforcement can be performed for subsequent casting of the new RC layer.

## 1.2. Scope of the thesis

The broad use of flat slabs as a structural solution led to the development of structural strengthening solutions when required. The characteristic slenderness of flat slabs leads to greater spans, which results in greater flexural stresses. These stresses can occur in the vicinity of the column supports, where shear and negative bending moments are greater. Flexural failure is often preceded by wide cracking and large deformations, which can be controlled beforehand. Punching failure, although a local phenomenon, can cause a major structural failure due to the progressive collapse of the structure. One advantage of strengthening flat slabs with a Reinforced Concrete

Overlay is the application on top face of the existing structure, with minimal or even without formwork, as illustrated in the figure below. The reduced thickness of the new layer (Figure 1.1, *a*), allows for easy levelling with new flooring, or if the existing rebar and respective clear cover allow for the new layer to be cast within the original slab thickness (Figure 1.1, *b*), thus resulting in an unobtrusive strengthening solution.

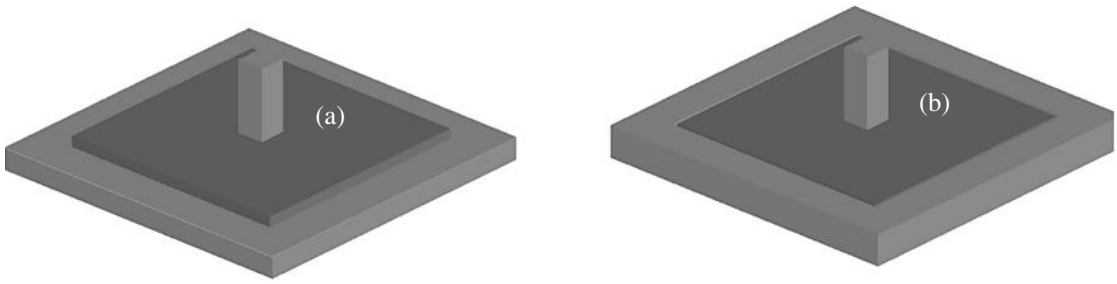


Figure 1.1 – RCO strengthening technique: a) Protruding from the existing slab (removal of concrete cover only); b) Embedded in the existing slab due to large concrete cover.

To guarantee the anchoring of added reinforcement, dimensions of the new layer in the column region must accommodate for the required anchorage length that envelops both the negative bending moment diagram and the punching of the slab. Anchoring the flexural reinforcement by embedding the added reinforcement at the edges of the RCO accounts for a stitching solution that further improves the performance of the strengthening system (Figure 1.2, a). Another solution for stitching the two layers is placing shear connectors distributed at the interface, arranged so that the interface shear and tensile stresses are increased (Figure 1.2, b and c).

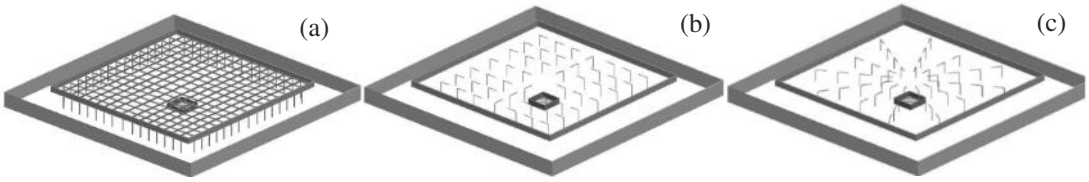


Figure 1.2 – Detailing of reinforcement crossing the interface between concrete layers.

A practical application of strengthening with an RCO in which specific punching reinforcement doubled as stitching of the new layer was performed on a building in Lisbon. Cracking denoted deformability issues of the flat slab, which resulted in radial and tangential cracking around the columns as observed in Figure 1.3. The adopted strengthening solution with an RCO comprised the punching strengthening solution with post-installed shear reinforcement, which doubled as stitching reinforcement. This further improves the monolithic behaviour of the resulting composite cross-section. The RCO after finish doubled its purpose by also concealing the shear reinforcement on top of the slab where functionality is important.

Figure 1.3 – Structural strengthening of the -1 and -2 floors of the Visconde de Alvalade building, Lisbon; Project by Versor - Consultas Estudos e Projetos, Lda; Contractor: HTecnic – Construções, Lda. (Photos by Versor, Lda.)

A better understanding on how the interface between two concrete layers behaves when applied on the tensile face of the slab is needed for proper design. Due to the flexural nature of this strengthening solution, testing of reinforced concrete specimens strengthened with new RC overlaid on the tensile face can assist the characterisation of the interface and the degree of monolithic behaviour. A composite cross-section behaving as monolithic is the main objective when improving structural interfaces. Such interaction depends on the stress transfer capacity of the interface, which in turn depends on the strength and stiffness of each layer. Layers with different flexural stiffnesses are responsible for the differential deformation and the consequent relative displacements that arise. Such displacements are the cause for debonding and should be controlled through either one of the aforementioned techniques or a combination of stitching reinforcement. Since punching is a failure mechanism of brittle nature, with small deformations prior to failure, flexural tests assist on analysing the structural response to relative displacements of the interface.

## 1.3. General structure of the thesis

This dissertation is organized in six chapters and two appendixes A and B, comprising an introduction and a conclusion, state of the art about the characterisation of concrete-to-concrete

interfaces, experimental program comprising flexural and punching tests, test results and discussion, with the proposal of design and assessment of interface strength parameters.

Chapter two is an overview on the strengthening of flat slabs, the behaviour of concrete-to-concrete interfaces and the behaviour of flat slabs as structural solution. The overview on the strengthening of flat slabs comprised the techniques that are stated in the literature and design codes, stating the impact that each technique has on the behaviour of the strengthened slab. The aesthetic and economic impact each technique has on the existing structure are defining characteristics when opting for either solution. The behaviour of concrete-to-concrete interfaces is also broadly addressed in this chapter, considering the existing surface conditions, which affect how the new RC layer will bond to the existing structure. Roughening of the existing surface is a nuclear task when applying new concrete to an existing structure due to the shear friction mechanism that characterises the interaction of concrete-to-concrete interfaces and is widely accepted in the literature. Both the process of roughening and the characterisation of the resulting surface are addressed in this chapter, considering destructive and non-destructive methods for the assessment of the interface capacity for transferring stresses. The analytical models that were developed over the years regarding the interface between concrete cast at different times are the basis for the design codes. Due to the nonlinearity of the debonding phenomenon, the numerical modelling of such interfaces stands as key for the correct numerical characterisation of non-monolithic cross-sections.

Chapters three and four present the experimental campaign that was carried out through flexural tests on rectangular one-way specimens and punching tests on square two-way specimens. The same order of slab thickness, reinforcement, and general span dimensions were adopted to relate the specimens. The surface preparation of the substratum was performed similarly on all tests, allowing for the direct comparison of results. Detailing of reinforcement crossing the interface was also similar on both geometries, allowing for the comparison of anchor loads when more or less relative deformation is present at the interface. The surface preparation was assessed through the measurement of its roughness parameters and tensile strength. The numerical simulation of the test results is also presented in both chapters, for both geometries, with good accordance to experimental results. The numerical characterisation of the interface is presented through a model in which the results were similar to measurements performed during testing for the relative displacements of the interface.

Chapter five is the application of knowledge gathered in previous chapters, with the aim of proposing an interface analysis of its capacity for transferring stresses in a flexural strengthening situation with RCO. The tensile characterisation through pull-off tests is addressed statistically in this chapter. The stress-state at the interface during the load history is also addressed in this chapter, with the characterisation of the shear stress transferred between layers and the monolithic degree attained. The application of an RCO strengthening solution to a design situation is not without the recommendations stated in this chapter. The nuclear parameters of geometry, reinforcement, surface preparation and material properties are discussed in order to more effectively impact the behaviour of the strengthened cross-section. Accounting for the parameters proposed in this chapter should result in a properly designed RCO strengthening solution.

Appendixes A and B present the deformations of rectangular one-way specimens and square two-way specimens over the load history, and roughness profiles of existing surface after preparation.

# 2. STATE OF THE ART

## 2.1. Anomalies on flat slabs

The inherent advantages of opting for a flat slab structure is a flat soffit – slender structures, allowing for irregular column layouts, less formwork and simpler reinforcement detailing, and consequent speed of construction – led to the broad use of this structural solution. Ever since the flat slab structural system was proven advantageous over traditional beam supported slabs, the need for strengthening such structures arose due to:

- Errors in the design phase, such as reduced thickness of the slab for the given span, insufficient flexural reinforcement, insufficient anchoring of such reinforcement or the lack of punching reinforcement;

- Errors in construction, from which can result the wrong thickness of the slab or the wrong placing of flexural reinforcement, from which can result the excessive clear cover and consequently insufficient effective depth of reinforcement;

- Changes in the original function of structures that lead to higher loads or the execution of openings in the slab close to the column supports.

The slender nature of a flat slab makes it sensitive to errors in the construction phase since its strength relies on the correct positioning of reinforcement and the resulting effective depth. When the latter is smaller than defined by design, the service limit state of the structure is compromised and may result in excessive deformation and cracking of concrete. The structure's ultimate limit state is also compromised, thus resulting in lower flexural and shear strengths. An example is shown in Figure 2.1 for the building "Visconde de Alvalade" in Lisbon, Portugal, where misplacing of flexural reinforcement close to the center of the slab resulted in visible cracks that were specific radial cracks of the punching failure mechanism. This can be an error in the design phase when an insufficient effective depth is preconised, or a mistake in the construction phase by using wrong spacer dimensions.

Figure 2.1 – Punching cracks on the column region of the -1 floor of the Visconde de Alvalade building, Lisbon; Project by Versor - Consultas Estudos e Projetos, Lda.; Contractor: HTecnic – Construções, Lda. (Photos by Versor, Lda.).

An inspection revealed that the concrete cover of the top reinforcement was 95 mm, instead of the 25 mm that were specified in the design of the 250 mm thick slab. This results in 40 % loss of flexural strength for negative moments and 60 % loss of punching strength. Another example of exploring the slenderness of flat slabs beyond their capabilities is a building in Oeiras, Portugal, illustrated in Figure 2.2. This can be an error in the design phase or a consequence of using lower class concrete or steel reinforcement. The large spans and columns with small cross-sections halted construction of such building until strengthening. The effort of strengthening was then divided into the enlargement of the supporting columns, stiffening of the column-slab support through column heads below the slab and overlaid reinforced concrete on top of the slab, altogether with radial punching reinforcement. The latter only contributes to the strength of the column-slab connection without effecting its stiffness.


Figure 2.2 – Strengthening due to excessive spans and insufficient cross-section on supporting columns in a building located in Oeiras, Lisbon; Project by Versor - Consultas Estudos e Projetos, Lda.; (Photos by Versor, Lda.).

Bibliographic case-studies of flat slab building failures can show the adverse result of the aforementioned errors or changes of the original function of structures:

- The Harbour Clay condominium in Florida, USA, which collapsed during construction. The lack of verification for punching strength in the design phase, the thickness of the slab of around 20 cm instead of the 28 cm preconised by design, and consequent placing of reinforcement with an effective depth of 135 mm instead of the 160 mm preconised by design, resulted in the progressive collapse of the entire structure;

Figure 2.3 – Harbour Clay condominium collapse in Florida, USA [1].

- Another well-known collapse of a flat slab building is the Sampoong Department Store in Seoul, South Korea, where the change of function of the top floor, along with the extra load and reduced cross-section of the supporting columns, resulted in the collapse of the top floor and progressive collapse of the structure.

Figure 2.4 – Sampoong department store collapse, Seoul, South Korea [2].

The aforementioned collapses of flat slabs are critical examples of errors in the construction phase or change of the structure's original function.

## 2.2. Strengthening of flat slab structures

### 2.2.1. Strengthening techniques for flat slabs

Strengthening techniques for flat slabs in the column region, depending on the scope of the strengthening solution adopted, may vary from the simplest enlargement of the column that supports the slab to more elaborate solutions that require composite materials. Usually cracking is related to tensile stress phenomena and spalling with compressive stresses. Flexural stresses combine both the aforementioned stress fields and require that the strengthening techniques become more elaborate to account for both. Shear is then the flow of stresses crossing the element, with shear failure being an undesired mechanism of structural collapse due to its brittle nature. An explanation of how strengthening affects the behaviour of a column-slab connection is presented by Koppitz [3], adapted from SIA code D-0226 [4], as shown in Figure 2.5. One should notice that structural unloading is a requisite prior to strengthening as stated on such document and depicted in the figures below by the residual rotation $\psi_{res}$ observed on all load-rotation graphs. By unloading a previously loaded structure, the reloading curve must account for the residual rotation that results from existing cracks unable to fully close.

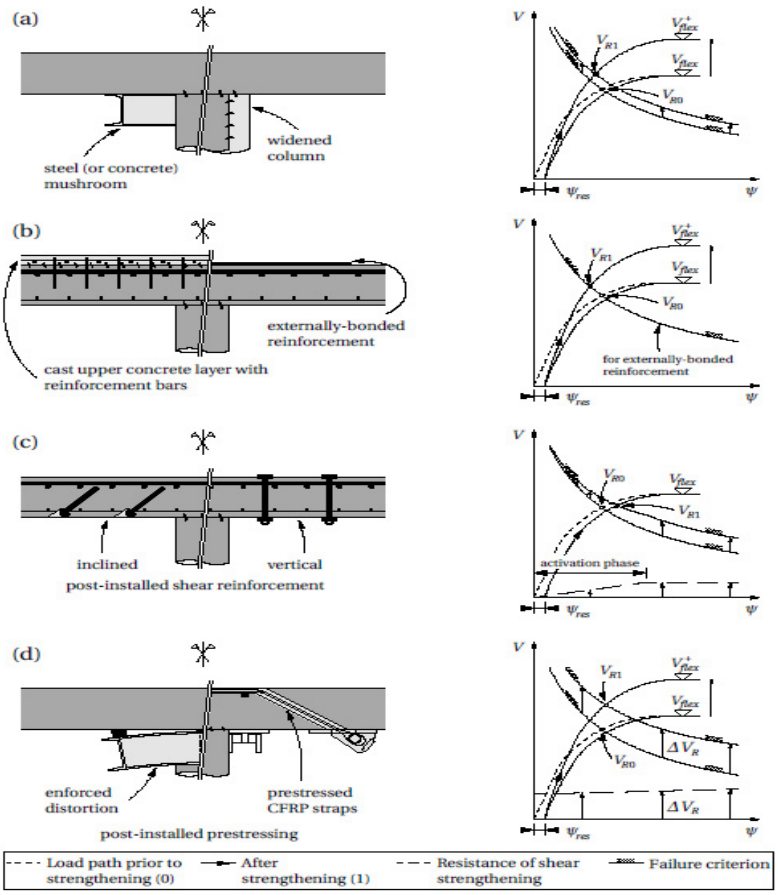


Figure 2.5 –Methods for punching strengthening on flat slabs: (a) a steel capital on top of the column, (b) flexural reinforcement on the tensile face, (c) post-installed shear reinforcement, and (d) post-installed pre-stressing (extracted from [3]).

The effects that each strengthening solution has on the column-slab connection is also depicted in the figure above:

(a) Increasing the area of the support, the failure criterion can be altered along with the control perimeter, and a higher failure load is attained. In [5] the strengthening of the column-slab connection with steel beams as column heads was analysed with good results considering the added steel beams worked monolithically with the existing structure;

(b) Flexural strengthening on the tensile face only impacts the failure criterion if the effective depth is changed, which happens with a new RC layer cast on top. The stiffening of the load curve ensures a higher failure load is attained. Strengthening the column-slab connection on the tensile face with fibre reinforced polymers was analysed in [6], attesting the performance of the strengthening solution depends on redistribution of bending moments in the flat slab and the load level at which strengthening is performed;

(c) Post-installed shear reinforcement does not impact the stiffness of the slab and therefore the loading curve is not affected, with such elements altering the stiffness of the loading curve and consequent direction of the critical shear crack, allowing for a higher failure load to be attained. In [7] the strengthening of the column-slab connection with post-installed transverse reinforcement is analysed considering the prestressing of such reinforcement, attesting the dependency of the punching strength to the force installed by prestressing;

(d) Post-installed prestressing can drastically alter the column-slab connection behaviour, since it induces a stress state contrary to loading, directly affecting the behaviour of the column-slab connection or introducing a negative rotation to the slab. In [8] the post-tensioning with anchorages embedded in the slab by bond was analysed and compared to design codes. The authors state a 50% increase in punching load capacity when compared to non-strengthened slabs, and a significant reduction in tensile strains of the flexural reinforcement in service.

The technique of enlarging the support is then validated due to the direct relationship with the punching reference perimeter. Such technique dates back to classical Greece where the shaft of columns was enlarged on the top and bottom, as so to reduce the punching phenomenon on the ends of a compressed structural element. Such principle is implemented on all behaviour models with the dimensions of the supporting column determining the control perimeter. The increase of the columns support area in a punching situation is noticeable in the Hassanzadeh and Sundquist's work [9], where the enlargement of the support yielded the largest increase in strength as illustrated below. Such modifications also affect the flexural behaviour of the slab, increasing $V_{flex}$, but also increasing the overall stiffness of the slab, as shown below through smaller rotations. This is also valid when considering the Critical Shear Crack Theory [10], in which increasing the column dimensions also causes the slab rotation to decrease.

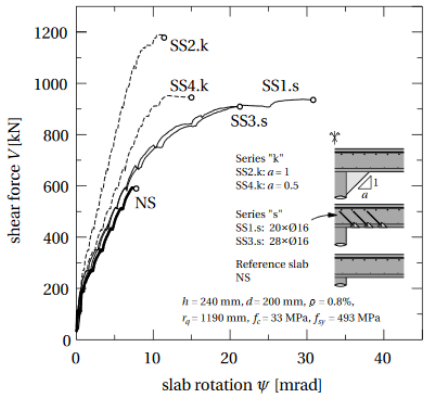


Figure 2.6 – Tests from [9] where the series "k" are the column enlarged specimens and present the largest increase in strength when compared to the reference slab "NS" (series "s" are strengthened with inclined post-installed shear reinforcement).

One way of directly controlling the punching phenomenon is by adding reinforcement crossing this critical zone of the shear crack, opposing the radial stresses and allowing for higher loads. This strengthening technique has been studied since 1974 by Ghali *et al.* [11], where the advantage of vertically prestressing the slab's cross-section has been explored with the purpose

of limiting the critical shear crack opening. Further improvement of the technique was performed by Ramos *et al*. [7], alongside repairing techniques for post-failure strengthening of the column-slab connection. This is an active measure for limiting the evolution of such crack, while specific punching shear reinforcement is a passive method of strengthening flat slabs. Such method has been extensively studied since the seventies, with the works by Hawkins being widely referenced, where different types of shear reinforcement like steel headed studs, bent-up bars, and stirrups were presented [12].

Flexural strengthening as a way of controlling slab rotation can be achieved by adding longitudinal reinforcement, or high tensile strength materials in the form of bars or laminates. Fibre-reinforced polymer strips or steel plates can be glued to regular and sound surfaces for controlling strain on the tensile region of the cross-section. Such technique was explored by Faria *et al*. [6], as shown below characterised by the failure criterion of the CSCT. One important aspect is the reduction of slab deformability, which also leads to brittle structures and is not desirable for flat slabs due to the progressive collapse mechanisms.

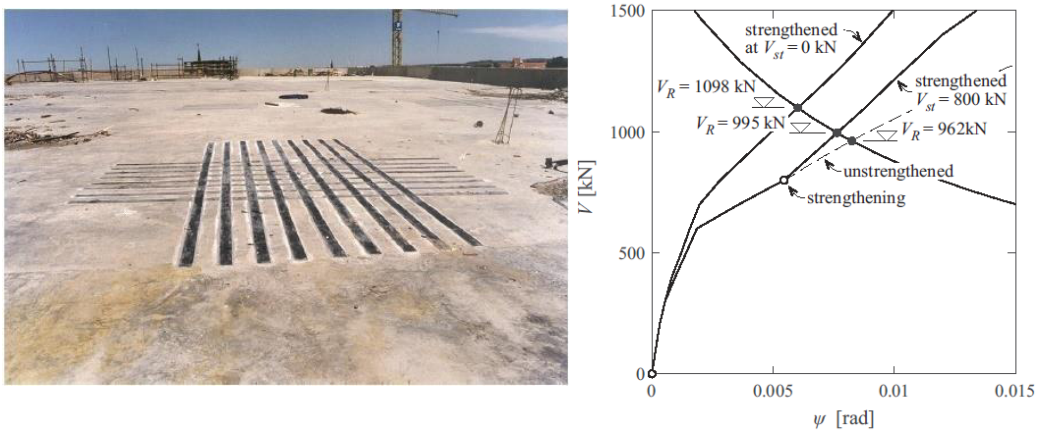


Figure 2.7 – FRP strengthening in a punching situation and respective change in behaviour of the strengthened slab (extracted from [6])

Strengthening of slabs poses several challenges regarding the differential deformation of concrete layers due to slenderness, and consequently higher flexural deformation of such elements. Datta and Seraj [13] performed a series of tests on overlay strengthened slab specimens, with the overlay on the compressed face of the slab. The specimens were relatively thin for current slabs, which contributes to its slenderness and flexural behaviour. The authors also compared the experimental results to design codes like the ACI 318-95 [14] and the MC 1978 [15], namely the strength increase estimated by the former, where a 40% increase in effective depth should result in 58% increase in punching capacity. The use of dowel bars as shear connectors also proved to be efficient for punching of flat slabs due to the higher degree of monolithic behaviour attained.

An example of real application of a bonded reinforced concrete overlay was analysed by Casal [16], where an existing structure was modelled as it was strengthened with a new reinforced concrete layer. Such technique was applied to the top of flat slabs in the column-slab connection area where the punching shear mechanism occurs, as depicted in Figure 2.8.

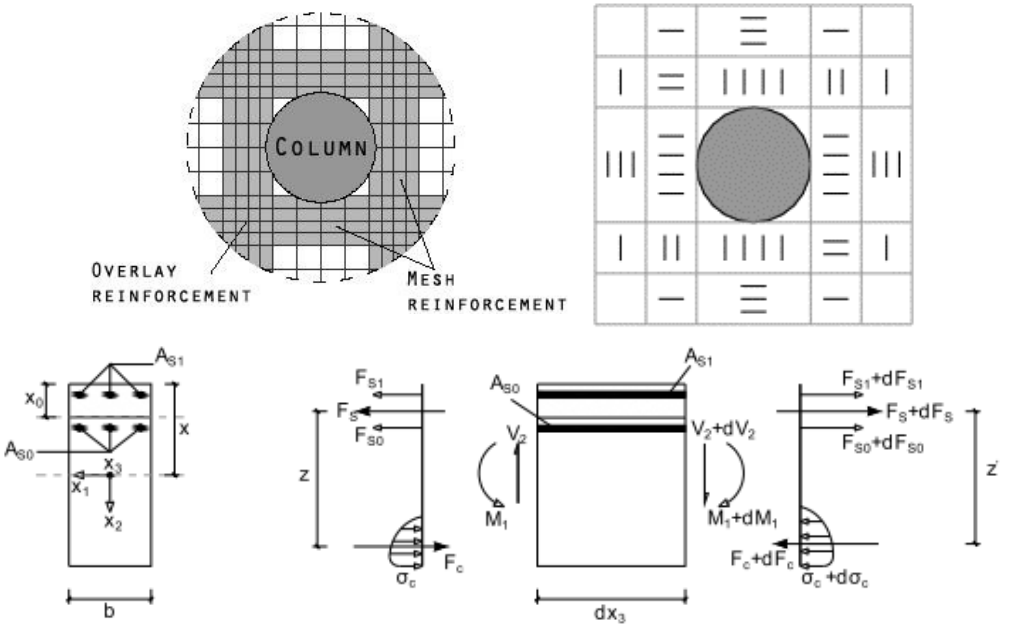


Figure 2.8 – Overlay strengthening in a punching situation on RC slab elements (adapted from [16])

Regarding the work of Casal [16] about the practical application of RC overlays, which consisted on the analysis of stresses in a column-slab connection and design of the concrete-to-concrete interface for such stresses, several conclusions were drawn. The author states that the ratio of reinforcement crossing the interface is able to govern its strength, and that reducing the diameter of such reinforcement can be balanced with more reinforcement. The weakest concrete strength is also relevant to the shear-friction mechanism and existing cracks can also significantly affect the interface behaviour.

### 2.2.2. Techniques for the flexural strengthening of slabs

Jacketing of beams and columns is the technique that mostly uses the interface between concrete cast at different times. Strengthening structural elements with a new RC layer can change the failure mechanism from flexural to shear due to the increased reinforcement ratio. Zhang *et al.* [17] addressed the problem of shear on the strengthening with overlaid concrete on the tensile face of RC beams. By analysing the crack pattern at failure, the authors devised a concrete tooth model that allows for determining the tensile stress of concrete that causes debonding. Such model is shown in Figure 2.9, where the tensile strength of concrete $\sigma_A$ is calculated considering the bending moment and its moment of inertia, $M_A$ and $I_A$, in the section of a $b$ wide shear tooth limited by crack spacing $S_{cr}$.

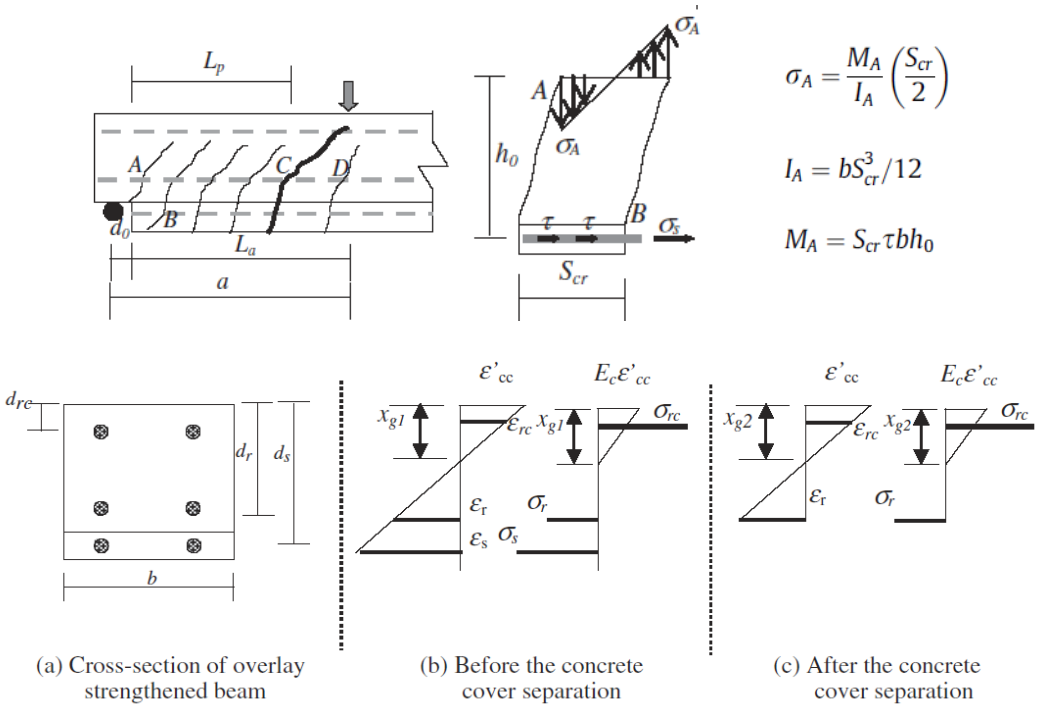


Figure 2.9 – Concrete tooth model according to Zhang *et al.* (extracted from [17])

The term $h_0$ accounts for the distance between the substratum reinforcement furthest from the strengthening layer and the centroid of tensile strengthening, being FRP or reinforcement in overlaid concrete. The authors assume a monolithic behaviour of the composite cross-section until debonding. They also define the stage when tensile stresses at the interface cause debonding of the overlaid concrete as when vertical stress $\sigma_A$ equals the concrete tensile strength $f_t$. Such premise states the weakest concrete as governing the interface capacity. Thus by rearranging the equations in Figure 2.9 results the horizontal stress $\tau_d$ from the equilibrium of the cross-section:

$$\tau_d = \frac{\sigma_A S_{cr}}{6.\,h_0} = \frac{f_t S_{cr}}{6.\,h_0} \tag{2.1}$$

Rodrigues Vaz *et al.* [18] analysed the feasibility of applying partial jacketing to a reinforced concrete beam on the tensile face, considering fatigue loading. The authors concluded that beam elements strengthened with such technique on the tensile face result in good behaviour of the strengthened structure, allowing also for less conservative considerations than current codes at the time like the MC 90 [19]. The work developed by Rocha [20] is an example in Portugal that contributes to the topic by exploring the use of reinforced concrete overlays on the tensile face of structural elements. The main difference from the latter is the exploring of the behaviour of RC beams with a finite length RC layer, where a performance increase was attained although the preferential failure mode was resumed to shear. This, in turn, validated the concrete overlay strengthening since the flexural reinforcement of the substratum was interrupted at midspan, as shown in Figure 2.10. This way, flexural strength depends on the stress transferring capacity of the interface.

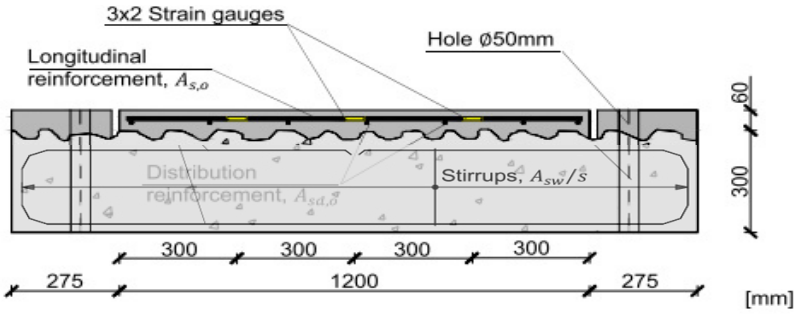


Figure 2.10 – Overlay strengthening in a shear situation on RC beam elements (adapted from [20])

The impact of detailing the reinforcement crossing the interface was analysed and significant performance gains were obtained when shear connectors or dowels were distributed over the interface. The authors also analysed the detailing of longitudinal reinforcement anchored at the ends of the strengthening layer on the existing structure. The preparation of the existing surface was also performed and was a requisite for activating shear and tensile strength of such reinforcement, which is attained through a rough finish. Such surface preparation allows for separation at the interface when relative sliding occurs, which activates the tensile capacity of reinforcement crossing the interface. The author states performance gains of 39% and 79% for failure load of strengthened specimens, respectively for dowels distributed over the interface and flexural reinforcement anchored at the ends of the strengthening layer. In terms of shear stress at the interface, the former yielded a stress of 1.40MPa and the latter a stress of 2.0MPa. Such values were calculated considering the average strains measured at the overlaid concrete reinforcement. One should notice that the performance gains were assessed considering the specimens strengthened with a new overlaid RC layer and no reinforcement crossing the interface. The gains over an unstrengthened structure could then be of greater magnitude.

## 2.3. Concrete-to-concrete interfaces

### 2.3.1. Characteristics of concrete-to-concrete interfaces

The performance of bonded concrete overlay applied on the tensile face of concrete elements relies on the quality of the bond between the two concrete layers, therefore changing with surface preparation, and with steel connectors crossing the interface if provided. If no connectors exist, adhesion is the only component at the interface, and brittle failure shall occur with increasing load and deformation. Such condition relies strongly on roughness, which allows for interlocking of the two layers and consequently bonding stresses to develop at the interface. With steel connectors crossing the interface between the two concrete layers, three components of the resisting mechanism illustrated in Figure 2.11 shall develop [21]:

1. Adhesion – due to chemical bond between the two layers, and mechanical interlocking if a macroscopic surface roughness is present – it shall be considered for slips up to 0.5 mm [22];

2. Friction – it is a direct consequence of external loads perpendicular to the interface, or due to steel connectors crossing the interface that are mobilized in tension for higher relative displacements, usually larger than 0.5 mm [22], with equilibrium guaranteed by compressive forces at the interface;

3. Dowel action – larger relative slips induced by bending, result in shear and bending of the steel connectors crossing the interface. The dowel action maximum value depends on the resistance of the steel connector (flexural + tension + shear) and the crushing of the surrounding concrete [23].

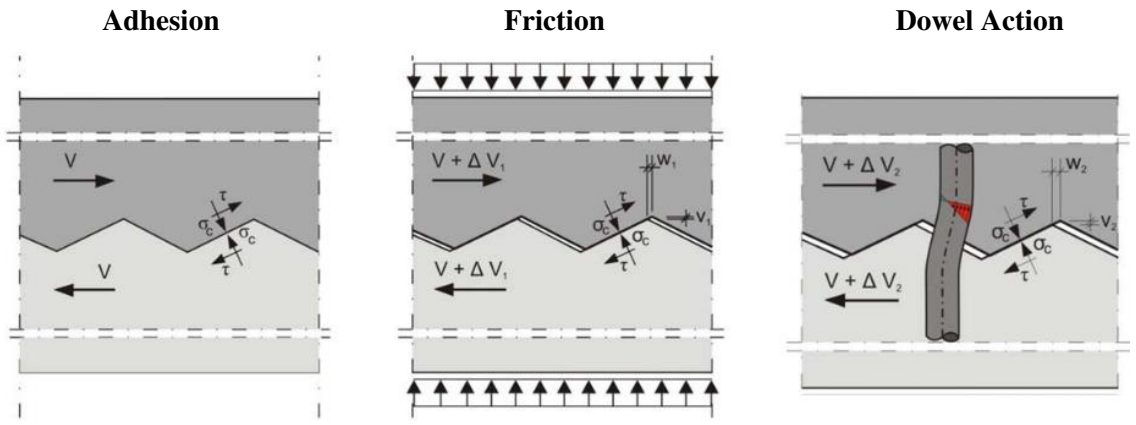


Figure 2.11 - Resisting mechanism for concrete-to-concrete interfaces with steel connectors (adapted from [24]).

The behaviour and strength of the interface depend on the following parameters:

- *Preparation of the interface* – Such parameter is the key for a higher degree of monolithic behaviour for the composite cross-section, since it will account for interlocking of the two layers and the development of the shear-friction mechanism. Macro-roughness of the interface will account for the interlocking of aggregates embedded in the cement matrix and micro-roughness will account for the cohesion of the interface. The last occurs due to the opening of the pores allowing for the cement paste of freshly poured concrete to bond with the existing surface, and thus a micro-interlocking effect along with chemical adhesion will develop. An intentionally roughened surface will also result in controlling of shrinkage of freshly poured concrete, helping to prevent the formation of an interface crack that could cause the loss of strength on concrete-to-concrete interfaces [25]. An important factor is also the method used for preparing the interface, which can negatively influence the interface behaviour due to the presence of microcracking and spalling of concrete [26].

- *Specific reinforcement crossing the interface* – It is recommended to use reinforcement crossing the interface, since structural integrity is compromised upon loss of bond. Reinforcement crossing the interface limits the interfacial crack dilation and relative slip of the two layers by dowel action and increases the friction forces at the interface. The required shear deformation to mobilize dowel action implies that a larger relative slip is attained, thus compromising the latter function of limiting relative deformations of the interface [27]. Therefore, the clamping effect of such reinforcement contributes to the resisting mechanism more than dowel action. Mattock and Hawkins [28] refer to this type of reinforcement as capable of restoring the interface strength after cracking due to the loss of the adhesion component.

- *Compressive and tensile strength of both concrete layers* – Compressive strength of concrete is also relevant mainly to the friction and interlocking mechanisms of the interface. The presence of reinforcement or external forces allow for higher compressive strains, optimizing contact upon sliding of the two concrete layers. Mattock and Hawkins [28] present early references to the contribution of concrete compressive strength. Tensile strength was later introduced to the shear friction mechanism, with references of its contribution to the cohesion strength of the interface by Randl [29] and by Santos [30]. The latter work relates tensile strength of concrete to a brittle failure scenario of the interface, not accounting for specific reinforcement.

- *Aggregate type, shape and size* – Aggregate type is also relevant to the strength of the interface since its compressive strength is higher than the cement matrix for normal weight aggregates. This makes such aggregate a strong link in the shear friction mechanism. A reference is made to the shape of the aggregate by Hoff [31] where angular aggregates provided higher strength after loss of adhesion than round aggregates. Aggregate size is also of the utmost importance to the shear friction mechanism since protruding aggregates of the existing surface allow for a higher degree of interlocking between that and newly cast concrete.

- *Confining forces* – Forces acting on the interface can be active or passive, depending on whether the source is an external force or the consequence of interface equilibrium due to compressive stresses resulting from activating the tensile stress of reinforcement. The presence of reinforcement properly anchored crossing the interface allows for the activation of compressive stresses and its contribution should be accounted for in the shear friction mechanism. One should note that these types of confining forces can act simultaneously on the interface and should be added.

### 2.3.2. Methods for intentionally roughening the surface

According to [32] and [33], the preparation of the substratum surface is fundamental for proper concrete repair and strengthening procedures. An interface between concrete layers should then be prepared for casting the new layer. Several methods and techniques that increase roughness and remove the laitance layer are possible, with caution due to the possible microcracking of the substratum, depending on whether heavy techniques are opted for.

Surface preparation plays a major role on the interface behaviour by increasing the interlocking of contacting layers, which causes the interface crack to open when relative slip occurs [34]. Surface preparation can be performed through several methods, from jackhammering the concrete cover, recognized as the most aggressive surface preparation method concerning the microcracking of concrete, to water jetting, the least aggressive and more efficient method for the selective removal of concrete, both in terms of depth and resulting roughness ([35], [36], [37], [38]). Roughening the existing surface is recommended and should be prescribed when designing concrete-to-concrete interfaces [32,33]. A rough surface increases the degree of monolithic behaviour by transferring stresses through the interlocking of contacting layers, thus controlling the differential creep and shrinkage of freshly poured concrete [36,39–41]. Achieving such surface characteristics is accomplished through scarification of the concrete surface, where the concrete cover is removed to a predetermined depth. Such depth depends on whether unsound concrete is present, or the depth preconised by the design of the new layer, usually limited by the cover of reinforcement.

Removal of the laitance layer and small aggregates with wire brushes, milling, needle scaling, bush hammering or sandblasting, are possible surface preparations for concrete surfaces, although not recommended for concrete-to-concrete interfaces with primary structural function [32,42]. Although sandblasting can be accounted for as a valid rough surface preparation method, it comes at a cost due to material consumption and resulting grit waste. Figure 2.12 shows two possible finished surfaces after sandblasting, lightly and heavy sandblasted.

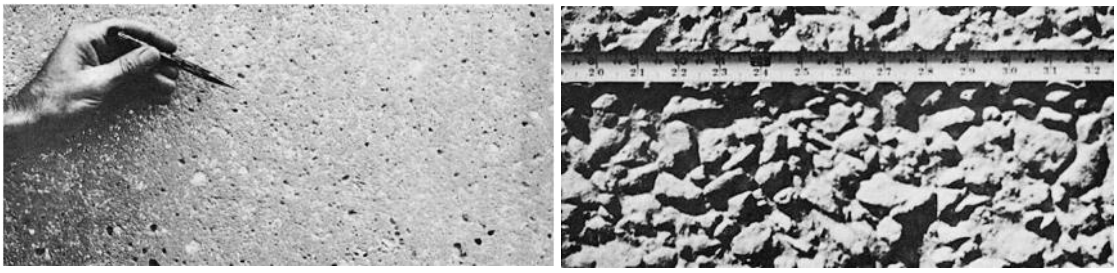

Figure 2.12 – Light (left) and heavy (right) sandblasted concrete surface (extracted from [43])

Julio *et al*. [44] assessed the performance of sandblasted surfaces in concrete-to-concrete interfaces and concluded that such method allowed for higher bond strength in shear and in tension, when compared to partially chipping the surface or wire brushing the laitance layer. Silfwerbrand also stated in [36] that bond strength between two concrete layers was the highest when sandblasting was the chosen method for surface preparation. A reference is made in [45] for the polishing effect of the sand-blasting technique that should be accounted for when a roughest contact surface is intended. Carter [46] stated sandblasting as a great method to remove spalled concrete and loose aggregates after performing a heavy surface preparation like jackhammering. The latter technique is one of the most aggressive for surface preparation, since it can induce microcracking of concrete, vibrations on the reinforcement that further damage bond to concrete, and damage to the reinforcement causing the loss of cross-section as shown in Figure 2.13 [47].

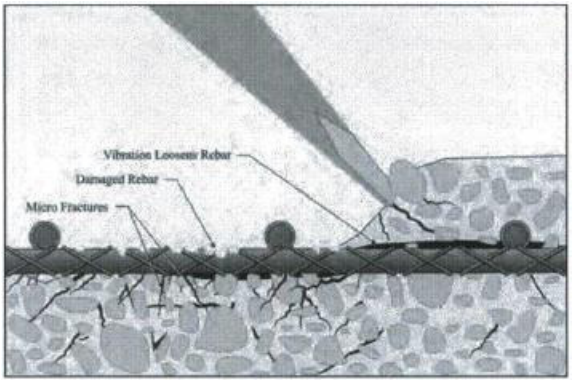


Figure 2.13 – Damage from jackhammering the existing concrete (extracted from [47])

The economic advantage of being the cheapest rough surface preparation when accounting for the cost and logistics, disposal of the generated waste and the level of specialization for performing such technique makes jackhammering the existing surface a valid choice for surface preparation. On the other end of the economic spectrum, we have high pressure water jetting, which is the most effective preparation of concrete surfaces. It works by removing the cement matrix and exposing aggregates with minimal vibration and no microcracking of the substratum. Such method is also the most expensive due to the required equipment, specialized labour and the generated waste. It works similarly to sandblasting but is more efficient and the generated waste consists of mud from eroded cement particles. A nozzle works closely to the surface and erodes the substratum as shown in Figure 2.14, where the angle of the water cone allows for reaching higher depths and cross the longitudinal reinforcement if required.

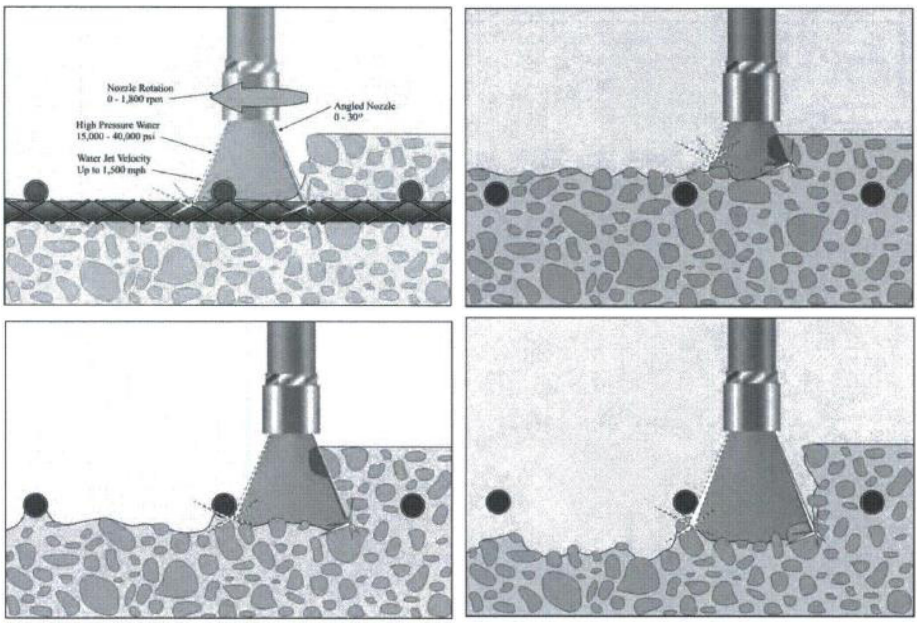


Figure 2.14 – Application of high pressure water jetting to existing concrete surface (extracted from [47])

Between the two more used methods of jackhammering or water jetting, the economic factor is what most separates the two, despite the known advantages of both:

- *Jackhammering the existing surface* – requires the least specialized operator and more economic tools to perform the surface preparation. It consists of electric or pneumatic hammers with a steel moil point or equivalent, attacking the existing surface at an angle that promotes the spalling of concrete and thus achieving the intended roughness. According to [48], each blow of the hammer can apply enough energy to result in microcracking of unspalled concrete. The resulting microcracks can lower the interface capacity since new concrete will be bonded to already spalled concrete. This technique is then limited to structures where concrete quality allows for such surface preparation with controlled depth of removed concrete. For structures where concrete quality decayed or low strength concrete is present, the water jetting technique is then recommended;

- *Water jetting the existing surface* – it remains as the most efficient surface preparation for existing concrete structures, both for exposing aggregates for the interlocking of the two layers and for the absence of microcracking when applying such technique [49]. It allows for the removal of a controlled depth of concrete cover, without microcracking, exposing the larger aggregates by removing the surrounding cement matrix. The depth of concrete removal is controlled by the time the nozzle spends at the surface, which can be controlled by the operator. It stands as the best technique for scarification of existing surfaces, with the greatest drawback being the economic character and logistics of applying such technique in terms of equipment needed, the required specialized operator and the amount of mud it produces by removing the cement matrix with pressurized water.

Some provisions state that proper surface preparation should be attained through the application of deep methods such as the aforementioned, followed by lighter methods like sandblasting the resulting surface for the removal of loose debris and spalled concrete [41,50]. This option becomes onerous due to the increased logistics of sandblasting a concrete surface. A compromise between good bond and effectiveness of applying a single surface preparation method is then sought-after, concerning the effective surface area that provides the bond capacity. The resulting surface can then be assessed through several parameters identified in the literature and accepted for characterising the bond capacity of concrete-to-concrete interfaces.

### 2.3.3. Existing surface condition before casting

Alexander *et al*. [51] state that cleanliness is a very important aspect of the interface between concrete cast at different times. Recommendation for cleaning the contact surface twice prior to casting the overlaid concrete is also referred to by the authors. Such procedure should occur right after surface preparation, since the loose particles, chunks of concrete or smaller aggregate particles, or mud from water-jetting, should be completely removed from the contact surface. The second cleaning of the interface should occur right before casting the new layer to ensure that debris, oils and other particles are not present at the interface. Such consideration is coherent with good practice for attaining proper bond, since washing the interface prior to casting can ensure the optimal conditions for bonding the new layer. It is stated by Emmons [52] that three conditions can occur and affect interface performance, all depicted in Figure 2.15, with one being the optimal:

- *Dry substratum* – This condition can result in the pores of the existing surface withdrawing the water needed for the hydration process of the cement matrix of the new layer, thus resulting in poor bond;

- *Free water in the surface of substratum* – Such condition states the existence of a water film on the existing surface, thus weakening bond between the two layers due to excessive water on the hydration process of the fresh concrete and resulting in voids at the interface;

- *Dry surface, saturated substratum* – This is then the optimal condition of the interface, where the dried surface can ensure that the hydration process will occur at the existing pores thus promoting bond, and the saturated substratum will ensure that no water is excessively withdrawn from the fresh concrete to be cast.

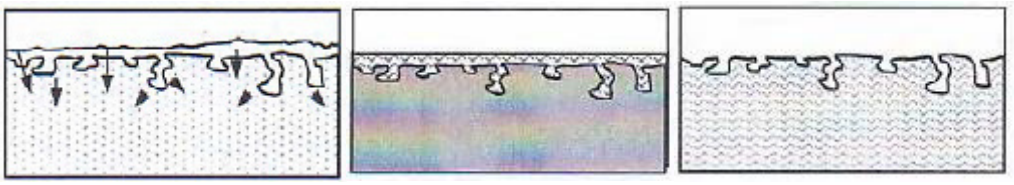

(a) (b) (c)

Figure 2.15 – Humidity degrees at the interface prior to casting the new concrete layer: (a) dry substrate, water from fresh concrete is withdrawn to the substratum; (b) saturated substratum, resulting in free water on the surface and poor bond; (c) optimal combination of dry surface and saturated substratum, existing pores available for maximum chemical adhesion and no water withdrawn from fresh concrete (adapted from [52])

The best combination of the aforementioned conditions for the contact surface is a requirement for good bonding capacity between the two concrete layers. The contact area is defined in [37] as a transition zone between the two layers, which can also create a layer of weakness, since small aggregates can accumulate close to the contact surface. This, in turn, creates a wall effect as depicted on the left of Figure 2.16. The authors also refer to the behaviour between fresh and hardened concrete to be similar to bond between aggregates and cement paste. In [53] this phenomenon was attested by bond tests in shear, with failure occurring in the overlaid concrete and near the interface. A good correlation was found between interface shear resistance and the overlaid concrete compressive strength, which is particularly important for design purposes. In [54] the transition zone is also identified between the two layers, depicted in Figure 2.16 to the right, and described as the zone where any interaction should occur that disturbs the stress fields of the other layer.

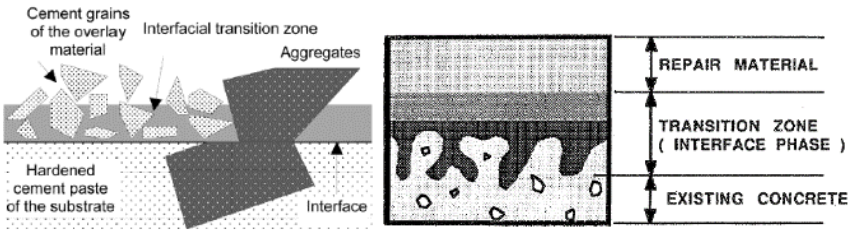


(a) (b)

Figure 2.16 - Transition zone between two layers: (a) the resulting aggregate condition at the interface (small aggregates – wall effect, large aggregates crossing the interface – mechanical effect on the strength of the interface); (b) depiction of the transition zone comprising the heterogeneity of interface phase (adapted from [37], [54]).

### 2.3.4. Assessment of the contact surface characteristics

Assessment of the contact surface can be divided in two ways: preliminary assessment of the existing surface through non-destructive methods after intentional roughening, and effective assessment after hardening of new concrete. A correlation has been established between the two [41,55], since roughness can assist on determining the degree of monolithic behaviour, along with specific reinforcement crossing the interface. Several methods are considered in [56] for evaluating surface roughness, namely the Sand Patch Method, which is referred to as not suitable for very rough surfaces or inclined surfaces [57]. Assessment of the existing surface before strengthening can be performed through several methods of profilometry [58]: mechanical profilometry [38]**,** laser profilometry [59], being the most accurate method available to date, photogrammetric techniques [60] or volumetric assessment of the groove volume in a predetermined area [61]. The latter method is defined as the Sand Patch Method (SPM) and has been the recommended method on design provisions due to its seniority as an accepted surface assessment method. The apparatus and schematics of applying such method are depicted in Figure 2.17.

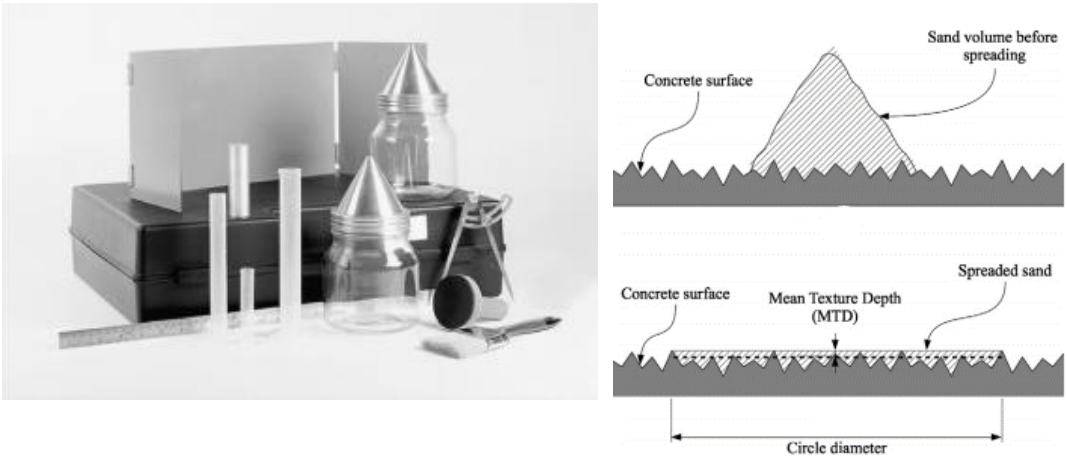


Figure 2.17 – The apparatus and application of the sand patch method (SPM, adapted from [62])

This test is performed by pouring a known volume of sand $V$ on the surface to be assessed, spreading it to form a relatively round patch until the highest ridges are noticeable. The requirements are that the surface needs to be dry and the method is limited for very rough surfaces due to the scatter of sand on the grooves, thus not forming a patch with an accountable mean radius, required for its characterisation [56]. The average diameter of such patch is calculated through the Mean Texture Depth (MTD) as:

$$MTD = \frac{4.V}{\pi.\emptyset^2} \tag{2.2}$$

Profilometry, as the name implies, focuses on tracing profiles for characterising the surface roughness. It is more or less effective depending on the quantity of points measured and the accuracy of traced profiles. In the matter of accuracy, laser profilometry through a 3D interferometer has become the standard, overcoming mechanical profilometry. The higher volume of data points and speed of digital data loggers when compared to discrete needles and manual logging were the vantage points. The latter's precursors were Abu-Tair *et al*. [63] where the proposed apparatus of needles would allow for a profile to be traced and texture parameters to be quantified. Such method was not practical for in-situ applications, and manual tracing of profiles can result in a great variability of results. Garbacz [64] used an apparatus that follows the same principles of mechanical profilometry with the particularity of a single stylus that works on a linear dimension and traces singular profiles of a given surface. The authors also assessed the sensitivity of measurement with different tips for the stylus, albeit round or conical, with best results for the latter, since it will pick up more signal changes of the profile slopes and smaller roughness.

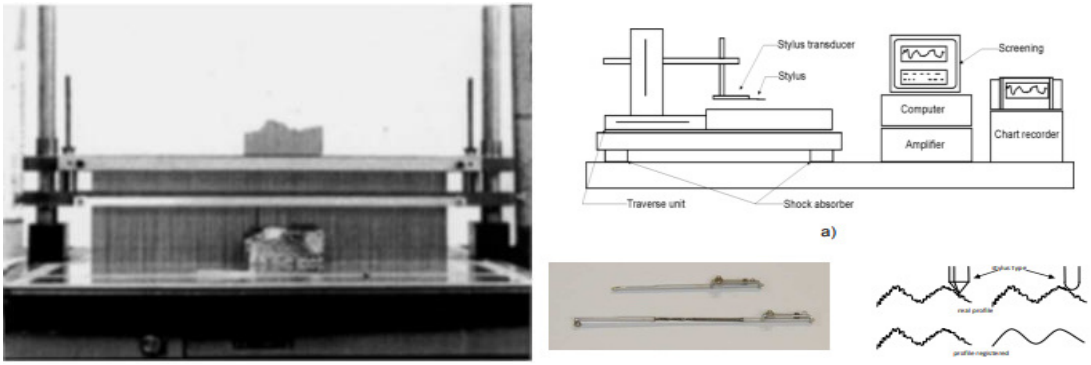


Figure 2.18 – Mechanical profilometry as initially proposed by Abu-Tair *et al*. [63] and later by Garbacz [64] (right)

Laser profilometry is then the state-of-the-art when it comes to surface assessment and is the most accurate technique with the largest volume of point measurements. Development of such method applied to concrete surfaces begins to be referenced by Maerz [58] applied to bonding of FRP strips to concrete. Several authors then developed such approach to the assessment of rough concrete surfaces, emphasizing the practicality of this method and the data processed automatically which reduces the uncertainty of results [59,65–67]. Santos and Julio [59] presented a solution for the laser assessment of rough surfaces, where an autonomous apparatus could measure the effective surface and its roughness, and calculate whatever parameter intended for

characterising such surface. Profile tracing would also be instantaneous and without external interference regarding the registered results due to data logging in-situ. This condition allowed for the correct assessment of surface parameters and correlation to bond capacity of the interface. The apparatus itself is composed of a laser sweep and a controlling unit, that also has the ability to store the measured data, as illustrated in Figure 2.19.

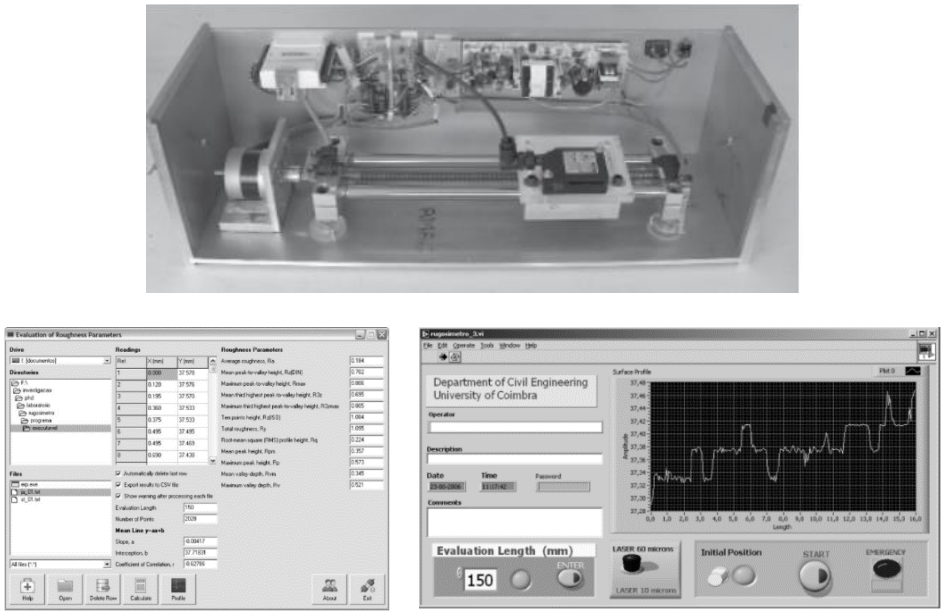


Figure 2.19 – The laser profilometer as presented by Santos and Júlio [59].

### 2.3.5. Texture parameters of intentionally roughened concrete surfaces

The profile of the existing surface is an important factor that governs the contact area and interlocking of the two layers. Garbacz *et al*. [68] state that parameters of roughness and waviness are enough for the assessment of bond quality. Roughness characterises the relationship between the grooves and ridges of the existing surface. Waviness of the contact area also contributes to the interlocking of contacting surfaces and should be accounted for [64]. Santos *et al*. [55,69] refer to several parameters that can attain good correlation to experimental tests, namely the maximum peak to valley height, total roughness height and maximum valley depth, along with the average and total roughness. Other parameters can be withdrawn from the data, regarding the intended surface characterisation. Average roughness and total roughness of the surface profile are the most recurrent surface parameters when characterising rough surfaces, calculated by equations (2.3) and (2.4), with its terms graphically depicted in Figure 2.20.

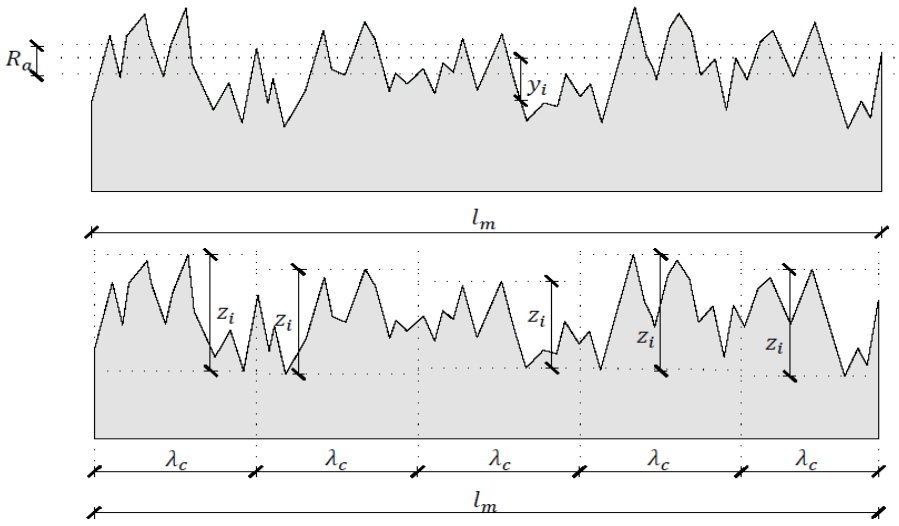


Figure 2.20 - Average roughness and mean peak-to-valley height for surface profile (adapted from [57]).

The average of measurements $\bar{y}$ that form the profile is calculated from the $n$ measurements $y_i$ performed with a fixed coordinate along the profile, allowing for the calculation of average roughness $R_a$ of a profile with a length $l_m$. The $R_z$ parameter that corresponds to the assessment of total roughness is calculated considering the peak-to-valley measurements $z_i$ of five reference lengths.

$$R_a = \frac{1}{l_m}.\int_0^{l_m} y(x)\,dx \approx \frac{1}{n}.\sum_{i=1}^{n} |y_i - \bar{y}| \tag{2.3}$$

$$R_z = \frac{1}{5}.\sum_{i=1}^{5} z_i \tag{2.4}$$

Roughness alone cannot be an absolute characterisation of the contact surface, since different profiles can have the same average roughness, as stated in [70] and depicted in Figure 2.21. Waviness can assist the characterisation of the interlocking capacity of the interface, which is relevant when account for the sliding of the two layers.

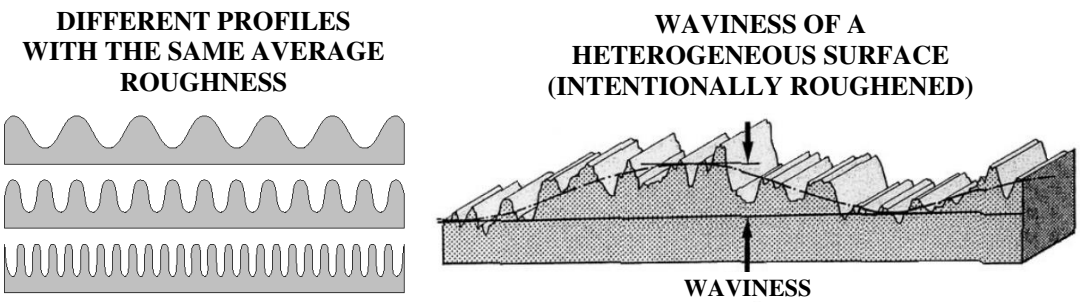


Figure 2.21 – Important characteristics that impact concrete-to-concrete interfaces: Roughness (left) and Waviness (right) (adapted from [70] and [71])

Since the mean texture depth that results from the SPM can only determine the equivalent to the average "peak-to-mean" roughness $R_p$ [57], such parameter can be calculated according to equation (2.5) as proposed by [24], where $n$ is the number of peak $p_i$ to mean $\bar{z}$ profile measurements.

$$R_p = \frac{1}{n} . \sum_{i=1}^{n} |p_i - \bar{z}| \tag{2.5}$$

The remaining aforementioned parameters of maximum peak-to-valley height $R_{max}$, total roughness height $R_y$ and maximum valley depth $R_v$, calculated according to equations (2.6) to (2.8), characterise the surface in terms of the grooves and ridges that interlock the two layers. The good correlation to test results on [55] state these parameters as accountable for characterising the interface between concrete cast at different times.

$$R_{max} = max\{z_i\} \tag{2.6}$$

$$R_y = p_{max} - v_{max} \tag{2.7}$$

$$R_v = max\{v_i\} \tag{2.8}$$

Therefore, $R_{max}$ can perform an absolute characterisation of the surface interlocking abilities through the highest ridge that will interlock with the new layer. Simultaneously, $R_v$ can characterise the same way, since a groove or ridge in the existing surface will result in ridges and grooves on the new layer. Total roughness height can characterise the interface in terms of the difference between highest ridges and lowest valleys, and therefore the interlocking capacity of the interface.

The waviness of a given surface can be perceived when very rough and heterogeneous surface preparations are used due to spalling of concrete. This parameter is relatively random and highly dependable on the method used for surface preparation, with more aggressive methods resulting in greater waviness of the surface. Courard *et al*. [72] analysed the difference in measurement of roughness and waviness of a given surface. The authors characterise micro-roughness as surface roughness and the macro-roughness as waviness of such surface.

Santos and Júlio [62] stated the importance of different surfaces yielding the same average roughness. For concrete-to-concrete interfaces, micro-roughness can have a secondary effect if

waviness is present and acting as macro-roughness, allowing for the interlocking of the contacting surfaces. Garbacz [64] states the waviness of a given surface as the lower frequency assessment of its roughness. Such statement requires that the length between two measurements is long enough for the assessment of waviness, without losing information from the slope sign throughout the assessment length. Figure 2.22 shows the real surface with its irregularities, roughness and waviness, and roughness as the real surface with attenuated waviness heights. This shows the impact of waviness as a macro-roughness on the assessed roughness, attesting its interlocking capacity.

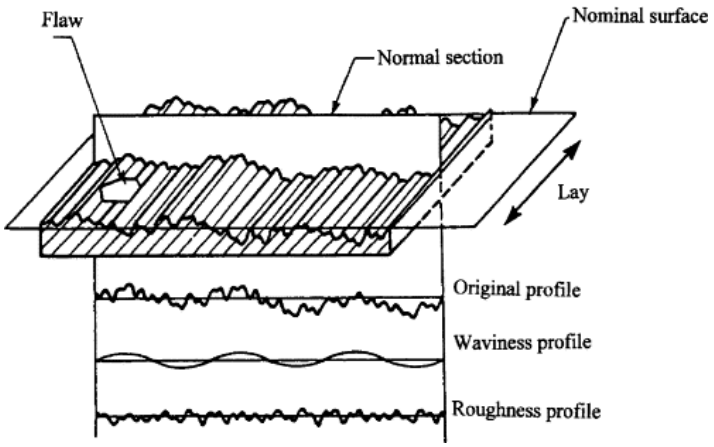


Figure 2.22 – Surface characteristics: real profile, the waviness profile and effective roughness (adapted from [73]).

Determining roughness parameters will reflect on code provisions, where characterisation of the surface roughness quantifies adhesion and friction stresses acting on the interface. In [35] the qualitative characteristic of surface roughness assessment methods adopted in code provisions is mentioned, and it is stated that it should be altered to quantitative methods, like the ones already referred to in the MC2010 [57]. Roughness and waviness can be perceived as a micro and macro roughness, as depicted in Figure 2.23, since its impact on tensile and relative slip of a concrete interface is different due to the effective area of the former and the friction of the latter.

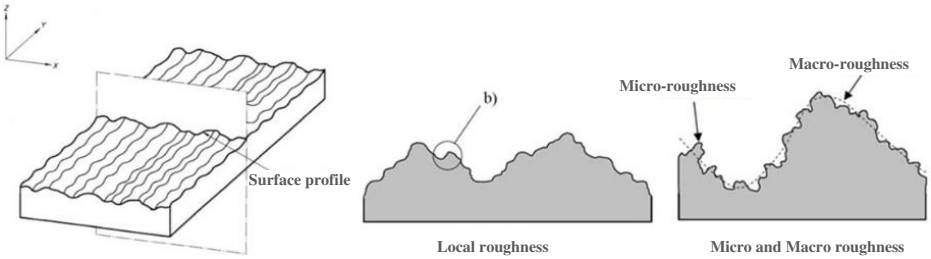


Figure 2.23 – Micro and macro roughness of a roughened concrete surface (adapted from [24])

Roughness alone does not implicitly improve tensile strength, although it improves the effective contact area and macroscopic interlocking. Adhesion comes from microscopic and sub-microscopic interlocking of the two layers, both chemically and mechanically. Figure 2.24 illustrates the same surface observed under different scales.

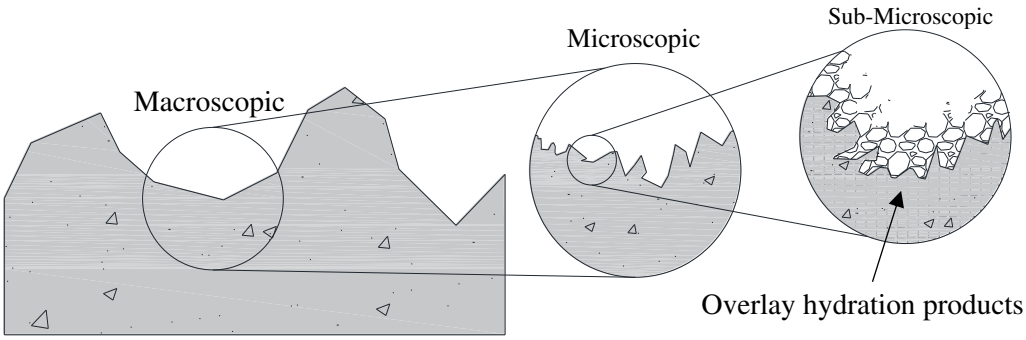


Figure 2.24 - Macroscopic, microscopic, and sub-microscopic surface roughness (adapted from [53]).

### 2.3.6. Reinforcing the concrete-to-concrete interface

Interfaces that have a structural function are recommended to be reinforced to improve the available shear mechanisms of concrete-to-concrete interfaces. These include the microscopic interlocking of the two layers, which promotes adhesion and friction, and macroscopic interlocking, which also promotes friction, dowel action and the tensile capacity of interface reinforcement. In the work of Cook *et al*. [74], a reference is made to the ratio of 50% between tensile and shear capacity both for pre-installed and post-installed shear connectors. Provisions for anchoring to the substratum and proper anchoring to the overlay are referred to in [36], for shear headed studs and rebar embedded in the former. The recommended geometry for the shear connectors and/or interface crossing reinforcement is shown in Figure 2.25.

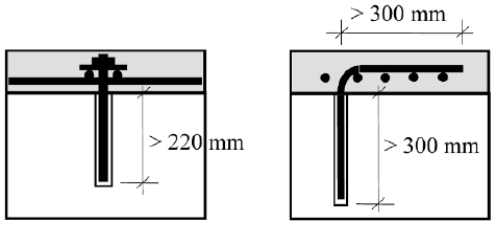


Figure 2.25 – Headed studs and rebar as shear connectors of concrete-to-concrete interfaces (extracted from [36])

Failure modes of interface crossing reinforcement comprise the flexural deformation that occurs for higher relative sliding of contacting layers. At this point adhesion would already have been lost and such reinforcement would provide structural integrity through friction and respective dowel action. Such deformation requires for the crushing of concrete and yielding of the shear connector, which depends on the strength of both materials and usually results in one of three possible failure modes represented in Figure 2.26.

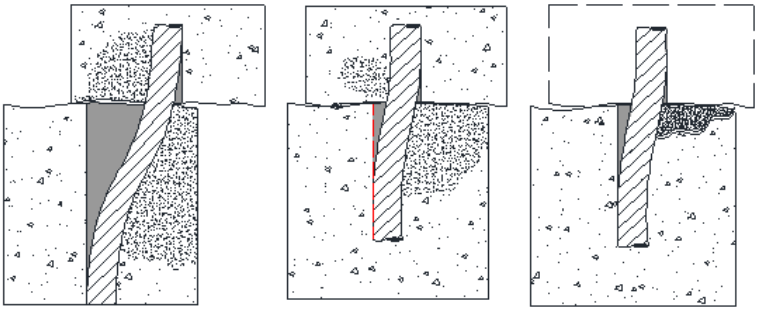

Figure 2.26 – Failure modes of shear connectors (adapted from [75])

Shear connectors with higher embedment lengths usually result in yielding of steel if proper anchoring is provided, with concrete crushing for higher relative slips (Figure 2.26 (1)). For a lower strength concrete on the substratum, the shear connector can crush the concrete material and consequently debond behind the anchorage, resulting in loss of stiffness and failure of the interface (Figure 2.26 (2)). Depending on the quality of the substratum and flexural stiffness of the shear connector, spalling of concrete can occur due to increased relative slip of the two layers, although overlaid concrete can provide some degree of confinement to the substratum (Figure 2.26, c). All the aforementioned assumptions rely on higher strength for the overlaid concrete and relatively sound substratum concrete. Provisions for the shear capacity of a properly anchored rebar in the Model Code 90 [19] are based in the theory by Leonhardt and Mönnig [76], calculated through equation (2.9), where $\varepsilon = 3.e/\emptyset_s . \sqrt{f_c/f_y}$ is the coefficient that accounts for the eccentricity of the shear load depicted in Figure 2.27 and $\zeta = \sigma_s/f_y$ the coefficient that accounts for the stress at the rebar. The limit $A_s.f_y/\sqrt{3}$ is the shear strength for a single rebar.

$$F_v = 1{,}30.\emptyset_s{}^2 \left\{\sqrt{1+(1{,}3.\varepsilon)^2} - 1{,}3.\varepsilon\right\}.\sqrt{f_c.f_y.(1-\zeta^2)} < \frac{A_s.f_y}{\sqrt{3}} \qquad (2.9)$$

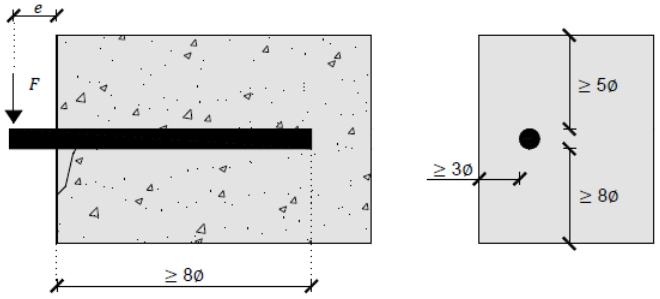


Figure 2.27 – Parameter of a properly anchored rebar in shear (adapted form [19])

The same provisions on the MC2010 [57] are an evolution of the previous, as illustrated by equation (2.10), and account for the shear deformation $s$ of the rebar, which is limited to $s_{máx}$ of about 10-20% of the rebar diameter.

$$F_v(s) = F_{0,máx}.\left(\frac{s}{s_{máx}}\right)^{0,5} = k.A_{s,i}.\sqrt{f_c.f_y}.\left(\frac{s}{s_{máx}}\right)^{0,5} \quad (2.10)$$

For greater relative deformations, pull-out of the shear connector can also occur if properly bonded to the overlaid concrete, with the traditional failure modes depicted in Figure 2.28. The failure modes of a pull-out mechanism comprise the clean pull-out by either the interface between the rebar and the bonding agent (2) or the bonding agent and the concrete where it is anchored (3). Extreme cases of reaching the tensile strength of reinforcement (1) or pull-out of a concrete cone (4) can also occur, although a state of pure tensile stress is difficult to obtain on shear connectors.

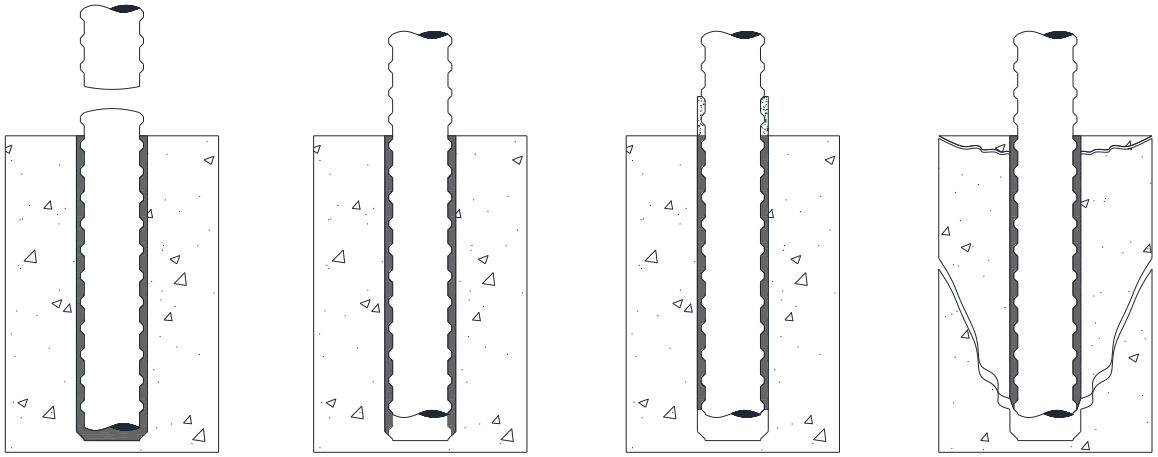

Figure 2.28 – Failure modes of post-installed shear connectors (adapted from Miltenberger [77])

Quantification of the pull-out force is then performed through equations (2.11) to (2.14), corresponding to the four failure situations shown in the figure above, where $A_s$, $\emptyset_s$ and $f_y$ are the reinforcement characteristic area, diameter and yield stress, respectively, $\emptyset_b$ the diameter of the drilled hole, $f_c$ the characteristic compressive strength of concrete and $l_{anc}$ the anchorage length. The bonding stresses of both the interfaces $f_{b,s}$ and $f_{b,c}$ should be taken from the bonding agent manufacturer or assessed experimentally prior to application.

$$F_{r,1} = A_s.f_y \quad (2.11)$$

$$F_{r,2} = \pi.\emptyset_s.l_{anc}.f_{b,s} \quad (2.12)$$

$$F_{r,3} = \pi.\emptyset_b.l_{anc}.f_{b,c} \quad (2.13)$$

$$F_{r,4} = 12{,}5.{f_c}^{0,5}.{l_{anc}}^{1,5} \quad (2.14)$$

### 2.3.7. Effective assessment of interface capacity

The effective assessment of interface capacity for bonding two concrete layers can be performed through testing of the tensile and shear capacity of the interface. Testing of such capacity can be performed through pull-off tests for tensile capacity and the push-off test for shear stress at the interface.

The pull-off test is the most common characterisation of bond capacity, with reference of its use from 1984 in [78]. This type of test can be performed in the field by coring the specimens in the existing structures using relatively light test equipment [79]. Pull-off testing is a type of direct tension test, with inherent limitations pointed by several authors regarding load eccentricity, damage during coring, and dispersion due to randomness of surface roughness and test results ([80], [81], [82]). General setup for pull-off testing and respective failure modes can be observed in Figure 2.29. Coring of the specimens is recommended to reach a depth of at least 25 mm through the substratum, enough to assess the condition of existing concrete through its tensile strength [33]. High strength epoxy glue is generally recommended for bonding the test dolly to the concrete surface [81], with previous removal the respective laitance layer.

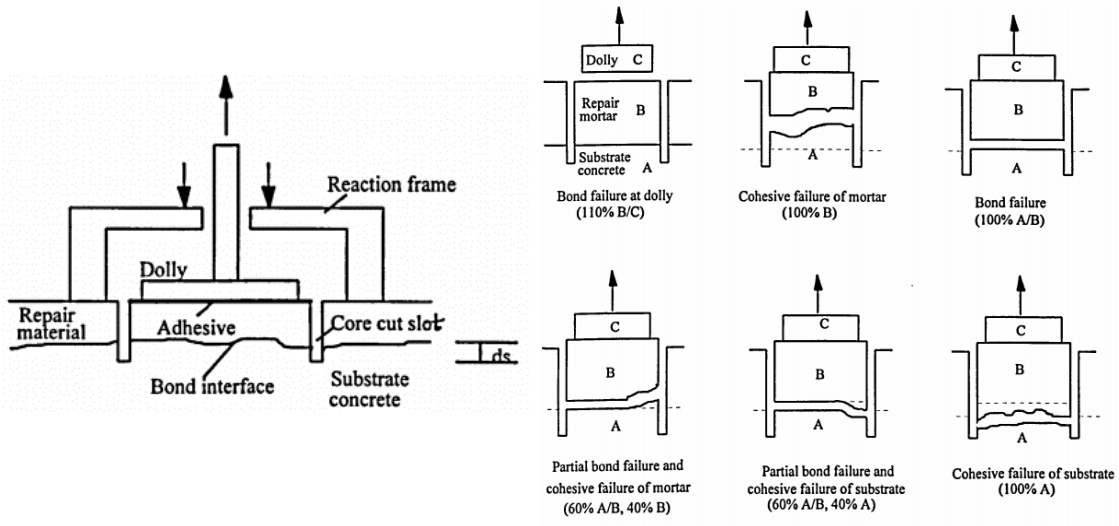


Figure 2.29 – General pull-off test setup and failure modes (extracted from [83]).

The failure modes associated with pull-off tests are divided into adhesive, depending on whether failure occurred at the interface between the steel dolly and concrete or concrete-to-concrete, or cohesive, if the tensile strength of concrete is reached before that of the interface. Indeed, even tensile failure modes of the contacting layers occurring close to the interface are all referred to as interface failure, since clean debonding of the overlaid concrete is difficult to obtain [53]. A failure surface that is commonly reported corresponds to the overlaid concrete near the interface, as shown in Figure 2.30. Such phenomenon then attests the substratum post-strengthening quality and is in accordance with [53].

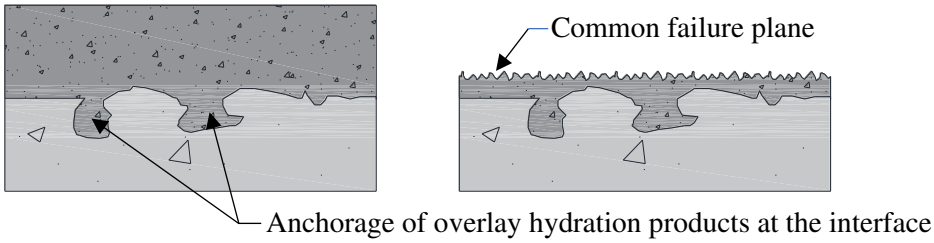


Figure 2.30 - Common failure plane for concrete-to-concrete interfaces (adapted from [53]).

Information on pull-off test conditions and preparation are provided in the EN 1504-3 [32]. This European standard specifies minimum surface cohesion values for structural repairs of 2,0 MPa and a minimum of five valid tensile bond tests. Pull-off testing is directly addressed in the EN 1542 [79], regarding general aspects for this type of test, mainly dolly sizes, angle of force application, and test procedure. This includes the size and shape of the dolly, the speed of loading, and how deep the specimen should be isolated from the rest of the substratum. This issue is addressed in [84], where a reference is made to the variability of results when specimens are not properly isolated from the surface of the substratum. A depth of 15±5mm, considered enough for isolating vertical stress and guarantee mainly vertical stresses at the base of the specimen, was then adopted in such work and according to previous works [85,86].

Other tests can be performed to assess the interface capacity like the push-off test, the slant-shear test, the splitting test or the wedge-splitting test. These tests allow for characterising the tensile or shear bond capacity of the interface. The push-off test has been referred to in 1960 by Hanson [87], and modified ever since by several authors [25,28,88], with its geometry allowing for reinforcement to be installed at the interface. The slant shear test is then another practical way to assess the shear stress at the interface. A prismatic or cylindrical two-material specimen that comprises the interface set at a slope of 30 degrees to the direction of loading, with confinement provided by the normal component of the compressive force applied. In [89] the main parameters of specimens are addressed, namely the angle of the interface and the ratio between loaded area and the height of the specimen, initially proposed as cylindrical. The referred value of 30 degrees to the axis of the specimen initially proposed in 1976 is still used. Other modifications have also been proposed regarding the geometry of the specimens, namely the change to square specimens, illustrated in Figure 2.31, allowing for practicality and more stable test results.

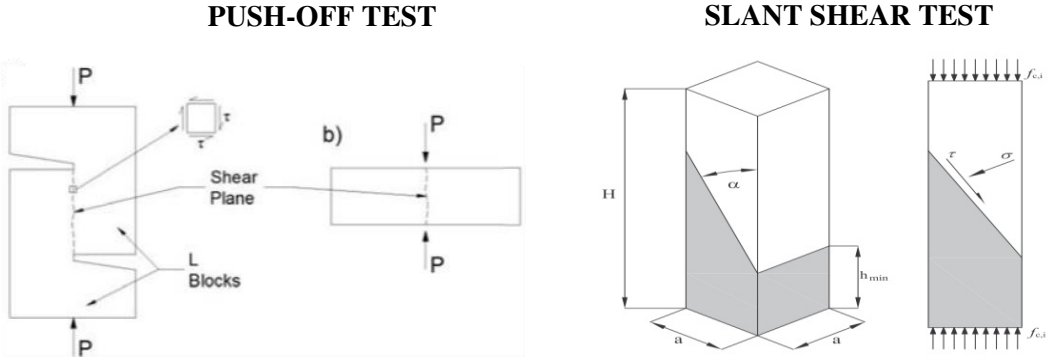


Figure 2.31 – The push-off test and slant shear test geometries (adapted from [90] and [89])

Characterisation tests on the bond capacity of concrete-to-concrete interfaces are referenced in the literature, namely the splitting test [91] and the wedge-splitting test [92], that induce a dominantly tensile field of stresses at the interface. The first requires that a prismatic or cylindrical specimen is cast with two materials whose interface is coincidental with the axis in the load direction. Load is then applied in the direction of the interface and the stress field induced by compressing the specimen as depicted in Figure 2.32. Such test is also known as the Brazilian Test with provisions for dimensions and material characteristics in EN 12390-6 [91]. In the wedge-splitting test a tensile stress state similar to the last but in a prismatic specimen, is induced as shown in Figure 2.33. Such test was developed by Linsbauer and Tschegg [92] for assessing the tensile strength of an interface, and later modified by Bruhwiler and Wittmann [93]. It stands as a more efficient and reliable test than loading notched beams on the three-point bending test [94].

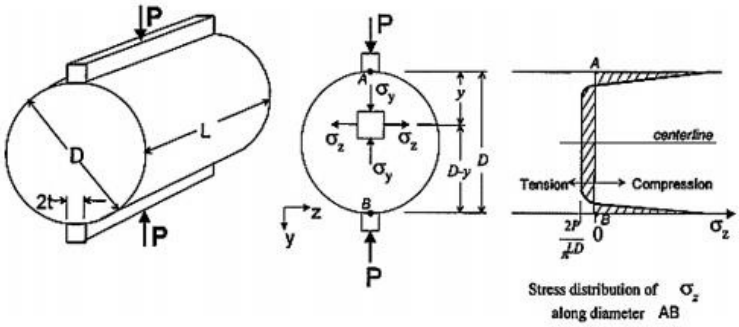


Figure 2.32 – Splitting test (extracted from EN12390-6 [91])

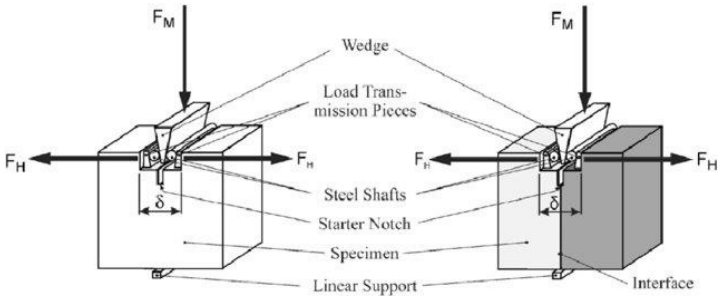


Figure 2.33 – Wedge splitting test (extracted from [92])

### 2.3.8. Bonding and Debonding of overlaid concrete

Bonding of newly cast concrete to an existing concrete surface depends on several components of the resisting mechanism that govern the interface behaviour:

- Curing of fresh concrete allows for bonding to an existing surface, roughened or not, due to the microscopic anchoring of new cement matrix to the pores of an existing surface. This makes for adhesion between the two concrete layers – which can be chemical or mechanical, depending whether it results from curing of concrete or anchoring to grooves of an existing rough surface;

- Friction is then a consequence of relative slip between the two layers, due to resulting compressive stresses on the interface, either by external compressive forces or the equilibrium of shear connectors' resulting stresses;

- Interlocking of contacting layers occurs due to the resulting antisymmetric profile of newly cast concrete at the interface with existing concrete – such effect is greatly improved by installing shear connectors.

Debonding occurs then after failure of either component of the resisting mechanism, which results in relative displacement between contacting layers. The failure mechanism usually starts at the boundaries of overlaid concrete, where the edge-lifting phenomenon is present due to the lack of neighbouring elements that restrain shrinkage and provide equilibrium of forces [95]. Although the interface pull-off strength is well-accepted as an all-purpose performance index for characterising tensile capacity [96], Perez *et al*. state in [41] that this parameter alone does not correctly assess the interface capabilities for structural integrity. Debonding occurs in a strengthening situation when a flexural or shear crack reaches the interface, being the path of least resistance, resulting in the tensile stress component orthogonal to the interface exceeding its tensile capacity. Chemical adhesion should be assessed through direct tension testing such as the pull-off test [97]. Full bonding between the two layers is a structural requirement since partial bonding is an heterogeneous condition and cannot be fully accounted for [33]. According to the authors, inhomogeneous bond at the interface according to Figure 2.34 can cause a restraint on the overlaid concrete and consequent cracking.

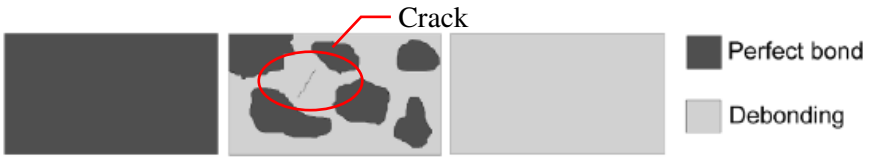


Figure 2.34 – Inhomogeneous bond between contacting layers can affect shrinkage and cause cracking of newly cast concrete (extracted from [33]).

This then relates to one of the main characteristics for tensile capacity in a rough interface, the effective surface area. This is typically larger than the geometric area, as depicted in Figure 2.35. This is an important parameter for bond capacity of concrete-to-concrete interfaces, according to [55] and [45]. Also, the effectiveness of mechanical adhesion depends on the penetration of the fresh cement paste in the grooves and pores of the existing surface which, after hardening, will help interlocking the two layers.

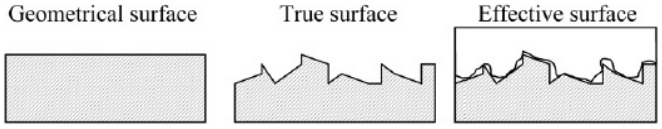


Figure 2.35 - Contact area between two layers: geometric, true, and effective (extracted from [33]).

This interlocking phenomenon is relevant in tension for mechanical adhesion when effective vertical anchorage of overlaid concrete in pores and voids, as shown in Figure 2.36, along with chemical adhesion, with both playing a major role in the tensile strength of the interface.

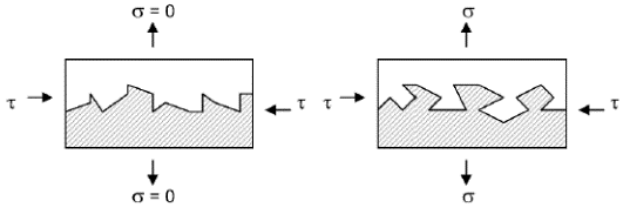


Figure 2.36 - Mechanical tensile and shear bond between two layers (extracted from [33]).

The debonding mechanism has been characterised by Granju [39] as initiating from a discontinuity of the overlay, being a crack on the boundary of overlaid concrete. Cracking is a broad subject of RC structures and should be accounted for when assessing the behaviour of RCO strengthened structures. The debonding phenomenon itself consists on the forming of a crack at the plane of the interface, with the reinforcement that crosses such interface controlling the opening and delaying the otherwise brittle failure. Perez *et al*. [50] analysed the behaviour of a concrete-to-concrete interface closer to the tensile face and the impact of flexural cracks reaching the interface, as shown in Figure 2.37.

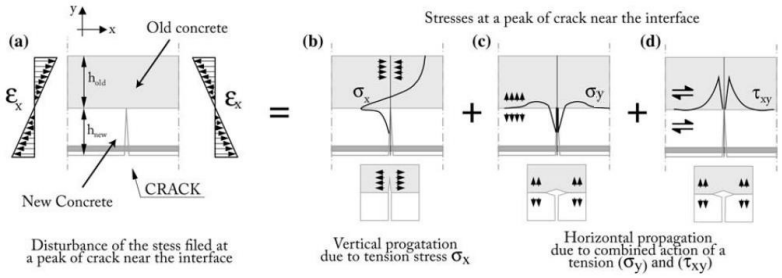


Figure 2.37 – Flexural crack reaching the interface between concrete layers (extracted from [50])

One can observe the impact on stress state when a flexural crack reaches the interface, with horizontal stresses concentrating at the interface level and the increased shear stress that results. The authors state that tensile strength of the overlaid concrete was reached upon cracking and the increased stresses at the interface would result in debonding initiating in tension, which leads to the tensile strength of the interface governing bond strength between the two layers. Such premise validates the assessment of the interface tensile strength for characterising its bond capacity.

Zhang *et al*. [17] characterise the failure modes and mechanism of overlay strengthened beam specimens. Cracking is then one of the main topics discussed in such work, since concrete overlaid on the tensile face of structural elements subjected to shear and bending forces will crack, and such cracks will then cross the interface, as depicted in Figure 2.38.

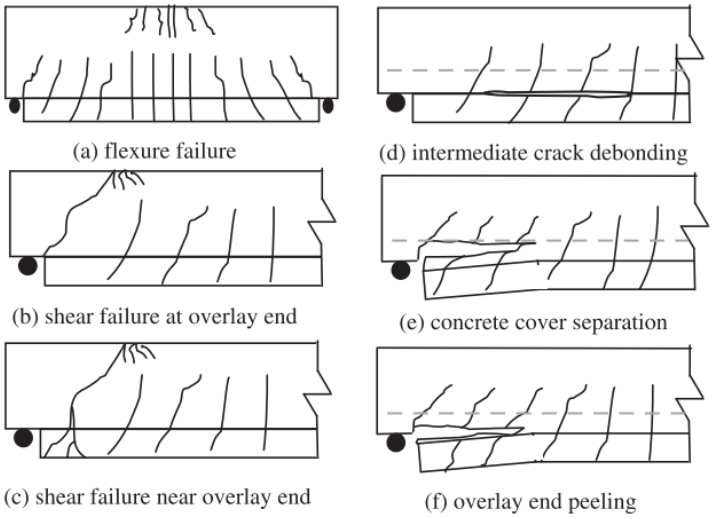


Figure 2.38 – Failure modes of overlay strengthened beams (extracted from [17])

The failure modes depicted above envelop the possible failure modes of overlay strengthening solutions. Bond of new-to-old concrete is usually weaker than the tensile strength of either layer, hence the failure mode usually being of flexural or shear nature, or debonding of the substratum concrete cover together with the debonded layer (Figure 2.38 a, b, c, f). The latter is a known consequence of surface preparation through mechanical methods, where microcracking near the surface of the substratum leads to spalling of concrete bonded to the overlaid concrete, resulting in a reduced bond capacity. This is a nuclear aspect of surface preparation, as stated by Silfwerbrand [36] when identifying the major factors affecting bond of new-to-old concrete as shown in Figure 2.39 scaled by a degree of influence on bond capacity:

- *Microcracks at the substratum* – a very important aspect since it may cause the loss of bond by spalling of cracked concrete from the substratum. It is a common consequence of unsound concrete or concrete that was intentionally roughened through impact mechanical methods (jackhammering, etc). In [32] it is stated that microcracked or delaminated concrete shall be removed from the contact surface prior to casting the new layer, whether it derived from unsound concrete or surface preparation;

- *The importance of removing the laitance layer and cleanliness of the existing surface prior to casting new concrete* – the laitance layer results as a low-strength barrier to bonding of new concrete due to the fine nature of the cement matrix it comprises. Cleanliness is also of the utmost importance to bond of new concrete since loose material and grease cause the loss of bond and premature failure of the interface.

- *The compaction and curing of overlaid concrete* – these aspects are also important due to the proper casting of new concrete to maximize bond to the substratum, since compaction removes the voids in fresh concrete and curing controls shrinkage that may result in premature cracking of such concrete.

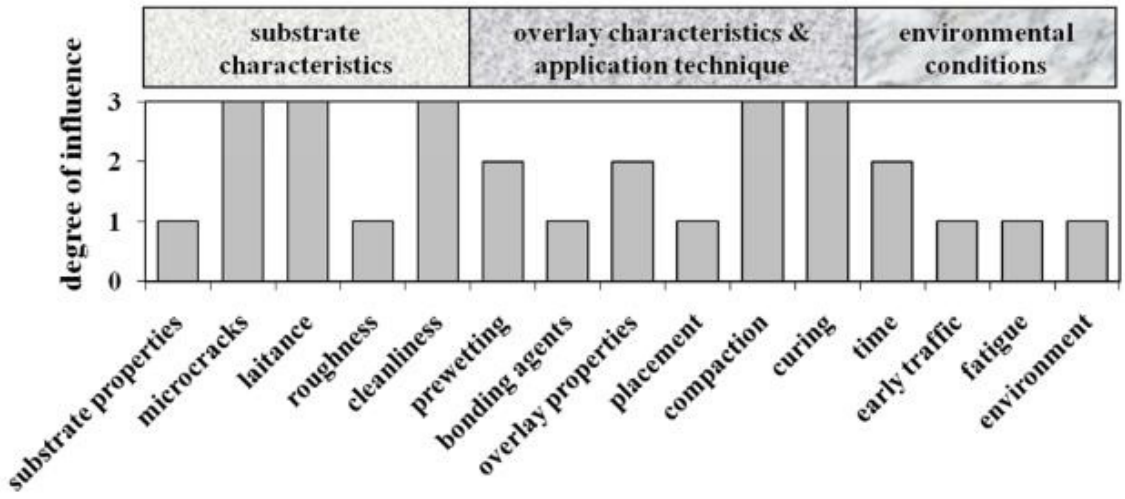


Figure 2.39 – Factors affecting bond between new-to-old concrete (adapted from [36])

Attempts at improving interface strength through the use of bonding agents were also performed. Julio *et al*. [98] present a complete description of the theory behind the use of epoxy-based bonding agents on concrete-to-concrete interfaces and the previous works that preceded. The authors state that the application of an epoxy-based bonding agent on a rough surface does not improve bond strength more than a sufficiently rough surface preparation. Such conclusion was also drawn by Saucier and Pigeon [37] for the use of cement grout as a bonding agent between two concrete layers. The use of a bonding agent can weaken the connection between such layers of concrete if not properly applied. For this matter, and due to the freshly poured concrete that should harden when the bonding agent is still fresh, Cleland and Long [80] state the use of a bonding agent in a concrete-to-concrete interface can have a negative result and should be cautiously proposed as a solution for bonding concrete layers cast at different times.

### 2.3.9. Analytical models

The analytical models for interface shear assessment started with the proposed calculation of the friction between two sliding surfaces by Birkeland and Birkeland (1966) [99] through equation (2.15), and thus the development of the Shear Friction Theory for concrete-to-concrete interfaces. The principle was that roughness of the interface could be theoretically defined as a saw-tooth, since it causes the interface to debond perpendicularly to its plane when a horizontal relative displacement is applied. The saw-tooth model is a tool that characterises the parameters of equation (2.15) and is accepted as an approximation of the heterogeneous surface of roughened concrete, as depicted in Figure 2.40.

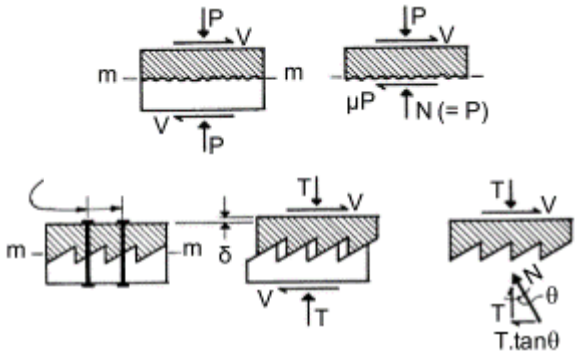


Figure 2.40 – Saw-tooth model of the Shear Friction Theory(adapted from [99])

$$\tau_R = \rho . f_y . \mu \text{ (MPa)} \quad (2.15)$$

Where $\rho$ and $f_y$ are the ratio of reinforcement crossing the interface and the yielding stress of such reinforcement, and $\mu$ is the coefficient of friction, which is the tangent of the internal friction angle $\theta$ resultant from the clamping compressive force on the interface. The friction coefficient was then defined as:

- $\mu = 1.7$ for monolithic concrete ($\theta \approx 59.5°$);
- $\mu = 1.4$ for normal strength concrete and interface intentionally roughened ($\theta \approx 54.5°$);
- $\mu = 0.8$ for steel-concrete interfaces ($\theta \approx 38.7° \; to \; 45°$).

Mattock and Hawkins (1972) [28] considered the contribution of material and interface properties to the behaviour and strength of concrete-to-concrete interfaces. Such contribution would state the Modified Shear Friction Theory, which would include the adhesion component to the shear friction mechanism. This component was considered to be constant at 1.38MPa and calculation of the interface shear strength was then:

$$\tau_R = 1.38 + 0.8 . \left(\rho . f_y + \sigma_n\right) \text{ (MPa)} \quad (2.16)$$

Other main contribution to the Shear Friction Theory was provided by Walraven and Reinhardt (1981) [100], in which the authors explicitly identify a phenomenon that would later on be implemented to the shear friction theory: aggregate interlock. Such phenomenon considers the interaction between the contacting surfaces at the interface through consideration for the components of reinforced concrete: the cementitious matrix and the aggregates it incorporates. Considering the superior strength of the latter, one would expect the cement matrix to crush when loaded by the aggregates. Such principle was considered in this theory, in which the interface is characterised by random spheres of heterogeneous sizes crossing it, as depicted in Figure 2.41.

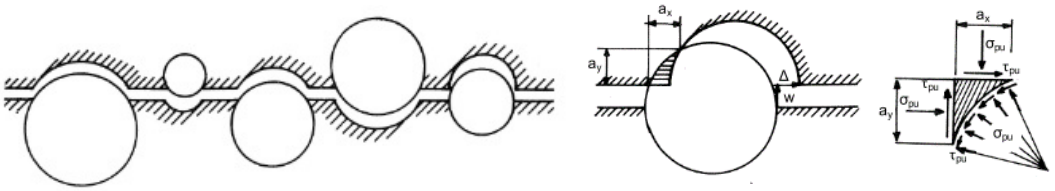


Figure 2.41 – Sphere model of Walraven and Reinhardt (extracted from [100])

One should note that the waviness of the interface was not accounted for in this model as it can be observed in the flat contact surface between aggregates. Deformation of the interface is then solely characterised by the plastic deformation of the cement matrix. The authors also evaluated the influence of reinforcement in the transmission of stresses between the two layers, and thus the weight of the reinforcement ratio when estimating the interface bond stress. These comprise the formation of diagonal struts in concrete, dowel action and tensile stresses of reinforcement due to relative slip of the two layers and the resulting crack opening. The equilibrium of all these components is depicted on the right of Figure 2.42, where $F_d$ is the dowel force and $H$ the tensile stress of each bar, $F_{iv}$ and $F_{ih}$ the forces resulting from aggregate interlock.

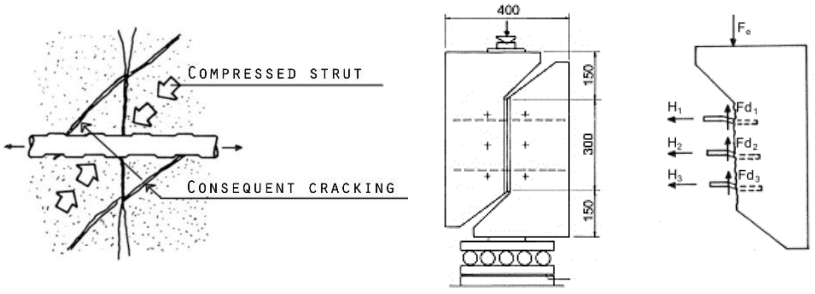


Figure 2.42 – Phenomena in the vicinity of reinforcement and resulting mechanisms at the interface (adapted from [100])

A design estimate based on such theory is then proposed by Walraven *et al* (1987) [88] through a power function of the term $\rho.f_y$, with factors $C_1$ and $C_2$ accounting for concrete compressive strength:

$$\tau_R = C_1.\left(\rho.f_y\right)^{C_2} \text{ (MPa)} \tag{2.17}$$

$$C_1 = 0.822.f_c^{\,0.406} \tag{2.18}$$

$$C_2 = 0.159.f_c^{\,0.303} \tag{2.19}$$

Considering the aforementioned effects on the shear bond mechanism of concrete-to-concrete interfaces, Randl (1997) [29] proposed an estimation of such strength considering all the sub-mechanisms, adhesion and aggregate interlock, friction and dowel action of reinforcement

crossing the interface. Dowel action, accounted by the term "$\alpha.\rho.\sqrt{f_c}.\sqrt{f_y}$" refers to the various mechanisms at the interface, namely the tensile capacity generating compressive stresses at the interface and flexural capacity limiting relative slip by compressing concrete at the anchored length of steel dowels. The proposed formulation was then quantified by:

$$\tau_R = \tau_c + \mu.\sigma_n + \alpha.\rho.\sqrt{f_c}.\sqrt{f_y} \leq \beta.\nu.f_c \text{ (MPa)} \quad (2.20)$$

Where $\alpha$ is a tabled factor that accounts for the flexural capacity of reinforcement for the dowel action. The term for adhesion $\tau_c$ is defined through the power function $c.(f_c)^{1/3}$, where $c$ is an empirical tabled coefficient. The term for friction $\mu.\sigma_n$ can account for the tensile capacity of reinforcement crossing the interface by adding the term "$\mu.\rho.k.f_y$", where $k$ is a tabled coefficient of efficiency for the tensile force transmitted between layers by the interface crossing reinforcement. The upper bound of such theory is set by the compressive capacity of a concrete strut through the term "$\beta.\nu.f_c$", where $\beta$ is the coefficient that accounts for the angle of a concrete diagonal strut and $\nu$ the reduction factor.

A correlation was observed between a higher degree of surface roughness and cohesive failure modes, along with higher shear stresses at the interface, with Santos [70] directly characterising the coefficient of cohesion and the coefficient of friction through interface characteristics, namely the mean valley depth $R_{vm}$. Such parameter will be discussed later on and directly characterises surface roughness and the interlocking capacity of the contacting surfaces. One should note that the authors accounted for the correlation of maximum valley depth $R_v$, but deprecated it since strong irregularities are not well accounted for, although it is referred to be the parameter that best correlates with bond strength of the interface [55]. An estimation of interface strength was then proposed regarding the mean valley depth of the surface texture through the expressions presented in equations (2.21) and (2.22), where the coefficient of cohesion and the coefficient of friction are characterised in terms of the latter parameter:

$$\tau_R = \begin{cases} 1.698.{R_{vm}}^{0.145}.f_{ctd} & (2.21) \\ 1.560.{R_{vm}}^{0.041}.(\sigma_n.\rho.f_y) & (2.22) \end{cases} \text{ (MPa)}$$

Where $f_{ctd}$ is the design tensile strength of concrete, and when in a design situation one should consider affecting equation (2.21) with factor $1/\gamma_{coh}$, with the value 2.6 for $\gamma_{coh}$, and affecting equation (2.22) with factor $1/\gamma_{fr}$, with the value 1.2 for $\gamma_{fr}$.

### 2.3.10. Design code rules and considerations

Design codes are the moderated result of all research performed in a field, since it will be widely used when designing a new structure or retrofitting an existing structure. Therefore, these are based on the state of the art so far, until each release of a new design code. Such principle applied to shear friction provisions of existing codes justifies the analysis of existing codes, even those that were replaced have a basis that should be considered, since it can somehow characterise the behaviour and strength of concrete-to-concrete interfaces. The main codes to consider are then presented in Table 2.1, ranging from the Model Code 1990 [19] to the Model Code 2010 [57].

Table 2.1 – Design codes that address the shear friction of concrete-to-concrete interfaces

| Design Code | Year | Design expression |
|---|---|---|
| Model Code 1990 [19] | 1993 | $\tau_R = c.f_{ctd} + \mu.(\sigma_n + \rho.f_y) \leq 0.25.f_{ctd}$ |
| Eurocode 2 [101] | 2004 | $\tau_R = c.f_{ctd} + \mu.\sigma_n + \rho.f_y.(\mu.\sin\alpha + \cos\alpha) \leq 0.5.\nu.f_{cd}$ |
| CSA A23.3-04 [102] | 2004 | $\tau_R = \lambda.\phi_c.\left(c + \mu.\left(\sigma_n + \rho.f_y.\sin\alpha\right)\right) + \phi_2.\rho.f_y.\cos\alpha \leq 0.25.\phi_c.f_c$ |
| ACI 318-11 [75] | 2011 | $\tau_R = \rho.f_y.(\mu.\sin\alpha + \cos\alpha)$ |
| Model Code 2010 [57] | 2013 | $\tau_R = c.{f_c}^{1/3} + \mu.\left(\sigma_n + \rho.k.f_y\right) + \alpha.\rho.\sqrt{f_c.f_y} \leq \beta_c.\nu.f_{cd}$ |

Where:

- *Model Code 1990* – It is divided in two terms, cohesion and friction, in a similar manner to the latest theories at the time, with tabled coefficients of cohesion $c$ and friction $\mu$, accounting for concrete tensile strength $f_{ctd}$ on the former, and external forces and reinforcement crossing the interface for the friction mechanism, and an upper bound for the interface shear capacity at 25% of concrete compressive strength ($0.25.f_{cd}$);

- *Eurocode 2* – Similar to MC90, with main differences being the updated coefficient values and the consideration for the angle of reinforcement $\alpha$ to the interface, which for orthogonal reinforcement equals to the previous model code, decomposing in the normal component $\mu.\rho.f_y.\sin(\alpha)$ responsible for friction and the horizontal component; the upper bound for interface shear capacity was set at $0.5.\nu.f_{cd}$, with $\nu$ being a strength reduction factor defined in the design code;

- *CSA A23.3* – The Canadian design code is also based on similar principles for shear friction, with a slightly different approach, accounting also for the angle of reinforcement to the interface, with updated tabled coefficients including the factor $\lambda$, and assuming that a crack shall be assumed to occur along the shear plane (interface) and relative displacement shall be resisted by cohesion and friction, guaranteed by the interface crossing reinforcement. The term $\lambda.\phi_c.\left(c + \mu.\left(\sigma_n + \rho.f_y.\sin(\alpha)\right)\right)$ shall be limited with the upper bound $0.25.\phi_c.f_c$;

- *ACI 318* – The American design code adopts a different approach to the shear friction mechanism, accounting only for the contribution from interface crossing reinforcement in a similar manner to the Eurocode 2, considering the angle of such reinforcement. Surface classification and the consideration of a modification factor $\lambda$ for concrete density is similar to that of the Canadian design code. The upper bound of such design code depends on whether or not new concrete is of normal density and cast on top of intentionally roughened hardened concrete. If so, shear capacity of the interface is limited by the minimum of $0.2.f_c$, $(3.3 + 0.08.f_c)$, or 11MPa. If any other condition should apply, the upper bound is then limited by the minimum of $0.2.f_c$ or 5.52MPa.

- *Model Code 2010* – The latest design code to date is based on the formulation of Randl [22] established the Extended Shear Friction Theory and explicitly accounts for all specific components of the shear friction mechanism, cohesion/interlocking, friction and dowel action. The model code states the principle that the overall strength of a concrete-to-concrete interface is obtained by combining the Coulomb friction hypothesis with the dowel action effect, thus obtaining the proposed expression above for interface strength. The use of such provisions should account for two scenarios regarding interface behaviour: one for brittle behaviour of the interface, and other for a more ductile behaviour. The first should characterise the strong bond assuming a rigid bond-slip behaviour, and the last where adhesion is neglected and other mechanisms govern the behaviour of the interface. Tabled values are provided in the design code for the coefficients of cohesion, friction, and tensile and dowel action efficiency. The upper bound for the assessment of shear strength through such provisions is set at $\beta_c . \nu . f_{cd}$, where $\beta_c$ is a tabled coefficient that correlates to the angle of the concrete strut and $\nu$ the reduction factor $0.55.(30/f_{ck})^{1/3} \leq 0.55$.

### 2.3.11. Flexural loading of composite concrete cross-sections

The shear-friction theory presented by Birkeland and Birkeland [99] requires that both normal and tangential relative displacements shall occur at the interface, with the last one being a consequence of the first due to the roughness that is recommended for attaining a higher degree of monolithic behaviour. The saw-tooth model illustrates how such roughness impacts deformation at the interface, with the interfacial crack evolving with the relative slip of the two layers, as shown in Figure 2.43. Also, the components of the shear friction mechanism, cohesion and dowel action, all compose the bond capacity of concrete-to-concrete interfaces, with its impact illustrated in the figure below for the evolution of the shear load and interface slip displacement.

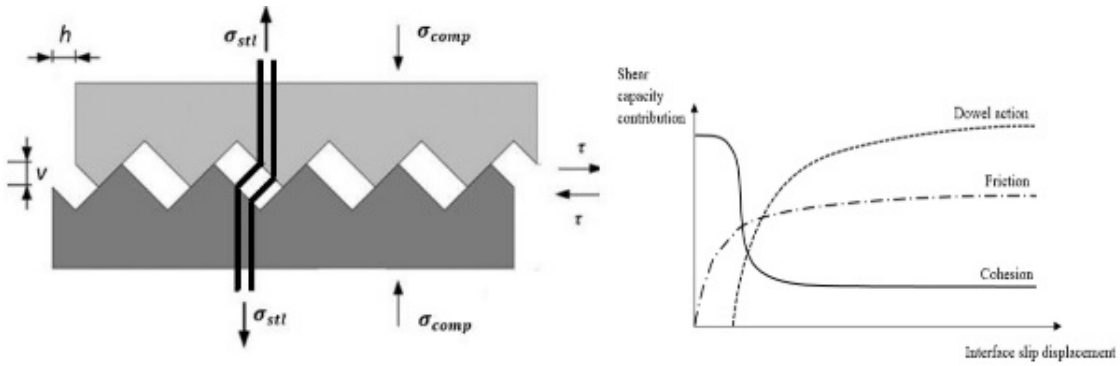


Figure 2.43 – Saw-tooth model presented in [99] and [34]

One can observe the initial impact of cohesion on bond capacity of the interface and loss of performance for smaller slips due to loss of adhesion between the two layers. Both friction and dowel action start low in the load history and become relevant with increased relative displacements, with dowel action becoming relevant for increased slips. Earlier in the load history, interlocking of the two layers increases friction due to compressive stresses of contacting

grooves and ridges of the interface, and aggregate interlock according to the interface model proposed by Walraven [103]. Shrinkage should then be accounted for on the interaction of the two layers, since the differential amount of deformation can cause stresses at the interface and therefore should be controlled to avoid premature debonding. Such phenomenon is worked analytically by Zhou *et al* [104], where the authors stated that differential shrinkage can induce a stress state of compression on the existing layer, with consequent tension of the new layer, as depicted in Figure 2.44, and therefore should be assessed.

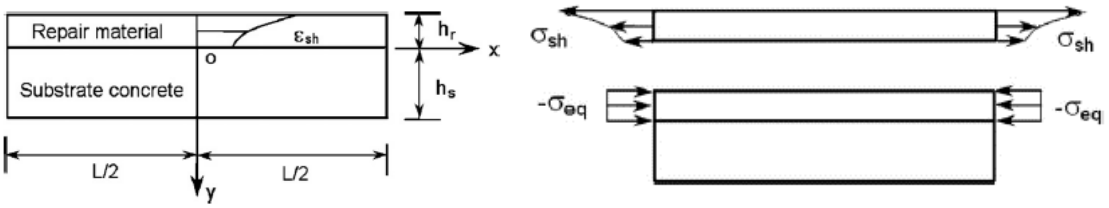


Figure 2.44 – The effect of shrinkage on the existing concrete layer (adapted from [104]).

The acting compressive stress on the existing layer $\sigma_{eq}$ is then calculated by integrating the stress due to shrinkage on the overlaid concrete $\sigma_{sh} = E_r . \varepsilon_{sh}$, where $E_r$ is the young modulus of the strengthening layer and $\varepsilon_{sh}$ is the strain due to shrinkage of such layer. The resulting calculation is then:

$$\sigma_{eq} = \frac{1}{h_r} . \int E_r . \varepsilon_{sh}(y)\, dy \tag{2.23}$$

Although previous studies presented in [40] suggest that thin overlays are easier to debond than thicker ones [105], others show no dependence on overlay thickness regarding bond strength [106]. When differential shrinkage between the substratum and overlay is significant, shear stresses in the interface and consequent cracking may result at the overlay, reducing bond between the substratum and the concrete overlay. Thickness of the concrete layer is especially relevant, since the greater thickness results in a greater lever-arm of rebar forces on the flexural reinforcement and consequently larger tensile and compressive stresses at the interface. Cracking that results from flexural loading the composite cross-section is usually composed of modes I (normal) and II (tangential) of fracture mechanics, in a mixed-mode manner as depicted in Figure 2.45 below.

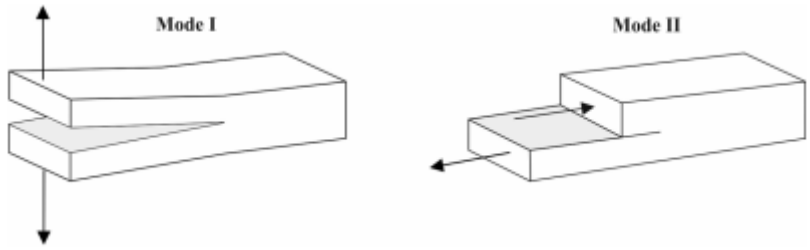


Figure 2.45 – Stresses on an infinitesimal concrete section in mixed-mode fracture (adapted from [107])

This figure also shows that validating the tensile performance through pull-off testing is accepted according to [33], since cracking in concrete occurs in a combination of modes I (tension) and II (in-plane shear) of fracture mechanics, respectively depicted in the same figure. Such publication also references the results of Van Mier *et al*. [108] where the author states that most interface shear failure initiates in mode I and true mode II failure is very difficult to obtain. Also, characterisation by Granju [39] stated that although the mixed mode stress state is common at the interface, debonding is always initiated by tensile stresses perpendicular to the interface (mode I).

### 2.3.12. Numerical modelling of concrete-to-concrete interfaces

To further improve the knowledge of the interface between concrete with different ages, numerical modelling can assist in identifying and characterising the behaviour of a concrete-to-concrete interface. The latter has been described in the literature, with its components identified and quantified through several design models. The nonlinear Finite Elements (FE) modelling software can numerically simulate the experimental tests, analysing cracking patterns and stress distribution through both layers, also accounting for the interface.

Atashi *et al*. [109] worked on the numerical modelling of overlaid concrete, mainly concerning the application on the tensile face, as illustrated in Figure 2.46. The authors mainly studied the uplift phenomenon on beam elements, with results that allowed to withdraw conclusions about overlay thickness, concrete strength of both layers and flexural reinforcement on the overlaid concrete. The latter has a direct impact on cracking of such layer, since it limits crack opening and improves flexural stiffness.

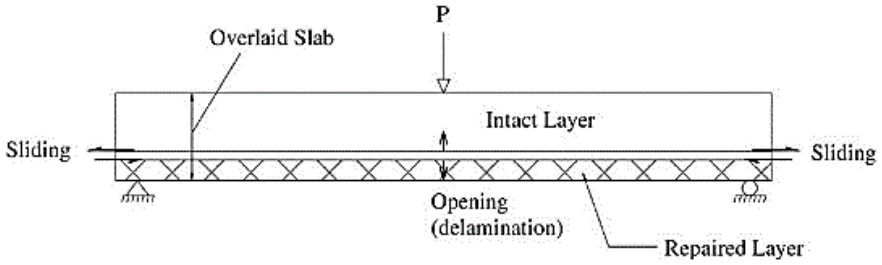


Figure 2.46 – Strengthening layer applied on the tensile face (adapted from [109]).

For an overlay with constrained edge deformation, sliding at the edge of the new layer due to the relative displacement being larger at this zone, and separation close to the midpoint due to the flexural deformation of the layers govern the uplift phenomenon. The inclusion of longitudinal reinforcement assists on controlling the uplift phenomenon and can shift the stresses that act on it to allowable values for controlling the debonding phenomenon, as illustrated in Figure 2.47.

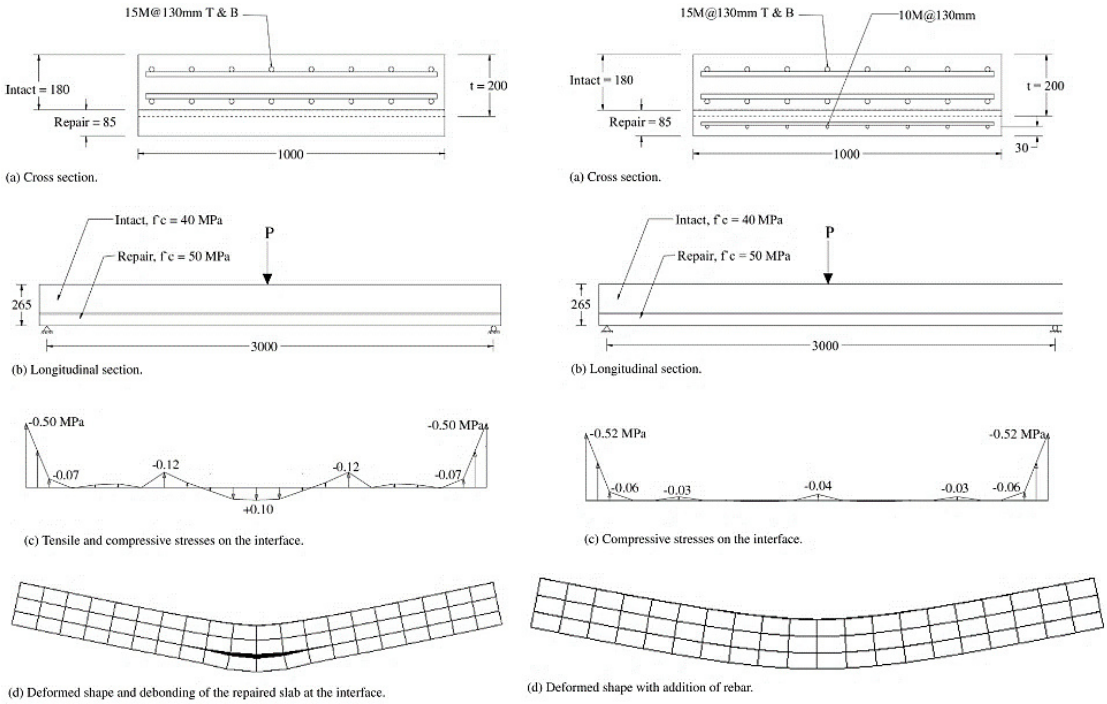


Figure 2.47 – Strengthening layer applied on the tensile face (adapted from [109]).

Other aspect denoted in this work is the importance of limiting stresses normal to the interface, where the authors recommend the use of bonding agents between the two concrete layers when strengthening is performed in the tensile face. Debonding as a result of perpendicular stresses further justifies the use of reinforcement crossing the interface, thus improving both the tensile and dowel action capability of steel reinforcement. Another decisive factor on the behaviour of concrete-to-concrete interfaces is cracking of the cross-section for tensile stresses. Flexural cracking of concrete structures occurs in the tensile regions, with cracks resulting from reaching the tensile strength of concrete as a release of stored energy. Due to reinforcement, these cracks result more or less regularly spaced in the span of the concrete element, depending on its flexural stiffness.

The work presented by Benzerzour *et al*. [110] on slab panels strengthened with overlaid concrete on the tensile face, as depicted in Figure 2.48, that were loaded cyclically to assess crack growth, showed that flexural cracking can change the signal of normal stresses at the interface between the two layers. In such work, the interface between the concrete layers was modelled through 5mm contact elements with elastic behaviour. Such option was to identify the interface stresses that develop through the load history of the specimen. One should consider that loading was cyclic, which causes the fatigue of structural elements and of the interface, as stated by the authors.

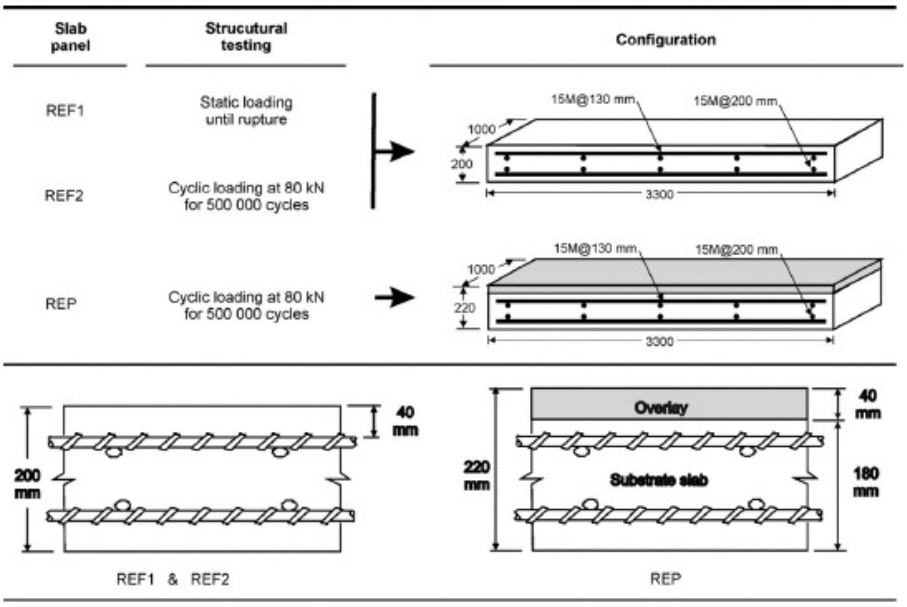


Figure 2.48 – Specimen geometry and overlay strengthening on the tensile face (extracted from [110]).

The local equilibrium of normal stresses on the interface between these cracks results then in tensile stresses closer to the cracks and compressive stresses further from these, as depicted in Figure 2.49. Such distribution of stresses results from the curvature due to the flexural deformation and the differential stiffness between the two layers. When the bending moment is increased, one can observe the evolution of the crack opening and the concentration of normal stresses further from the cracks. The authors recall the capability of reinforcement or fibres on the overlaid concrete to control the debonding phenomenon at a premature stage. This happens due to the limiting of tensile stresses thus reducing cracking and consequently the normal stresses at the interface that cause debonding.

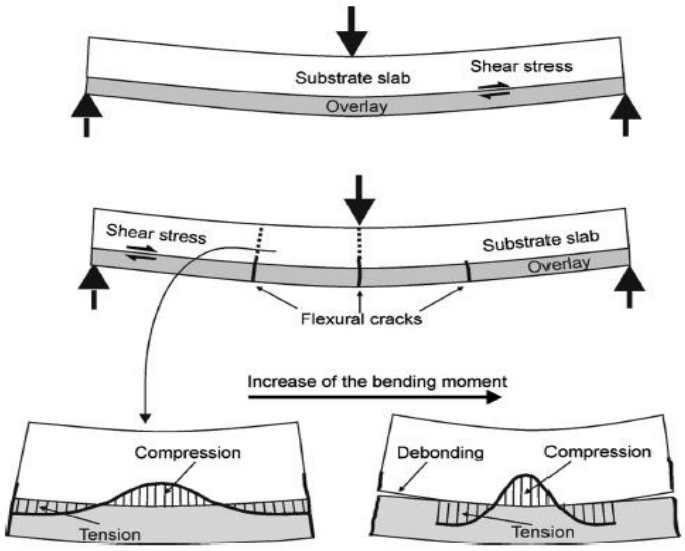


Figure 2.49 – Normal stresses at the interface between cracks (extracted from [110]).

The authors also reported a good correlation to the cracks assessed experimentally, validating the numerical model and the behaviour of the interface through the adopted method for modelling such structural discontinuity. The unreinforced concrete overlay considered allowed for a smaller number of flexural cracks closer to midspan, that caused the signal inversion of the interface normal stresses as depicted in Figure 2.50. One can extrapolate that for a reinforced concrete overlay such signal inversion would occur throughout the interface and the aforementioned concentration of stresses would also form between cracks.

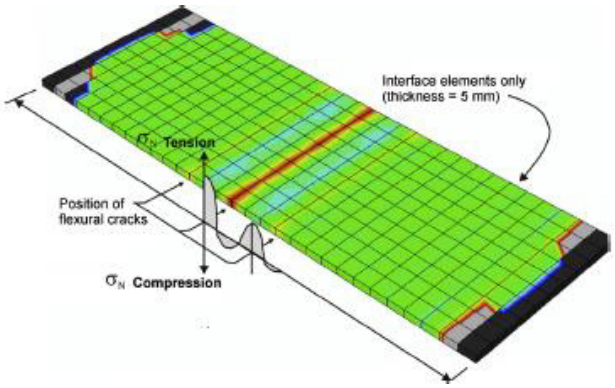


Figure 2.50 – Signal inversion of normal stresses at the interface between cracks (adapted from [110]).

Nowadays, the nonlinear analysis software for structural concrete can predict structural failure by using complex constitutive models for concrete with several material parameters defined according to experimental data. These are usually based on a predictor-corrector method for the analysis, mainly the Modified Newton Raphson method with tangent predictor and line search [111]. When reinforcement crossing an interface is provided, ductilization of such interface results in the relative slip or sliding of the two layers prior to failure. This relative slip then relates to the shear stress at the interface, as considered by several models [21,29,112–114], which depends on the roughness profile, crack opening, and concrete strength. When no reinforcement crosses the crack, a linear or multilinear stress-displacement curve with a kink point like the one on the left of

Figure 2.51 can be applied. The kink point is referenced in the bibliography and determined according to empirical data collected from various tests [115–117]. When a minimum amount of reinforcement crosses the crack, the progressive softening occurs, with exponential and power curves best fitting the relationship between stress and relative displacement.

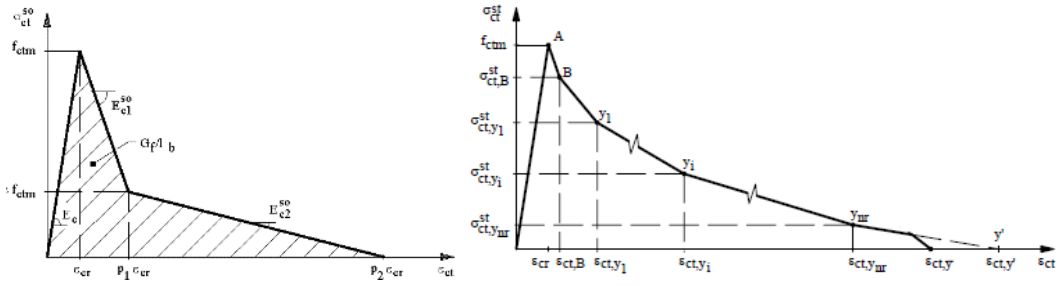


Figure 2.51 - Softening of stresses without/with reinforcement crossing the interface (extracted from [118]).

A softening law for that interface is important for the nonlinear modelling of the interface between two materials, for the characterisation of the debonding phenomenon. FE modelling of a concrete-to-concrete interface can be performed with discrete or zero-thickness elements, with the latter elements composed by a set of parameters that characterise the stiffness and bond capacity of the interface. In [119] this type of elements are referred to as a contact or damage/plasticity models, whichever work best with the intended behaviour of the composite cross-section, as depicted in Figure 2.52 for zero-thickness interface elements.

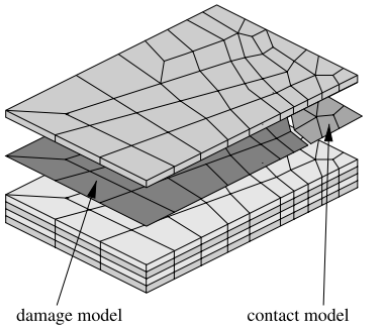


Figure 2.52 – Zero-thickness elements (adapted from [119]).

These elements should be fitted with a law for debonding, if such phenomenon should be brittle, quasi-brittle or ductile. The brittle case is the one where failure occurs after the peak bonding stresses are reached, decreasing the interface capacity to zero. The most common cases are the ones referred in [119], quasi-brittle and ductile, with the respective stress-displacement relationships depicted in Figure 2.53.

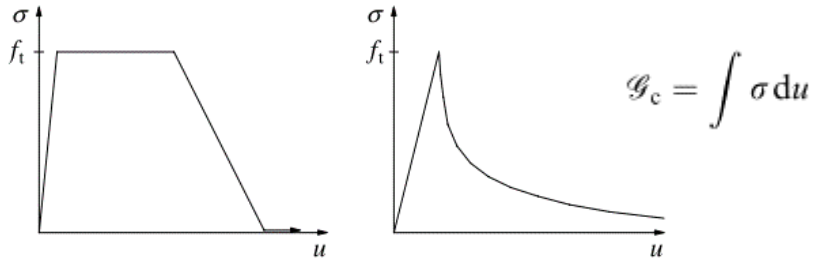


Figure 2.53 – Interface stress-displacement relationships (ductile and quasi-brittle, adapted from [120]).

The size required for a patch of overlaid concrete is considerable when accounting for all the phenomena that develops when a structure is loaded, mainly cracking, shrinkage and anchoring of reinforcement. Therefore, the cohesive forces that develop in the fracture process zone should be accounted for, with Hillerborg's fictitious crack model suitably fitting such behaviour [121]. This model states that crack initiation starts with the reaching of tensile capacity by the interface normal stress. When the relative deformation reaches a critical value that limits stress transfer, the real crack starts to occur due the null characteristic of normal stresses.

The simple constitutive model for a general three-dimensional case is given in terms of normal and tangential stresses, and respective relative displacements, by:

$$\begin{Bmatrix}\tau_1\\ \tau_2\\ \sigma\end{Bmatrix} = \begin{bmatrix}k_{tt} & 0 & 0\\ 0 & k_{tt} & 0\\ 0 & 0 & k_{nn}\end{bmatrix}.\begin{Bmatrix}\Delta v_1\\ \Delta v_2\\ \Delta \mathrm{u}\end{Bmatrix} \tag{2.24}$$

Where $\tau_1$, $\tau_2$ and $\sigma$ are the shear stresses on directions 1 and 2 of the interface and tensile stresses, respectively, with $\Delta v_1$, $\Delta v_2$ and $\Delta u$ the respective relative displacements of contacting layers, $k_{tt}$ and $k_{nn}$ the interface tangential and normal stiffnesses. For a two-dimensional analysis, the second row and column can be omitted. $k_{tt}$ and $k_{nn}$ denote the initial elastic shear and normal stiffness, respectively. Interface width $t$ is a relative term when evaluating rough concrete interfaces because no discrete interface can be identified, hence no direct value can be assessed. A recommended calculation is provided in the software ATENA 3D® documentation [122], regarding the lowest young modulus and respective FE dimensions, to estimate stiffness values using the following:

$$k_{nn} = \frac{E}{t} \tag{2.25}$$

$$k_{tt} = \frac{G}{t} = \frac{k_{nn}}{2.(1+\upsilon)} \tag{2.26}$$

Such parameters are important when characterising interface behaviour until the stress peak due to loss of adhesion, with the softening of stresses composing the next stage of the debonding phenomenon. The peak of stresses after the initial positive slope are illustrated in Figure 2.54, where the exponential softening of stresses is also shown.

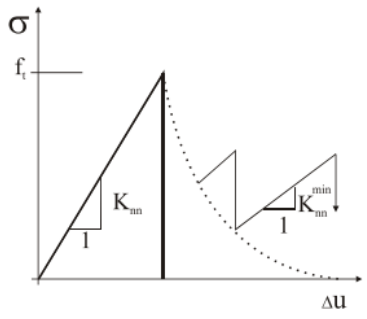


Figure 2.54 - Behaviour of the interface between two macroelements regarding normal and tangential stresses (extracted from [123]).

$k_{nn,min}$ and $k_{tt,min}$ parameters are related to numerical stability and recommended to be taken as 100 or 1000 times smaller than the respective normal and tangential stiffnesses [122]. The adopted failure criterion was the Mohr-Coulomb with tension cut-off, as illustrated in Figure 2.55, where $f_t$ is the interface tensile stress, $c$ the cohesion of the interface, $\phi$ the angle of friction, and $\tau$ and $\sigma$ respectively the interface tangential and normal stresses.

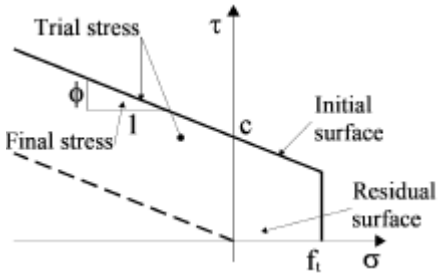


Figure 2.55 - Mohr-Coulomb failure criterion at the interface [124].

This surface is governed by equation (2.27) until tensile limit stress is reached, then by equation (2.28) when shear stress becomes null because no contact exists between the surfaces.

$$|\tau| \leq c + \sigma.\phi \text{ for } \sigma \leq f_t \tag{2.27}$$

$$\tau = 0 \text{ for } \sigma \geq f_t \tag{2.28}$$

After stresses violate this condition, the failure surface collapses to a residual surface. This is due to the larger displacements that no longer include the material cohesion or tensile strength, accounting only for friction between the two layers. The tensile and shear softening are defined based on the fracture energy associated with each mode.

## 2.4. Bending and punching of flat slabs

### 2.4.1. Bending and shear on flat slabs

The inherent improvement of a flat slab over other structural solutions, such as slabs with beams, needs to meet some requirements before it is validated as such. The main advantage of flat slabs over slabs with beams is the attained slenderness due to its comparatively low thickness. The problem poses then due to the discrete supports of the flat slab, which are the columns that guarantee the clear ceiling height between floors. Concrete material then allows for certain span lengths between such supports without the need for beams, intrinsically related to the slab's thickness. Such relationship is stated in the current design codes and regulations, namely on the Eurocode 2 [101] for flat slabs, where the span-to-depth-ratio (L/d) is defined according to the reinforcement ratio of the slab. Depending on whether concrete is lightly reinforced ($\rho \leq 0{,}5\%$) or heavily reinforced ($\rho \geq 1{,}5\%$), the ratio L/d is respectively 24 or 17, taken for average material conditions of a class C30 concrete and a steel stress of 310MPa. The ratios L/d in-between can be interpolated, and for two direction flat slabs the longer span should always be considered. A reference is made to the conservative aspect of such ratios, allowing for slabs that are even more slender than those preconised. This is then a problem for the structure's service state, where deformation and consequent cracking need to be controlled to prevent second order effects to the structure. Vollum and Hossain [125] also address this characteristic, stating the rules on such design code being conservative although it allows for thinner slabs than other design codes. The authors also address the fact of concrete cracking during construction which affects the structure's

long term condition, leading to excessive deformation and therefore exceeding the design code limit of L/250. Consequently, rebar protection is not guaranteed due to cracking, thus affecting structural integrity and the ultimate limit state. The slenderness of flat slabs leads to the bending moment being preponderant to the design of such structural elements, considering the sagging moments at midspan and hogging moments at the column supports, as illustrated in Figure 2.56.

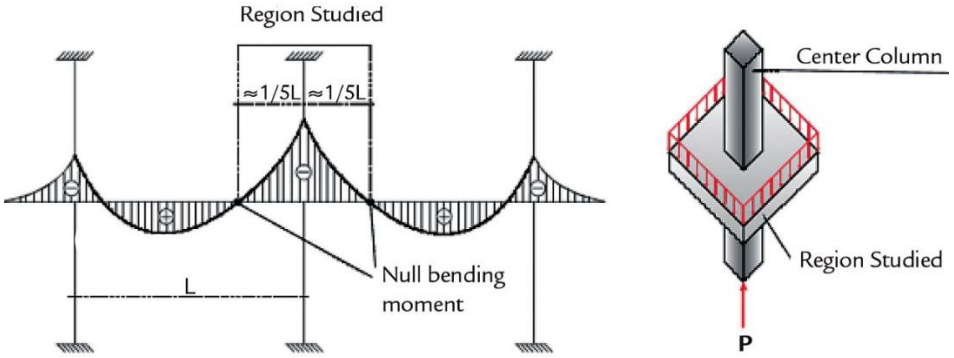


Figure 2.56 – Sagging and hogging moments on continuous slabs (extracted from [126]).

The larger the spans of column-supported slabs can lead to insufficient reinforcement for sagging moments, also resulting in greater hogging moments, and consequent cracking on the lower face at midspan and upper face near the column regions. The latter regions are prone to punching due to the concentrated load of the supporting column, whose failure mode comprises a critical shear crack that reaches the upper face of the slab. Cracking due to poor flexural design can then result in pre-cracking of the punching control perimeter, reducing the structure's service and ultimate limit state capacity.

Due to the slenderness of flat slabs, shear is usually dealt with through the arch effect of compressive stresses in the upper face of the slab's span which direct to the column support. Such effect is depicted in Figure 2.57, along with the two shear failure mechanisms of flat slabs. Shear failure can occur in a slab with insufficient reinforcement, usually a one-way slab or a specific slab span that is lightly reinforced. Punching of the slab by the supporting column is a particular failure mechanism by shear in two-way slabs and the more recurrent type of failure on flat slabs.

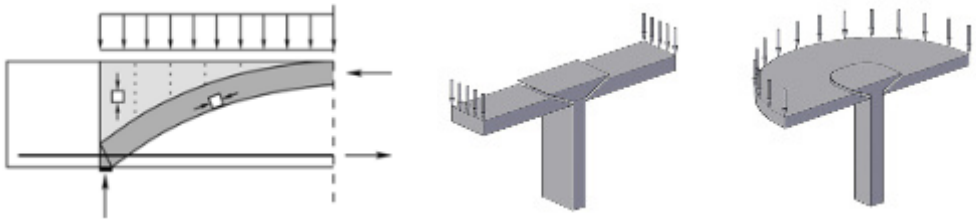

Figure 2.57 – Arch effect, one-way shear and punching shear of flat slabs (adapted from [127]).

The analysis of two-way flat slabs is usually performed considering strips of a given width connecting the supporting columns as depicted in Figure 2.58. Such width can be determined for each case depending on the intended analysis, with the quarter length of the perpendicular span generally adopted as illustrated in the figure below, or simply limited by the null-moment (contra-flexure) line of the slab illustrated in Figure 2.58 at a distance of L/5 from the column face.

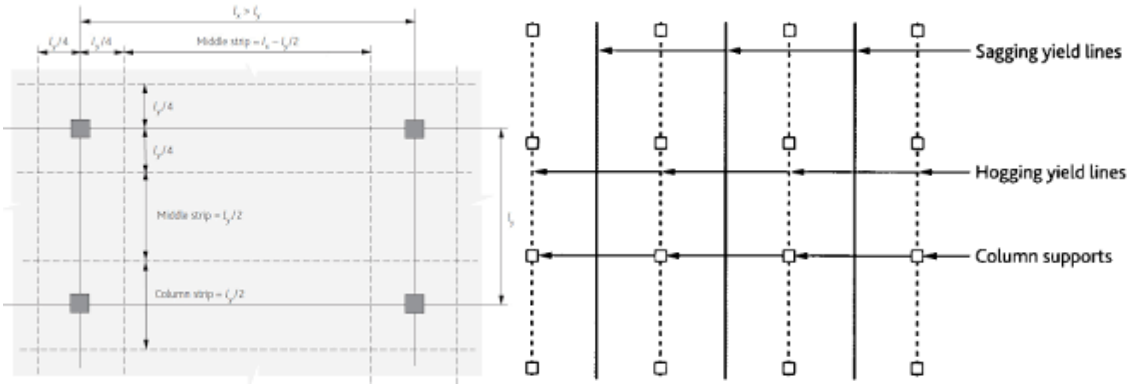


Figure 2.58 – Strips connecting the column supports for flexural design and lines of contra-flexure (adapted from [126]).

The depiction above of the null-moment lines reflects then the case of a one-way flexural analysis. A two-way flexural analysis presented in Figure 2.59 shows the small region of the column supports where the hogging moments are concentrated, thus concentrating stresses on such zones where punching failure can occur. Due to the magnitude of hogging moments in the column region when compared to sagging moments at midspan, detailing determines the behaviour of the column-slab connection and capacity for punching.

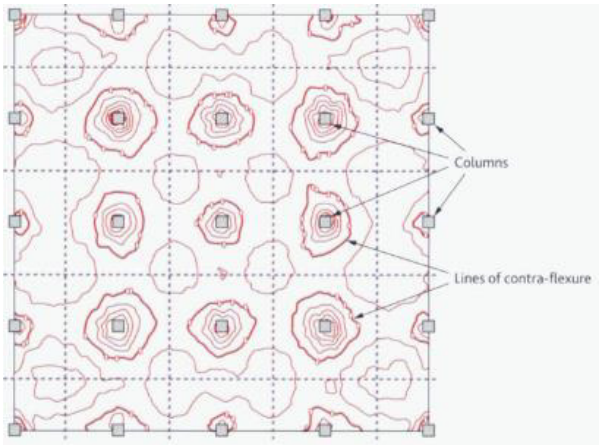


Figure 2.59 – Lines of contra-flexure on two-way slabs (extracted from [126]).

Punching of flat slabs can be related to the flexural capacity of the slab. In [128], it is stated that early literature suggests punching shear a second order effect, had yielding of reinforcement already occurred before in the load history. Yielding of reinforcement leads to radial cracking in the column region and further opening of tangential cracks due to the punching mechanism. Guandalini *et al*. [129] state that design codes, by not accounting for the flexural reinforcement, can yield unsafe estimate of punching shear strength. Lower reinforcement ratios can govern the slab behaviour through yielding of reinforcement and reduced punching strength. The yield lines presented in Figure 2.60 show the expected tipping lines due to the rectangular column geometry. These are the lines of the governing flexural cracks, although several radial cracks shall form due to punching stresses on the column region.

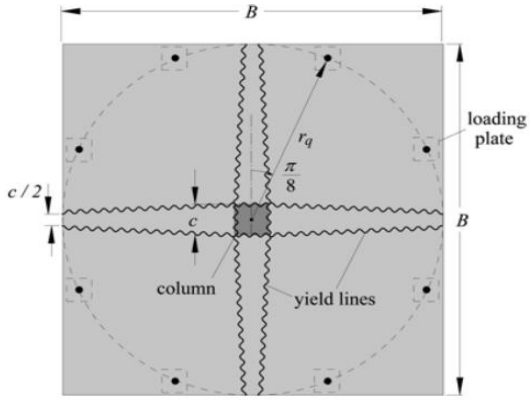


Figure 2.60 – Yield-lines due to flexural punching (extracted from [129]).

### 2.4.2. Punching on flat slabs

The mechanical models that nowadays allow for the analysis and prediction of the failure load and behaviour of the column-slab connection in flat slabs are based on the continuous development of behaviour models introduced in the beginning of the twentieth century. Such models are still valid due to the verified nature of its physical and mechanical principles and consist on a strong reference to the study of the punching phenomenon. Although earlier references exist to the study of the punching phenomenon, the renowned mechanical model of Kinnunen and Nylander originated in Sweden in 1960 [130] is recognized as one of the first models able to characterise the punching behaviour in flat slabs. The schematics of the parameters illustrated in Figure 2.61 serve as the basis for other behavioural models of punching on flat slabs. Over sixty tests in circular slabs composed the basis of such model, loaded by circular columns with its reinforcement placed radially and tangentially to the latter. Rectangular shaped slabs can also use this model, using the equivalent perimeter that can be inscribed in its shape. The failure mode considered on such model was observed on all tests, where a tangential crack around the column was the radial inclined failure crack from the column face.

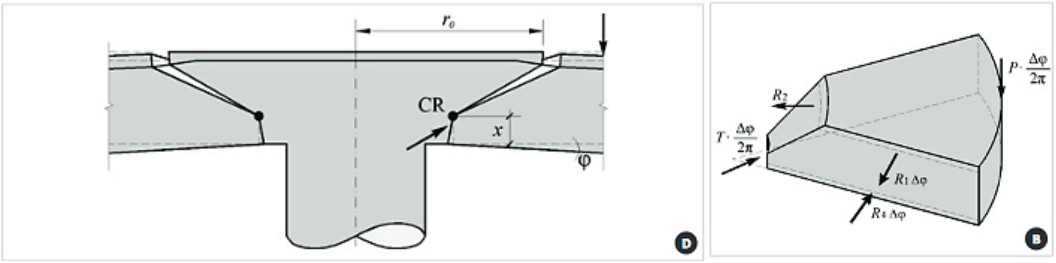


Figure 2.61 – Kinnunen and Nylander mechanical model for punching (extracted from [130]).

One key factor from this model is the consideration for slab rotation, and hence its deformation, allowing to characterise the kinematic equilibrium of each element between radial cracks, the tangential critical shear crack and the edge of the slab. Such rotation requires a center of rotation which is also coincidental with the compressed strut that is also one of the main characteristics of this model. The increase of compressive strains on the strut results in the release of stored energy

through the critical shear crack, with the center portion inside this perimeter remaining undeformed and the rigid bodies outside such perimeter deforming according to the level of load.

The model presented by Muttoni [131] also made use of Kinnunen and Nylander's theory and definition of the main parameters of column-slab connections and in a punching situation. Thus, derived the Critical Shear Crack Theory (CSCT), where a flexural crack evolves with the increase of the slab's deformation and becomes critical to the shear stress transfer between the column-supported portion and the rigid segments that rotate with the increase of slab load, as depicted in Figure 2.62. Such behaviour leads to the reduction of strength of the inclined strut and failure by punching of the slab may occur.

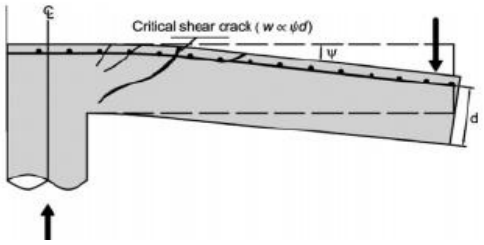


Figure 2.62 – Muttoni critical shear crack model (extracted from [131]).

The geometric characteristics of the crack are key to the model proposed by Muttoni, since the opening and sliding of this crack govern the behaviour and response of the loaded column-slab connection. Therefore, aggregate interlock plays a major role in governing the behaviour of the critical shear crack and can be described as the aggregate's effect on the sliding of the contacting surfaces that further assists opening of the crack and contributes with the strength to crushing of both aggregate and concrete. One should note that such contribution occurs solely on the compressed portion of the crack where friction can be generated by compressive forces for the aggregate interlock. The failure criterion to be considered results as a function of the width of the critical shear crack $w \propto \psi . d$ according to [131], where $\psi$ is slab rotation and $d$ the effective depth of the slab. The figure below illustrates the relationship between material properties of concrete and the behaviour of a rough crack opening. Such formulation allowed for the good fitting of 99 punching tests from the literature at that time, as depicted in Figure 2.63.

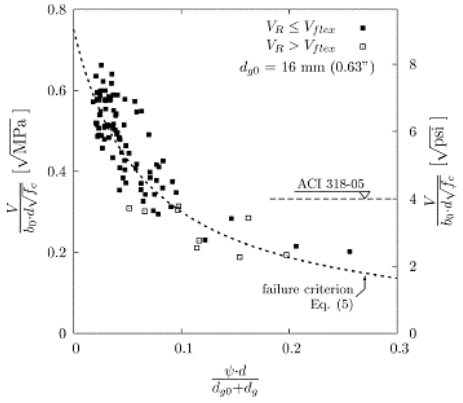


Figure 2.63 – Depiction of the failure criterion according to CSCT fitting experimental results from the literature (extracted from [131]).

The failure criterion depicted above is the basis of the CSCT, where punching stress $\upsilon_{Rd} = \frac{V_{Rd}}{b_0.d}$ is scaled by the inverse of square root of concrete compressive strength $\frac{1}{\sqrt{f_c}}$ and crack width $w$ is scaled by aggregate size factor $\frac{1}{(d_{g0}+d_g)}$, for the equality:

$$\frac{V_{Rd}}{b_0.d.\sqrt{f_c}} = \frac{3/4}{1 + 15.\frac{w}{(d_{g0} + d_g)}} \tag{2.29}$$

The evolution of slab rotation is accompanied by the curvature of the slab due to reinforcement strains that allows for tension stiffening. Such relationship can be characterised as the quadrilinear relationship between moment and curvature in Figure 2.64. A reference is made to the dashed line depicted in the figure below, which results from neglecting concrete tensile strength and tension stiffening, thus not accounting for the cracking phenomenon and only the yielding of flexural reinforcement.

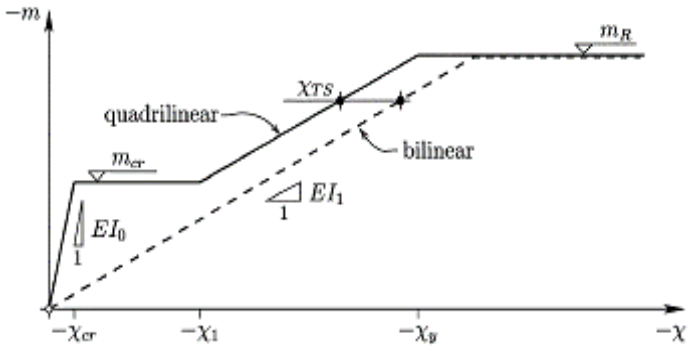


Figure 2.64 – Depiction of the quadrilinear moment-curvature relationship for punching of a flat slab (adapted from [131]).

The angle of the critical shear crack can identify the structural response of the column-slab connection, whether mainly shear or flexural capacity of the cross-section will govern failure. A higher slope of the critical shear crack identifies the higher flexural stiffness of the cross-section, and therefore failure occurring in shear close to the column region. Consequently, a lower slope identifies a lower flexural stiffness and horizontal stresses develop on the cross-section. Considering the infinitesimal equilibrium provided by the Mohr Coulomb theory, increasing compressive stresses results in tensile stresses on the perpendicular direction, hence the critical shear crack when the tensile capacity of concrete is reached.

Bompa and Onet [132] proposed a calculation of the punching strength of flat slabs, assuming it depends on the slope of a singular critical shear crack responsible for the conical shape of the failure cone of column-slab connections. The premise is that the slope of this crack can identify the amount of shear on such mechanism, depending on the amount of reinforcement and where such reinforcement is crossed by the critical shear crack by accounting for the slenderness of the slab and concrete size effect. The angle of such crack also governs the loaded area and thus the punching control perimeter depicted in Figure 2.65. The conical shape characterised by angle θ,

slenderness characterised by the effective depth $d$, and the Mohr-Coulomb theory principles can be observed in the figure below.

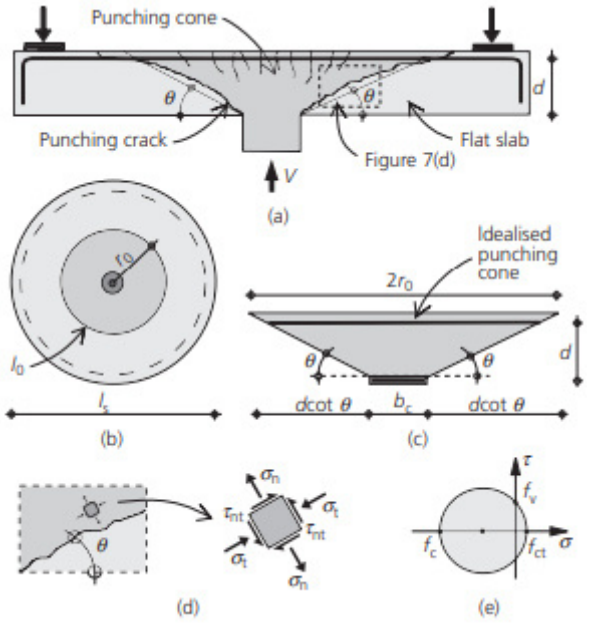


Figure 2.65 – Punching control perimeter and the Mohr-Coulomb criterion for the critical shear crack (extracted from [132]).

Considering concrete as a Coulomb material, typical failure modes are sliding and separation when the tensile strength is reached. Prior to separation of the two bodies, concrete can withstand a stress equal to the tensile strength in the normal direction to the crack ($\sigma_n$=$f_{ct}$). The shear strength $f_v$ in the region can be predicted using the Mohr–Coulomb criterion illustrated by Figure 2.65 (e). All these considerations result in a punching control perimeter also depending on the slope of the critical shear crack, with the proposed method for calculating such parameter in equation (2.30). Considering a set of 21 tests with resulting angles from the observation of saw-cuts between 20º and 49º, a correlation was attained with the punching strength of such slabs.

Calculation of the punching strength is then performed through equation (2.30), where $r_0$ is the punching control perimeter and ξ the parameter that accounts for the fracture mechanics of concrete.

$$V_R = 2.\pi.d.{f_c}^{1/3}.\left(0{,}4.d + \rho.{f_y}^{1/3}.r_0\right).\xi \qquad (2.30)$$

According to such work, punching strength of a given slab can be directly related to the angle of the critical shear crack, directly affecting the punching control perimeter $r_0 = d.cotg(\theta) + r_c$, where $r_c$ is the column size. Concrete fracture mechanics also play a role in such quantification of the punching strength through parameter $\xi = 0.75 + (d/l_{ch})^{-0.2}$, with $l_{ch} = E_c.G_F/{f_{ct}}^2$ the characteristic length parameter that accounts for the concrete elastic modulus $E_c$, concrete tensile strength $f_{ct}$, and concrete fracture energy according to provisions on MC2010 [57] ($G_F = 73.{f_c}^{0,18}$). The authors state that accounting for a variable angle of the critical shear crack, the

proposed calculation can predict the ultimate punching strength for extreme geometrical and material configurations such as low reinforcement ratios and high-strength concretes.

Another approach to the punching mechanism where the angle of the critical shear crack is explicitly accounted for was proposed by Birkle *et al*. [133]. The authors then propose that a rectangular loading plate can generate four failure surfaces from the sides of such loading plate, in analogy to the homothetic projection from one side to the other of a given slab thickness $h$. The shear force at the failure surface $S$ results from the compressive strut of the punching mechanism. The homothetic projection of a loading plate results on a perimeter dimension on the opposite side of the slab which is given by the tangent relation of angle $\theta$. These parameters are illustrated in Figure 2.66 for a rectangular loading plate and consequently asymmetric failure surfaces on both directions.

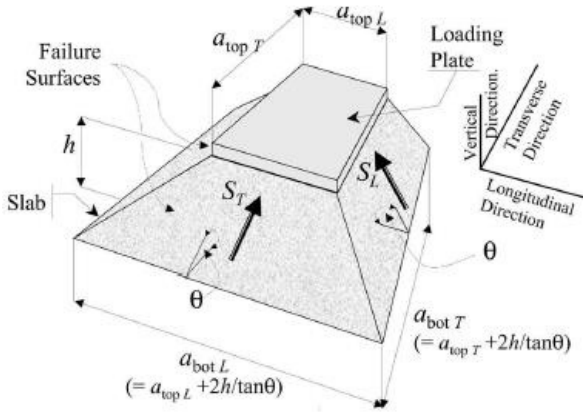


Figure 2.66 – Punching model considering the failure surfaces of the critical shear crack (adapted from [133]).

The effective area $A$ of each failure surface can then be calculated according to geometrical considerations, allowing for the characterisation of shear stress $\tau$ on the shear crack surface, considering the shear force $S$ ($\tau = S/A$). Punching strength of each side of the loading plate is then calculated according to equation (2.31), with total punching capacity resulting from the sum of the strength on each side ($V_R = \sum V_{r,s}$). For square loading plates, the punching capacity is then four times the strength of one side of such plate.

$$V_{r,s} = \frac{3}{8} \cdot \left(\frac{30}{f'_c}\right)^{1/4} \cdot \left(\frac{500}{h}\right)^{\frac{1}{4}} \cdot (f'_c)^{\frac{1}{2}} . A . \tan(\theta) \tag{2.31}$$

The punching model proposed by the author was then compared to current design codes at the time, with good correlation between these and the application of the punching model as depicted in Figure 2.67, where the ratio between experimental and theoretical results close to the unity can be observed.

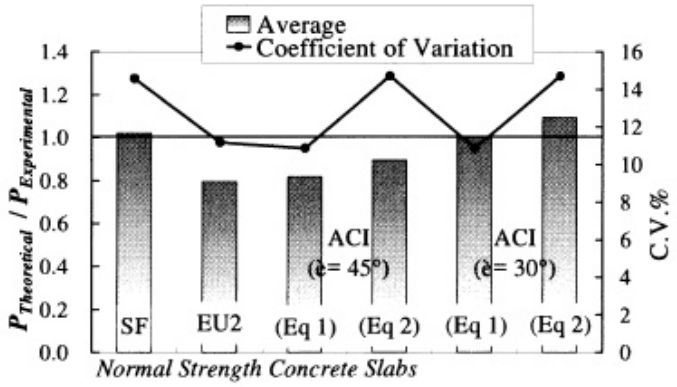


Figure 2.67 – Comparison of the proposed model to design codes (extracted from [133]).

## 2.4.3. Code provisions for punching design

### 2.4.3.1. Model Code 1978 and REBAP

The provision for the verification of shear in concrete structures on the Portuguese code REBAP – Regulamento de Estruturas de Betão Armado e Pré-esforçado [134] was based on provisions of the Model Code 1978 (MC1978) [15]. Such provisions were based on a variation of the Mörsch theory for trusses. Designing with such principle is based on the limitation of the compressive stresses on the concrete struts and tensile stresses on the longitudinal reinforcement. The particular case of punching shear required that a laminar structural element was loaded by a significant concentrated load, distant enough from other loads and from the edge of the slab at least five times the effective depth of the slab. This model can account for specific punching reinforcement and shifting of flexural moments for detailing the longitudinal reinforcement on the slab, specifically on the column-slab connection.

Quantification of punching strength was then calculated according to equation (2.32), where $u$ is the control perimeter for loading regarding the punching phenomenon, $d$ is the effective depth of the loaded slab, and $\tau_1$ is a reference shear stress provided on chapter 53.2 of that norm. This coefficient is quantified by $\tau_1 = 0.6.f_{ctk,0.05}/\gamma_c$, where $f_{ctk,0.05}$ is the lower percentile characteristic tensile stress for concrete and $\gamma_c$ the minoring factor of 1.5 for concrete, and the coefficient $\eta = (1.6 - d) \geq 1.0$.

$$V_{Rd} = \upsilon_{Rd}.u = (\eta.\tau_1.d).u \text{ (kN)} \quad (2.32)$$

Limitations of this norm state that the loaded area should not exceed 3.5 times the effective depth of the slab for a circular control perimeter, 11 times the effective depth and the length or width should not exceed twice the other for a rectangular loaded area.

Parallel to the provisions of the MC1978, the REBAP norm sets the control perimeter for the punching phenomenon at half the effective depth of the slab, from the column face. Such conditions must be verified for columns of all geometries as identified in Figure 2.68.

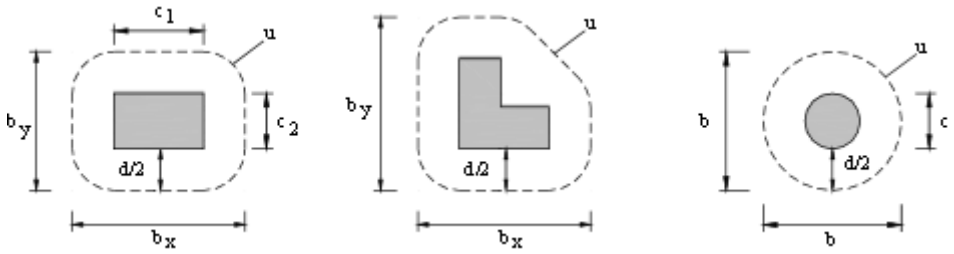


Figure 2.68 – Control perimeter for the punching phenomenon (extracted from [134]).

When reinforcement specific for punching is installed, the norm preconises that the resulting punching capacity should not exceed four thirds of the rebar strength on the perpendicular direction, limiting its yield stress $f_{syd}$ to 350MPa. Quantification of the increased strength due to specific reinforcement can be calculated through equation (2.33), where $A_{sw}/s$ is the area of the regularly spaced perimeter of specific reinforcement, and $\alpha$ the angle of such reinforcement and the plane of the slab. Such quantification should not exceed 60% in excess of the punching strength.

$$V_{Rd} = \frac{4}{3}.\frac{A_{sw}}{s}.f_{syd}.sen(\alpha) \text{ (kN)} \quad (2.33)$$

### 2.4.3.2. Model Code 1990 and Eurocode 2

The subsequent Model Code 1990 (MC1990) [19] and the Eurocode 2 (EC2) [101] also present several parallelisms to its provisions, namely the control perimeter for the punching phenomenon at a distance not smaller than two times the slab's effective depth, according to the schematics depicted in Figure 2.69.

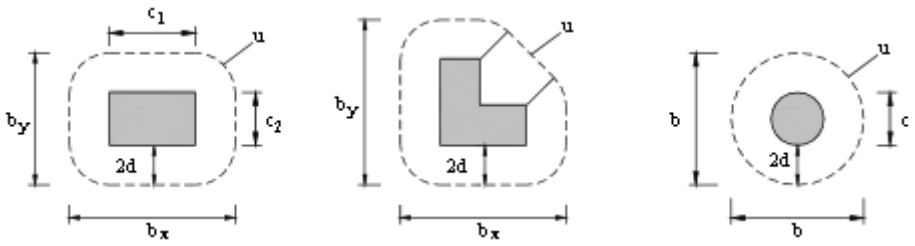


Figure 2.69 – Control perimeter for the punching phenomenon acc. to MC1990 and EC2 (extracted from [101]).

The foundations for such perimeter were that the shear stress was uniform at that distance from the column face, as stated in the MC90 [19]. The EC 2 [101] adopted the principles of the MC90, with the calculation of the slab's punching strength resulting very similar between both codes, and can be calculated through equation (2.34) for the concrete strength without specific reinforcement on both codes. Such quantification of the punching strength of concrete flat slabs is derived from experimental tests and therefore empirical in its nature. The main parameters that define it are the ratio of flexural reinforcement $A_{sl}$, calculated as $\rho_l = \sqrt{\rho_{lx}.\rho_{ly}}$ (with $\rho_{lx}$ or $\rho_{ly} = A_{sl}/(b.d)$)

within a slab width equal to the column plus $3d$ to each side, and the size effect factor $\xi = 1 + \sqrt{200/d}$.

$$V_{Rd,c} = \frac{0{,}18}{\gamma_c}.\xi.(100.\rho.f_{ck})^{1/3}.u_1.d \leq 0{,}035.(\xi)^{\frac{2}{3}}.(f_{ck})^{0{,}5}.u_1.d \text{ (kN)} \quad (2.34)$$

The control perimeter for the punching phenomenon $u_1$ is then set at $2d$ from the column face, and the concrete characteristic strength $f_{ck}$ is considered for the calculation of the slab's punching strength. The right side of the inequation represents the minimum strength of the column-slab connection, governed mainly by concrete strength characteristics regarding the compressed strut of the punching mechanism.

For situations when concrete strength is not enough and specific reinforcement is needed for dealing with the punching phenomenon, both codes provide the quantification for such condition by considering 75% of the connection strength without specific reinforcement and calculating the required amount of reinforcement through:

$$V_{Rd,s} = 0{,}75.V_{Rd,s} + 1{,}5.\frac{d}{S_r}.A_{sw}.f_{ywd,ef}.sen(\alpha) \text{ (kN)} \quad (2.35)$$

Where $S_r$ is the specific reinforcement spacing and $f_{ywd,ef} = 250 + 0.25.d$. An assumption is made that specific reinforcement for the punching phenomenon is anchored on both ends with no slip occurs during the load history, with headed studs being recommended for such purpose.

### 2.4.3.3. CSCT and Model Code 2010

The Critical Shear Crack Theory, as proposed by Muttoni [10], is a theoretical model based on the assumption of failure governed by the opening of a critical shear crack in the vicinity of the column that supports the slab, coherent with the punching failure region of such connection. The punching mechanism is then composed by the interaction of the contacting surfaces of the critical shear crack and the upper layer of flexural reinforcement.

Such theory was the basis of code provisions on the Model Code 2010 [57], where the slab rotation $\psi$ is accounted for and governs failure of the column-slab connection. For better suiting the needs of design or the analysis of such connection, four levels of approximation (LOA) are provided as illustrated in Figure 2.70.

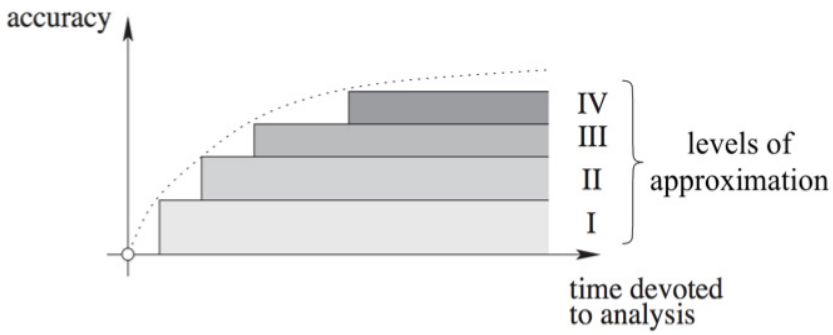


Figure 2.70 – Accuracy regarding the adopted LOA for the application of CSCT (extracted from [57]).

Levels one to three are intended for design, with level three being recommended for special geometries of the column/slab or particularities near this area, and level four being recommended with the use of Finite Element Analysis for the assessment of particular column-slab connections. The difference of the three levels of approximation resides on the calculation of slab rotation like:

- $\psi = 1.5.\frac{r_s}{d}.\frac{f_{yd}}{E_s}$, for the LOA I, as a simple approach that considers $m_{Sd} = m_{Rd}$ which implies that reinforcement has yielded at failure on the support strip, and is a conservative estimate since it results in larger crack openings that decrease the punching strength;

- $\psi = 1.5.\frac{r_s}{d}.\frac{f_{yd}}{E_s}.\left(\frac{m_{Sd}}{m_{Rd}}\right)^{3/2}$, for the LOA II, where $r_s$ is the control perimeter radius, the average bending moment per unit width in the support strip $m_{Sd}$ is taken as $V_{Ed}/8$ and $m_{Rd}$ the design average flexural strength per unit width in the support strip. The remaining parameter are geometrical and material properties of the column-slab connection;

- $\psi = 1.2.\frac{r_s}{d}.\frac{f_{yd}}{E_s}.\left(\frac{m_{Sd}}{m_{Rd}}\right)^{3/2}$, for the LOA III, where the coefficient of 1.2 can be used if the perimeter $r_s$ and the average bending moment $m_{Sd}$ on the support strip are calculated using a linear elastic model. Such approximation is recommended for irregular slabs or when the ratio between span lengths is less than $1/2$ or over $2$.

The flexural moment capacity of the slab $m_R$ can be calculated through equation (2.36), where $f_{cp} = f_c.(30/f_c)^{1/3} \leq f_c$ is the plastic compressive strength of concrete for uniaxial compression that accounts for the influence of concrete brittleness in compression.

$$m_R = \rho.f_y.d^2.\left(1 - \frac{\rho.f_y}{2.f_{cp}}\right) \tag{2.36}$$

The width of the support strip can be calculated through $b_s = 1.5.\sqrt{r_{s,x}.r_{s,y}}$, where $r_{s,x}$ and $r_{s,y}$ are the radius $r_s$ on both directions increased $1.5$ times, which is also where to integrate the flexural moments on the slab.

The theory states that when no reinforcement specific for punching is installed, the shear strength of flat slabs depends on the width $w$ and roughness of the critical shear crack through aggregate size $d_g$, as:

$$\frac{V_R}{b_0.d} = \sqrt{f_c}.f(w, d_g) \tag{2.37}$$

Where $b_0$ is the control perimeter for the punching phenomenon that is set at a distance of $d/2$ from the column face as depicted in Figure 2.71 according to such theory, which states that such perimeter should be set at the minimum distance for a regular polygon.

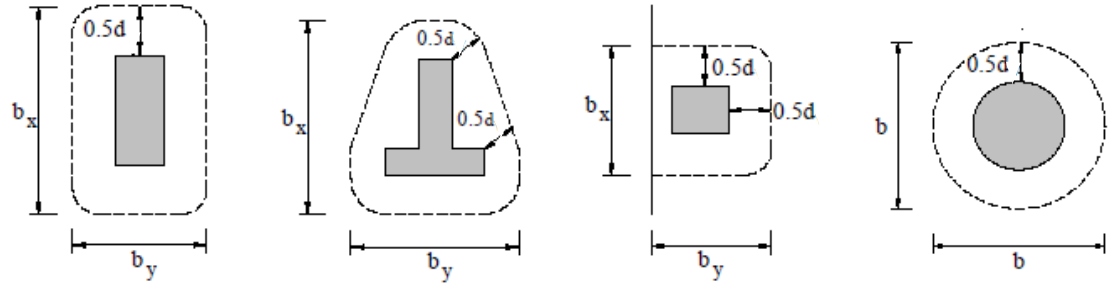


Figure 2.71 – Illustration of the control perimeter for the punching phenomenon (adapted from [57]).

The width $w$ of the critical shear crack can be calculated by considering the product of the slab rotation $\psi$ and the effective depth $d$ of the slab ($w \propto \psi.d$). Half of this rotation is assumed to occur in the critical shear crack and, as the slab rotates, the concrete component of shear resistance at the crack is assumed to decrease, while the component from the shear reinforcement increases up to yield strength. Such considerations led to the formulation of the failure criterion in terms of average strength proposed in [10] and depicted in Figure 2.72, where $d_{g0}$ is the reference aggregate size of 16mm:

$$\frac{V_R}{b_0.d.\sqrt{f_c}} = \frac{3/4}{1 + 15.\frac{\psi.d}{d_{g0} + d_g}} \quad [MPa] \tag{2.38}$$

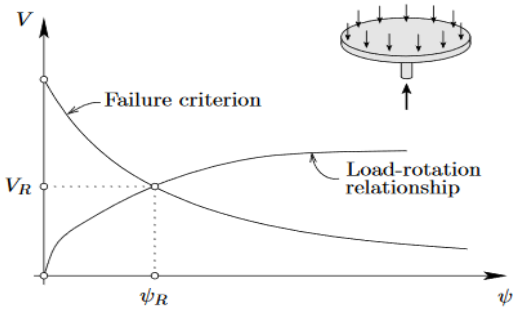


Figure 2.72 – Illustration of the failure criterion (extracted from [135]).

In the CSCT, punching resistances are related to the rotation ψ of the slab, outside a critical crack. The rotation ψ is related to the ratio $V/V_{flex}$, where $V_{flex}$ is the shear force corresponding to the flexural capacity, calculated by the yield-line theory as $V_{flex} = 2.\pi.m_R.r_s/(r_q - r_c)$, with $m_R$

being the flexural moment per unit length of yield line, and the remaining parameters are those that characterise the column-slab connection. A simplified approach is also provided by such theory by assuming a parabola with a 3/2 exponent for the latter ratio, and yielding of flexural reinforcement is reached at 75% of the radius $r_s$, which results in:

$$\psi = 1{,}5.\frac{r_s}{d}.\frac{f_y}{E_s}.\left(\frac{V_s}{V_{flex}}\right)^{3/2} \tag{2.39}$$

The MC2010 [57] provisions regarding the punching strength without specific reinforcement consider equation (2.40) for the calculation of such strength, where the coefficient $k_\psi$ accounts for the rotation of the slab and consequently the opening of the critical shear crack ($w \propto \psi.d$), and such coefficient also accounts for roughness of the critical shear crack through coefficient $k_{d_g}$.

$$V_{Rd,c} = k_\psi.\frac{\sqrt{f_c}}{\gamma_c}.u.d \quad [MPa] \tag{2.40}$$

With $k_\psi = \frac{1}{1{,}5+0{,}6.\psi.d.k_{d_g}} \leq 0{,}6$ and $k_{d_g} = \frac{32}{16+d_g}$ being the coefficients that account for the main characteristics considered on the CSCT, deformation of the slab and roughness of the critical shear crack. One should note the absence of the control perimeter in such calculation. Nonetheless, application of equation (2.40) implies that punching strength is calculated considering the control perimeter $b_0$ set at $d/2$ from the column face.

## 2.5. Final remarks

By analysing the bibliographic references and design codes in this chapter, one can assess the main parameters of a concrete-to-concrete interface, namely the condition of the existing surface and the procedures for optimizing bond between both layers. The extensive research surrounding the topic of the shear friction mechanism allowed for several theories characterising its behaviour and should be accounted for when analysing or designing a structural dependent concrete-to-concrete interface.

Knowledge of the flexural and punching stresses that develop in the column region of flat-slabs allows for an optimized definition of the strengthening solution, since most relevant parameters that govern the stiffness and strength of the column-slab connection can be assessed and optimized, namely the control perimeter and effective depth of flexural reinforcement, and the impact each parameter has on the strength and stiffness of the slab. Applying a new concrete layer on top of an existing slab will alter its stiffness and if properly bonded to the latter, will result in higher punching and flexural capacity of the slab in the column region.

Success in the numerical modelling of composite cross-sections presented in bibliographic references allow for considering the nonlinear finite element modelling technique for characterising the behaviour of overlay strengthened slabs subjected to debonding of the overlaid concrete.

# 3. UNIDIRECTIONAL SLABS STRENGTHENED WITH RCO ON THE TENSILE FACE

## 3.1. Foreword

Strengthening of concrete slabs with a new reinforced concrete (RC) layer applied on the tensile face has proved to be effective for service and ultimate limit states. Although it requires the consideration for premature failure by debonding of the new layer, correctly designed it can be an efficient and economical method for structural strengthening. An experimental campaign was programmed for assessing the performance of fresh concrete overlaid on the tensile face of existing structures. Such campaign comprised the design and conception of unidirectional slab specimens to be strengthened with RC overlaid at midspan. This new layer was detailed with the least thickness possible while comprising the minimum clear cover and spacing to the interface between the two layers. Such limits are a design requirement for proper behaviour of a RC structure, guaranteeing the bond of embedded reinforcement. Isolating the stresses at the interface to one direction allows for the definition of longitudinal stress distribution over the strengthened area and comparison to existing behaviour models.

Different detailing solutions for the reinforcement crossing the interface between the two concrete layers were tested and analysed to identify the main factors that influence the behaviour of the composite section. Such reinforcement was defined in two ways: evenly distributed on the interface through steel dowels; anchoring of the new layer's reinforcement on the edge of the strengthened area; or a combination of the two. All specimens had the substratum surface worked for greater roughness through the milling with percussion tools and chisels. Such preparation of the existing surface further activates the interface crossing reinforcement contributing for greater interaction and less brittle behaviour of the composite cross-section.

Numerical modelling of the tested specimens was also performed to assess the stress distribution at the interface, contribution of the interface reinforcement, and stress distribution of the composite cross-section. The numerical models were calibrated according to geometric and material data from experimental specimens to analyse different detailing solutions of the interface.

Such combination of experimental testing and numerical modelling allowed for the characterisation of RCO strengthened slabs' behaviour and analysis of the effects from different detailing solutions of the interface. The knowledge from this study was then applied to the strengthening of column-supported flat slab specimens, where a large stress concentration occurs at the column-slab connection. The usual brittle failure of these zones by punching further influences the behaviour of the interface between the two concrete layers.

## 3.2. Strengthened specimens

### 3.2.1. Description of the specimens

To characterise the behaviour of the strengthening situation, three different reinforcement detailing solutions of the interface and one unreinforced for reference, were tested. The reference specimens comprised only surface roughening and no rebar crossing the interface between the two layers. Two sets of reference specimens were tested: one with 1.00 m and another one with 1.70 m in length of overlaid concrete. The subscripts "S" and "L" were added to the definition of rectangular specimens "R" to differentiate short overlays of 1.00 m from long overlays of 1.70 m, respectively. Relevant data regarding the geometry of specimens is provided in Table 3.1, where $A_{s,o}$ and $A_{s,s}$ are the area of longitudinal reinforcement for the overlay and substratum, respectively. $A_{s,i}$ is the area of the reinforcement, shear dowels or longitudinal rebar, crossing the interface. The experimental tests comprised the following specimens:

1. REF – specimens with surface roughening only;

2. STC - specimens with steel connectors distributed along the interface, with 50 mm of anchorage length (STC1 to 3), and 80 mm of anchorage length (STC4 and 5);

3. ANC - specimens with anchoring of the longitudinal reinforcement bars of the new layer at the ends, since the deformation of the specimens in bending suggests the lifting of the overlaid concrete in this zone [42], with 50 mm of anchorage length (ANC 1 to 3) and 80 mm of anchorage length (ANC 4 and 5);

4. STANC - specimens with the two aforementioned techniques combined for improving bond at the interface.

Table 3.1 - Relevant rectangular specimens' geometrical parameters.

| | | $R_S$ / $R_L$ | | | |
|---|---|---|---|---|---|
| | | **REF** | **STC** | **ANC** | **STANC** |
| **Overlay** | **Thickness [m]** | 0.07 | | | |
| | **Length [m]** | 1.00 / 1.70 | | | |
| | **Width [m]** | 0.60 | | | |
| | **$A_{s,o}$ [-]** | 2Ø12//0.10m (22.6cm²/m) / 2Ø10//0.10m (15.7cm²/m) | | | |
| **Interface** | **$A_{s,i}$ [mm²]** | - | 336 | 678 | 1014 |
| **Substratum** | **$A_{s,s}$ [-]** | 2Ø10//0.10m (15.7cm²/m) | | | |
| | **Width [m]** | 1.00 | | | |
| | **Length [m]** | 2.30 | | | |
| | **Thickness [m]** | 0.12 | | | |

Slender slab specimens were adopted for allowing larger deformations and relative displacements. Structural integrity until debonding was guaranteed by double bars as longitudinal reinforcement, which resulted in double the flexural capacity for the same effective depth. Reducing the contact area longitudinally and laterally between the two layers increased the bond stress and resulted in

larger relative displacements. The substratum of the specimens was reinforced with 2x10 mm grouped longitudinal bars spaced 100 mm and the overlaid concrete layer was reinforced with 2x12 mm or 2x10 mm bars, also spaced 100 mm, respectively, for the short and long overlays (Figure 3.1 to Figure 3.8).

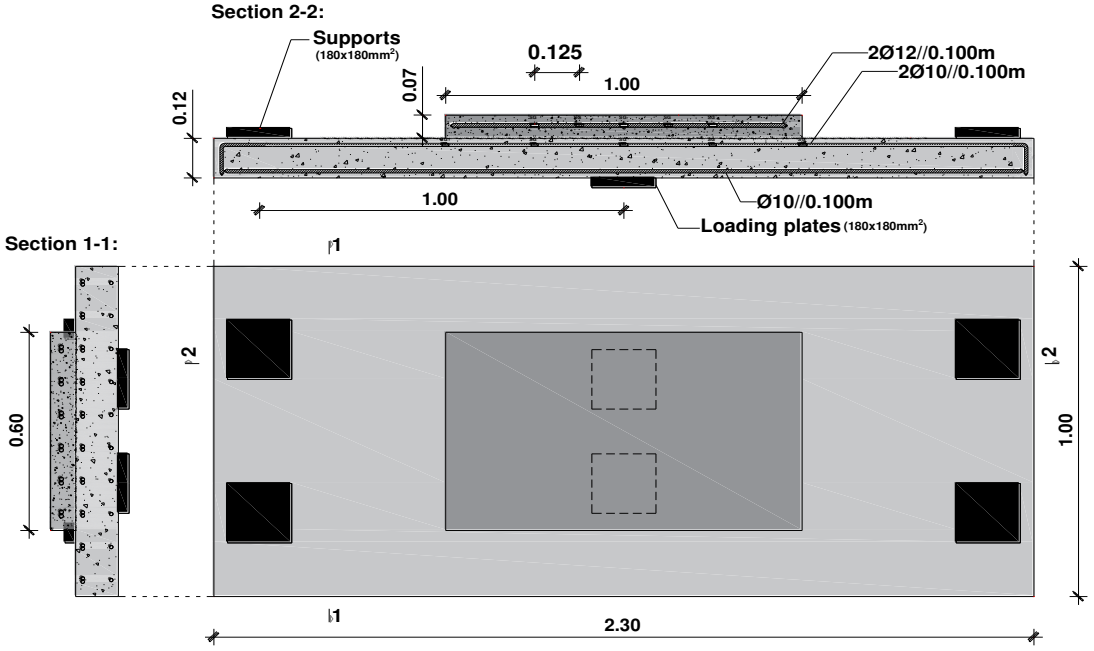


Figure 3.1 - Rebar detailing and strain gauge placing for reference specimens ($R_S$-REF).

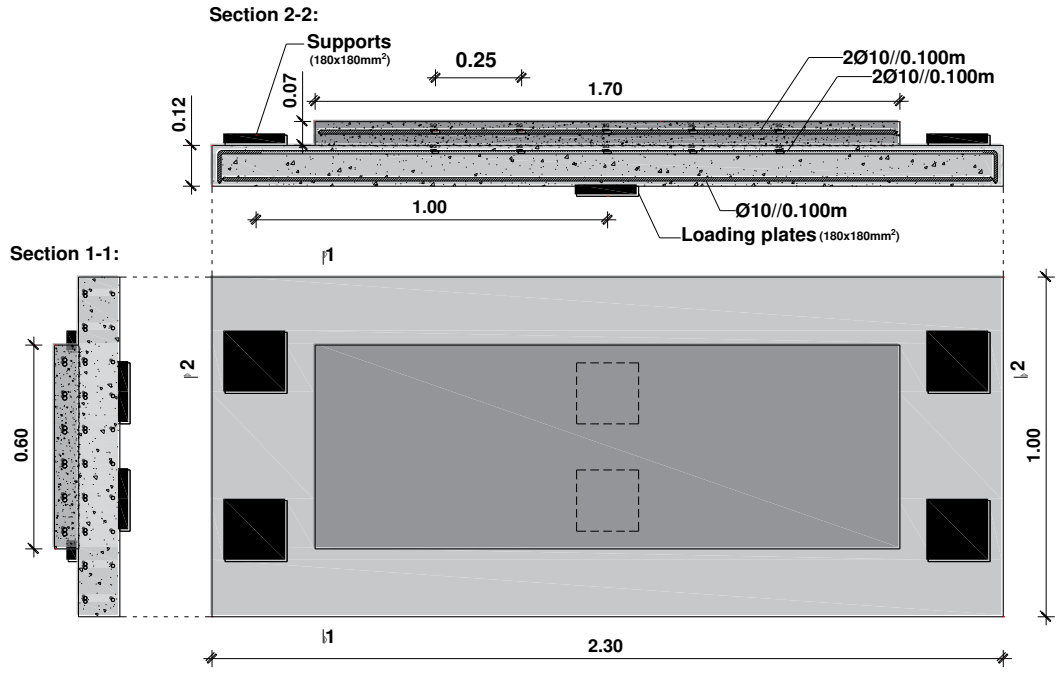


Figure 3.2 - Rebar detailing and strain gauge placing for reference specimens ($R_L$-REF).

Reinforcement was designed regarding the ultimate shear and flexural strengths of the slab specimens since the intended result was the debonding of the overlaid concrete. Longitudinal reinforcement grouped in pairs allowed for a flexural stiffness that led to larger interface stresses prior to failure.

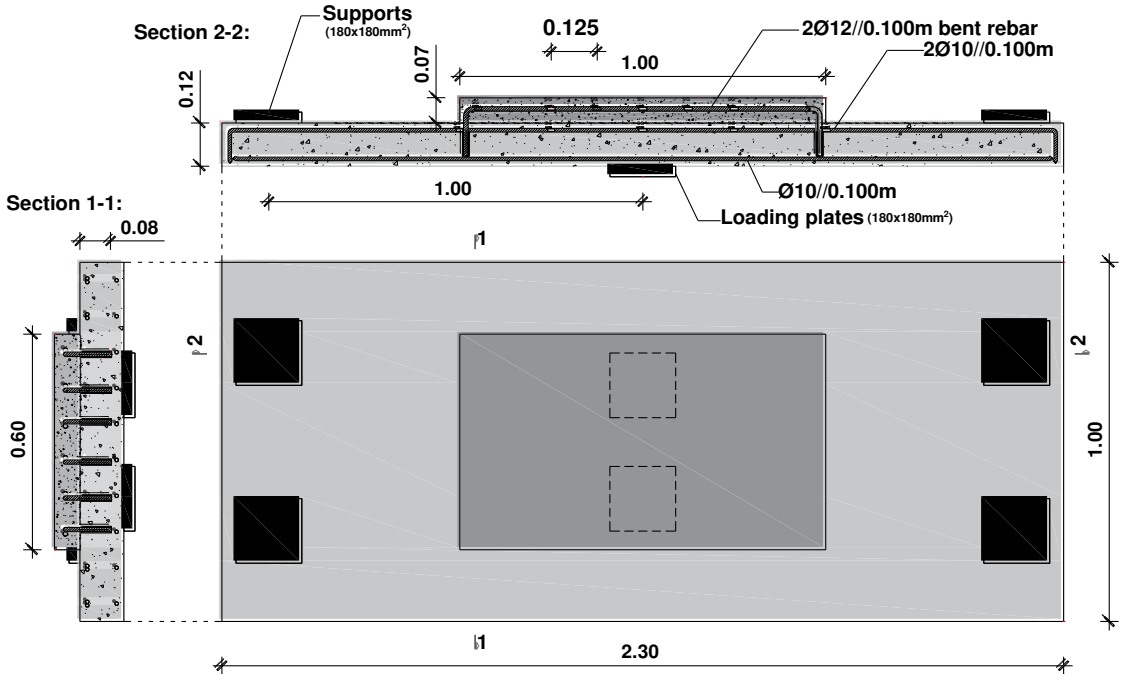


Figure 3.3 - Rebar detailing and strain gauge placing for the $R_s$-ANC specimens.

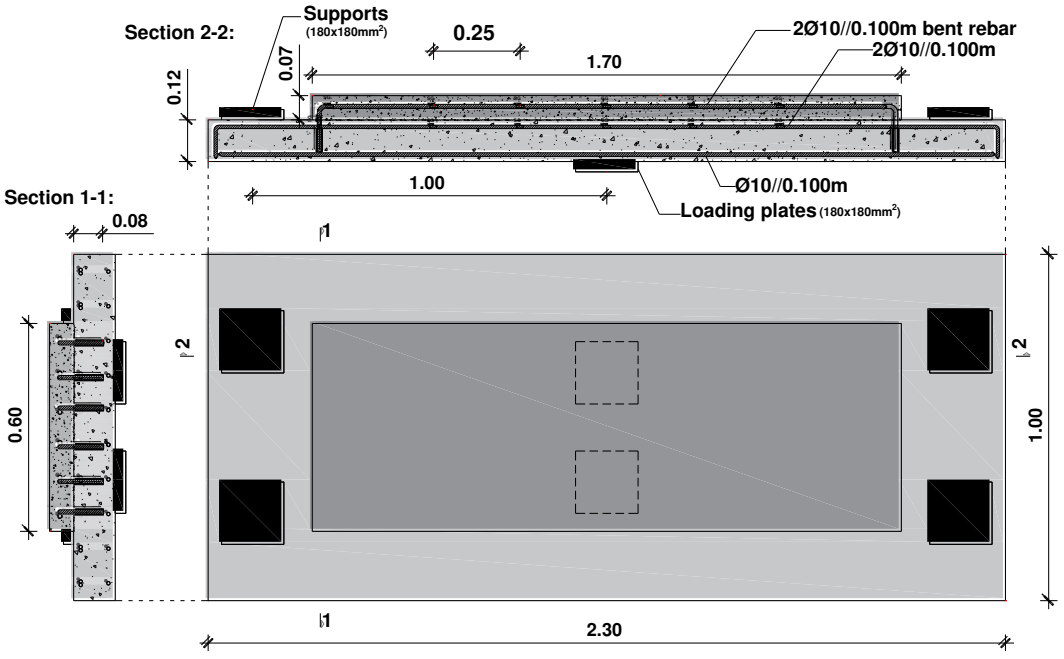


Figure 3.4 - Rebar detailing and strain gauge placing for the $R_L$-ANC specimens.

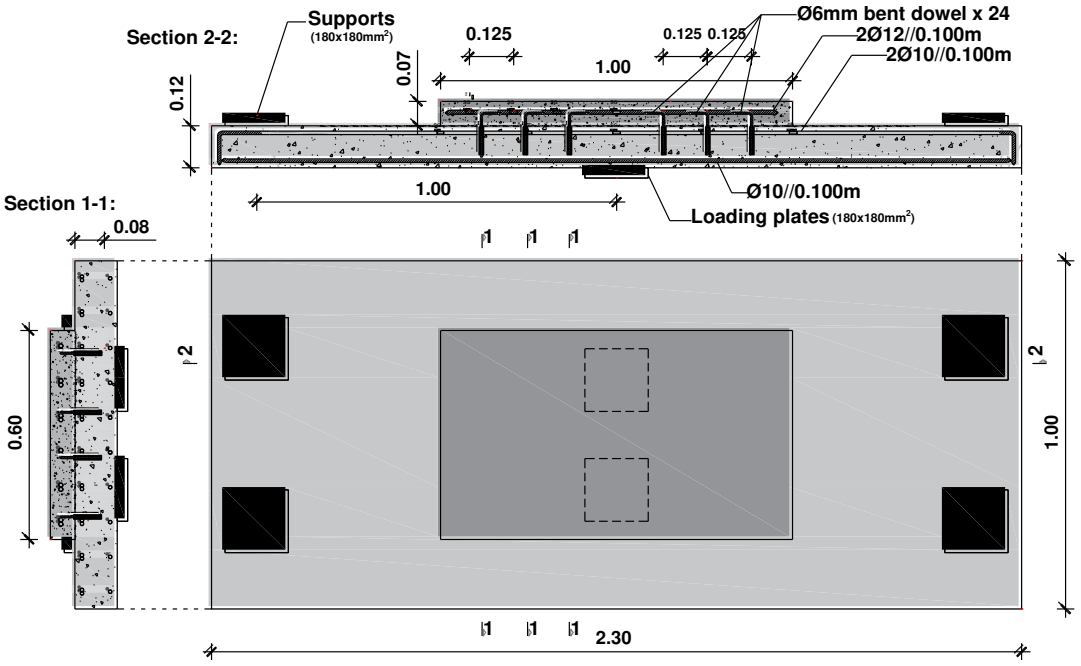


Figure 3.5 - Rebar detailing and strain gauge placing for $R_S$-STC specimens.

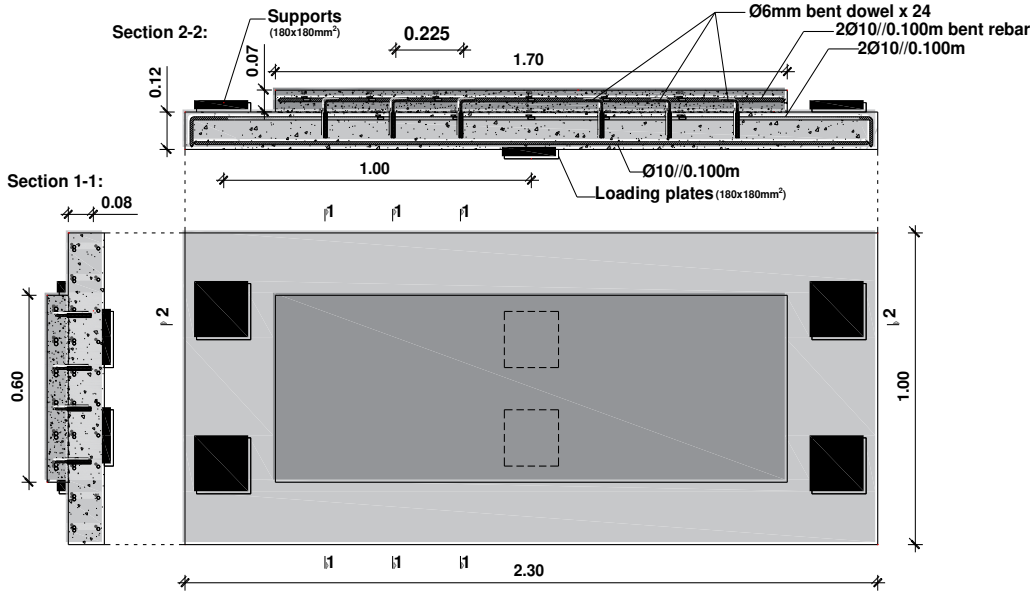


Figure 3.6 - Rebar detailing and strain gauge placing for $R_L$-STC specimens.

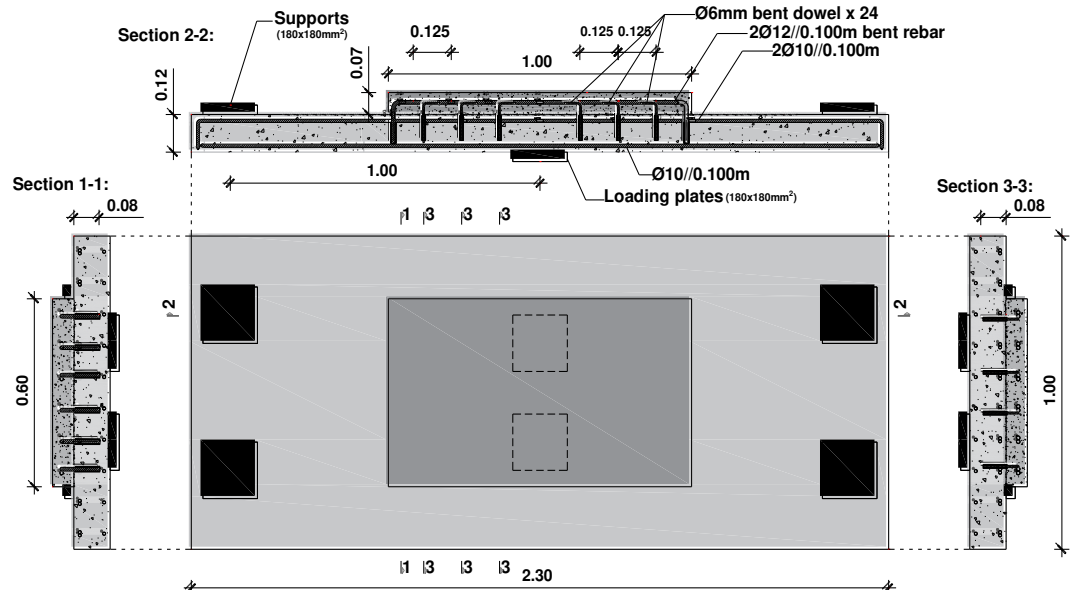


Figure 3.7 - Rebar detailing and strain gauge placing for $R_S$-STANC specimens.

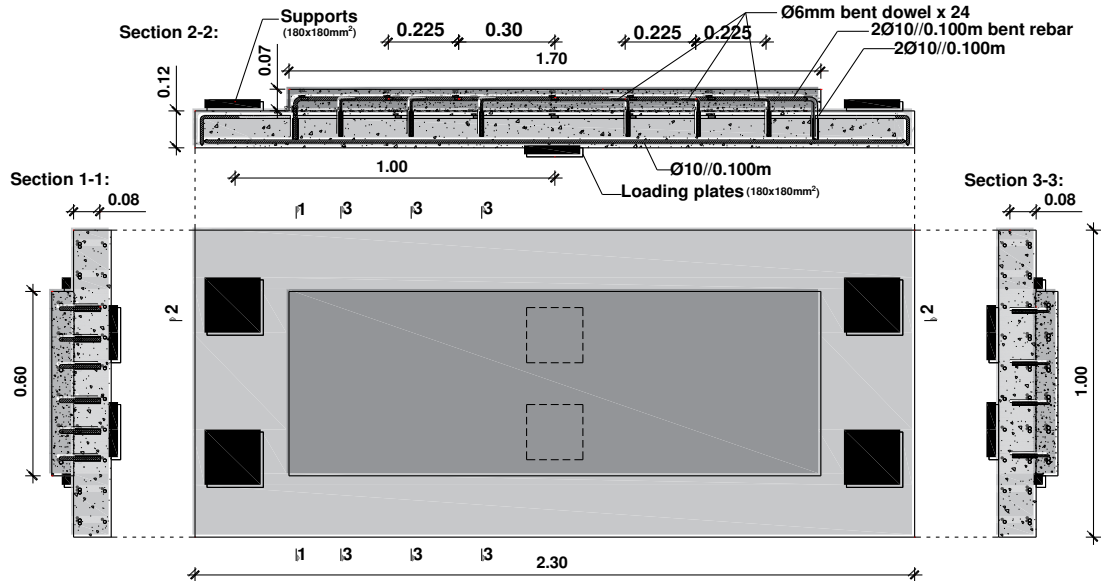


Figure 3.8 - Rebar detailing and strain gauge placing for $R_L$-STANC specimens.

Shear connectors consisting on right angle steel bars, were embedded in the substratum layer with Sika® Grout and tied to the longitudinal reinforcement of the overlay. The choice for a cement-based bonding agent rather than epoxy was due to the economy and ease of application in a practical situation with less specialized labour. The anchorage lengths of reinforcement crossing the interface (steel dowels and longitudinal reinforcement) were 50 mm and 80 mm. The first value resulted from not accounting for surface preparation on the anchorage length, since roughening the surface removes some of the concrete material, thus reducing the actual anchorage length. This phenomenon, along with the error margin when drilling holes in concrete, resulted in less 20 mm of anchoring for the first three specimens (STC and ANC).

The problem of anchorage length in bored holes was addressed by increasing the design length by at least the total roughness of the surface profile ($R_t$). Such parameter will be addressed in the sub-chapter of surface characterisation (3.2.4).

### 3.2.2. Strain gauges

Strain gauges (SG) were installed on reinforcement for assessing the stresses that develop at key locations of the specimens. These were installed in pairs on ach point monitored with strain gauges diametrically opposed, accounting for the flexural deformation of reinforcement. Longitudinally, only one steel bar and one row of steel dowels were instrumented in general for each specimen. The instrumented coordinates are presented in Figure 3.9 below for the $R_S$-STC specimens. Assessing longitudinal rebar strains between each row of steel dowels allows for assessing the shear capacity of interface crossing reinforcement. Placing of SG's on steel dowels was carried out coincident with the interface, where anchoring starts, and tensile and shear force are greater.

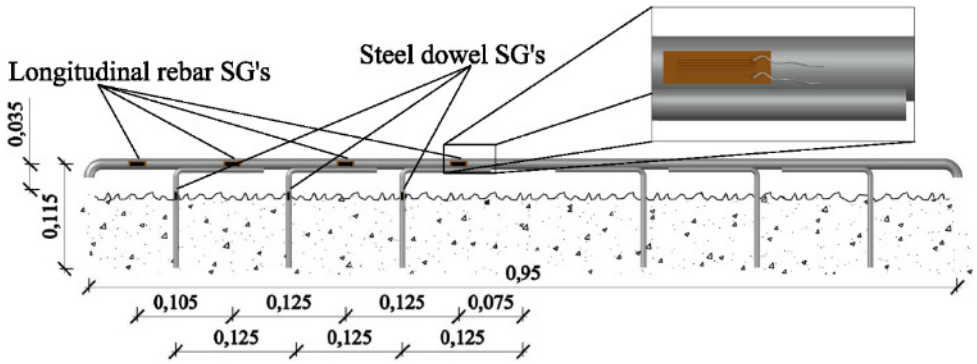


Figure 3.9 – Example of strain gauge placing for the $R_S$-STC specimens.

The process of installing each strain gauge was divided into:

1. Grinding of the rusting finish and ribs of steel until a smooth surface is attained;
2. Cleaning and degreasing the new surface for effective bonding of the strain gauge;
3. Placing the strain gauge in line with the rebar longitudinal axis;
4. Gluing to the steel surface with a cyanoacrylate bonding agent;
5. Waterproofing the strain gauge and respective contacts with a dielectric sealant;
6. Shock proofing the strain gauge with a silicone or a styrene-acrylic sealant.

The question of choosing between the latter components arose since fixation of the wire leads to the rebar is usually performed with zip ties, that interrupt the rebar contact area and interfere with the anchorage to surrounding concrete, and shock proofing with silicone sealant results much larger than actual strain gauge size, as observed in Figure 3.10.

Figure 3.10 – Strain gauge wire leads with zip tie and silicone shock proofing.

Since the silicone sealant has a weak bond to the steel surface of the grinded rebar, applying a styrene-acrylic sealant from Sika® was an improvement to the strain gauge installation. The latter is responsible for both shock proofing the strain gauge and the fixation of wire leads, thus removing the need for zip ties and optimizing the stain gauge installation procedure. The final aspect can be observed in Figure 3.11, where the strain gauge is fixed to the reinforcement solely relying on the new sealant.

Figure 3.11 – Strain gauge shock proofed with styrene-acrylic sealant from Sika®.

### 3.2.3. Casting of specimens with surface preparation

The specimens were produced in the precast concrete factory CONCREMAT, in Pinhal Novo, Portugal (Figure 3.12).

Figure 3.12 – Casting of the substratum layer.

The effective depth of the top reinforcement of the substratum was set at 0.095 m from the bottom of the formwork to guarantee 20 mm of clear cover suitable for surface preparation. This value was assessed later after saw cutting the specimens. For characterising the concrete strength, six Ø150x300 mm cylindrical specimens and three 150 mm cube specimens were also cast for each of the strengthened specimen's layers.

Marking of the holes was performed in the specimen surface before roughening due to the ease of marking and drilling the holes on a flat surface. An assessment of the existing reinforcement

was performed with a magnetic scanner HILTI® PS200S Ferroscan, shown in Figure 3.13, in order to avoid damaging the top reinforcement. The holes were then drilled to the depth referred in 3.2.1.

Figure 3.13 – Rebar assessment, hole marking, and drilling for anchoring reinforcement.

Surface preparation was performed with an electric Bosch® GSH 5 CE Professional chipping hammer and steel moil point chisel, eighteen days after casting of the substratum layer for each specimen, until a rough appearance and a homogeneous surface could be observed (Figure 3.14).

Figure 3.14 – Surface preparation and resulting roughness.

Despite the disadvantages concerning microcracking of the existing surface, this method was chosen because it is practical and economical. Surface roughness was evaluated for each specimen, with concern that the moil tip should not go deeper than 10 mm, thus protecting the longitudinal rebar and the minimum concrete cover for bond to develop. Due to the adopted method of milling and the available resources, roughness was determined with the point measurement system illustrated in Figure 3.15, equivalent to the mechanical stylus system described in [136]. This type of roughness assessment is referred in [68] as adequate for concrete surfaces prepared with more aggressive methods. The system composed of a two degree of freedom structure for the displacement transducer illustrated in the figure below, allowed for forty equally spaced point measurements with a 50 mm TML® CDP-50 displacement transducer, along a 90-cm span. The supports of such structure were levelled with each specimen. Several profiles were evaluated for characterising the surface roughness of each specimen.

Figure 3.15 - Substratum surface roughness assessment setup and detail.

After assessing the surface roughness, reinforcement was placed for the new layer and anchored to the substratum. Grouting was performed by pouring the previously mixed cement grout until 80% of the hole was filled. Reinforcement was then inserted and topping the cement grout as necessary until properly anchored (Figure 3.16). The contact surface was pre-wetted a few hours before for the layer to be saturated, and then the free water was removed with compressed air just before casting. This way, according to [52,80], maximum bond is achieved due to the porosity in the existing concrete being able to bond with the cementitious matrix of the fresh poured concrete. Casting of the new layer then followed, together with casting of cylindrical and cubic specimens for the assessment of concrete strength.

Figure 3.16 – Dowel placement with spacers and detail of grouted anchor.

According to [42], the newly added layer should be of greater strength than the substratum and low shrinkage, and should be fluid enough to penetrate the grooves of the existing surface. Cleanliness of the interface is described in [33] as the most important parameter influencing

interface performance. The existing surface should be free of any contaminants, both micro and macro particles, and moistened prior to casting the new layer. Water saturation is also of the utmost importance in concrete-to-concrete interfaces since the porosity of the existing layer will draw water from fresh concrete. This results in poor hydration and weak cement matrix, which can weaken the connection between the two layers. In [80] several scenarios for water saturation at the existing surface were considered. The opposites of an excessively dry or a saturated surface both resulted in poor bond, whereas good bond resulted from apparently dry surface and saturated substratum. This is in accordance with test results from [52], which recommends the same combination of dry surface and saturated substratum. Following these recommendations, the new layer was cast seventy-five days after the substratum, with the same number of specimens for characterisation of compressive and tensile strength of concrete. For characterising the interface tensile strength, six prismatic specimens were also cast on each of the strengthened specimens, with the same thickness as the overlay layer and a contact area of 150x150 $mm^2$. The cast layer and respective pull-off test specimens can be observed in Figure 3.17.

Figure 3.17 – Casting of the overlay layer.

### 3.2.4. Surface characterisation

One of the main parameters that determines how two surfaces interact relatively to one another is roughness. Such parameter can account for the grooves and ridges of a given surface and characterise how the two surfaces interlock. This in turn defines how the normal and tangential relative displacements will evolve with load. The interaction of the two surfaces is then related to roughness and varying from null to full in terms of the shear stresses, as shown in Figure 3.18.

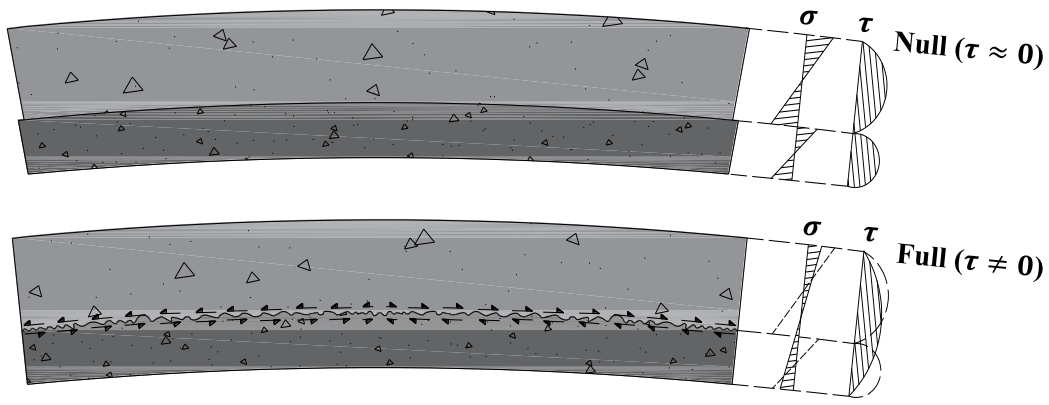


Figure 3.18 – Interaction of surfaces regarding the transfer of shear stresses.

Silfwerbrand states in [36] that there is an upper bound for roughness regarding the tensile capacity between two concretes of different ages and that this threshold is given by the roughness obtained from sandblasting the existing surface. It is also stated that greater roughness will not significantly affect the interface tensile capacity. Such level of roughness will be effective for relative sliding of contacting surfaces, since interlocking and waviness will play a major role on the interaction of the two layers interlocking at the interface.

Of the methods to characterise roughness , the Sand Patch Method (SPM) is the reference method on the concrete-to-concrete section of the MC2010 [57], despite its limitation that it can only determine the mean texture depth $R_{t,SPM}$, losing accuracy on very rough or inclined surfaces. The laser roughness analyser allows for the characterisation of several parameters [55], namely the average roughness $R_a$ and the mean peak-to-valley height $R_{z(DIN)}$ more accurately. The fact that surfaces with a different macro roughness can yield the same parameters above [35] leads to the consideration of some type of quantification that better describes the concrete-to-concrete interface. Such need leads to considering the "peak-to-mean" roughness parameter for characterising rough concrete surfaces, which can be related to the output of the SPM, and thus is relatable to current design codes. In [24] a correlation is given for both parameters regarding the rough and very rough surface grades, presented on Table 3.2.

Table 3.2 – Limit values for surface roughness assessment [24].

| | **Rough** | **Very rough** |
|---|---|---|
| **$R_t$ (mm)** | ≥1.5 | ≥3.0 |
| **$R_p$ (mm)** | ≥1.1 | ≥2.2 |

This way, both area and linear methods of surface characterisation can be related, and relevant coefficients withdrawn from the codes. Using point measurement, the peak-to-mean roughness parameter can be calculated according to equation (2.5), where *n* is the number of peak $p_i$ to mean $\bar{z}$ profile measurements [35].

The probe tip adopted was conical with a diameter of 1.5 mm at the largest section and 1.5 mm high, with a detailed illustration in Figure 3.19, allowing for the evaluation of deeper grooves in the substratum surface.

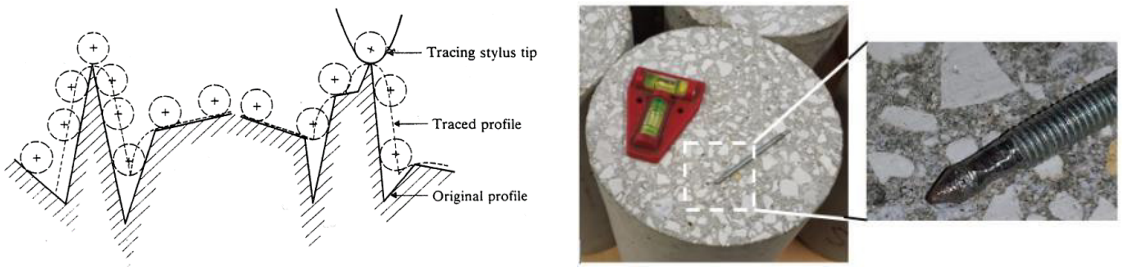


Figure 3.19 – Assessment for smaller grooves conditioned by the probe tip size (adapted from [137]) and probe tip used.

Probe tip size was machined for the smallest attainable, since caution is advised in [35] regarding the grooves on the existing surface that keep the probe tip from correctly assessing the true roughness. A depiction is presented in [24] regarding the discretization of point measurements in surface roughness assessment. Such problem can be solved through high resolution measuring equipment like laser profilometry. Mechanical profilometry, however, yields an approximate surface profile, detailed enough for assessing its roughness. Spacing between measurements, i.e. the resolution of the chosen profilometry technique, determines the degree of detailing and quality of the assessment performed, accounting for more or less irregularities that compose roughness, as illustrated in Figure 3.20.

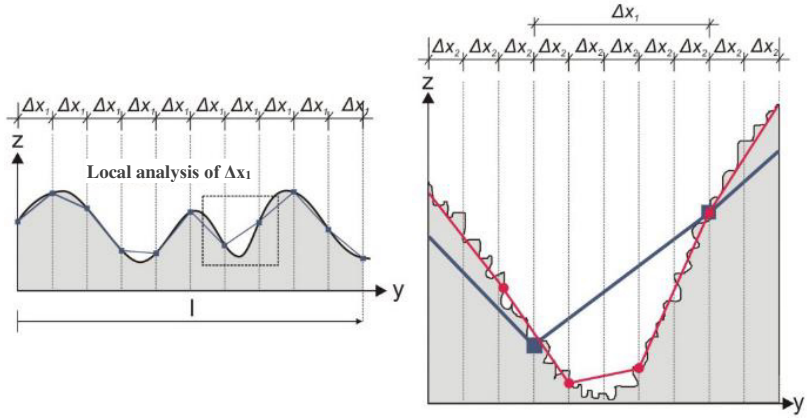


Figure 3.20 – Resolution of the measurement points affecting roughness assessment (adapted from [24]).

The resulting profiles could then be plotted for assessing the parameters that would characterise the surface of each specimen and are presented on Annex B. The average surface roughness $R_a$, total roughness $R_t$ and peak-to-mean roughness $R_p$ were calculated, since: the first allows for a general characterisation of surface roughness; the second allows for a quantitative measurement of the interlocking capacity of the contacting surfaces; and the third intrinsically accounts for the aforementioned parameters allowing for the classification of the interface as very-rough. Such classification is important when analysing the interface shear capacity. The resulting parameter $R_p$ for each of the specimens is presented in Table 3.3, where six assessment lengths (n=6) were considered.

Table 3.3 - Average peak-to-mean roughness parameter.

| $R_p$ (mm) | Reference (REF) | Steel connectors (STC) | Anchorage (ANC) | Steel connectors + Anchorage (STANC) |
|---|---|---|---|---|
| **R-1** | 2.2 | 2.2 | 2.2 | 2.6 |
| **R-2** | 2.2 | 2.2 | 2.9 | |
| **R-3** | 2.2 | 2.3 | 2.3 | |
| **R-4** | - | 2.6 | 2.9 | |
| **R-5** | - | 2.4 | 2.7 | |
| **R-EXT** | 2.6 | 2.6 | 2.2 | 3.2 |

Characterisation of the surface roughness was performed according to [24], where a lower limit roughness is set at 3.0 mm for using the SPM ($R_{t,SPM}$), or 2.2 mm when considering the $R_p$ parameter. The $R_p$ parameter allowed then for a surface classification of "very rough" for all specimens, also the classification provided on the MC2010 [57].

Roughness can directly influence the interaction between the two concrete layers regarding the shear capacity of the interface. Such characteristic of the interface is the main contributor to the interaction between the differential deformations of the layers, surpassed only by interface reinforcement. Horizontally, the capacity of the interface can be characterised by a coefficient of friction, which in turn relates such stresses with vertical stresses. Such coefficient was calculated with equation (3.1) as proposed in [57] and also in [138] for very rough interfaces, where $R_{vm}$ is the mean valley depth accounting for five consecutive measurements on each roughness profile.

$$\mu = 1.37.{R_{vm}}^{0.041} \tag{3.1}$$

This parameter accounts for the valleys on a given roughness profile and is calculated according to equation (3.2), where $R_v$ is the difference between the depth of valleys and the average profile roughness.

$$R_{vm} = \frac{1}{5}.\sum_{i=1}^{5} R_{vi} \tag{3.2}$$

The values for the mean valley depth and respective coefficient of friction are presented on Table 3.4. The reason for using such parameter is stated in [69] due to its lower coefficients of variation.

Table 3.4 - Substratum surface roughness parameters $R_{vm}$ and $\mu$.

| Specimen | $R_{vm}$ (mm) | $\mu$ (-) |
|---|---|---|
| **$R_S$-STC-4** | 2.46 | 1.42 |
| **$R_S$-STANC-4** | 2.36 | 1.42 |
| **$R_S$-ANC-4** | 2.46 | 1.42 |
| **$R_L$-REF** | 3.05 | 1.43 |
| **$R_L$-ANC** | 2.07 | 1.41 |
| **$R_L$-STC** | 2.47 | 1.42 |
| **$R_L$-STANC** | 3.18 | 1.44 |
| **$R_S$-STC-5** | 2.04 | 1.41 |
| **$R_S$-ANC-5** | 2.48 | 1.42 |
| **$R_S$-REF-1/2/3** | 2.39 | 1.42 |
| **$R_S$-ANC-1/2/3** | 2.86 | 1.43 |
| **$R_S$-STC-1/2/3** | 2.51 | 1.42 |

Analysing the table above, one can observe that the resulting coefficient of friction results in values of order 1.40. The very low fluctuation of this value is due both to the consistency of the mean valley depth parameter on all specimens and the very small order of power on equation (3.1) for this parameter.

### 3.2.5. Characterisation of materials

Material characterisation was performed for the different concrete layers, rebar sizes, and bonding agent used for anchoring the rebar crossing the interface. The latter was defined as cementitious grout due to the economic aspect and ease of use that is more tolerant than epoxy based bonding agents. A water-binder ratio of 0.13 L/kg was defined for the grout mixture, to allow for good workability and enough flow for filling the holes drilled into the substratum. The mechanical properties of the latter were assessed through compressive and tensile tests, and with pull-out tests for anchoring bond strength. The former were performed according to RILEM PC-5 (Method of test for compressive strength of polymer concrete and mortar, [139]) through simple compression tests on 40x40 mm$^2$ specimens at a speed of 1.6 kN/s, illustrated on Figure 3.21.

Figure 3.21 – Compressive testing of 40x40x40 mm$^3$ grout specimens.

Tensile strength was assessed according to RILEM PCM-8 (Method of test for flexural strength and deflection of polymer-modified mortar, [140]) through three-point flexural tests with a span of 160 mm, displacement controlled at a speed of 1.0 mm/min. Nine specimens were tested, in which the resulting halves were used for the aforementioned compressive test, thus resulting in eighteen compressive test specimens. The cementitious grout could then be classified with a flexural tensile strength of 9.7 MPa, calculated through, and a compressive strength of 78.8 MPa. Such values are in accordance to the manufacturer's technical sheet which states a flexural tensile strength of 5-8 MPa and a compressive strength of 55-65 MPa are preconised.

The anchoring capacity of the bonding agent (Sika Grout®) was assessed through the pull-out of a rebar embedded in the substratum with an anchorage length of 50 mm, as illustrated in Figure 3.22.

Figure 3.22 – Pull-out testing of rebar embedded with grout (example for 6 mm rebar with a 50 mm embedment length).

The resulting behaviour of anchored reinforcement is shown in Figure 3.23 for 6 mm steel bars embedded 50 mm, in 14 mm diameter drilled holes. The procedure for preparing such test was similar to anchoring the interface crossing reinforcement, with pouring of the cementitious grout and inserting the rebar carefully. Anchorage failure resulted from the pull-out of rebar, sliding through the steel-grout interface with the resulting anchorage stress-slip relationship shown below.

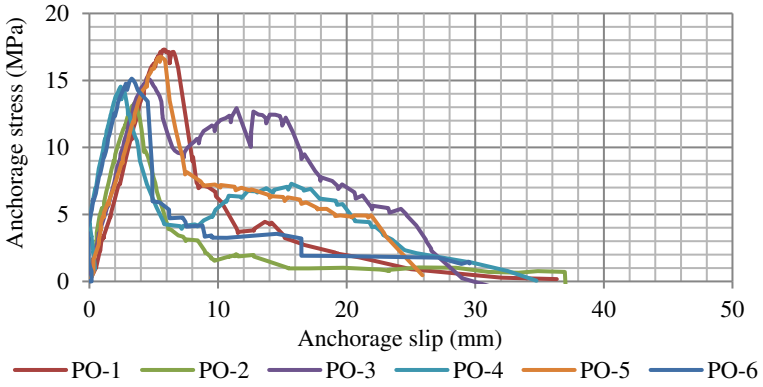


Figure 3.23 – Anchorage stress-slip relationship of 6 mm rebars embedded with Sika® grout.

Anchorage stress was calculated considering the lateral contact area of reinforcement effectively embedded by the bonding agent. In this particular case, six specimens were tested, each consisting of a 6 mm diameter rebar embedded 50 mm in the substratum. The average pull-out force was about 22.9 kN, corresponding to an average stress of 16.2 MPa. Such result characterises the cementitious grout for bonding the reinforcement crossing the interface and is in accordance to the manufacturer's values that state a bonding stress of 15.0 MPa for rebar.

Tensile strength testing of rebar specimens was performed at LNEC, in Lisbon, Portugal, according to specifications on EN 10002-1 [141], which prescribes control by deformation of the specimen at a rate of 9.0 MPa/s. The setup was composed of a INSTRON® 1343 press with hydraulically controlled claws for gripping the ends of the rebar specimens, illustrated on Figure 3.24, and HBM® Spider8 datalogger controlled by HBM® CATMAN software.

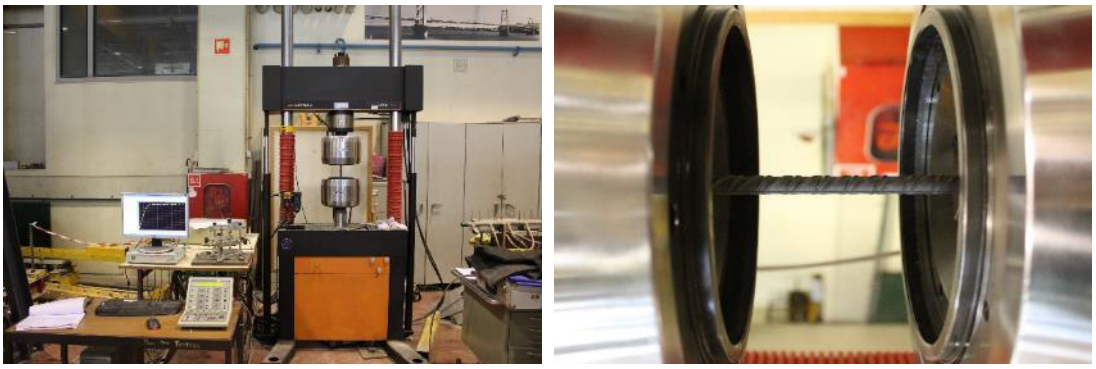

Figure 3.24 – Steel bar tensile strength test apparatus.

Specimens were all A500 NR SD steel reinforcement, with respective results presented on Table 3.5 and Table 3.6, where k denotes the ratio between maximum and yielding load, which is expected between 1.15 and 1.35 according to LNEC E 460-2002 [142].

Table 3.5 – Rebar tensile strength characteristics for the $R_S$ specimens.

| | Specimen | Free span (mm) | Yield stress $\sigma_y$ (MPa) | $\sigma_{y,med}$ (MPa) | Maximum Stress $\sigma_u$ (MPa) | $\sigma_{u,med}$ (MPa) | k (-) |
|---|---|---|---|---|---|---|---|
| **Ø12** | A1 | 158 | 538,3 | 532,1 | 643,3 | 627,4 | 1,19 |
| | A2 | 158 | 526,1 | | 616,6 | | 1,17 |
| | A3 | 159 | 531,9 | | 622,4 | | 1,17 |
| **Ø10** | B1 | 158 | 524,5 | 530,6 | 623,5 | 627,5 | 1,19 |
| | B2 | 158 | 549,5 | | 640,8 | | 1,17 |
| | B3 | 159 | 517,7 | | 618,0 | | 1,19 |
| **Ø6** | C1 | 159 | 549,3 | 541,0 | 689,3 | 692,7 | 1,25 |
| | C2 | 159 | 538,7 | | 697,1 | | 1,29 |
| | C3 | 159 | 535,1 | | 691,8 | | 1,29 |

Table 3.6 – Rebar tensile strength characteristics for the $R_L$ specimens.

| | Specimen | Yield stress $\sigma_y$ (MPa) | $\sigma_{y,med}$ (MPa) | Maximum Stress $\sigma_u$ (MPa) | $\sigma_{u,med}$ (MPa) | k (-) |
|---|---|---|---|---|---|---|
| Ø10 | G1 | 526 | 524 | 620 | 620 | 1.18 |
| | G2 | 521 | | 618 | | 1.18 |
| | G3 | 524 | | 623 | | 1.19 |
| Ø6 | H1 | 585 | 586 | 682 | 688 | 1.17 |
| | H2 | 586 | | 683 | | 1.16 |
| | H3 | 587 | | 699 | | 1.19 |

Concrete compressive and tensile strengths were assessed for the two layers of each specimen. Due to some errors in logistics, the specimens for concrete testing were not produced for some layers. Concrete compressive strength was assessed according to EN 12390-3 [143] through the monotonic loading in compression of cubic specimens, with a side length of 150 mm. Such tests were force controlled, at a rate of 11.25 kN/s. Concrete tensile strength was assessed according to EN 12390-6 [91] through the splitting tensile test on cylinder specimens, which allowed for assessing the concrete splitting tensile strength $f_{ct,sp}$, which is calculated according to equation (3.3), where $P$ is the failure load of the specimen, $L$ is the height and $\emptyset$ the diameter of the cylindrical specimen.

$$f_{ct,sp} = \frac{2.P}{\pi.L.\emptyset} \tag{3.3}$$

The relationship between such strength and the effective concrete tensile strength $f_{ct}$ is referred to in [144] as 10 to 15 percent higher. The ratio $f_{ct}/f_{ct,sp}$ was then taken as 0.9. Tensile strength is preconised in [101] through equation (3.4), where $f_{ck} = f_{cm} - 8$ and $f_{cm}$ is the average compressive strength of cylinder specimens.

$$f_{ctm} = 0.30.{f_{ck}}^{2/3} \tag{3.4}$$

Tensile strength, however, was quantified through splitting test results for all specimens and affected with factor 0.9, thus resulting in concrete average tensile strength. The values for concrete compressive strength on cubic specimens and tensile strength are presented below. A minimum of three specimens were tested both in compression and splitting tensile strength, with the average of such values presented below for each specimen on Table 3.7 and Table 3.8.

Table 3.7 – Concrete strength characteristics for the $R_S$ specimens.

| | | **$R_S$-REF 1 to 3** | **$R_S$-STC 1 to 3** | **$R_S$-ANC 1 to 3** | **$R_S$-STC 4 / 5** | **$R_S$-ANC 4 / 5** | **$R_S$-STANC** |
|---|---|---|---|---|---|---|---|
| **$f_{ccm}$ (MPa)** | Substratum | 45.3 | 40.6 | 37.4 | 55.5 / 49.2 | 54.8 / 42.8 | 56.4 |
| | Overlay | 47.8 | 47.8 | 47.8 | 41.1 / 38.0 | 39.4 / 36.7 | 41.5 |
| **$f_{cm}$ (MPa)** | Substratum | - | - | - | - / 45.1 | - / 34.6 | - |
| | Overlay | - | - | - | 40.6 / 36.8 | 39.8 / 33.3 | 40.5 |
| **$f_{ct}$ (MPa)** | Substratum | 3.8 | 3.5 | 3.4 | 4.2 / 3.2 | 4.3 / 2.9 | 4.1 |
| | Overlay | 3.9 | 3.8 | 3.3 | 3.6 / 2.7 | 3.5 / 2.9 | 3.6 |

$f_{ccm}$ – mean value for the compressive strength of concrete in cubic specimens.
$f_{cm}$ – mean value for the compressive strength of concrete in cylindrical specimens.
$f_{ct}$ – mean value for the tensile splitting strength of concrete.

Table 3.8 – Concrete strength characteristics for the $R_L$ specimens.

| | | **$R_L$-REF** | **$R_L$-STC** | **$R_L$-ANC** | **$R_L$-STANC** |
|---|---|---|---|---|---|
| **$f_{ccm}$ (MPa)** | Substratum | 37.3 | 56.8 | 53.1 | 52.8 |
| | Overlay | 34.9 | 33.2 | 36.7 | 38.0 |
| **$f_{cm}$ (MPa)** | Substratum | 36.6 | 49.7 | 42.5 | 45.3 |
| | Overlay | 29.7 | 32.9 | 33.3 | 31.6 |
| **$f_{ct}$ (MPa)** | Substratum | 2.7 | 3.2 | 3.1 | 3.1 |
| | Overlay | 2.8 | 2.1 | 2.9 | 2.5 |

The Young modulus was also assessed experimentally, following LNEC E-397 [145] guideline for the concrete material of each specimen's layers through the apparatus illustrated in Figure 3.25, which measures the deformation of the specimen in a range up to 40% of the failure load, which was already assessed by compression of cylindrical specimens of the same batch.

Figure 3.25 – Young modulus assessment apparatus.

Test procedure prescribes four cycles that should be completed without exceeding a set threshold that validates the test. Respective Young modulus assessed experimentally was then:

Table 3.9 – Young modulus for the $R_S$ and $R_L$ specimens.

| | | Substratum | | Overlay | |
|---|---|---|---|---|---|
| | | $f_{cm,sub}$ (MPa) | $E_{cm,Exp}$ (GPa) | $f_{cm,ol}$ (MPa) | $E_{cm,Exp}$ (GPa) |
| $R_S$ | **$REF_{1,2,3}$** | 36.2 | 33.29 | 35.1 | 32.35 |
| | **$STC_{1,2,3}$** | 32.5 | 30.88 | 35.1 | 34.49 |
| | **$STC_4$** | 44.4 | 30.89 | 32.9 | 31.27 |
| | **$STC_5$** | 39.4 | 31.33 | 30.4 | 31.59 |
| | **$ANC_{1,2,3}$** | 29.9 | 29.69 | 35.1 | 30.03 |
| | **$ANC_4$** | 43.8 | 32.10 | 31.5 | 32.78 |
| | **$ANC_5$** | 34.2 | 32.55 | 29.4 | 31.02 |
| | **STANC** | 45.1 | 29.88 | 33.2 | 30.33 |
| $R_L$ | **REF** | 29.8 | 30.23 | 27.9 | 30.89 |
| | **STC** | 45.5 | 33.10 | 26.6 | 31.05 |
| | **ANC** | 42.5 | 31.98 | 29.4 | 31.01 |
| | **STANC** | 42.3 | 33.56 | 30.4 | 28.79 |

### 3.2.6. Characterisation of the interface

#### 3.2.6.1. Dolly size and design

Common dolly sizes for pull-off testing are circular with a diameter of 50 mm [79], or square with 100 mm sides [146]. For concrete with an aggregate size of up to 20 mm, a heterogeneous surface arises when intercepting the interface, as shown in Figure 3.26. The maximum dimension of aggregates can rule the contact surface for a small area due to the ratio between aggregate section area and dolly contact area ($A_{d_g}/A_{Spec}$). Such ratio should be minimized for less heterogeneity of the contact surface.

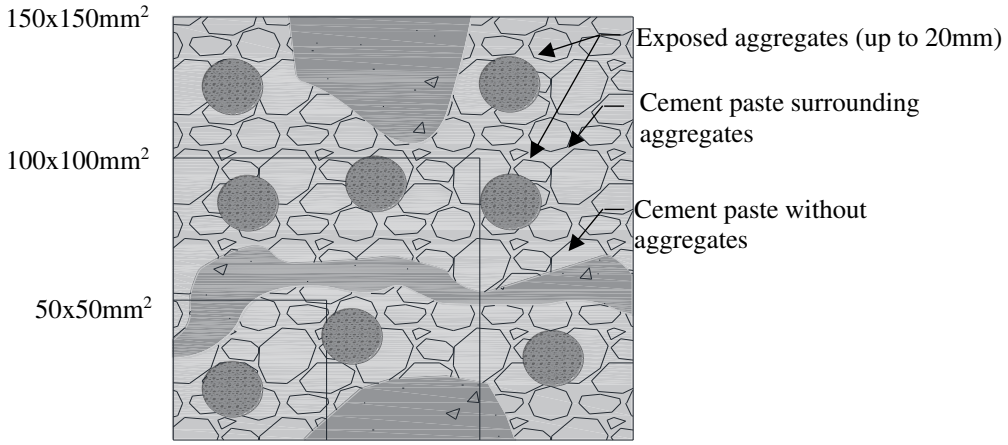


Figure 3.26 – Differences in the contact surface heterogeneity for different dolly sizes.

Also, standard 50 mm dollies are relatively small when compared to the mean spacing between grooves and ridges in the existing surface. Eurocode 2 [101] states in section 6.2.5 (2) that rough surfaces should have ridges with a minimum height of 3.0 mm and spaced 40 mm between consecutive ridges. The intended surfaces to be classified as rough or very rough fall short of this requisite with 50 mm dollies. A test setup for larger dollies was then developed to allow for surface characterisation with a very rough profile where aggregates do not govern the contact area.

Several factors according to Vaysburd *et al*. [81] determined the contact area for dollies used in this work. Expected interface performance in tension results in higher loads for increased contact areas, since the relationship between both is linear. This limits the test setup, which must guarantee a stiff reaction for these loads until failure of the specimen by pull-off. Also, stiffness of the steel dolly must be guaranteed not to influence test results. A larger round dolly would require heavy core drilling for the partial coring of the substratum layer below the test specimen as recommended in [85,86]. A square dolly allows for a straight partial coring of the substratum with regular concrete-cutting equipment. Following these premises, a parametric study regarding several dolly dimensions was carried out with ATENA 3D® software, according to the FE model and test results depicted in Figure 3.27. Concrete material was the same on both layers and the interface was parametrized with a 1.0 MPa tensile capacity. Loading was monotonic as depicted in the last picture in Figure 3.27**.**

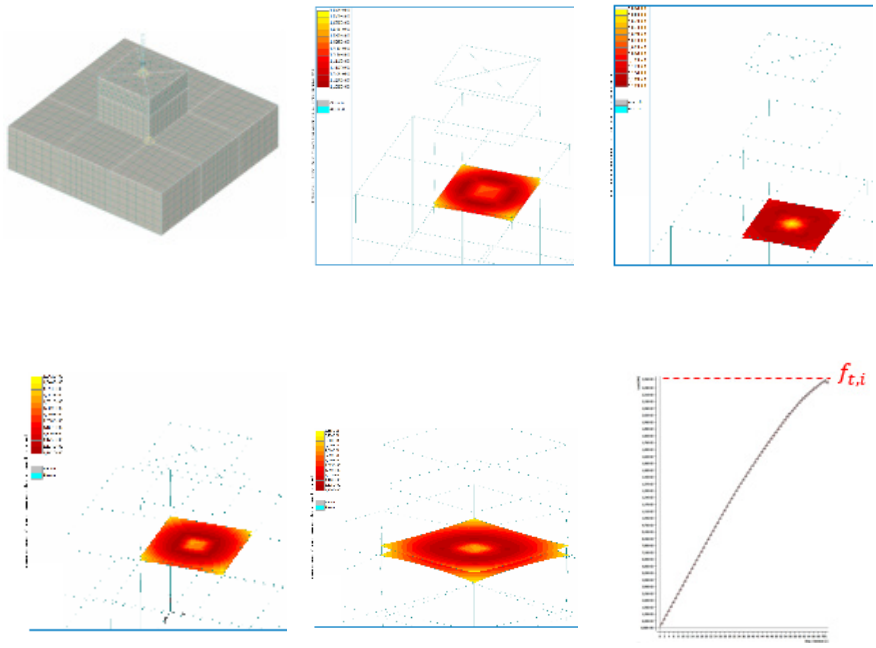


Figure 3.27 – Numerical analysis for the detailing of pull-off test dolly.

For the same parametrization of the interface, 50mm, 100mm, 150mm and 200mm square dollies were considered, with the former yielding the largest tensile capacity and the latter the smallest tensile capacity. One possible justification is the deformation on the boundaries of the test specimen that for larger specimens show some flexural deformation, thus debonding at the edge. The latter results were accompanied by a more uniformly distributed stresses on the larger dolly which also attested its choice. After all considerations, a dolly with a side length of 150 mm was chosen, as depicted in Figure 3.28. This enables a test setup that can be assembled by one person, and both test setup and steel dolly are stiff enough for reliable test results for higher loads. For this matter, 15mm-thick steel dollies were symmetrically strengthened to prevent the bending phenomenon to occur. Such dimension is also the preconised contact-face side length for concrete prismatic specimens.

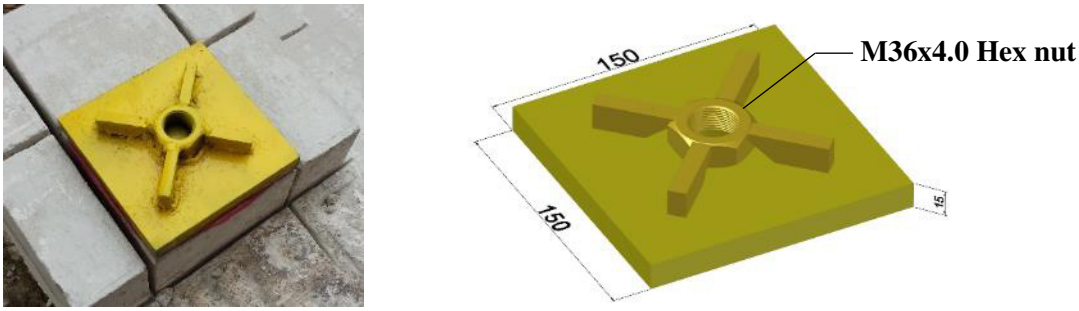


Figure 3.28 – Pull-off test dolly detail.

A least heterogeneous contact surface can be achieved through dollies with larger areas, as depicted in the previous figure, balancing the equilibrium between aggregates of different sizes and the cement matrix, allowing for a better assessment of interface properties. Not accounted for in the schematics above are the air bubbles that latch to the surface of existing concrete and become voids in the contact surface with the new hardened concrete layer, thus promoting the heterogeneity of the interface as stated in [33]. An evidence of such phenomenon can be observed on a saw cut shown in Figure 3.29 for specimen $R_L$-ANC, where the voids due to air bubbles could not be controlled through the vibration of concrete upon casting and are easily observed.

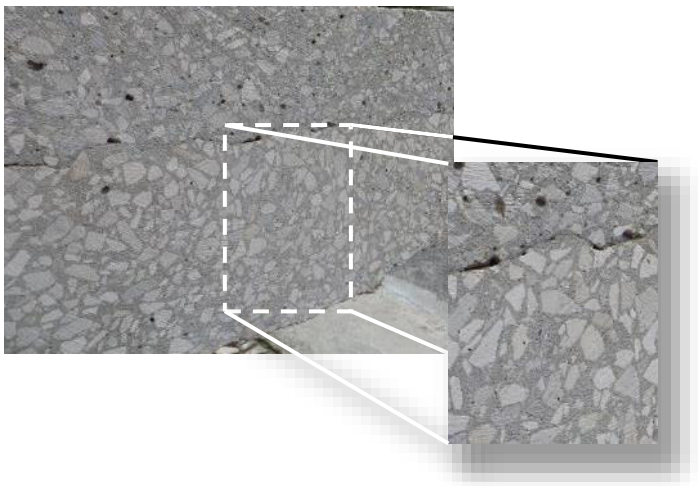

Figure 3.29 – Voids as a result from air bubbles trapped at the interface level of the $R_L$-ANC specimen.

### 3.2.6.2. Test setup and failure modes

Test setup consisted on a 20mm-thick steel plate with a side length of 300 mm. Three holes were threaded in the plate for the supporting 22 mm diameter threaded rods, allowing for the levelling of the steel plate as required for this type of test. Details can be observed in Figure 3.30 regarding the general schematics of the test reaction apparatus and supporting rods.

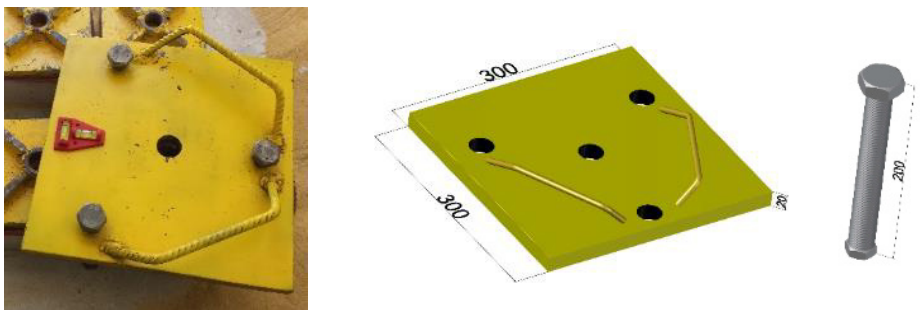


Figure 3.30 – Reaction plate and threaded rod support for pull-off test setup.

Specimens were axially loaded in tension through a threaded rod with a diameter of 32 mm fixed to the specimen with a hex nut welded to the steel dolly and to the reaction plate with another hex nut. A hollow cylinder ENERPAC® RCH-206 and a load-cell TML® CLC200KNA were used,

both with 200 kN capacity. General test setup, as well as the full data-logging equipment, can be observed in Figure 3.31.

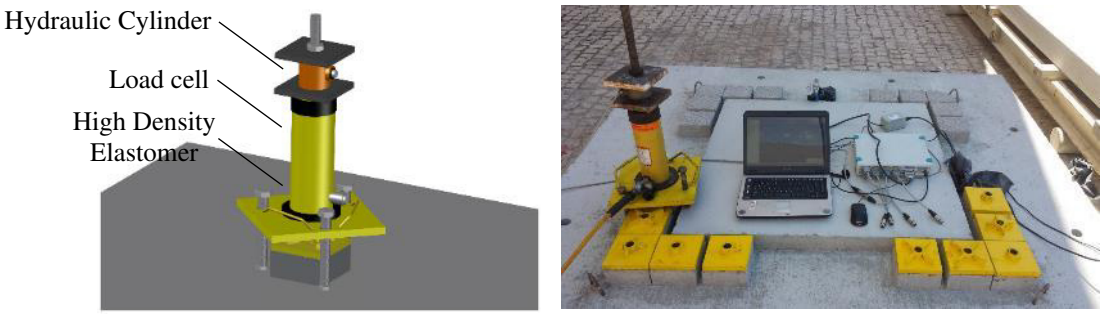


Figure 3.31 – General setup for pull-off testing with loading and data-logging equipment.

A high-density elastomer with a thickness of 10 mm was placed between the hydraulic jack and the steel plate to allow for the correction of verticality when preparing the specimens. The intended effect for the elastomer can be observed in Figure 3.32 where the vertical off-axis eccentricity is corrected, thus reducing flexural stresses at the interface that cause premature debonding. Loading was performed with an electronic hydraulic pressure controller WALTER+BAI® PKNS19D at an approximate rate of 0,005 MPa/s until failure. A load history example can also be observed in Figure 3.32.

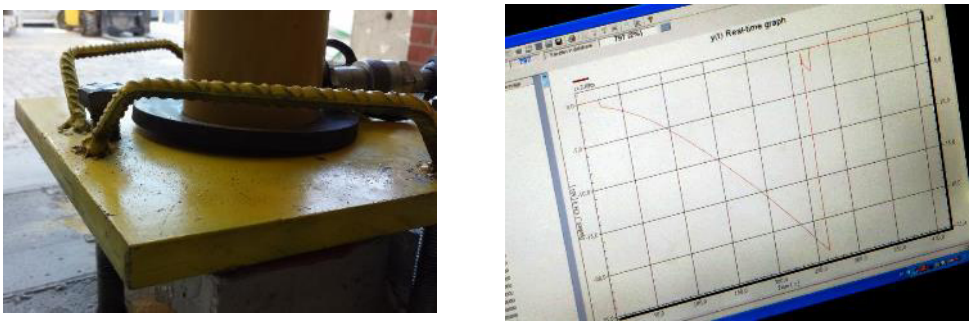

Figure 3.32 – Elastomer for the off-axis vertical correction (left) and load history example (right).

Adhesive failure mode of the concrete-to-concrete interface was the general result for all tests. Exceptions were when failure occurred through the bonding agent at the steel dolly contact surface with concrete. Several measures were taken to avoid this type of failure, namely the removal of the laitance layer through sandblasting, cutting grooves in the surface of specimens, and cleaning the prepared concrete surface with pressurized air. Procedure and final aspect can be observed in Figure 3.33 (left and center). Bonding of the steel dolly was performed with an epoxy HILTI® HIT-RE500 bonding agent, whose tensile bonding capacity is greater than required for the expected test loads, and its viscosity guaranteed no influence in test results.

Figure 3.33 – Removal of laitance layer through sandblasting (left), groves for improved dolly adhesion (center), and bonding of steel dolly (right).

Pre and post-failure can be observed in Figure 3.34 (left and center), with the adhesive failure at the concrete-to-concrete interface visible in Figure 3.34 (right). Debonding resulted clean through the interface, with the markings of the steel moil point still visible on the substratum contact surface and in reverse at the debonded specimen surface. Such failure mode is characteristic of the aggressive surface preparation method chosen, where pieces of the substratum and/or the overlay concrete randomly stuck upon debonding, which was also in accordance with test results in [26].


Figure 3.34 – Concrete-to-concrete adhesive failure of pull-off specimens.

### 3.2.6.3. Results

Assessment of the interface tensile strength was then performed through the pull-off testing of specimens cast on the same surface and at the same time as the RCO. Table 3.10 presents the average pull-off strength ($\sigma_{Pull\text{-}off}$) of each set of specimens. Such strength was calculated through the tensile strength of the interface, which is the measured tensile failure load divided by the pull-off specimen area (ap. 150x150mm$^2$).

Table 3.10 - Concrete properties and interface tensile capacity for all specimens.

| | Nr. of specimens | $\sigma_{Pull-off}$ (MPa) | Standard Deviation (MPa) | Coefficient of Variation |
|---|---|---|---|---|
| **$R_S$-STC-4** | 5 | 1.25 | 0.14 | 0.11 |
| **$R_S$-STANC-4** | 5 | 1.14 | 0.13 | 0.11 |
| **$R_S$-ANC-4** | 6 | 1.44 | 0.12 | 0.08 |
| **$R_L$-REF** | 6 | 0.70 | 0.13 | 0.18 |
| **$R_L$-ANC** | 5 | 0.88 | 0.12 | 0.13 |
| **$R_L$-STC** | 6 | 0.94 | 0.08 | 0.08 |
| **$R_L$-STANC** | 6 | 0.90 | 0.15 | 0.16 |
| **$R_S$-STC-5** | 6 | 0.91 | 0.06 | 0.07 |
| **$R_S$-ANC-5** | 6 | 0.88 | 0.07 | 0.08 |
| **$R_S$-REF-1/2/3** | 6 | 1.36 | 0.12 | 0.09 |
| **$R_S$-ANC-1/2/3** | 6 | 0.73 | 0.13 | 0.18 |
| **$R_S$-STC-1/2/3** | 6 | 1.16 | 0.15 | 0.13 |

The resulting pull-off strength varied in terms of average stress from a minimum of 0.70 MPa to a maximum of 1.44 MPa. A large scatter could be observed through high coefficients of variation, which are also characteristic on tensile test results. The sample of 69 test results can be considered statistically relevant for defining interface tensile capacity. The results that scattered more than 15% from the average of tensile stresses were discarded. Distribution of the resulting stress for each specimen by its pull-off specimens can be observed in Figure 3.35, where the average stress of approximately 1.02 MPa was attained with such preparation of surface of existing concrete.

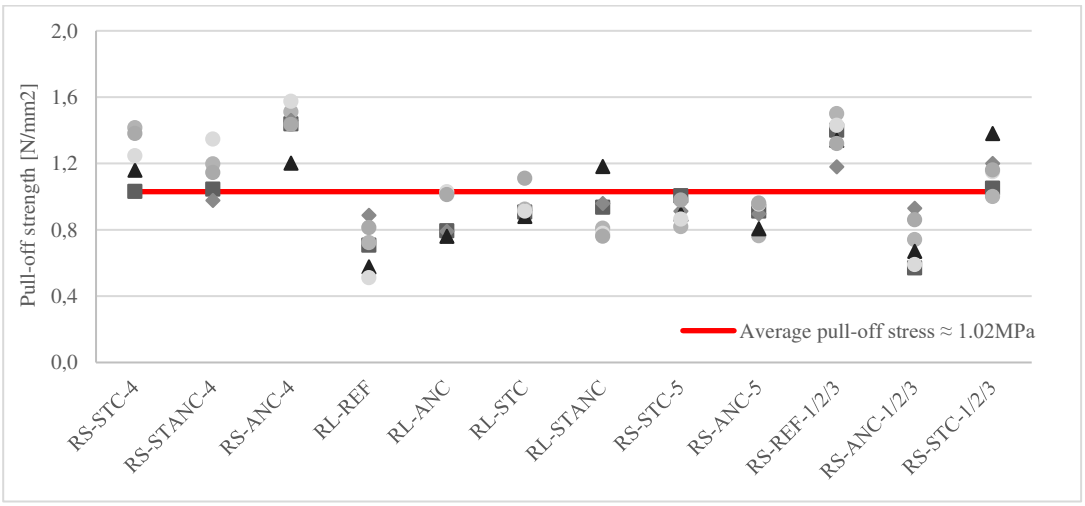


Figure 3.35 – Pull-off strength for the $R_S$ and $R_L$ specimens tested.

### 3.2.7. Test setup

The specimens were subjected to monotonic loading in a three-point bending test, with respective dimensions and layout depicted in Figure 3.36 and Figure 3.37. Loading was imposed at midspan with hydraulic jacks, and reactions at two symmetrical supports, according to the figures below. Forces at the supports were measured with four TML® CNC-200KNA load cells and the deformation at the coordinates identified in the pictures below, with TML® CDP-100 displacement transducers. These tests were performed with prestressing strands fixed to the laboratory strong floor that guaranteed the kinematic boundary conditions at the supports.

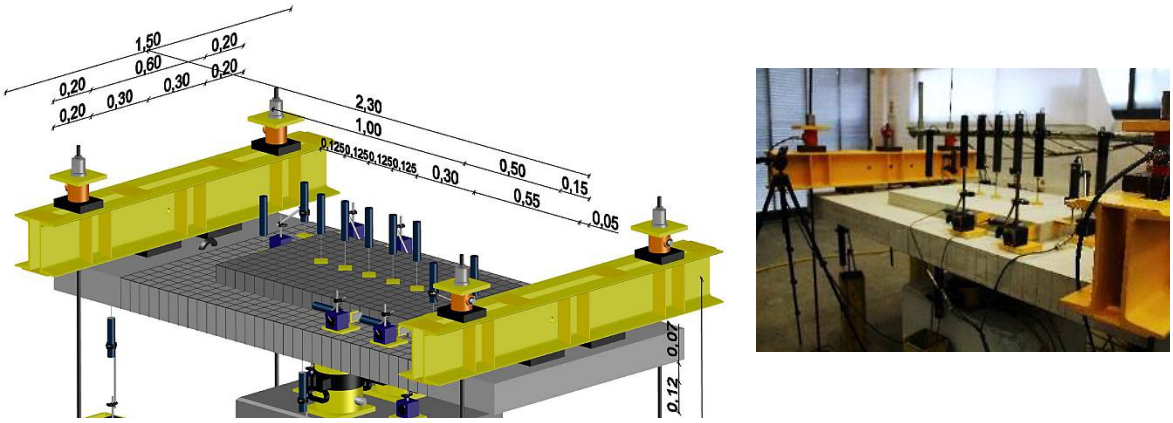


Figure 3.36 – General test layout for $R_S$ (short overlay) geometry: conceptual and real test setup.

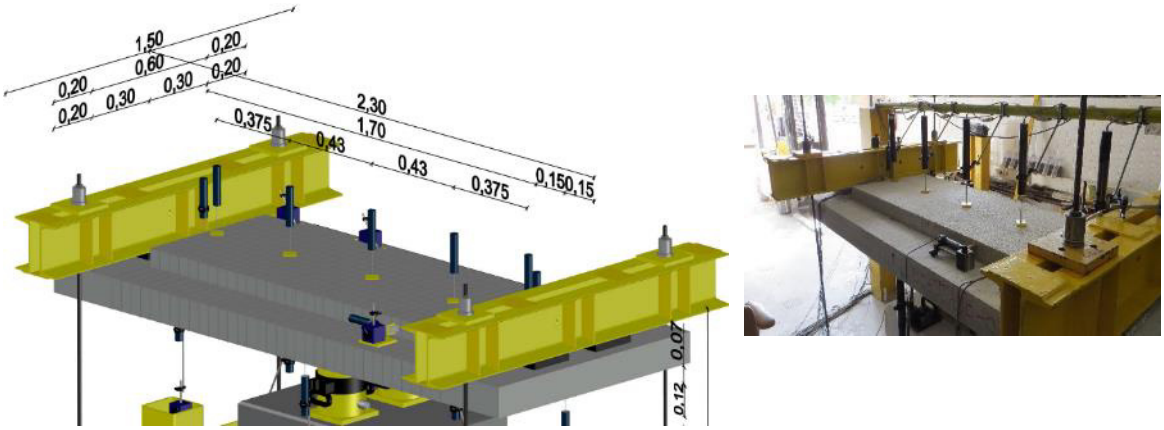


Figure 3.37 – General test layout for $R_L$ (long overlay) geometry: conceptual and real test setup.

Initially, the load cells were installed on top of the spreader beams. The choice for installing the load cells below the laboratory strong floor on the tests that followed was due to the simplicity of assembling the test setup, removing the need for balancing heavy objects on top of the spreader beams, as illustrated in Figure 3.38 and Figure 3.39. Displacement transducers installed below the slab specimens allowed for measuring the settlement at the supports and measure the deformation of the substratum span. Transducers placed directly below the ones above the slab

specimen allowed for estimating differential deflection, which can be translated to crack opening at the midpoint between the midspan and the ends of the overlay.

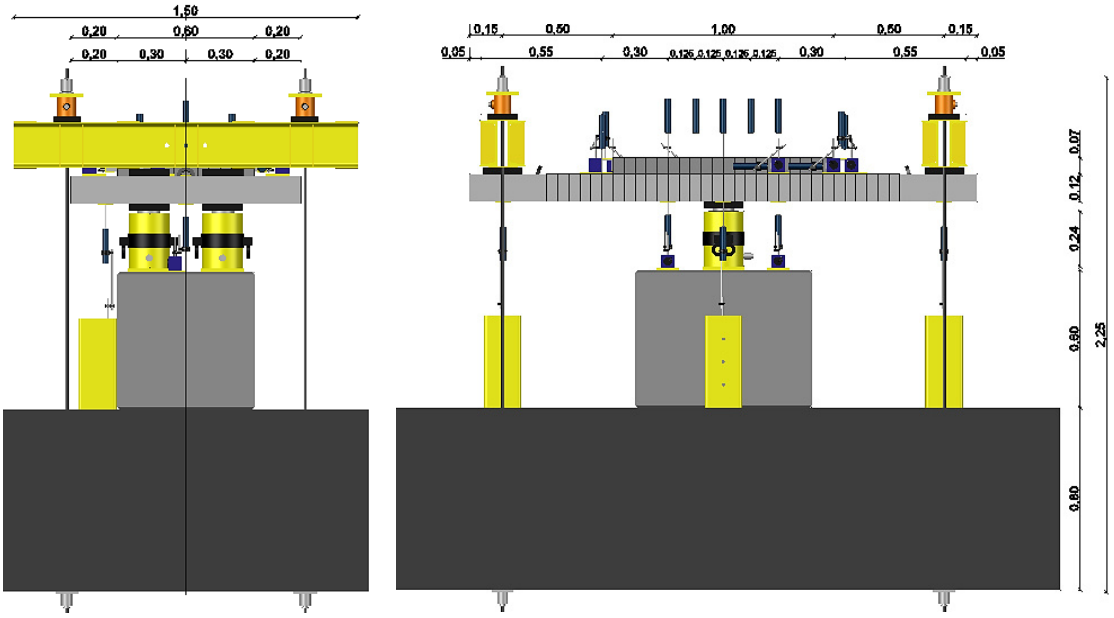


Figure 3.38 – Dimensions (front and side view) of $R_S$ test layout.

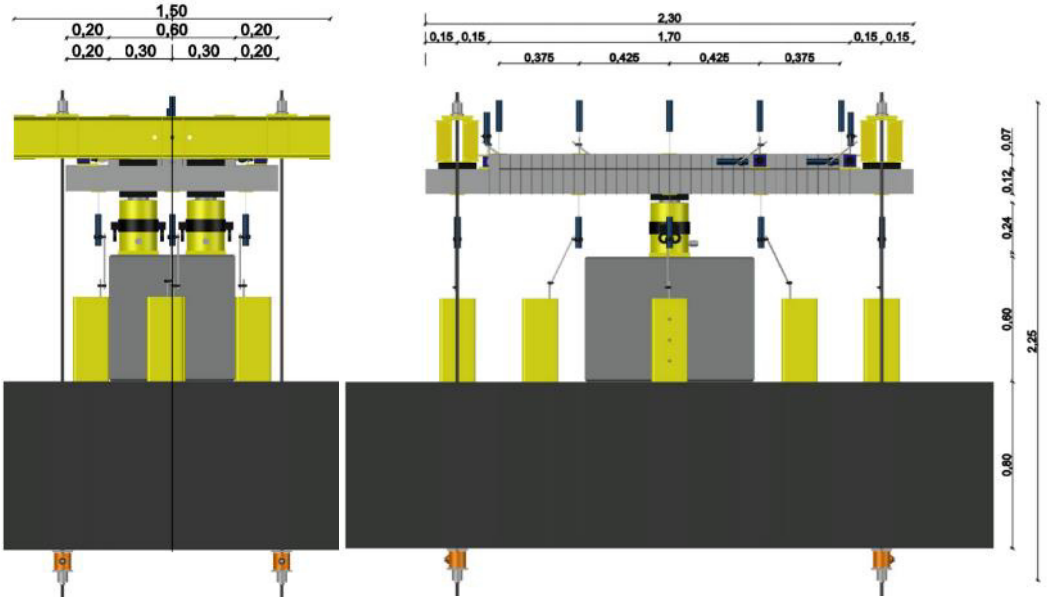


Figure 3.39 – Dimensions (front and side view) of $R_L$ test layout.

For directly assessing relative displacements between the two layers, TML® CDP-50 displacement transducers were fixed on the slab substratum, as shown in Figure 3.40 and Figure 3.41. Such equipment was composed of 50 mm transducers measuring horizontal relative displacement at the midpoint from midspan and at the ends of the overlay, where the vertical relative displacement was also measured.

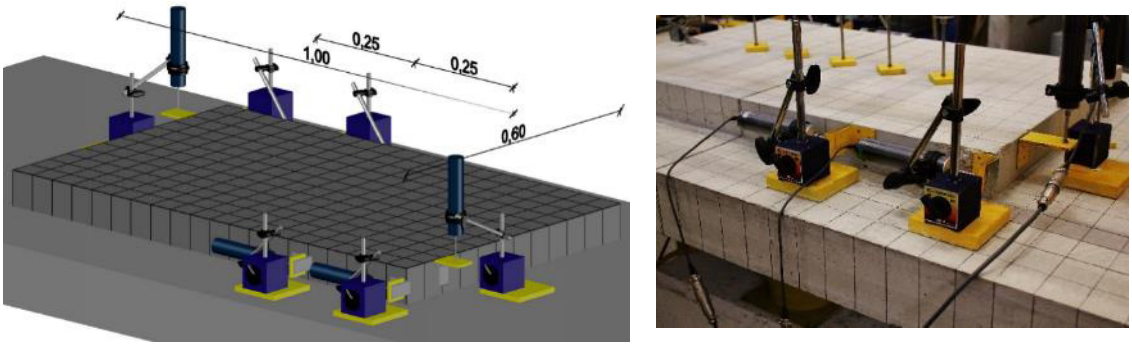


Figure 3.40 – Relative displacement measurement setup for the short overlay geometry ($R_S$).

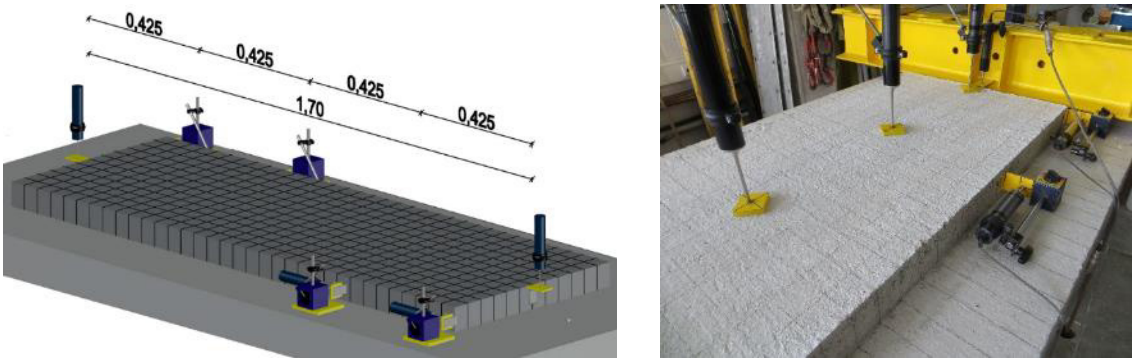


Figure 3.41 – Relative displacement measurement setup for the long overlay geometry ($R_L$).

For data acquisition, four HBM® Spider8 datalogger units were used for the load cells and displacement transducers. Strain gauges were measured with one UPM100 datalogger unit at the beginning, and later by more advanced QuantumX datalogger unit, all from HBM®. The dataloggers were monitored by HBM® Catman V6.0 software. Loading was force controlled with a WALTER+BAI® PKNS19D electronically controlled hydraulic pump, at a speed of 0.10kN/s for all tests, as shown in Figure 3.42.

Figure 3.42 – Data acquisition and load control apparatus.

## 3.3. Results of RCO strengthened one-way specimens

The behaviour of the strengthened specimens could be observed and characterised until failure, according to each detailing of the interface. Complete debonding occurred when no reinforcement crossed the interface, with subsequent loading of the substratum until flexural yielding of tensile reinforcement. The debonding phenomenon started at the ends of the overlaid concrete, where the horizontal and vertical relative displacements were the largest. In Figure 3.43 the starting of interface cracking can be observed along with the data being collected during the tests that registered a discontinuity in the linearity of loading.

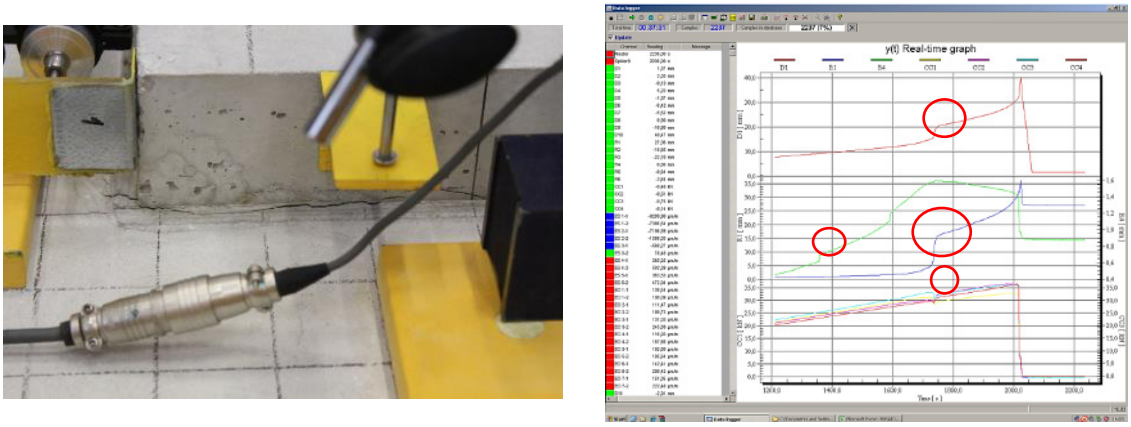


Figure 3.43 – Beginning of cracking at the interface: visual and data proof.

Due to the geometric discontinuity, that is the variation of cross-section between the strengthened and unstrengthened portion of the slab span, cracking started at the ends of the overlaid concrete on all specimens. The evolution of such crack, that leads to debonding of this layer, was controlled by the stitching reinforcement crossing the interface, in the form of steel dowels across the interface or anchored longitudinal rebar in the ends of the overlaid concrete. These solutions combined with a rough surface preparation played a major role on stress transfer between the two layers by interlocking both layers in a controlled debonding of the overlaid concrete.

### 3.3.1. Evolution of interface cracking/debonding

The slenderness of the slab specimens leads to flexural cracking before other cracks can form. The discontinuity that is the interface between the two layers leads to energy dissipation through its area and subsequent debonding. The reference specimens allowed for the full separation of the concrete cross-section and observation of the cracking phenomenon for overlaid concrete layers in tension. Cracking of the reference specimens at the interface evolved from the ends of the overlaid concrete, along the interface to midspan. Full debonding is shown in Figure 3.44 for the short ($R_S$-REF-1) and long ($R_L$-REF) overlay geometries.

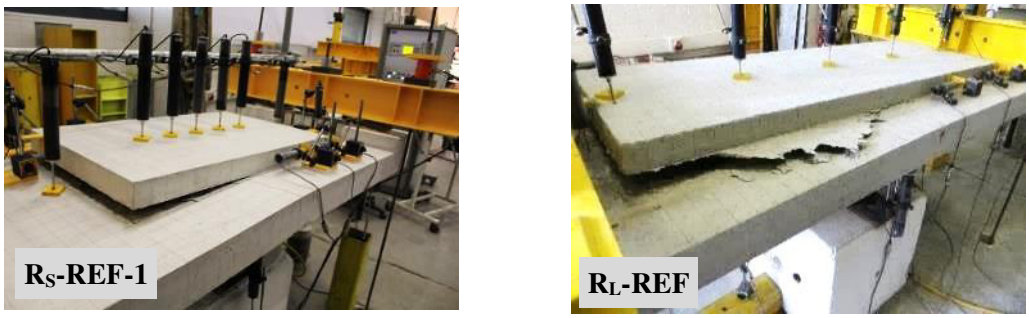


Figure 3.44 – Interface failure for the reference specimens.

For specimens with longitudinal rebar anchored on the substratum layer, beginning of interface cracking was similar to the reference specimens, occurring again at the ends of the overlaid concrete. Failure of these specimens was divided into flexural and shear failure modes, with the former being characteristic of the short anchoring of the reinforcement crossing the interface ($R_S$-ANC, 2 and 3), observed on Figure 3.45 for the $R_S$-ANC-2 specimen. Characteristic of such failure is the pull-out of the anchorage from the substratum through the grout-concrete interface. Also, the degradation of the substratum at the contact surface, with spalling of concrete and concrete cones that were also pulled out with the anchorages, was also observed (Figure 3.45).

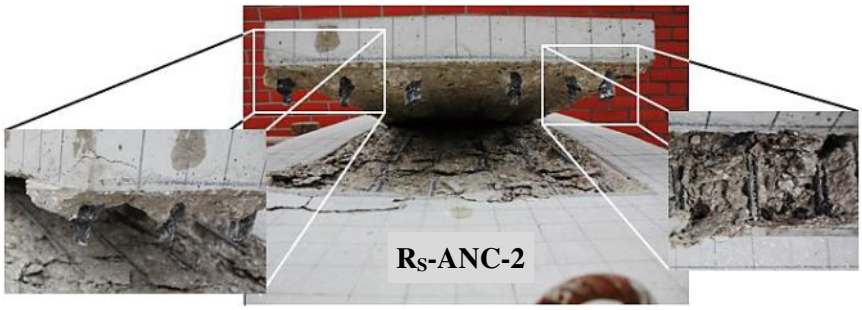


Figure 3.45 – Failure for specimens with small anchorage length of the longitudinal rebars ($R_S$-ANC-2).

Shear of the substratum with incomplete debonding of the overlaid concrete was then the common failure mode of such detailing of the interface for one of the short anchorages ($R_S$-ANC-1), and for the longer anchorages, on both short ($R_S$-ANC, 4 and 5) and long ($R_L$-ANC) overlay geometries, shown in Figure 3.46. Analysing the shear crack, a similarity was identified on these specimens, regarding the most prominent shear crack that started at around 0.40 m from the ends of the overlay.

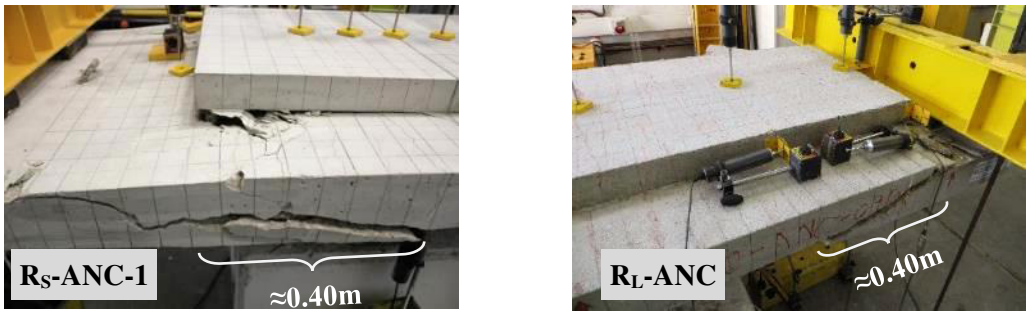


Figure 3.46 – Shear failure for the ANC specimens.

Regarding the specimens with steel connectors distributed on the interface, cracking was similar to anchored rebar ones, where two specimens failed in shear, with an example illustrated in Figure 3.47 for $R_S$-STC-1 specimen. Full debonding of the overlaid concrete was never attained on these specimens, with failure occurring with the two layers still transferring stresses through the interlocking of both layers. The predominant failure mode was shear of the substratum for the $R_S$-STC specimens 1 and 3, and for the $R_L$-STC specimen, with both short and long overlay geometries illustrated in Figure 3.47.


Figure 3.47 – Shear failure for the STC specimens.

Two of the short overlay specimens ($R_S$-STC-2 and $R_S$-STC-5) failed in bending. The first specimen failed due to the short anchoring of the dowels, which allowed for the slipping of the stitching reinforcement. Anchorage failure occurred then with pull-out at the steel-grout interface visible through the interface crack right after testing (Figure 3.48, left). The longitudinal saw cutting allows for assessing the evolution of the shear crack for the specimen that failed in bending. The insufficient anchorage length caused the shear crack to fail intercepting the steel connectors, as observed in the figure below, and again the weakened concrete of the substratum spalled in a cone shape at the anchorages similar to the ANC specimens above.


Figure 3.48 – Steel connectors anchorage detail and sawcut of the $R_S$-STC-2 specimen.

The STANC specimens, that combined all detailing solutions for the interface on the short and long geometries of the overlay, also failed in shear of the substratum, as observed in Figure 3.49.


Figure 3.49 – Shear failure for the STANC specimens.

One can observe that the specimens with the larger anchorage length of reinforcement crossing the interface (80 mm) failed in shear. This attests the need for sufficient anchorage length of reinforcement crossing the interface, thus allowing the transfer of stresses between the two layers throughout the load history. When reinforcement crosses the interface, the proper anchoring to the substratum is then a requirement for structural integrity and achieving an almost monolithic behaviour.

### 3.3.2. Sawcuts of the specimens

Analysing the sawcuts of the specimens, one can observe how cracking was deflected by the stitching reinforcement. Due to the expensive resources needed for saw-cutting reinforced concrete, only selected specimens were cut and analysed visually. These were selected by singularity of the failure mode, or if the visual inspection of the interface was not possible. Analysing the specimens with dowels crossing the interface in the next figures, one can observe how the most prominent shear crack was deflected further away from the column face before reaching the interface. On the left side of the $R_S$-STC-4 specimen, such phenomenon occurred on the last row of dowels, also corresponding to where shear failure occurred for the substratum. On the right side, the most prominent crack reached the top reinforcement of the substratum right after the first row of dowels, having evolved horizontally and close to the interface. From the post-failure spalling of the concrete surface observed in Figure 3.50 for the substratum, the evolution of cracking slightly below the interface is expected.

Figure 3.50 – Spalling of the substratum at failure ($R_S$-STC-4 specimen).

Regarding the long overlay specimen $R_L$-STC, one can observe in Figure 3.51 the asymmetry of cracking due to the longer span of the slab, with failure occurring on the right side of the specimen, where the most prominent shear crack also evolved. Cracking of the specimens with such detailing of the interface suggests that this reinforcement worked like shear reinforcement. A change in the direction of principal stresses and the partial pull-out of the bottom part of the dowel's anchorage by intersecting the last row of dowels indicate a deformation in shear.

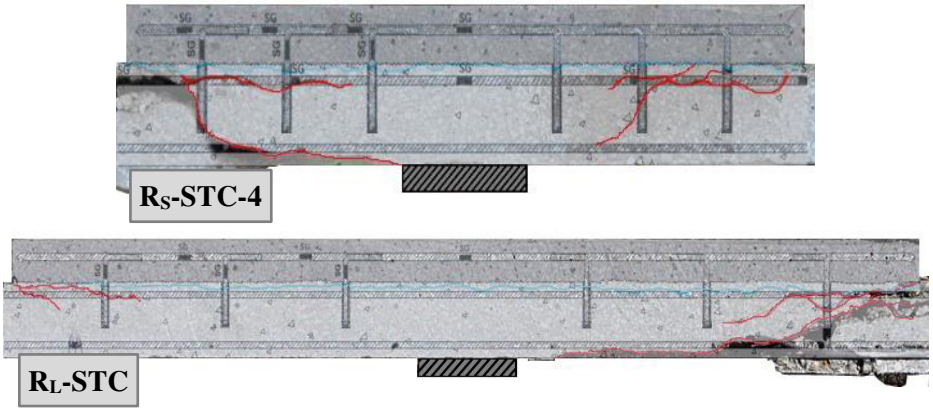


Figure 3.51 – Sawcut detail of the short and long overlay STC specimens.

Analysing the specimens with the overlaid concrete reinforcement anchored in the substratum on Figure 3.52, one can observe a major difference between the short and long overlay geometries, namely the flexural cracks that are very prominent in the $R_L$ specimen. Although both geometries failed due to shear of the substratum, the $R_S$-ANC-4 specimen resulted on almost symmetric cracking of the cross-section between the column face and the end of the strengthened layer. Such cracking crossed the interface until reaching the overlaid concrete reinforcement. Analysing both overlay geometries, one can observe the strut that is coherent with the characteristic for shear on concrete slabs and beams without reinforcement specific for shear. The latter phenomenon was coherent with failure of the $R_L$ specimen, observed in Figure 3.52.

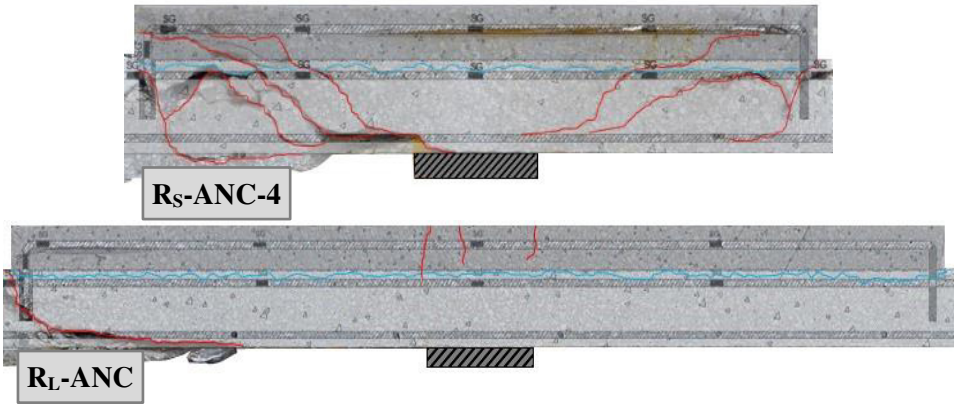


Figure 3.52 – Sawcut detail of the short and long overlay ANC specimens.

Analysing the specimens where all the specific reinforcement was applied, the same kind of cracking similar to the aforementioned specimens could be observed on Figure 3.53. Crack pattern for the $R_S$-STANC specimen resulted almost symmetrical, with two prominent shear cracks on each side. Failure occurred similarly to the ANC specimens above, by the strut that reached the end of the overlay. The dowels caused the prominent shear crack to deflect to the top of the cross-section before reaching the ends of the overlay on the $R_L$-STANC specimen, with the shear crack at failure resulting before the end of the overlay. Crossing of the interface for the innermost shear cracks is also noteworthy since it denotes an almost monolithic behaviour of the composite cross-section.

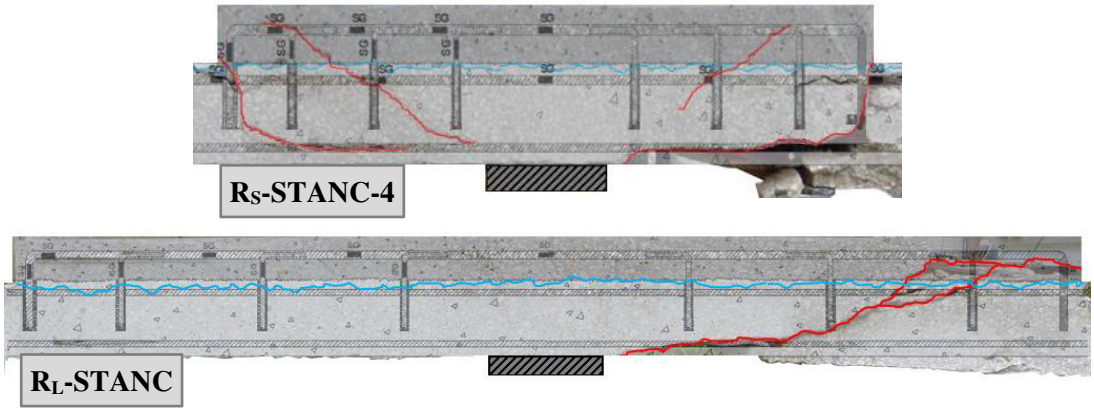


Figure 3.53 – Sawcut detail of the short and long overlay STANC specimens.

### 3.3.3. Debonding and failure loads

The load - deflection diagrams at midspan are analysed for characterising the behaviour of overlaid concrete strengthened specimens. Relative displacements are also measured on all specimens for assessing the interaction between the two layers regarding relative slip and interface crack dilation. Stresses at the longitudinal reinforcement are estimated regarding the measured strain on the instrumented rebars, and the shear stress at the interface are also estimated considering the flexural equilibrium of the composite cross-section.

Figure 3.54, Figure 3.56 and Figure 3.57 present the vertical load - deflection at midspan diagrams for all unidirectional specimens, comparing between the ones with reinforcement crossing the interface and reference ones, for both short ($R_S$) and long ($R_L$) overlay geometries.

The load-deflection diagrams of the first set of tests that comprised reference ($R_S$-REF), $R_S$-ANC, and $R_S$-STC specimens, can be observed in Figure 3.54. One can observe where the reference specimens show clearly the debonding phenomenon through a plateau in such diagrams. Specimens with reinforcement crossing the interface, which had a small anchorage length of 55 mm, emphasize the importance of this reinforcement, with brittle debonding occurring when the interface capacity is reached (ANC specimens). Subsequently, the substratum is loaded until flexural failure occurs.

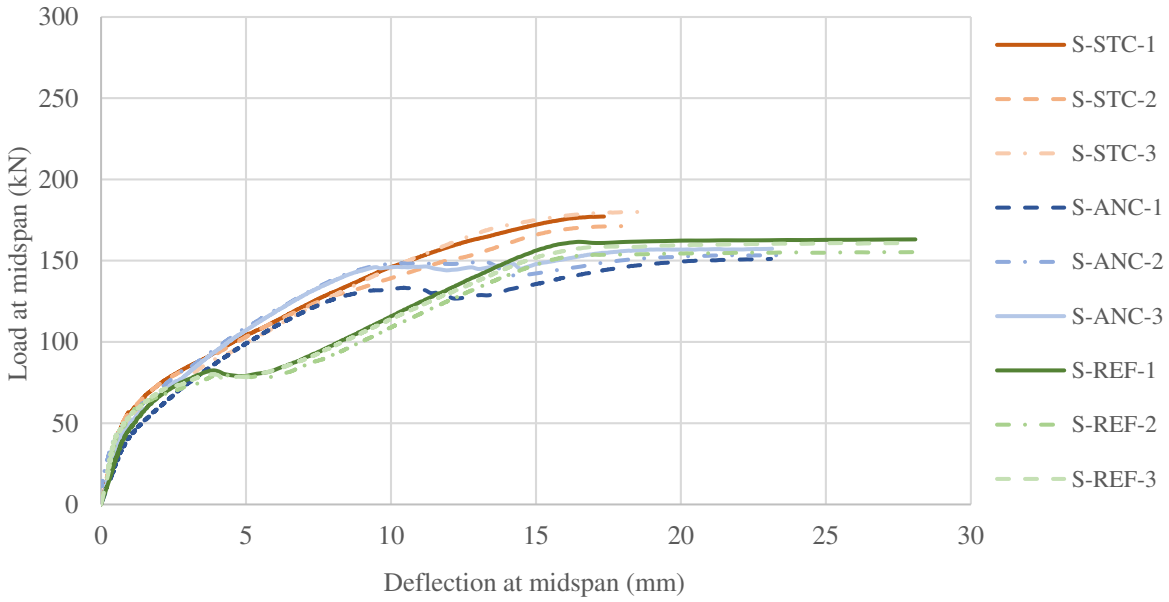


Figure 3.54 – Load-deflection at midspan diagrams for the first short overlay ($R_S$) specimens.

The load-deflection curves above show an approximately linear behaviour for all tests up to a load close to 40 kN at midspan, followed by a reduction in stiffness. Such load was characterised by the initiation of the cracking phenomenon due the loss of stiffness. For assessing this load, the cracking moment $M_{cr}$ was calculated according to equation (3.5) for the composite cross-section considering its inertia I as a monolithic section since the interface still holds its stress transferring capacity. The chosen tensile strength was that of the overlay since cracking begins at the outermost tensile fibre v from the section's neutral axis.

$$M_{cr} = f_{ctm} . \frac{I}{v} \tag{3.5}$$

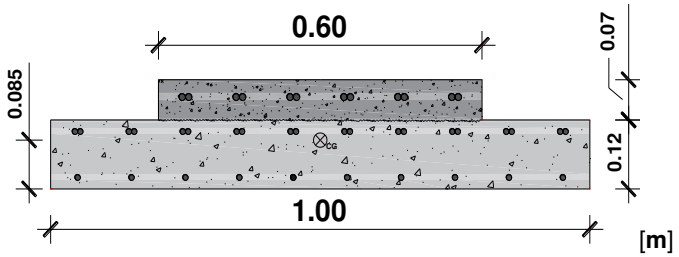


Figure 3.55 – Separation of the two components of the composite cross-section – 7cm thick and 0.60m wide (overlay), and 12cm thick and 1.00m wide (right).

The flexural modulus of the composite cross-section allowed for calculating the section's cracking moment and respective load at midspan. The cracking load at midspan considering the composite cross-section results in values ranging from 29-kN to 37-kN at midspan, considering the respective concrete tensile strengths of 2.7 to 3.9-MPa. Such values are in accordance to the behaviour observed on the load-deflection curves of the strengthened specimens. The exact value of the cracking load on such curves is of difficult assessment due to the data resolution and nonlinear behaviour of concrete. This phenomenon also affects the bond capacity of the interface since it consists of a sudden change in the specimen's geometry at the end of the overlay. These zones are characterised by stress concentration and change in the direction of stress paths. For the reference specimens ($R_S$-REF, 1 to 3), debonding of the overlaid concrete occurred for a load at midspan of 80 kN. Stiffness was reduced to approximately zero, observed graphically by a horizontal plateau. This was followed by reloading of the substratum, until flexural failure occurred for a load at midspan around 160 kN.

For the specimens with longitudinal rebar anchored 50 mm in the substratum ($R_S$-ANC, 1 to 3), the ultimate failure load was about the same as the reference specimens, which is explained by the debonding of the overlaid concrete that also occurred on these specimens. Such behaviour and change in stiffness suggests the initiation of the interface cracking phenomenon similar to the reference specimens. A debonding load around 142 kN presents an increase of 79 % when compared to the latter specimens, also resulting very close to its failure load. The insufficient anchoring of the overlaid concrete did not allow for controlling the edge lifting phenomenon further in the load history.

For specimens with steel connectors anchored 50 mm in the substratum ($R_S$-STC, 1 to 3), the debonding load increased about the same as the latter (76 %), with the resulting failure load being 10 % higher than the reference specimens. Despite the small anchorage length of the steel connectors, these specimens showed a difference in terms of the load-deflection diagrams since no clear debonding could be identified in the load history. Although full debonding was not visible during testing, this phenomenon was identified through the strain measurement at the longitudinal rebars.

The three specimens with 80 mm anchorage length ($R_S$-ANC-4, $R_S$-STC-4, and $R_S$-STANC) differed from the first set of tests mainly due to greater debonding and failure loads, with the vertical load - deflection at midspan diagrams for these specimens presented below in Figure 3.56. Common to these specimens was also the shear failure of the specimen's substratum, as mentioned in 3.3.1.

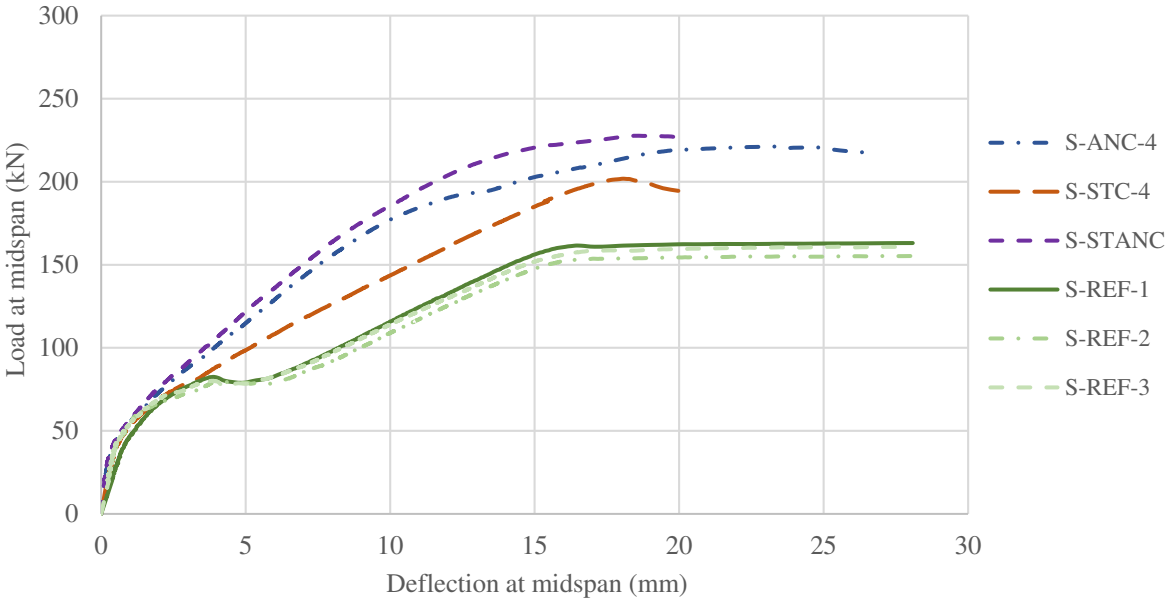


Figure 3.56 – Load-deflection diagrams at midspan for the second short overlay ($R_S$) specimens.

From the load-deflection diagrams, one can observe the increase of debonding and failure loads due to the 80 mm anchorage length. The latter showed an increase of 39% for the anchored longitudinal rebar specimens (ANC), 27% for the slabs with steel connectors (STC), and 43% for when all techniques were combined (STANC). Also noticeable is the small increase of the failure load on the STANC specimen when compared to the ANC specimen. This attests the impact of the latter detailing on the overall behaviour of the interface, due to the positioning at the overlaid concrete ends where the edge lift phenomenon occurs. The limitation in the evolution of both interface crack dilation and relative slip in the edge of the overlay results in smaller relative displacements that reach the steel connectors, limiting its contribution to the capacity of the interface. However, these are activated later in the loading. Observing the stiffness of the STC specimen after the debonding stage set by the reference specimens suggests the substratum governing such stiffness. The absence of rebar crossing the interface at the ends of the overlay allows for the edge lifting phenomenon to occur, with consequent debonding propagating towards the midspan, only controlled by the steel dowels crossing the interface.

Analysing the specimens with long overlays ($R_L$, Figure 3.57), one can observe the largest increase in terms of ultimate failure load, which resulted close to double that of the original reference specimens. Debonding occurred for a load around 140 kN on the reference specimen, which is a 75% increase over the $R_S$-REF specimens. The larger area of contact and respective edge further from midspan can both justify such behaviour. The increase observed for the debonding load is coherent with the 70% geometric increase in contact area between the two layers. However, the reloading stage of the specimen's load history did not result in any increase for the ultimate failure load. Load loss after debonding of the $R_L$-REF specimen was different than that of the $R_S$-REF specimen, which plateaued with no reduction of load. A load loss could be observed for the former specimen after debonding since the flexural strength is smaller than the debonding load. Also, noticeable in the figure below is the proximity of ultimate failure loads between ANC and STANC specimens, similar to the short overlay specimens.

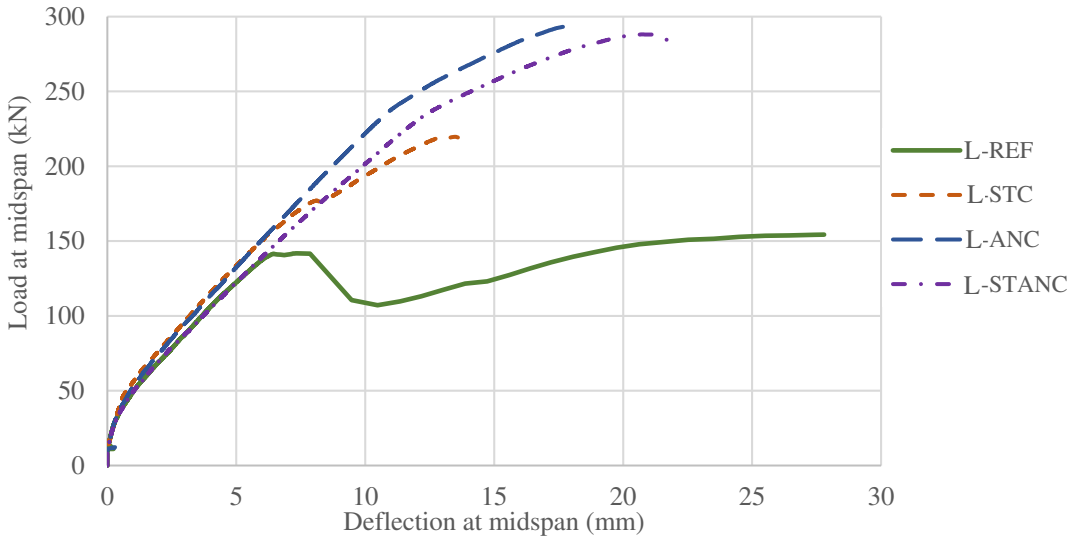


Figure 3.57 – Load-deflection diagrams at midspan for the long overlay ($R_L$) specimens.

A governing stiffness for all specimens can be identified until debonding of the overlaid concrete on the reference specimen, with the specimens superimposing each load-deflection diagrams in pairs, respectively REF with STANC, and STC with ANC. The STC specimen was the one that registered the lowest failure load of the specimens with reinforcement crossing the interface, although with the same failure mode. Shear failure on these specimens could be observed in 3.3.1 and 3.3.2 and consisted on a shear crack on the substratum that reached the edge of the overlay. STC was the only detailing that didn't provide reinforcement in this zone of the cross-section, therefore not controlling the shear failure mode observed. Coupled with the edge lifting phenomenon, again such behaviour emphasizes the importance of the edge reinforcement crossing the interface. The specimens with such reinforcement ANC and STANC then resulted in the largest failure loads of this series, with no relevant debonding of the interface, doubling the debonding load of the reference specimen.

Table 3.11 lists the loads at midspan for failure and for maximum strain at the overlay $P_{MS}$ reinforcement, allowing to assess the ratio between such load-states. The respective force on the tensile reinforcement of the substratum $F_S$ and overlay $F_{SO}$ are also presented for understanding the differential strength between both layers. Such load also corresponds to maximum shear stress at the interface. Failure modes are identified as shear of the substratum ("Shear") or flexural failure of the substratum reinforcement ("Flex"). Due to the absence of strain gauges at the time of specimen production, some specimen's reinforcement could not be instrumented, thus being left blank in the table below regarding strain measurement.

Table 3.11 – Loads for maximum strain at the overlaid concrete reinforcement and failure – $R_S$ specimens.

| Specimen | | Load at Maximum Strain (MS) in the overlay rebars | | | | Failure Load | $\frac{P_{MS}}{P_{max}}$ | Failure mode |
|---|---|---|---|---|---|---|---|---|
| | | $P_{MS}(kN)$ | $F_{so}(kN)$ | $F_s(kN)$ | $\frac{F_{so}}{F_s}$ | $P_{max}\ (kN)$ | | |
| **$R_S$-REF** | 1 | 82.4 | 138.9 | 90.8 | 1.53 | 163.1 | 0.51 | Flex |
| | 2 | --- | --- | --- | --- | 155.3 | --- | Flex |
| | 3 | 80.1 | 141.3 | 88.6 | 1.59 | 160.8 | 0.50 | Flex |
| **$R_S$-STC** | 1 | 140.3 | 218.7 | 179.7 | 1.22 | 177.2 | 0.79 | Shear |
| | 2 | --- | --- | --- | --- | 171.2 | --- | Flex |
| | 3 | 144.3 | 226.5 | 175.9 | 1.29 | 180.1 | 0.80 | Shear |
| | 4 | 200.3 | 408.1 | 375.9 | 1.09 | 201.8 | 0.99 | Shear |
| | 5 | 153.1 | 388.0 | 254.3 | 1.53 | 185.0 | 0.83 | Flex |
| **$R_S$-ANC** | 1 | --- | --- | --- | --- | 151.1 | --- | Shear |
| | 2 | 150.2 | 305.5 | 153.6 | 1.99 | 153.6 | 0.98 | Flex |
| | 3 | 140.6 | 273.6 | 137.3 | 1.99 | 157.3 | 0.89 | Flex |
| | 4 | 190.3 | 408.2 | 272.7 | 1.50 | 221.2 | 0.86 | Shear |
| | 5 | 134.1 | 279.7 | 258.5 | 1.08 | 210.9 | 0.64 | Shear |
| **$R_S$-STANC** | | 214.7 | 483.4 | 235.2 | 2.06 | 227.7 | 0.94 | Shear |

Maximum strain and failure of the composite cross-section were characterised by the debonding of the overlaid concrete and subsequent substratum capacity. The ratio for the two load states considered, debonding and failure, was larger than 80% for all specimens on Table 3.11, except for the reference specimens and the $R_S$-ANC-5 specimen. The ratio for the former was about 50% and the latter showed some inconsistent values and great strain loss for no apparent reason. The $R_S$-STC-5 specimen resulted the most different, with larger strains for the substratum than the overlay. Such behaviour can be due to strain gauge malfunction that didn't allow for a reliable measurement throughout the test. The $R_S$-STANC specimen's failure load was almost that of debonding, resulting also in the greatest value for the latter.

Regarding the specimens with the long overlay geometry ($R_L$), the debonding and failure loads are presented in the table below. The same criteria were considered as for the $R_S$ specimens.

Table 3.12 – Loads for maximum strain at the overlaid concrete reinforcement and failure – $R_L$ specimens.

| Specimen | Load at Maximum Strain (MS) in the overlay rebars | | | | Failure Load | $\frac{P_{MS}}{P_{max}}$ | Failure mode |
|---|---|---|---|---|---|---|---|
| | $P_{MS}(kN)$ | $F_{so}(kN)$ | $F_s(kN)$ | $\frac{F_{so}}{F_s}$ | $P_{max}\ (kN)$ | | |
| **$R_L$-REF** | 141.7 | 206.9 | 144.7 | 1.43 | 154.2 | 0.92 | Flex |
| **$R_L$-STC** | 219.7 | 484.4 | 393.3 | 1.23 | 219.7 | 1.00 | Shear |
| **$R_L$-ANC** | 230.1 | 561.7 | 459.3 | 1.22 | 293.6 | 0.78 | Shear |
| **$R_L$-STANC** | 235.5 | 688.0 | 524.0 | 1.31 | 288.1 | 0.82 | Shear |

The larger contact area between the two layers leads to higher debonding loads and consequently higher failure loads. Shear failure of the substratum was common on all specimens with reinforcement crossing the interface. These specimens reached the highest loads of all specimens tested, attesting that the longer overlays result in better behaviour and capacity of the strengthened specimens. The ratio between the debonding and failure loads was also larger than 80 % on all specimens, which states the good contribution of the strengthening layer during the load history.

### 3.3.4. Rebar strains on both layers

The strain gauges installed for the assessment of strain on longitudinal and transverse reinforcement crossing the interface allowed to identify the development of the strain profile of the specimens tested. The differences between the stresses in both steel layers correspond to the stress transferred through the interface. The organization of strain data was divided by detailing solution of each strengthened specimen, and by overlay size.

The lateral distribution of strain on the flexural reinforcement was analysed on the first specimens – $R_S$-REF 1 and 3, $R_S$-STC 1 and 3, and $R_S$-ANC 2 and 3 – by instrumenting the adjacent reinforcement to the fully instrumented rebar, as illustrated in Figure 3.58.

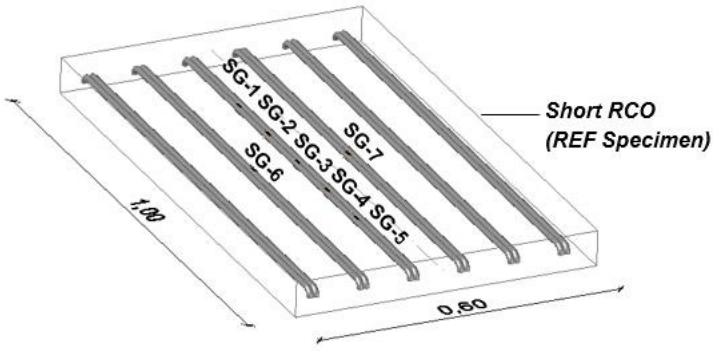


Figure 3.58 – Lateral instrumentation of overlay reinforcement on $R_S$-REF specimens.

The resulting strain profiles allowed for assessing a difference in strains of adjacent reinforcement to the main instrumented rebar, as illustrated in Figure 3.59. The resulting error was then evaluated for each of the specimens, ranging from 6-24% on the $R_S$-REF specimens, mainly due to the lower strains measured, 7-10% for the $R_S$-ANC specimens, and 4-6% for the $R_S$-STC specimens. The error between adjacent instrumentation reduces with increasing strains as expected. The resulting error between adjacent strain gauges allows for considering a uniformly distributed strain across the transverse cross-section.

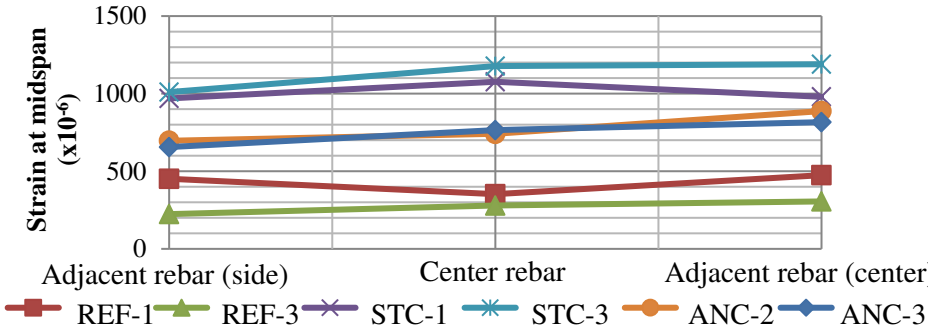


Figure 3.59 – Transversal distribution of overlay reinforcement strains on $R_S$-REF specimens.

### 3.3.4.1. Reference specimens

These specimens were characterised for not having reinforcement crossing the interface, hence were characterised for having smaller strains on the overlay reinforcement than other specimens. Three specimens were considered for such detailing of the interface: two with shorter overlays ($R_S$-REF, 1 and 3) and one where such layer was extended closer to the supports ($R_L$-REF). The $R_S$-REF-1 specimen can be observed on Figure 3.60 regarding the strains on the longitudinal reinforcement of both layers.

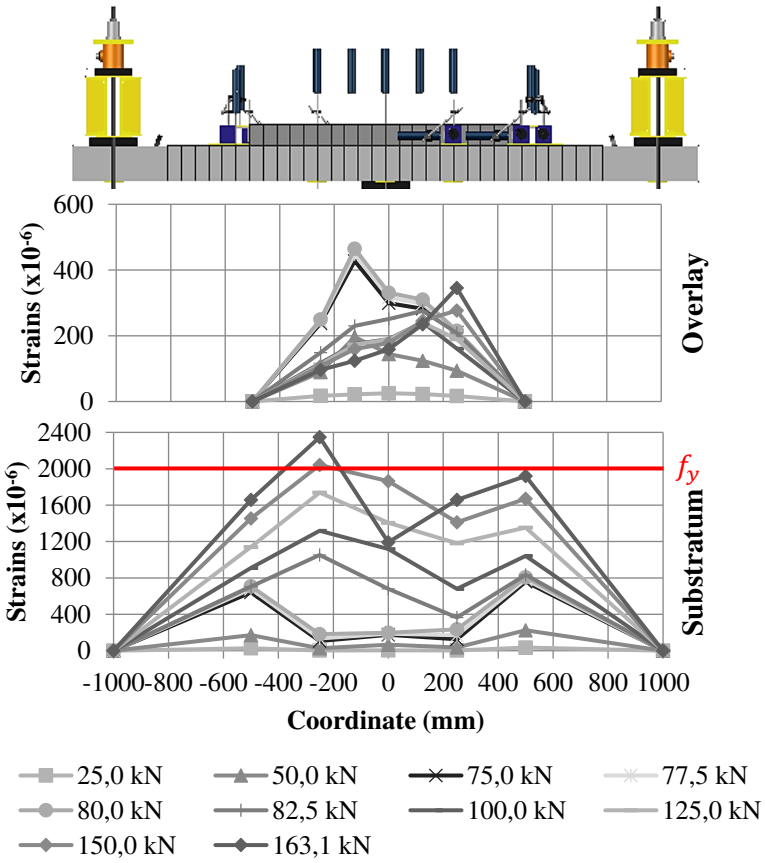


Figure 3.60 – Strain profiles by load step on both layers of $R_S$-REF-1 specimen.

One can observe the concentration of strains in the figure above on the left side of the overlay reinforcement until debonding occurs for a load around 80 kN. After such plateau, the strains increase mainly on the left side of this specimen and debonding occurs on either side of the specimen.

Analysing the strains on coincidental coordinates of both layers, the point in the load history where the strains of both layers intersect globally identifies completion of the debonding phenomenon. This can be graphically observed on Figure 3.61. The difference between rebar strain on both layers is transferred through the interface, thus resulting the shear stress that is favourable to such phenomenon. The load-strain relationship also changes on the substratum, with an increase due to cracking of the cross-section and the loss of effective cross-section after debonding, since the overlay contribution is minimized at this stage.

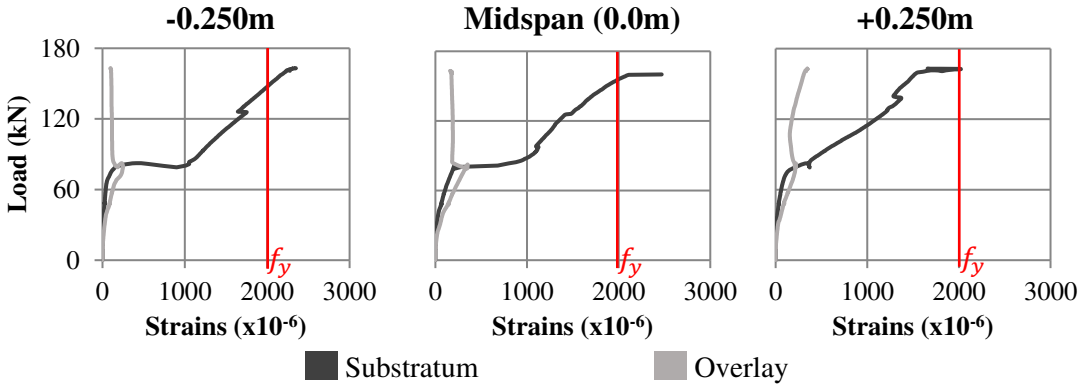


Figure 3.61 – Evolution of strain at coincident coordinates on both layers of the $R_s$-REF-1 specimen.

Strains regarding the specimen where the overlay dimension was extended closer to the supports ($R_L$-Ref) revealed a greater concentration at midspan on both layers until debonding. After this plateau the strains on the overlay dropped and the strains on the substratum were increased on the right side of the specimen, opposite to where debonding occurred. All this can be observed in Figure 3.62.

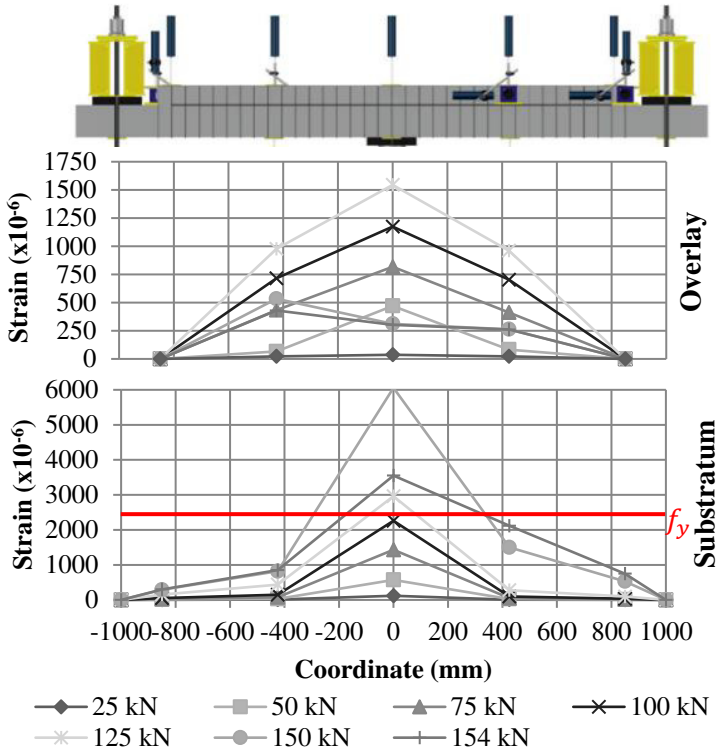


Figure 3.62 – Strain profiles by load step on both layers of $R_L$-REF specimen.

Analysing the strains on the coincidental coordinates of both layers on Figure 3.63, one can observe the major change in behaviour of these specimens when compared to short overlays. On opposite coordinates, the strains kept the same magnitude and larger strains were registered at the overlay. Strains at midspan were significantly larger for the substratum, which may indicate an incorrect reading of the strain gauge. Such observations can identify the shifting of stresses further from midspan for longer overlay geometries.

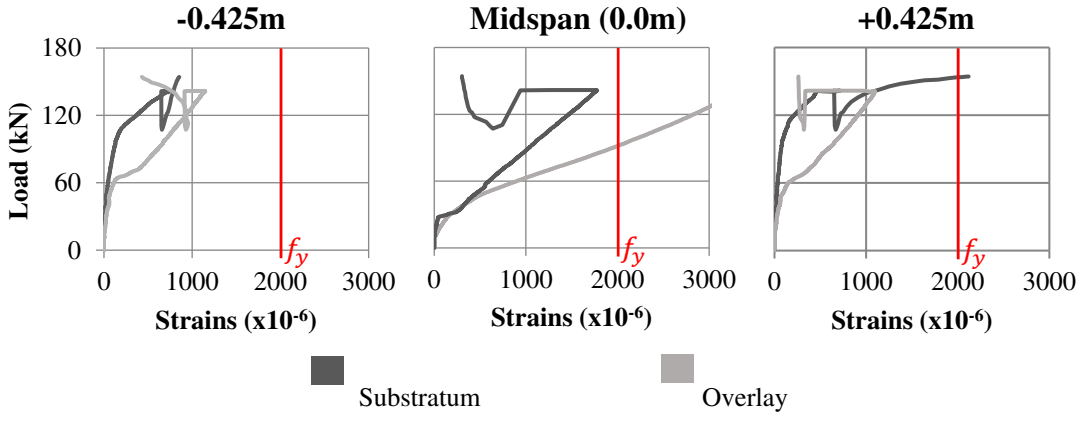


Figure 3.63 – Evolution of strain at coincident coordinates on both layers of the $R_L$-REF specimen.

### 3.3.4.2. Specimens with dowels crossing the interface

These specimens were characterised for controlling the debonding phenomenon further in the load history, therefore enabling the reinforcement in the overlaid concrete to reach higher strains. Consequently, the interface was also required to withstand higher stresses, both normal and tangential, since reinforcement crossing the interface increases the interlocking of the two surfaces and more friction. The resulting strains of the short overlay specimen $R_S$-STC-1 are presented below for both layers.

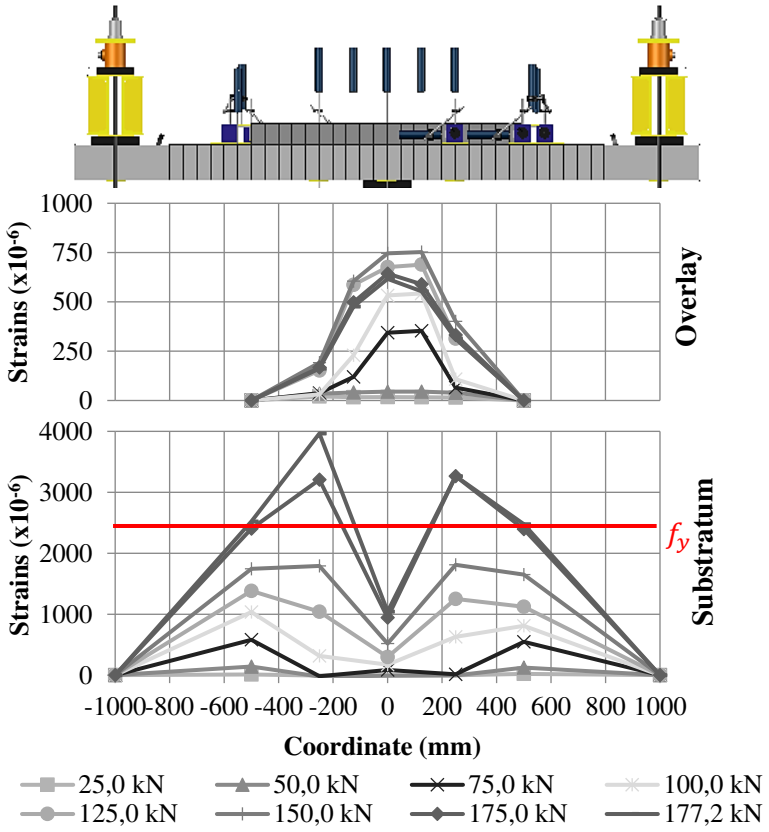


Figure 3.64 – Strain profiles by load step on both layers of $R_S$-STC-1 specimen.

One can observe in the figure above that the stitching reinforcement with steel dowels allowed for greater strains at the overlay reinforcement. This behaviour is attested by the smaller strains on the center of the substratum when compared to strains on each side of the overlaid concrete. The magnitude of such difference could also be explained by the improper reading of the strain gauge since the strain gauges next to midspan show a linear evolution. The expected flexural crack at midspan due to maximum bending moment places the strain gauge directly on it prone to damage. This specimen allowed for an 85% increase in the maximum strain measured at the overlay when compared to the respective reference specimen in 3.3.4.1.

Analysing the strains at the coincidental coordinates on both layers, the debonding phenomenon is identified as the maximum strain on the overlay reinforcement. One can observe that the strains equalize close to failure. This can be graphically observed on Figure 3.65, although more progressive than the reference specimens without stitching reinforcement. The strains at midspan behave like the reference specimen, where the strains of the overlay reinforcement rise after cracking and then intersect with the strains of the substratum reinforcement, as consequence of the debonding phenomenon.

Larger strains were attained on both sides of the overlay, and even larger on the substratum. Such behaviour denotes the difference in deformation between fixed and non-fixed ends. The ends of substratum reinforcement are fixed, allowing for the reinforcement to deform according to the curvature of the flexural deformation. The ends of overlay reinforcement are non-fixed, which allows for a loss of strain due to the change of its initial coordinate, thus explaining the behaviour observed at the instrumented coordinates -0.250m and +0.250m.

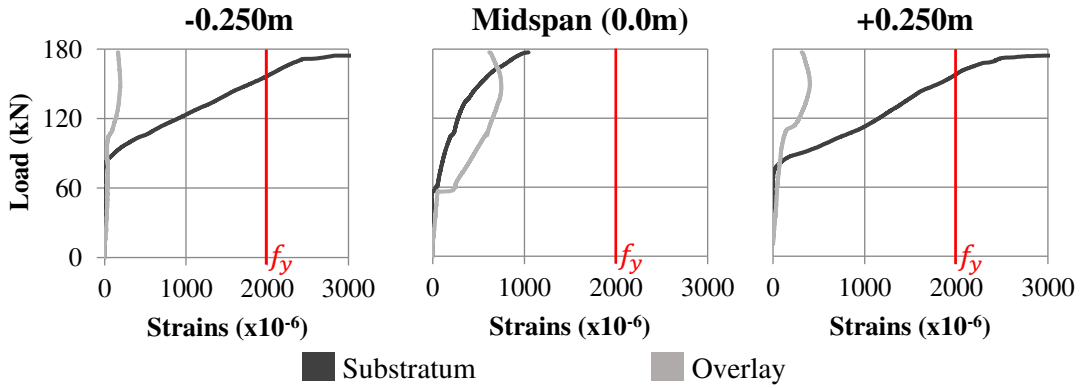


Figure 3.65 – Evolution of strain at coincident coordinates on both layers of the $R_s$-STC-1 specimen.

Regarding the strains on the $R_L$-STC specimen, one can observe in Figure 3.66 the order of values on both layers were almost the same, with marginally larger strains on the overlay. A great change in the behaviour could be observed when compared to the $R_S$ specimen, with the evolution of strain resulting similar on both layers.

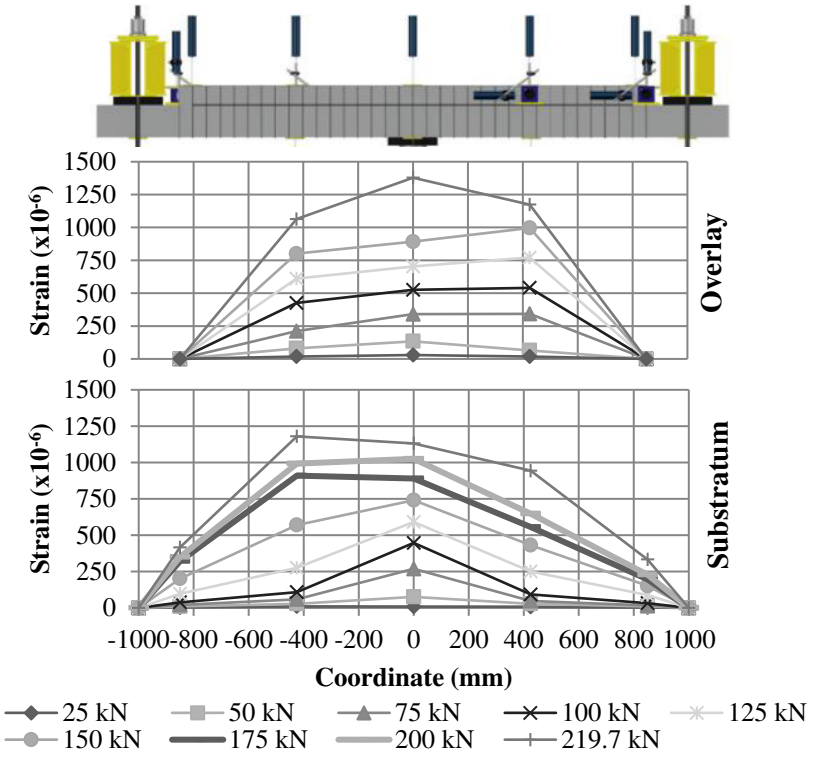


Figure 3.66 – Strain profiles by load step on both layers of $R_L$-STC specimen.

Analysing the strains on coincidental coordinates of the specimen on Figure 3.67, these were always greater on the overlaid concrete reinforcement, evolving linearly at midspan and more susceptible to the debonding phenomenon further from midspan.

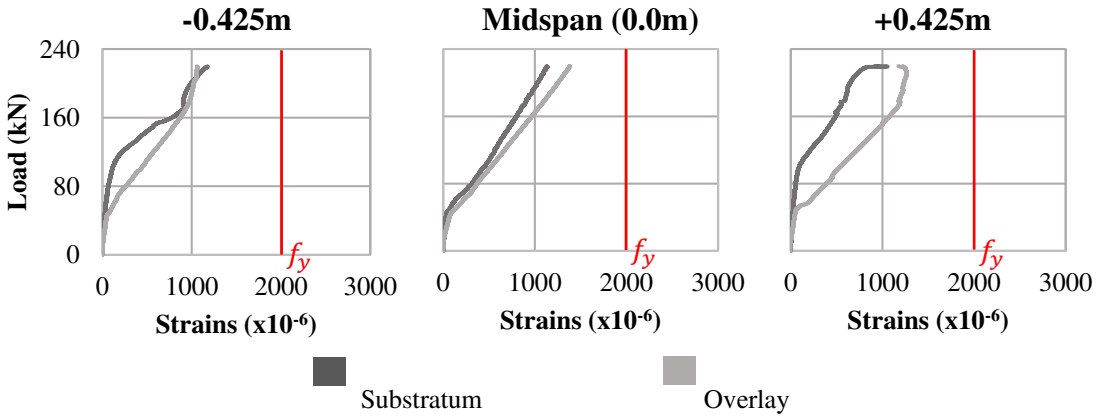


Figure 3.67 – Evolution of strain at coincident coordinates on both layers of the $R_L$-STC specimen.

Strains at the steel dowels were also measured at the interface level, in the direction of the anchored portion on the substratum. An example is presented in Figure 3.68 for the $R_S$-STC-4 specimen since the anchorage length was the preconised 80 mm, enough for guaranteeing the anchorage pull-out strength. Analysing the evolution of strain on steel dowels and longitudinal reinforcement on the figure above, one can observe the more prominent vertical stresses closer to the edge rather than closer to midspan. The negative strain on the intermediate row of steel dowels

can be explained by the shear crack observed in Figure 3.51 of chapter 3.3.2 possibly damaging the strain gauge. Load loss between the rows of dowels was around 60 % for the closest to midspan, 33 % for the intermediate row, and 13 % for the row furthest from midspan.

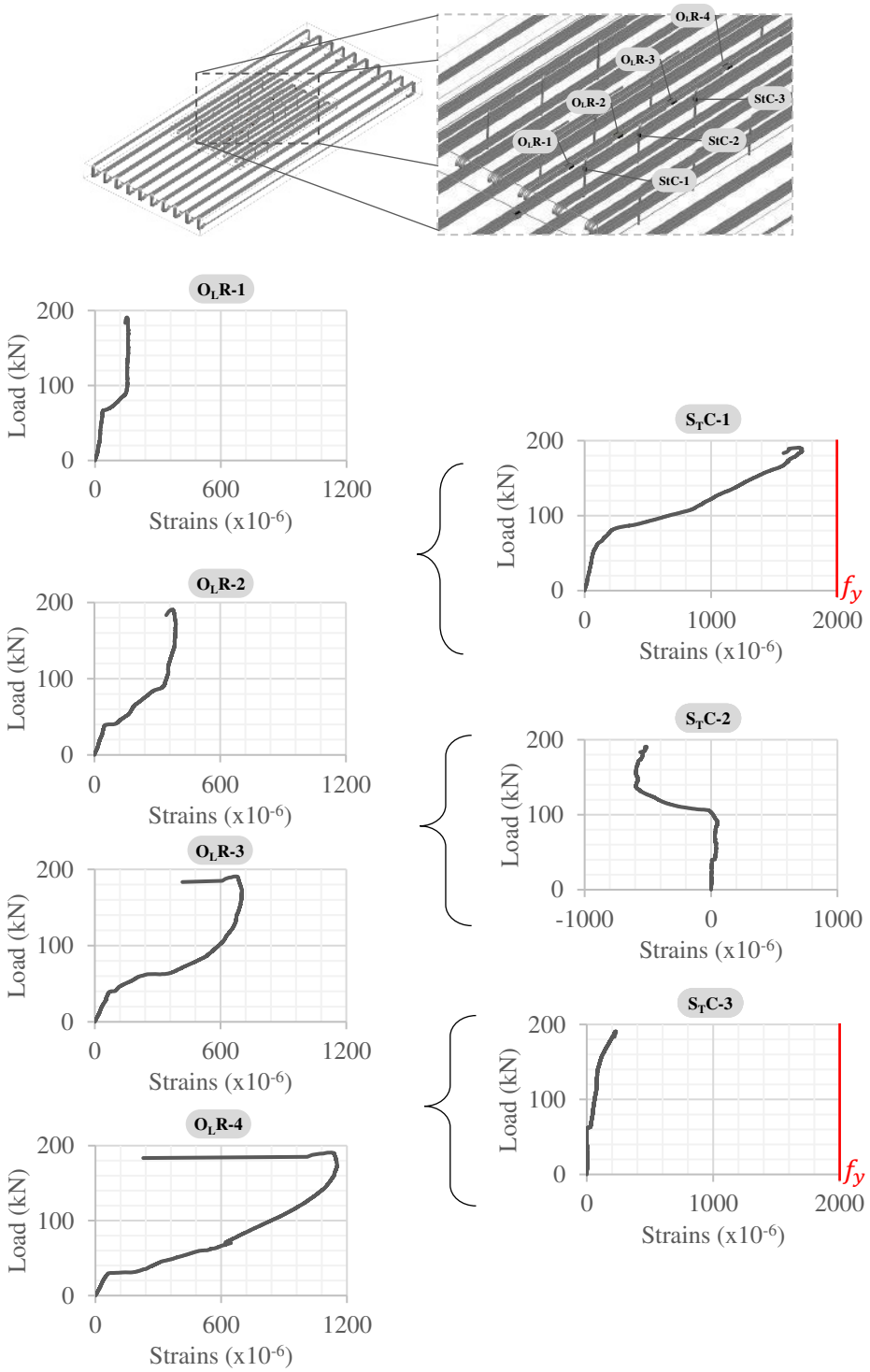


Figure 3.68 – Instrumented steel dowels and longitudinal reinforcement on $R_S$-STC-4 specimen, and respective strains measured.

The same analysis was performed on the $R_L$-STC specimen to assess strain distribution on the longitudinal reinforcement of overlaid concrete regarding the steel dowel layout, with results presented below in Figure 3.69.

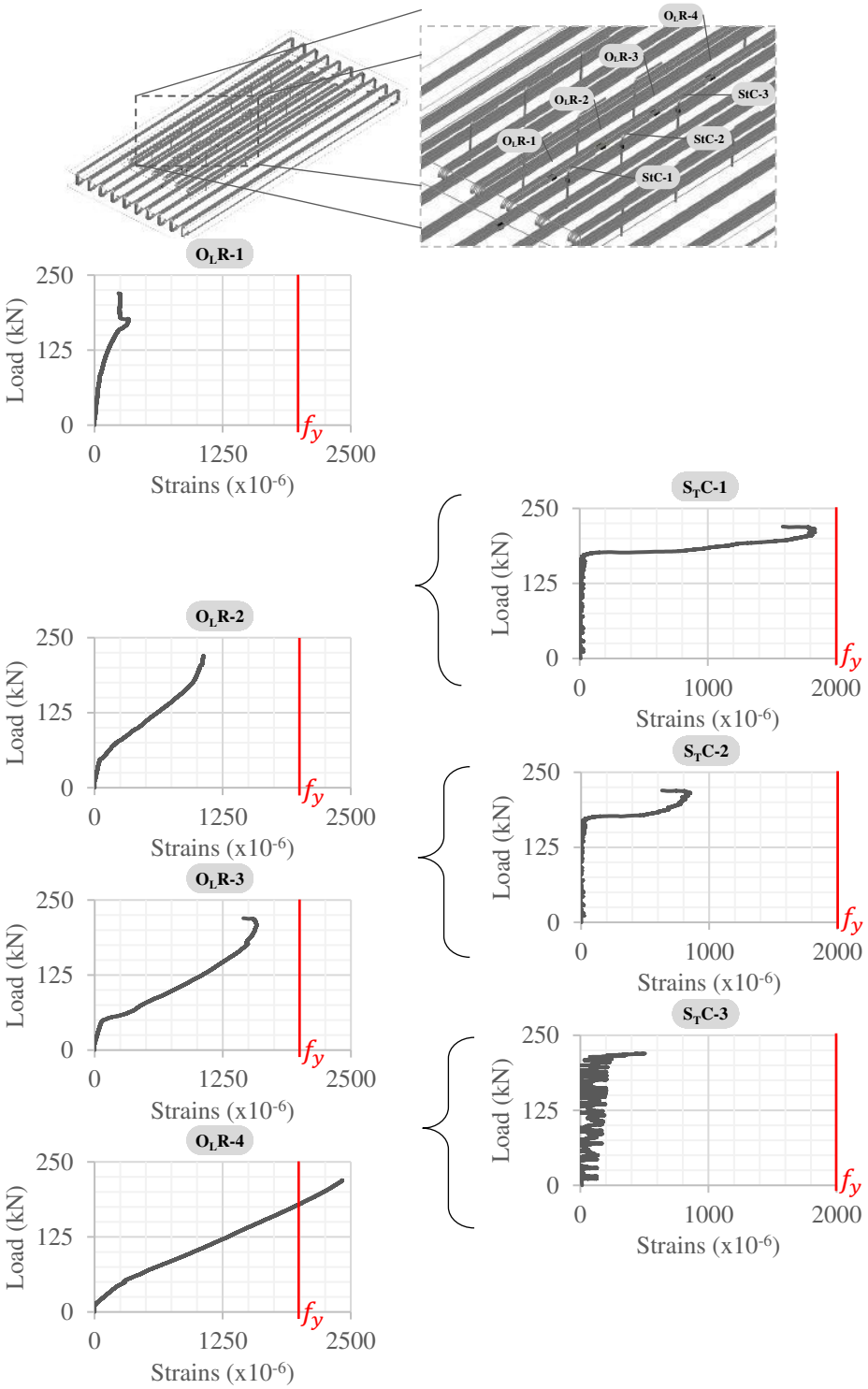


Figure 3.69 – Instrumented steel dowels and longitudinal reinforcement on $R_L$-STC specimen, and respective strains measured.

The same trend as the $R_S$-STC specimen in strain increase from the edge of the overlay to midspan could be observed, with respective strain decrease in the steel dowels over the same length.

Analysing the strains on longitudinal reinforcement one can observe the loss of strain on the first and third strain gauges, denoting the debonding phenomenon. Also noticeable is the lack of strain decrease on the middle strain gauge, which could be explained by the placing between the stitched portions of the strengthened slab span. Regarding the strains on the steel dowels one can observe the decrease in strain before failure, coherent with the debonding phenomenon and pull-out of the embedded reinforcement. Such phenomenon can be explained by the reduction on anchorage length due to the shear crack intersecting the last row of steel dowels observed in Figure 3.51. Load loss between the rows of dowels was around 66 % for the closest to midspan, 41 % for the intermediate row, and 12 % for the row furthest from midspan.

#### 3.3.4.3. Specimens with overlay reinforcement anchored in the substratum

These specimens were characterised for directly addressing the edge lifting phenomenon characteristic bonded concrete overlays by stitching the ends of such layers with bent longitudinal reinforcement already from structural design. For the sake of good comparison between test results, the $R_S$-ANC-4 specimen was considered, which had a longer anchoring of reinforcement in the substratum (80 mm) and did not debond like the first set of tests. Although bond between the two layers was prolonged further in the load history, strains were consistently larger in the substratum reinforcement, except at midspan where these were similar until failure (Figure 3.70).

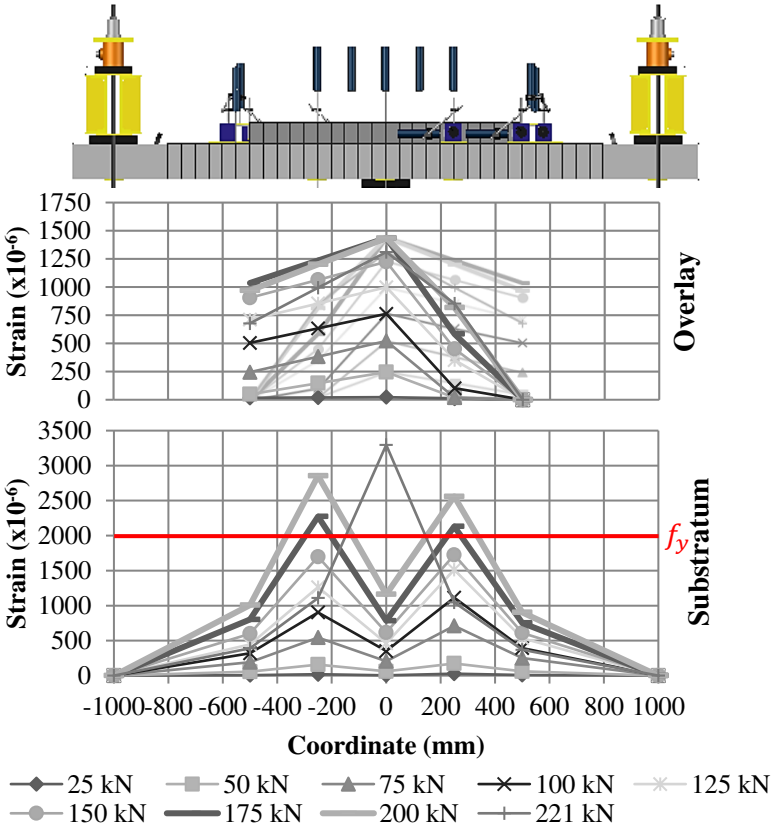


Figure 3.70 – Strain profiles by load step on both layers of $R_S$-ANC-4 specimen.

One can observe in the figure above that the longitudinal reinforcement anchored in the substratum controlled the edge lifting phenomenon. Strains on the overlay reinforcement at midspan reached double the strains registered for the same reinforcement on the $R_S$-STC specimen. The interpretation of the graph for the overlay reinforcement should be considered mirrored for the twin rebar that composes one of twelve pairs, anchored on each ends of the overlay, with such mirrored strains shown faded.

Analysing the strains at coincidental coordinates of both layers, the debonding phenomenon is again identified at the maximum strain of the overlay. The strains equalize right before failure occurs. This can be graphically observed for the midspan graph in Figure 3.71. The strains at midspan rise after cracking and then intersect with the strains of the substratum due to the debonding phenomenon, similarly to other specimens. Larger strains were again measured on both sides of the overlay than on midspan, with yielding occurring at a distance of 0.25m from midspan but not at midspan, where maximum bending stresses are attained.

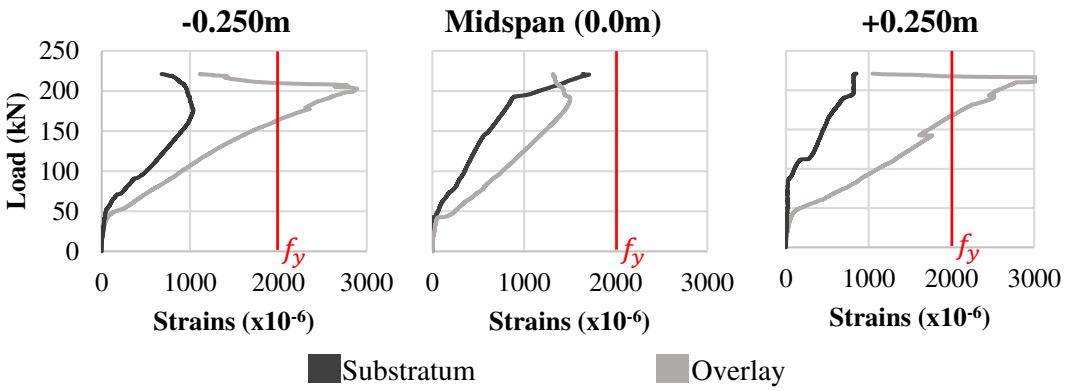


Figure 3.71 – Evolution of strain at coincident coordinates on both layers of the $R_s$-ANC-4 specimen.

Regarding the strains on the $R_L$-ANC specimen, one can observe in Figure 3.72 that this specimen was more susceptible to the variation of strain in the length of the reinforcement. Such values were significantly larger on the anchored side, almost reaching the yielding strain for steel reinforcement close to the bend and the anchored end. Strains on the substratum resulted almost symmetric throughout the load history and marginally larger at midspan than the overlay. Again, on the latter layer one must account for the bundle pair, which can be simplified by mirroring the data registered for one rebar as depicted below.

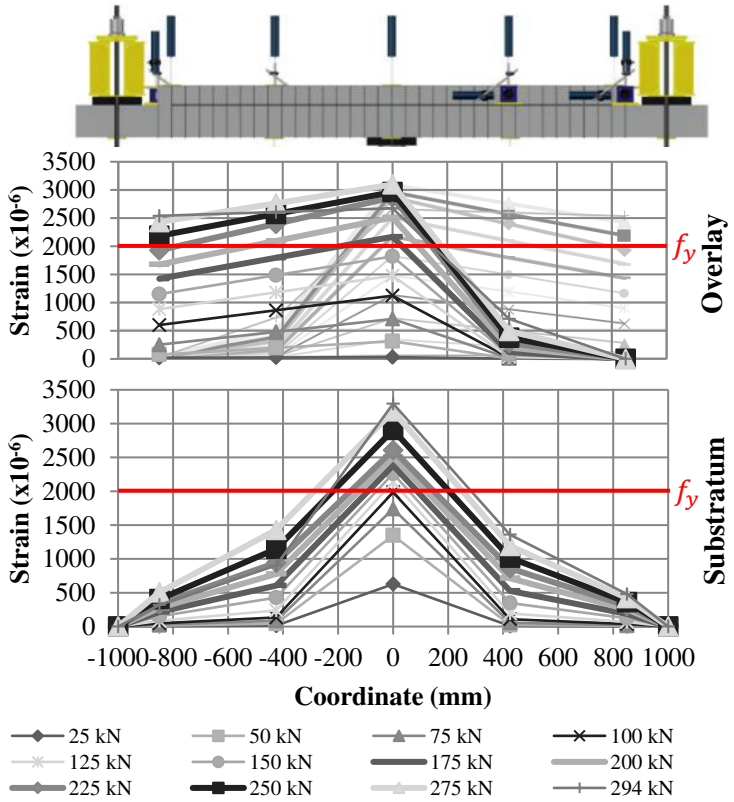


Figure 3.72 – Strain profiles by load step on both layers of $R_L$-ANC specimen.

Analysing the strains on coincidental coordinates of the specimen in Figure 3.73, one can observe the difference on each side of the overlay reinforcement with consistently larger strains on the anchored edge. Although the load-strain relationship crosses at midspan in Figure 3.73, the debonding phenomenon could not be considered, since the strains in the overlay continued to evolve linearly for this load. Such phenomenon may be justified by a malfunction of the strain gauges at midspan or by the local slipping of the substratum reinforcement close to midspan, regaining a linear evolution for strains close to the yielding strain for rebar.

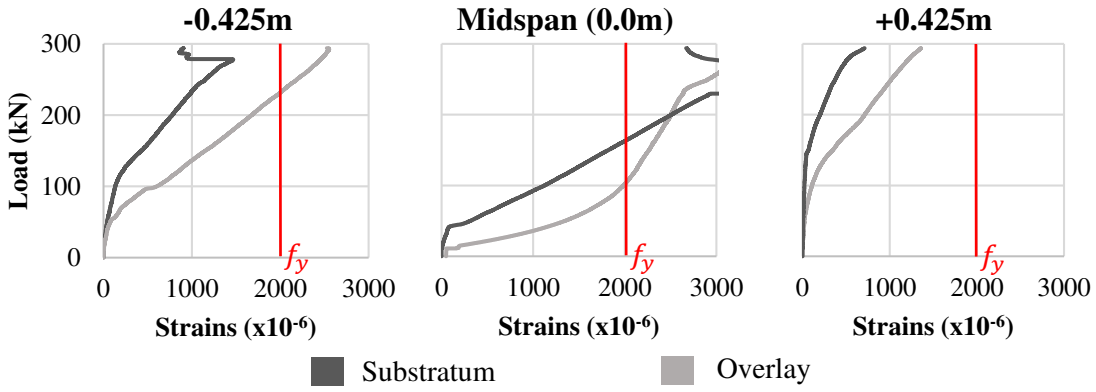


Figure 3.73 – Evolution of strain at coincident coordinates of both layers for the $R_L$-ANC specimen.

### 3.3.5. Relative displacements between layers

The resistance and stiffness of a composite cross-section depend highly on the interaction of the layers that compose it. The relative displacements between the two layers of the composite slab were measured according to the schematics presented on Figure 3.40 and Figure 3.41. The vertical and horizontal relative displacements at the ends of the overlay were measured for each detailing of the interface. The horizontal relative displacement was also measured halfway from midspan to the ends of the overlay. The latter was installed for assessing the evolution of the debonding phenomenon over the length of the interface. The load-displacement diagrams are presented in Figure 3.74 to Figure 3.81 for a specimen of each interface detailing. The rest of the load-displacement relationships of test specimens are presented in Annex A.

The key stages when analysing these diagrams are the softening of the load-displacement curves as evidence of the debonding phenomenon occurring at the interface. Changes in the behaviour of such curves occurs in pairs of horizontal and vertical displacements, often identifying the debonding of the overlay and consequent relative sliding between the two layers. Failure is often identified as a sudden rise in relative displacements. Relative displacements effectively start with the beginning of the debonding phenomenon by cracking the interface at the end of the overlaid concrete. The sudden change in the cross-section leads to cracking at this zone due to the change in the direction of stresses. The relationship between stress and the horizontal and vertical relative displacements can be observed in Figure 3.74 to Figure 3.77 for each example of the $R_S$ specimens. The load-displacement curves are organized in horizontal to the left and vertical to the right of the load scale, by colours, where the blue and red identify either sides of the specimens: R1 and R4, vertical displacement or interface crack opening; R2 and R5 horizontal displacement or relative sliding.

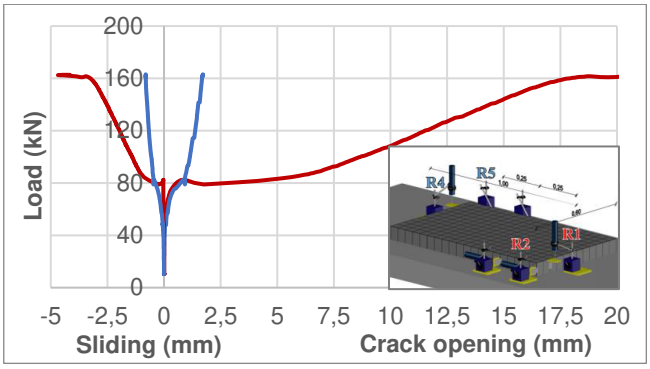


Figure 3.74 – Relative displacements between concrete layers for the $R_S$-REF-1 specimen.

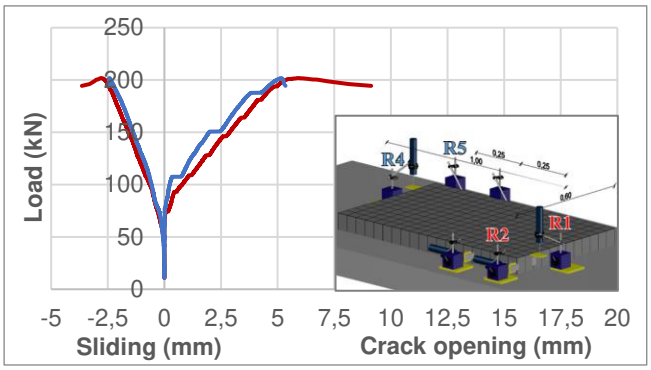


Figure 3.75 – Relative displacements between concrete layers for the $R_S$-STC-4 specimen.

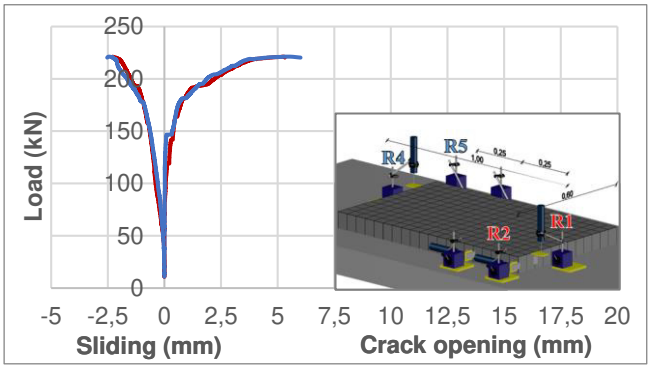


Figure 3.76 – Relative displacements between concrete layers for the RS-ANC-4 specimen.

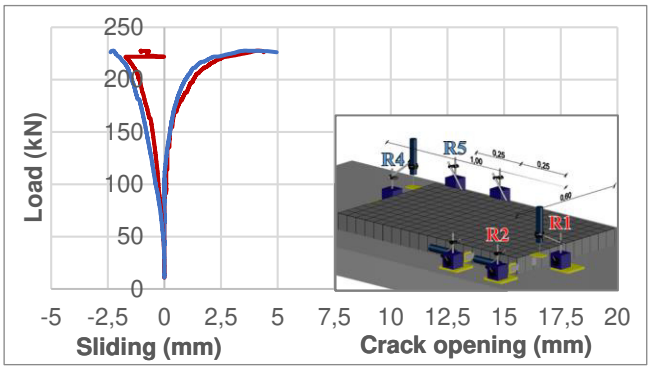


Figure 3.77 – Relative displacements between concrete layers for the $R_S$-STANC specimen.

Analysing the reference specimens, one can observe the exponential evolution of the interface crack opening with load until it becomes horizontal, characterising the full debonding of the overlaid concrete for a load around 80 kN. After such load, both values continued to evolve, paired with the evolution of the substratum vertical deformation until flexural failure of such layer, characterised on the figures above by another horizontal plateau. The debonding phenomenon can be identified starting for a load around 40 kN, with the load-displacement relationship vertical until such load. Both interface crack opening and sliding of the overlaid concrete evolved in the same way, with an exponential function. Due to the brittle nature of the

REF specimens, debonding occurred on one side of the specimens, hence the asymmetry between both sides of the specimens on the load-displacement relationships above.

The load-displacement relationship regarding the STC specimens allowed for a bilinear relationship, which peaked before failure, denoting the yielding of reinforcement and also the debonding phenomenon. The horizontal and vertical deformation on both sides of the overlay were similar for these specimens, attesting the integrity provided by reinforcement crossing the interface. Such reinforcement controlled the debonding phenomenon allowing for a symmetric deformation on both sides of the slab specimen. Analysing the relative displacements on the ANC specimen above, one can observe the behaviour of the load-displacement relationship close to a power function until failure. The behaviour of the relative displacements was similar to the STC specimen, with coincident values measured on both sides of the overlay. The anchoring of the longitudinal reinforcement resulted in a stiffer structural response due to the direct impact on the edge lifting phenomenon.

The specimen that combined all the aforementioned techniques resulted in the larger load capacity of all the short overlay geometry specimens, as expected, since the stitching of the two layers from the ends of the overlay to midspan allowed for a more controlled debonding, as observed in Figure 3.77. The stiffness of this specimen was only marginally greater than the latter specimen, which attests the anchoring of longitudinal reinforcement as the more behaviour changing detailing to be applied on a concrete-to-concrete interface.

Regarding the load-displacement diagram of the long overlay geometry ($R_L$) depicted in Figure 3.78 to Figure 3.81, one can observe that despite the longer overlay the relative displacements resulted similar to those of the short overlay specimens.

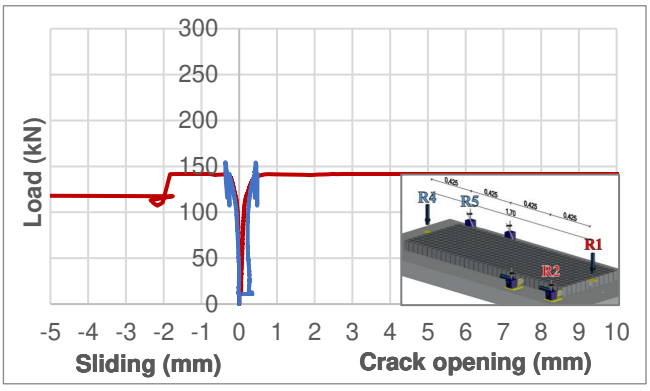


Figure 3.78 – Relative displacements between concrete layers for the $R_L$-REF specimen.

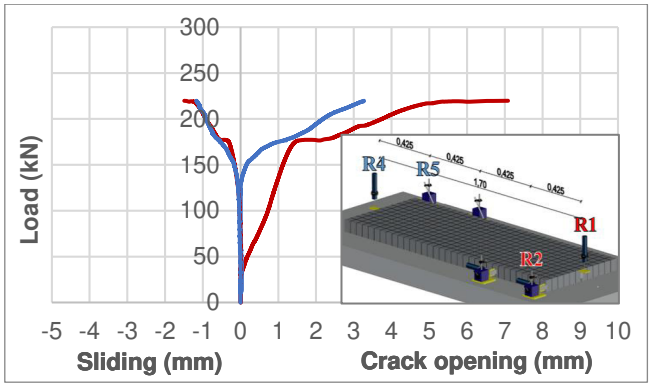


Figure 3.79 – Relative displacements between concrete layers for the $R_L$-STC specimen.

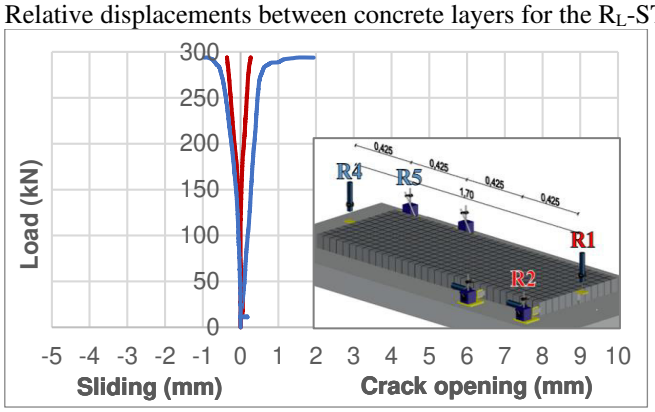


Figure 3.80 – Relative displacements between concrete layers for the $R_L$-ANC specimen.

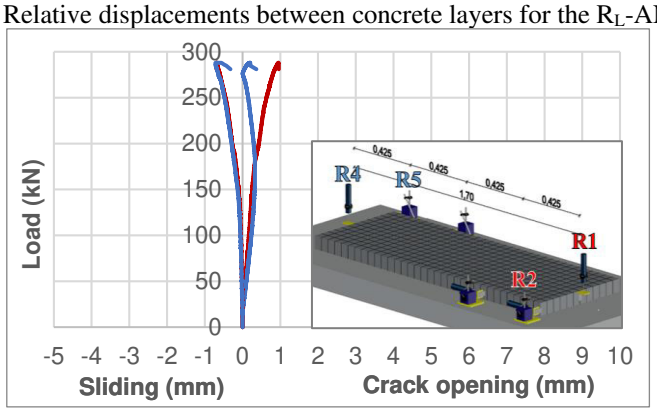


Figure 3.81 – Relative displacements between concrete layers for the $R_L$-STANC specimen.

Regarding the reference specimen in Figure 3.78, debonding is clear on the load-displacement diagram by a horizontal evolution of the relative displacement. On the STC specimen in Figure 3.79, a change in behaviour can be observed on the load-displacement diagram, characterised by a horizontal plateau for a load around 175 kN. Such plateau and the interruption in the linearity of the load-deflection diagram denotes the debonding phenomenon, but not full debonding of the interface, since some gain in stiffness could also be observed.

Relative displacement of the ANC and STANC specimens were the smallest registered on all tests. Such behaviour can be explained by the longer overlay allowing for a more progressive

cracking of the overlaid concrete, thus resulting in less relative deformation between the two layers. The ANC specimen resulted in a closely linear relationship between load and relative displacement (Figure 3.80) with a great loss of stiffness close to the maximum strain measured on such specimen. The supposed closing of the interface crack registered on $R_4$ transducer of the STANC specimen in Figure 3.81 can be justified by the opening of a flexural crack on the cross-section and perturbation of the displacement transducer. The evolution of the relative displacement on the other side of the strengthened span evolved as an opened state until failure.

The main parameter to be assessed is then the debonding of the overlaid concrete, which accounted for critical opening of the interface crack and relative slip of the two layers. Debonding, as stated before from a reinforcement strain point-of-view, is when strains at the overlaid concrete peak. Such phenomenon was observed to occur close to failure or early in the load history.

The significant values of interface crack dilation (ICD) and relative slip (RS), respectively vertical and horizontal relative displacements, are presented in Table 3.13, in particular:

- Specimens where the overlaid concrete fully debonded, the displacement values were considered for maximum steel strain at midspan of the overlay reinforcement;
- Specimens without strain gauge information, this value was estimated based on the respective load-deflection curve presented above, comparing with instrumented specimens with the same detailing of the interface (REF-2, STC-2 and ANC-1).

Table 3.13 - Relative displacements at the end of the overlay before debonding.

| Specimen | | Load at midspan (kN) | Interface Crack Dilation (mm) | Interface Slip (mm) |
|---|---|---|---|---|
| **$R_S$-REF** | **1** | 82.4(1) | 1.52 | 0.58 |
| | **2** | 79.6(3) | 0.87 | 0.39 |
| | **3** | 80.1(1) | 1.42 | 0.57 |
| **$R_S$-STC** | **1** | 177.2(2) | 4.11 | 1.45 |
| | **2** | 148.1(3) | 2.89 | 1.02 |
| | **3** | 180.1(2) | 4.33 | 1.43 |
| | **4** | 201.8(2) | 4.98 | 2.38 |
| | **5** | 153.1(1) | 4.26 | 1.63 |
| **$R_S$-ANC** | **1** | 151.1(3) | 2.33 | 0.35 |
| | **2** | 150.2(1) | 2.06 | 0.51 |
| | **3** | 140.6(1) | 2.51 | 0.49 |
| | **4** | 221.2(2) | 5.46 | 2.49 |
| | **5** | 210.9(2) | 1.71 | 1.66 |
| **$R_S$-STANC** | | 227.7(2) | 4.18 | 2.21 |

(1) Load for maximum strain at debonding of overlaid concrete;
(2) Load for maximum strain at specimen's (shear) failure;
(3) Estimated load for maximum strain at specimen's failure or debonding.

The results also show higher crack dilation and interface slip for the higher failure loads of specimens' $R_S$-STC-4, $R_S$-ANC-4, and $R_S$-STANC, denoting the activation of reinforcement crossing the interface with proper anchoring in the substratum. The sudden increase in relative displacement due to shear cracks was avoided by accounting only for values at maximum strain of reinforcement. The same parameters were considered for the longer overlay geometry specimens, where smaller values of relative displacement were measured, which can be observed on Table 3.14. Such phenomenon can be justified by the discontinuity in the cross-section taking place further from midspan where flexural loads are greater and more favourable to debonding. Also, the longer overlays are less sensitive to the impact of flexural cracking, allowing for cracks to evolve progressively and impacting less on the edge of the overlay where debonding is more prominent.

Table 3.14 - Relative displacements at the end of the overlay before debonding.

| Specimen | Load at midspan (kN) | Interface Crack dilation (mm) | Interface slip (mm) |
|---|---|---|---|
| **$R_L$-REF** | 141.7(1) | 2.58 | 0.77 |
| **$R_L$-STC** | 219.7(2) | 3.27 | 1.17 |
| **$R_L$-ANC** | 293.6(2) | 1.94 | 0.96 |
| **$R_L$-STANC** | 288.1(2) | 0.96 | 0.69 |

(1) Load for maximum strain at debonding of overlaid concrete;
(2) Load for maximum strain at specimen's (shear) failure.

## 3.4. Numerical simulation and analysis of the test results

The calibration of numerical models with the test results is considered relevant, since the nonlinear analysis software allows for the assessment of stress and deformation that either were not measured, nor such measuring was possible during experimental tests. An example of the latter is the actual stress state at the interface which cannot be directly measured and can only be estimated through the monitoring of other data. Modelling composite cross-sections and the respective interfaces poses a challenge since the calibration of the interface fracture energy is needed according to experimental results. The flexural and shear deformation of reinforcement is also relevant when assessing dowel action of the interface crossing reinforcement. Since linear discrete elements only work for axial stress the definition of actual macroelements to model reinforcement crossing the interface is needed. Stress distribution on the interface could then be assessed, mainly tensile and longitudinal shear stress, which combined are responsible for interface failure by debonding. The crack pattern was also assessed numerically and compared to cracking observed on experimental specimens.

### 3.4.1. Definition of numerical models

The numerical analysis of the specimens was performed then with the nonlinear analysis software ATENA 3D®. The defined macroelements for the concrete sections were sectioned at relevant geometry changes and particularities, like the vicinity of supports and the edge of either layer. To guarantee a numerically converged solution, a sensitivity analysis was performed, analyzing the

influence of the number of load steps and element size. The specimen's double symmetry allowed to model only one quarter of each specimen as shown in Figure 3.82, saving time and effort of calculating symmetrical coordinates with equal conditions.

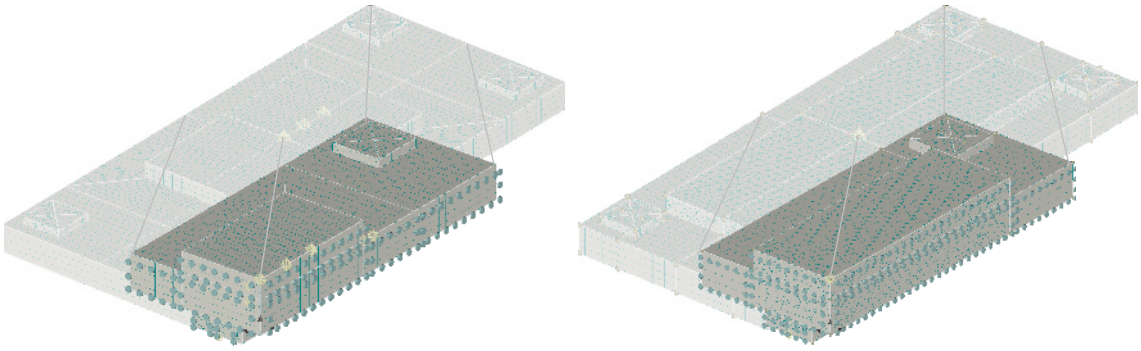

Figure 3.82 – One quarter numerical models of experimental $R_S$ and $R_L$ specimens.

Longitudinal reinforcement was modelled through linear truss elements with constrained slip at the axis of symmetry and the ends of the substratum, since reinforcement in the test specimens was detailed bent down. Slip of the reinforcement was allowed at the ends of the overlay, since the rebars are only anchored when specifically detailed. Slip of reinforcement relative to surrounding concrete is defined in the ATENA software through predefined laws: the one on the Model Code 1990 [19] and Bigaj bond-slip model [147]. The former was considered for this work with the simple input of concrete cubic strength and good bond quality. Such models depend on material and/or geometric characteristics such as concrete compressive strength or the rebar diameter, which was input later for each element. An example of the discretization of longitudinal reinforcement is presented in Figure 3.83.

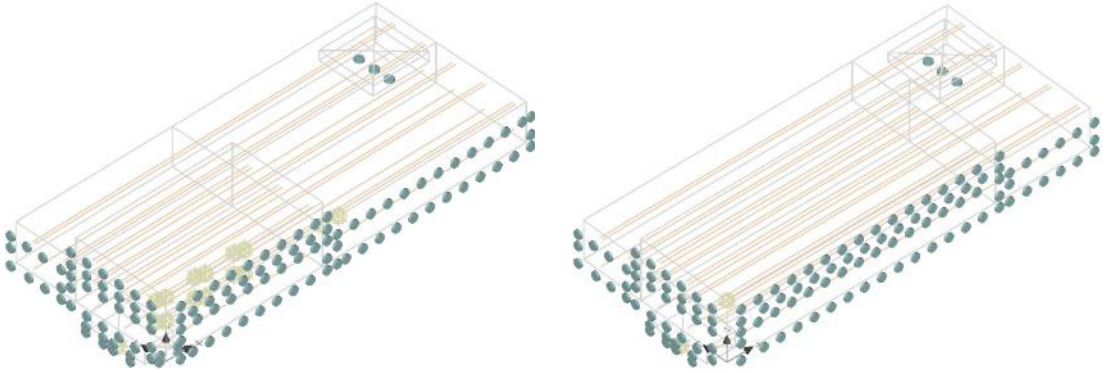

Figure 3.83 – Detailing of discrete reinforcement on the $R_S$ (left) and $R_L$ (right) models.

Macroelement meshing was then divided into brick and tetra elements. No relevant losses could be observed due to the less integration nodes during the numerical modelling of the specimens when using tetra elements. Such option resulted in detriment of brick elements due to the difficulty of modeling the embedded reinforcement crossing the interface. Since the linear discrete elements used for modelling reinforcement in the software do not account for the shear and flexural deformation of dowel action, the interface crossing reinforcement was modelled with macroelements. On the models with tetra meshing, the procedure for embedding reinforcement

in the substratum consisted on using the functions available on the software's pre-processor for defining approximately circular objects and subtracting the necessary volume for embedding the reinforcement that crosses the interface. Two examples are presented on Figure 3.84 for a shear dowel and anchored longitudinal reinforcement.

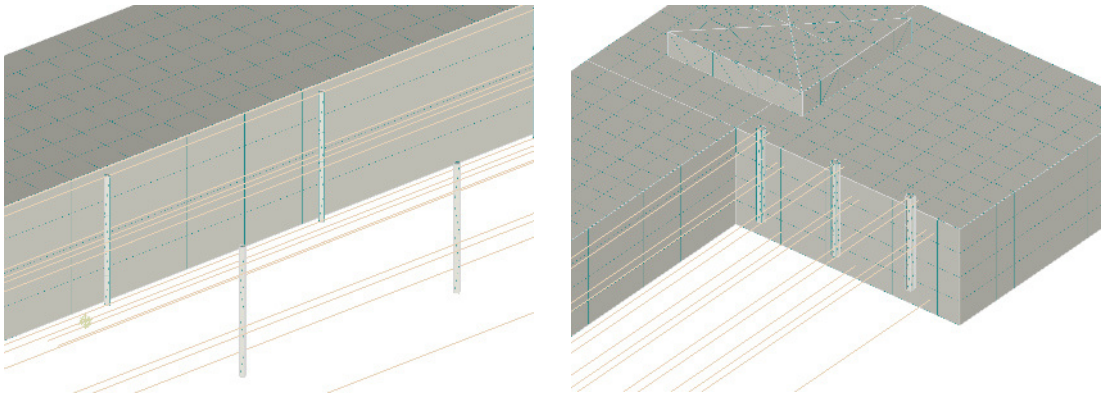

Figure 3.84 – Modelled shear dowels (left) and anchoring of longitudinal reinforcement (right).

Such openings in the substratum resulted on an irregular macroelement that could not be meshed with regular brick elements, and therefore tetra elements were used. The meshing elements used consisted then on two kinds, 8-node brick elements and 4-node tetra elements, illustrated on Figure 3.85.

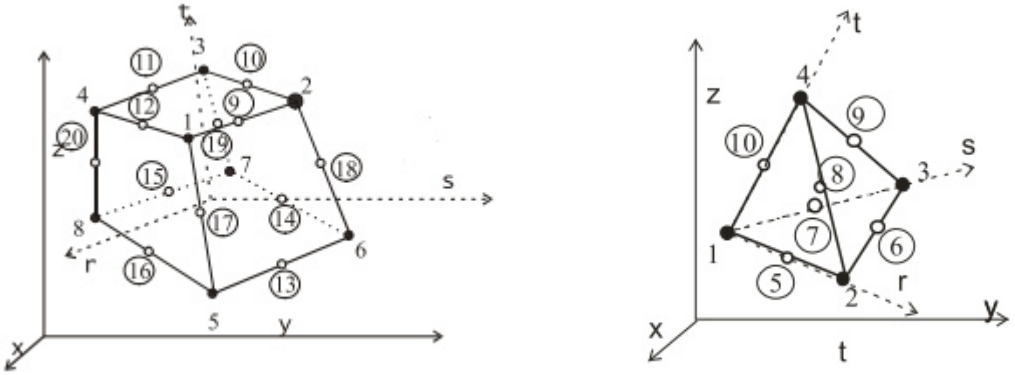


Figure 3.85 – 8-node brick and 4-node tetra elements [123].

Due to the larger number of integration points, brick elements are desired over the tetra elements. The need for the latter is due to the irregular shape of the macroelements when more nodes are introduced, or an irregular prismatic shape is formed.

An attempt was performed to model the $R_S$ specimens entirely with brick elements (Figure 3.82, left), leading to an intricate discretization of the specimens macroelements through smaller prismatic macroelements. This allowed for the number of nodes needed when creating brick elements as desired for the macroelements. Such premise led to a great number of contact surfaces, but also allowed to generate a regular mesh with quadrilateral elements, despite the hexagonal shape of the rebar modelled with 3D macroelements (Figure 3.86).

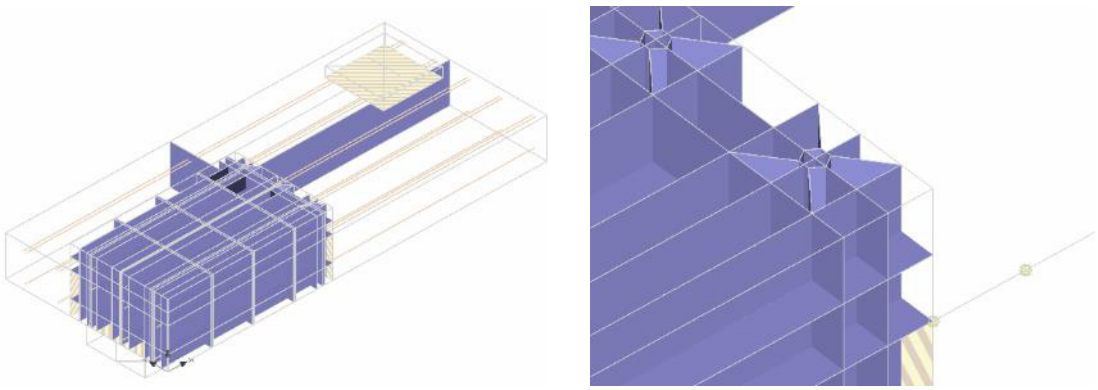

Figure 3.86 – Contacts for modelled specimens with anchored longitudinal reinforcement (ANC and STANC, left) and anchorage detail (right).

Reinforcement crossing the interface was then modelled with macroelements to account for shear and bending because of the relative displacement of the contact surfaces. The shear dowels distributed across the interface were modelled by prismatic specimens with 5x5 $mm^2$ and 50 mm and 80 mm embedded in the substratum, as illustrated in Figure 3.87. Elements smaller than such dimensions reach the threshold and cannot be meshed by the software mesh generator.

Figure 3.87 – Reinforcement embedded on the substratum: shear dowel (left); anchored end of longitudinal reinforcement (right).

A calibration was performed considering models with regular brick elements and models with tetra elements on single layer slab models (unstrengthened), with both resulting very close. Meshing of a strengthened specimen was also performed with only tetra elements. No refinement of the mesh was performed in the column region for the models with brick elements. Mesh compatibility was enabled at contacting surfaces to minimize mesh distortion and its impact on results. For the slab specimens modelled with tetra elements, the macroelements outside the strengthened two-layer portion of the slab remained as brick elements in the FE mesh.

Monitoring points were defined at key coordinates of the numerical models, namely measuring load at the point where the prescribed deformation is applied and deflection on top of the slab at the midspan of specimens. Such monitoring points allowed for tracing the load-deflection curves to compare with experimental specimens.

### 3.4.2. Definition of material properties

Material parametrization was performed based on the concrete compressive and tensile strength on Table 3.7 and Table 3.8 of section 3.2.5, steel tensile strength on tables Table 3.5 and

Table 3.6 of section 3.2.5, cement grout tensile strength and pull-out strength of embedded anchorages, also on section 3.2.5. Interface parameters such as the tensile strength and coefficient of friction considered were taken from section 3.2.4 and section 3.2.6.3.

The modelling of materials relies strongly on the chosen theory with respect to strain softening/hardening and cracking of structural elements. The concrete material defined by the software is based on the SBETA constitutive model. This model mainly includes nonlinear behaviour in compression, softening and hardening of the material, cracking in tension, tension stiffening, and fixed and rotated crack modelling [111]. After cracking occurs, the concrete material can perform in a fracture-plastic behaviour, also comprising the crushing of concrete, and combining the constitutive relations for tensile and compressive behaviour (Figure 3.88, left).

The option for the modelling of discrete truss elements allowed for accurately placing all rebars as intended, with known spacing, effective depth and clear cover. A limitation arises when modelling the reinforcement crossing the interface, since the linear truss elements only work for axial loading [122]. To account for the shear and bending of such reinforcement, macroelements were defined with a polygonal geometry that would allow for the intended cross-section and contact area close to the circular reinforcement. A bilinear stress-strain relationship was considered for the behaviour of all reinforcement material (Figure 3.88, right).

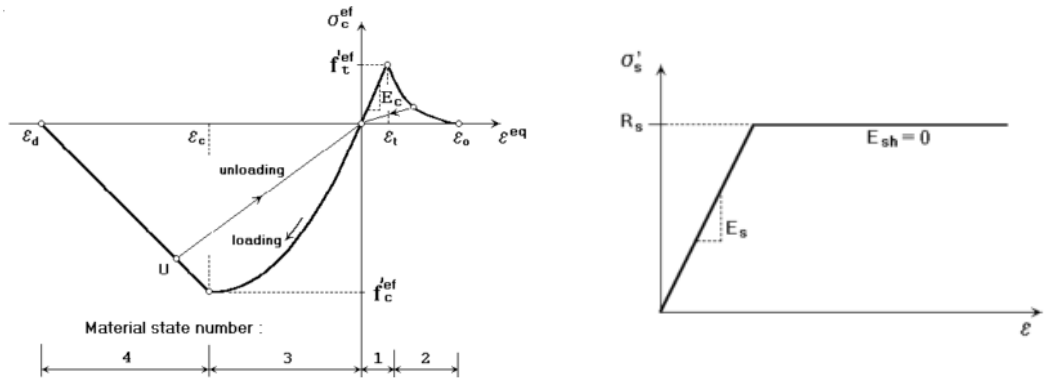


Figure 3.88 –Concrete and reinforcement steel constitutive relations considered [123].

Reinforcement can be modelled by discrete truss elements or smeared in the concrete macroelements. The software allows for two predefined bond-slip or user-defined laws. In this work the Model Code 1990 illustrated in Figure 3.89 was adopted. Such model requires for concrete compressive strength, rebar diameter, rebar type, and bond quality parameters. Interface crossing reinforcement bond-slip capacity was defined based on the pullout tests performed and was custom-defined similarly to the interface, as shall be presented further in this chapter.

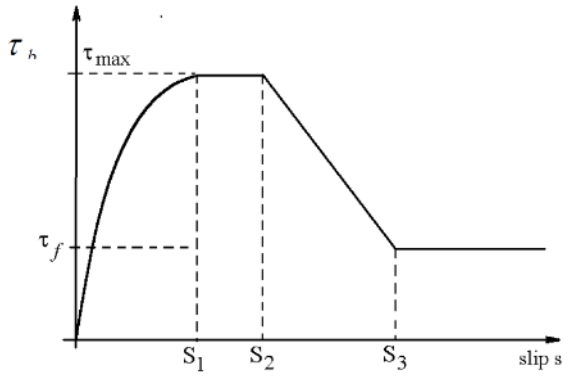


Figure 3.89 – Model Code 1990 bond-slip model (adapted from [123]).

The concrete material in particular is based on the Rankine failure criterion, which allows for discrete and smeared crack approaches, and both fixed (FCM) and rotated (RCM) crack models [148]. Both are illustrated in Figure 3.90, where the greatest difference can be observed with shear strain occurring only on the FCM due to the principal stress direction coinciding with principal strains.

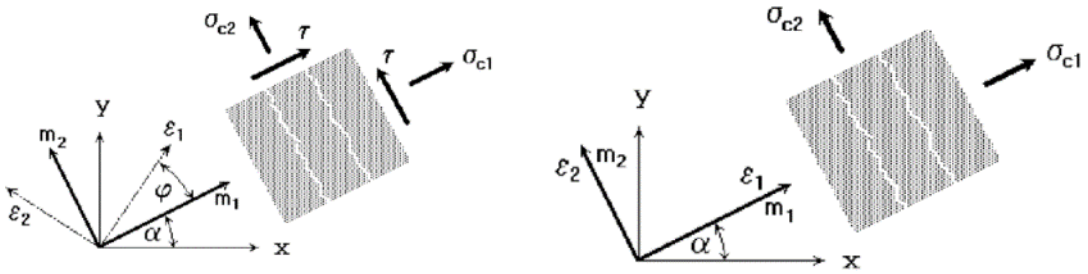


Figure 3.90 – Fixed and rotated crack models (adapted from [123]).

The software's concrete model uses the smeared crack approach combined with the crack band method. In the fixed crack model, crack direction and material axes are defined by the principal stress direction at the onset of cracking when the principal stress exceeds the tensile strength. In both models a crack is formed as the principal stresses reach the concrete tensile strength. In the fixed crack model, the crack direction is given by the direction of the principal stress and is fixed at crack initiation, whilst in the rotated crack model the direction of the crack coincides with the direction of the principal stress. If the latter changes, the direction of the crack rotates. In a real reinforced concrete structure, the cracks might change their courses, however they cannot rotate as the rotated crack model proposes. A ratio of 0.5 between both was assumed to give a more realistic description of the cracking progress in this study.

### 3.4.3. Definition of the interface parameters

The interface itself as defined by the software consists on zero thickness elements, defined geometrically by the contact area between the two layers for each specimen. The input parameters for a 3D interface in ATENA software are stiffness, normal and tangential to surface, tensile strength, cohesion, and a friction coefficient. The software allows for the complete debonding between two finite elements, as stated in [123], where the 3D interface is characterised as open or closed. While the latter state is the one that allows for the mobilization of stresses, the former is the one that allows for the realistic behaviour of the concrete-to-concrete interface with full separation of surfaces. Such behaviour is characterised by shear and tensile strengths, and respective softening models for the opening and sliding of the contact elements. The tensile strength was taken directly from experimental pull-off tests for each specimen presented in 3.2.6. Such tests allowed for assessing each specimen average interface tensile capacity considered for all numerical models. Cohesion was then calculated considering the Mohr-Coulomb failure criterion with tension cut-off, as illustrated in Figure 3.91.

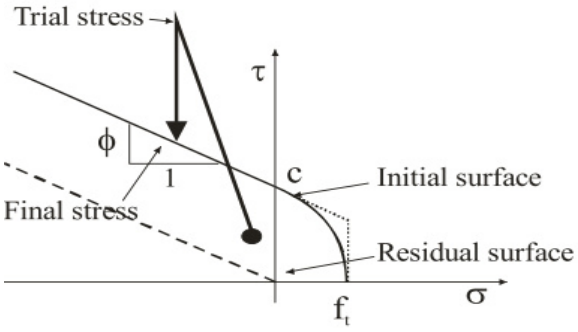


Figure 3.91 – Mohr-Coulomb failure criterion at the interface [123].

The initial surface is governed by equation (3.6) for the compressive stress state, and then by equation (3.7) until the tensile limit imposed by the failure criterion. After such limit, shear stress becomes null because no contact exists between the surfaces.

$$\tau = c - \sigma.\tan(\phi), \sigma \leq 0 \tag{3.6}$$

$$\tau = \tau_0.\sqrt{1 - \frac{(\sigma - \sigma_c)^2}{(f_t - \sigma_c)^2}}, 0 < \sigma \leq f_t \tag{3.7}$$

The choice for the elliptical form of the failure criterion on the tensile portion of Figure 3.91 was due to the expected behaviour of the interface from the experimental tests. The relationship between load and relative displacement showed to evolve as a power function, thus suggesting a relationship between tensile and tangential loads of the same nature. A friction coefficient needs to be considered when normal and tangential stresses are accounted for. Such parameter was calculated according to [138] and the values presented on Table 3.3 of section 3.2.4. Cohesion was calculated iteratively until the minimum shear stress was reached at the vertical axis that

could relate the slope given by the friction coefficient and the tensile capacity of the interface, according to Figure 3.91.

The behaviour of an interface loaded in tension can be divided into two stages that differ with the interface cracking due to debonding, illustrated in Figure 3.92 by the vertical axis that separates the ascending and descending stages of stress at the interface. The lack of a clear and accountable intersection between both layers required the calculation of interface stiffnesses regarding the adjacent materials fracture energy. For this method, a negative theoretical displacement in the bond stress-slip relationship of the interface was considered (Figure 3.92), with the stiffness calculated according to a linear stress growth until maximum stress was reached. This is the energy needed for the first crack to appear, with the softening of stresses beginning right after, until degradation of the interface and no stress is transferred. Although this method allowed for a good agreement with experimental results, it is still an approximate way of accounting for interface fracture energy and calculating interface stiffness. For simplification, it is recommended by the software developers to consider interface tangential stiffness ($K_{TT}$) with the same value as the interface normal stiffness ($K_{NN}$). This procedure was adopted in this work with good results. To calculate interface stiffness, a variation of the concrete stress-strain relationship was used, considering the very small displacement needed for concrete to crack.

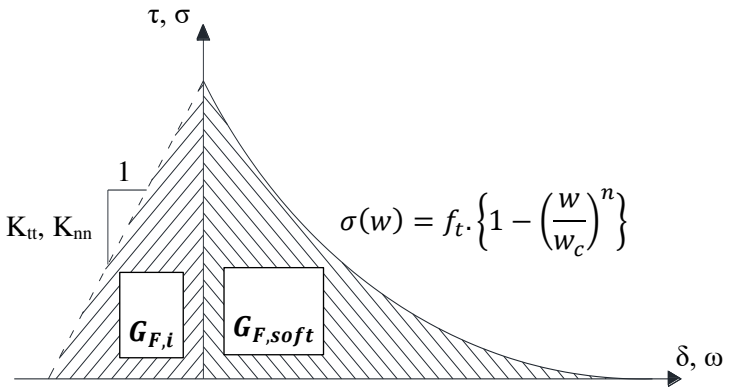


Figure 3.92 – Relationship between stress and relative displacements at the interface.

The positive slope, or interface normal stiffness $K_{NN}$ (or tangential stiffness $K_{TT}$), is governed by the interface fracture energy needed for cracking to occur, and is calculated according to:

$$K_{NN}(or\ K_{TT}) = \frac{{f_{t,i}}^2}{2.G_{F,i}} \tag{3.8}$$

Where $f_{t,i}$ is the interface tensile capacity and $G_{F,i}$ is the interface fracture energy, calculated by:

$$G_{F,i} = \frac{f_{t,i}}{f_{t,Conc}}.G_{F,WeakConc} \tag{3.9}$$

The former is assessed directly through experimental tensile testing of specimens bonded to a substratum, and the latter can be calculated considering the weakest neighbouring concrete fracture energy ($G_{F,WeakConc}$). Good results were obtained when calculated according to the approximation on Model Code 1990 [19]:

$$G_{F,WeakConc} = G_{F0}\left(\frac{f_{cm}}{f_{cm0}}\right)^{0,7} \quad (3.10)$$

Where $G_{F0}$ and $f_{cm0}$ are standard values provided on [19] of the base value of concrete fracture energy [N/mm] and a scale value of concrete compressive strength, respectively. The former varies with maximum aggregate size of concrete, and the latter has a fixed value of 10 MPa. The weakest concrete compressive strength $f_{cm}$ of the two layers was then considered for such calculation.

The model that best described the relationship between stress and relative displacement at the interface after cracking was Reinhardt's exponential curve [149]. Stress for each relative displacement is calculated with equation (3.11), where n is a fitting parameter.

$$\sigma(w) = f_t.\left\{1 - \left(\frac{w}{w_c}\right)^n\right\} \quad (3.11)$$

To characterise the descending portion that corresponds to the softening of stresses, it was considered that the energy corresponding to the area below the stress-displacement softening curve ($G_{F,soft} = \int \sigma(w)$) was the same as the fracture energy determined above for cracking the interface.

Interface parameters regarding equations (3.8) to (3.10) for the short overlay geometries are presented on Table 3.15, where the definition of the interface fracture energy was performed considering the smaller values yielded by equation (3.9), highlighted in bold.

Table 3.15 – Concrete-to-concrete interface parameters for the modelling of $R_S$ specimens.

| | **Concrete-to-concrete interface parameters** | | | |
|---|---|---|---|---|
| | **REF** | **ANC** | **STC** | **STANC** |
| $\mathbf{G_{F,sub}}$ **(x10$^{-5}$ MN/m)** | 6.77 | 5.92 | 6.27 | 7.90 |
| $\mathbf{G_{F,ol}}$ **(x10$^{-5}$ MN/m)** | 7.03 | 7.03 | 7.03 | 6.37 |
| $\mathbf{f_{t,sub}}$ **(MPa)** | 3.42 | 3.06 | 3.15 | 3.69 |
| $\mathbf{f_{t,ol}}$ **(MPa)** | 3.51 | 2.97 | 3.42 | 3.24 |
| $\mathbf{f_{t,i}}$ **(MPa)** | 1.36 | 0.73 | 1.16 | 1.22 |
| $\mathbf{G_{F,i(sub)}}$ **(x10$^{-5}$ MN/m)** | **2.69** | **1.41** | **2.31** | 2.61 |
| $\mathbf{G_{F,i(ol)}}$ **(x10$^{-5}$ MN/m)** | 2.72 | 1.73 | 2.39 | **2.40** |
| $\mathbf{K_{nn}}$ **(x10$^{4}$ MN/m$^3$)** | **3.43** | **1.89** | **2.91** | **3.10** |
| $\mathbf{K_{tt}}$ **(x10$^{4}$ MN/m$^3$)** | **3.43** | **1.89** | **2.91** | **3.10** |
| **μ (-)** | 1.41 | 1.42 | 1.41 | 1.41 |
| **C (MPa)** | 3.84 | 2.08 | 3.28 | 3.45 |

Such premise states the strength of the interface to be conditioned by the weakest neighbouring material. Cohesion was calculated considering the Mohr-Coulomb failure criterion depicted on Figure 3.91 and equations (3.6) and (3.7). The criteria chosen was to find a cohesion value that would allow for the slope of the Mohr-Coulomb failure criterion ruled by equation (3.6), to

converge the elliptical curve ruled by equation (3.7). Such curve crosses the horizontal axis on the interface tensile capacity $f_{t,i}$, as depicted in Figure 3.93.

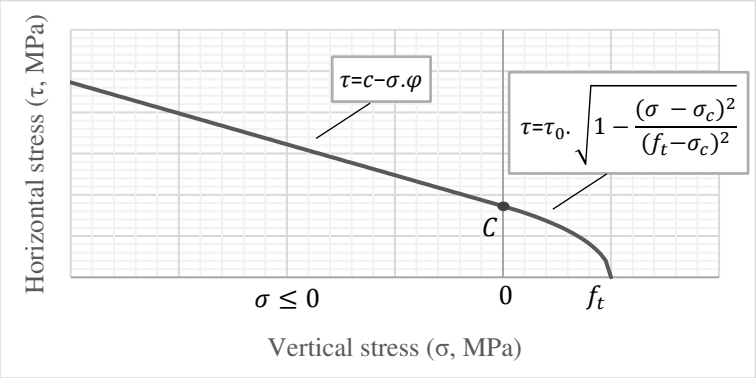


Figure 3.93 – Determination of Cohesion through the Mohr-Coulomb failure criterion.

For tracing the crack dilation and cohesion softening curves with equation (3.11), the relative displacements on Table 3.13 were considered. Interface parameters regarding equations (3.8) to (3.10) for the long overlay geometries ($R_L$) are presented on Table 3.16, where definition of the interface fracture energy was performed considering the smaller values yielded by equation (3.9), highlighted in bold. For tracing the crack dilation and cohesion softening curves with equation (3.11), the relative displacements on Table 3.14 were considered.

Table 3.16 – Concrete-to-concrete interface parameters for the modelling of $R_L$ specimens.

| | **Concrete-to-concrete interface parameters** | | | |
|---|---|---|---|---|
| | **REF** | **ANC** | **STC** | **STANC** |
| **$G_{F,sub}$ (x10$^{-5}$ MN/m)** | 5.91 | 7.57 | 7.94 | 7.54 |
| **$G_{F,ol}$ (x10$^{-5}$ MN/m)** | 5.64 | 5.84 | 5.45 | 5.99 |
| **$f_{t,sub}$ (MPa)** | 2.67 | 3.12 | 3.26 | 3.05 |
| **$f_{t,ol}$ (MPa)** | 2.84 | 2.89 | 2.18 | 2.47 |
| **$f_{t,i}$ (MPa)** | 0.70 | 0.80 | 0.94 | 0.90 |
| **$G_{F,i(sub)}$ (x10$^{-5}$ MN/m)** | 1.55 | 1.94 | **2.29** | 2.23 |
| **$G_{F,i(ol)}$ (x10$^{-5}$ MN/m)** | **1.39** | **1.62** | 2.35 | **2.18** |
| **$K_{nn}$ (x10$^4$ MN/m$^3$)** | **1.76** | **1.98** | **1.93** | **1.85** |
| **$K_{tt}$ (x10$^4$ MN/m$^3$)** | **1.76** | **1.98** | **1.93** | **1.85** |
| **μ (-)** | 1.42 | 1.41 | 1.42 | 1.43 |
| **C (MPa)** | 2.04 | 2.32 | 2.77 | 2.65 |

Definition of the steel-concrete interface for the reinforcement anchored in the substratum followed the same procedure as for the concrete-to-concrete interface. The specific fracture energy was taken from [150], where several mortars were tested and respective fracture energy

was assessed. Considering the grout properties in 3.2.5, a specific fracture energy of 0.037 N/mm was accounted for when calculating the steel-concrete interface fracture energy with equation (3.9). The required parameters on such equation are also the grout tensile strength and tensile bond. The former parameter was calculated considering provisions by [151], where a ratio of 0.7 is stated between such material's tensile strength and flexural tensile strength. Since no information about tensile bond on steel-concrete interfaces could be assessed, tensile bond of the interface was estimated regarding provisions on [122] that state a factor of 0.5 regarding the tensile strength of the weakest neighbouring material, in this case, the cementitious grout. Cohesion of the interface was calculated with equation (3.6), considering a coefficient of friction of 0.5. According to [152], coefficient of friction between steel plates and concrete can vary from 0.57 to 0.65 in normal conditions, and in 2.3.9 is stated the value of 0.8 from the Shear Friction Theory. The value of 0.5 was then considered regarding the Troubleshooting Manual for the ATENA 3D® [122] software which recommends such value to improve numerical stability due to the interface parameters. Considering such premises and grout strength properties in 3.2.5, the resulting interface parameters calculated using equations (3.8) to (3.10) are presented on Table 3.17.

Table 3.17 – Steel-concrete interface parameters.

| | **Steel-concrete interface parameters** |
|---|---|
| **$G_{F,grout}$ (x $10^{-5}$ MN/m)** | 3.70 |
| **$f_{t,grout}$ (MPa)** | 6.72 |
| **$f_{t,i}$ (MPa)** | 3.36 |
| **$G_{F,i}$ (x $10^{5}$ MN/m)** | 1.85 |
| **$K_{NN}$ (x $10^{5}$ MN/m$^3$)** | 3.05 |
| **$K_{TT}$ (x $10^{5}$ MN/m$^3$)** | 3.05 |
| **$\tau_{bond}$ (MPa)** | 16.2 |
| **$\mu$ (-)** | 0.5 |
| **C (MPa)** | 14.52 |

Since the main purpose of defining a steel-concrete interface was to allow slipping of the anchored reinforcement, as observed in experimental testing on sections 3.3.1 and 3.3.2, a softening law was also defined with equation (3.11). Calculation of such curve requires a maximum displacement which was defined according to results presented on Figure 3.23 of section 3.2.5, which state an anchorage slip ranging from 2.5 mm to 5.5 mm for the maximum pull-out load.

### 3.4.4. Numerical results

In order to gain confidence on numerical results, simplified local models were also performed for assessing the effective tensile strength of the concrete material, pull-off strength at the interface, and pull-out strength of anchored reinforcement.

Since concrete in tension is a parameter of difficult assessment and mostly estimated through indirect tensile tests, a direct tensile specimen was modelled through regular macroelements and

brick meshing, illustrated in Figure 3.94 with an example of a resulting Stress-Strain curve. Modelling the concrete material based on the experimental results presented at Table 3.7 and Table 3.8 resulted in a constant behaviour of the nonlinear material, with differences smaller than 5 % to concrete tensile values assessed experimentally.

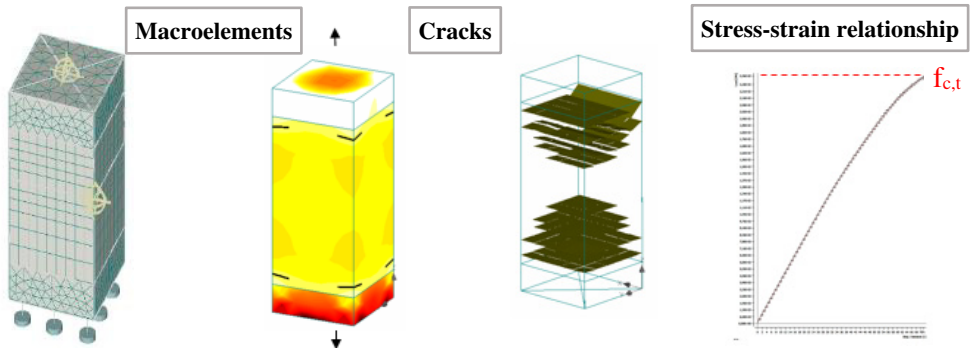


Figure 3.94 – FE modelling of direct concrete tensile strength.

Pull-out of rebar embedded in the substratum layer was modelled for a single 6 mm and 10 mm. Rebar anchorages were embedded in a larger concrete substratum, as shown in Figure 3.95, so stresses could dissipate with no influence of boundary conditions. Pull-out force measured was 22.2 kN on the Ø6 mm model and 33.4 kN on the Ø10 mm model, which results in bond stresses of 16.8 MPa for the former and 15.2 MPa for the latter. Such values are in accordance to assessed material strength on section 3.2.5. Also noteworthy was the behaviour of the Ø6 mm model similar to the behaviour observed experimentally in Figure 3.23 of the same chapter. No comparison was performed for the Ø10 mm model, since no experimental test was performed for the anchoring of such rebar diameter, although FE cracking of such anchorage is displayed for reference.

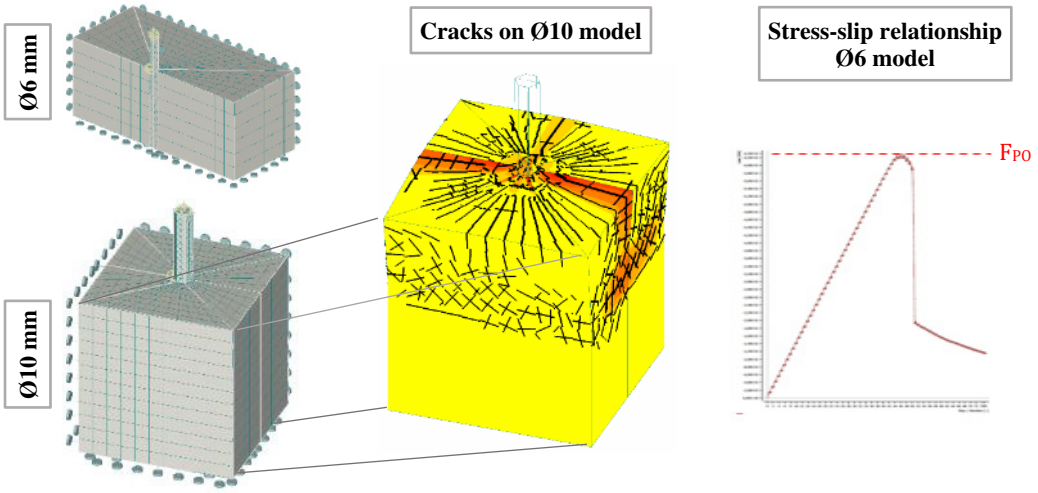


Figure 3.95 – FE modelling of rebar pull-out strength when embedded with cement grout.

After numerical characterisation of the materials, the one quarter models of the experimental specimens were tested. The load step was defined with an increment of 0.1 mm at midspan, with good stability for the Newton-Raphson solution method of the FE analysis. As observed in experimental testing, loading of the reference specimens can be divided into two stages: loading of the composite cross-section until debonding of the overlaid concrete; and loading of the substratum layer until flexural yielding of reinforcement. The phenomena regarding interfacial debonding was identified in the analysis, with the plateau in the load-deflection curve identifying this stage on the loading. In Figure 3.96, the numerical and experimental load-deformation curves show a good correlation, with both debonding and flexural yielding of reinforcement characterising the behaviour of the reference specimens. The numerical modelling of the substratum layer alone was also performed (A3D$_S$-SUB, plotted in blue). One can observe in the figure below the substratum layer for comparison with strengthened specimens (A3D$_S$-REF, plotted in red). Since there were no experimental specimens with only the substratum layer, the added value for these FE models is recognized.

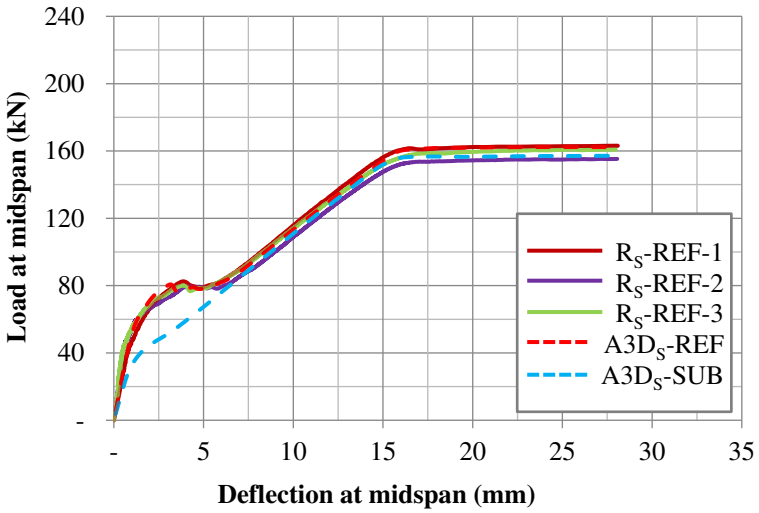


Figure 3.96 – Comparison between numerical and experimental results for the modelling of REF specimens.

A good correlation was also attained when comparing the numerical models with reinforcement crossing the interface to experimental specimens. Also evident was the change in the behaviour due to such reinforcement that stiffens the strengthened slabs, also noticeable when comparing to reference specimens. Numerical models for both anchorage depths adjusted accordingly to the experimental results. A comparison between the numerical and experimental results is shown in Figure 3.97 to Figure 3.99 for the ANC, STC, and STANC detailings of both 50 mm and 80 mm anchored reinforcement crossing the interface. The reference load-deflection curves are shown on all figures below for scaling the difference in specimen behaviour when compared to the former.

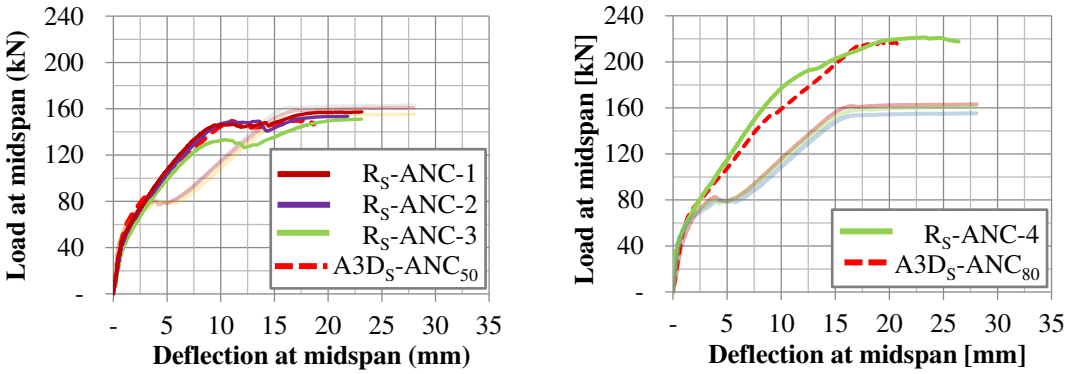


Figure 3.97 – Comparison between numerical and experimental results of 50 mm and 80 mm anchored longitudinal reinforcement.

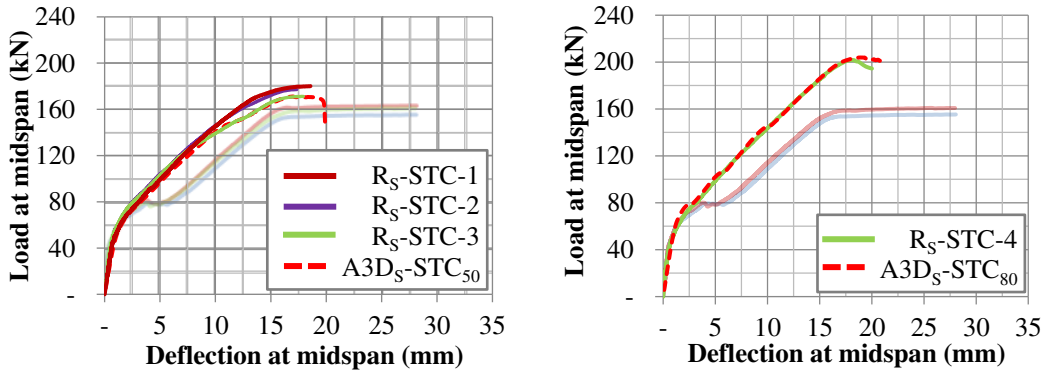


Figure 3.98 – Comparison between numerical and experimental results of 50 mm and 80 mm anchored steel connectors.

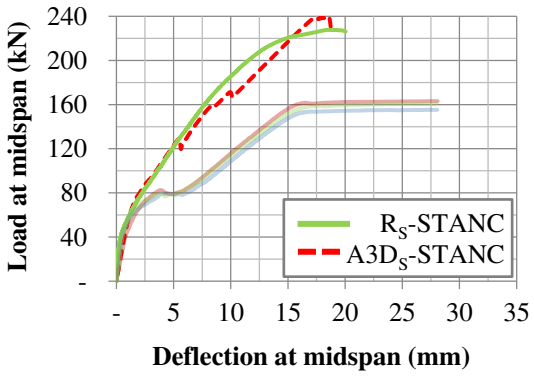


Figure 3.99 – Comparison between numerical and experimental results of 80 mm anchored longitudinal reinforcement and steel connectors.

A good correlation could be observed for all detailings of the interface reinforcement with the key aspects of the experimental specimen's behaviour modelled correctly, like the initiation of cracking and its respective loss of stiffness, and the debonding of the two layers. The difference in terms of the maximum load or deflection were marginal and within accepted tolerances.

Observing the figures above, the good approximation for the 50 mm anchored longitudinal reinforcement, as well as for 50 mm and 80 mm steel dowels, is evident. The greater divergence in terms of the load-deflection relationship could be observed for 80 mm anchored longitudinal reinforcement (ANC and STANC).

In Figure 3.100 an example is presented for comparison of the crack pattern and similar macro cracking between the numerical models and experimental specimens. Surface cracks were similar on both the numerical models and experimental specimens, with special attention to the main cracks that occur very close on both. The example below is composed by specimens' $R_S$-STC-2 whose debonding of overlaid concrete allowed for the surface cracks on the overlay to close, and $R_S$-ANC-4 where cracks reached the interface before the anchored end, but failure resulted through the shear crack close to the anchored reinforcement.

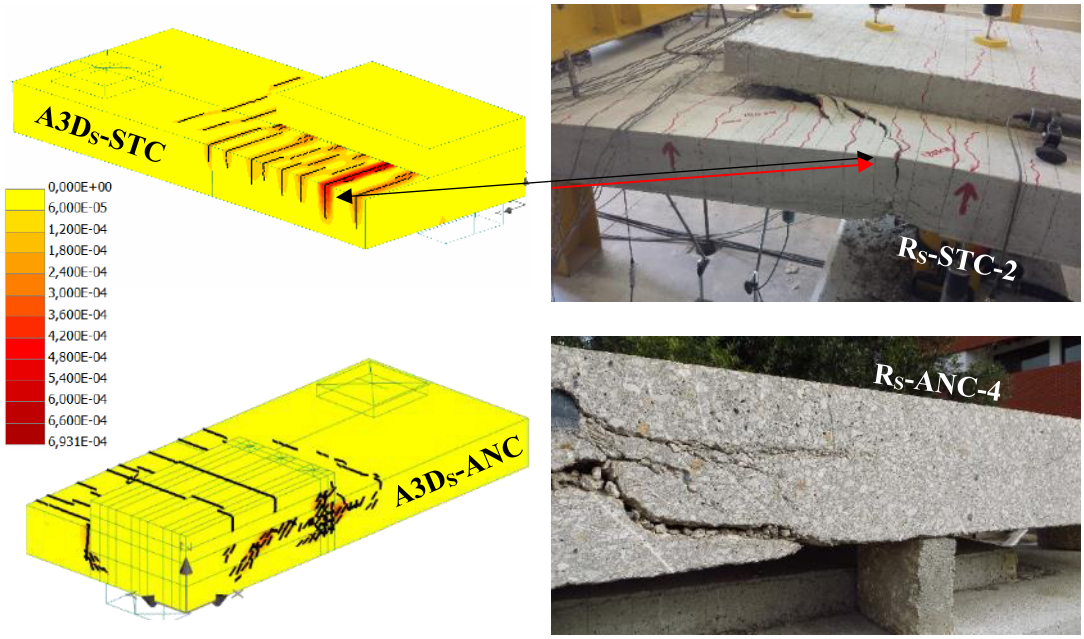


Figure 3.100 – Cracking of the numerical models and experimental specimens for the long overlays ($A3D_S$ and $R_S$).

Considering the long overlay geometries, the resulting load-deflection relationship also fitted the experimental test results, with little divergence until maximum load and deflection, as observed in Figure 3.101 to Figure 3.104.

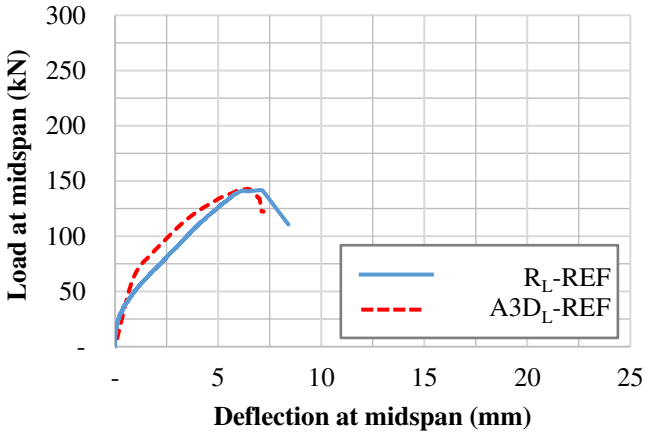


Figure 3.101 – Comparison between numerical and experimental results for the modelling of the $R_L$-REF specimen.

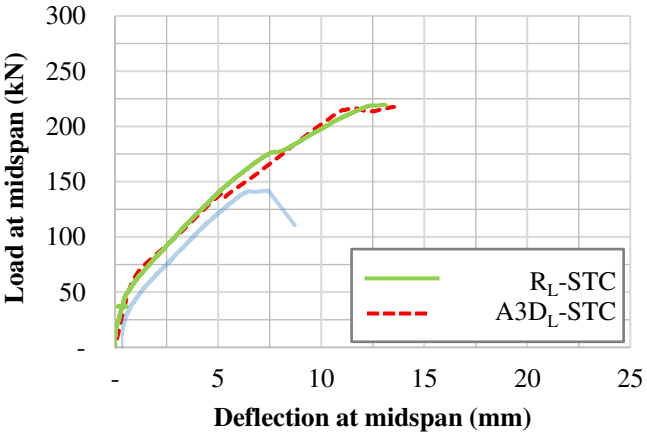


Figure 3.102 – Comparison between numerical and experimental results for the modelling of the RL-STC specimen.

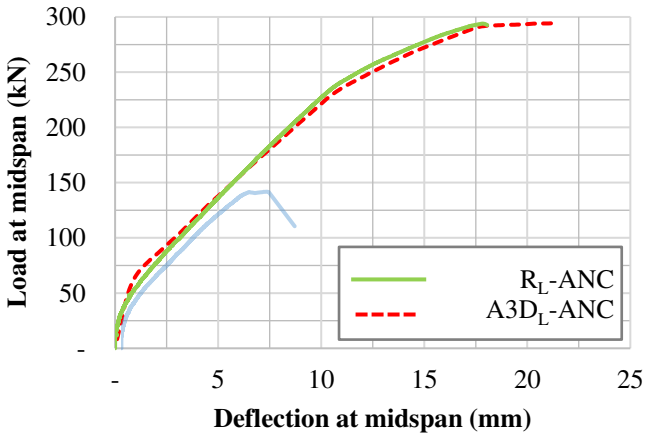


Figure 3.103 – Comparison between numerical and experimental results for the modelling of the RL-ANC specimen.

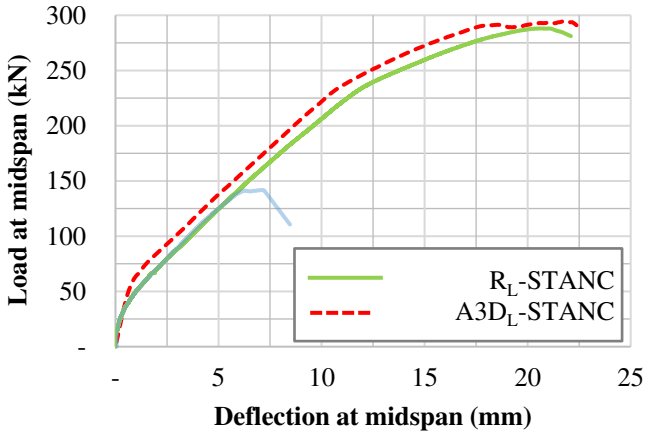


Figure 3.104 – Comparison between numerical and experimental results for the modelling of the $R_L$-STANC specimen.

Observing the load-deflection relationships above, one can attest for the good fitting of the numerical modelling on experimental results for the long overlay geometry specimens. Both the maximum load and deflection were reached on all numerical models with an accepted level of error for the stiffness change throughout the model's load history.

In Figure 3.105 an example is presented similar to that of the short overlays, for comparison of the crack pattern and similar macro cracking between the numerical models and experimental specimens. Cracking of the STC model on the long overlays was coherent with the experimental specimen, with debonding of the overlaid concrete and cracks on the substratum close to the edge of the overlay. Cracking of the STANC model on such overlays resulted closer to the edge of the overlay than on the experimental specimen, with continuity of cracks crossing the interface.

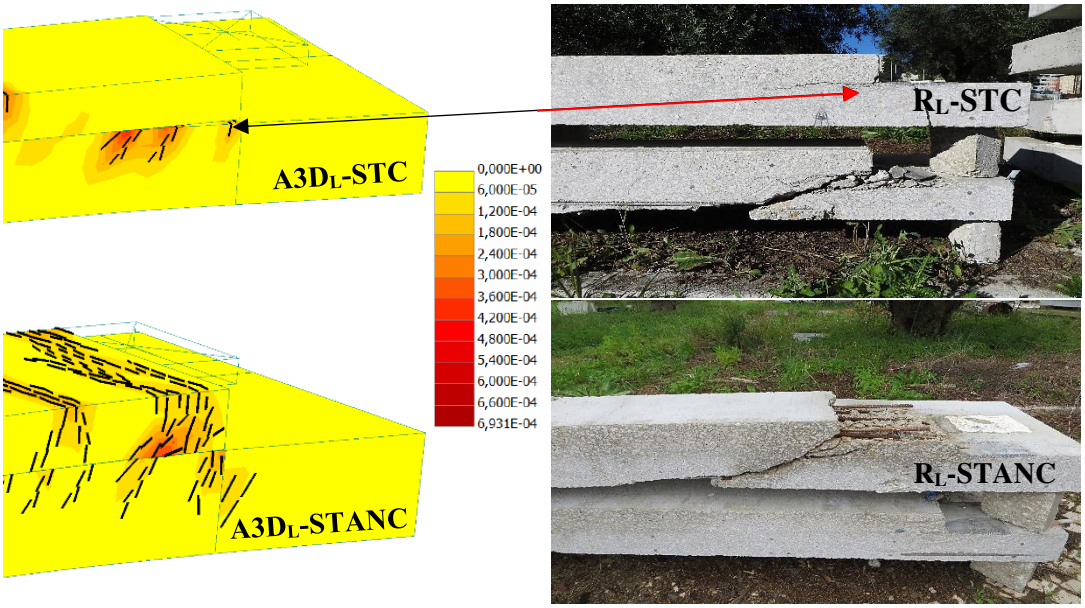


Figure 3.105 – Cracking of the numerical models and experimental specimens for the long overlays ($A3D_L$ and $R_L$).

The respective failure loads for all the modelled specimens and comparison to experimental average results are presented on Table 3.18. Due to the numerical behaviour observed for the $R_L$-REF specimen, the experimental value considered was the one of the plateau observed upon debonding, coherent with maximum strain at the overlay reinforcement. Experimental values for multiple specimens were taken as the average of each group of interface detailing results presented before on Table 3.11.

Table 3.18 – Experimental and numerical failure loads of rectangular specimens.

| Failure loads | REF | | STC | | ANC | | STANC | |
|---|---|---|---|---|---|---|---|---|
| | $R_S$ | $R_L$ | $R_S$ | $R_L$ | $R_S$ | $R_L$ | $R_S$ | $R_L$ |
| **Experimental (kN)** | 159.7 | 141.7 | 176.2 | 219.7 | 154.0 | 293.6 | 227.7 | 288.1 |
| **Numerical (kN)** | 162.1 | 143.0 | 170.6 | 217.6 | 149.8 | 294.2 | 238.1 | 294.5 |
| **EXP/NUM (-)** | 0.99 | 0.99 | 1.03 | 1.01 | 1.03 | 1.00 | 0.96 | 0.98 |

A good correlation was attained for the numerical models of $R_S$ specimens when comparing to the equivalent experimental slab specimens, with a maximum difference of 4 % for the $A3D_S$-STANC model. The correlation level remained very good also for the modelling of long overlay geometries, with a maximum difference of 2 % also for the $A3D_L$-STANC model.

### 3.4.5. Discussion of numerical results

The good correlation between experimental specimens and numerical models in terms of its global behaviour, deformation and failure load, allowed for assessing the stress and crack patterns at the interface. A concentration could be observed on the corner further from midspan where the geometry changes on both directions, as illustrated in Figure 3.106. Tangential stresses are shown to grow from midspan to the overlay's edge, where the maximum relative displacement of the two layers results in maximum shear stress. The deformed shapes below illustrate the stress-state at the interface for half the failure load of the $A3D_S$-STC model.

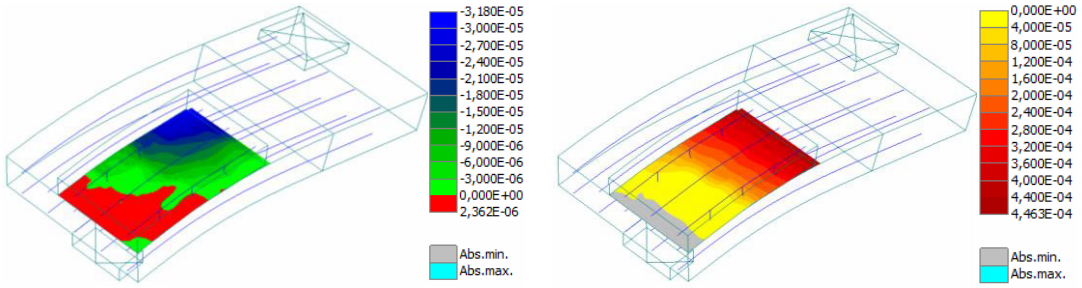


Figure 3.106 – Normal and Tangential stresses at the interface (deformation magnified 10x).

The relationship between alternating stress fields and the position of the steel connectors did not verify the theoretical assumption that rebar crossing the interface would lead to only tensile stresses. The horizontal relative displacement led to a concentration of compressive stresses due to the stitching provided by the rows of steel connectors and its flexural capacity. Discrete zones then formed around such elements that resulted, from midspan, in compression on one side, and tension on the other side of the steel connector elements. An example is presented in Figure 3.107 for the A3D-STANC model where the binary of stresses is more evident at the anchored reinforcement, but also at the steel dowels.

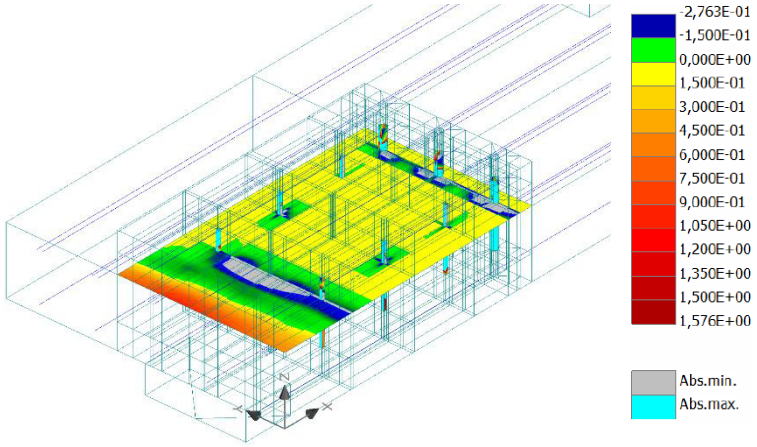


Figure 3.107 – Compressive vertical stresses near the shear connectors (A3D$_S$-STANC, MPa).

Such phenomenon illustrated the interlocking effect caused by reinforcement stitching the interface, generating compressive stresses that are favourable to the resisting mechanism of concrete-to-concrete bond. Although the stress distribution at the interface depends on the detailing of the reinforcement crossing the interface, it also depends on the geometry of the slabs and the loading conditions. This can be observed in Figure 3.108 for the intermediate row of steel connectors of the A3D$_S$-STC model, where the interface has debonded on a great portion and this row of steel connectors is guaranteeing the binary of forces at that distance from midspan. One can notice the furthest row from midspan is already on a debonded zone, contributing only with the tensile strength provided by the anchoring to the substratum. In such case, debonding has occurred until the second row of steel dowels, denoting the stitching reinforcement work at preventing the full debonding of the interface.

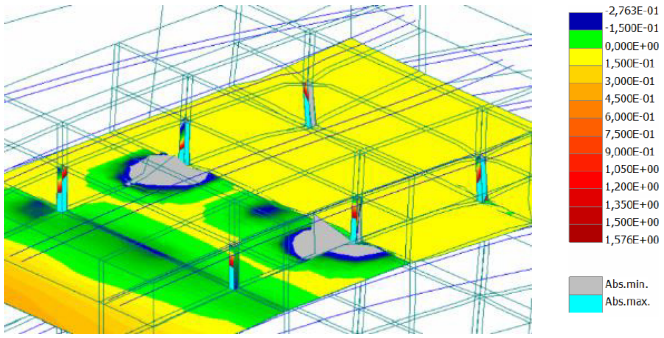


Figure 3.108 – Interface partially debonded and tensile-compressive stresses around the steel dowels (A3D$_S$-STC, MPa).

The steel dowels interference on stress distribution could also be assessed through the analysis of the reinforcement stress and bond stress over the slab span depicted in Figure 3.109. The local stiffening of the steel dowels causes the reduction of such reinforcement bond stress although the steel stress distribution remained.

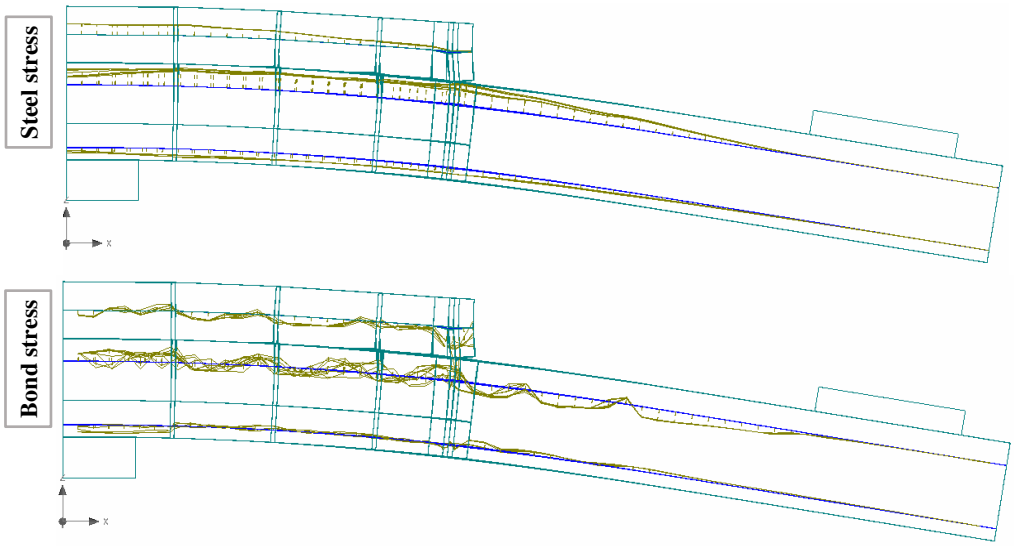


Figure 3.109 – Steel stress and bond stress of longitudinal reinforcement (A3D-STANC model).

One of the main subjects intended for assessing through numerical modelling was the dowel action of reinforcement crossing the interface. Such phenomenon could be observed on the FE models through the inversion of stresses on the reinforcement crossing the interface and through the augmented deformed shape of such elements on Figure 3.110.

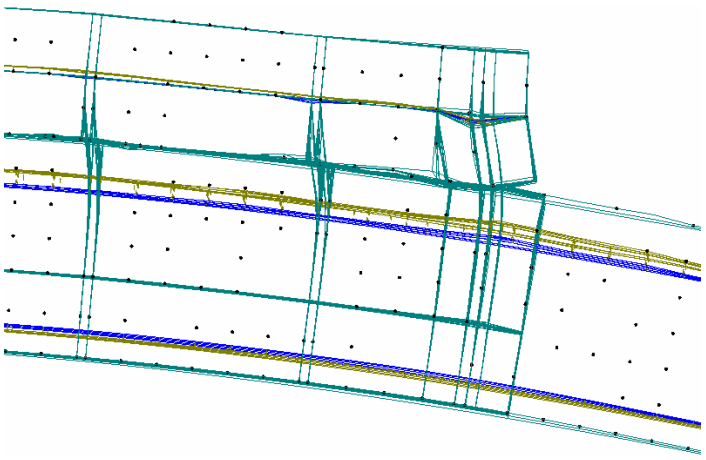

Figure 3.110 – Change of normal stresses' sign for the shear connectors at half the embedment length.

This attests for the expected behaviour of the slabs where this particular resisting mechanism is accounted for. Stress distribution for the steel connectors resulted according to [22] and can be observed in Figure 3.111 for the A3D-STANC model. The maximum compressive stresses were observed until a certain depth, with bending stresses changing the sign below such depth, illustrated by the switch from cool to warm colours. Such behaviour was proof of shear and bending stresses on the anchored reinforcement as a result of differential deformation between layers.

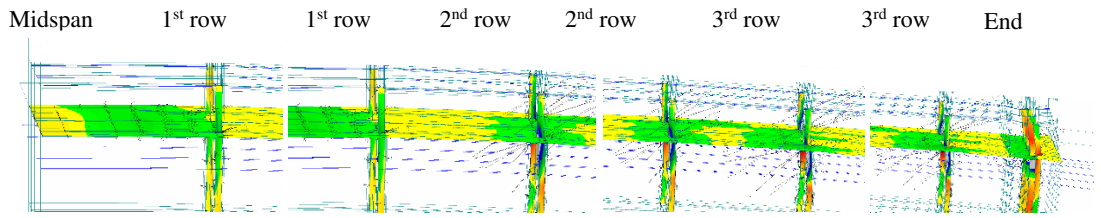


Figure 3.111 – Steel connectors stress sign change at half the embedment length (A3D-STANC model, MPa).

When analysing the direction of the principal compressive stress inside the slabs for the A3D-STANC detailing of the interface, a clear concentration of stresses that led to cracking occurred mainly near the second and third rows of reinforcement crossing the interface. A path is identified for these stresses where they cross the last row of steel connectors up to the overlaid concrete rebar, and equilibrium occurs at the node where the rebar is anchored. A strut and tie model can be defined for these slabs according to Figure 3.112.

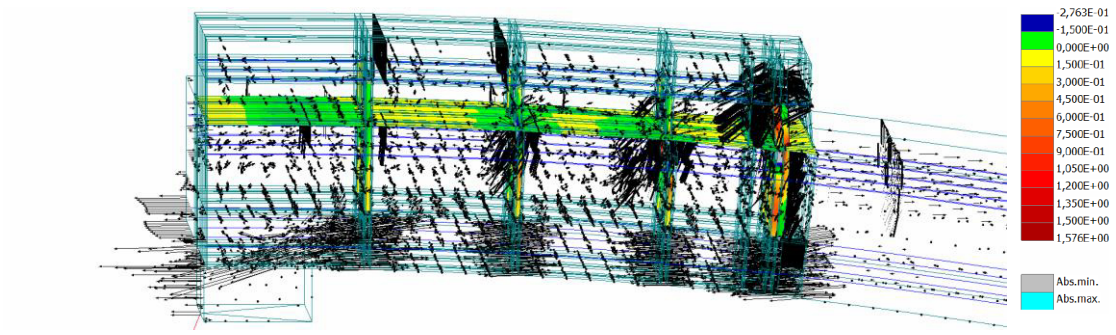


Figure 3.112 – Principal compressive stress path, anchorage normal stress, and concrete cracking (A3D-STANC model).

The cracking pattern observed for this detailing of the interface was coherent with the inclined cracks observed in the anchored rebar regions for the experimental specimens. This behaviour can be observed in Figure 3.113, where a horizontal crack shifts from the interface to the rebar level.

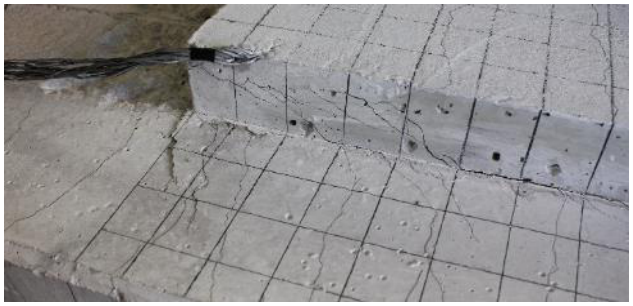

Figure 3.113 – Inclined cracks at the anchored rebar region (STANC detailing).

The use of reinforcement crossing the interface further enhances the resisting mechanism by bond, adding interlock of the contacting surfaces and friction, along with dowel action of such reinforcement, to the standard component of bond, adhesion. When analysing the contribution of each component of the bond mechanism, it is important to affect the amount of stress at the interface that is mobilized for each of the latter components. Such distribution is of difficult assessment without effectively measuring the load at each coordinate of the test specimen, and this is where numerical modelling can assist directly the analytical approach.

Analysing the horizontal stress at the interface of the numerical model, one can assess the area and degree of stress that is mobilized, with the remaining stress mobilized by dowel action of the interface reinforcement. Figure 3.114 to Figure 3.116 illustrate the shear stress at the interface for all detailings (STC, ANC, and STANC). On the STC models, one can assess around 70 % of shear stress at the interface of the $A3D_S$ model and around half that value (35 %) on the $A3D_L$ model. Such distribution of stresses can be withdrawn from graphically analysing the grade of stresses at the interface and the area of the interface actually mobilizing shear stress, shown with an array of warm colours. Yellow and Green colours are considered null stresses due to the low stresses they represent. Since structural integrity is maintained throughout the load history until the experimental failure loads, one can consider that the remaining horizontal stresses are mobilized through dowel action of the interface crossing reinforcement.

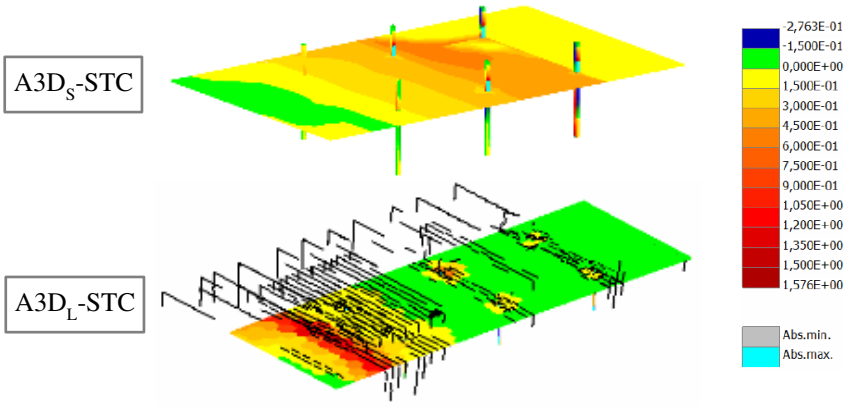


Figure 3.114 – Shear stress at the interface for the $A3D_S$ and $A3D_L$ models of the STC specimens.

Such distribution of shear stress to the interface is observed on the ANC models with half the distribution determined for the STC models, 35 % and 17.5 %, respectively. Such drop in interface contribution through its shear stress capacity can be explained by the main role that controlling the edge lifting phenomenon can play on the debonding of concrete-to-concrete interfaces.

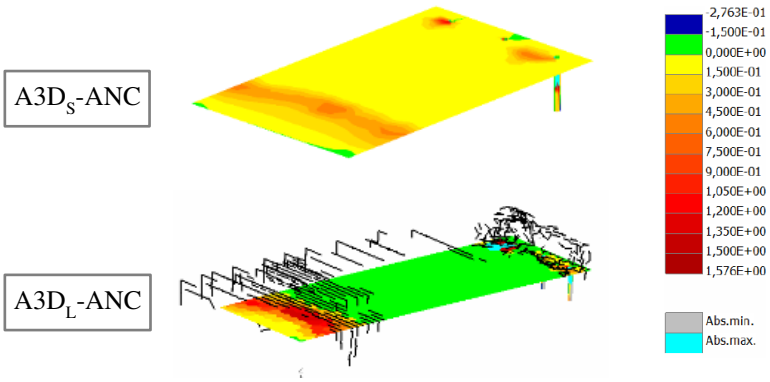


Figure 3.115 – Shear stress at the interface for the A3D$_S$ and A3D$_L$ models of the ANC specimens.

The STANC models follow the stated distribution of horizontal stress for the ANC models since reinforcement crossing the interface responsible for controlling the edge lifting phenomenon is also present. The distribution of 35 % of horizontal stress for interlocking and friction were then considered for the A3D$_S$ model, in accordance to interface stress assessed visually in Figure 3.116. The value of 17.5 % determined for the analogous geometry above was then considered also for the A3D$_L$ model of the STANC detailing, consistent with the visual data observed below.

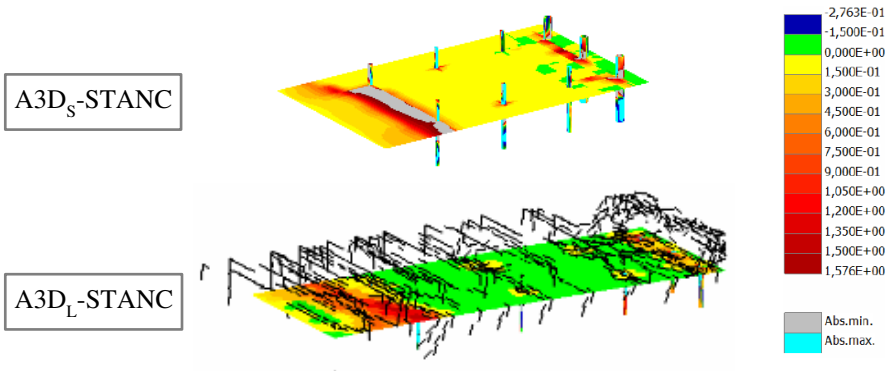


Figure 3.116 – Shear tress at the interface for the A3D$_S$ and A3D$_L$ models of the STANC specimens.

## 3.5. Final remarks

The experimental campaign on rectangular slabs contributed to the understanding of strengthening with overlaid concrete on the tensile face of slabs by simplifying the horizontal shear stress problem to one direction. The concrete-to-concrete interaction phenomenon on a tensile face is a complex and material dependent strengthening solution which requires the correct considerations regarding the existing structure. The increase of flexural and shear strengths attained allowed for attesting the application of a reinforced concrete overlay on the tensile face of existing slabs.

Characterisation of the tensile capacity of an interface between two concrete layers allowed for assessing an average tensile stress enough for considering the adhesion component of the shear friction mechanism. The structural dependency of the strengthened specimens on the integrity of the interface is apparent when debonding of the overlaid concrete occurs. The evolution of such phenomenon is dependent on the detailing of interface crossing reinforcement, since loss of contact stops the stress transfer capacity between layers and reduces the flexural stiffness to less than that of the original structure due to damaging of the cross-section during the load history.

Numerical modelling of strengthened specimens allowed for the calibration of a nonlinear finite element 3D model for each specimen geometry and detailing of the interface. The small errors that resulted from such models allowed for considering such technique as valid when analysing overlay strengthened structures. The correct characterisation of the debonding phenomenon is important since consideration of a full monolithic section is an unconservative approach.

Results presented in this chapter allowed for evolving the problem to column-supported slabs, where the mesh of flexural reinforcement and the point load of column supports leads to dispersions of stresses on both directions of the slab.

# 4. COLUMN-SUPPORTED SLABS STRENGTHENED WITH RCO

## 4.1. Foreword

Flat slab strengthening on the column region is the object of several studies in Structural Engineering, with available methods ranging from the enlargement of the support [9], through the use of post-installed reinforcement [11], to the bonding of composite materials on the tensile surface [6]. All techniques have their advantages and disadvantages, usually regarding workmanship and economic aspects. Strengthening an existing structure usually requires at least partial unloading before strengthening, at least for passive strengthening methods. Active methods that involve prestressing [8] have the ability to restore some deformations.

Enlargement of the support is the most common method for controlling the behaviour of the column-slab connection. Such technique can be performed in both the design stage or when strengthening is needed, either by a capital or column head, or through a drop panel around the column that stiffens the slab. By enlarging the slab thickness, both flexural and punching strength will increase. The advantages that result from the stiffening of the slab can also be attained if such layer is applied on the top face of the slab. The new reinforcement then is core on the resistance of the cross-section and can only work if stresses are transferred from the slab to this new layer. To provide such behaviour, the interface must be prepared through the roughening of the existing surface and reinforcement properly anchored on both layers.

Strengthening with overlaid reinforced concrete on existing structures is then a valid option, since it can provide stiffness, strength and a new protection to deteriorated structures. Such option comes with an increase on the structure self-weight, which should be accounted for, but it remains an economic and least specialized way for structural strengthening or retrofitting. An important aspect is the technical condition of the existing structure, which must always be assessed prior to the decision for strengthening, mainly regarding damage state and quality of the existing structural elements. To improve the bond between the overlaid reinforced concrete and the substratum, roughening of the existing surface is required [56]. When performing such preparation of the surface, one must choose the roughening technique adequately, since the more aggressive percussion methods with heavy pneumatic or electric hammers can cause microcracking of the existing concrete [153]. One of the advantages of concrete jacketing or overlaying is the ability to substitute some of the deteriorated or damaged material with sound concrete, thus improving the structural longevity. Some work has been performed regarding the structure state before strengthening [154,155]. A poor-quality of the substratum concrete will result in poor bond to the new layer. Deteriorated or damaged concrete should then be replaced with sound concrete, thus guaranteeing concrete strength and protection of new and existing reinforcement.

The latter reinforcement should be assessed through available methods, preferably non-destructive, regarding the design quantity and respective layout on the existing structure. The possible way to improve bonding of the new layer to the existing structure is by adding mechanical connectors in the form of dowels for stitching the two layers together and improving the degree of monolithic behaviour for the strengthened slab. This post installed reinforcement

can work for both tensile and shear forces on the interface of the two layers [21], controlling relative displacements on both directions, and the edge lifting phenomenon at the ends of the overlay [42].

When all considerations regarding the connection between layers have been taken, strengthening with a concrete overlay is then viable and able to guarantee the structural integrity in the column-slab connection. Such region is characterised for being susceptible to high hogging moments, with consequent cracking and deformation, and to punching of the slab, which is a brittle failure mode for concrete elements, with the possibility of causing progressive collapse of the global structure.

## 4.2. Experimental research

Since the strengthening system analyzed in this work is intended for existing structures and working spaces, minimizing such interference is important, and therefore two strengthening areas were considered. An upper bound radius from the column face was set at *4d* from the column face, deemed enough for anchoring the longitudinal reinforcement and doubling the control perimeter set for punching by the EC2 [101] at *2d,* where *d* is the effective depth of the overlay reinforcement. Accounting for the needed anchorage length of longitudinal reinforcement and the latter control perimeter for the punching phenomenon, the lower bound radius of the strengthened area was set at a distance *3d* from the column face. This work is backed by experimental results and conclusions from the previous chapter, regarding the material and interface properties as well as the experimental and numerical behaviour of the debonding phenomenon.

### 4.2.1. Test specimens

The experimental programme for assessing the performance of this strengthening method consisted of nine interior column reinforced concrete flat slab specimens, strengthened with an overlaid reinforced concrete layer. They were divided into two series: with the strengthening layer up to four times, $S_{4D}$, or three times the resulting cross-section effective depth, $S_{3D}$, from the column face. Relevant data regarding the geometry of specimens is provided in Table 4.1, where $A_{s,o}$ and $A_{s,s}$ are the area of longitudinal reinforcement for the overlay and substratum, respectively. The detailing of the interface was then organized as:

- SUB – For the reference value of the existing structure without strengthening (thickness of 120 mm, only directly comparable to *3d* specimens);
- REF – Reference specimen, strengthened with reinforced concrete overlay and no stitching reinforcement;
- STC – Shear connectors (steel dowels) distributed across the interface, embedded 80 mm with a cementitious grout (SikaGrout® 213) in the existing substratum;
- ANC – Longitudinal reinforcement of the overlaid concrete anchored in the ends by embedding 80 mm with cementitious grout (SikaGrout® 213) in the existing substratum;
- STANC – Combination of all the detailings of the interface.

Table 4.1 - Relevant geometrical parameters of the square specimens.

| | | $S_{4D}$ / $S_{3D}$ | | | |
|---|---|---|---|---|---|
| | | **REF** | **STC** | **ANC** | **STANC** |
| **Overlay** | **Thickness [m]** | 0.06 / 0.07 | | | |
| | **Length [m]** | 1.70 / 1.10 | | | |
| | **Width [m]** | 1.70 / 1.10 | | | |
| | **$A_{s,o}$ [-]** | 2Ø10//0.10m (15.7cm$^2$/m) | | | |
| | **$d_{s,o}$ [m]** | 0.175 / 0.155 | | | |
| **Interface** | **$A_{s,i}$ [mm$^2$]** | - | 1344 | 4740 / 3476 | 6084 / 4820 |
| **Substratum** | **$d_{s,s}$ [m]** | 0.125 / 0.100 | | | |
| | **$A_{s,s}$ [-]** | Ø16//0.10m (20.11cm$^2$/m) / 2Ø10//0.10m (15.70cm$^2$/m) | | | |
| | **Width [m]** | 2.30 | | | |
| | **Length [m]** | 2.30 | | | |
| | **Thickness [m]** | 0.15 / 0.12 | | | |

Strain gauges were installed on both the substratum and overlaid concrete reinforcement, both in the longitudinal reinforcement and in the reinforcement crossing the interface. The specimen's substratum comprised the dimensions of 2300x2300 mm$^2$ and thicknesses of 150 mm and 120 mm, respectively for the $S_{4D}$ and $S_{3D}$ specimens illustrated in Figure 4.1.

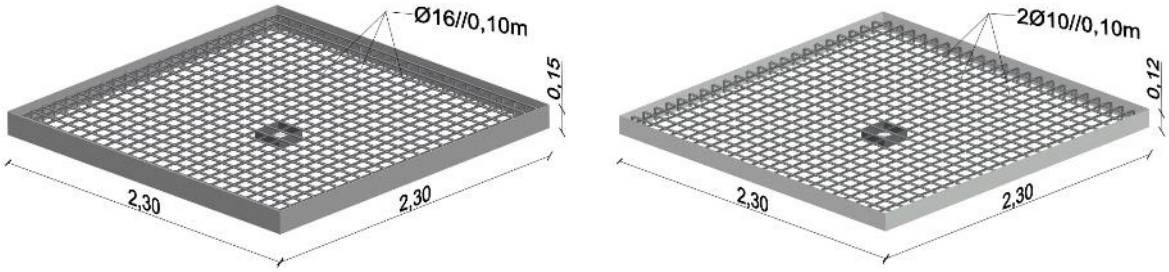


Figure 4.1 – Detailing of the substratum reinforcement for both sets – $S_{4D}$ (left) and $S_{3D}$ (right).

The bottom reinforcement of the substratum consisted of 8 mm bars spaced every 200 mm on each direction, for both slab sets. Such detailings were performed on the substratum of both $S_{4D}$ and $S_{3D}$ specimens as shown in Figure 4.2, where the rebar placement and casting are depicted for the conception phase.

Figure 4.2 – Placing of the substratum reinforcement for both sets – $S_{4D}$ and $S_{3D}$.

Strain gauges were installed on key coordinates of the reinforcement for assessing strains and estimate the stresses on reinforcement, similar to the rectangular specimens on chapter 3. Such coordinates consisted on the column face and at a distance *2d* from that on both sets, and at the anchorage of such reinforcement, at a distance of *4d* and *3d* from the column face, respectively for the $S_{4D}$ and $S_{3D}$ specimens, as depicted in Figure 4.3.

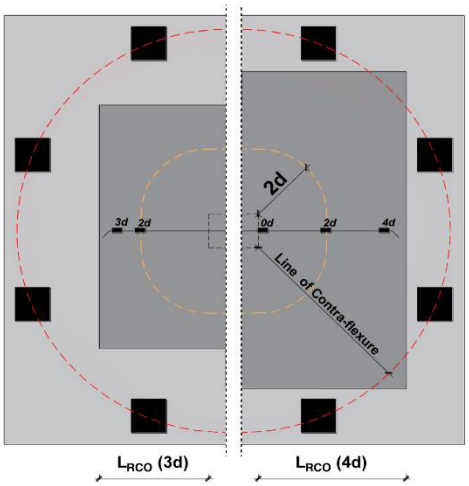


Figure 4.3 – Key locations of strain gauges in the $S_{3D}$ (left) and $S_{4D}$ (right) specimens.

An example of the strain gauges installed on these coordinates can be observed in Figure 4.4.

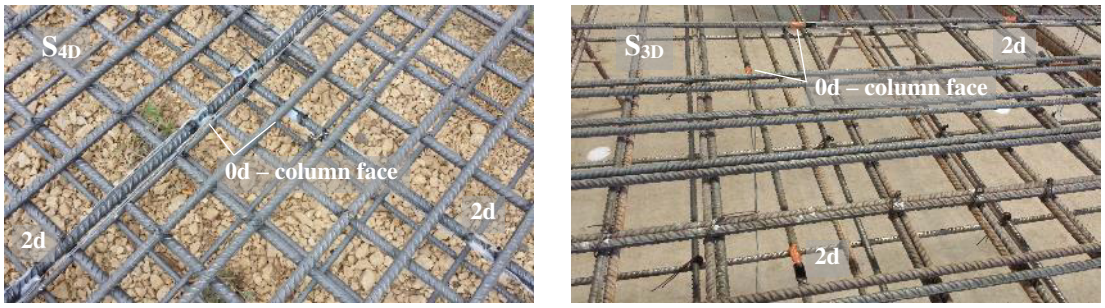


Figure 4.4 – Strain gauges on key coordinates of the substratum – $S_{4D}$ and $S_{3D}$ .

To adequately replicate the application of the strengthening solution, holes for the interface crossing reinforcement were drilled after hardening of the substratum concrete. Such task required the assessment of the installed reinforcement to avoid intercepting any longitudinal rebar. This assessment was performed with a magnetic scanner HILTI® PS200S Ferroscan, illustrated in Figure 4.5.

Figure 4.5 – Assessment of substratum reinforcement, mapping and drilling of holes for the stitching reinforcement.

Due to the reduced area of the overlaid concrete patch on the $S_{3D}$ specimens, anchoring of longitudinal reinforcement was performed close to the edge of the overlay, as observed in Figure 4.6.

Figure 4.6 – Hole boring on the $S_{3D}$ specimens.

Time between casting of both layers was about two months for the $S_{4D}$ specimens, and two weeks for the $S_{3D}$ specimens. Preparation of the substratum top surface consisted in chipping with an electric hammer and steel moil point, with concern that the moil tip should not go deeper than 10 mm at each stroke. Such consideration allowed for protecting the longitudinal reinforcement of the substratum and its minimum concrete clear cover as illustrated in Figure 4.7.

Figure 4.7 – Surface preparation with chipping hammer and steel moil point – $S_{4D}$ and $S_{3D}$.

Characterisation of the resulting surface roughness is addressed in section 3.2.6. The resulting surface could then be classified as very rough, as recommended for proper concrete-to-concrete bond. The overlaid concrete area dimensions were then 1700x1700 mm$^2$ for the $S_{4D}$ specimens and 1100x1100 mm$^2$ for the $S_{3D}$ specimens, illustrated in Figure 4.8.

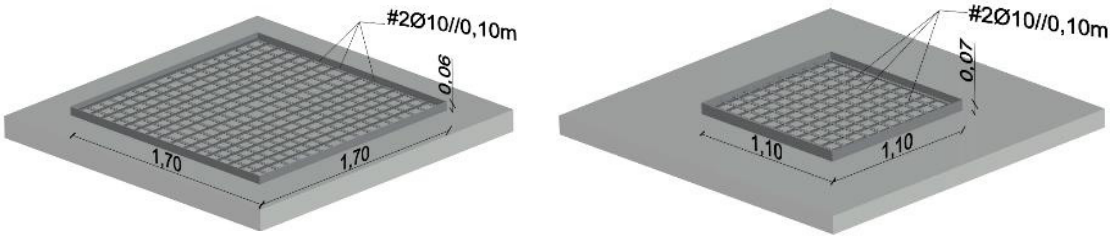


Figure 4.8 – Detailing of the reference specimen overlay reinforcement – $S_{4D}$ and $S_{3D}$.

The $S_{4D}$ set comprised a 60 mm thick overlaid reinforced concrete layer, which was also the minimum thickness to accommodate for the rebars, concrete cover, and the minimum spacing to the interface. The $S_{3D}$ set comprised a 70 mm thick layer. The longitudinal reinforcement on both geometries consisted of pairs of 10 mm bars, spaced every 100 mm in each direction, as illustrated in Figure 4.9. Pairs of bars with smaller diameter were chosen in order to reduce the diameter of the overlay reinforcement, and consequently the overlay thickness.

Figure 4.9 – Detailing of the reference specimen overlay reinforcement – $S_{4D}$ (left) and $S_{3D}$ (right).

Due to the edge lifting phenomenon, observed in several works and included in some design codes ([42], [57]), detailing with reinforcement crossing the interface near the ends of the new layer (ANC specimens, illustrated in Figure 4.10) directly addresses this phenomenon, controlling the interface crack opening. The figure below presents an example for the $S_{4D}$ specimen. Loading of the specimens was performed by imposing a load at midspan and reactions on the supports that guarantee the boundary conditions.

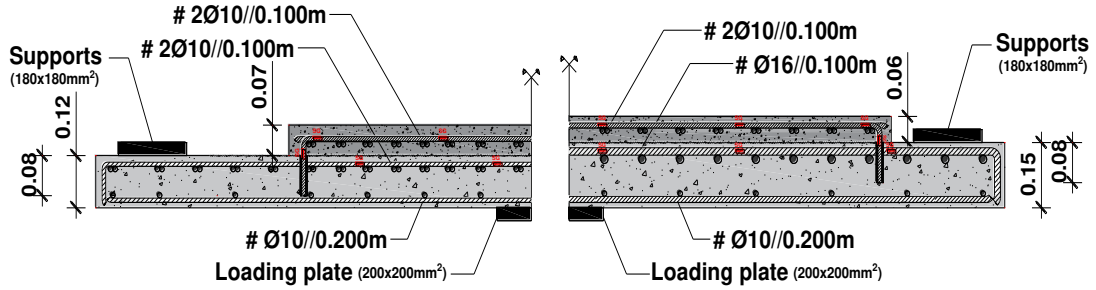


Figure 4.10 – Detailing of the ANC specimen overlay reinforcement – $S_{3D}$ and $S_{4D}$.

Stitching the interface with steel dowels was also performed on both sets, with a regular orthogonal distribution across the interface, totalling 48 steel dowels crossing the interface on each set. The difference between the two sets was the distance between each row of steel dowels, with 0.20 m on the $S_{4D}$ specimens and 0.15 m on the $S_{3D}$ specimens. An example is presented in Figure 4.11, also for the $S_{4D}$ specimen.

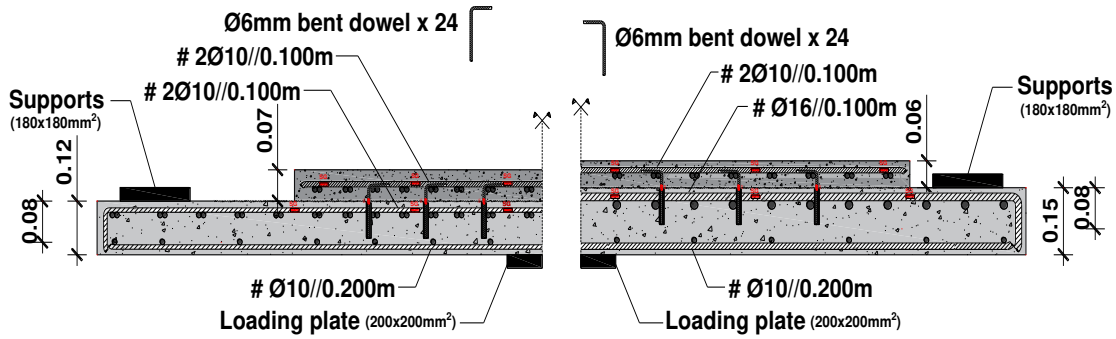


Figure 4.11 – Detailing of the STC specimen overlay reinforcement – $S_{3D}$ and $S_{4D}$.

Due to the need for structural redundancy in a real strengthening situation, the STANC specimen aims at combining the advantages of the STC and ANC detailings of the interface. Hence, two stitching solutions are used in the strengthened area, controlling both the edge lifting phenomenon and the evolution of interface crack dilation. An example is presented in Figure 4.12 also for the $S_{4D}$ specimen.

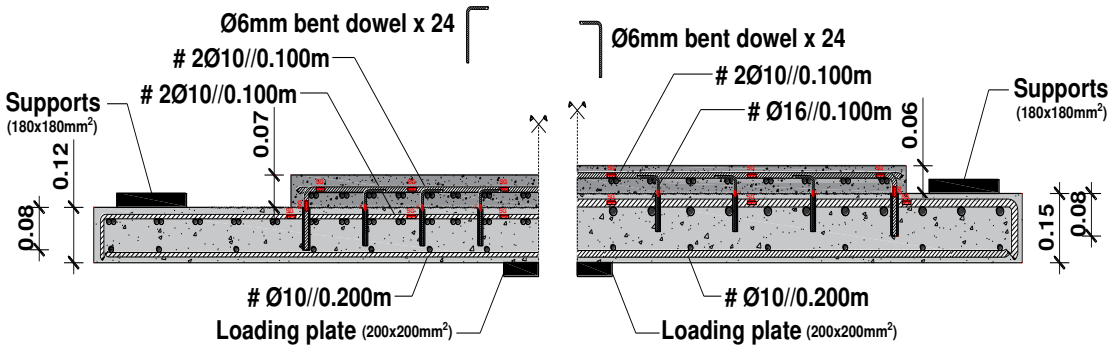


Figure 4.12 – Detailing of the STANC specimen overlay reinforcement – $S_{3D}$ and $S_{4D}$.

Grouting of reinforcement crossing the interface was performed similarly to the rectangular specimens, with a cementitious grout bonding agent (SikaGrout® 213), directly poured into the

holes, followed by the insertion of the steel bar to be anchored. Both procedures were performed with close attention to air being trapped inside the anchorage length of the steel bar, through the slow pouring of the bonding agent and twisting the steel bar whenever possible. Although the latter was only possible for the steel dowels, all reinforcement was inserted slowly into the bonding agent until the hole was filled to the surface of the substratum, as illustrated in Figure 4.13.

Figure 4.13 – Grouting of longitudinal reinforcement and steel dowels in the substratum.

The steel dowels were also instrumented with strain gauges at the interface level, coincident with instrumentation on the substratum and the overlay. Such coordinates were defined at the column face and at a distance of *2d* from the column face, right before and right after the bend of anchored longitudinal reinforcement at the top of the anchored length of steel dowels. A practical example is depicted for the last two in Figure 4.14.

Figure 4.14 – Anchorage instrumentation of longitudinal steel bars (left) and steel dowels (right).

A minimum of 48 hours was respected, as recommended by the manufacturer for the cement grout matrix to properly harden, anchoring the embedded steel bars. Casting of the overlaid concrete was performed two months after casting the substratum on the $S_{4D}$ specimens and two weeks on the $S_{3D}$ specimens. An assessment of horizontal and vertical rebar spacing was performed prior to casting the overlay, as depicted in Figure 4.15 (top, right), with the final aspect of the strengthened specimens one day after casting the overlay also illustrated in Figure 4.15.

Figure 4.15 – Casting of the overlaid concrete on the S4D (left) and S3D (right) specimens.

### 4.2.2. Materials and surface characterisation

The characterisation of materials was performed similarly to rectangular specimens. Concrete compressive and tensile strengths were assessed along with the Young modulus of each layer. Also, the strength characteristics of the bonding agent responsible for anchoring reinforcement to the substratum SikaGrout@ 213 had already been presented in section 3.2.5 of the previous chapter.

Concrete compressive and tensile strength assessment was performed similarly to rectangular specimens presented on chapter 3.2.5, with respective results presented in tables Table 4.2 and Table 4.3, where both cube and cylinder specimens were accounted for when available for material characterisation.

All specimens from the Young modulus assessment test were then tested to failure by compressive strength of concrete since the former test only reaches about 40% of the material's strength.

Table 4.2 – Concrete strength characteristics for the $S_{4D}$ specimens.

| $S_{4D}$ specimens | | REF | STC | ANC | STANC |
|---|---|---|---|---|---|
| $f_{ccm}$ (MPa) | Substratum | 32.8 | 26.4 | 34.8 | 25.6 |
| | Overlay | 36.9 | 34.3 | 37.2 | 39.3 |
| $f_{cm}$ (MPa) | Substratum | 28.5 | 22.0 | 27.5 | 20.7 |
| | Overlay | 30.5 | 29.2 | 30.3 | 32.1 |
| $f_{ct}$ (MPa) | Substratum | 3.2 | 2.8 | 3.3 | 2.8 |
| | Overlay | 3.4 | 3.2 | 3.4 | 3.5 |

Table 4.3 – Concrete strength characteristics for the $S_{3D}$ specimens.

| $S_{3D}$ specimens | | SUB | REF | STC | ANC | STANC |
|---|---|---|---|---|---|---|
| $f_{ccm}$ (MPa) | Substratum | 44.8 | 41.6 | 52.8 | 38.2 | 45.1 |
| | Overlay | - | 35.5 | 38.0 | 34.6 | 35.7 |
| $f_{cm}$ (MPa) | Substratum | 38.2 | 34.5 | 43.8 | 35.7 | 36.2 |
| | Overlay | - | 30.9 | 35.5 | 32.6 | 32.2 |
| $f_{ct}$ (MPa) | Substratum | 3.8 | 3.1 | 3.1 | 3.2 | 2.5 |
| | Overlay | - | 2.8 | 2.5 | 3.4 | 2.3 |

The Young modulus was also assessed similarly to the procedure presented in the last chapter, following LNEC E-397 [145] for the concrete material of each specimen's layers through the apparatus illustrated in Figure 3.25 of that section, and are presented in Table 4.4.

Table 4.4 – Young modulus for the $S_{4D}$ and $S_{3D}$ specimens.

| Specimen | | Substratum | | Overlay | |
|---|---|---|---|---|---|
| | | $f_{cm,sub}$ (MPa) | $E_{cm,Exp}$ (GPa) | $f_{cm,ol}$ (MPa) | $E_{cm,Exp}$ (GPa) |
| $S_{4D}$ | **REF** | 26.2 | 30.7 | 29.5 | 31.1 |
| | **STC** | 21.1 | 29.7 | 27.5 | 29.0 |
| | **ANC** | 27.9 | 30.1 | 29.7 | 32.2 |
| | **STANC** | 20.5 | 31.1 | 31.5 | 32.1 |
| $S_{3D}$ | **SUB** | 44.8 | 34.9 | - | - |
| | **REF** | 33.3 | 31.7 | 28.4 | 31.0 |
| | **STC** | 42.3 | 32.6 | 30.4 | 31.2 |
| | **ANC** | 36.1 | 34.9 | 27.7 | 31.4 |
| | **STANC** | 30.5 | 30.2 | 28.5 | 32.2 |

Tensile strength testing of A500 NR SD rebar specimens was performed similarly to section 3.2.5, according to specifications on EN 10002-1 [141], with results presented in Table 4.5 for the $S_{4D}$ specimens. Values for the $S_{3D}$ specimens were coincident with $R_L$ specimens, already presented in Table 3.6 of section 3.2.5.

Table 4.5 – Rebar tensile strength characteristics for the $S_{4D}$ specimens.

| | Specimen | Yield stress $\sigma_y$ (MPa) | $\sigma_{y,med}$ (MPa) | Maximum stress $\sigma_u$ (MPa) | $\sigma_{u,med}$ (MPa) | k (-) |
|---|---|---|---|---|---|---|
| Ø16 | D1 | 553 | 550 | 651 | 649 | 1.18 |
| | D2 | 551 | | 650 | | 1.18 |
| | D3 | 547 | | 647 | | 1.18 |
| Ø10 | E1 | 546 | 553 | 624 | 632 | 1.14 |
| | E2 | 544 | | 623 | | 1.15 |
| | E3 | 570 | | 650 | | 1.14 |
| Ø6 | F1 | 534 | 538 | 655 | 657 | 1.23 |
| | F2 | 540 | | 656 | | 1.22 |
| | F3 | 539 | | 670 | | 1.22 |

Surface characterisation was performed similarly to the rectangular specimens already presented on chapter 3.2.4, through the measurement of the existing surface roughness after preparation and the pull-off testing of prismatic 150x150mm$^2$ specimens. The main difference to the rectangular specimens of the previous chapter was the assessment of roughness in two directions, with three profiles traced on each orthogonal direction, as presented in Table 4.6. The roughness attained through milling of the concrete surface could then be classified as very rough on both directions, according to the limit of 2.6 mm for the peak-to-mean roughness parameter stated on [24] and the table below. Only the $S_{3D}$-STC specimen did not meet such requirement in one of the directions assessed, yielding a marginally lower roughness parameter.

Table 4.6 - Substratum surface peak-to-mean roughness $R_p$.

| Specimen | | $R_p$ (mm) | |
|---|---|---|---|
| | | xx | yy |
| $S_{4D}$ | REF | 3.3 | 3.1 |
| | STC | 2.7 | 3.8 |
| | ANC | 3.9 | 3.8 |
| | STANC | 3.3 | 2.9 |
| $S_{3D}$ | REF | 3.1 | 2.8 |
| | STC | 2.4 | 2.7 |
| | ANC | 3.5 | 2.9 |
| | STANC | 3.4 | 3.5 |

The coefficient of friction was calculated for the column-supported specimens through equation (3.1) of the previous chapter, where $R_{vm}$ is the mean valley depth calculated according to equation (3.2) of that chapter. The values for the mean valley depth and respective coefficient of friction are presented on Table 4.7. Assessment of the surface mean valley depth was also performed in both directions as are presented in the table below.

Table 4.7 - Substratum surface roughness parameters $R_{vm}$ and $\mu$.

| Strengthened Specimen | $R_{vm}$ (mm) | | $\mu$ (-) | |
|---|---|---|---|---|
| | xx | yy | xx | yy |
| **S3D-REF** | 4.46 | 3.46 | 1.46 | 1.44 |
| **S3D-STC** | 2.64 | 1.99 | 1.43 | 1.41 |
| **S3D-ANC** | 2.61 | 3.93 | 1.42 | 1.45 |
| **S3D-STANC** | 3.56 | 3.46 | 1.44 | 1.44 |
| **S4D-REF** | 2.23 | 3.43 | 1.42 | 1.44 |
| **S4D-STC** | 3.52 | 2.69 | 1.44 | 1.43 |
| **S4D-ANC** | 3.45 | 3.94 | 1.44 | 1.45 |
| **S4D-STANC** | 2.38 | 3.20 | 1.42 | 1.44 |

Analysing the table above, one can observe again similarly to the rectangular specimens on the previous chapter that the resulting coefficient of friction results in values of order 1.40 due both to the consistency of the mean valley depth parameter on all specimens and the very small order of power on equation (3.1) of that chapter for this parameter.

Assessment of the interface tensile strength was then performed similarly to the rectangular specimens through the pull-off testing of specimens cast on the same surface and at the same time as the RCO. Table 4.8 presents the average pull-off strength ($\sigma_{Pull\text{-}off}$) of each set of specimens and respective statistical data regarding the standard deviation and coefficient of variation.

Table 4.8 - Interface tensile capacity of column-supported specimens.

| Strengthened Specimen | Nr. of specimens | $\sigma_{Pull\text{-}off}$ (MPa) | Standard Deviation (MPa) | Coefficient of Variation |
|---|---|---|---|---|
| **S3D-REF** | 16 | 0.81 | 0.19 | 0.23 |
| **S3D-STC** | 16 | 0.85 | 0.15 | 0.18 |
| **S3D-ANC** | 16 | 1.02 | 0.10 | 0.10 |
| **S3D-STANC** | 16 | 1.00 | 0.16 | 0.16 |
| **S4D-REF** | 16 | 0.85 | 0.31 | 0.36 |
| **S4D-STC** | 15 | 1.08 | 0.11 | 0.10 |
| **S4D-ANC** | 16 | 0.82 | 0.18 | 0.22 |
| **S4D-STANC** | 14 | 0.83 | 0.13 | 0.15 |

The resulting pull-off strength varied in terms of average stress from a minimum of 0.81 MPa to a maximum of 1.08 MPa. A large scatter could be observed through high coefficients of variation, which are also characteristic on tensile test results, as observed also for the rectangular specimens on 3.2.6.3. The sample of 125 test results can be considered statistically relevant for defining interface tensile capacity. Distribution of the resulting stress for each specimen by its pull-off specimens can be observed in Figure 4.16, where the average stress of approximately 0.91 MPa was attained with such preparation of existing concrete's surface.

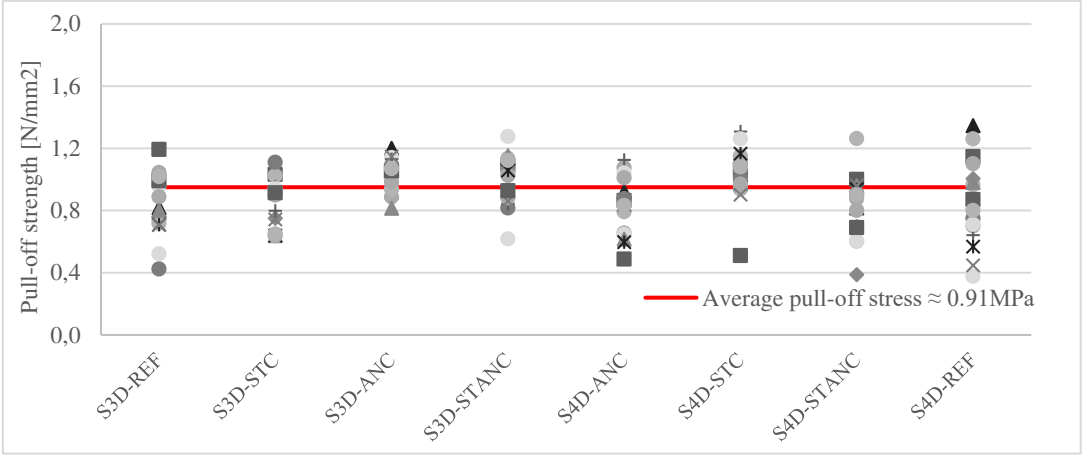


Figure 4.16 – Pull-off strength of all tests on column-supported specimens.

### 4.2.3. Test setup

Square specimens were loaded from below the slab at the centre, imposing a force up to failure by shear or flexural punching. The test setup is illustrated in Figure 4.17 and Figure 4.18 for both the $S_{4D}$ and $S_{3D}$ set of specimens, illustrating the real and conceptual test setups, on the left and on the right, respectively.

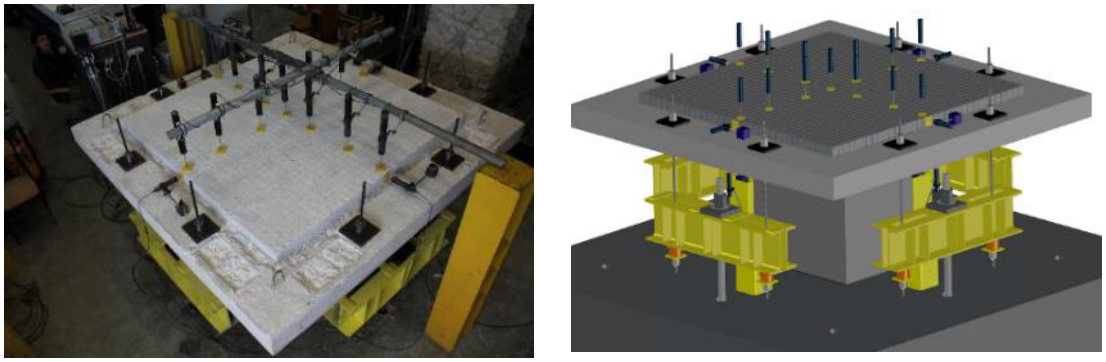

Figure 4.17 – General test setup, real life (left) and conceptual (right) – $S_{4D}$ specimens.

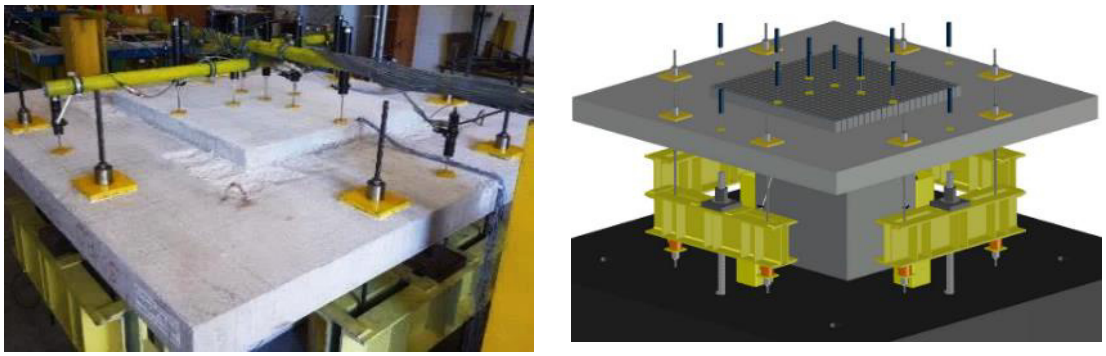

Figure 4.18 – General test setup, real life (left) and conceptual (right) – $S_{3D}$ specimens.

The test specimens were loaded monotonically by a 1000 kN hydraulic jack (ENERPAC® RCH-1003), positioned below the slab at the geometric center. Loading was performed in the upwards direction through a steel plate with 200x200 mm$^2$ area and 50 mm thickness. Eight steel plates with an area of 150x150 mm$^2$ and 20 mm thickness guaranteed boundary conditions at the zero-moment line of the specimens, illustrated in Figure 4.19 and Figure 4.20. These elements were linked to spreader beams by 15.2 mm high strength steel strands, and the whole setup for the supports was fixed to the laboratory strong floor by four high strength 40 mm steel threadbars.

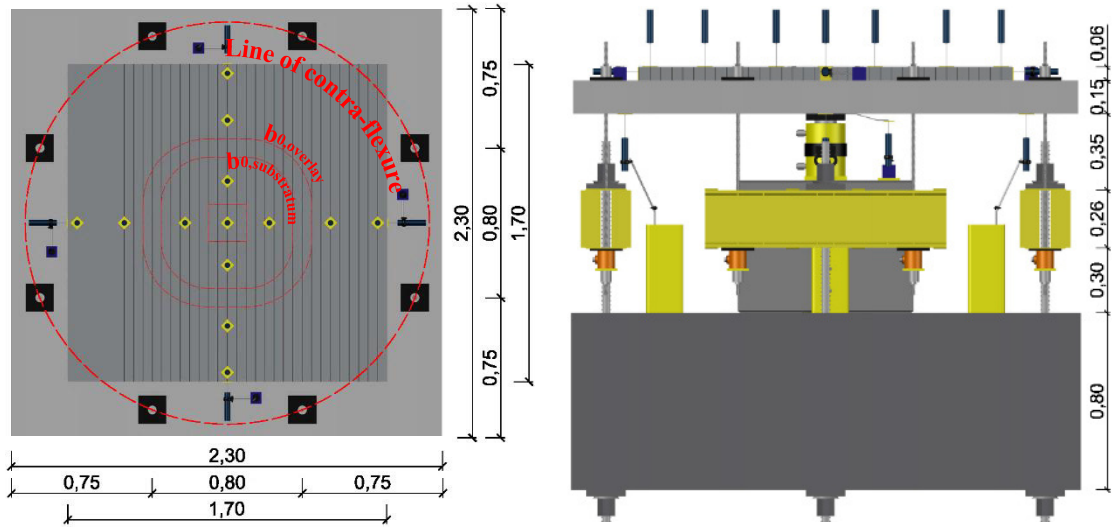


Figure 4.19 – Test layout dimensions, top view (left) and side view (right) – $S_{4D}$ specimens.

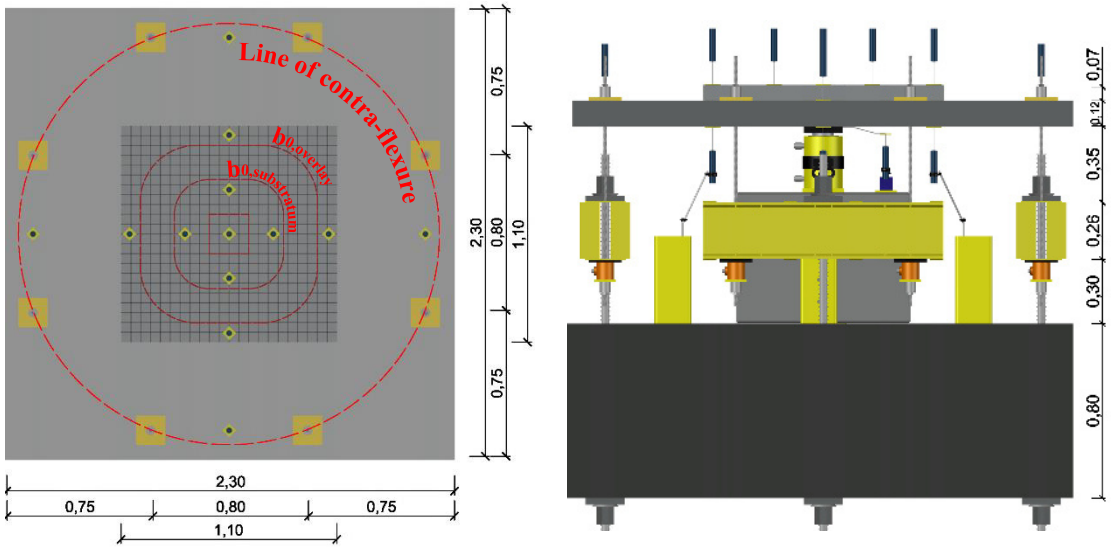


Figure 4.20 – Test layout dimensions, top view (left) and side view (right) – $S_{3D}$ specimens.

Applied load was measured at the supports by eight TML® CNC-200KNA load cells installed below the spreader beams. Vertical displacements were measured by 100 mm TML® CDP-100 displacement transducers, on the top and bottom faces, and 50 mm TML® CDP-50 displacement transducers at the supports, all illustrated in Figure 4.21 and Figure 4.22, for the $S_{4D}$ and $S_{3D}$ specimens.

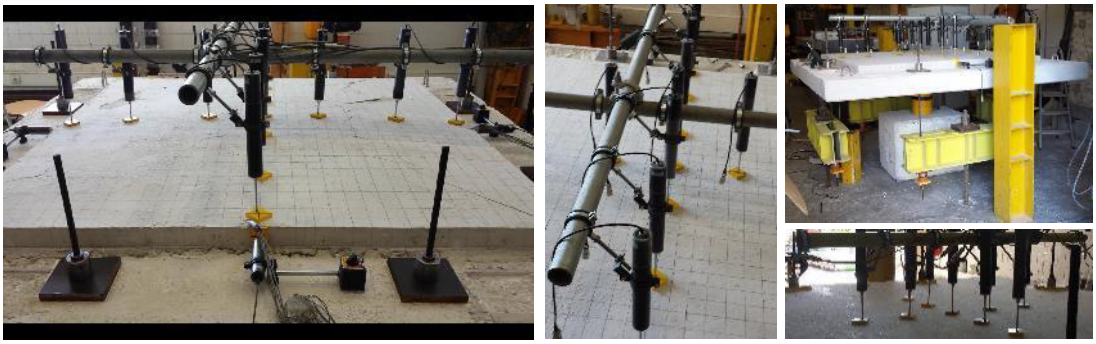

Figure 4.21 – Test layout for the $S_{4D}$ specimens.

Figure 4.22 – Test layout for the $S_{3D}$ specimens.

Relative horizontal displacement between layers was measured directly with four 50 mm TML® CDP-50 displacement transducers for the $S_{4D}$ specimens, with only the vertical displacement measured on the $S_{3D}$ specimens, as illustrated in Figure 4.23.

Figure 4.23 – Measurement of relative displacement on $S_{4D}$ specimens (left) and $S_{3D}$ specimens (right).

Data acquisition was performed with Spider8, Centipede, and QuantumX data-loggers from HBM®, all monitored by HBM® Catman V6.0 software and illustrated in Figure 4.24. Loading until failure of the specimens was controlled by a WALTER+BAI® PKNS19D hydraulic pump, at a rate of 0.25 kN/s.

Figure 4.24 – Hardware for data acquisition and load application.

## 4.3. Results of RCO strengthened square specimens

### 4.3.1. Load-deflection relationship of column-supported specimens

Loading until failure was monotonic for all specimens, imposing a deformation at the center of the slab, controlled by force. The load-deflection graph at the centre of the specimens can be observed in Figure 4.25 for both sets of specimens ($S_{4D}$ and $S_{3D}$).

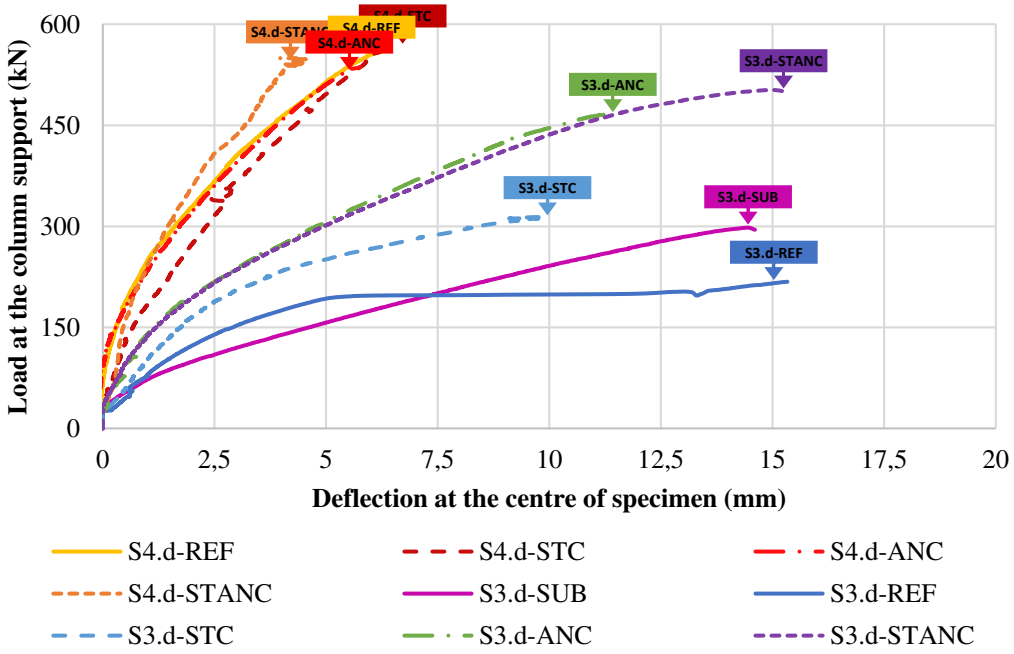


Figure 4.25 – Load-deflection diagrams of the $S_{4D}$ and $S_{3D}$ specimens.

Analysing the above diagrams, one can state the main difference between both strengthening geometries was the stiffness of the load-deflection diagram. Two main factors contributed for such difference:

- The substratum thickness was reduced in 30mm, from 150mm on the $S_{4D}$ specimens to 120mm on the $S_{3D}$ specimens;

- Flexural reinforcement of the substratum, similarly to the latter, was also reduced in 22%;

- The smaller area of RCO, together with the former reduction allowed for a less stiff response of the strengthened specimens, due to the lower flexural reinforcement available in the column strip.

One can observe in the figure above the small difference between the $S_{4D}$ specimens geometry, both in terms of the ultimate failure load and stiffness, particularly the $S_{4D}$-REF and the $S_{4D}$-ANC specimens that almost overlap for the entire load history. Such behaviour can be explained by the distance of the overlay's edge from the zone of maximum flexural stresses. For the other specimen's geometry, the higher failure load of the unstrengthened $S_{3D}$-SUB specimen when compared to the $S_{3D}$-REF can be explained by the loss of reinforcement upon debonding which can be graphically observed by the plateau in Figure 4.25. The higher initial stiffness of the latter can then be explained by the larger strengthened composite cross-section before debonding. The values for maximum load and respective deflection at failure are presented in Table 4.9.

Table 4.9 – Experimental results of the column-supported slab specimens.

| | **$S_{4D}$ specimens** | | **$S_{3D}$ specimens** | |
|---|---|---|---|---|
| **General layout** | 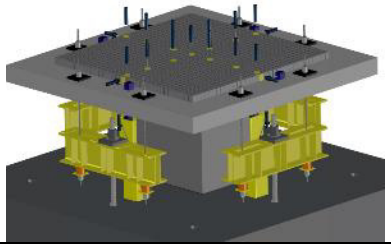 | | 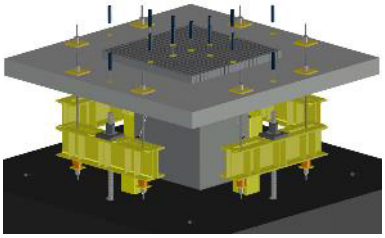 | |
| **Self-weight** | 33.5 kN | | 26.6 kN | |
| **Specimens** | **Failure load (kN)** | **Deflection (mm)** | **Failure load (kN)** | **Deflection (mm)** |
| **SUB** | - | - | 298.0 | 14.6 |
| **REF** | 559.8 | 6.3 | 217.8 | 15.3 |
| **STC** | 567.6 | 6.6 | 313.8 | 9.9 |
| **ANC** | 535.8 | 5.8 | 467.3 | 11.4 |
| **STANC** | 549.8 | 4.5 | 502.5 | 15.3 |

The failure loads allow for the assessment of strengthening performance with RCO on a column-slab connection. Graphically, one can observe that this load increment can result in more than double the original punching capacity for interior slab-column connections. This was observed on the $S_{4D}$ specimens that did not debond (STC and STANC), and for the $S_{3D}$ specimens that punched through the interface (ANC and STANC). The little increment of the $S_{3D}$-STC specimen attests the poor performance of the detailing with dowels stitching the two layers, for a small area of overlaid concrete. The $S_{3D}$ specimens allowed for the greater performance gains in terms of stiffness and ultimate failure load, when compared to the particular poor performance of the $S_{3D}$-

REF specimen, where the overlaid concrete contributed very little to the stiffness gains of such specimen. Debonding occurred very soon in the load history, corresponding to an even lower resistance than the $S_{3D}$-SUB specimen, which was unstrengthened. Such result can be explained by a lower quality concrete together with poor bond between the two layers. Comparing the strengthened $S_{3D}$ specimens with the unstrengthened $S_{3D}$-SUB specimen it is possible to see the impact on stiffness and load increment of a small area of RCO, when properly bonded to the substratum.

The results of the $S_{3D}$ specimens allowed for comparing the difference between the deformation of unstrengthened and strengthened specimens, due to the unstrengthened SUB specimen. No significant change in deformation was registered for the specimen that performed better ($S_{3D}$-ANC and $S_{3D}$-STANC) when compared to the latter. For $S_{4D}$ specimens there was no unstrengthened specimen for comparison. For the sake of comparison, a numerical model of the substratum was provided for each specimen, performed on ATENA 3D® with respective concrete and rebar strength characteristics presented in section 4.2. These models were calibrated based on the structural response of the $S_{3D}$-SUB specimen, with a punching load of 298.0 kN, and respective numerical failure load of 304.1 kN, which resulted on a ratio $V_{exp}/V_{num}$ of 0.98. With such premise, the substratum of each specimen was modelled, and the load increment could then be assessed, as illustrated in Figure 4.26 below. The reference specimen of the $S_{3D}$ set is not presented since the correct acquisition of the experimental results could not be provided.

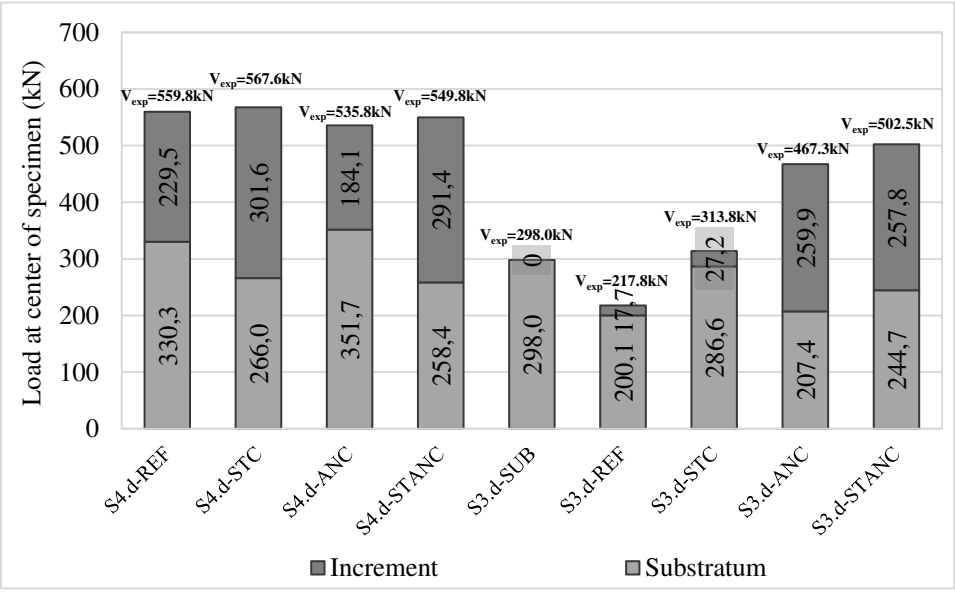


Figure 4.26 – Punching capacity regarding the contribution of each layer.

### 4.3.2. Failure modes and sawcuts of the specimens

The general failure mode observed for the $S_{4D}$ and $S_{3D}$ specimens was the punching of the substratum layer, with transmission of stresses to the overlaid concrete, which conditioned the slope of the critical shear crack and the respective punching strength. Analysing the sawcuts of the slab specimens tested, one can see where the critical shear crack was deflected by the stitching reinforcement. Such sectioning of the concrete cross-section also allowed for some assumptions regarding the behaviour of the strengthened specimens analogous to the procedure for the rectangular specimens on chapter 3.

The failure modes of the $S_{4D}$ specimens were identified as punching failure of the full cross-section for the specimens with reinforcement crossing the interface (STC, ANC, and STANC), and debonding of the overlaid concrete with punching of the substratum for the REF specimen, all observed in Figure 4.27, right after failure of the specimens.

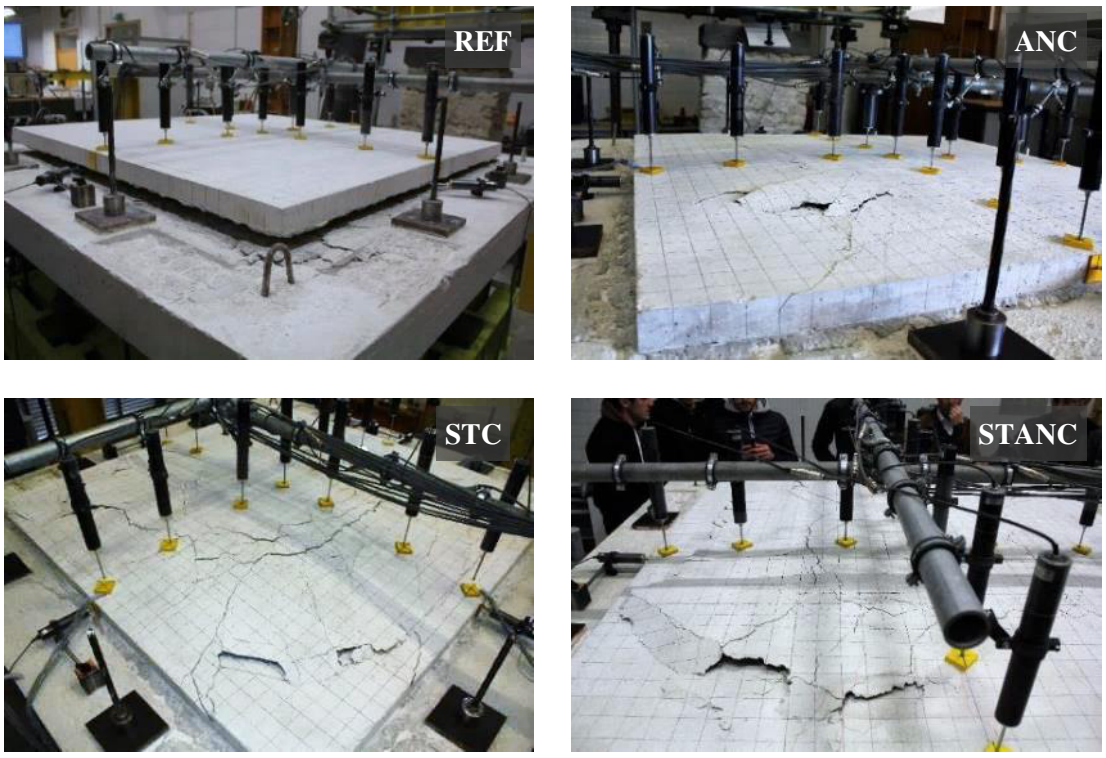


Figure 4.27 – Observed failure modes of the $S_{4D}$ specimens after failure.

The former two specimens presented two different paths of the critical shear crack, reaching only the interface on the REF specimen and intersecting the already cracked interface on the ANC specimen. During testing of the reference specimen, radial cracks could be observed on the top face of the overlaid concrete, which indicate a significant amount of stress being transferred to the top layer. Such fact is also significant due to the failure load similar to the other specimens with interface reinforcement. Debonding then occurred when no more deformation could be resisted by the interface, since no stitching reinforcement was provided. Cracking never evolved

from hairline cracks, which closed right after debonding. Removing the overlaid concrete layer, the punching shear cone that developed in the substratum can be observed in Figure 4.28. Analysing the resulting surface after debonding, one can observe that the top layer debonded clean from the bottom layer, with almost no visible damage.

Figure 4.28 – Failure surfaces (substratum and overlay) of the $S_{4D}$-REF specimen.

Debonding also occurred on the $S_{4D}$-ANC specimen, but to a lesser degree, since the anchored longitudinal reinforcement controlled the debonding phenomenon until failure of the specimen. From the sawcut presented in Figure 4.29, a characteristic punching failure in the substratum can be observed. Due to debonding, the punching crack becomes horizontal when it reaches the interface.

Figure 4.29 – Debonding of the overlaid concrete on the $S_{4D}$-ANC specimen.

After saw cutting the ANC specimen, one can observe that debonding also occurred at the interface between the two layers, with the anchored longitudinal reinforcement guaranteeing the structural integrity until failure. The crack path observed in Figure 4.30 shows the change in the direction of the crack to the interface. One can also observe some cracking on the right side that evolved vertically to the overlaid concrete until the reinforcement level.

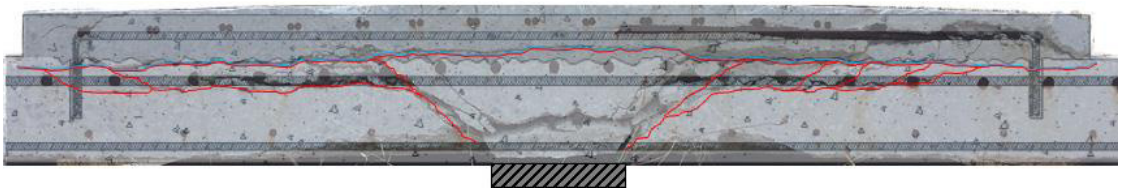

Figure 4.30 – Sawcut detail of the $S_{4D}$-ANC specimen.

Detailing with shear connectors allowed for the critical punching crack to reach the overlaid concrete, as illustrated in the sawcut of Figure 4.31, where a great amount of damage can be

observed on this layer. Debonding occurred selectively where the punching crack crossed the interface and higher stresses were transferred between rebar layers, with cracking reaching the overlay rebars at the last dowel. Typical radial and tangential cracks could also be observed in Figure 4.27, coherent with the figure below, denoting an almost monolithic behaviour of these specimens.

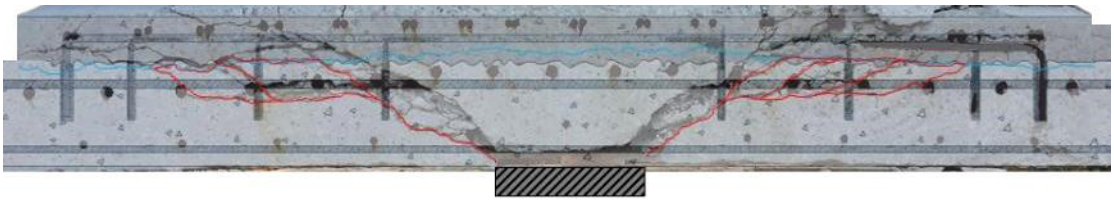

Figure 4.31 – Sawcut detail of the $S_{4D}$-STC specimen.

Cracking could then be identified with a characteristic cone above the centre support, and a fan of cracks that cross the steel dowels and reach the interface between the two rows further from the centre support. Such cracking was similar to that of the $S_{4D}$-STANC specimen, illustrated in Figure 4.32, where the critical shear crack reached the overlaid concrete with an almost monolithic behaviour, and cracking reached the interface also in the last row of dowels. A characteristic cone could also be observed above the centre support with the critical shear crack showing a typical slope for punching of column-slab connections.

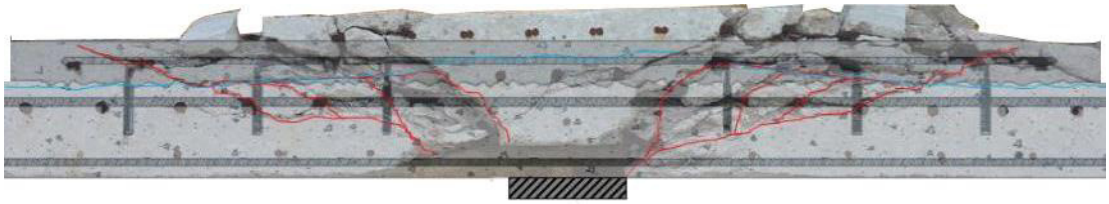

Figure 4.32 – Sawcut detail of the $S_{4D}$-STANC specimen.

Observing the figure above and comparing with the behaviour of the STC and ANC specimens, one can hypothesize on the contribution of the anchored longitudinal reinforcement for a patch of overlaid concrete up to a distance of *4d* from the column face. Debonding occurred on the ANC specimen similarly to the REF specimen, except being controlled in the former by the anchored longitudinal reinforcement, but with no gains in terms of ultimate failure load. Cracking was similar between the STC and STANC specimens, denoting the relationship between both regarding the steel dowels distributed across the contact area between layers. Concerning the premises based on the observed behaviour of the specimens, one can conclude that for such an RCO patch, the steel dowels is the best of the considered solutions for achieving a monolithic behaviour. Nonetheless, the STANC solution is advised to create structural redundancy.

The set of tests regarding the $S_{3D}$ specimens allowed to assess the sensitivity of the RCO patch size to debonding of the strengthening layer. They also assisted on determining the lower limit dimensions when applying such technique.

The $S_{3D}$ specimens were defined with the same detailing of the interface as the $S_{4D}$ specimens, but comprising two reference specimens: one unstrengthened substratum $S_{3D}$-SUB for scaling the

RCO strengthening performance and behavioural improvement; and one strengthened substratum $S_{3D}$-REF, similar to the $S_{4D}$-REF specimens, with only milling of the existing surface, as illustrated in Figure 4.33.

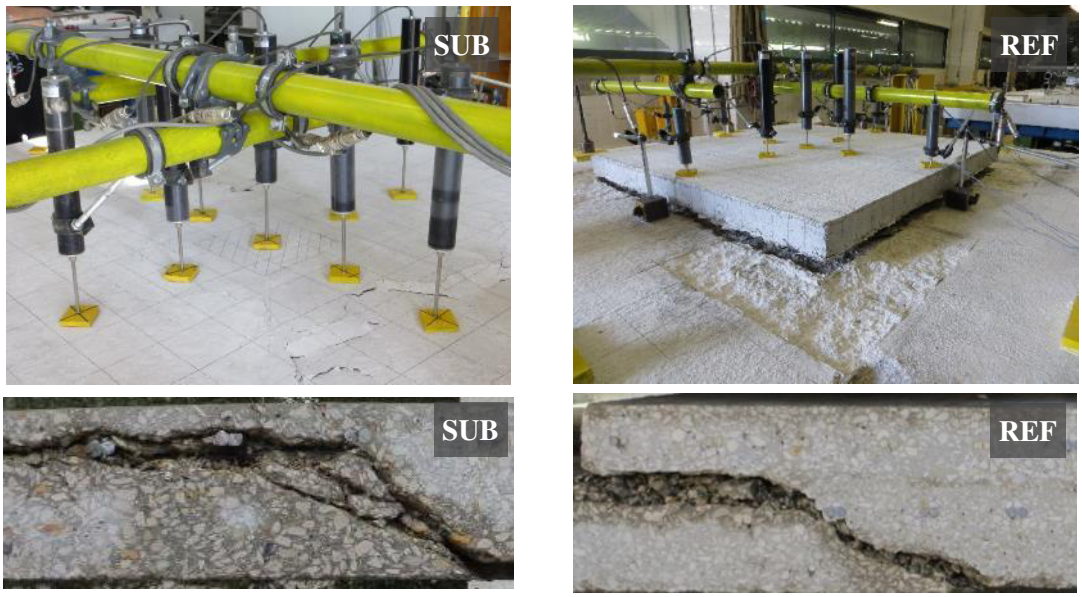


Figure 4.33 – Failure of the $S_{3D}$-SUB and $S_{3D}$-REF specimens.

Failure of the SUB specimen was typical for a center column on a slender flat slab, despite the resulting failure load, which was lower on the REF specimen when compared to the SUB specimen. Observing the sawcuts of both specimens, one can attest the shift in the slope of the critical shear crack on the REF specimen. The RCO patch applied until 3d from the column face shifted the slope angle to half the value of the slope angle observed on the unstrengthened SUB specimen. A schematic illustration of the critical shear crack crossed with the original design and detailing of reinforcement can be observed in Figure 4.34. Such condition results in larger horizontal stresses, which together with the absence of stitching reinforcement resulted in the premature debonding of the interface.

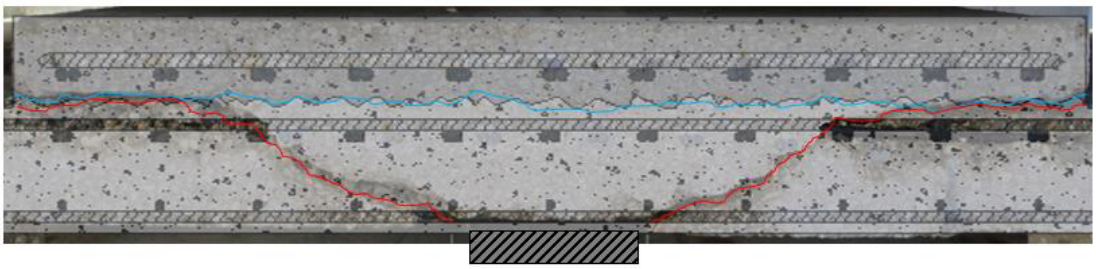

Figure 4.34 – Sawcut detail of the $S_{3D}$-REF specimen.

Analyzing the top face of the ANC and STANC specimens after failure in Figure 4.35, two main flexural cracks can be observed in the direction of highest effective depth. This is coherent with the smaller flexural capacity on the orthogonal direction due to the respective lower effective depth. This phenomenon adds to the more ductile behaviour of these specimens. The prominent

crack on the side of the overlay, visible on the figure below, attests the lower limit size of the strengthening layer when compared to the respective $S_{4D}$ specimens' behaviour.

Figure 4.35 – Failure of the $S_{3D}$-ANC and $S_{3D}$-STANC specimens.

The specimens with stitching reinforcement resulted in an approximately monolithic behaviour regarding the interface, with no significant debonding of the top layer and no significant shift of the critical shear crack crossing the interface. Schematically, one can observe the crack path and the slope of the critical shear crack in Figure 4.36 and Figure 4.37.

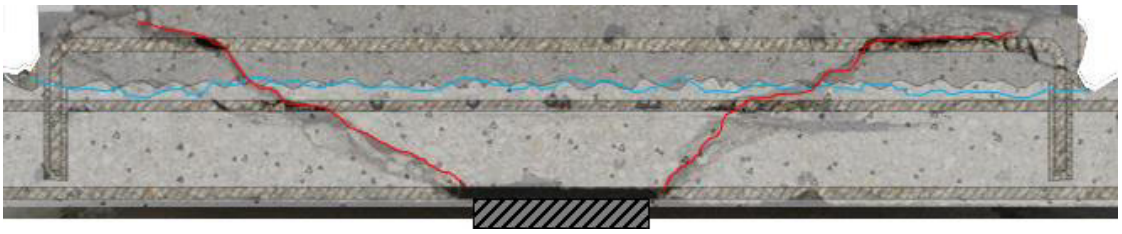

Figure 4.36 – Sawcut detail of the $S_{3D}$-ANC specimen.

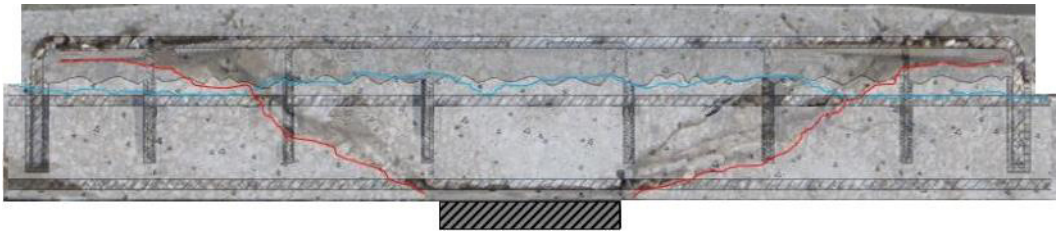

Figure 4.37 – Sawcut detail of the $S_{3D}$-STANC specimen.

Two rigid bodies can be identified on each side of the critical shear crack, attesting the performance of the stitching reinforcement. The slope inclination of the critical shear crack is of the same order as the one observed on the REF specimen, attesting the standard behaviour of

RCO strengthening until *3d*, with the stitching reinforcement controlling the debonding phenomenon until failure. The behaviour was similar on the ANC and STANC specimens, with slightly larger load and deformation at failure on the latter, which was the strongest of the three specimens with reinforcement crossing the interface.

Regarding the STC specimen, visually the failure mode after testing was similar to the one observed for the REF specimen, with apparent debonding of the interface, as observed in Figure 4.38.

Figure 4.38 – Failure of the $S_{3D}$-STC specimen.

Due to the dowels stitching the two layers on the $S_{3D}$-STC specimen, the critical shear crack was deflected until it reached the interface at the overlay's edge, resulting in a larger control perimeter for punching. Analyzing the evolution of the critical shear crack schematically with the original detailing of reinforcement in Figure 4.39, one observes that the crack evolves below the steel dowels, only intersecting the last row. Such condition results in a lower slope of such failure surface.

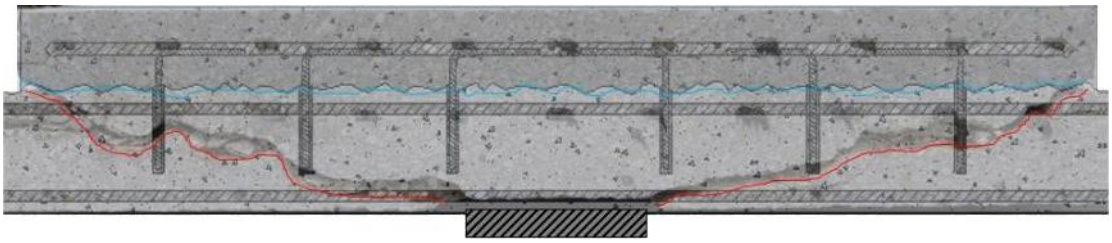

Figure 4.39 – Sawcut detail of the $S_{3D}$-STC specimen.

This also indicates that the considered dimension for the overlay concrete layer for the specimens $S_{3D}$ was not enough, and in practical applications should be at least *4d* from the column face. Externally, this specimen showed only hairline and barely visible cracks on the top face of the overlay after failure. The latter condition is not enough for guaranteeing the structural integrity after strengthening as proven by the $S_{3D}$-STC specimen that debonded for a very small load increment over the reference specimens.

### 4.3.3. Evolution of strain with load history

Instrumentation of the column-supported slabs with strain gauges on both directions of reinforcement allowed for assessing the difference in strain on key coordinates of the longitudinal reinforcement. Such key locations were the column face, where the bending moment is maximum, and reinforcement at *2d* from the former, where the critical shear crack usually develops. Other key coordinates were before the bent anchored end of the overlay reinforcement and at the interface level of anchored reinforcement. The priority was to consider the strains on the reinforcement with higher effective depth, which would result in higher strains and consequently higher stresses at the interface. Such locations were identified in Figure 4.3 of section 4.2.1.

Analysing the strains of the two longitudinal reinforcement layers, shown in Figure 4.40, one can observe that these remain about the same for both layers until flexural cracking of the specimens. Then, strain is greater on the overlay rebars, attesting the stress transfer capabilities of the interface. It is possible to identify some particularities of the composite cross-section behaviour, like the beginning of cracking or debonding at the interface, important for characterising the behaviour of the strengthened slab. Cracking can be identified by an abrupt increment of the steel strain correspondent to the transfer of the internal tensile forces from the concrete to the steel. From this point, strains grew larger for the overlaid concrete due to the greatest effective depth and integrity of the interface that allowed to keep the stress transfer throughout the load history.

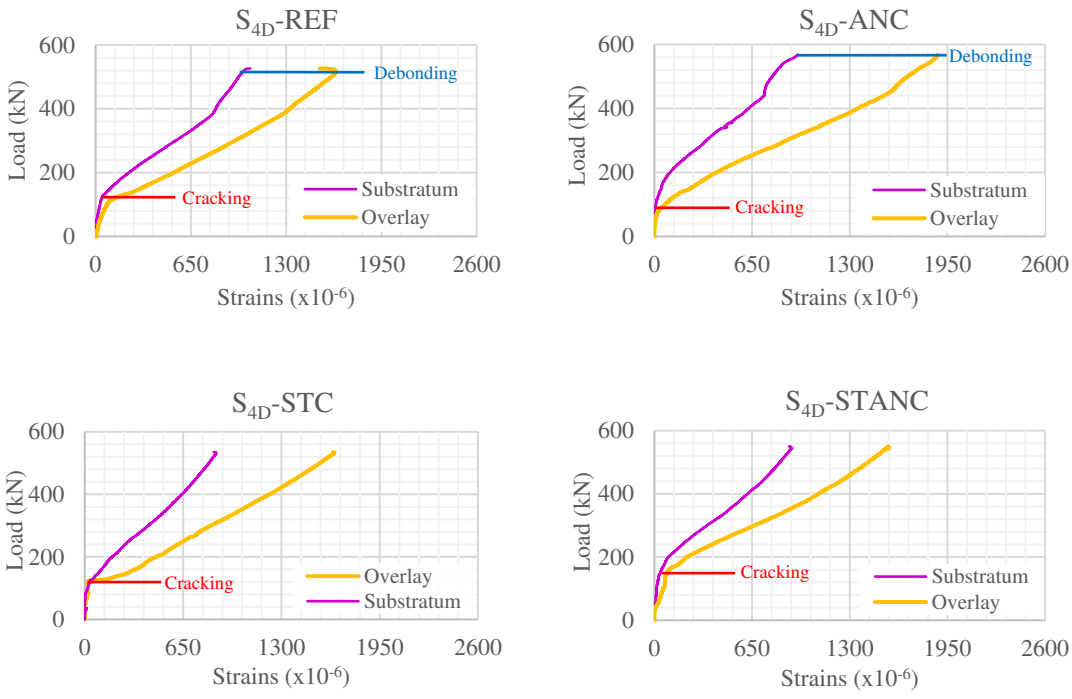


Figure 4.40 – Load-strain diagram measured in the rebars at the column face of the $S_{4D}$ specimens.

The debonding phenomenon can be identified on the $S_{4D}$-REF specimen that fully debonded at the interface through the decrease of strain on the overlay rebars, along with an increase of strains on the substratum reinforcement. To a lesser degree, the same behaviour can be identified at the end of the load history of the $S_{4D}$-ANC, where the increase of the substratum reinforcement strains is visible, and debonding at the interface can be observed in Figure 4.29. A variation in the slope of the load-strain diagrams of the aforementioned specimens for loads close to 400 kN can be seen in Figure 4.40. The same phenomenon was not observed on the load-strain diagrams of the other two specimens of the $S_{4D}$ set, coherent with the saw-cuts in the previous section.

The load-strain diagrams above can attest for the uniformity of strain evolution throughout the load history for all specimens, with no significant phenomenon other than the referred debonding on two specimens. Clear debonding could only be registered for the REF specimen with a decrease in the overlay strain, observed in the figure above right before failure. The highest strain was registered on the overlay reinforcement of the ANC specimen, but still lower than the yield strain of steel reinforcement at $2.0 \times 10^{-6}$m/m, which no specimen reached.

The reduced RCO area on the $S_{3D}$ specimens resulted in a different behaviour for each detailing of the interface. Debonding on the $S_{3D}$-REF specimen was clearly identified through a plateau in the load-deflection diagram (Figure 4.25) prior to punching of the substratum. The same phenomenon can be observed for strain on this specimen through a decrease in the strain of the overlay and an increase in the substratum, as shown in Figure 4.41 for $S_{3D}$-REF diagram.

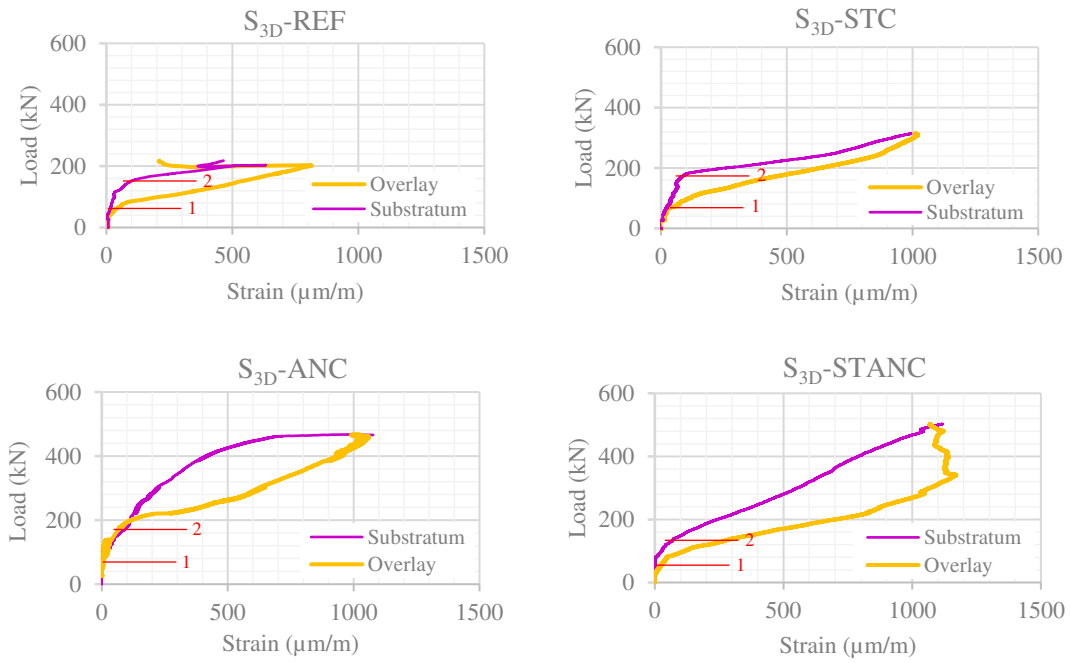


Figure 4.41 – Load-strain relationship measured at the column face of the $S_{3D}$ specimens.

The $S_{3D}$-STANC resulted in the maximum load registered for these specimens. The $S_{3D}$-ANC resulted in a very similar load-deflection diagram to the latter specimen until 90% of its failure load. This attests the impact of the rebar anchored in the ends of the overlaid concrete on the behaviour of RCO strengthened structures. As for the behaviour of the $S_{3D}$-STC specimen, the shift on the slope of the critical shear crack observed in the previous section resulted in a less stiff load-strain diagram, attesting the influence of dowels stitching the two layers for a small area of strengthening with RCO. Such considerations can be observed in Figure 4.41, where cracking of each layer was more prominent due to the less stiff structural response of these specimens. These were identified as *1* for the overlay, furthest tensile fiber of the composite cross-section, and *2* for when the crack reaches the substratum. Despite the cracking observed in Figure 4.35 for the ANC and STANC specimens, there was no yielding of reinforcement, as strains were generally lower than the $S_{4D}$ specimens.

Analyzing the load-strain diagrams of the longitudinal reinforcement for the $S_{3D}$ specimens, one can observe the change in behaviour when the strengthened area is reduced, with strains generally smaller than the $S_{4D}$ specimens. A general tendency for the sudden rise of strain on the overlaid concrete can be identified on all specimens, with the particularity of the strain values meeting again right before failure. This was the main difference in the behaviour when comparing to the $S_{4D}$ specimens, where the strains kept evolving further apart. The tendency for the strains to meet before failure suggests the vertical redistribution of horizontal stresses in the composite cross-section. Such condition can be justified with the RCO patch being closer to the loaded region. The sudden rise can be explained with the attainment of the section's cracking load, with subsequent reduction of strain justified by the debonding of the interface in the REF specimen, as observed in the figure above. Only the $S_{3D}$-STANC specimen reached the peak strain of the overlay considerably before the failure load. The rest of the specimens reached the peak strain at the overlay marginally before failure.

The maximum strain at the reinforcement of the overlay, the respective strain at the substratum reinforcement, and the load at the center of the specimen, can be observed in Table 4.10 below. The values for maximum strain were taken for the same load as the maximum strain on the other layer was reached, with the example of the $S_{3D}$-STANC specimen which yielded the largest difference for maximum strain on both layers. One should notice that there was no yielding of reinforcement on any column-supported specimens.

Table 4.10 – Maximum strain of overlay reinforcement at the column face and respective substratum.

| | **$S_{4D}$ specimens** | | | **$S_{3D}$ specimens** | | |
|---|---|---|---|---|---|---|
| | **Load (kN)** | **Substratum (µm/m)** | **Overlay (µm/m)** | **Load (kN)** | **Substratum (µm/m)** | **Overlay (µm/m)** |
| **REF** | 526.3 | 1054.8 | 1639.5 | 203.0 | 627.9 | 814.4 |
| **STC** | 528.2 | 867.9 | 1644.1 | 312.8 | 988.7 | 1022.4 |
| **ANC** | 567.6 | 956.9 | 1883.2 | 465.5 | 1077.4 | 1057.8 |
| **STANC** | 547.6 | 909.0 | 1559.4 | 338.7 | 642.7 | 1166.3 |

The strains before and after the bend on the anchored end of the longitudinal reinforcement were analysed for the higher and lower effective depths of reinforcement on the ANC and STANC specimens of both $S_{4D}$ and $S_{3D}$ sets. Figure 4.42 and Figure 4.43 present the diagrams for the horizontal and vertical strains of the $S_{4D}$-ANC and $S_{4D}$-STANC specimens.

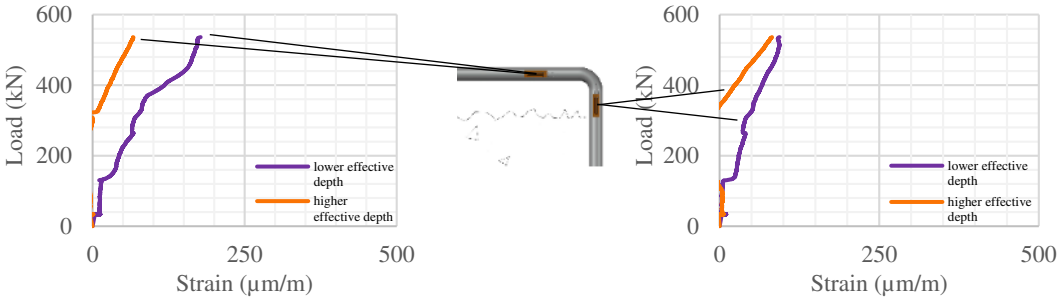


Figure 4.42 – Strains at the anchorage of the $S_{4D}$-ANC specimen longitudinal reinforcement.

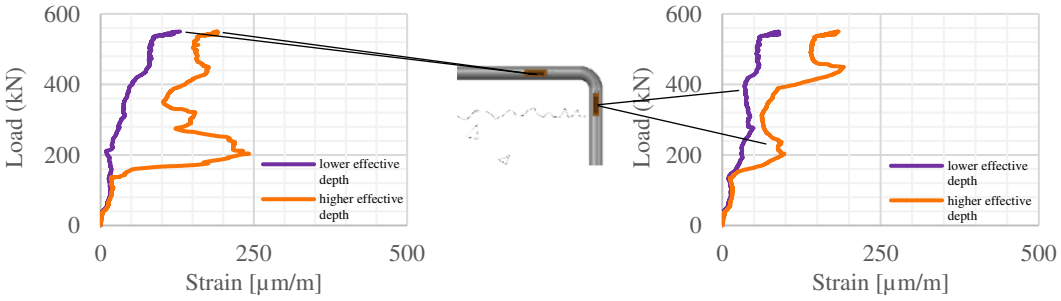


Figure 4.43 – Strains at the anchorage of the $S_{4D}$-STANC specimen longitudinal reinforcement.

Analysing the strains above, one can observe the low degree of vertical strain on the anchored end of longitudinal reinforcement for the $S_{4D}$ specimens. The location further from the column face of such reinforcement's anchored end, and closer to the null moment radius, can justify the lower strains measured. Such consideration attests the lower stresses on the anchorage of reinforcement, in spite of its importance to the integrity of the strengthened slab as attested by the failure mode of the $S_{4D}$-REF specimen. The lower stresses are also important for controlling the interface crack opening, despite only reaching about one quarter of the steel strength before yielding. Also noticeable is the switch between higher strains on the lower and higher effective depths respectively for the $S_{4D}$-ANC and $S_{4D}$-STANC specimens.

Regarding the strains at the steel dowels of the $S_{4D}$-STC and $S_{4D}$-STANC specimens, measurements were performed on both directions for one steel dowel of each row, aligned with the axis of the slab. Such results are presented in Figure 4.44 and Figure 4.45 respectively.

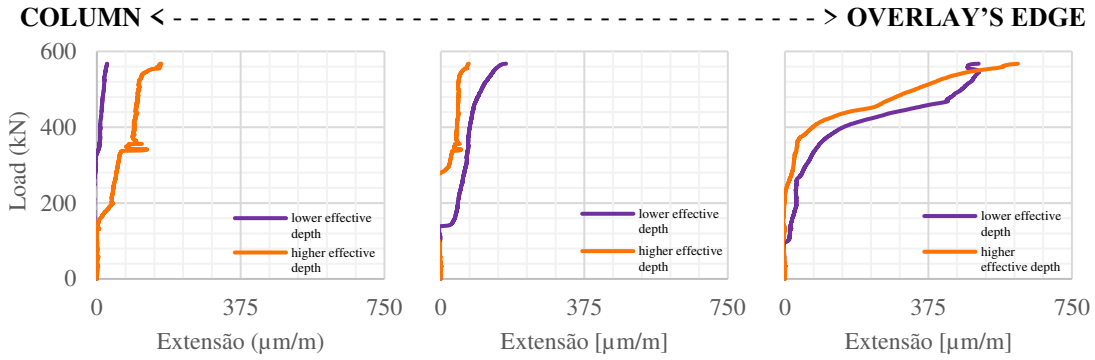
COLUMN < - - -

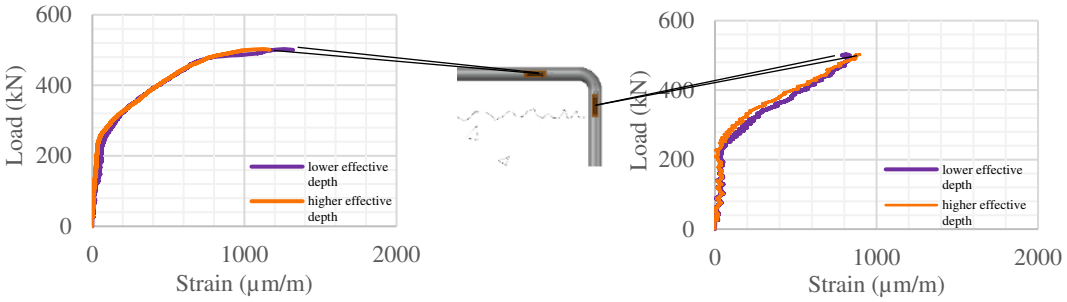


Figure 4.47 – Strains at the anchorage of the $S_{3D}$-STANC specimen longitudinal reinforcement.

The figures above illustrate the plateau of the horizontal strains before failure, without yielding of reinforcement. A shift in the load-strain relationship can be observed on both specimens, but more clearly in Figure 4.47 for a load around 225kN. Vertical strains decrease the stiffness of such relationship, coherent with the opening of the interface crack probably due to the critical shear crack reaching the interface.

The hypothesis of the critical shear crack resulting in a perimeter larger than the strengthened area arises when observing the $S_{3D}$-STC specimen failure in the previous section. The steel dowels on such specimen changed the failure mode so the critical shear crack did not cross the interface. The readings observed on the shear connector strain gauges resemble a faulty data acquisition but can be taken into account when observing the sawcut specimen. The shifting of the critical shear crack and the undamaged interface could justify the small readings measured in Figure 4.48.

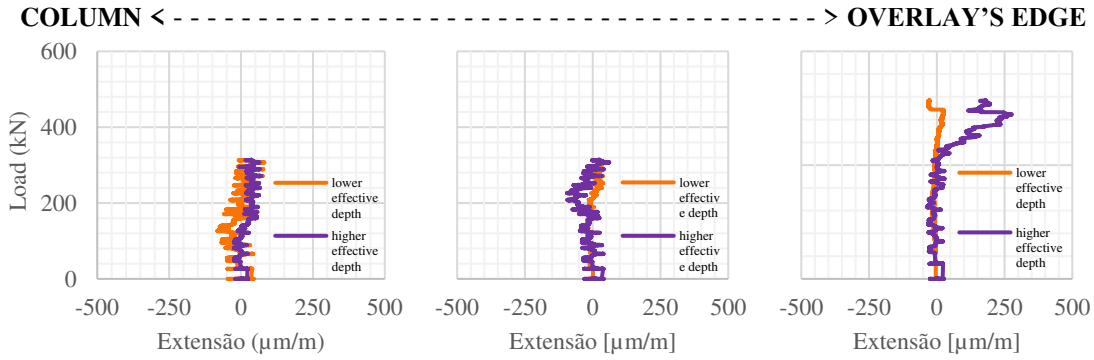
COLUMN < - - -

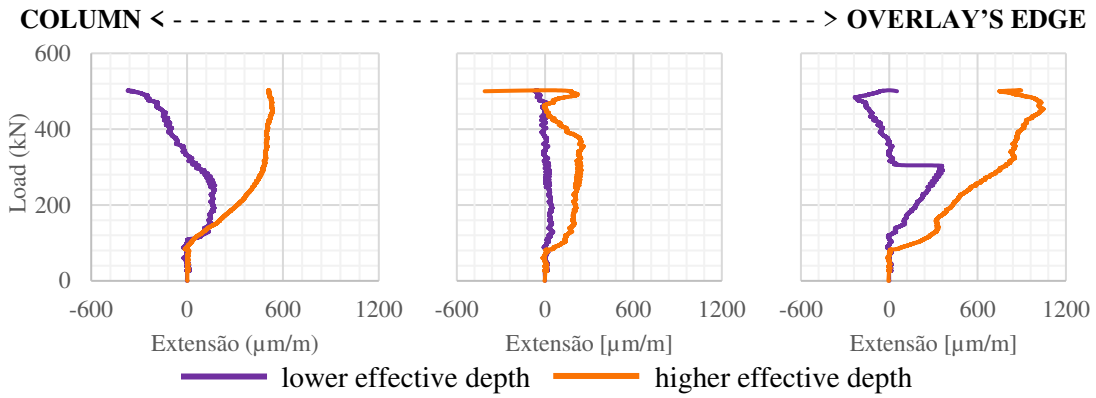
COLUMN < - - -

In Figure 4.51, one observes the discretization of macroelements on both models' geometries for the STANC detailing of the interface, which is the most complex model with all types of macroelements and interfaces.

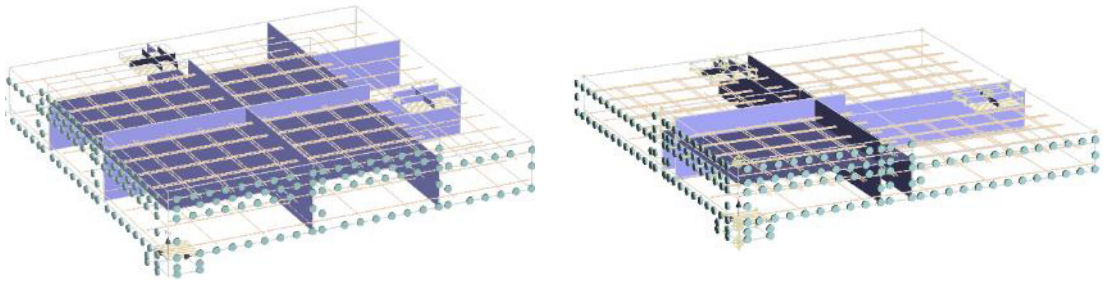

Figure 4.51 – Discretization of macroelements on the numerical FE models: $S_{4D}$, left; $S_{3D}$, right.

Definition of material properties was carried out similarly to the rectangular specimens in section 3.4.2 through the SBETA constitutive model, which allows for the nonlinear behaviour and cracking of concrete, discrete truss elements with bilinear behaviour and a bond-slip model for the longitudinal reinforcement, bilinear behaviour 3D Von Mises for the interface crossing reinforcement modelled through macroelements, and zero-thickness elements defined like in section 3.4.3 for the contact area between the two layers. Material parametrization was performed based on the concrete compressive and tensile strength on Table 4.2 and Table 4.3 of section 4.2.2, steel tensile strength on tables Table 4.5 of the same section and Table 3.6 of section 3.2.5, cement grout tensile strength and pull-out strength of embedded anchorages, also in section 3.2.5. Interface parameters such as the tensile strength and coefficient of friction considered were taken from Table 4.6 and Table 3.10 of section 3.2.6. Interface parameters regarding equations (3.8) to (3.11) of section 3.4.3, are presented on Table 4.11 for the $S_{4D}$ specimens, where the definition of the interface fracture energy was performed considering the smaller values yielded by equation (3.9), highlighted in bold.

Table 4.11 – Concrete-to-concrete interface parameters for the modelling of $S_{4D}$ specimens.

| **$S_{4D}$** | **Concrete-to-concrete interface parameters** | | | |
|---|---|---|---|---|
| | **REF** | **ANC** | **STC** | **STANC** |
| $G_{F,sub}$ **(x10$^{-5}$ MN/m)** | 5.40 | 5.63 | 4.64 | 4.54 |
| $G_{F,ol}$ **(x10$^{-5}$ MN/m)** | 5.87 | 5.90 | 5.57 | 6.13 |
| $f_{t,sub}$ **(MPa)** | 3.2 | 2.8 | 3.3 | 2.8 |
| $f_{t,ol}$ **(MPa)** | 3.4 | 3.2 | 3.4 | 3.5 |
| $f_{t,i}$ **(MPa)** | 0.85 | 0.82 | 1.04 | 0.82 |
| $G_{F,i(sub)}$ **(x10$^{-5}$ MN/m)** | **1.44** | 1.65 | **1.46** | **1.33** |
| $G_{F,i(ol)}$ **(x10$^{-5}$ MN/m)** | 1.47 | **1.51** | 1.71 | 1.44 |
| $K_{nn}$ **(x10$^{4}$ MN/m$^{3}$)** | **2.52** | **2.22** | **3.70** | **2.53** |
| $K_{tt}$ **(x10$^{4}$ MN/m$^{3}$)** | **2.52** | **2.22** | **3.70** | **2.53** |
| $\mu$ **(-)** | 1.43 | 1.44 | 1.43 | 1.42 |
| $C$ **(MPa)** | 2.44 | 2.37 | 2.98 | 2.33 |

Parametrization of the interface was performed based on tensile strength and surface parameters assessed in section 4.2.2. Although the surface assessment was performed on both directions of the specimens, the interface properties were set for the weakest of the two directions. Similarly, the interface parameters for the $S_{3D}$ specimens were also assessed through the same principles as the $S_{4D}$ specimens and are presented in Table 4.12.

Table 4.12 – Concrete-to-concrete interface parameters for the modelling of $S_{3D}$ specimens.

| $S_{3D}$ | Concrete-to-concrete interface parameters | | | |
|---|---|---|---|---|
| | **REF** | **ANC** | **STC** | **STANC** |
| $G_{F,sub}$ (x10$^{-5}$ MN/m) | 6.38 | 6.01 | 7.54 | 6.75 |
| $G_{F,ol}$ (x10$^{-5}$ MN/m) | 5.71 | 5.61 | 5.99 | 5.73 |
| $f_{t,sub}$ (MPa) | 3.1 | 3.1 | 3.2 | 2.5 |
| $f_{t,ol}$ (MPa) | 2.8 | 2.5 | 3.4 | 2.3 |
| $f_{t,i}$ (MPa) | 0.81 | 1.02 | 0.85 | 1.00 |
| $G_{F,i(sub)}$ (x10$^{-5}$ MN/m) | 1.67 | **1.98** | 2.00 | 2.70 |
| $G_{F,i(ol)}$ (x10$^{-5}$ MN/m) | **1.65** | 2.29 | **1.50** | **2.49** |
| $K_{nn}$ (x10$^{4}$ MN/m$^{3}$) | **1.99** | **2.63** | **2.41** | **2.01** |
| $K_{tt}$ (x10$^{4}$ MN/m$^{3}$) | **1.99** | **2.63** | **2.41** | **2.01** |
| $\mu$ (-) | 1.42 | 1.42 | 1.41 | 1.43 |
| $C$ (MPa) | 2.31 | 2.90 | 2.40 | 2.87 |

The steel-concrete interface of the anchored reinforcement was also calculated similarly to section 3.4.3, regarding stiffness, strength, and the post-peak softening of stresses that allow for anchorage slip. The input of parameters for such interface followed that of [150] due to the available data on grout strength.

### 4.4.2. Numerical results

The relationship between load and deflection at the centre of each specimen can be observed for both the experimental tests and numerical models of the specimens strengthened up to *4d* from the column face in Figure 4.52. Since no unstrengthened substratum was preconised for this set of tests, the load-deflection relationship presented for such layer alone was attained through the numerical modelling of a single layer without the overlaid concrete elements.

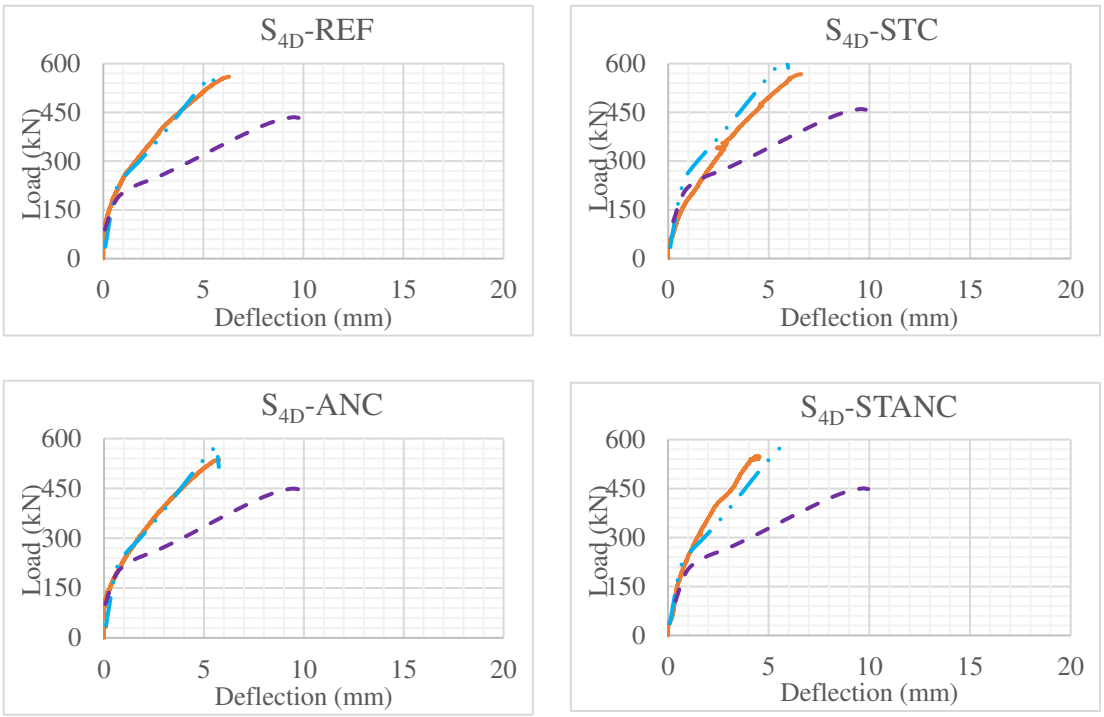


Figure 4.52 – Load-deflection relationship of the $S_{4D}$ specimens:
Experimental (——), Numerical (— · · —), Substratum (– – –).

The above load-deflection diagrams show a greater correlation between the experimental tests and numerical models where debonding occurred ($S_{4D}$-REF and $S_{4D}$-ANC). Analyzing the experimental and numerical failure loads, one can verify that they are of the same magnitude. Numerical behaviour denotes a point of change for stiffness around 200 kN, coherent with major cracks appearing on the model and progressive debonding of the interface.

When comparing the results between the experimental specimens and numerical models of the $S_{3D}$ specimens, one can see the less stiff structural response on the load-deflection diagram. The shorter reach of the RCO results on the substratum governing a larger area of the column region and thus the strengthened cross-section contributing only closer to the column face. As observed by the numerical load-deflection diagram illustrated in Figure 4.53, a small discrepancy is evident between these and the experimental specimen STC. The premature failure of the $S_{3D}$-REF specimen deemed it unfit for comparing to a numerical model since its particular behaviour could not be replicated numerically. Therefore, such comparison is not presented in the next figure.

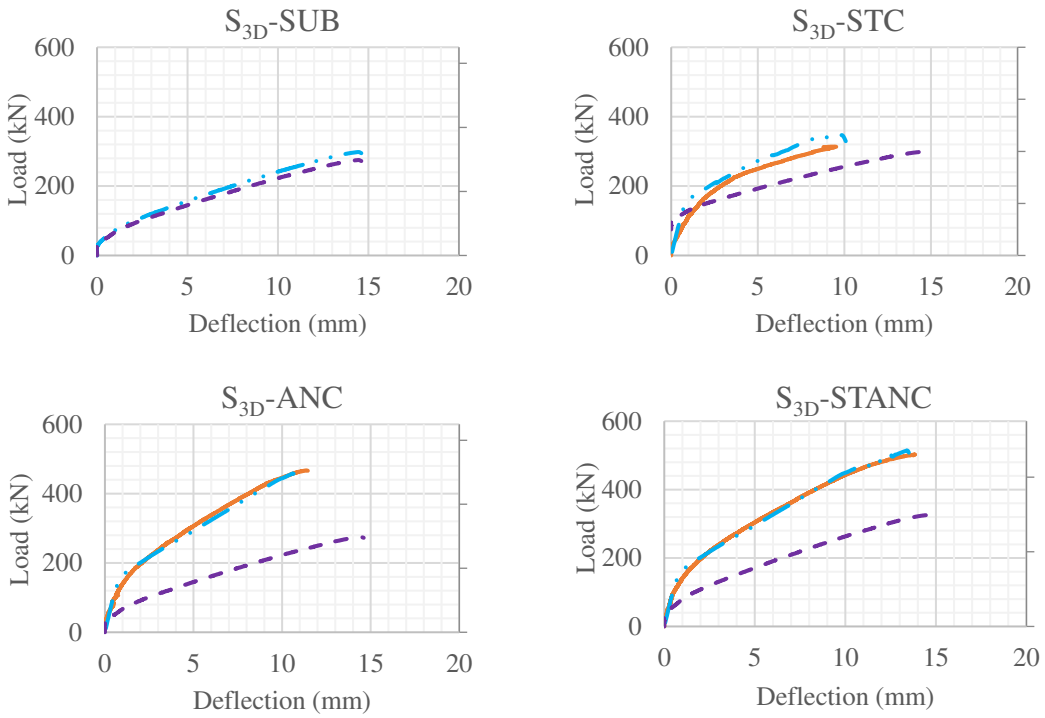


Figure 4.53 – Load-deflection relationship of the $S_{3D}$ specimens: Experimental (——), Numerical (— · · —), Substratum (– – –).

A good correlation is inherent to all FE model results when compared to the respective experimental equivalent specimens. The attainment of such results was possible due to calibration of the software according to experimental data, which mainly concerned material properties, but also the displacements measured. This allowed for some tuning of the interface response and thus better results. For interface detailings with and without reinforcement, definition according to experimental data was the main parameter that affected global behaviour and failure loads. Graphically, one can observe that this strengthening system can result in more than double the original punching capacity for interior slab-column connections (Figure 4.54). Such condition implies a behaviour close to monolithic, where stresses can be transferred to the top layer reinforcement.

The impact of the increased effective depth and the behaviour close to monolithic resulted in a considerable increase for the punching failure load. This was observed for the $S_{4D}$ specimens that did not debond (STC and STANC), and for the $S_{3D}$ specimens that punched through the interface (ANC and STANC). The little increment of the $S_{3D}$-STC specimen attests the poor performance of the detailing with dowels stitching the two layers for a contact area close to the punching control perimeter. Numerical test results also attest the good correlation between these and the experimental tests, with small differences between both failure loads attained.

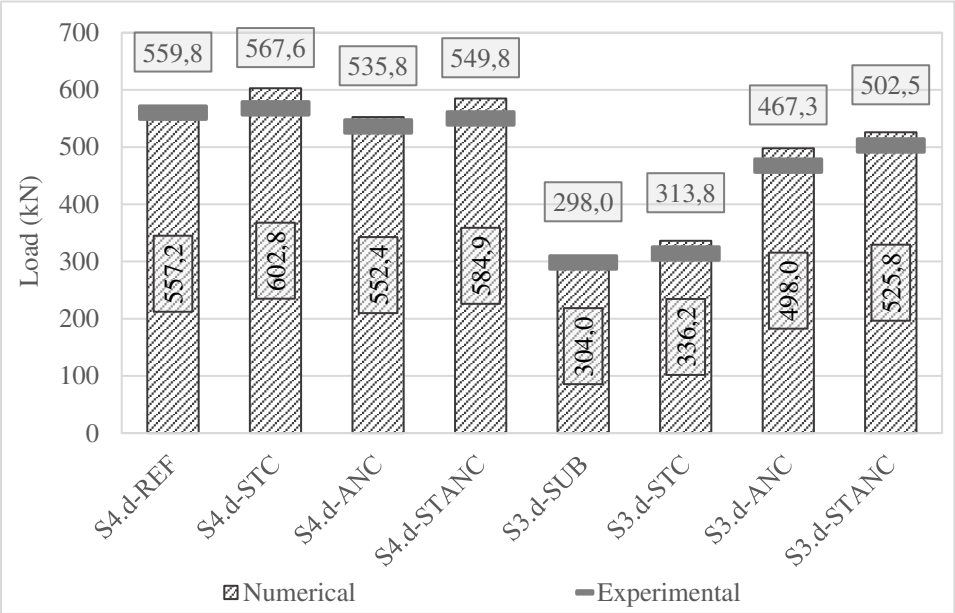


Figure 4.54 – Punching capacity regarding each layer and numerical failure load.

The good correlation of all results can also be observed in Figure 4.54, where the maximum difference between the numerical models and experimental tests of 7 % is shown for the $S_{3D}$-STC detailing. One should account that the critical shear crack shifted its slope on such specimen, intersecting the surface after the overlay's edge. Due to the lack of substratum specimens for all the strengthened specimens tested and the knowledge developed around numerical modelling, an estimation of the substratum strength was performed with the software. Failure loads from numerical modelling of the strengthened specimens are also presented in Table 4.13.

Table 4.13 – Experimental and numerical failure loads for all square specimens.

| | | **Substratum Only** | **Strenghtened with overlaid reinforced concrete** | | | | | | |
|---|---|---|---|---|---|---|---|---|---|
| | | **Numerical** | **Experimental** | **Increment over Substratum** | | **Numerical** | **Increment over Substratum** | | **Experimental / Numerical** |
| | | **(kN)** | **(kN)** | **(kN)** | **(%)** | **(kN)** | **(kN)** | **(%)** | **(-)** |
| **$S_{4D}$** | **REF**(*) | 330.3 | 559,8 | 229.5 | 69 | 557.2 | 226.9 | 68.7 | 1.00 |
| | **STC** | 266.0 | 567,6 | 301.6 | 112 | 602.8 | 336.8 | 127 | 0.94 |
| | **ANC**(*) | 351.7 | 535,8 | 184.1 | 52 | 552.4 | 200.7 | 57.1 | 0.97 |
| | **STANC** | 258.4 | 549,8 | 291.4 | 113 | 584.9 | 326.5 | 126 | 0.94 |
| **$S_{3D}$** | **SUB** | - | 298.0 | - | - | 304 | - | - | 0.98 |
| | **STC** | 286.6 | 313.8 | 27.2 | 9.0 | 336.2 | 49.6 | 17.3 | 0.93 |
| | **ANC** | 207.4 | 467.3 | 259.9 | 125 | 463.2 | 290.6 | 140 | 1.01 |
| | **STANC** | 244.7 | 502.5 | 257.8 | 105 | 514.8 | 281.1 | 115 | 0.98 |

(*) debonding failure

### 4.4.3. Discussion of numerical results

Analysing the failure modes of the numerical models, one can observe concentrated cracks at the zone of the critical shear crack, with an example presented in Figure 4.55 for the reference substratum specimens considered for both 150 mm and 120 mm.

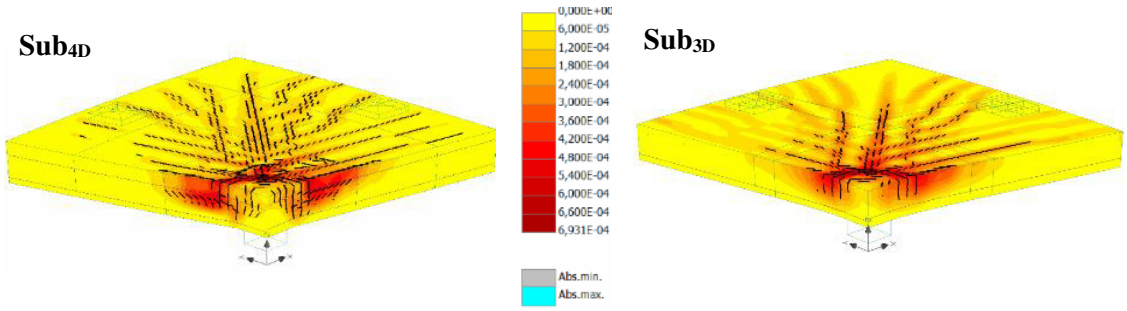


Figure 4.55 – Post failure cracking of the reference substratum specimens – crack width in mm.

Analysing the numerical models of the strengthened specimens, a discontinuity in the substratum cracks can be observed when they reach the interface, denoting the importance of the interface to transfer stress between layers. Figure 4.56 shows this phenomenon and the consequent cracking occurring at the overlay top surface from the stresses transferred between layers.

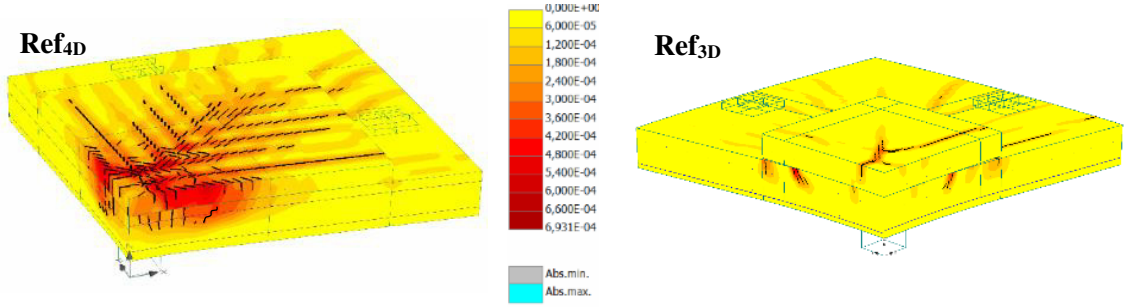


Figure 4.56 – Post failure cracking of the reference strengthened specimens – crack width in mm.

Observing the output in terms of cracking, one sees the difference in terms of flexural and shear failure of both geometries. The $S_{4D}$ specimens resulted in a great concentration of cracks in the critical shear crack area and the $S_{3D}$ specimens show a significant flexural crack in the direction of the higher effective depth of the longitudinal reinforcement, coherent with the lower flexural stiffness provided by the longitudinal reinforcement in the other direction. Also observable are the different distances the critical shear crack reaches the interface on both directions: closer to the column face on the higher effective depth of reinforcement, and further on the opposite direction. Such behaviour suggests the critical shear crack has a lower slope on this direction, which could limit for a smaller patch of overlaid concrete.

Magnifying the deformation of the numerical models, one can observe the effective contact occurring at the interface on the $S_{3D}$ models. Although the interface is assumed bonded over the contact area, such assumption may not be true and debonding can be non-continuous, as depicted in Figure 4.57.

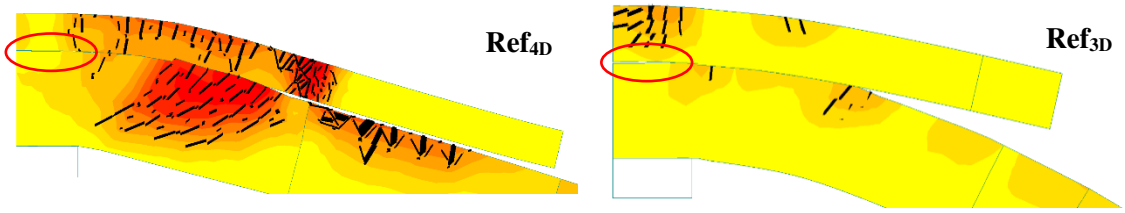


Figure 4.57 – Debonding on top of the center support (column) for the $S_{4D}$ and $S_{3D}$ specimens.

The figure above shows the debonding phenomenon occurring on top of the center support, suggesting the tipping point at the compressive strut that results from the punching mechanism. Such behaviour can help to justify the interface crack observed in Figure 4.29 for the specimen $S_{4D}$-ANC, where debonding of the overlaid concrete was visible after saw-cutting and observing the post-failure cross-section. The numerical model for such specimen shows, in Figure 4.58, that the shear stresses at the interface are very close to null on top of the center column. This behaviour explains how the interface debonded, although compressive stresses from the struts of the punching mechanism are loading the interface. The perimeter of compressive stresses can also be observed in the figure below near the column.

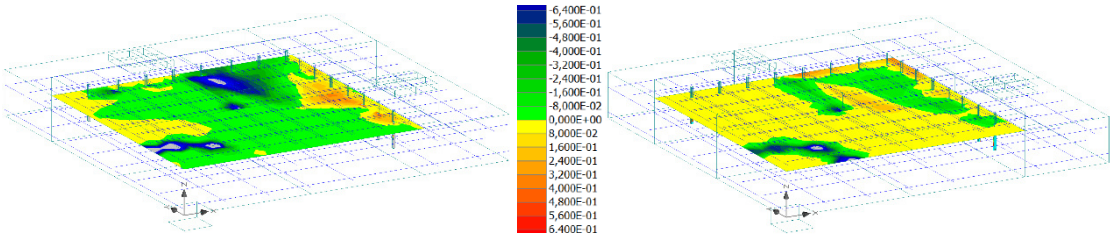


Figure 4.58 – Normal stresses on the contact surface of the $S_{4D}$-ANC specimen at failure.

Analyzing the shear stresses $\tau_{xz}$ e $\tau_{yz}$ on the strengthened specimen, cross-section denotes a great concentration of stresses in both directions on the zone of the critical shear crack, beginning from the column face to interface of the two layers. The latter could be justified by the dissipation of energy through interface debonding. An example is shown in Figure 4.59 for both the reference models of the $S_{4D}$ and $S_{3D}$ specimens.

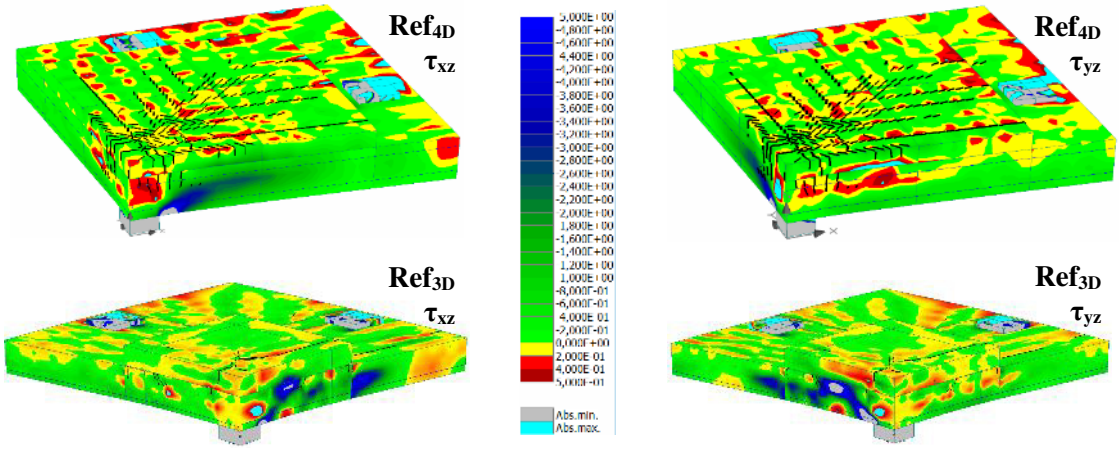


Figure 4.59 – Shear stresses at the axis of the strengthend specimens – stress in MPa.

Analyzing the stresses at the interface reveals a difference in behaviour between the $S_{4D}$ and $S_{3D}$ specimen geometries. In the $S_{4D}$ specimens, a perimeter of stresses can be observed for both the normal and tangential directions, as shown in Figure 4.60. The behaviour is similar to the $S_{3D}$ specimens on such perimeter, coincidental with the cracks observed in Figure 4.56. Tangential stresses are overtaken by tensile stresses on the $S_{4D}$ specimens right before the critical shear crack for both the $S_{4D}$ and $S_{3D}$ specimens, thus resulting in the debonding of the overlaid concrete. A trend could be identified for the stress distribution as the debonding of the interface evolves through a frontline of null stresses and the inversion of the stress signal with the strut from the punching mechanism. Such inversion of stresses could help in justifying the debonding phenomenon observed in the $S_{4D}$-ANC specimen that debonded despite the stitching provided by the anchored reinforcement and compressive stresses from the punching strut.

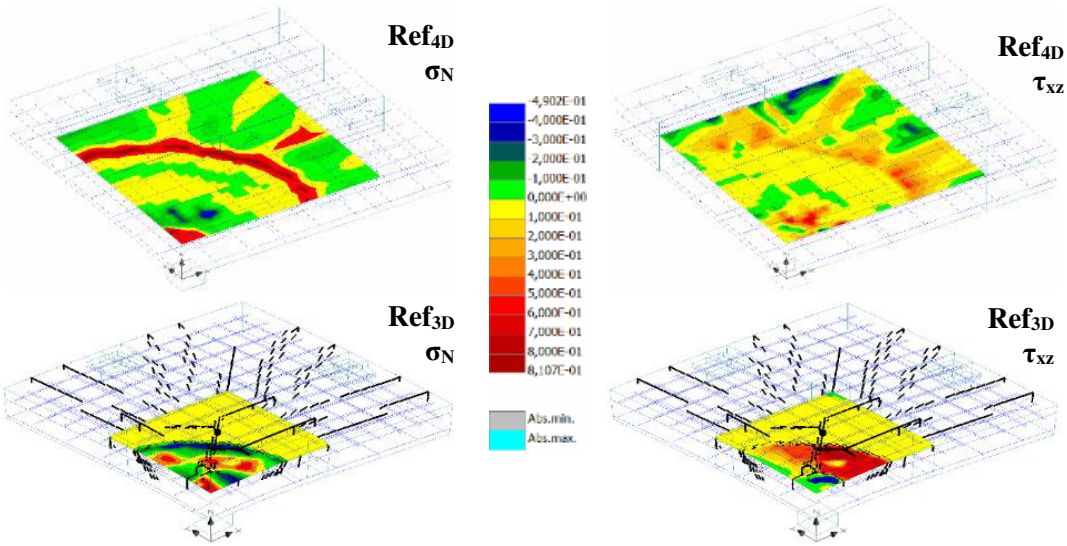


Figure 4.60 – Normal and tangential stresses at the interface – stresses in MPa.

Another important aspect of the square specimens occurred for the $S_{3D}$-STC specimen, where a shifting of the critical shear crack was the main phenomenon that conditioned structural response and led to a fully bonded interface at failure, despite the lower punching capacity. This shift in the slope of the critical shear crack could be observed on the respective numerical model through the adaptation of the Fixed Crack Model coefficient. Tuning of such parameter to a value of 0.3 allowed for adjusting the response of the model and good correlation was attained with the experimental specimen, observed in Figure 4.61.

Figure 4.61 – Shifting of the critical shear crack slope: numerical (left) and experimental (right).

The slope of the critical shear crack for a traditional failure by punching of a concrete slab is usually set at around 26.6º. A smaller angle of such crack implies that the compressive strut of the punching mechanism is predominantly horizontal, thus inducing larger strains on the longitudinal reinforcement. In a case of RCO strengthening, these horizontal stresses discard the full composite cross-section capacity. Even the shear strength of the substratum is compromised by the RCO since the slope of the resulting shear crack is smaller than the unstrengthened specimen in Figure 4.33. The main difference of this specimen to the $S_{3D}$-STANC specimen is the lack of stitching reinforcement at the edge of the overlay. Such condition lead to the evolution of the interface crack to critical shear cracks on both directions, otherwise controlled by the aforementioned reinforcement. Also noteworthy is the relationship between the slope of the critical shear crack and the effective depth of the rebar layers. The behaviour was stiffer on the direction with higher effective depth, denoted by the higher slope of the critical shear crack illustrated in Figure 4.62. The smaller effective depth also coincided with the critical shear crack with smaller slope due to the less flexural stiffness. Such condition was also observed on the numerical model of this specimen in Figure 4.61 where different slopes of the critical shear crack can be observed on each direction.

Figure 4.62 – Higher slope of the critical shear crack on the direction of rebar with higher effective depth for the S3.d-STC specimen.

A good correlation could then be observed between the numerical models and experimental specimens, which denotes the numerical modelling suitability to experimental tests when considering concrete-to-concrete interfaces and the punching mechanism. Despite the change in the behaviour due to the shifting of the critical shear crack slope, failure occurred for a similar load. A decrease in strain on the experimental specimen can be observed in Figure 4.63 for the substratum reinforcement at a distance from the column face at *0d*, *2d* and the edge of the overlay. Such behaviour can result in the decrease of strains in the longitudinal reinforcement since energy was released with such progressive deformation. A sudden rise in strain due to interface cracking could also be observed on the flexural reinforcement of the substratum layer, where the equilibrium of the cross-section suggests the smaller slope observed for the critical shear crack rather than the standard slope. A comparison of the strains assessed experimentally and numerically at the overlay's edge allowed for the comparison of both the specimen and model behaviour in Figure 4.63.

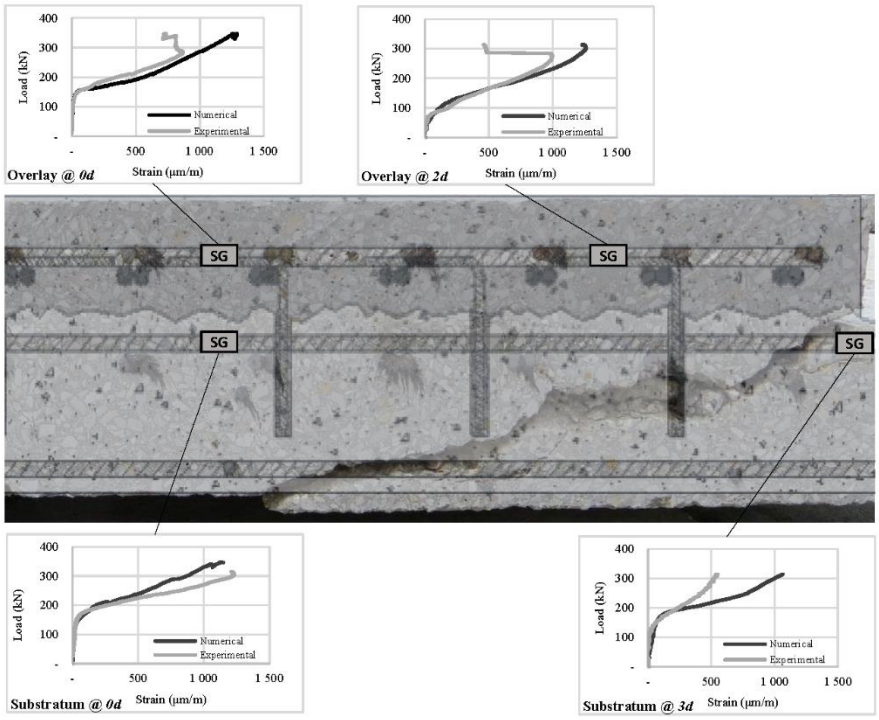


Figure 4.63 – Comparison of strain reading on key coordinates of longitudinal reinforcement for $S_{3D}$-STC specimens.

The strains of both the experimental specimens and numerical models result close to each other, attesting the numerical modelling capability for accounting such phenomena, like the debonding of concrete-to-concrete interfaces, along with punching of flat slabs. One noticeable difference can be observed regarding the decrease in strain right before failure on the experimental specimens. Such decrease is in accordance with the behaviour observed during testing of these specimens, with the critical shear crack opening and evolving before failure. This phenomenon allows for the dissipation of energy and redistribution of stresses, which results in a decrease of the longitudinal reinforcement strain.

Failure modes close to a monolithic behaviour were observed on the ANC and STANC detailing for both the numerical models and experimental specimens. Such failure modes can be observed and compared in Figure 4.64 and Figure 4.65, where the critical shear crack resulted with a slope close to nominal values for punching, and equivalent to a monolithic cross-section.

Figure 4.64 – Critical shear crack on the numerical model and experimental specimen of the $S_{3D}$-ANC detailing of the interface.

Figure 4.65 – Critical shear crack on the numerical model and experimental specimen of the $S_{3D}$-STANC detailing of the interface.

Numerically, the higher strains of the substratum reinforcement can be observed in the figures above through the concentration of larger crack openings after the overlay's edge. Such phenomenon is a consequence of the reduction in the cross-section geometry, which concentrates strains on the reinforcement. Experimentally, one can observe the effective difference in strain at the overlay's edge on both the substratum and overlay reinforcement. Such results attest the capacity of the anchored longitudinal reinforcement to control the concrete-to-concrete interface crack opening where it is more prominent. Comparing to the result of the STC specimen, the role of such reinforcement resulted in an equilibrium of stresses at the edge of the overlay, where the punching capacity was determinant for the failure of the composite slab. Load was transferred to the longitudinal reinforcement in a standard punching mechanism, with the anchored end guaranteeing the length of reinforcement required for flexural equilibrium of the cross-section. Thus, the punching capacity was reached before all other phenomena.

## 4.5. Final remarks

Testing of column-supported slabs allowed for attesting the RCO strengthening technique on the column region as valid, stiffening the column-slab connection and allowing for higher punching and flexural capacity of the slab. A general difference could be observed between the $S_{3D}$ specimens and the $S_{4D}$ specimens regarding the behaviour of the overlaid concrete, with the $S_{4D}$ specimens all resulting in punching inside the RCO perimeter. Stitching reinforcement allowed for a higher degree of monolithic behaviour of the specimens when compared to REF specimens of each set. The $S_{3D}$-STC specimen resulted in punching through the substratum only, with a smaller slope of the critical shear crack. Such condition attests the need for controlling the edge lifting phenomenon when closer to the column face due to the higher flexural stresses in the column region.

The numerical modelling of the strengthened specimens allowed for assessing the capacity of nonlinear FE models to replicate the behaviour of a composite cross-section. Even the specimen that resulted with a different behaviour regarding the slope of the critical shear crack ($S_{3D}$-STC) could be modelled after tuning the Fixed Crack Model coefficient of the nonlinear modelling software. Another possibility of such software was to observe and assess the perimetral distribution of stresses at the interface, whose compressive stresses were coherent with the slope of the punching shear strut.

# 5. ANALYSIS OF RESULTS AND DESIGN PROPOSALS

## 5.1. Concrete-to-concrete tensile strength

### 5.1.1. Tensile capacity of the interface

Assessment of the interface tensile strength was performed through the pull-off testing of specimens cast on the same surface and at the same time as the RCO. Two-hundred pull-off tests were carried out in the vicinity of the strengthening layer of RCO.

For improved performance of the interface, a very rough profile is recommended, with an average roughness parameter equal or greater than 3.0mm, since it directly affects all other components of the resisting mechanism. Due to the fact that the assessment of different surface geometries can result in the same average roughness as stated in [70], one can resort to different parameters for surface assessment and classification [35]. For very rough worked concrete surfaces, the mean-to-peak roughness parameter can be considered since it accounts for the variations in the surface profile due to grooves and ridges of different length in the surface profile [24].

Empirical values for adhesive tensile stress are provided in [36] for the steel moil point and the high-pressure water jet techniques of 1.10 MPa and 1.46 MPa, respectively. Courard *et al*. [96] advise caution in the selection of the surface preparation method due to its aggressiveness and the substratum concrete strength and soundness, with a lower limit of concrete strength class of C30/37 advised for the most aggressive methods. This is a critical aspect, since the discontinuity due to microcracking of the substratum results in premature spalling of the substratum concrete that leads to failure of the interface. In [36] this problem is addressed when comparing several methods of surface preparation, with reference to the high-pressure water-jetting technique that removes concrete selectively, which is particularly important in scenarios of unsound or deteriorated concrete.

Table 5.1 presents the average pull-off strength ($\sigma_{Pull\text{-}off}$) of each set of specimens. Such strength was calculated through the tensile strength of the interface, which is the failure load divided by the pull-off specimen area (ap. 150x150mm$^2$).

Table 5.1 - Concrete properties and interface tensile capacity for all specimens.

| Strengthened Specimen | $\sigma_{Pull-off}$ (MPa) | Number of pull-off specimens | Standard Deviation (MPa) | Coefficient of Variation |
|---|---|---|---|---|
| **$S_{3D}$-REF** | 0.81 | 20 | 0.19 | 0.23 |
| **$S_{3D}$-STC** | 0.85 | 20 | 0.15 | 0.18 |
| **$S_{3D}$-ANC** | 1.02 | 20 | 0.10 | 0.10 |
| **$S_{3D}$-STANC** | 1.00 | 20 | 0.16 | 0.16 |
| **$S_{4D}$-ANC** | 0.82 | 16 | 0.18 | 0.22 |
| **$S_{4D}$-STC** | 1.04 | 15 | 0.19 | 0.18 |
| **$S_{4D}$-STANC** | 0.82 | 14 | 0.22 | 0.26 |
| **$S_{4D}$-REF** | 0.85 | 16 | 0.31 | 0.36 |
| **$R_S$-STC-4** | 1.34 | 5 | 0.25 | 0.19 |
| **$R_S$-STANC-4** | 1.22 | 5 | 0.21 | 0.17 |
| **$R_S$-ANC-4** | 1.44 | 6 | 0.12 | 0.08 |
| **$R_L$-REF** | 0.70 | 6 | 0.13 | 0.18 |
| **$R_L$-ANC** | 0.80 | 5 | 0.19 | 0.24 |
| **$R_L$-STC** | 0.94 | 6 | 0.08 | 0.08 |
| **$R_L$-STANC** | 0.90 | 6 | 0.15 | 0.16 |
| **$R_S$-STC-5** | 0.91 | 6 | 0.06 | 0.07 |
| **$R_S$-ANC-5** | 0.88 | 6 | 0.07 | 0.08 |
| **$R_S$-REF-1/2/3** | 1.36 | 4 | 0.12 | 0.09 |
| **$R_S$-ANC-1/2/3** | 0.73 | 4 | 0.13 | 0.18 |
| **$R_S$-STC-1/2/3** | 1.16 | 4 | 0.15 | 0.13 |
| **Mean values** | **0.95** | **-** | **0.16** | **0.17** |

The resulting pull-off strength varied in terms of average stress from a minimum of 0.70 MPa to a maximum of 1.44 MPa. A large scatter could be observed through high coefficients of variation, which are also characteristic on tensile test results. The sample of 200 test results can be considered statistically relevant for defining interface tensile capacity. Distribution of the resulting stress for each slab specimen by its pull-off specimens can be observed in Figure 5.1. The weighed average stress of 0.95 MPa was attained with the preparation of surface of existing concrete, which despite the aggressive method for surface preparation is in accordance with [36].

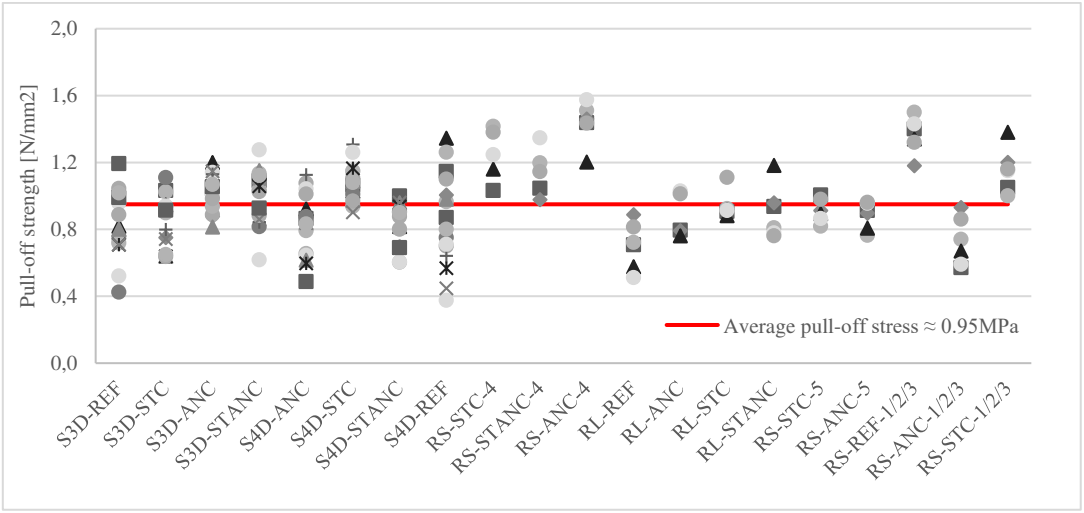


Figure 5.1 – Pull-off strength of all specimens tested.

Accounting for concrete compressive strength of both layers, a positive correlation factor of 0.41 was achieved when the substratum concrete was compared to the pull-off strength of all specimens. A positive correlation factor of 0.43 for the overlaid concrete also resulted when the latter was compared to the interface tensile capacity. Both results can be graphically observed in Figure 5.2 and Figure 5.3.

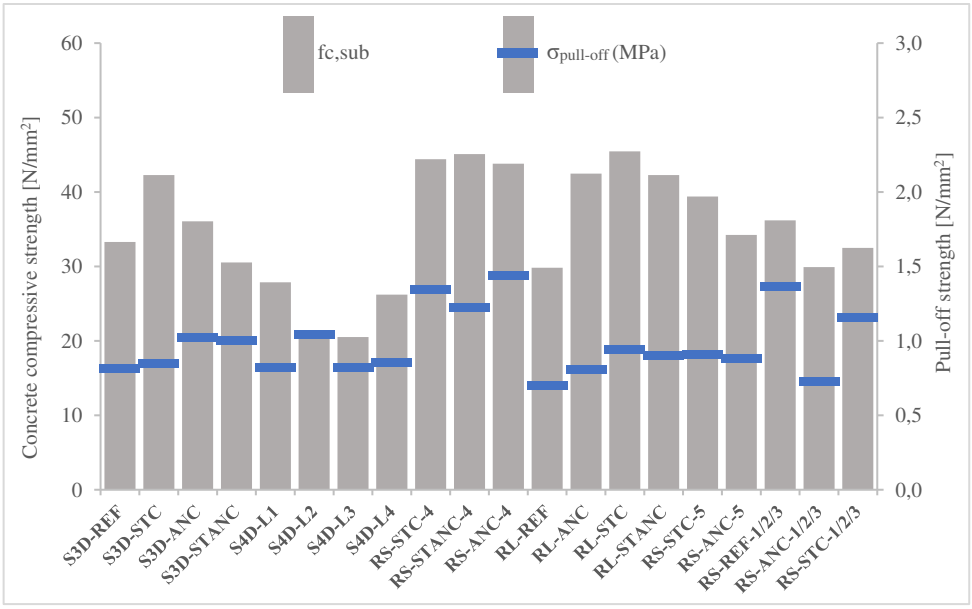


Figure 5.2 – Relationship between the interface pull-off strength and the compressive strength of substratum concrete.

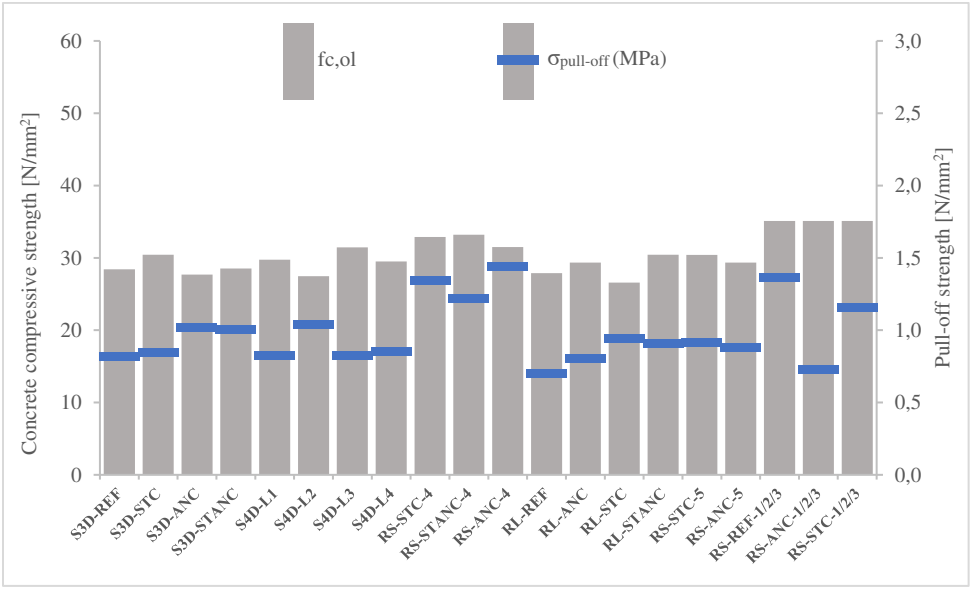


Figure 5.3 – Relationship between the interface pull-off strength and the compressive strength of overlaid concrete

Regarding concrete tensile strength, pull-off test results yielded positive correlation factors of 0.77 for substratum concrete tensile strength and 0.52 for the tensile strength of the overlaid concrete. Both can be graphically observed in Figure 5.4 and Figure 5.5.

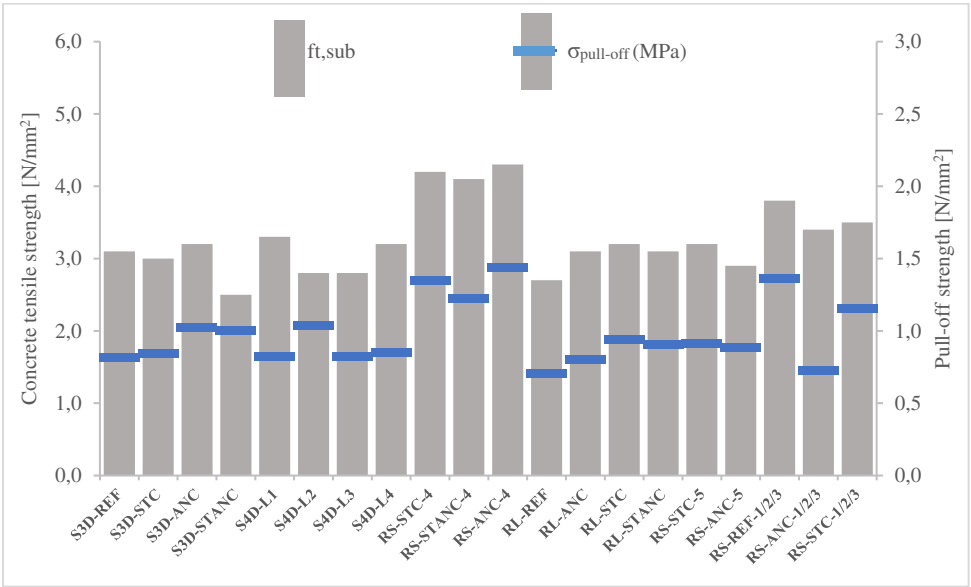


Figure 5.4 – Relationship between interface pull-off strength and concrete tensile strength for substratum concrete.

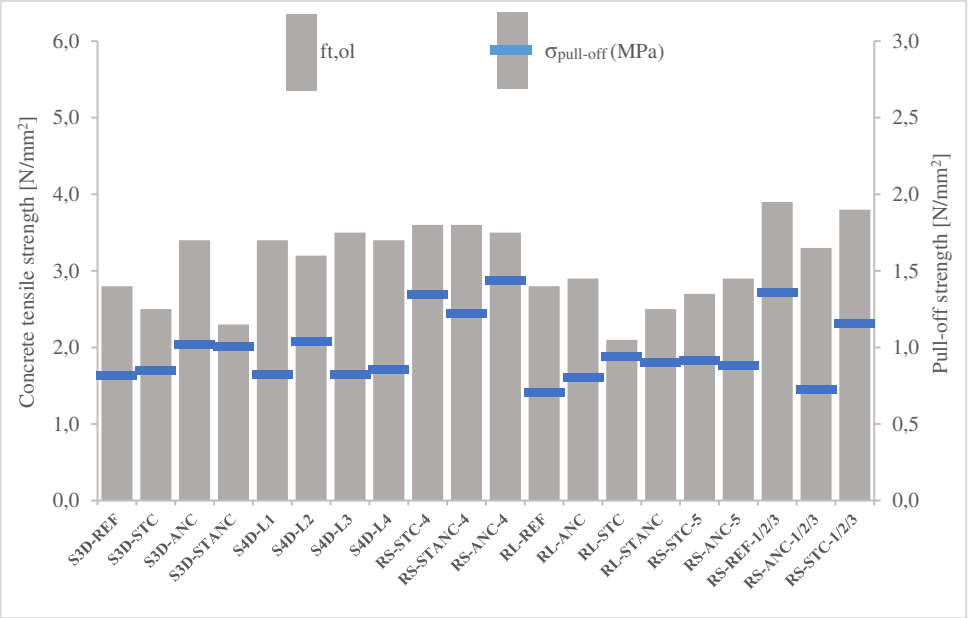


Figure 5.5 – Relationship between interface pull-off strength and concrete tensile strength for overlaid concrete.

Considering the weak links in a concrete-to-concrete interface as the material of the contacting layers other than the interface itself, the correlations between pull-off strength and the lowest compressive and tensile strengths were also assessed, with positive correlations of 0.49 for the former and 0.57 for the latter. Graphically, these correlations can be observed in Figure 5.6 and Figure 5.7.

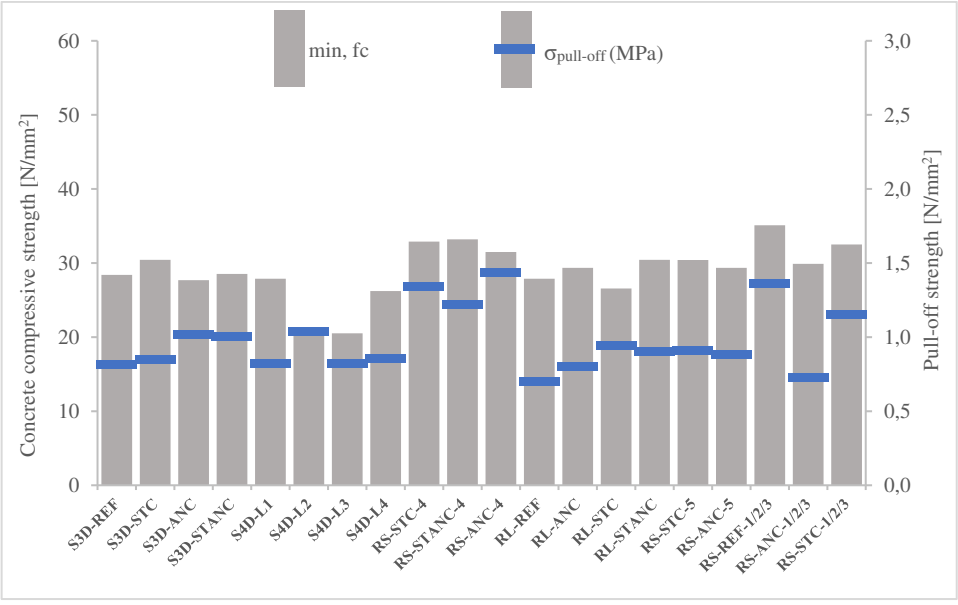


Figure 5.6 – Relationship between interface pull-off strength and the lowest concrete compressive strength of both layers.

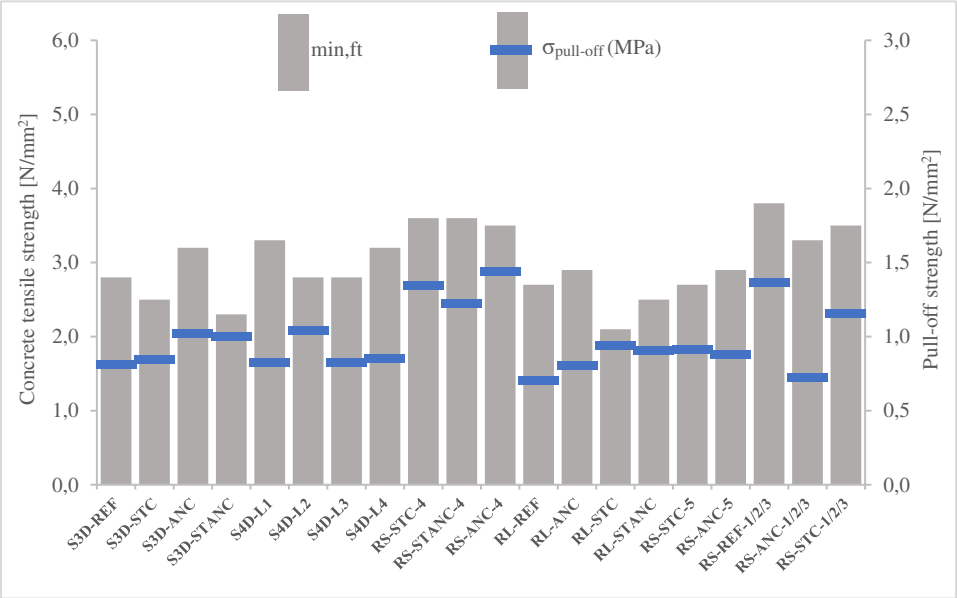


Figure 5.7 – Relationship between interface pull-off strength and the lowest concrete tensile strength of both layers.

Observing the results above, no strong correlation between the pull-off strength and concrete compressive and tensile strengths can be drawn. The best correlation with pull-off tests was attained for the substratum concrete tensile strength, which states a stronger relationship between the tensile strength of such layer and the interface. This statement differs from results by Beushausen [53] where failure occurs preferably on the overlaid concrete near the interface. Since the preparation of surface chosen comprised an aggressive method that promotes microcracking of the existing surface, one can correlate this fact with the results obtained, and attest the scatter of results. Although the latter fact is inherent to tensile testing, microcracking of the surface is favourable to the scatter of results and weakening of the interface tensile strength between the two concrete layers. This fact is also justified by the failure surface occurring at the interface on all test specimens.

### 5.1.2. Tensile capacity between different levels of roughness

To assess the effectiveness of surface preparation, eighteen tests were performed on a surface prepared with a diamond grinder (DG) that removed the laitance layer and exposed the top of aggregates and the pores on existing concrete. The results are presented in Table 5.2 and compared with the previous surface preparation technique with steel moil point (SMP) of $R_S$-STC-4, $R_S$-STANC-4 and $R_S$-ANC-4 specimens. The average (AVG) pull-off stress is then presented for each set of specimens, along with the statistical standard deviation (SD) and coefficient of variation (COV). The ratio SMP/DG presents the increment in terms of tensile stress of the interface when considering a least rough and a very rough surface preparation.

Table 5.2 - Comparison between surface preparation techniques.

| $\sigma_{Pull-off}$ (MPa) | $R_S$-STC-4 | | $R_S$-STANC-4 | | $R_S$-ANC-4 | |
|---|---|---|---|---|---|---|
| | SMP | DG | SMP | DG | SMP | DG |
| **1** | 1.03 | 0.99 | 1.04 | 0.70 | 1.44 | 0.80 |
| **2** | 1.42 | 0.85 | 1.20 | 0.55 | 1.51 | 0.66 |
| **3** | 1.83 | 1.06 | 0.98 | 0.84 | 1.46 | 1.14 |
| **4** | 1.16 | 1.02 | 1.62 | 0.35 | 1.20 | 1.02 |
| **5** | 1.25 | 0.91 | 1.35 | 0.71 | 1.57 | 1.26 |
| **6** | 1.38 | 1.13 | 1.14 | 0.49 | 1.43 | 1.41 |
| **AVG (MPa)** | 1.34 | 0.99 | 1.22 | 0.61 | 1.44 | 1.05 |
| **SD (MPa)** | 0.25 | 0.09 | 0.21 | 0.16 | 0.12 | 0.26 |
| **COV** | 0.19 | 0.10 | 0.17 | 0.26 | 0.08 | 0.25 |
| **SMP/DG** | 1.35 | | 2.01 | | 1.37 | |

Results show that for more aggressive surface preparation techniques an increment of approximately one third of the tensile bond strength was attained for the $R_S$-STC-4 and $R_S$-ANC-4 specimens and double the tensile bond capacity for $R_S$-STANC-4. This was a direct assessment of the impact surface preparation has on the tensile bond capacity between two concrete layers. Despite being the specimen that resulted in double the bond capacity between both techniques, the $R_S$-STANC-4 specimen was also the least rough of the three tested, as it will be presented next. This suggests an upper bound for surface roughness in tension, also according to a conclusion stated in [36], since for very rough surfaces there is no significant increment to the effective contact area. This can justify the impact of a smaller roughness that could result in higher tensile capacity.

### 5.1.3. Tensile capacity regarding surface roughness

Since surface roughness can impact the effective contact area between two concrete layers, this parameter was assessed and accounted for when analysing the interface tensile capacity. The two main surface parameters considered for classifying the surface, as recommended by current design codes, are the average roughness and total roughness. The former is the arithmetic average value of the surface profile measurements, and the latter states the relationship between highest peaks and lowest valleys, which can attest the interlocking capacity of the two layers for larger relative displacements. The Peak-to-Mean Roughness (PMR) was also calculated in sections 3.2.4 and 4.2.2 since it is a valid roughness assessment parameter and used in current design codes. A lower limit of 2.2 mm for this parameter is considered for very-rough surfaces in [24]. The values of the three parameters are presented in Table 5.3, where the PMR parameter is presented in two directions due to the square specimen assessment that was performed, as presented in Annex B. Such assessment of roughness was performed in two directions for specimens with a larger area of contact since different profiles can impact the sliding of the surfaces relative to one another differently.

Table 5.3 - Substratum surface roughness parameters: average roughness $R_a$, total roughness $R_t$ and peak-to-mean roughness $R_p$.

| Specimen | $R_a$ (mm) | $R_t$ (mm) | $R_p$ (mm) | |
|---|---|---|---|---|
| | | | xx | yy |
| **$S_{3D}$-REF** | 3.0 | 7.6 | 3.1 | 2.8 |
| **$S_{3D}$-STC** | 2.6 | 8.6 | 2.4 | 2.7 |
| **$S_{3D}$-ANC** | 3.2 | 8.4 | 3.5 | 2.9 |
| **$S_{3D}$-STANC** | 3.4 | 9.1 | 3.4 | 3.5 |
| **$S_{4D}$-ANC** | 3.8 | 9.2 | 3.9 | 3.8 |
| **$S_{4D}$-STC** | 3.3 | 7.4 | 2.7 | 3.8 |
| **$S_{4D}$-STANC** | 3.1 | 8.3 | 3.3 | 2.9 |
| **$S_{4D}$-REF** | 3.4 | 8.9 | 3.3 | 3.1 |
| **$R_S$-STC-4** | 2.9 | 7.9 | 2.6 | |
| **$R_S$-STANC-4** | 2.5 | 8.2 | 2.6 | |
| **$R_S$-ANC-4** | 3.0 | 8.4 | 2.9 | |
| **$R_L$-REF** | 2.6 | 8.0 | 2.6 | |
| **$R_L$-ANC** | 2.2 | 6.2 | 2.2 | |
| **$R_L$-STC** | 2.6 | 6.1 | 2.6 | |
| **$R_L$-STANC** | 3.2 | 7.3 | 3.2 | |
| **$R_S$-STC-5** | 2.4 | 6.6 | 2.4 | |
| **$R_S$-ANC-5** | 2.7 | 6.8 | 2.7 | |
| **$R_S$-REF-1/2/3** | 2.8 | 9.9 | 2.2 | |
| **$R_S$-ANC-1/2/3** | 2.9 | 10.6 | 2.7 | |
| **$R_S$-STC-1/2/3** | 2.9 | 10.2 | 2.3 | |

The average resulting values for the average roughness ranged from 2.2 mm (specimen $R_L$-ANC) to 3.8 mm (specimen $S_{4D}$-ANC). The former resulted below the limit of 3.0 mm stated in current design codes, although its pull-off tensile capacity resulted close to the strength of other specimens. The peak-to-mean roughness parameter can assist on classifying a surface as very-rough due to the lower bound of 2.2 mm. According to pull-off strength results in Table 3.10 and the strengthened specimen results in chapters 3 and 4, this stands as a valid characterisation for a rough surface preparation such as the one in this work, since the interface behaved similarly to other specimens. These results are in agreement with Beushausen's [53], which state that the pull-off test is less sensitive to small variations of surface roughness that impact greatly relative sliding of surfaces but not the effective area of contact. It is the case of the surface preparation in question, where the macro-roughness in the form of waviness is explored for interlocking the two layers sliding relative to one another. It should be noted that surface roughness is also a user-dependent variable when preparing the surface for casting the new layer, and not exclusively material-dependent. Surface classification through these values can't be absolute, since surfaces with the same average roughness can present different profiles as stated in [35].

In Figure 5.8 the relationship between the pull-off tensile capacity and the aforementioned parameters can be graphically observed with average values highlighted in red on both axis.

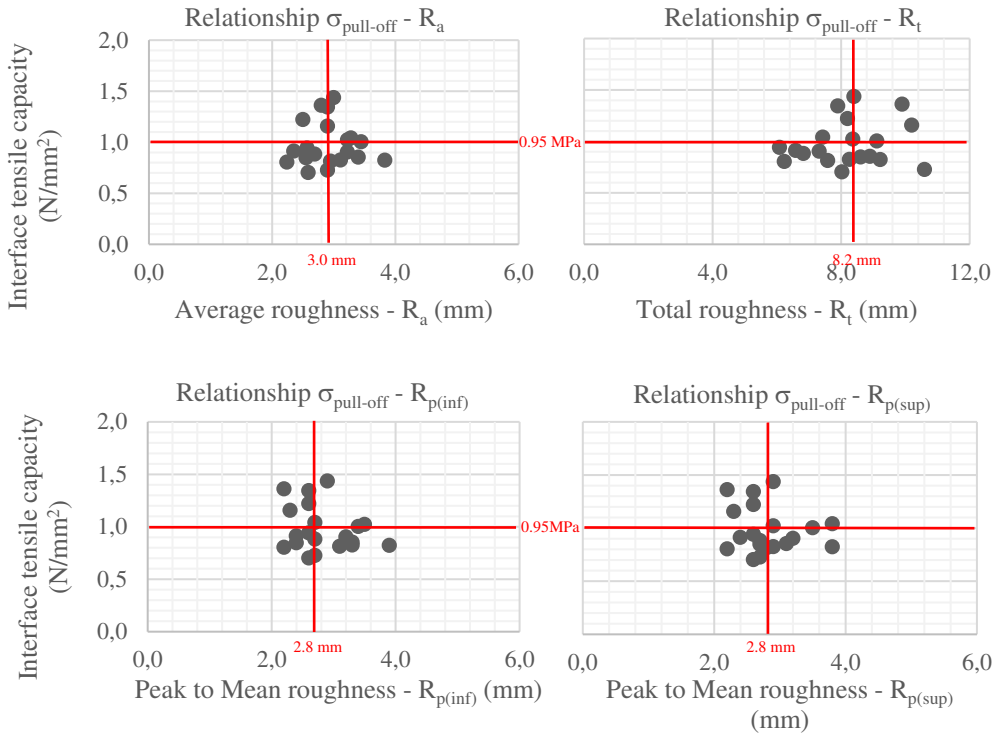


Figure 5.8 – Relationship between average, total, and peak-to-mean roughness and interface tensile capacity.

### 5.1.4. Analysis of interface tensile strength results

Tensile strength of a concrete-to-concrete interface is a parameter that depends on the adjacent materials and therefore varies with their strength. The pull-off tests performed allowed for assessing the variability of such strength with material properties of the contacting layers. Since the energy release depends on the weakest strength of adjacent materials, the relationships were plotted between the minimum tensile and compressive strengths of such materials, and the interface tensile strength. Figure 5.9 and Figure 5.10 show such relationships assessed by linear regression trendlines that best fit the experimental results.

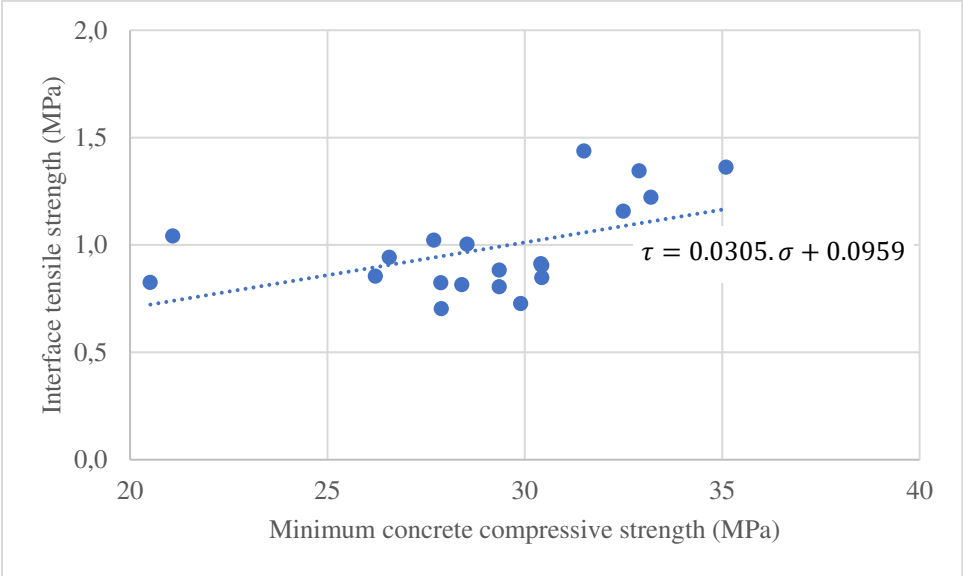


Figure 5.9 – Relationship between interface tensile strength and concrete minimum compressive strength.

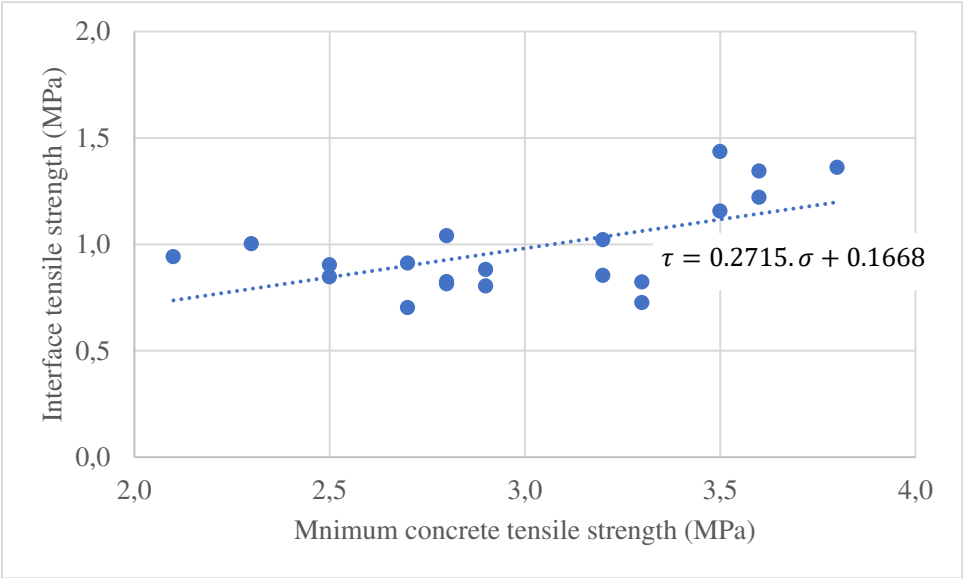


Figure 5.10 – Relationship between interface tensile strength and concrete minimum tensile strength.

Analysing the figures above, one can observe the average interface tensile strength close to 1.0MPa can be considered for a concrete compressive strength of 30MPa. Such value is close to the assessed weighed average of all pull-off test results of 0.95MPa. Compressive strengths higher than 30MPa tend to a higher interface tensile stress which work on the safe side for design purposes. Lower strength concrete resulted in values close to the same value for tensile strength, although no significant data could be assessed to attest for interface strength on lower strength concrete.

## 5.2. Proposal for RCO strengthening of unidirectional slabs

Flexural strengthening of unidirectional slabs was performed on two main sets of test specimens with shorter ($R_S$) and longer ($R_L$) reinforced concrete overlays according to the dimensions in Table 3.1, comprising the detailing of flexural and interface crossing reinforcement preconised for stitching the two layers.

The provisions on concrete-to-concrete interface strength presented in the Model Code 2010 [57] were considered for behaviour characterisation and for quantifying aggregate interlock, friction, and dowel action. Such provisions allowed for experimental results to be characterised in terms of the aforementioned components of the shear friction mechanism, with slight modifications in terms of the weight of each parameter. The proposed modifications account for the variation in terms of specimen geometry, which directly affects the contact area between the two layers, type and ratio of interface reinforcement.

Shear stresses at the interface are a consequence of the variation of force on the longitudinal rebars $\Delta F_{so}$ of the overlaid concrete, which are transferred to the substratum layer. These stresses are responsible for the integrity of the composite cross-section, since the local failure at the interface can cause the global failure of the strengthened element. Shear stress can be evaluated in terms of force transferred through the interface between the two concrete layers. Considering the concrete element of length $\Delta l$ between cracked sections illustrated in Figure 5.11, the equilibrium of forces leads to an average shear stress $v_i$ at the interface.

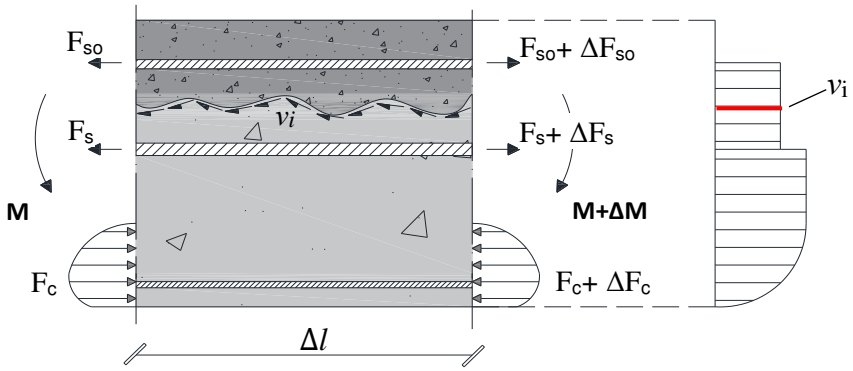


Figure 5.11 – Forces and stresses on a concrete element with composite cross-section, of length Δl.

This is proportional to the variation of forces over the length of overlaid concrete rebars, according to equation (5.1), where $b$ is the width of the interface, as follows:

$$v_i = \frac{\Delta F_{so}}{\Delta l . b} \tag{5.1}$$

The strain gauges installed in the longitudinal rebars provided a linear distribution of steel strains, which is consistent with a uniform distribution of shear stresses across the interface. The values for the steel strains at midspan $\varepsilon_s$ and corresponding values for shear stress at the interface ($v_i$) can be observed in Table 5.4. These values are the maximum strains registered for the longitudinal

rebars at the overlaid concrete. Note that not all specimens of each detailing were instrumented with strain gauges at the rebars.

Table 5.4 - Overlay steel strains and shear stress at the interface for shorter overlays.

| Specimen | | $\varepsilon_{s,o}$ (x10$^{-6}$) | $v_i$ (MPa) |
|---|---|---|---|
| **$R_S$-REF** | **1** | 511.7 | 0.46 |
| | **3** | 520.6 | 0.47 |
| **$R_S$-STC** | **1** | 805.7 | 0.73 |
| | **3** | 834.5 | 0.76 |
| | **4** | 1384.9 | 1.25 |
| | **5** | 1551.2 | 1.40 |
| **$R_S$-ANC** | **2** | 1125.5 | 1.02 |
| | **3** | 1008.0 | 0.91 |
| | **4** | 1503.9 | 1.36 |
| | **5** | 1499.3 | 1.36 |
| **$R_S$-STANC** | | 1780.9 | 1.61 |

Such parameters were also evaluated on the longer overlay geometry, which can be observed in Table 5.5, where a reduction of the shear stresses at the interface was measured on all specimens in relation to the values of the short overlay specimens, varying from 16 % (*STANC* detailing) to 27 % (*STC* detailing). A reduction of the interface shear stresses was expected due to the increase of the contact area increase over the original specimen's geometry and the decrease of 70% for the overlay reinforcement.

Table 5.5 - Overlay steel strains and shear stress at the interface for longer overlays.

| Specimen | $\varepsilon_{s,o}$ (x10$^{-6}$) | $v_i$ (MPa) |
|---|---|---|
| **$R_L$-REF** | 1097.3 | 0.49 |
| **$R_L$-STC** | 2552.1 | 0.94 |
| **$R_L$-ANC** | 2982.3 | 1.10 |
| **$R_L$-STANC** | 3651.7 | 1.35 |

Evaluation of the shear capacity at the interface was carried out according to Randl [22] and MC2010 [57]. The resisting mechanisms at the interface are divided into three main components: aggregate interlock, friction, and dowel action of the reinforcement crossing the interface, all calculated according to equations (5.2) and (5.3) taken from [22].

In [22] a distinction is made between stiff and more brittle behaviour of the interface in terms of the relative slip ($s$). This limit is set at 0.05 mm, governed by aggregate interlock and friction from external actions. For slips over this limit, the behaviour is considered more ductile, with adhesion replaced by friction/interlocking and dowel action.

$$s \leq 0.05mm, v_{R,ad} = c_a . f_{ctd} \leq 0.5 . \nu . f_{cd} \quad (5.2)$$

$$s \geq 0.05mm, v_{R,il+fr+dow} = c_r . f_{ck}^{\frac{1}{3}} + \mu . \rho_i . k_1 . f_{yd} + k_2 . \rho_i . \sqrt{f_{yd} . f_{cd}} \leq \beta_c . \nu . f_{cd} \quad (5.3)$$

These equations quantify both scenarios of rigid and ductile interface, without accounting for external actions that are favourable to the resisting mechanism, where:

$v_{R,ad}$ is the design value for the adhesive shear stress for the interface;

$c_a, c_r$ are the coefficients for surface condition, with reference values of 0.20 for $C_r$, considering a very rough finish of the existing surface;

$f_{ctd}$ is the design value for concrete tensile strength;

$\nu$ is the reduction coefficient for compressive forces ($\nu = 0.55.(30/f_{ck})^{1/3} \leq 0.55$);

$f_{cd}$ is the design value for concrete compressive strength;

$v_{R,il+fr+dow}$ is the design value for shear stress of the interface for interlocking, friction, and dowel action;

$f_{ck}$ is the characteristic compressive strength for concrete;

$\mu$ is the friction coefficient with reference values of 0.8 for characteristic concrete strengths greater than 20MPa, or 1.0 for such strengths greater than 35MPa;

$\rho_i$ is the ratio of reinforcement crossing the interface ($\rho_i = A_{s,i} / A_i$);

$k_1$ is the reinforcement performance reduction factor ($k_1 = \sigma_{s,i} / f_y \leq 1.0$) where $\sigma_{s,i}$ is the actual tensile stress in the steel crossing the concrete interface;

$f_{yd}$ is the design value for steel yielding stress;

$k_2$ is the interaction coefficient for flexural resistance of the rebar (≤ 1,6 for circular cross-sections and C20/25 - C50/60);

$\beta_c$ is the coefficient that accounts for the strut inclination of concrete in compression.

Coefficient $c_r$ is proposed as the standard value for very rough surfaces of 0.20 as recommended in [22,57]. One should notice that for the present case the interface comprises perpendicular tensile stresses at the ends of the overlay where debonding starts to occur, whereas the $c_r$ values according to [22,57] refer to non-tensioned interfaces (shear only). Considering the specimens with only surface preparation and no reinforcement crossing the interface, the resisting

mechanism can only account for the interlocking of contacting surfaces. From equation (5.2) the shorter and longer overlays thus resulted in 0.66 MPa ($R_s$-*REF*, 1 and 3) and 0.62 MPa ($R_L$-*REF*), respectively. Such calculations were performed considering the lower concrete compressive strength of each pair of layers in tables Table 3.7 and Table 3.8. These values overestimate the test results of tables Table 5.4 and Table 5.5 in 40% and 26%, respectively. The micro-cracking due to the surface preparation and the tensile stresses that result from equilibrium at the end of the interface (Figure 5.12) can justify this behaviour, debonding prematurely for a brittle resisting mechanism.

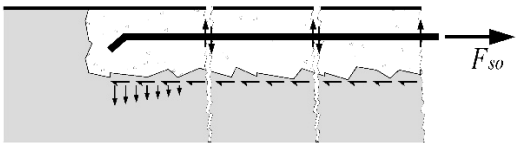


Figure 5.12 – Vertical tensile stresses at the end of an unreinforced interface.

The coefficient of friction $\mu$ was calculated with equation (3.1) in chapter 3, as proposed in [57] and also in [138] for very rough interfaces, where $R_{vm}$ is the mean valley depth accounting for five consecutive measurements on each roughness profile. Considering the roughness classification presented in section 3.2.1 and the values presented in Table 3.4, the friction coefficient takes the general value of 1.4. For the coefficient $k_I$ a new method is proposed, that contemplates the amount of horizontal force at the interface not resisted by dowel action of the rebar. This shear force at the interface ($k_{-F} \cdot \Delta F_{so}$) is accounted for in the quantification of the steel stresses for the rebars crossing the interface, by means of a coefficient '$k_{-F}$' as follows:

$$\sigma_{si} = \frac{(F_{s,anc} \text{ or } F_{s,c})}{A_{si}} = \frac{(k_{-F}.\Delta F_{so}).\tan\theta}{A_{si}} = \frac{k_{-F}.\nu_i.\tan\theta}{\rho_i} \tag{5.4}$$

Where $F_{s,c}$ is the tensile force in the steel connectors or longitudinal rebar anchorage and $\rho_i$ is the reinforcement ratio crossing the interface ($A_{si}/A_i$). $\theta$ is the angle between the interface plane and the concrete strut that results from nodal equilibrium, as illustrated in Figure 5.13.

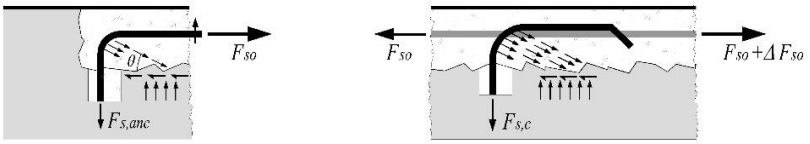


Figure 5.13 – Resisting mechanism of the overlay rebars anchorage (left) and shear connectors (right).

The values for the coefficient $k_{-F}$ were determined according to the amount of stresses resisted by dowel action of the rebar crossing the interface. Around 70 % of the total horizontal load at the interface for the steel connectors was determined for the aggregate interlock and friction resisting mechanisms ($k_{-F}$ = 0.7). The remaining stresses were then resisted by dowel action of the rebars. For the specimens with longitudinal rebar anchored, the value $k_{-F}$ was reduced in half ($k_{-F}$ = 0.35) empirically with good approximation to the test results, since the edge lifting phenomenon is

present, thus resulting in tension of the anchored rebars. An angle $\theta$ of 21.8 º was considered, with good correlation to test results, which is also the lower bound for the angle of concrete struts according to [101]. The considered values for these parameters are a tentative approach to account for the rather complex situation at the overlay edges subjected to delamination. Such premises were confirmed through the experimental tests and respective correlation of analysis results. Dowel action resistance alone can be calculated according to [22] with equation (5.5), where maximum allowable dowel action of the reinforcement is scaled down due to the interaction between bending and tensile stresses in the rebars ($\sqrt{1-k_1^2}$), and due to the relative slip of the interface crack ($\sqrt{s/s_{max}} \leq 1.0$). This phenomenon is particularly important for surfaces with a higher roughness, where horizontal relative displacement leads to vertical displacement, causing the interface crack to open.

$$V_F(s) = V_{F,máx} \cdot \sqrt{s / s_{máx}} \cdot \sqrt{1 - k_1{}^2} \leq \frac{A_{si} \cdot f_y}{\sqrt{3}} \tag{5.5}$$

Where:

$V_{F,máx} = k_2 . A_{si} . \sqrt{f_{c,cube} \cdot f_y}$ is the maximum allowable force for dowel action;

$A_{si}$ is the area of the reinforcement crossing the interface;

$f_{c,cube}$ is the concrete compressive strength in cubic specimens;

$f_y$ is the steel yield stress;

$s$ is the relative slip of the layers at the interface;

$s_{\max}$ is the relative slip for $V_{F,\max}$ , limited to 0.10Ø - 0.20Ø.

The coefficient $k_2$ is taken as 1.5, fitting within the values prescribed in [22], without safety factor. The value for the resisting stress that results from dowel action, considering the limit $s_{max} = 0.10Ø$, are presented in the table below:

Table 5.6 - Dowel action resistance for shorter overlays.

| Specimen | $R_S$-STC | | | | $R_S$-ANC | | | | $R_S$-STANC | |
|---|---|---|---|---|---|---|---|---|---|---|
| | 1 | 3 | 4 | 5 | 2 | 3 | 4 | 5 | Ø6 | Ø12 |
| $A_{si}$ (mm²) | 336 | | | | 678 | | | | 336 | 678 |
| s (mm) | 0.48 | 0.53 | 2.38 | 1.63 | 0.51 | 0.49 | 1.32 | 1.66 | 1.69 | |
| $k_1$ (-) | 0.34 | 0.35 | 0.59 | 0.66 | 0.24 | 0.21 | 0.32 | 0.16 | 0.25 | |
| $V_F$ (kN) | 62.5 | 62.2 | 60.6 | 61.8 | 91.1 | 91.7 | 140.1 | 146.1 | 72.7 | 146.7 |
| $v_F$ (MPa) | 0.21 | 0.21 | 0.20 | 0.21 | 0.30 | 0.31 | 0.47 | 0.49 | 0.73 | |
| $v_F/v_i$ (-) | 0.29 | 0.27 | 0.16 | 0.15 | 0.30 | 0.34 | 0.34 | 0.36 | 0.45 | |

Contribution of the rebar crossing the interface is significant, accounting in the $R_S$-STANC solution for almost half the horizontal load at the interface by dowel action of the rebar. For most

of the other specimens, this mechanism accounted for around one third of the horizontal load at the interface. The remaining resisting mechanisms at the interface can then be estimated according to [22] with equation (5.6), and are presented in Table 5.7 along with the total value for the resisting strength of the interface.

$$v_{il+fr} = c_r \cdot f_{cm}^{1/3} + \mu \cdot k_1 \cdot \rho_i \cdot f_y \tag{5.6}$$

Table 5.7 - Shear stress for friction and interlocking of protruding aggregates.

| Specimen | RS-STC | | | | RS-ANC | | | | RS-STANC |
|---|---|---|---|---|---|---|---|---|---|
| | 1 | 3 | 4 | 5 | 2 | 3 | 4 | 5 | |
| $v_{il}$ [MPa] | 0.64 | | 0.64 | 0.68 | 0.62 | | 0.63 | 0.65 | 0.64 |
| $v_{fr}$ [MPa] | 0.29 | 0.30 | 0.49 | 0.55 | 0.20 | 0.18 | 0.27 | 0.27 | 0.31 |
| $v_{fr+il}/v_i$ [-] | 1.27 | 1.24 | 0.90 | 0.88 | 0.81 | 0.88 | 0.66 | 0.67 | 0.59 |
| $v_{fr+il+F}$ [MPa] | 1.13 | 1.14 | 1.33 | 1.44 | 1.12 | 1.11 | 1.37 | 1.40 | 1.69 |
| $v_{fr+il+F}/v_i$ [-] | 1.55 | 1.51 | 1.06 | 1.02 | 1.10 | 1.21 | 1.00 | 1.03 | 1.05 |

Analysing the table above one can observe that when enough anchoring is provided to reinforcement crossing the interface, aggregate interlock and friction can account for 90 % of the resisting mechanism when using steel connectors (STC, 4 and 5). This value can decrease to two-thirds of the shear capacity of the interface when longitudinal reinforcement is anchored at the end of the overlay (ANC, 4 and 5). Such phenomenon attests to the importance of the edge lifting phenomenon on differential deformations between layers. Figure 5.14 shows how the estimated components of the resisting mechanism weigh on the capacity of the strengthened specimen's strength, and the corresponding correlation to experimental results.

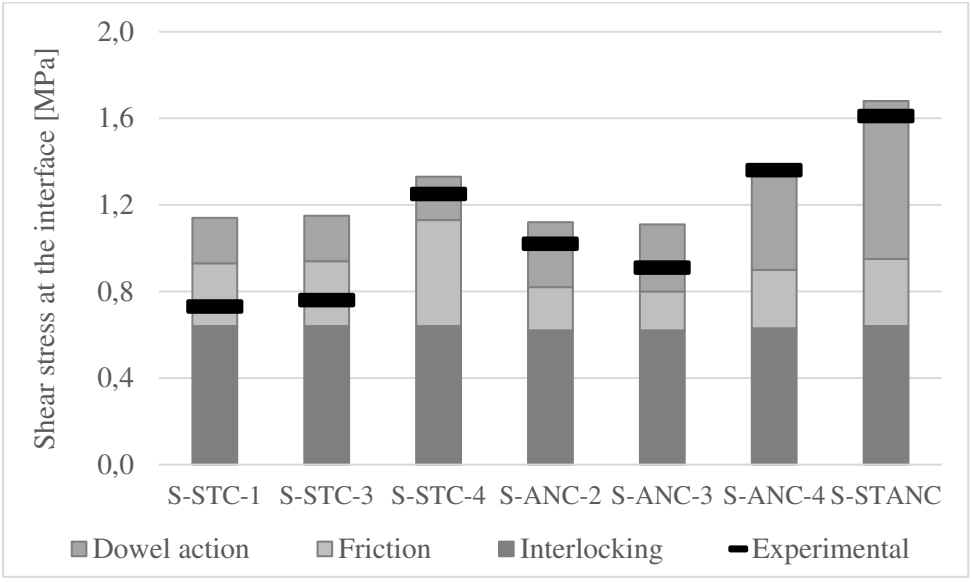


Figure 5.14 – Short overlays' estimated shear stresses at the interface and experimental shear stresses.

An overestimation for the shear resistance at the interface seems characteristic for the specimens with smaller anchoring of the reinforcement crossing the interface ($R_S$-STC-1, $R_S$-STC-3, $R_S$ ANC-2 and $R_S$-ANC-3, see Figure 5.14). A good correlation with the model is found for the specimens with proper anchoring of the reinforcement crossing the interface ($R_S$-STC 4 and 5, $R_S$-ANC 4 and 5, and $R_S$-STANC, see Figure 5.14). The anchorage length of the reinforcement crossing the interface shall be determined considering the resistance of the grout used in the hole, the total roughness of the surface, and the failure mechanisms of grouted anchors under shear and tension, according to [30].

The same considerations regarding the specimens with longer overlays resulted in a very good correlation to experimental results, considering the adaptation of the proposed coefficient $k_{-F}$ to values half of the previously stated, respectively 0.35 for shear connectors and 0.175 for anchored reinforcement. The correspondent shear stresses that result from dowel action, again considering the same limit as before ($s_{max}$ = 0.10Ø) are presented in Table 5.8.

Table 5.8 - Dowel action resistance for longer overlays.

| Specimen | $R_L$-STC | $R_L$-ANC | $R_L$-STANC Ø6 | $R_L$-STANC Ø12 |
|---|---|---|---|---|
| **$A_{si}$ (mm²)** | 336 | 678 | 336 | 678 |
| **s (mm)** | 1.17 | 0.96 | 0.69 | |
| **$k_1$ (-)** | 0.37 | 0.11 | 0.18 | |
| **$V_F$ (kN)** | 38.8 | 88.0 | 73.9 | 168.2 |
| **$v_F$ (MPa)** | 0.13 | 0.29 | 0.47 | |
| **$v_F/v_i$ (-)** | 0.14 | 0.27 | 0.35 | |

Analysing the table above, one observes the reduction in dowel action contribution to the resisting mechanism. Such reduction resulted in around 40 % less contribution in terms of $V_F$ on specimens STC and ANC, with the STANC specimen results in the same order as the shorter overlay specimens'. Such behaviour can be explained with the overlaid concrete being uniformly anchored to the substratum through the steel connectors and the anchored longitudinal reinforcement. The same ratio could also be observed for $V_F$ between the STC and ANC specimens, and each of the respective components on the STANC specimen. Contribution of dowel action threshold was set at one third of the horizontal load for the STANC specimen, and lower on the other two specimens. The remaining resisting mechanisms at the interface can then be estimated the same way as before according to [22] with equation (5.6). The resulting values are presented on the table below, along with the total value for the resisting strength of the interface.

Table 5.9 - Shear stress for friction and interlocking of protruding aggregates.

| Specimen | $R_L$-STC | $R_L$-ANC | $R_L$-STANC |
|---|---|---|---|
| **$v_{il}$ (MPa)** | 0.62 | 0.70 | 0.70 |
| **$v_{fr}$ (MPa)** | 0.18 | 0.11 | 0.22 |
| **$v_{fr+il}/v_i$ (-)** | 0.85 | 0.73 | 0.68 |
| **$v_{fr+il+F}$ (MPa)** | 0.93 | 1.10 | 1.39 |
| **$v_{fr+il+F}/v_i$ (-)** | 0.99 | 1.00 | 1.03 |

Contributions of the several components of the resisting mechanism can also be graphically observed in Figure 5.15, similar to shorter overlay specimens' analysis, showing the good correlation to experimental loads measured.

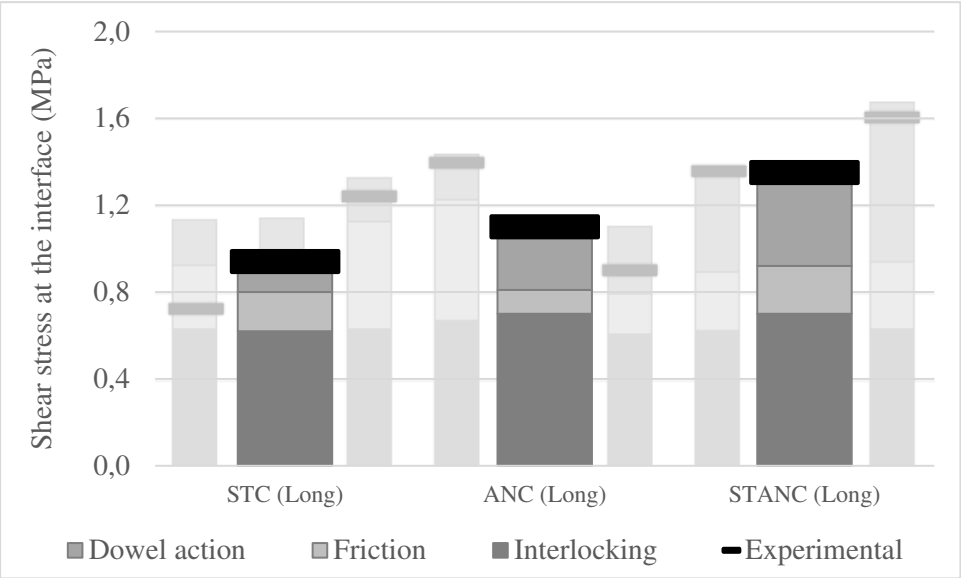


Figure 5.15 – Long overlays estimated shear stresses in the interface and experimental shear stresses.

Analysing the figure, the good correlation of the estimated resistance with experimental values is evident, verifying the applicability of the method to concrete slabs strengthened with overlaid concrete. A decrease in dowel action contribution could also be observed on the ANC and STANC specimens. This phenomenon can be justified by the variation in cross-section geometry occurring further from midspan and the longer strengthened portion of the slab span, which allows for a more evenly distributed cracking of the overlaid concrete.

Such considerations allowed for an estimation of the stress at the interface in accordance to experimental test results and suggest a variation in terms of the behaviour due to short or long overlays. Since dowel action is activated for higher horizontal relative displacements, the behaviour observed on specimens with longer overlays suggests that flexural cracking of concrete reduces the relative displacement between the two layers at the edge of the overlay and therefore dowel action is deprecated by aggregate interlock and friction. For continuous overlays, the proposed coefficient $K_{-F}$ could be taken as a unit value.

Regarding the anchorage itself, strains were also measured to assess the pull-out force due to relative displacement between layers. The anchored portion on the edge after the bend of longitudinal reinforcement in the overlay is subjected to tension. The change in direction of forces due to the bent reinforcement results in a Compression-Tension-Tension (C-T-T) node where a strut develops on the concrete inside the bend of reinforcement.

Since the anchored reinforcement crosses the surface of the substratum, relative displacement between both layers leads to a shear deformation of the former. Also, the coordinate chosen for strain measurement was at the interface level. Relative deformation is greater when further away from midspan, but due to the placing of strain gauges, it also measures the kinking effect [156] from the higher shear deformation, hence the higher strains presented below in Figure 5.16.

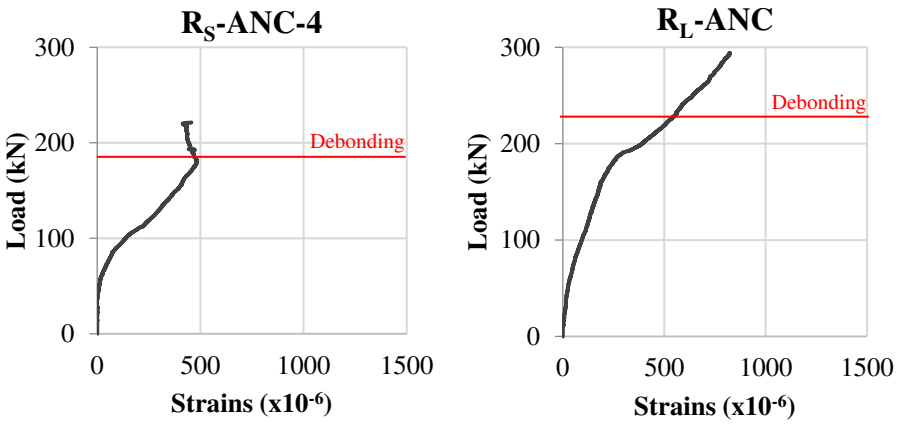


Figure 5.16 – Strains on the longitudinal reinforcement anchorage of rectangular ANC specimens.

Analysing the figure above, one can notice the increase in strain on the $R_L$ specimen for the same load as when reinforcement strains of both layers at midspan crossed each other (Figure 3.73). The angle θ in Figure 5.13 can then be calculated at debonding and at failure and is presented in Figure 5.17.

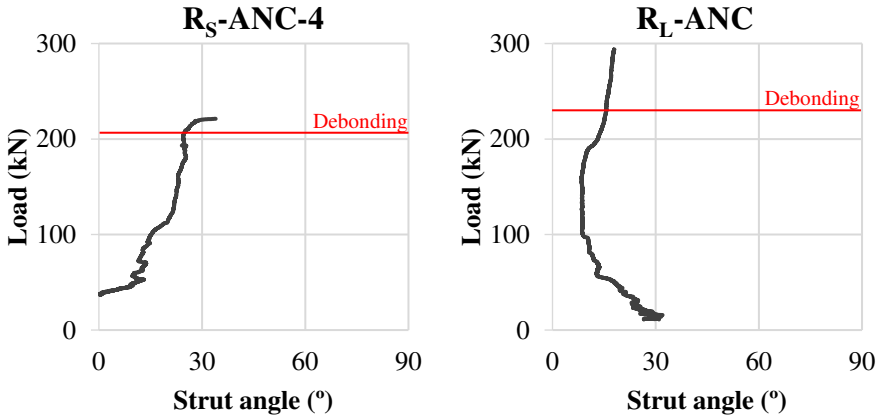


Figure 5.17 – Angle of the strut on the reinforcement bend of rectangular ANC specimens.

The evolution of such angle differed between specimens. It started small on the $R_S$ specimen, evidence of higher horizontal stresses at the anchored end and consequently higher shear. Over the loading history, this angle rose as an evidence of higher tensile stresses due to the interface crack. The $R_L$ specimen's strut angle decreased over the loading history. Observing the sawcuts in 3.3.2, one can see the critical shear crack reaching the anchored reinforcement horizontally in

the $R_S$ specimen and vertically on the $R_L$ specimen. This is in accordance with the angles observed below, where the horizontal crack denotes higher vertical stresses, although the vertical crack may not be directly related to horizontal stresses.

## 5.3. Proposal for RCO strengthening of column-supported slabs

Punching testing of column-supported slabs was performed on two main sets of test specimens with different perimeters of the RCO strengthening patch ($S_{4D}$ and $S_{3D}$) according to the dimensions in Table 4.1, comprising the detailing of flexural and interface crossing reinforcement preconised for stitching the two layers. The dimensions of the second set of tests ($S_{3D}$) were defined similarly to the rectangular specimens regarding the thickness and flexural reinforcement on both layers.

Given the nature of concentrated stresses in the column region, the limitation of the column-slab connection can result in punching of the slab. Current design codes then allow for the calculation of punching capacity of a simple column-slab connection with an orthogonal mesh of flexural reinforcement and specific shear reinforcement. The strengthening solution in this work results in multi-layer flexural reinforcement in the column region, along with a concrete-to-concrete interface between the contacting layers. Such condition requires the analysis of the code provisions for fitting the behaviour or RCO strengthened slabs due to the multi-layer reinforcement and different concrete strength of the existing structure and strengthening.

Due to the different concrete strengths of each specimen and also between the two layers of the strengthened cross-section, failure loads were normalised on all specimens for assessing the increase in strength due to the RCO. This was performed according to equation (5.7) below, where $V_{Spec}$ is the punching strength of the specimen, $f_{c,Ref}$ and $f_{c,Spec}$ are the reference and respective specimen compressive strength. The power of 0.41 was taken from [157], where good correlation was achieved when normalising punching failure loads by concrete compressive strength.

$$V_{Norm} = V_{Spec} \cdot \left( \frac{f_{c,Ref}}{f_{c,Spec}} \right)^{0.41} \tag{5.7}$$

The concrete strength of each strengthened specimen was considered according to [155] as the substratum compressive strength $f_{c,Sub}$, taken as a conservative approach due to the lower compressive strength of existing concrete ($f_{c,Spec} = f_{c,Sub}$). Since only the $S_{3D}$ specimens comprised an unstrengthened specimen ($S_{3D}$-SUB), normalisation of the failure load was performed by considering the compressive strength for the reference specimen of each set ($S_{4D}$-REF and $S_{3D}$-REF). The values for the unstrengthened variants of the specimens were attained through numerical modelling of the substratum geometry of each specimen, also normalised to the reference specimens' concrete strength. With such premises, the performance gains were assessed and are presented on Table 5.10.

Table 5.10 – Normalised and substratum failure loads of the column-supported slab specimens.

| | $S_{4D}$ specimens | | | $S_{3D}$ specimens | | |
|---|---|---|---|---|---|---|
| | **Unstrengthened** | **Strengthened** | **Strengthened / Unstrengthened** | **Unstrengthened** | **Strengthened** | **Strengthened / Unstrengthened** |
| **REF (kN)** | 330.3 | 559.8 | 1.69 | 200.1 | 217.8 | 1.09 |
| **STC (kN)** | 285.2 | 608.6 | 2.13 | 265.6 | 290.8 | 1.09 |
| **ANC (kN)** | 345.3 | 526.0 | 1.52 | 203.5 | 458.5 | 2.25 |
| **STANC (kN)** | 273.5 | 582.0 | 2.13 | 250.3 | 513.9 | 2.05 |

Due to the proximity of the RCO's edge to the column face on the $S_{3D}$ specimens, anchoring of flexural reinforcement is of the utmost importance, since the short overlay is in a zone of higher stresses. For such cases, steel dowels are not effective due to the higher stresses that result in the edge of the overlaid concrete and lead to the formation of the critical shear crack or debonding. Analysing the table above one can observe how the increase in the ultimate failure load of RCO strengthened slabs was affected, namely:

- The $S_{4D}$ specimens, due to the limit of the larger RCO area closer to the line of contra-flexure, allowed for a significant increase in strength of the specimens since smaller stresses at the ends of the overlay delay the debonding phenomenon further in the loading history. This fact can help characterise the failure load of the $S_{4D}$-REF specimen close to the load of the $S_{4D}$-ANC specimen;

- Due to the fact that anchoring of longitudinal reinforcement is far from the column face, the importance of steel connectors rises and thus results the failure load of the $S_{4D}$-STC close to the failure load of the $S_{4D}$-STANC specimen;

- In the $S_{3D}$ specimens, the edge of the RCO area further from the line of contra-flexure results in greater stresses of the anchored ends of longitudinal reinforcement due to the higher flexural stress state closer to the column support. This assists the importance of the flexural reinforcement and the increase in strength of the $S_{3D}$-STC of the $S_{3D}$-STANC, where anchoring of such reinforcement allowed for the effective mobilization of stresses on the RCO reinforcement and consequent higher failure load;

- The RCO strengthening was not effective on the $S_{3D}$-REF specimen, since stresses of the RCO flexural reinforcement were not mobilized. The same principle could be observed on the $S_{3D}$-STC specimen where the steel connectors were not enough for mobilizing stresses on the RCO flexural reinforcement, as stated by the observed failure mode.

The lowest strength gain of the $S_{4D}$ specimens could be observed for the $S_{4D}$-ANC specimen, which still guaranteed a 50% increase in punching capacity of the strengthened cross-section. For comparison, the analogous specimen of the $S_{3D}$ set attained a load increase larger than two times the original punching strength. The highest strength gains allowed for a strength increase larger than double the initial strength of the substratum on both the $S_{4D}$ and $S_{3D}$ sets, accounting for the specimens with stitching reinforcement on the former and anchoring of reinforcement on the latter.

Strengthening with RCO alters the slab stiffness since the height of the section is changed to accommodate the overlaid concrete. Such change is susceptible to impact the slab behaviour in a way that the size of the strengthened area could impact the structural response of the column-slab connection. The Critical Shear Crack Theory (CSCT) sets a failure criterion that characterises punching strength of a given slab when intersected by the load-rotation relationship of the slab. Such failure criterion is characterised by a semi-empirical approach quantified by equation (2.29), as introduced by Muttoni [127]. One of the main parameters of the CSCT is the effective depth *d* of the structural element, which is altered with a new concrete overlay well bonded to the existing slab [158]. Such parameter should be weighed according to the stiffness of each layer, resulting a new effective depth $d_{eq}$:

$$d_{eq} = \frac{d_s . A_s + d_o . A_o}{A_s + A_o} \tag{5.8}$$

The concrete strut that for a proper degree of monolithic behaviour should develop through the interface between the two layers leads to weighing the aggregate size by the geometric parameters of each layer, thus resulting in the equivalent aggregate size $d_{g,eq}$. Such consideration has also been used by Inácio [159] with good correlation to test results.

$$d_{g,eq} = \frac{d_{g,s} . h_s + d_{g,o} . (h_{sc} - h_s)}{h_{sc}} \tag{5.9}$$

This term rules the interlocking phenomenon responsible for stress transfer in the shear crack, depending on the aggregate size ($d_g$) and reference aggregate size ($d_{g0}$). This model allows for accounting slab rotation ($\psi$), which rules the shear crack opening ($w = \psi \cdot d$) and is calculated according to the level of approximation deemed required for the analysis.

Calculation of the critical shear crack opening $\omega$ depends on the slab rotation $\psi$ that can be calculated by the semi-analytical equation (2.39). The factor of proportionality $k_m$ can yield the values of 1.5 or 1.2, depending on whether a level of approximation II or III is considered according to [160]. $V_{flex}$ is the load necessary for developing the flexural mechanism of the slab, as illustrated by the yield lines in Figure 2.60, given by the yield line theory presented in [129], quantified by Equation (5.10):

$$V_{flex} = \frac{4 . m_R}{r_q . \left(\cos\left(\frac{\pi}{8}\right) + \sin\left(\frac{\pi}{8}\right)\right) - c} . \frac{B^2 - B . c - c^2/4}{B - c} \tag{5.10}$$

Where $r_q$ is the radius of the applied load, $\pi/8$ is the angle between point loads or axis of symmetry, $B$ is the length of the slab and $c$ is the column size. The resisting moment of the slab $m_R$ is given by equation (2.36), considering the equivalent effective depth and respective equivalent reinforcement ratio. The latter ratio accounts for reinforcement on both layers, since both contribute for the flexural and punching capacity of the slab. Therefore, a $\rho_{eq}$ parameter, weighed on the geometric characteristics of each layer should be calculated. The flexural yielding moment provided by both layers of reinforcement is then $f_y.(d_s.A_s + d_o.A_o)$, which equals the flexural yielding moment provided by the equivalent reinforcement tensile capacity $f_y.\rho_{eq}.{d_{eq}}^2$. Considering the quantification of $d_{eq}$ provided by equation (5.8) results the equivalent reinforcement ratio:

$$f_y.\rho_{eq}.{d_{eq}}^2 = f_y.(d_s.A_s + d_o.A_o) \cong \rho_{eq} = \frac{A_s + A_o}{d_{eq}} \tag{5.11}$$

Such consideration requires for a higher degree of monolithic behaviour, provided by the interface detailing that was performed on the strengthened specimens. An important parameter is the radius of the slab $r_s$. Such parameter states the distance from the axis of the column to the line of contra-flexure. Such consideration of strengthening with RCO and the punching phenomenon requires proper anchoring of the longitudinal tensile reinforcement on discrete layers, whose geometrical discontinuities lead to the edge lifting phenomenon and premature debonding of overlaid concrete [47,169]. Considering the distance *2d* preconised on [101] for the punching control perimeter, the lower bound dimension of the overlay patch should always exceed this value. The effective lower bound for the RCO dimensions should be at least three times the strengthened cross-section effective depth, accounting for the anchorage length of reinforcement. This is the minimum distance for comprising the punching phenomenon within the RCO area.

The Eurocode 2 (EC2) [101] shear provisions for slabs without shear reinforcement present an empirical design equation for estimating the punching shear strength of flat slabs, calculated according to equation (2.34). On the MC2010 [57], the basic control perimeter ($b_0$) is set at a distance of half the slab's effective depth. Accounting for the values of each reinforcement cross-sectional area and respective effective depth yields the equivalent effective depths of approximately 0.138m and 0.120m respectively for the $S_{4D}$ and $S_{3D}$ specimens. The punching strength calculated according to each design code is presented in Table 5.11, where the Level of Approximation III was considered for the MC2010 approach. Calculation of the punching strength was performed considering the cylindrical compressive strength of the substratum concrete since its where the greater portion of compressive stresses occur. The equivalent effective depth of the strengthened cross-section given by equation (5.8) and respective equivalent reinforcement ratio given by equation (5.11) were also considered for estimating punching strength through both codes. The equivalent aggregate size preconised before through equation (5.9) was also considered for the MC2010 approach. The premature failure of the $S_{3D}$-REF specimen results in an overestimation of its failure load through both codes considered. Therefore it is only qualitatively presented in the following table, yielding a ratio around 50% when compared to current design codes.

Table 5.11 – Failure loads and comparison to code provisions of both test specimen geometries.

| | | Failure loads of strengthened specimens | | | | |
|---|---|---|---|---|---|---|
| | | **EXPerimental** | **Euro Code 2** | **EXP/EC2** | **Model Code 2010** | **EXP/MC2010** |
| | | **(kN)** | **(kN)** | **(-)** | **(kN)** | **(-)** |
| $S_{4D}$ | **REF**(*) | **559.8** | 566.4 | 0.99 | 580.5 | 0.96 |
| | **STC** | **567.6** | 526.7 | 1.08 | 520.6 | 1.09 |
| | **ANC**(*) | **535.8** | 578.1 | 0.93 | 598.6 | 0.90 |
| | **STANC** | **549.8** | 522.0 | 1.05 | 513.5 | 1.07 |
| $S_{3D}$ | **SUB** | **298.0** | 292.6 | 1.02 | 315.4 | 0.94 |
| | **REF** | **217.8** | 407.8 | 0.53 | 488.9 | 0.45 |
| | **STC** | **313.8** | 441.5 | 0.71 | 550.8 | 0.57 |
| | **ANC** | **467.3** | 396.4 | 1.18 | 468.5 | 1.01 |
| | **STANC** | **502.5** | 418.8 | 1.20 | 508.5 | 0.99 |

(*) – debonding failure

Analysing the above results, it is possible to realise the difference between code provisions applied to both geometries of the RCO patch area:

- The larger area of the $S_{4D}$ specimens allowed for code provisions to suit the experimental results with the same degree of approximation, overestimating the punching strength of the STC and STANC specimens, and underestimating it for the REF and ANC specimens;

- Differences arise when applying the code provisions to the smaller RCO patch area, where an overestimation of the $S_{3D}$-STC specimen failure load resulted in excess of 30% for the EC2 and 40% for the MC2010;

- Specimens with a higher degree of monolithic behaviour – $S_{3D}$-ANC and $S_{3D}$-STANC – were underestimated in excess of 20% by the EC2, with MC2010 suiting such results with a minimal variation.

The different failure mode of the $S_{3D}$-STC specimen resulted in lack of adjustment from current design codes. The smaller angle of the critical shear crack resulted in the intersection of only the substratum, with no visible shear cracking of the overlaid concrete nor debonding of the interface. Monolithically, stresses would reach the overlaid concrete reinforcement at a distance close to two times the effective depth of the composite cross-section, as observed on the $S_{3D}$-ANC and $S_{3D}$-STANC specimens. In Figure 4.39 one can observe the critical shear crack evolving below the shear connectors until reaching the edge of the strengthened area where geometry changes abruptly. Such consideration results in a critical shear crack with a slope close to 15º, from the column face to the edge of the RCO patch, as shown in Figure 5.18. Despite the lack of anchored reinforcement on such boundary, it did not debond and failure occurred only on the substratum. Experimentally, the punching failure surface resulted about the same as the RCO patch. Consequently, the angle of the critical shear crack resulted smaller than current punching failure results.

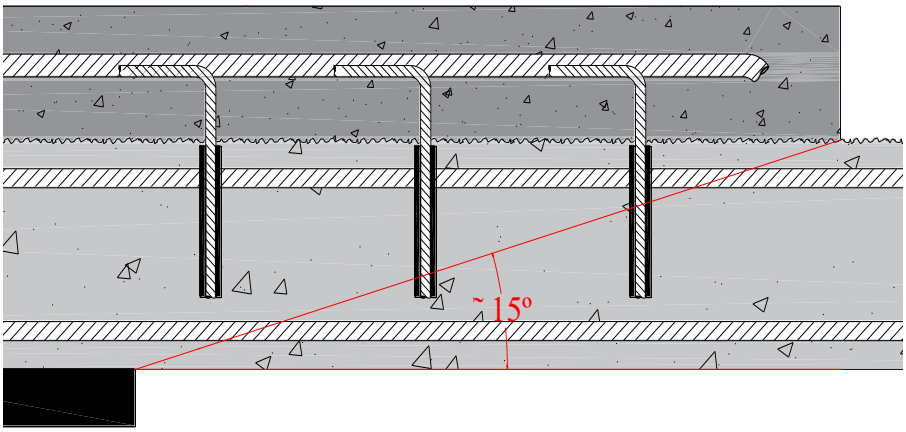


Figure 5.18 – Resulting angle of the critical shear crack for the $S_{3D}$-STC specimen.

When considering the behaviour model by Bompa and Onet [132] presented in Figure 2.65 of chapter 2, a punching capacity of 343kN can be calculated. Such value is considerably smaller than the one predicted by the design codes, given the smaller slope of the critical shear crack, resulting in a better fit to the experimental result of this specimen.

## 5.4. Designing a concrete-to-concrete interface

### 5.4.1. Materials and overall economy of the process

The use of the standard and traditional materials concrete and steel, along with the cementitious grout for anchoring reinforcement on the existing structure, validates the use of RCO strengthening on concrete structures. Higher performance materials can be opted for, such as self-compacting concrete (SCC) for thin RCO applications, due to difficult vibration of concrete, or when vibrating concrete may cause damage either to the surface or the reinforcement detailing and respective shear connectors. Such material was used in the structural strengthening of slabs presented in Figure 1.3 of section 1.1. The use of fibre-reinforced concrete (FRC) with either steel or composite fibres, can also be used and is compatible with this strengthening technique, mainly due to its application on the tensile face of structures, thus controlling the crack opening. Regarding the anchoring of reinforcement, the option for an epoxy-based bonding agent can result in an improved behaviour of interface crossing reinforcement. That option arises when the existing structure allows only for small anchorage lengths.

The degree of compatibility between existing and strengthening materials is then decided by the soundness of the existing structure. Such condition is also one of the advantages of RCO strengthening, which can repair the existing structure by replacing deteriorated concrete with sound concrete of a higher strength class. This practice is recommended on [42], where proper bond between the two concrete layers requires sound concrete and no bond-inhibiting foreign materials such as loose particles or grease present at the interface. The same document states the mechanical evaluation of the existing structure's surface capacity for good bond through tensile testing.

Concrete is a brittle material that is prone to cracking. Techniques for preparing the existing surface are more or less damaging to the existing structure depending on the equipment adopted. The two techniques of milling with a jackhammer or hydro-blasting the existing surface differ on the capacity for causing microcracks on existing concrete. The latter is the most efficient and less damaging to the existing structure. It is also the technique with the heaviest logistics in size of the machines required and processing of residues, mainly the resulting mud from the cement. Such technique poses the problem of wet materials indoors, besides the concrete required for the overlay, and is recommended for larger areas or when accessible by such equipment. The former technique of milling with a jackhammer is the cheapest, with less specialized labour and simpler logistics. Therefore, it shall be considered for practical applications and also suitable for small or large areas. The aspect of the resulting surface when preparing the strengthened specimens in this work showed no evidence of brittle areas, with a uniformly rough surface throughout the interface, as observed in Figure 5.19.

Figure 5.19 – Milling the existing surface with a jackhammer: progressive milling and loose particles prior to cleaning the resulting surface.

Analysing the interface after failure of the specimens allowed to assess its integrity and identify where clear debonding occurred (adhesive failure) or when cohesive failure of any layer occurred. Overall, one can conclude that the surface preparation through milling with a jackhammer worked well, despite the resulting microcracking that could condition failure of the strengthened specimens nor the interface itself. Such statement was valid both for larger areas of the RCO and for smaller areas of pull-off specimens.

Consideration for this technique, along with the traditional materials, steel and cementitious grout, results in the overall economy of structural strengthening when compared to the use of steel bars or composite materials bonded to the existing structure. The technique of RCO can be on the lower-end of the economy spectrum since the use of traditional materials and non-specialized labour can keep the cost down to current strengthening of concrete structures.

Since concrete is the material responsible for the fire protection of steel reinforcement, and according to [162] is a material with highest class of fire protection, the technique of RCO strengthening is then adequate for fire resistance.

### 5.4.2. Preparation of the existing concrete

The work of removing the existing concrete is an important step towards the correct application of a strengthening technique that relies on bonding to an existing structure. The latter statement contemplates the soundness of existing concrete and the protection of existing reinforcement. According to Eurocode 2 [101], reinforcement requires a minimum concrete cover, not only for protection, but also for the correct dispersion of stresses around the rebar. A requirement for the correct preparation of the existing surface is then knowing the depth of existing reinforcement, preferably through non-destructive methods such as electromagnetic steel reinforcement detectors. Specifically in this work, a HILTI® Ferroscan® (PS200S) was used before preparing the surface of each specimen as illustrated in Figure 5.20, thus limiting the intersection of existing reinforcement. For assuring instrument readings or when no such instruments are available, the partial demolition of the existing concrete is recommended to assess the effective concrete clear cover.

Figure 5.20 – Using a magnetometer (left) and drilled holes (right) without intersecting the existing reinforcement.

This allows for an optimized concrete removal that guarantees protection of the existing reinforcement and the effective strengthening of the existing structure. Such characteristic is of the utmost importance to functioning structures where strengthening needs to be embedded within the existing structure. The removal of concrete from the surface for depths up to 10 mm can be performed directly with current tools such as the electric or pneumatic jackhammer.

Performing the surface preparation should be phased and not executed at once, with clearing of the debris between each turn of the jackhammer (phase). For depths greater than 10 mm, previous cutting of grooves with the desired depth are recommended. An example was performed in this work and is illustrated in Figure 5.21, where 30 mm of concrete were removed from the existing surface with previously cut grooves serving as guides to the desired depth.

Figure 5.21 – Proposed technique for removing concrete at depths greater than 10 mm.

### 5.4.3. Roughness of the existing concrete surface

Since roughness is an important factor for the monolithic behaviour of a concrete-to-concrete interface, its quantification becomes a priority on designing such interface. Despite the inclusion of interface crossing reinforcement, roughness still weighs on interface performance, as it is responsible for activating the tensile capacity of such reinforcement. Current design codes relate roughness to the interface strength, stating the need for very rough surfaces to attain higher shear stresses at the interface.

Assessment of the surface roughness can be performed through several methods, with the laser profilometer being the most accurate and advanced measuring of interface characteristics available [59]. The MC2010 (7.3.3.6) [57] suggests the Sand Patch Method as suitable for the correct assessment of surface roughness, despite its limitations to horizontal and rough to very-rough surfaces. This poses several limitations to using such method, with moisture, large grooves or a slope of the surface possibly altering the results. The same code also specifies that more advanced surface assessment methods can be used to determine surface characteristics, including laser profilometry, mechanical profilometry or photogrammetry. The method utilized in this work was the mechanical profilometry, which resulted in good assessment of surface characteristics and ease of use. The ongoing development of laser profilometry will state this method as the standard for the assessment of surface characteristics due to its, precision, practicality, portability and automatic calculation of surface parameters.

These parameters can quantify several profile characteristics as stated in section 2.3.5 of chapter 2, with the recommended parameters being the average roughness ($R_a$), total roughness ($R_t$) and mean-to-peak roughness ($R_p$). The latter is the parameter accounted for in the MC2010 (6.3.2) [57], taken directly from applying the sand patch method, but can also be calculated directly from the surface roughness profile. Average roughness and mean-to-peak roughness can assist on characterising the existing surface roughness, with the limits of 3.0 mm and 2.2 mm respectively for classifying as very-rough. Such classification is recommended for structural strengthening, where concrete-to-concrete interaction can govern the behaviour and capacity of the strengthened structure.

### 5.4.4. Reinforcement crossing the interface – anchoring and design

The need for reinforcement crossing the interface can be of two kinds:

- Anchoring the longitudinal reinforcement to the existing structure, thus reducing the need for a longer anchorage length and effective mobilization of stresses for the added reinforcement;

- Shear connectors on the interface for the dispersion of stresses over the interface, redundancy of the debonding mechanism and stitching of the added layer for strengthening.

Anchoring of longitudinal reinforcement at the ends of the overlay has proven to contribute to the monolithic behaviour of the strengthened structure. Such condition is true due the roughness of the interface which allows for stresses to be transferred between layers over the strengthened span. Therefore, the composite cross-section can work monolithically, although it is only anchored at the ends of the overlaid concrete. Failure then depends on the local failure of such anchorages, leading to debonding of the overlaid concrete, or reaching the cross-section's shear or flexural capacity. These also limit the interface crack opening, thus maintaining the contacting surfaces further in the loading history of the strengthened structure.

According to the experimental campaign presented in chapter 3, anchorage lengths up to 50 mm are susceptible to pull-out and should therefore be avoided. Such length depends on the need for shear and tensile strength of anchored reinforcement, which must be calculated for every case or structure. The local analysis for anchoring this reinforcement can be performed considering the equilibrium of the node where interface reinforcement meets longitudinal reinforcement. The resulting compressive strut with an inclination of $\theta$ shall guarantee the equilibrium between horizontal and vertical forces, where the increment of stress characterised for force $\Delta F_s$ has to be balanced by the anchored reinforcement $F_{anc}$, balanced by the concrete strut of force $F_c$. Due to the small relative slip of tenths of millimetre, the shear strength of reinforcement is therefore discarded.

$$\begin{cases} F_{anc} - F_c.\sin\theta = 0 \\ F_s + \Delta F_s - F_c.\cos\theta = F_s \end{cases} \equiv F_{anc} = \Delta F_s.\tan\theta \tag{5.12}$$

After determining the anchored force, one can calculate with equation (5.13) the needed lateral area for resisting the tensile stress and calculate the anchorage length ($l_{anc,calc}$) required for effectively embedding such reinforcement. Such capacity is determined by the bonding agent interface strength ($\tau_{anc}$), both for the steel - bonding agent and for the bonding agent - concrete interface. Due to the adopted technique for surface preparation of milling with a jackhammer, the resulting irregular surface of the interface leads to a shorter hole depth, thus resulting in smaller anchored lengths of reinforcement. The adopted method for compensating such loss of anchoring capacity consisted on accounting the total roughness ($R_t$) of the resulting contact surface cumulatively to the anchorage length. Thus, adding the total roughness of the resulting surface profile to such parameter was performed, resulting the required length ($l_{anc,req}$).

$$l_{anc,calc} = F_{anc} \cdot \tau_{anc} \tag{5.13}$$

$$l_{anc,req} = l_{anc,calc} + R_t \tag{5.14}$$

The adopted anchorage length in this work of 80 mm mentioned in section 3.2.1 of chapter 3 followed such principles, resulting without failure by pull-out of reinforcement. The horizontal force is balanced by the concrete strut and the tensile force of the shear connector. Such assumption can be accounted for due to the roughness of the interface and the capacity of concrete to resist the compressive stresses from bending of the shear connector. The angle of the compressive strut on this mechanism was assessed on section 5.2. The variation of such angle throughout the load history and the different result between the short and long overlays leads to the consideration of the value of 21.8º on the design proposal also in section 5.2. This value presented good approximations to experimental results on both short and long overlays and should therefore be considered.

A hole-diameter twice the size of the anchored rebar was defined in this work, with good results regarding the pull-out and the crushing of the bonding agent due to shear. Such parameter is then a requirement for grouted anchors, where the cementitious grout comprises small aggregates that can range up to 3.0 mm. This limitation becomes less important when prescribing an epoxy-based bonding agent, where the absence of aggregates leads to holes with a smaller diameter, always according to the manufacturer's specification.

### 5.4.5. Applying an RCO patch to existing structures

The application of an RCO patch to an existing structure requires full accountability for all the aforementioned parameters of surface roughness, anchoring of the added flexural reinforcement and the shear connectors crossing the interface. The perimeter of the strengthening with an RCO patch is then determined by a combination of the bending moment and the limits of the punching failure surface in flat slabs. Such perimeter was then assessed on the column-supported slab specimens of chapter 4, where the structural sensitivity to the RCO area was tested.

The line of contra-flexure of the bending moment was then taken as the upper bound limit of the RCO perimeter, which must account for the anchoring of flexural reinforcement. The anchoring of such reinforcement can be performed by extending the length of flexural reinforcement further from the line of contra-flexure, or by embedding in the existing structure through post-installed anchorages. Regarding the work in chapter 4, the distances of *4d* and *3d* were tested. Such distances of four and three times the strengthened cross-section's effective depth were defined greater than the larger perimeter of the punching failure surface, accounting also for the needed anchoring of flexural reinforcement after this perimeter. The latter is a requirement for the dowel action of such reinforcement on the punching mechanism.

Although possible, the small RCO at a distance of *3d* from the column perimeter led to consideration for the safer distance of *4d*. This was attested when testing the $S_{3D}$-STC specimen, where the perimeter of the critical shear crack resulted greater than the perimeter of the overlay. Observing the failure mode of this specimen on Figure 5.22, one can see the smaller slope of the critical shear crack that reached the edge of the overlaid concrete. It should be noticed that no

debonding phenomenon was observed, simply a shift in the slope of the critical shear crack. Comparing the failure mode of this specimen with its equivalent $S_{4D}$-STC specimen, one can observe how the shear connectors can shift the slope of the critical shear crack similar to specific punching reinforcement. An illustration of both specimens can be observed on the figure below.

Figure 5.22 – Critical shear crack slope on the STC specimens of the $S_{4D}$ (left) and $S_{3D}$ (right) sets.

The slope of the critical shear crack was around 28º (marked in yellow in Figure 5.22) for the $S_{4D}$-STC specimen, and generally close to such value for the rest of the specimens that failed through punching. The damage rendered unclear where the critical shear crack is effectively located on this particular specimen, but the rigid body portion that could be identified on the $S_{4D}$ specimen revealed an angle similar to that of the $S_{3D}$ specimen. Such conditions can identify a trend in the behaviour of such detailing with shear connectors on the interface of RCO strengthened structures. This leads to the need for analysing whether the structure's punching capacity governs failure and the respective control perimeter. If the latter accounts for specific punching reinforcement, then failure at the outer perimeter of such reinforcement is possible, and the distance of *4d* must be adjusted accordingly. Distances smaller than *4d* from the column perimeter should be avoided according to the results observed in this work and also due to the proximity of the punching failure surface.

## 5.5. Final remarks

The assessment of interface tensile capacity and comparison to several surface parameters, although not strongly correlated, assists in finding a way of characterising the surface capacity for bonding to a new concrete layer without direct tensile testing. Indirect methods for assessing surface characteristics are easier to use in situ and do not require destructive ways for assessing surface conditions. Since no strong correlation could be assessed between tensile strength and roughness parameters, the limits preconised on current codes and bibliography of 3.0 mm for the average roughness or 2.2 mm for the peak-to-mean roughness are recommended for classifying the surface as very rough. This is the recommended surface grade of finish, since a very rough surface can promote interlocking of two sliding layers, further activating the tensile capacity of interface crossing reinforcement.

Knowledge from the surface characterisation allowed for tuning the modified shear friction theory on current design codes for assessing the strength of concrete-to-concrete interfaces. Such tuning allowed for the characterisation of each component of the shear friction mechanism, adhesion, interlocking, friction and dowel action, thus fully characterising the interface behaviour. The results from the numerical modelling of rectangular specimens allowed for assessing stress distribution at the interface, which assisted in applying the dowel action component of the shear friction mechanism. The multiple rows of steel dowels led to a stress distribution dependent on the limiting capacity of such elements to interface crack opening. The vertical and horizontal measurement of strains also assisted on determining the horizontal and vertical stress components on the interface.

Since no significant relative displacement could be observed on the column-supported specimens, a general good fitting of experimental results could be observed when considering the current design codes, by weighing material properties to the stiffness of each layer. The optimization of the RCO patch resulted in some constraints to the application of such technique, namely due to the proximity to a higher stress field closer to the column support. Controlling the edge lifting phenomenon is then a requirement, allowing for a higher degree of monolithic behaviour and thus fitting with current design codes.

The determination of equivalent geometrical properties allowed for a good correlation to current design codes, namely the equivalent effective depth which allowed for quantifying an equivalent reinforcement ratio. When in the presence of multi-layer tensile reinforcement, an assessment of the equivalent tensile capacity can assist on determining the monolithic degree of a composite cross-section. The $S_{4D}$ specimens, due to the edge of the overlay being further from the higher flexural stresses that develop close to the column support, resulted more predictable when considering the quantification through current design codes.

Relating horizontal flexural stresses with vertical tensile stresses of the interface was performed by accounting for the inclination of the concrete compressed strut, thus allowing for designing the needed anchoring capacity of interface crossing reinforcement. This way, the differential of stresses of the longitudinal reinforcement can be effectively resisted by the interface reinforcement , therefore optimizing the behaviour and strength of the interface. Although the dowel action capacity is, conservatively, not accounted for in the design stage, such component of this reinforcement can contribute to the more ductile behaviour of the concrete-to-concrete interface.

Finally, the determination of an effective lower bound of *4d* from the column face when applying this strengthening technique should be considered to avoid the premature failure of strengthened structures. This makes for practical applications of the RCO strengthening technique on the tensile face of flat slabs at the column support region, where flexural and punching stresses are greater.

# 6. CONCLUSIONS AND FUTURE WORKS

This chapter presents the main conclusions withdrawn from the experimental testing and numerical modelling performed when assessing the performance of RCO strengthened slabs. Both geometries that were assessed allowed for the characterisation of a concrete-to-concrete interface's behaviour when on the tensile half of the composite cross-section.

The unidirectional specimens allowed for characterising the behaviour of the composite cross-section for dominant flexural stresses and greater relative displacements of the two layers. The column-supported slabs allowed for characterising the behaviour of such interface for dominant shear stresses, with a more rigid behaviour with small relative displacements of the two layers.

Such results were fitted with current design codes and theories, with proper calibration of relevant parameters and consequently good approximation to experimental values. Assisting this task with numerical modelling results allowed for better fitting of the results, namely the stress distribution across the interface which is of difficult assessment.

Guidelines were then defined for the proper application of an RCO strengthening method on flat slabs that are in service. Proper definition of a concrete-to-concrete interface using the analysis software ATENA 3D® was also presented, relying on the good results attained upon calibration of the numerical models.

## 6.1. Regarding the concrete-to-concrete interface

Roughness assessment and pull-off tests were performed to characterise the contact area between concrete layers cast at different times. Two-hundred and ten very rough interface specimens and eighteen specimens with light surface preparation through diamond grinding were tested to assess the tensile strength of the interface. This allowed for the characterisation of the substratum surface after preparation with heavy or light technique prior to casting the concrete overlay.

Surface roughness was assessed through a mechanical profilometry method by point measurement, which allows for assessing linear continuous profiles of rough surfaces. A very rough surface characterisation could be assessed due to the resulting surface profiles, when considering the peak-to-mean roughness parameter ($R_p$). Values for such parameter ranging from 2.2 mm ($R_L$-ANC specimen) to 3.8 mm ($S_{4D}$-ANC specimen) could be assessed, allowing for the characterisation of the existing surface as very rough. Pull-off testing was performed with a test setup developed specifically for this work, which allowed for assessing the interface tensile capacity with larger dollies than usually prescribed by the standards. These dollies, measuring 150x150mm$^2$, allowed for a larger and least heterogeneous contact surface for the specimens, by reducing the ratio between larger aggregates that are exposed during surface preparation and the total contact surface of the specimen ($A_{d_g}/A_{Spec}$).

Tensile capacity of the interface resulted from pull-off tests varied from 0.70 MPa to 1.44 MPa. This variability can be explained by each layer of the twenty specimens accounted for being of a different concrete mix and the heterogeneous surface preparation performed at different times, by

different people. Curing conditions, as well as the relationship between time of casting and testing were also different for each set of tests. Considering the adopted method for surface preparation, a weighed average tensile capacity of approximately 0.95MPa could be assessed, considering all the very rough interface test results.

Debonding was characterised on zones where the interface surface could be observed as adhesive or cohesive, thus classifying the bond failure and the resisting mechanism. The latter could be observed generally in the substratum layer, where concrete was weakest due to surface preparation that promotes microcracking and can decrease concrete's integrity. No strong correlation could be assessed for the several parameters of the interface in terms of cause and effect between surface roughness or concrete strength and the interface tensile capacity. The greatest correlation with pull-off strength was attained when considering the substratum tensile strength. This can be explained due to the aggressiveness of surface preparation that weakens the surface of the existing concrete, thus increasing the chance of the failure mode right below the interface.

Due to the statistical nature of the tensile failure, enriching the population of results through more tests is always needed for a more accurate assessment of the interface tensile capacity. The present dimensions seem sufficient for reducing the contribution of aggregates to the uncertainty of the results, so a variation in the size of the dollies should not be a priority due to the logistics of a larger test setup. A combination with horizontal loads should be designed for this type and size of dolly, since this is an important matter for sliding surfaces. The binary of forces that arise in a sliding situation should be reduced by designing the test system of combined forces with the least possible eccentricity regarding the sliding surface.

## 6.2. Regarding the flexural strengthening

Eighteen flexural tests were performed on slab specimens strengthened with a new concrete overlay divided in fourteen specimens with a shorter concrete overlay and four with a longer concrete overlay. Failure mode for each detailing of the interface was identified, along with several constraints to the application of this strengthening technique. Full debonding of the new layer occurred on the reference specimens, attesting the importance of stitching reinforcement crossing the interface. The difference of the anchorage length of such reinforcement attested the importance of sufficient anchoring for the integrity of the interface and proper capacity for transferring stresses. The small dispersion of results attests the constant behaviour of concrete elements strengthened with this technique, thus crediting its application in actual strengthening and retrofitting situations. A difference was observed for whether the change in the cross-section geometry occurred closer or further from midspan, where flexural stresses are higher.

One constraint identified after testing was the insufficient anchorage length of the reinforcement crossing the interface in a first series of tests with shorter overlays, which led to complementary tests. Insufficient embedment of interface crossing reinforcement in the existing layer penalized the capacity of the interface, leading to premature debonding. The embedment length of the steel connectors or anchoring of flexural reinforcement must account for both the tensile and shear anchorage failure mechanisms and the total roughness of the interface. This parameter should be

controlled on site, since it can affect the integrity of the strengthened structure due to the structural dependency of the interface.

When compared to the reference specimens, detailing with reinforcement crossing the interface reached a performance gain for each solution in terms of maximum shear stress at the interface. Rebar crossing the interface with greater anchorage length resulted in a performance gain of more than double the shear stress of the reference specimens. Even with insufficient anchorage length, the reinforcement crossing the interface resulted in a performance gain of 60 % to 110 % for the shear stress at the interface. For the solution with both steel connectors and longitudinal rebar anchored (STANC), the shear stress at the interface was over three times and over two times that of the reference specimens, respectively for the short and long overlays.

Provisions on the Model Code 2010 [57] for concrete-to-concrete interfaces fit well with the experimental results for specimens with proper anchoring of the reinforcement crossing the interface, considering the proposed coefficients. This was valid for both short and long concrete overlays. The method is dependent on good interaction between concrete layers for a good correlation to experimental results or estimation of interface bond capacity when designing a strengthening solution with overlaid concrete. The contribution of all components was identified on several scenarios of reinforcement crossing the interface and its variation with overlay dimensions.

The numerical FE models allowed to verify the stress distribution of the interface and the stress fields inside the concrete layers. The latter allows for the identification of the main stress paths that load the interface and impact stress distribution. This was the main topic to be analysed, since no access and no measurement was provided at the interface on experimental testing environment. Analysing all results from the numerical FE modelling on rectangular specimens, a good correlation with the experimental specimens was attained, with the behaviour observed during these tests occurring also in the computational environment. Numerical FE models load-deflection curves adjusted properly to experimental specimens, with differences smaller than 5%.

The unidirectional nature of the rectangular specimens allowed for isolating the stress transfer between concrete layers to one direction. Such characteristic is shared also with linear elements such as beams. As a future development, the parametric study by increasing the thickness of both the substratum and the overlay is relevant for assessing the behaviour of RCO strengthened elements with increasing stiffness. This study, besides enriching the population of results and allowing for better calibrating the calculation of the RCO strengthening technique, would allow for determining the optimal ratio of thickness between both layers and the change in structural response for stiffer strengthened cross-sections. This work should be preceded by a parametric FE modelling study of the same nature for future assessment through experimental testing, which would also contribute for the calibration of the concrete-to-concrete numerical interface.

## 6.3. Regarding the column-supported slabs

The test results presented allowed for assessing the performance and behaviour of the column-slab connection strengthened with an overlaid reinforced concrete layer on the top face. This type of strengthening increases the bending and punching strength, reduces cracking and increases the

stiffness of slabs. Two perimeters of strengthening were considered for assessing the lower bound distance from the column face. The perimeter of the strengthening layer was set at four times and three times the composite cross-section effective depth from the column face. Even though the shorter specimens resulted in less predictable behaviour, all specimens with reinforcement crossing the interface resulted in performance gains in terms of punching capacity and overall stiffness of the column-slab connection. Both the $S_{4D}$ specimens and the $S_{3D}$ specimens allowed for double the structural strength of the column-slab connection to punching.

The MC2010 [57] code provisions allowed for a more conservative load prediction when compared to the EC2 [101], both for the substratum and the full composite cross-section when no debonding occurred. The latter cross-section comprised two reinforcement layers working together, which led to estimating an equivalent effective depth that could characterise the theoretical effective depth considering a monolithic cross-section. This value was weighed between the effective depth of each layer, resulting below the interface on both geometries tested. Given that the composite cross-section worked throughout the loading history, this accounts for a monolithic factor of the cross-section.

The small variation in terms of punching capacity attests how concrete strength affected the results of the $S_{4D}$ specimens, largely varying its compressive strength throughout the tests. Considering the concrete strength of the substratum when analysing the RCO strengthened specimens allowed for the good approximation of experimental test results. Both the MC2010 [57] and EC2 [101] punching provisions reflected concrete strength, with the punching load of specimens with higher concrete strength overestimated on both codes. The punching load of specimens with a lower strength concrete was then underestimated on both codes.

The numerical analysis allowed for assessing the stress distribution, especially at the interface between the concrete layers, where stress transfer is of utmost importance for structural integrity. A maximum difference of 6 % was attained for the $S_{4D}$ specimens with reinforcement crossing the interface (STC and STANC), with the debonding phenomenon correctly modelled. A maximum difference around 10 % was attained for the specimens of the $S_{3D}$ geometry. The stress distribution could be identified for the cross-section and the interface, coherent with the behaviour of flat slabs subjected to a punching load. A perimeter of stresses at the interface was observed tangentially around the column, coherent with the punching phenomenon, stating the location of critical tensile stresses at the interface that cause debonding.

More tests are required for the correct assessment of the monolithic degree on a concrete-to-concrete interface like the one presented in this work. The variation of geometry, by varying the ratio of the RCO sides or its thickness, along with detailing of both longitudinal and stitching reinforcement size and ratio should be tested, aiming at further calibrating the design models of this strengthening technique. As a future development, performing punching tests on RCO strengthened specimens with eccentric loading would allow to assess the behaviour of the interface subjected to unbalanced loading of the flat slab. The asymmetric assessment of the interface strength should for the optimization of design to different scenarios where RCO strengthening may be applied.

## 6.4. Future developments

The results attained from the experimental tests, numerical models and respective analysis, allowed for making some considerations regarding the characterisation of concrete-to-concrete interfaces. Namely, the RCO strengthening method applied to structures in service requires some premises that account for the structural condition, geometric constraints and the need for strengthening. Several variations should be tested regarding the aforementioned topics, namely accounting for unloading the structure that comprises also cracking and residual deformation due to the load history.

An important factor to analyse in future developments of the technique is the strengthening of loaded structures. Strengthening during the load history of the structure can impact the behaviour of the composite cross-section, since cracking and shrinkage have already occurred on the existing structure. A variation of the strengthening technique by externally prestressing in the column region proposed by Faria [8] for punching of flat slabs, could be adapted to column-supported specimens for simulating an already loaded structure. This would be performed by loading a specimen up to 70-80% the punching failure load, for simulating the need for strengthening. Secondly, applying the aforementioned technique by inverting it to the compressed face of the specimen for holding the residual deformation, the existing cracks would remain open as the specimen is loaded. After strengthening with RCO, the specimen would then be loaded until failure, thus simulating the strengthening of a loaded structure, namely a building in service.

More tests are required for better characterisation of flat slabs strengthened with overlaid reinforced concrete. Variations in the detailing of the interface can also affect the overall behaviour of the strengthened structure. This should be assessed through varying parameters, such as cross-sectional area and placing of the stitching reinforcement near or further from the column face. The sensitivity of the critical shear crack slope should also be analysed since the potential for failure resulting outside the strengthened area increases with smaller areas of RCO. The possibility of doubling specific punching shear reinforcement as stitching reinforcement can shift the failure mode outside the strengthened area and should also be assessed on smaller and larger overlays.

The work performed on FE modelling of the strengthened specimens still requires the parametric numerical validation through non-linear analysis to assess the stress distribution at the interface due to the punching phenomenon. Such study should account for varying the geometry of the specimens, namely the thickness of each layer and its effect on the stiffness of the load-deflection relationship. Although the availability of several products on the field of nonlinear analysis software for structural concrete, the definition of a concrete-to-concrete interface should be feasible on most. This allows for the broader application of nonlinear analysis software, other than purchasing a specific software for concrete-to-concrete interface analysis. Other than the specific zero-thickness interface elements of ATENA 3D®, modelling the thickness of the transition zone should be accounted for. This should improve stress dispersion in the transition zone between layers of the composite cross-section.

Material-wise, there is room for improving the behaviour of RCO applied on the tensile face of flat slabs. The consideration for traditional materials like normal strength concrete (NSC) and reinforcing steel, without any bonding agents at the interface, was performed aiming at the least favourable conditions for applying the RCO strengthening technique. Due to the thin nature of concrete overlays, the use of self-compacting concrete (SCC) should be considered as a valid option for casting RC overlays. Therefore, such consideration should be tested and validated, both numerically and experimentally. Due to the application of RCO in the tensile face of flat slabs, the use of fibre-reinforced concrete (FRC) should be held valid since its ability to control cracking could result in the stiffer response of strengthened structures. By limiting the crack opening of concrete, the impact on the edge lifting phenomenon should be analysed since there is no immediate energy release mechanism like cracking in NSC.

Given the importance of stiffness in a column-slab connection, cyclic testing of RCO strengthened specimens is necessary for assessing the non-symmetrical loading of a concrete-to-concrete interface. This connection's stiffness relies on the monolithic behaviour of the latter interface and is directly affected by bonding of the two layers. The test setup developed by Almeida [163] would allow for the assessment of RCO strengthened specimens' behaviour when subjected to horizontal cyclic loads. This test setup would allow also for the eccentric loading of column-supported slabs and the analysis of the respective punching load and failure modes.

# 7. BIBLIOGRAPHIC REFERENCES

[1] Lew, H.; Center for Building Technology.; United States. Occupational Safety and Health Administration.; Investigation of construction failure of Harbour Clay Condominium in Cocoa Beach, Florida, NBS Building Science Series 145, 1982.

[2] Park, T.; Inspection of collapse cause of Sampoong Department Store, Forensic Science International, Vol. 217: pp. 119–26, 2012.

[3] Koppitz, R.; Effect of Deformation History on Punching Resistance of Reinforced Concrete Slabs PAR 2015, Vol. 6472, 2015.

[4] D 0226 Documentation.; Sécurité structurale des Parkings couverts, Zürich: Swiss Society of Engineers and Architects; 2008.

[5] Ramos, A. e Lúcio, V.; Reforço de Lajes Fungiformes ao Punçoamento com Perfis Metálicos, 6º Encontro Nacional Sobre Estruturas Pré-Esforçadas, 1996.

[6] Faria, D.; Einpaul, J.; Ramos, A.; Fernández, M.; Muttoni, A.; On the efficiency of flat slabs strengthening against punching using externally bonded fibre reinforced polymers, Construction and Building Materials, Vol. 73: pp. 366–77, 2014.

[7] Ramos, A.; Lúcio, V.; Regan, PE.; Repair and Strengthening Methods of Flat Slabs for Punching, International Workshop on Punching Shear Capacity of RC Flat Slabs, pp. 125–33, 2000.

[8] Faria, D.; Lúcio, V.; Ramos, A.; Strengthening of flat slabs with post-tensioning using anchorages by bonding, Engineering Structures, Vol. 33: pp. 2025–43, 2011.

[9] Hassanzadeh, G.; Sundquist, H.; Strengthening of bridge slabs on columns, Nordic Concrete Research, 1998.

[10] Muttoni, A.; Punching shear strength of reinforced concrete slabs without transverse reinforcement, ACI Structural Journal, Vol. 105: pp. 440–50, 2008.

[11] Ghali, A.; Sargious, M.; Huizer, A.; Vertical prestressing of flat plates around columns, Shear in Reinforced Concrete, ACI Special Publication, Vol. 2: pp. 905–920, 1974.

[12] Hawkins, N.; Shear Strength of Slabs with Shear Reinforcement. Spec. Publ. 42 - Shear Reinf. Concr., p. 785–816, 1974.

[13] Datta, A.; Seraj, S.; Effect of Overlay on Punching Shear Capacity of Slabs, Journal of Civil Engineering, Vol. 31: pp. 67–82, 2003.

[14] ACI 318.; Building code requirements for structural concrete : (ACI 318-95) ; and commentary (ACI 318R-95), Farmington Hills, MI : American Concrete Institute, 1995.

[15] CEB/FIP.; Model Code for Concrete Structures, Lausanne: Fédération Internationale du Béton, Thomas Telford Services Ltd; 1978.

[16] Casal, B.; Ligações Entre Betões de Idades Diferentes - Aplicações Diversas. Master's Dissertation, Instituto Superior Técnico, Lisbon, 2011.

[17] Zhang, D.; Ueda, T.; Furuuchi, H.; Concrete cover separation failure of overlay-strengthened reinforced concrete beams, Construction and Building Materials, Vol. 26: pp. 735–45, 2012.

[18] Vaz, A.; Shehata, I.; da Conceição Domingues Shehata, L.; Gomes, RB.; Behaviour of RC beams strengthened by partial jacketing under cyclic loading, Materials and Structures, Vol. 47: pp. 383–96, 2014.

[19] CEB/FIP; CEB Bulletin No. 213/214: CEB-FIP Model Code 90, Fédération Internationale du Béton, pp. 460, 1993.

[20] Rocha, D.; Flexural Strengthening By Means of a RC Overlay in the Tension Zone, Master's Dissertation, Universidade Nova de Lisboa, 2012.

[21] Münger, F.; Wicke, M.; Randl, N.; Design of Shear Transfer in Concrete-Concrete Composite Structures. IABSE Reports, p. 163–8, 1997.

[22] Randl, N.; Design recommendations for interface shear transfer in fib Model Code 2010, Structural Concrete, Vol. 14: pp. 230–41, 2013.

[23] Koseki, K.; Breen, J.; Exploratory Study of Shear Strength of Joints For Precast Segmental Bridges, 1983.

[24] Lenz, P.; Beton-Beton-Verbund Potenziale für Schubfugen, PhD Thesis, Technische Universität München, 2012.

[25] Hofbeck, J.; Ibrahim, I.; Mattock, A.; Shear transfer in reinforced concrete, ACI Journal Proceedings, pp. 119–28, 1969.

[26] Courard, L.; Garbacz, A.; Piotrowski, A.; Sustercic, J.; Surface properties of concrete and criteria for adhesion of repair systems, KSPC 2013, pp. 69-82, Pristina, 29-30 May, 2013.

[27] Millard, S.; Johnson, R.; Gambarova, P.; Karakog, C.; Shear transfer across cracks in reinforced concrete due to aggregate interlock and to dowel action, Magazine of Concrete Research, Vol. 36: pp. 47–51, 1985.

[28] Mattock, A.; Hawkins, N.; Shear Transfer in Reinforced Concrete−Recent Research, Journal of the Prestressed Concrete Institute, Vol. 17: pp. 55–75, 1972.

[29] Randl, N.; Investigations on load transfer between old and new concrete at different surface roughnesses. Leopold-Franzens-Universität Innsbruck, 1997.

[30] Santos, P.; Júlio, E.; Recommended improvements to current shear-friction provisions of model code. 3rd fib Int. Congr., 2010.

[31] Hoff, G.; High Strength Lightweight Aggregate Concrete for Arctic Applications—Part 3: Structural Parameters., ACI Special Publication, pp. 175–246, 1993.

[32] European Committee for Standardization; EN 1504-3:2005 - Products and systems for the protection and repair of concrete structures - Definitions, requirements, quality control and evaluation of conformity - Part 3: Structural and non-structural repair, 2006.

[33] Silfwerbrand, J.; Beushausen, H.; Courard, L.; Bonded Cement Based Material Overlays

for the Repair, the Lining or the strengthening of slabs or pavements, Springer Netherlands, pp. 51–79, 2011.

[34] Santos, P.; Júlio, E.; Interface shear transfer on composite concrete members, ACI Structural Journal, Vol. 111: pp. 113–21, 2014.

[35] Santos, P.; Júlio, E.; A state-of-the-art review on roughness quantification methods for concrete surfaces, Construction and Building Materials, Vol. 38: pp. 912–23, 2012.

[36] Silfwerbrand, J.; Improving Concrete Bond in Repaired Bridge Decks., Concrete International, Vol. 12, p. 61–6, 1990.

[37] Saucier, F.; Pigeon, M.; Durability of new-to-old concrete bonding. Proc. ACI Int. Conf. Eval. Rehabil. Concr. Struct. Innov. Des., Hong Kong, p. 689–707, 1991.

[38] Abu-Tair, A.; Rigden, S.; Burley, E.; Testing the bond between repair materials and concrete substrate, ACI Materials Journal1, Vol. 93: pp. 553–8, 1996.

[39] Granju, J.; About the debonding of thin cement-based overlays, Special section: fracture mechanics in concrete repair/strengthening, p. 1751–60, 2001.

[40] Bissonnette, B.; Courard, L.; Beushausen, H.; Fowler, D.; Trevino, M.; Vaysburd, A.; Recommendations for the repair , the lining or the strengthening of concrete slabs or pavements with bonded cement-based material overlays, Materials and Structures, Vol. 46: pp. 481–94, 2012.

[41] Perez, F.; Morency, M.; Bissonnette, B.; Correlation between the roughness of the substrate surface and the debonding risk, Civil Engineering, 2009: pp. 949–56.

[42] Bissonnette, B.; Courard, L.; Fowler, DW.; Granju, JL.; Bonded Cement Based Material Overlays for the Repair , the Lining or the Strengthening of Slabs or Pavements: State-of-the-Art Report of the RILEM Technical Committee 193-RLS, 2011.

[43] Hunt, T.; Sandblasting of concrete surfaces, Publication nr. C680449, 1968: pp. 4.

[44] Júlio, E.; Branco, F.; Silva, V.; Concrete-to-concrete bond strength. Influence of the roughness of the substrate surface, Construction and Building Materials, Vol. 18: pp. 675–81, 2004.

[45] Talbot, C.; Pigeon, M.; Beaupre, D.; Morgan, DR.; Influence of surface preparation on long-term bonding of shotcrete, ACI Materials Journal, Vol. 91: pp. 560–6, 1994.

[46] Carter, P.; Gurjar, S.; Wong, J.; Debonding of Highway Bridge Deck Overlays, Concrete International, Concrete International, Vol. 24, pp. 51-28, 2002.

[47] International Concrete Reparation Institute.; Guide for the Preparation of Concrete Surfaces for Repair Using Hydrodemolition Methods, 2004.

[48] Bissonnette, B.; Courard, L.; Garbacz, A.; Concrete Surface Engineering, Modern Concrete Technology, CRC Press; pp. 256, 2017.

[49] Summers, D.; Waterjetting Technology, CRC Press; pp. 900, 1995.

[50] Perez, F.; Bissonnette, B.; Gagné, R.; Parameters affecting the debonding risk of bonded overlays used on reinforced concrete slab subjected to flexural loading, Materials and Structures, Vol. 42: pp. 645–62, 2009.

[51] Alexander, M.; Beushausen, H.; Dehn, F.; Moyo, P.; Concrete Repair, Rehabilitation and Retrofitting, Cape Town: 2005.

[52] Emmons, P.; Concrete Repair and Maintenance Illustrated: Problem Analysis; Repair Strategy; Techniques., R.S. Means Company Ltd; 1994.

[53] Beushausen, H.; Long-term performance of bonded concrete overlays subjected to differential shrinkage. University of Cape Town, 2005.

[54] Emmons, P.; Vaysburd, A.; Performance Criteria for Concrete Repair Materials, Vicksburg, MS: 1995.

[55] Santos, P.; Júlio, E.; Silva, V.; Correlation between concrete-to-concrete bond strength and the roughness of the substrate surface, Construction and Building Materials, 2007, Vol. 21: pp. 1688–95.

[56] Bissonnette, B.; Vaysburd, A.; von Fay, K.; Best Practices for Preparing Concrete Surfaces Prior to Repairs and Overlays, 2012.

[57] FIB - Fédération Internationale du Béton.; MC2010 - fib Model Code for Concrete Structures 2010, Berlin: Ernst & Sohn; 2013.

[58] Maerz, N.; Mo, R.; Concrete Roughness Characterization Using Laser Profilometry for Fiber- Reinforced Polymer Sheet Application 2001: pp. 1–12.

[59] Júlio, E.; Santos, P.; Development of a laser roughness analyser to predict in situ the bond strength of concrete-to-concrete interfaces, Magazine of Concrete Research, 2008, Vol. 60: pp. 329–37.

[60] Sarsam, S.; Ali, .; Assessing Pavement Surface Macrotexture Using Sand Patch Test and Close Range Photogrammetric Approaches 2015, Vol. 1: pp. 124–31.

[61] ASTM E965-15.; Standard Test Method for Measuring Pavement Macrotexture Depth Using a Volumetric Technique, 2015.

[62] Santos, P.; Júlio, E.; A state-of-the-art review on roughness quantification methods for concrete surfaces, Construction and Building Materials, 2013, Vol. 38: pp. 912–23.

[63] Abu-Tair, AI.; Lavery, D.; Nadjai, A.; Rigden, SR.; Ahmed, T.; A new method for evaluating the surface roughness of concrete cut for repair or strengthening, Construction and Building Materials, 2000, Vol. 14: pp. 171–6.

[64] Garbacz, a.; Górka, M.; Courard, L.; Effect of concrete surface treatment on adhesion in repair systems, Magazine of Concrete Research, Vol. 57: pp. 49–60, 2005.

[65] Yaacob, H.; Hassan, NA.; Hainin, MR.; Rosli, MF.; Comparison of sand patch test and multi laser profiler in pavement surface measurement, Jurnal Teknologi, Vol. 70: pp. 103–6, 2014.

[66] Vogler, N.; Kühne, H.; Charakterisierung von Bauteiloberflächen mittels Lasertriangulation bei der Instandsetzung 2015.

[67] D'Andrea, A.; Tozzo, C.; Boschetto, A.; Bottini, L.; Interface Roughness Parameters and Shear Strength, Modern Applied Science, Vol. 7: pp. 1–10, 2013.

[68] Garbacz, a.; Courard, L.; Bissonnette, B.; A surface engineering approach applicable to concrete repair engineering, Bulletin of the Polish Academy of Sciences: Technical Sciences, Vol. 61, 2013.

[69] Santos, P.; Júlio, E.; Effect of filtering on texture assessment of concrete surfaces, ACI Materials Journal, Vol. 107: pp. 31–6, 2010.

[70] Santos, P.; Assessment of the Shear Strength between Concrete Layers, PhD Thesis, Universidade de Coimbra, 2009.

[71] Tavares, S.; Analysis of surface roughness and models of mechanical contacts, Master's Dissertation, Universidade do Porto, 2005.

[72] Courard, L.; Perez, F.; Bissonnette, B.; Gorka, M.; Garbacz, A.; Two different techniques for the evaluation of concrete surface roughness, Concrete Repair, Rehabilitation and Retrofitting - Proceedings of the International Conference on Concrete Repair, Rehabilitation and Retrofitting, ICCRRR 2005, 2006.

[73] CSDA-ST-115.; Measuring Concrete Micro Surface Texture, Standard from the Concrete Sawing & Drilling Association, 2014.

[74] Cook, R.; Collins, D.; Klingner, R.; Polyzois, D.; Load-deflection behavior of cast-in-place and retrofit concrete anchors, ACI Structural Journal, Vol. 89: pp. 639–49, 1992.

[75] American Concrete Institute; Building Code Requirements for Structural Concrete (ACI 318-11) 2011: pp. 509.

[76] Leonhardt, F.; Mönnig, E.; Calcolo di progetto & techniche costruttive. Vol. II Casi Spec. di Dimens. nelle Costr. c. a. e c.a.p., 1979.

[77] Miltenberger, M.; Capacity design of grouted anchors. 16th Int. Conf. Struct. Mech. React. Technol., 2001.

[78] Long, A.; Murray, A.; The "Pul l-Off" Partially Destructive Test for Concrete, Special Publication, 1984, Vol. 82: pp. 327–50.

[79] BS EN 1542:1999.; Products and systems for the protection and repair of concrete structures. Test methods. Measurement of bond strength by pull-off, British Standard Institute; 1999.

[80] Cleland, D.; Long, A.; The Pull-Off Test For Concrete Patch Repairs. Proc. Inst. Civ. Eng. Struct. Build., vol. 122, ICE Publishing; 1997, p. 451–60.

[81] Vaysburd, A.; McDonald, J.; An evaluation of equipment and procedures for tensile bond testing of concrete repairs, Technical Report REMR-CS-61, US Army Corps of Engineers, Washington, DC, 1999.

[82] Delatte, N.; Wade, D.; Fowler, D.; Laboratory and Field Testing of Concrete - Bond Development for Expedited Bonded Concrete Overlays, Materials Journal, Vol. 97: pp. 272–80, 2000.

[83] Pan, Y.; Bond Strength of Concrete Patch Repairs - An Evaluation of Test methods and the Influence of Workmanship and Environment. Loughborough University of Technology, 1995.

[84] Bonaldo, E.; Barros, J.; Lourenço, P.; Bond characterization between concrete substrate and repairing SFRC using pull-off testing, Vol. 25: pp. 463–74, 2005.

[85] Austin, S.; Robins, P.; Pan, Y.; Tensile bond testing of concrete repairs, Materials and Structures, Vol. 28: pp. 249, 1995.

[86] Austin, S.; Robins, P.; Pan, Y.; Shear bond testing of concrete repairs, Cement and Concrete Research, 1999, Vol. 29: pp. 1067–76.

[87] Hanson, N.; Precast-prestressed concrete bridges 2. Horizontal shear connections, Development Department Bulletin D35, Portland Cement Association, Vol. 2: pp. 38–58, 1960.

[88] Walraven, J.; Frenay, J.; Pruijssers, A.; Influence of concrete strength and load history on the shear friction capacity of concrete members, PCI Journal, Vol. 32: pp. 66–84, 1987.

[89] Saldanha, R.; Júlio, E.; Dias-Da-Costa, D.; Santos, P.; A modified slant shear test designed to enforce adhesive failure, Construction and Building Materials, Vol. 41: pp. 673–80, 2013.

[90] Echegaray-Oviedo, J.; Navarro-Gregori, J.; Cuenca, E.; Serna, P.; Upgrading the push-off test to study the mechanisms of shear transfer in FRC elements, Proceedings of the 8th International Conference on Fracture Mechanics of Concrete and Concrete Structures, FraMCoS 2013, 2013: pp. 1012–21.

[91] European Comitee for Standardization.; EN 12390-6:2000 - Testing hardened concrete Part 6 - Tensile splitting strength of test specimens, 2000.

[92] Linsbauer, HN.; Tschegg, E.; Fracture energy determination of concrete with cube-shaped specimens, Zement Und Beton, 1986: pp. 38–40.

[93] Brühwiler, E.; Wittmann, F.; The wedge splitting test: a new method of performing stable fracture mechanics tests, Engineering Fracture Mechanics, 1990: pp. 117–25.

[94] Seitl, S.; Nieto García, B.; Merta, I.; Wedge splitting test method: Quantification of influence of glued marble plates by two-parameter fracture mechanics, Frattura Ed Integrita Strutturale, Vol. 30: pp. 174–81, 2014.

[95] Granju, J-L.; Debonding of Thin Cement-Based Overlays, Journal of Materials in Civil Engineering, Vol. 13: pp. 114–20, 2001.

[96] Courard, L.; Piotrowski, T.; Garbacz, A.; Near-to-surface properties affecting bond strength in concrete repair, Cement and Concrete Composites, 2014, Vol. 46: pp. 73–80.

[97] Carter, P.; Gurjar, S.; Wong, J.; Debonding of Highway Bridge Deck Overlays, Concrete

International, 2002, Vol. 24: pp. 51–8.

[98] Branco, F.; Silva, V.; Júlio, E.; Concrete-to-concrete bond strength: influence of an epoxy-based bonding agent on a roughened substrate surface, Magazine of Concrete Research, Vol. 57: pp. 463–8, 2005.

[99] Birkeland, P.; Birkeland, H.; Connections in Precast Concrete Construction, Journal of the American Concrete Institute, Proceedings, Vol. 63: pp. 345–67, 1966.

[100] Walraven, J.; Reinhardt, H.; Theory and Experiments on the Mechanical Behaviour of Cracks in Plain and Reinforced Concrete Subjected To Shear Loading., Heron, Vol. 26, 1981.

[101] European Committee for Standardization.; EN 1992-1-1: Eurocode 2-Design of Concrete Structures - Part I: General Rules and Rules for Buildings, Brussels: 2004.

[102] CAN/CSA-A23.3-04.; A23.3-04 - Design of concrete structures, CSA Group; 2004.

[103] Walraven, J.; Aggregate interlock: A theoretical and experimental analysis, PhD Thesis, Delft University Press; 1980.

[104] Zhou, J.; Ye, G.; Schlangen, E.; van Breugel, K.; Modelling of stresses and strains in bonded concrete overlays subjected to differential volume changes, Theoretical and Applied Fracture Mechanics, Vol. 49: pp. 199–205, 2008.

[105] Banthia, N.; Bindiganavile, V.; Repairing With Hybrid-Fiber-Reinforced Concrete, Concrete International, Concrete International., Vol. 23, pp. 29-32, 2001.

[106] Laurence, O.; Bissonnette, B.; Pigeon, M.; Rossi, P.; Effect of Steel Macro Fibres on Cracking of Thin Concrete Repairs. In: Chanvillard PR and G, Fifth Int. RILEM Symp. Fibre-Reinforced Concr., RILEM Publications SARL; 200AD, p. 10.

[107] Chaves, F.; da Silva, L.; de Moura, M.; Dillard, D.; Esteves, V.; Fracture Mechanics Tests in Adhesively Bonded Joints: A Literature Review, The Journal of Adhesion, Vol. 90: pp. 955–92, 2014.

[108] Van Mier, J.; Nooru-Mohamed, M.; Timmers, G.; An Experimental Study of Shear Fracture and Aggregate Interlock in Cementbased Composites, Heron Journal, Vol. 4: pp. 104, 1991.

[109] Atashi, M.; Lachemi, M.; Kianoush, M.; Numerical modeling of the behavior of overlaid slab panels for reinforced concrete bridge decks, Engineering Structures, Vol. 29: pp. 271–81, 2007.

[110] Benzerzour, M.; Gagné, R.; Abriak, N.; Sebaibi, N.; Experimental and numerical study of the structural and cracking behavior of an overlaid slab panel under cyclic flexural loading, Construction and Building Materials, Vol. 52: pp. 24–32, 2014.

[111] Cervenka, V.; Eligehausen, R.; Simulation of Cracking and Failure of Concrete Structures. FEMCAD. STRUCENG Optim., p. 323–8, 1990.

[112] Walraven, J.; Reinhardt, H.; Theory and experiments on the mechanical behavior of cracks in plain and reinforced concrete subjected to shear loading. Concrete Mechanics, Vol. 26,

p. 65, 1981.

[113] Murray, T.; Cousins, T.; Horizontal Shear Connectors for Precast Prestressed Bridge Decks. Virginia Polytechnic Institute and State University, 2002.

[114] Cornelissen, H.; Hordijk, D.; Reinhardt, H.; Experimental Determination of Crack Softening Characteristics of Normalweight and Lightweight Concrete., Heron, Vol. 31: pp. 45–56, 1985.

[115] Bažant, Z.; Concrete fracture models: Testing and practice, Engineering Fracture Mechanics, Vol. 69: pp. 165–205, 2001.

[116] Bažant, Z.; Gambarova, P.; Crack Shear in Concrete: Crack Band Microflane Model, Journal of Structural Engineering, Vol. 110: pp. 2015–35, 1984.

[117] Park, K.; Paulino, G.; Roesler, J.; Determination of the kink point in the bilinear softening model for concrete, Engineering Fracture Mechanics, Vol. 75: pp. 3806–18, 2008.

[118] Barros, J.; Figueiras, J.; Póvoas, R.; Modelos constitutivos para o betão armado fendilhado, Universidade do Minho; Encontro Nacional de Betão Estrutural, pp. 55-70, 1994.

[119] de Borst, R.; Remmers, J.; Computational modelling of delamination, Composites Science and Technology, Vol. 66: pp. 713–22, 2006.

[120] de Borst, R.; Numerical aspects of cohesive-zone models, Engineering Fracture Mechanics, Vol. 70: pp. 1743–57, 2003.

[121] Hillerborg, A.; Modéer, M.; Petersson, PE.; Analysis of crack formation and crack growth in concrete by means of fracture mechanics and finite elements, Cement and Concrete Research, Vol. 6: pp. 773–81, 1976.

[122] Pryl, D.; ATENA Program Documentation Part 11- Troubleshooting Manual, 2013.

[123] Červenka, V.; Jendele, L.; Červenka, J.; ATENA Program Documentation Part 1 Theory, Atena, 2012: pp. 1–282.

[124] Dobromil, P.; Jan, C.; Radomir, P.; Material model for finite element modelling of fatigue crack growth in concrete, Procedia Engineering, Vol. 2: pp. 203–12, 2010.

[125] Hossain, T.; Vollum, R.; Are existing span-to-depth rules conservative for flat slabs?, Magazine of Concrete Research, Vol. 54: pp. 411–21, 2002.

[126] The Concrete Society Working Group.; Guide to the Design and Construction of Reinforced Concrete Flat Slabs, Technical Report N.º 64, 2007.

[127] Muttoni, A.; Ruiz, MF.; Shear strength of members without transverse reinforcement as function of critical shear crack width, ACI Structural Journal, Vol. 105: pp. 163–72, 2008.

[128] Gesund, H.; Kaushik, YP.; Yield line analysis of punching failures in slabs, Publication of Kajima Institute of Construction Technology, Japan, 1970.

[129] Guandalini, S.; Burdet, O.; Muttoni, A.; Punching tests of slabs with low reinforcement

ratios, ACI Structural Journal, Vol. 106: pp. 87–95, 2009.

[130] Kinnunen, S.; Nylander, H.; Punching of Concrete Slabs Without Shear Reinforcement, Transactions of the Royal Institute of Technology, 1960: pp. 112.

[131] Muttoni, A.; Punching Shear Strength of Reinforced Concrete Slabs without Transverse Reinforcement, ACI Structural Journal, Vol. 105, 2008.

[132] Bompa, D.; Oneţ, T.; Punching shear strength of RC flat slabs at interior connections to columns, Magazine of Concrete Research, Vol. 68: pp. 24–42, 2016.

[133] Birkle, G.; Loov, R.; Dilger, WH.; Design of slabs using Shear Friction, Proceedings, Annual Conference - Canadian Society for Civil Engineering, 2003: pp. 1320–9.

[134] REBAP - Regulamento de Estruturas de Betão Armado e Pré esforçado, Decreto-Lei nº 349-C/83 de 30 de Julho, 1985.

[135] Muttoni, A.; Ruiz, M.; The levels-of-approximation approach in MC 2010: Application to punching shear provisions, Structural Concrete, Vol. 13: pp. 32–41, 2012.

[136] Whitehouse, D.; Surfaces and Their Measurement, Elsevier; 2002.

[137] Bhushan, B.; Surface Roughness Analysis and Measurement Techniques, Modern Tribology Handbook, 2001.

[138] Santos, P.; Júlio, E.; A state-of-the-art review on shear-friction, Engineering Structures, Vol. 45: pp. 435–48, 2012.

[139] RILEM Committee TC113.; PC-5: Method of test for compressive strength of polymer concrete and mortar, 1995.

[140] RILEM Committee TC113.; PCM-8: Method of test for flexural strength and deflection of polymer-modified mortar, 1995.

[141] European Committee for Standardization.; EN 10002: Metallic materials—tensile testing—part 1: method of test at ambient temperature, 2001.

[142] LNEC E460-2008.; Varoes de aço A500 NR de ductilidade especial para armaduras de betão armado: caracteristìcas, ensaios e marcação, 2008.

[143] European Committee for Standardization.; EN 12390-3:2001 - Testing hardened concrete Part 3 - Compressive strength of test specimens, 2001.

[144] Mehta, P.; Monteiro, P.; Concrete: microstructure, properties, and materials, Third Edition, McGraw-Hill, 2006.

[145] LNEC E-397.; Betões - Determinação do módulo de elasticidade em compressão., 1993.

[146] ABNT; NBR 13528:2010: Render made of inorganic mortars applied on walls - Determination of bond tensile bond strength, Technical Norm from Brazil, 2010.

[147] Bigaj, A.; Structural dependence of rotation capacity of plastic hinges in RC beams and slabs, PhD Thesis, Delft University of Technology, 1999.

[148] Ericsson, S.; Punching Shear in Reinforced Concrete Slabs Supported on Edge Steel Columns - Assessment of response by means of nonlinear finite element analyses, Master's Dissertation, Chalmers University Of Technology, Sweden, 2010.

[149] Reinhardt, H.; Crack softening zone in plain concrete under static loading, Cement and Concrete Research, Vol. 15: pp. 42–52, 1985.

[150] Ishiguro, S.; Experiments and analyses of fracture properties of grouting mortars, Part 1: Theoretical and Numerical Methods in Fracture Mechanics of Concrete, Fracture Mechanics for Concrete and Concrete Structures, Proceedings, 2007.

[151] Melis, L.; Meyer, A.; Fowler, D.; An Evaluation of Tensile Strength Testing, Research Report 432-lF, 1985.

[152] Rabbat, B.; Russell, H.; Friction Coefficient of Steel on Concrete or Grout, Journal of Structural Engineering, Vol. 111: pp. 505–15, 1985.

[153] Warner, J.; Bhuyan, S.; Smoak, WG.; Hindo, KR.; Sprinkel, M.; Surface Preparation for Overlays, Concrete International, Vol. 20: pp. 43–6, 1998.

[154] Lapi, M.; Martini, D.; Zagli, E.; Orlando, M.; Ramos, A.; Spinelli, P.; Comparison of flat slab strengthening techniques against punching-shear, NBSC2016 - The New Boundaries of Structural Concrete, 2016.

[155] Lapi, M.; Fernandes, H.; Orlando, M.; Ramos, A.; Lúcio, V.; Performance assessment of flat slabs strengthened with a bonded reinforced-concrete overlay, Magazine of Concrete Research, Vol. 70, 2017.

[156] Randl, N.; Load Bearing Behaviour of Cast-in Shear Dowels, Beton- Und Stahlbetonbau, Vol. 102: pp. 31–7, 2007.

[157] Mamede, N.; Ramos, A.; Faria, D.; Experimental and Parametric 3D Nonlinear Finite Element Analysis on Punching of Flat Slabs with Orthogonal Reinforcement, Engineering Structures, Vol. 48: pp. 442–57, 2013.

[158] Kunz, J.; Fernández, M.; Muttoni, A.; Enhanced safety with post-installed shear reinforcement. FIB Symposium, Tel-Aviv, p. 4, 2013.

[159] Inácio, M.; Comportamento ao Punçoamento de Lajes Fungiformes em Betão de Elevada Resistência, PhD Thesis, Universidade Nova de Lisboa, 2016.

[160] Muttoni, A.; Ruiz, M.; The levels-of-approximation approach in MC 2010: Application to punching shear provisions, Structural Concrete, Vol. 13: pp. 32–41, 2012.

[161] Carlswärd, J.; Shrinkage cracking of steel fibre reinforced self compacting concrete overlays - Test methods and theoretical modelling, PhD Thesis, Luleå University of Technology, 2006.

[162] TCC/03/62 - Concrete and fire safety: guidance on the use of concrete and masonry for fire resistant and efficient structures, MPA - The Concrete Centre; TCC Publication, 2008.

[163] Almeida, A.; Inácio, M.; Lucio, V.; Ramos, A.; Punching behaviour of RC flat slabs under reversed horizontal cyclic loading, Engineering Structures, Vol. 117: pp. 204–19, 2016.

# 8. APPENDIX A

## Contents



## Index of figures

## 8.1. Deformed shape by load step of rectangular specimens

The relative deformation of the composite cross-section results from concrete layers cast at different times which although bonded to one another, have a finite capacity for transferring stresses. Such capacity translates in terms of the interface shear, tensile and compressive strengths. When such interface is loaded in shear with tensile stresses, the different flexural stiffness of each contacting layer results in relative deformation, which in turn results in normal and tangential relative displacements at the interface. Assessment of such displacements can assist on characterising the interface behaviour and the debonding phenomenon. Measurement of relative deformation was performed with the measuring equipment comprised of LVDT's installed above and below the slab according to the schematics in Figure 8.1 and Figure 8.2.


Figure 8.1 – Measuring equipment for vertical deflection of the $R_S$ specimens.

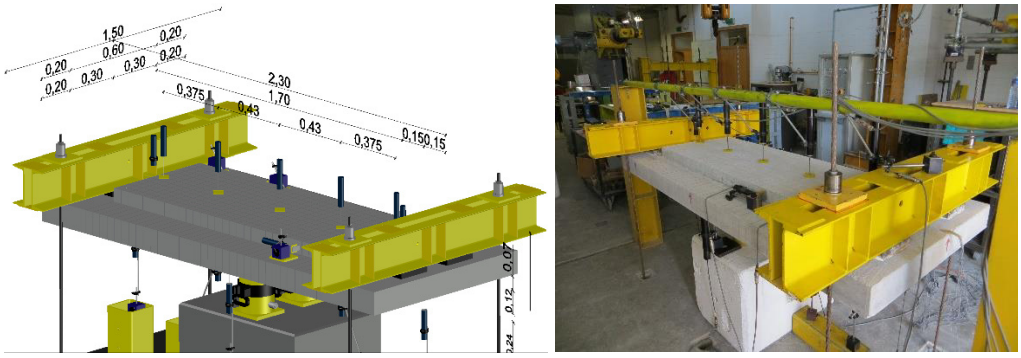


Figure 8.2 – Measuring equipment for vertical deflection of the $R_L$ specimens.

The vertical deflection of each layer was measured and the respective relative displacement between both layers could then be plotted. Figure 8.3 to Figure 8.6 illustrate the relative deformation between contacting layers for the rectangular specimens where the asymmetry of the

relative deformation between layers can be graphically observed. Load-stepping was considered at every 50 kN for the sake of simplicity of reading the resulting graphs.

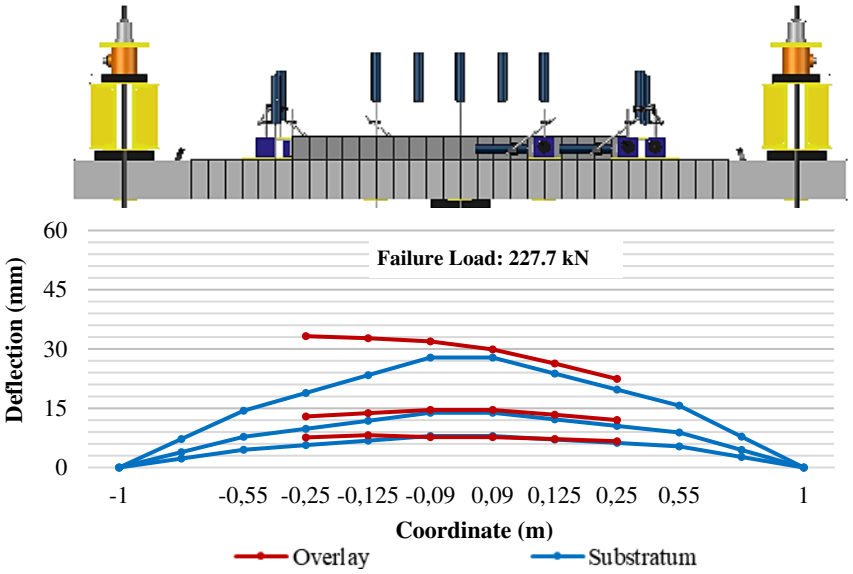


Figure 8.3 – Relative deformation between concrete layers for the $R_S$-REF specimen.

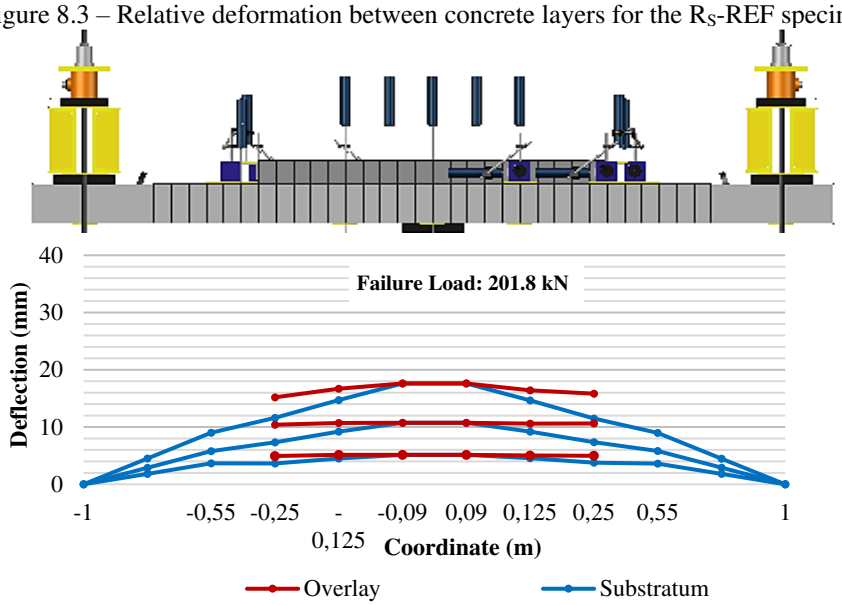


Figure 8.4 – Relative deformation between concrete layers for the RS-STC-4 specimen.

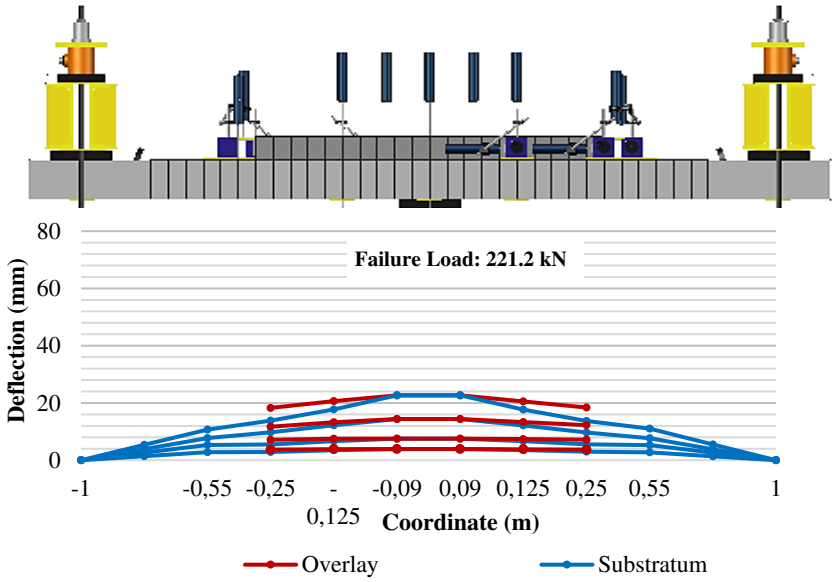


Figure 8.5 – Relative deformation between concrete layers for the $R_S$-ANC-4 specimen.

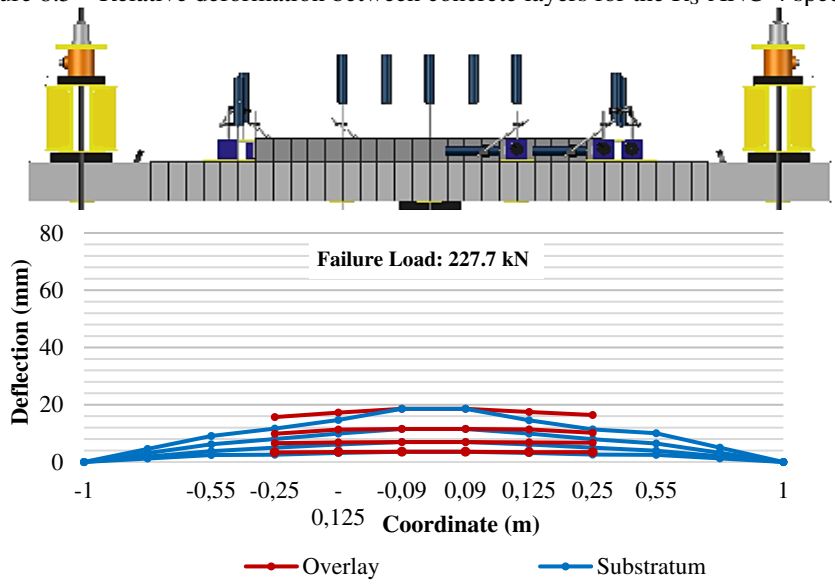


Figure 8.6 – Relative deformation between concrete layers for the $R_S$-STANC specimen.

Analysing the relationship between load and vertical relative displacement, one can observe that reinforcement crossing the interface yields a higher structural integrity. Proof of such impact are the almost symmetric deflections of these specimens. The same behaviour can be observed for the long overlay specimens on Figure 8.7 to Figure 8.10 where the ends of the longer RCO resulted further from midspan where bending stresses are greater.

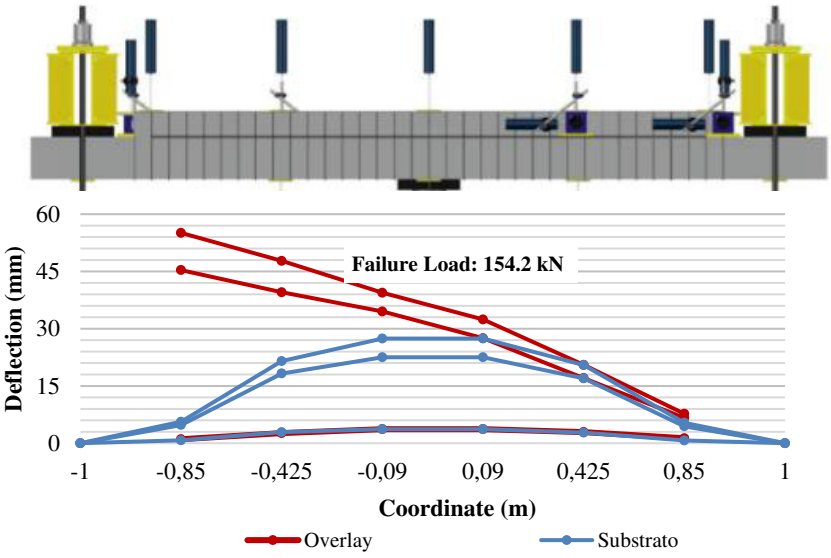


Figure 8.7 – Relative deformation between concrete layers for the RL-REF specimen.

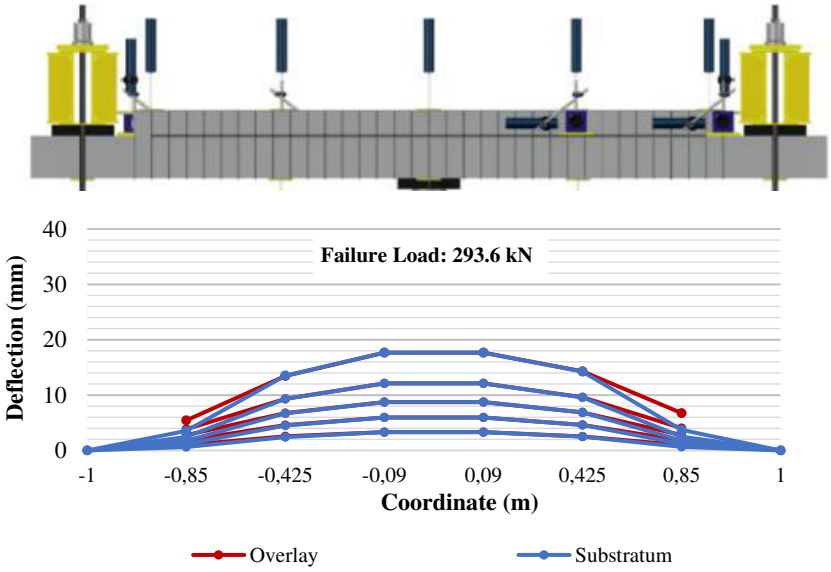


Figure 8.8 – Relative deformation between concrete layers for the RL-ANC specimen.

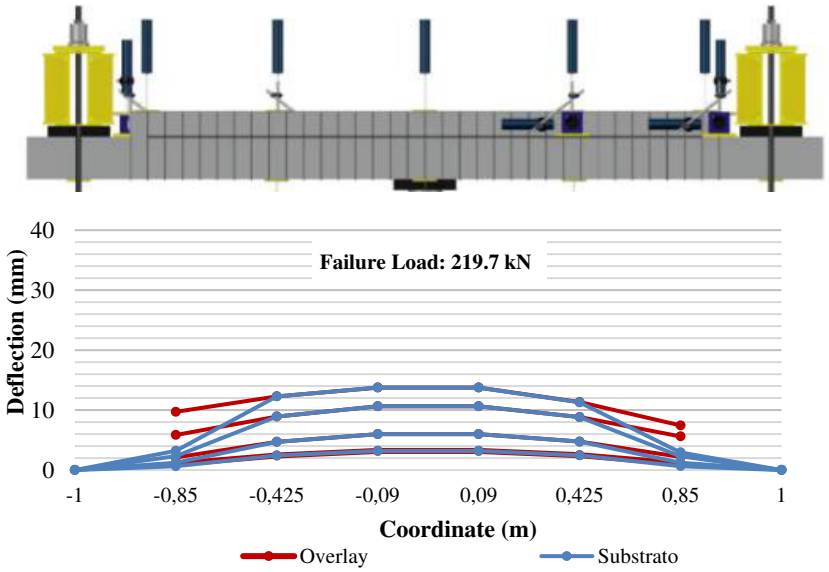


Figure 8.9 – Relative deformation between concrete layers for the RL-STC specimen.

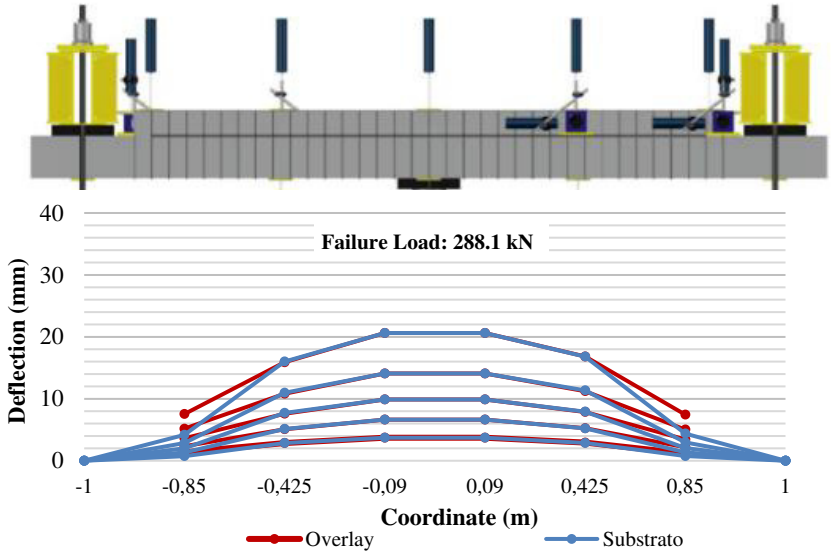


Figure 8.10 – Relative deformation between concrete layers for the $R_L$-STANC specimen.

Observing the figures above, one realises that the larger relative displacements are located on the ends of the overlay. This is due to the symmetrical flexural deformation of the strengthened specimens that results in higher relative deformation close to the ends of the specimens. The debonding phenomenon can be observed through the differential deflection between substratum and overlay. The longer overlays can accommodate the cracking of concrete tensile fibres due to bending stresses without debonding the edge of the overlaid concrete. Positioning of such edges further from midspan reduces bending stresses, thus resulting in a better control of the interface crack opening.

## 8.2. Deformed shape by load step of square specimens

The deformed shape of square specimens was graphically plotted to assess the evolution of deflection with loading of the strengthened specimens. No significant differential deformation could be observed between layers and therefore no differential deformation profiles were plotted. The system of LVDT's for measuring deflection throughout the load history of the strengthened specimens can be observed in Figure 8.11 and Figure 8.12 for both the $S_{4D}$ and $S_{3D}$ specimens.

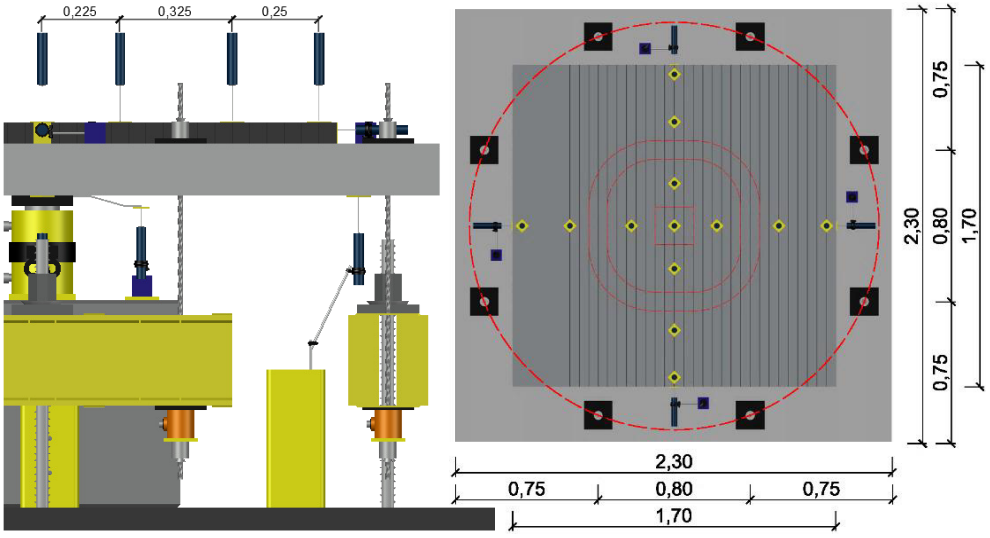


Figure 8.11 – Position of LVDT's on the $S_{4D}$ tests.

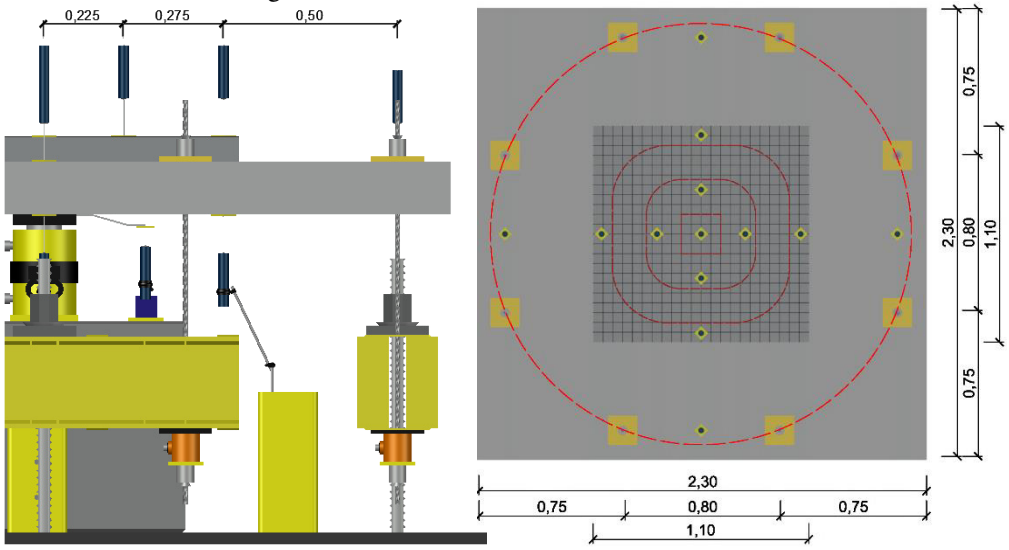


Figure 8.12 – Position of LVDT's on the $S_{3D}$ tests.

The vertical deflection, assuming a load step of 50 kN, can then be observed on Figure 8.13 to Figure 8.20.

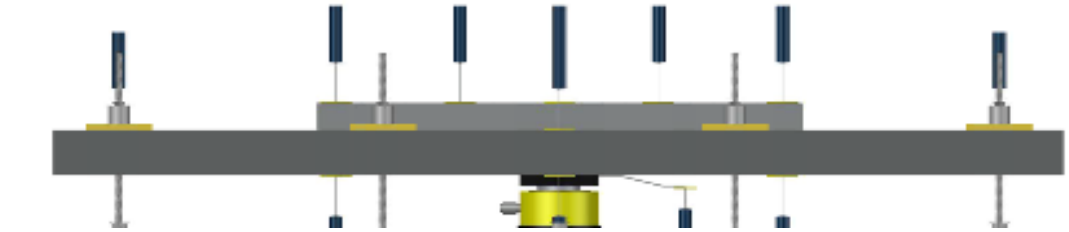

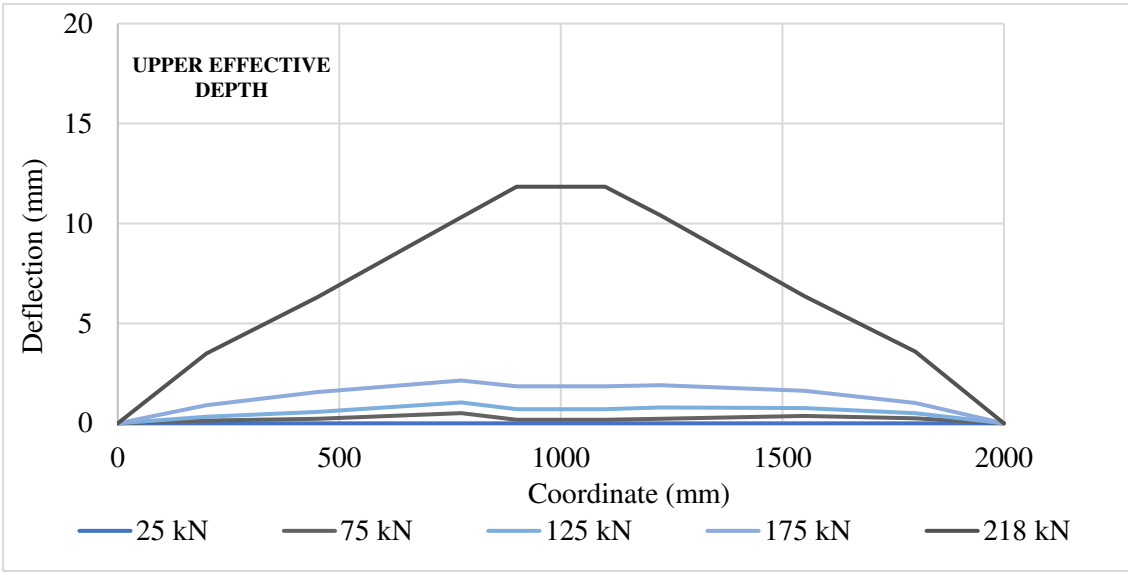


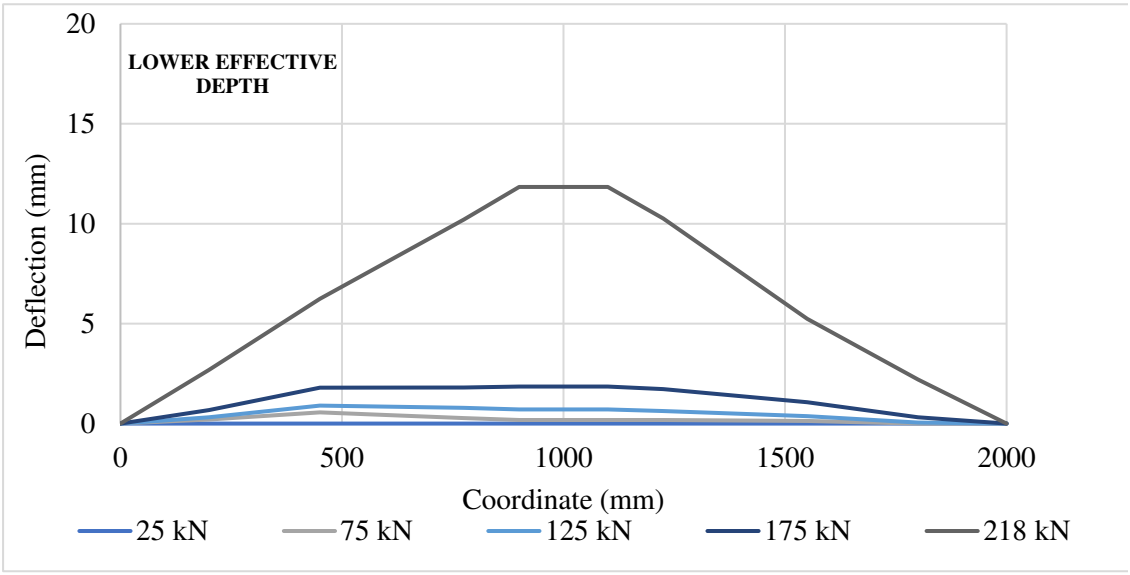


Figure 8.13 – Relative deformation between concrete layers for the $S_{3D}$-REF specimen.

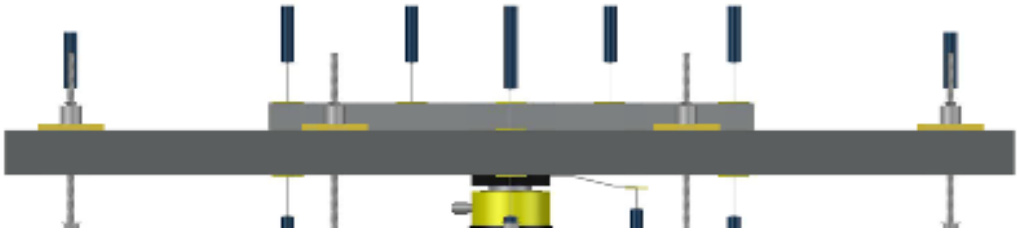

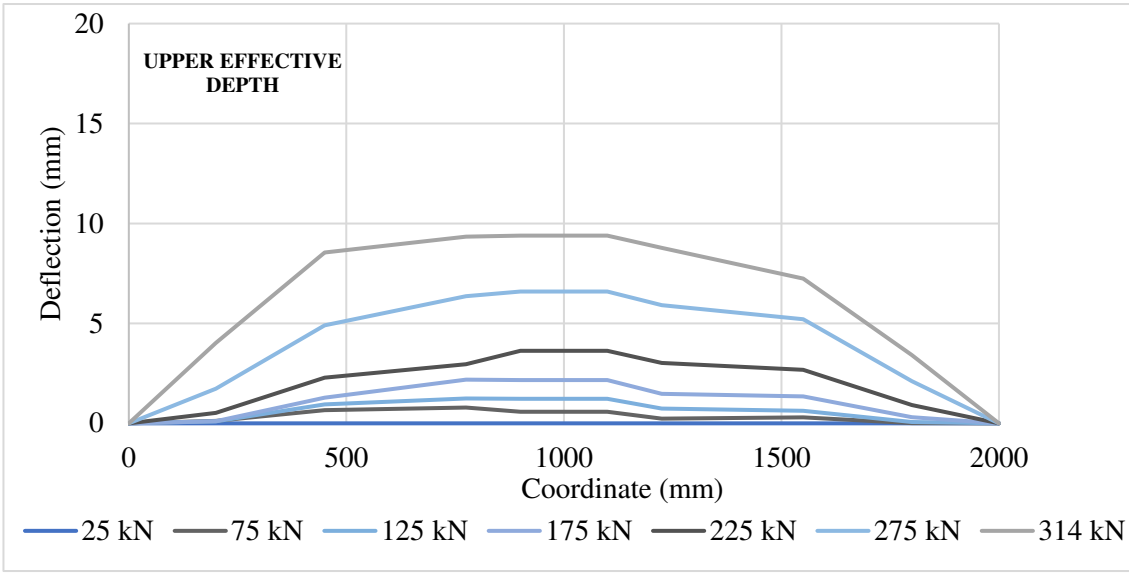


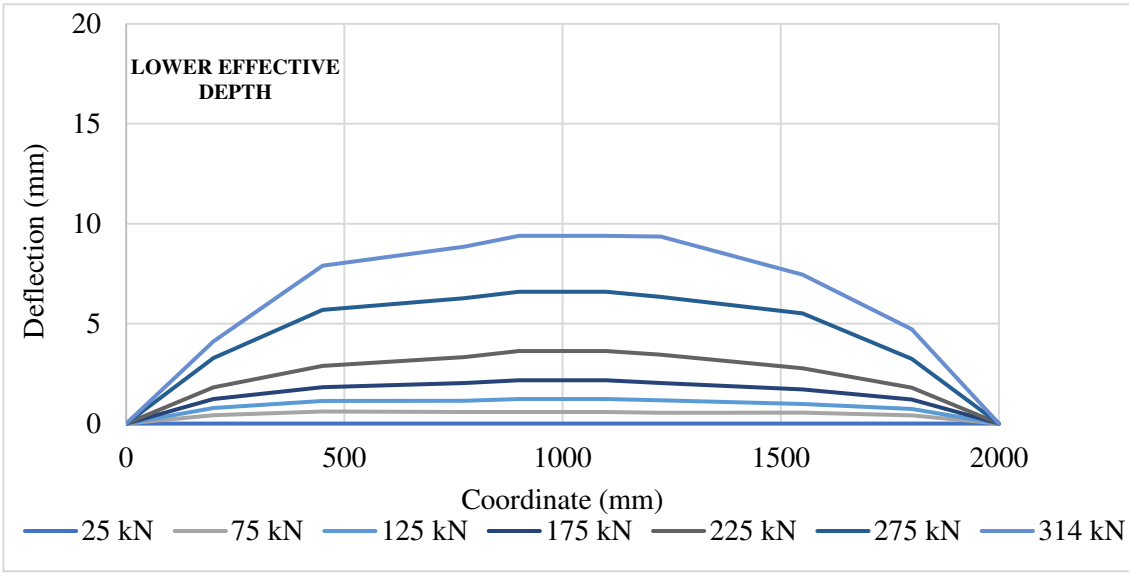


Figure 8.14 – Relative deformation between concrete layers for the $S_{3D}$-STC specimen.

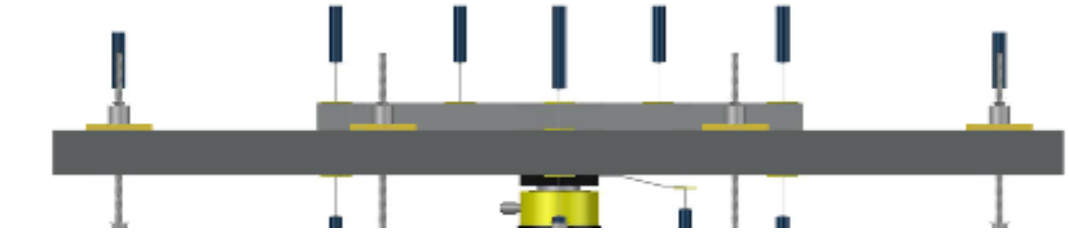

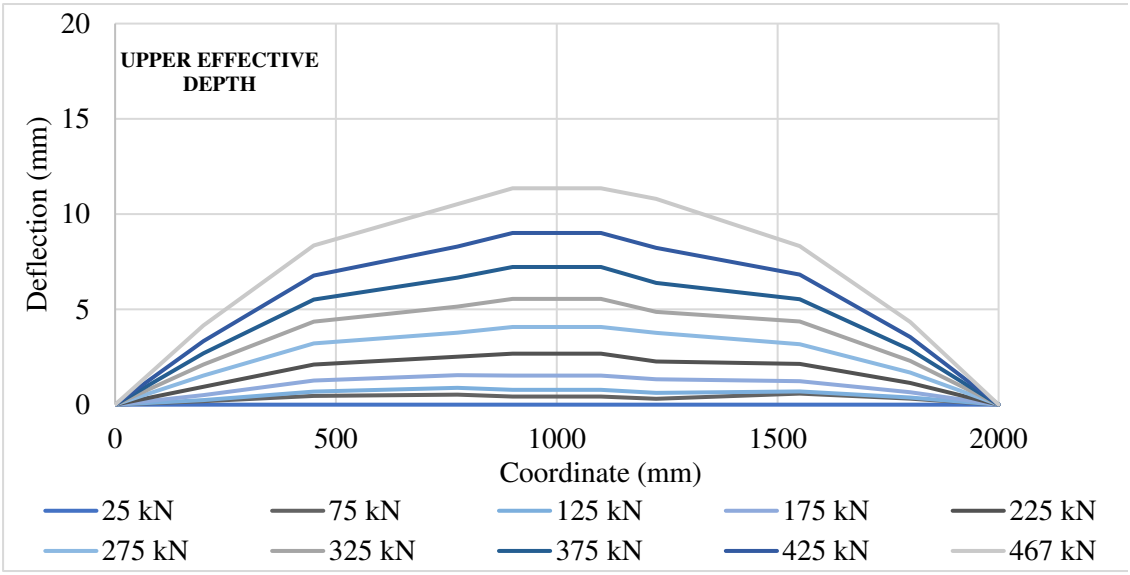


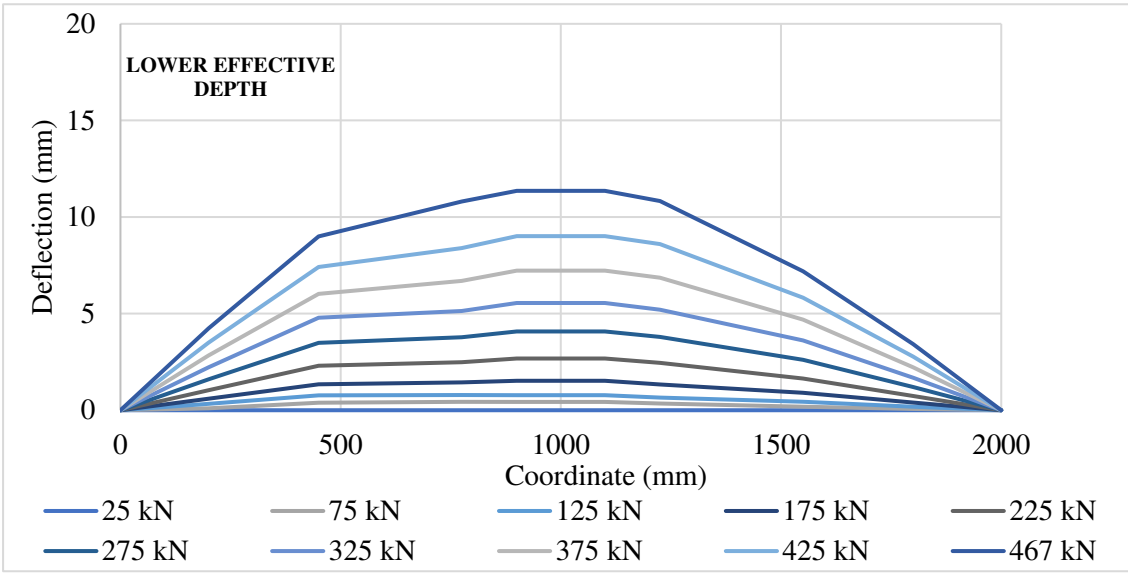


Figure 8.15 – Relative deformation between concrete layers for the $S_{3D}$-ANC specimen.

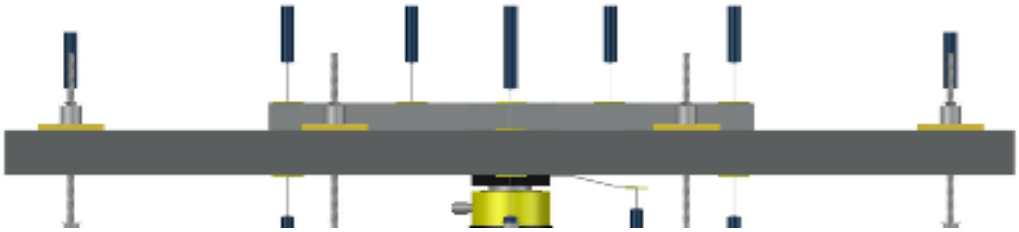

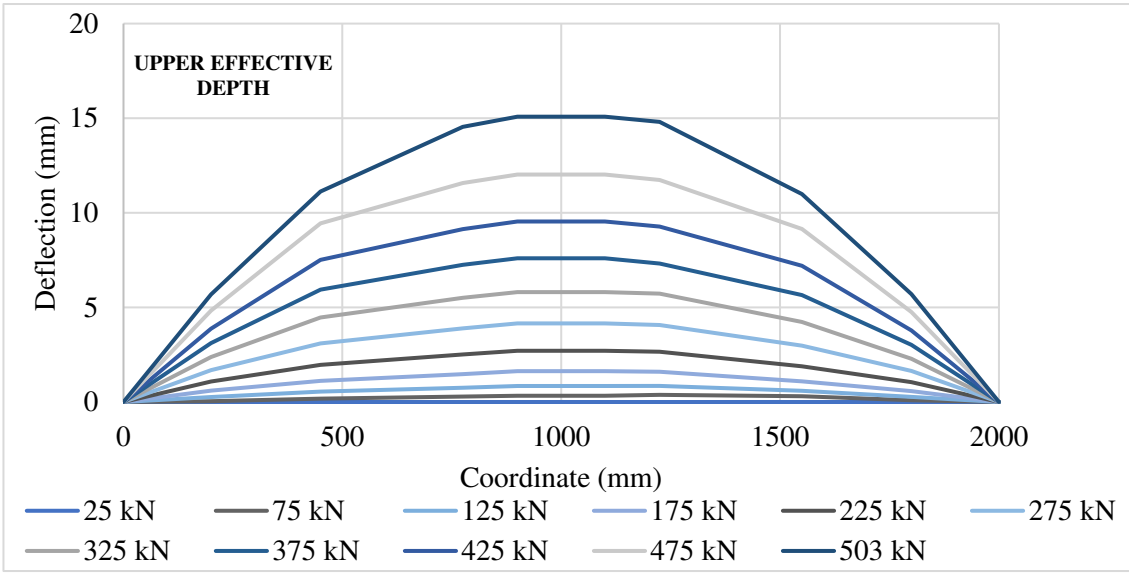


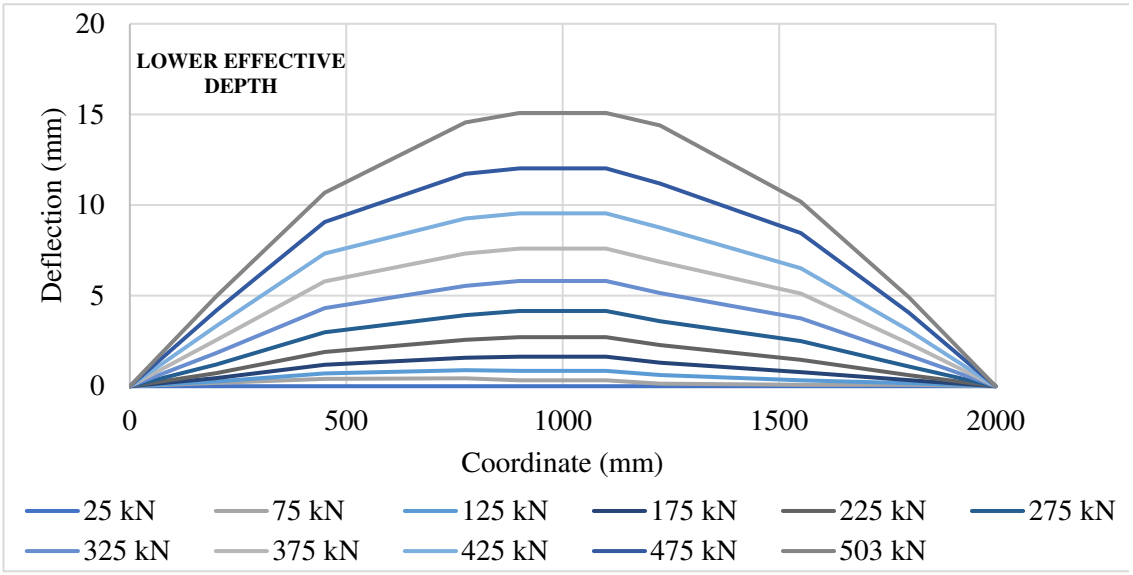


Figure 8.16 – Relative deformation between concrete layers for the $S_{3D}$-STANC specimen.

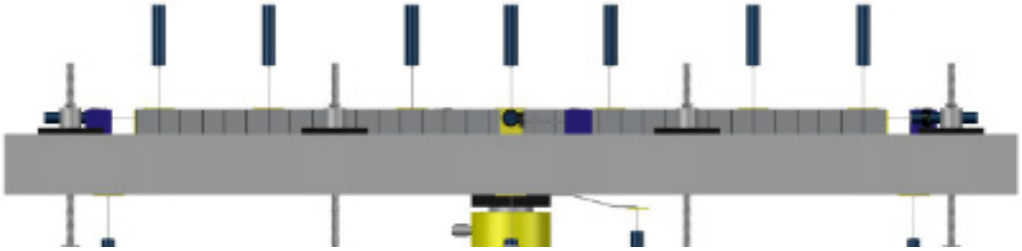

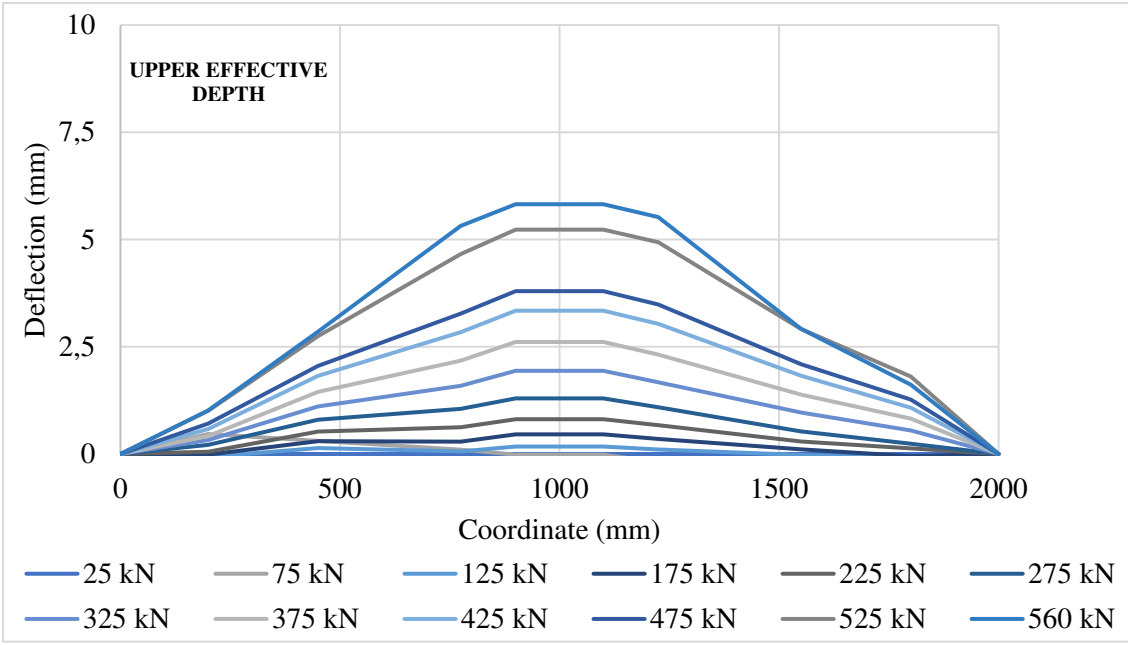


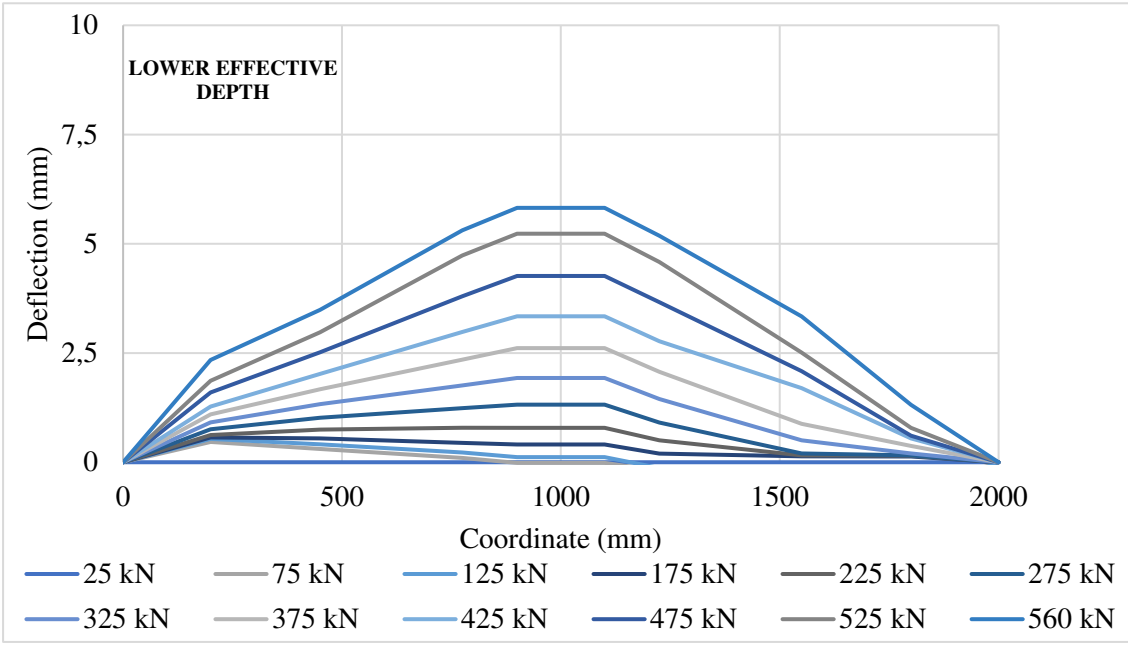


Figure 8.17 – Relative deformation between concrete layers for the $S_{4D}$-REF specimen.

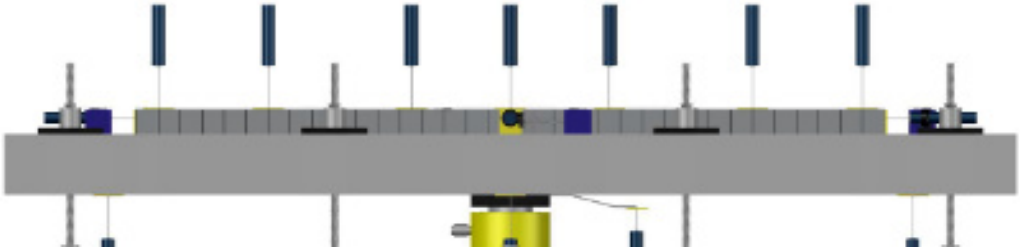

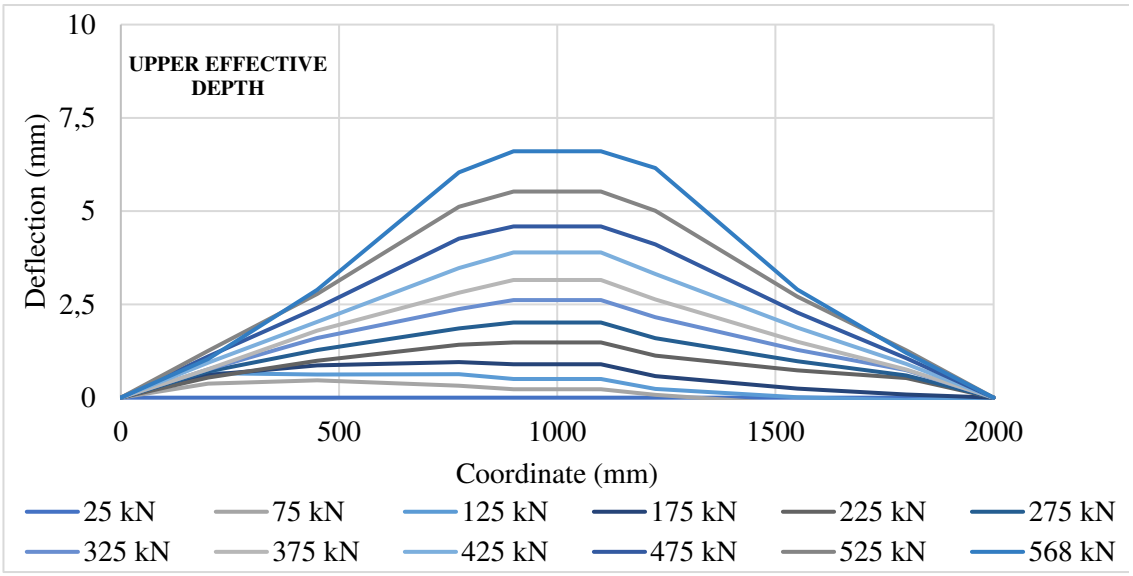


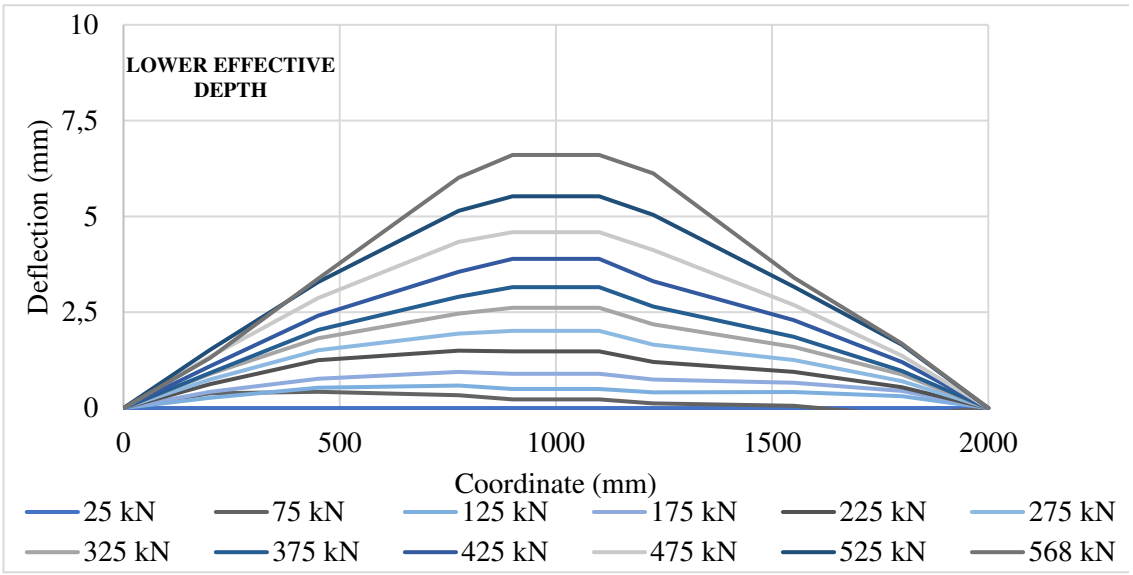


Figure 8.18 – Relative deformation between concrete layers for the $S_{4D}$-STC specimen.

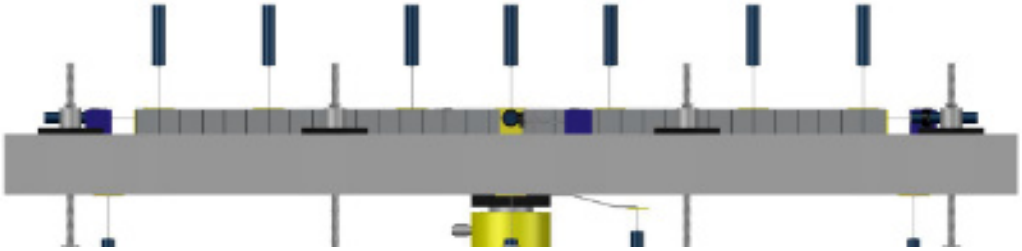

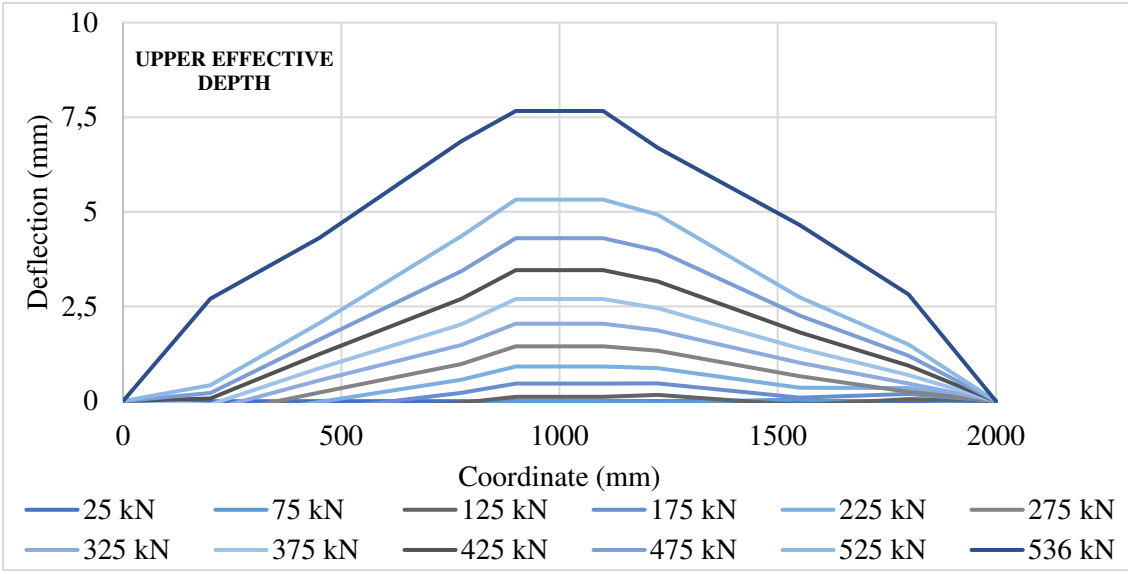


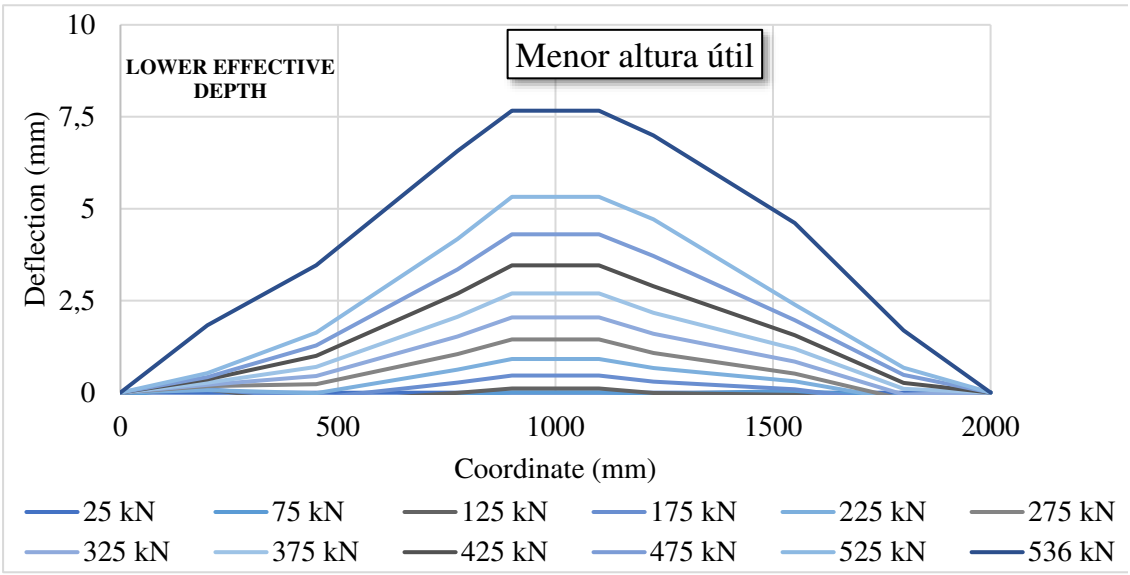


Figure 8.19 – Relative deformation between concrete layers for the $S_{4D}$-ANC specimen.

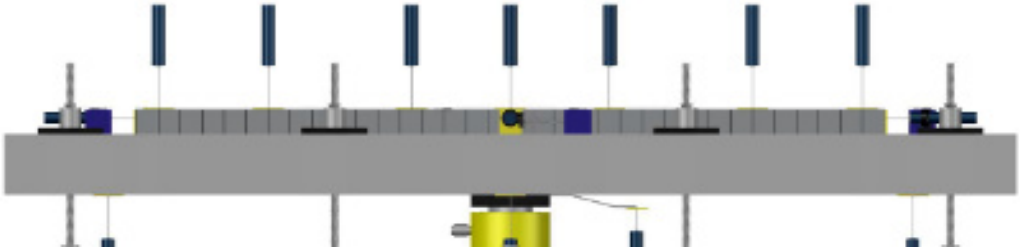

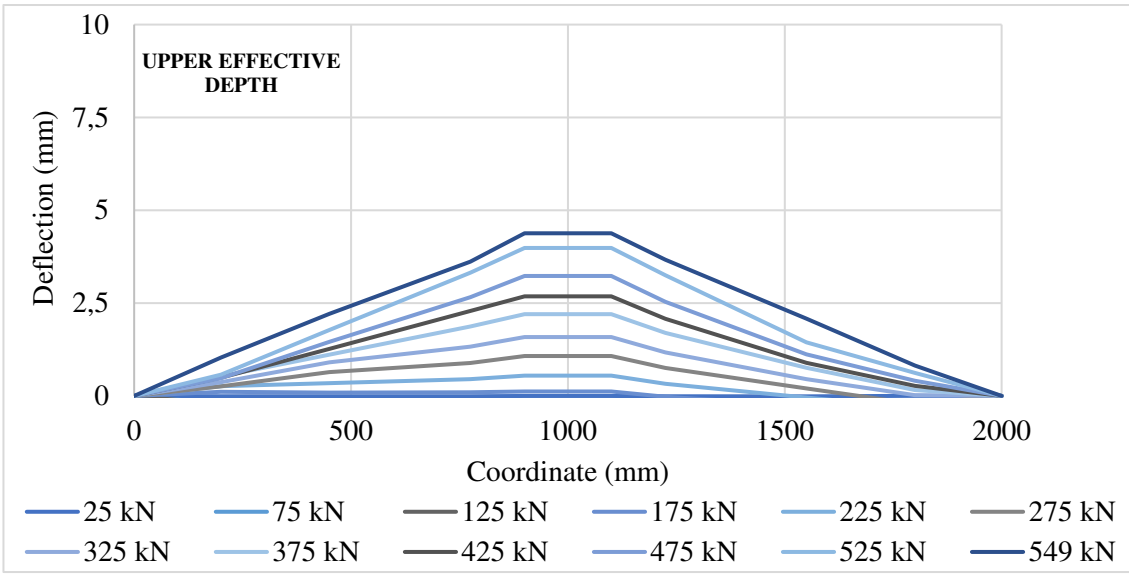


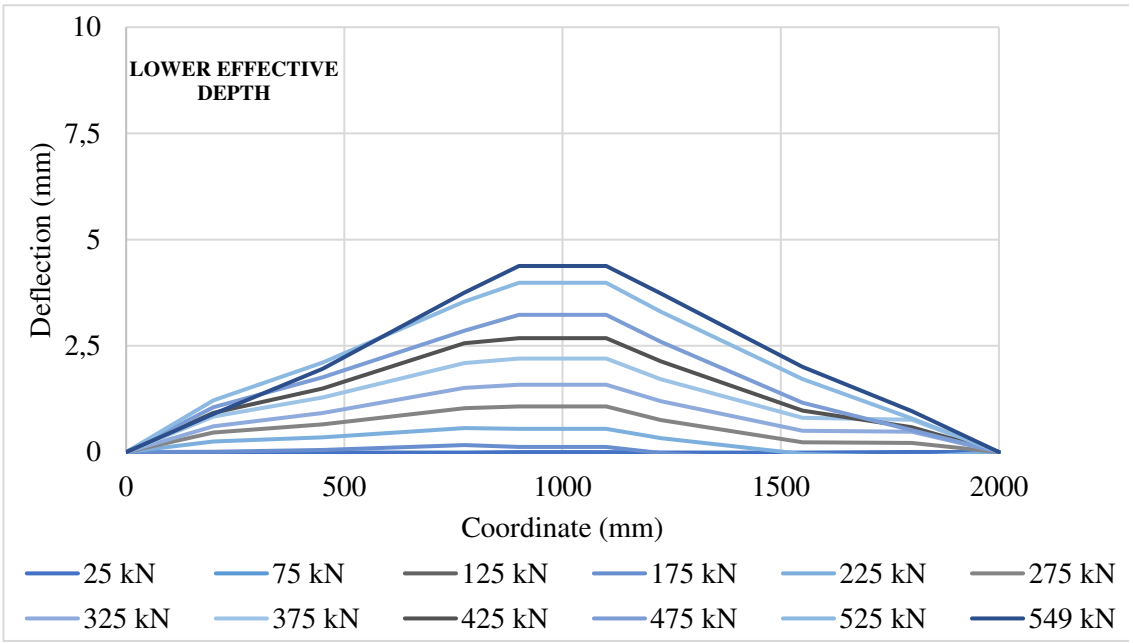


Figure 8.20 – Relative deformation between concrete layers for the $S_{4D}$-STANC specimen.

# 9. APPENDIX B

## Contents



## Index of Figures

# Index of Tables

## 9.1. Roughness profiles of rectangular specimens

The roughness of the substratum surface prior to casting the overlaid concrete was assessed after surface preparation and cleaning of debris and loose particles. The apparatus for measuring the substratum roughness profiles started as a 50 mm LVDT installed in a two degree-of-freedom system that measured the distance from a fixed referential to the existing surface, as illustrated in section 3.2.4 of chapter 3. Due to the lightness of the 50 mm LVDT, handling could be performed with one hand. This led to using a simplified version consisting on the fixed referential, levelled with the existing surface, where the 50 mm LVDT travels and acquires data on 37 predefined measurement points. Such operation is carefully performed by hand, with no significant error or instability of the light apparatus, as illustrated in Figure 9.1.

Figure 9.1 – Roughness profiles of the $R_L$-ANC specimen.

Discretization of the data acquired consisted on 37 equally spaced points of measurement in a 90-cm length. Assessment of the existing surface roughness was performed by tracing three profiles for each specimen according to the schematics in Figure 9.2.

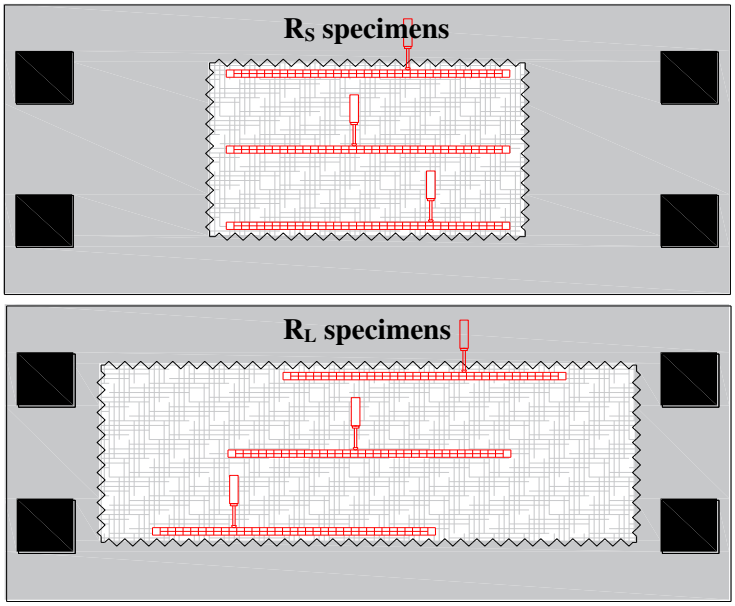


Figure 9.2 – Location of roughness assessment profiles on rectangular specimens.

The resulting profiles were then traced considering the average of points measured, according to equation (9.1) below, where $y_i$ is the measurement acquired on site and $\bar{y}$ the average of such measurements. Such profiles are illustrated on Figure 9.3 to Figure 9.11 for the rectangular specimens.

$$Z_i = |y_i - \bar{y}| \tag{9.1}$$

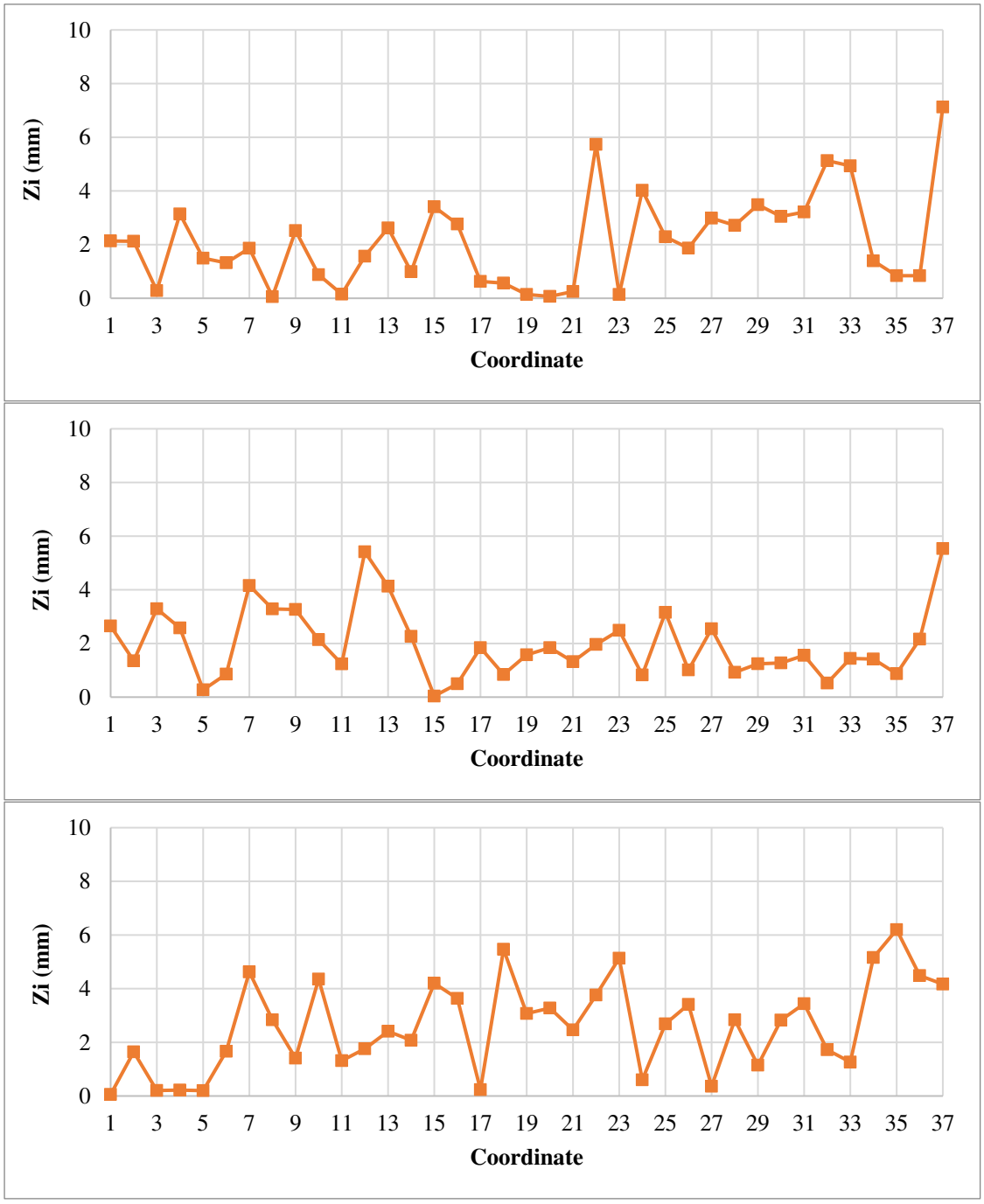


Figure 9.3 – Roughness profiles of the $R_L$-ANC specimen.

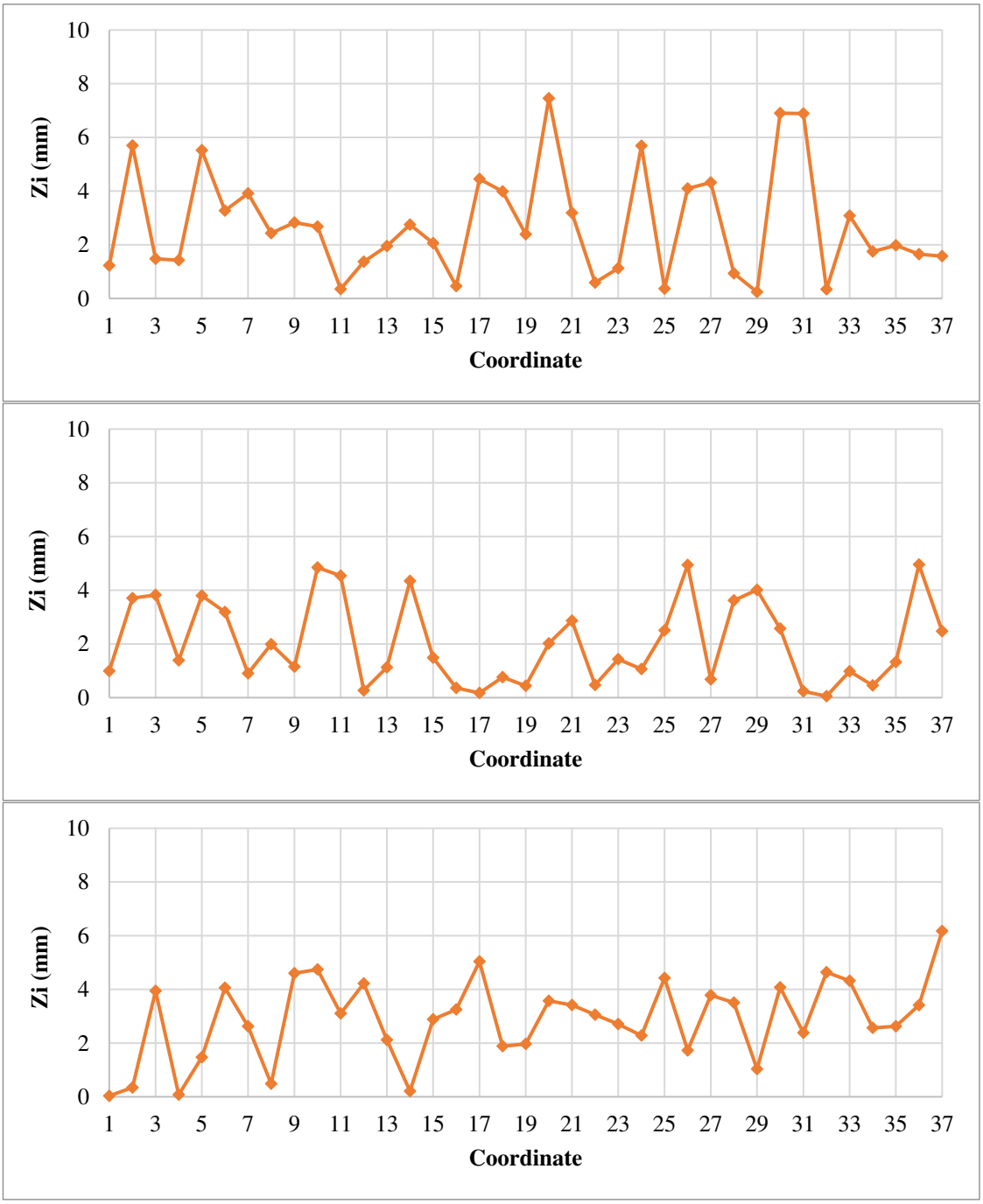


Figure 9.4 – Roughness profiles of the $R_L$-STC specimen.

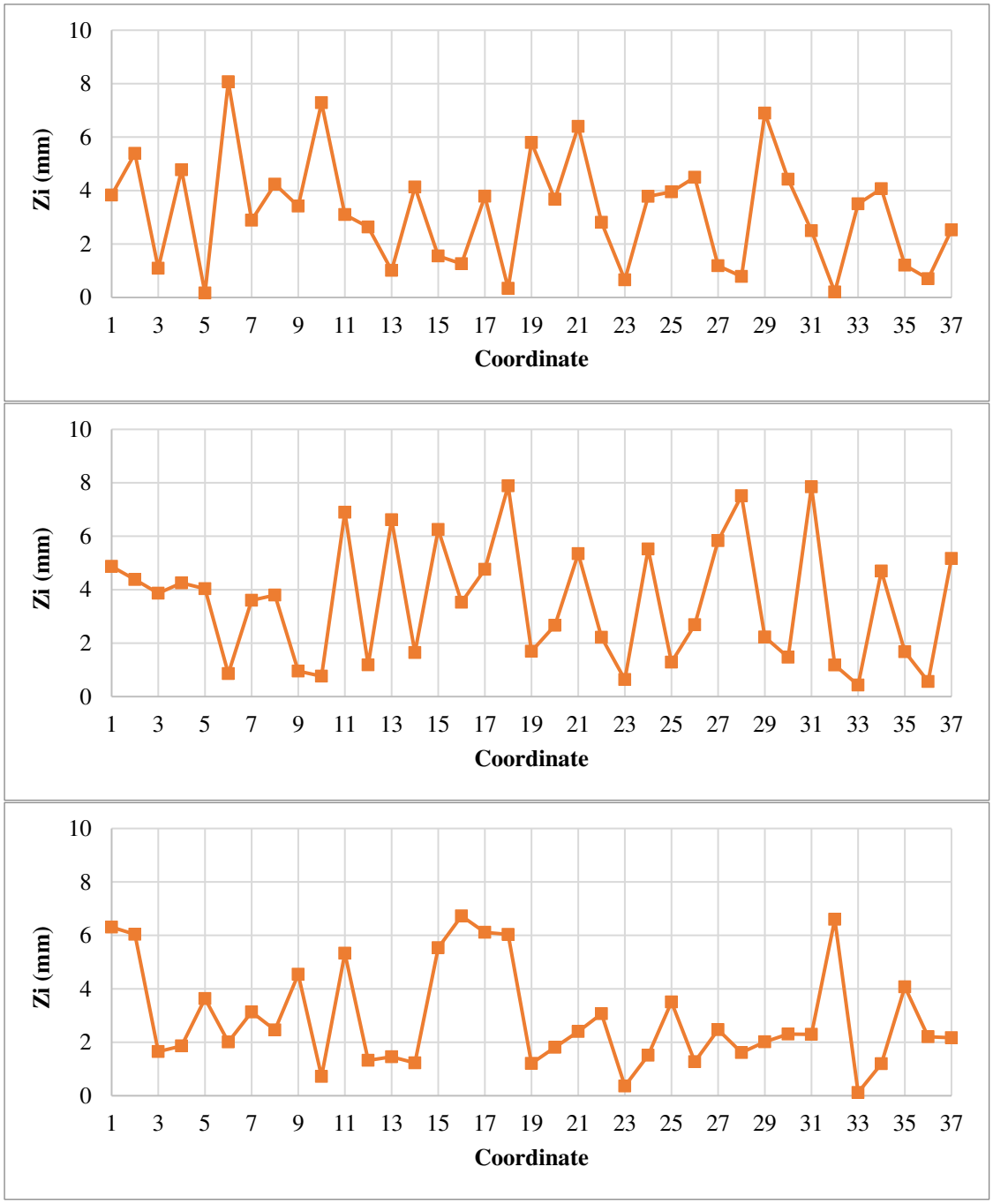


Figure 9.5 – Roughness profiles of the $R_L$-STANC specimen.

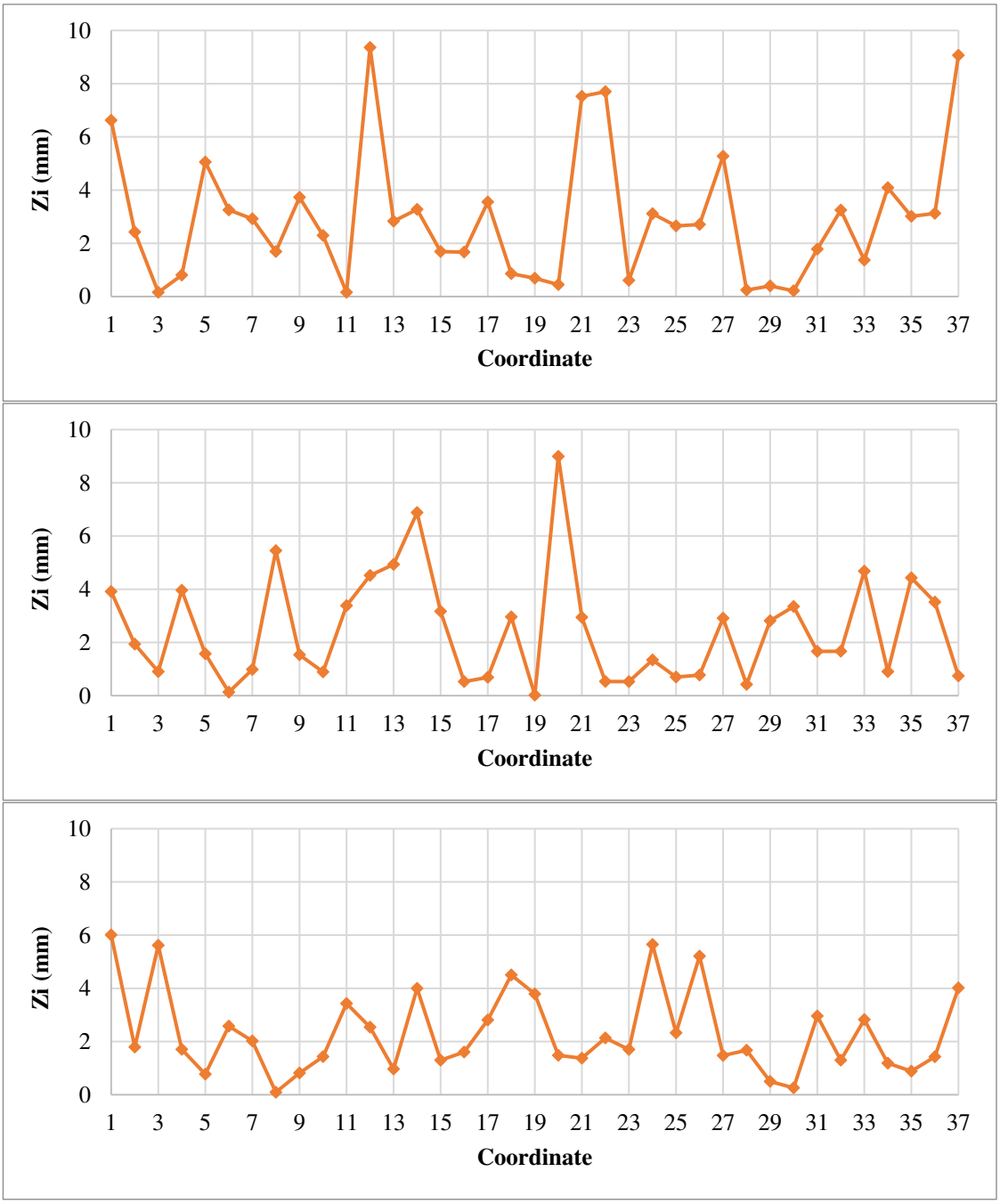


Figure 9.6 – Roughness profiles of the $R_L$-REF specimen.

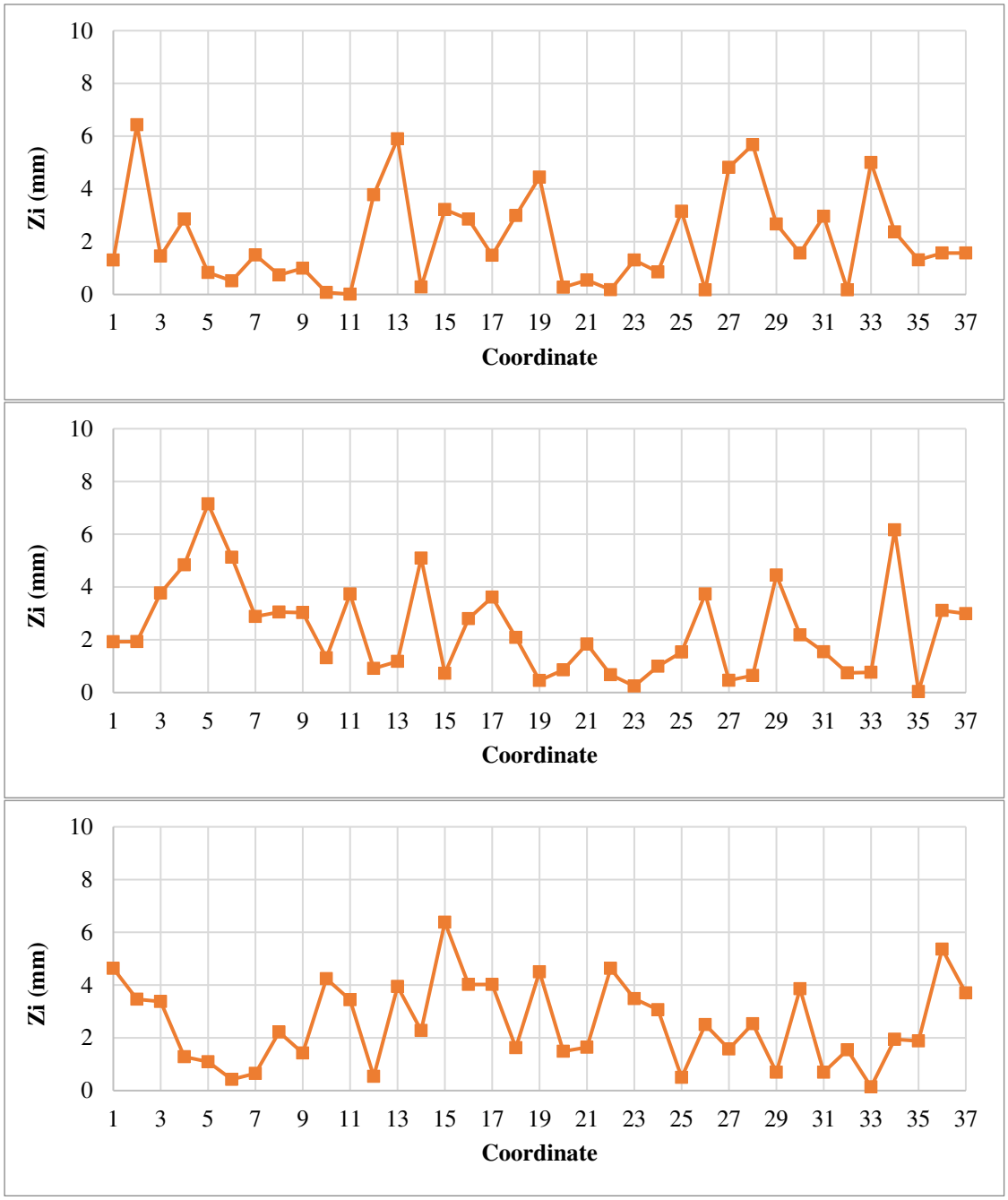


Figure 9.7 – Roughness profiles of the $R_S$-STC-5 specimen.

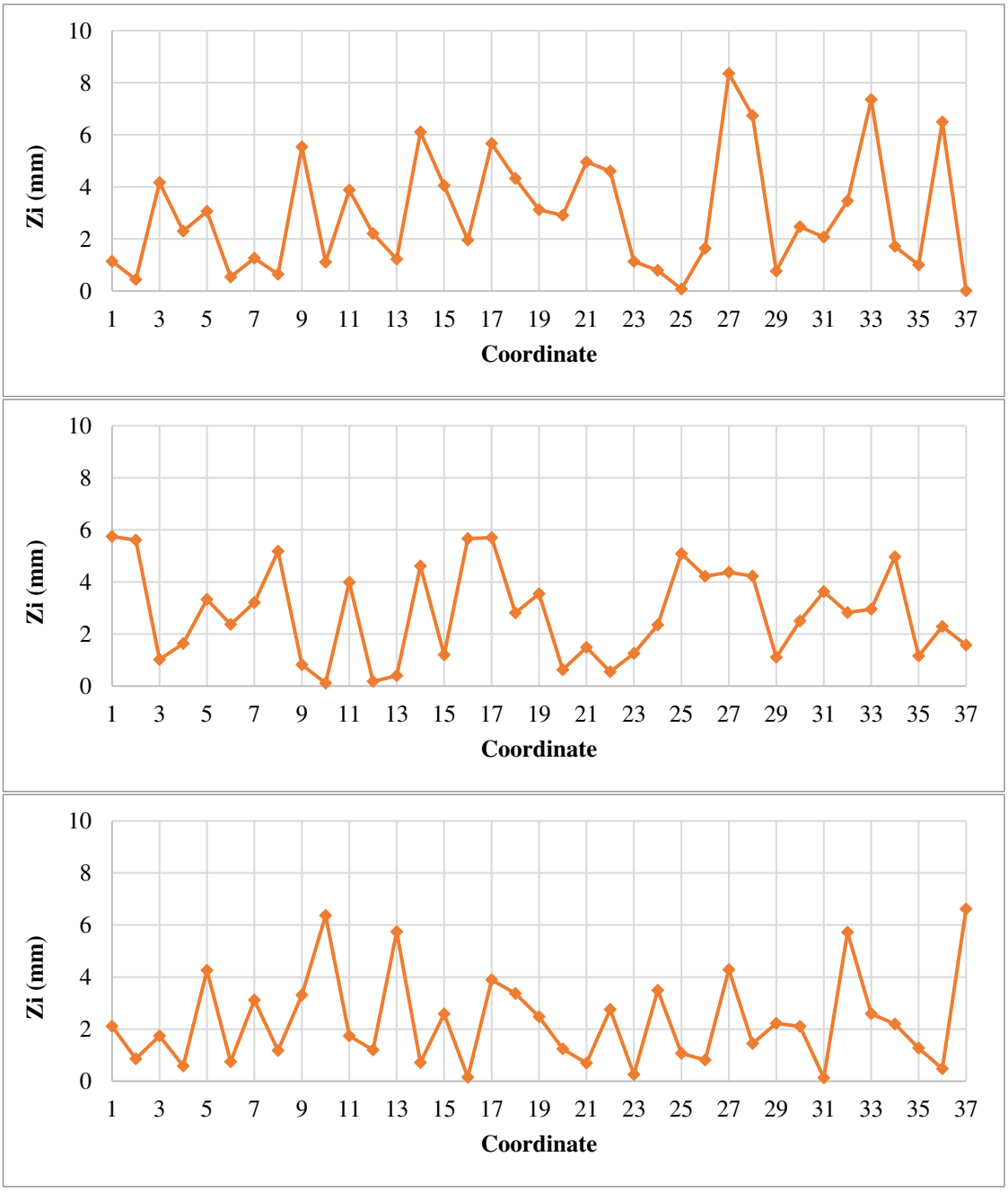


Figure 9.8 – Roughness profiles of the $R_S$-ANC-5 specimen.

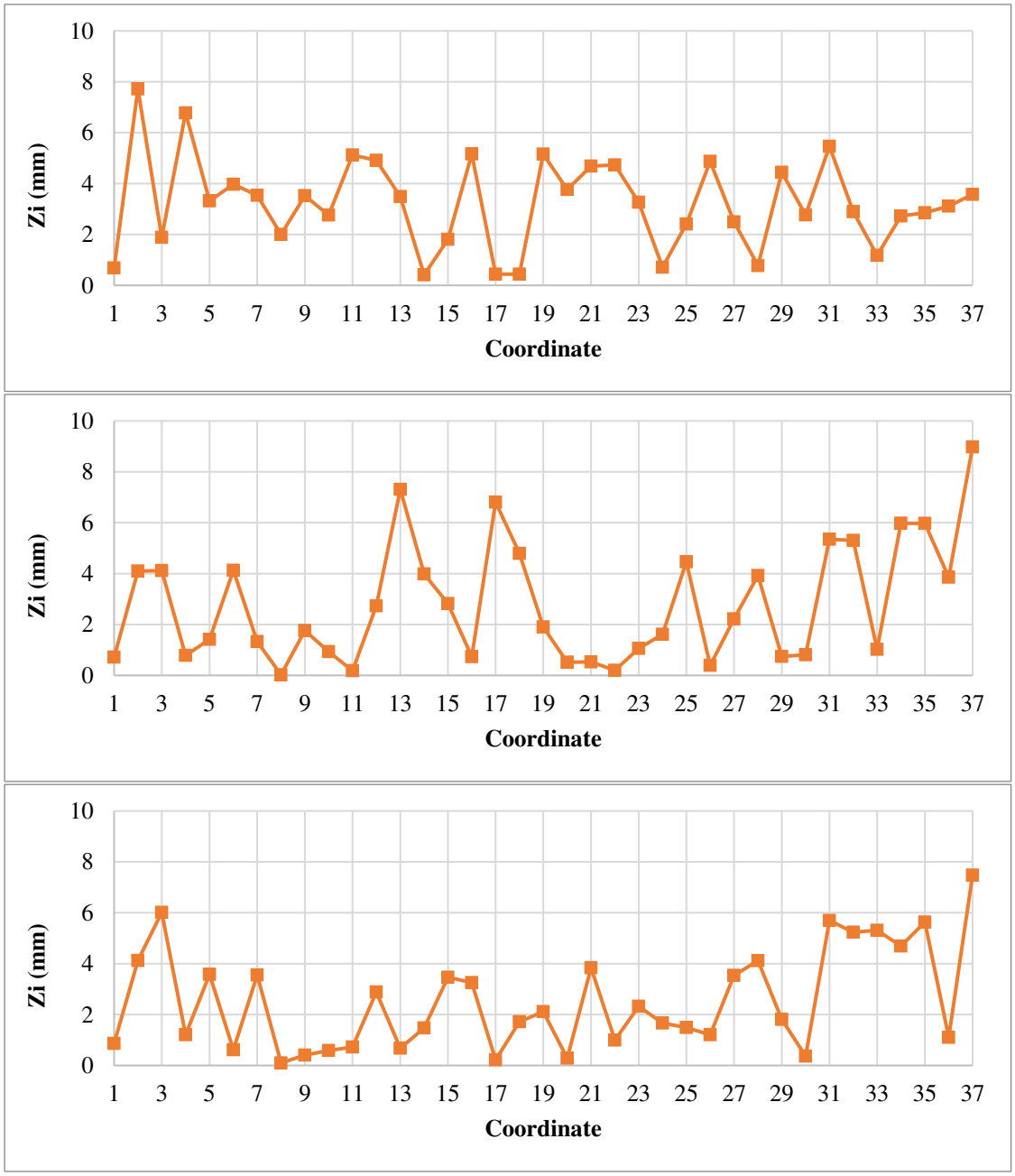


Figure 9.9 – Roughness profiles of the $R_S$-STC-4 specimen.

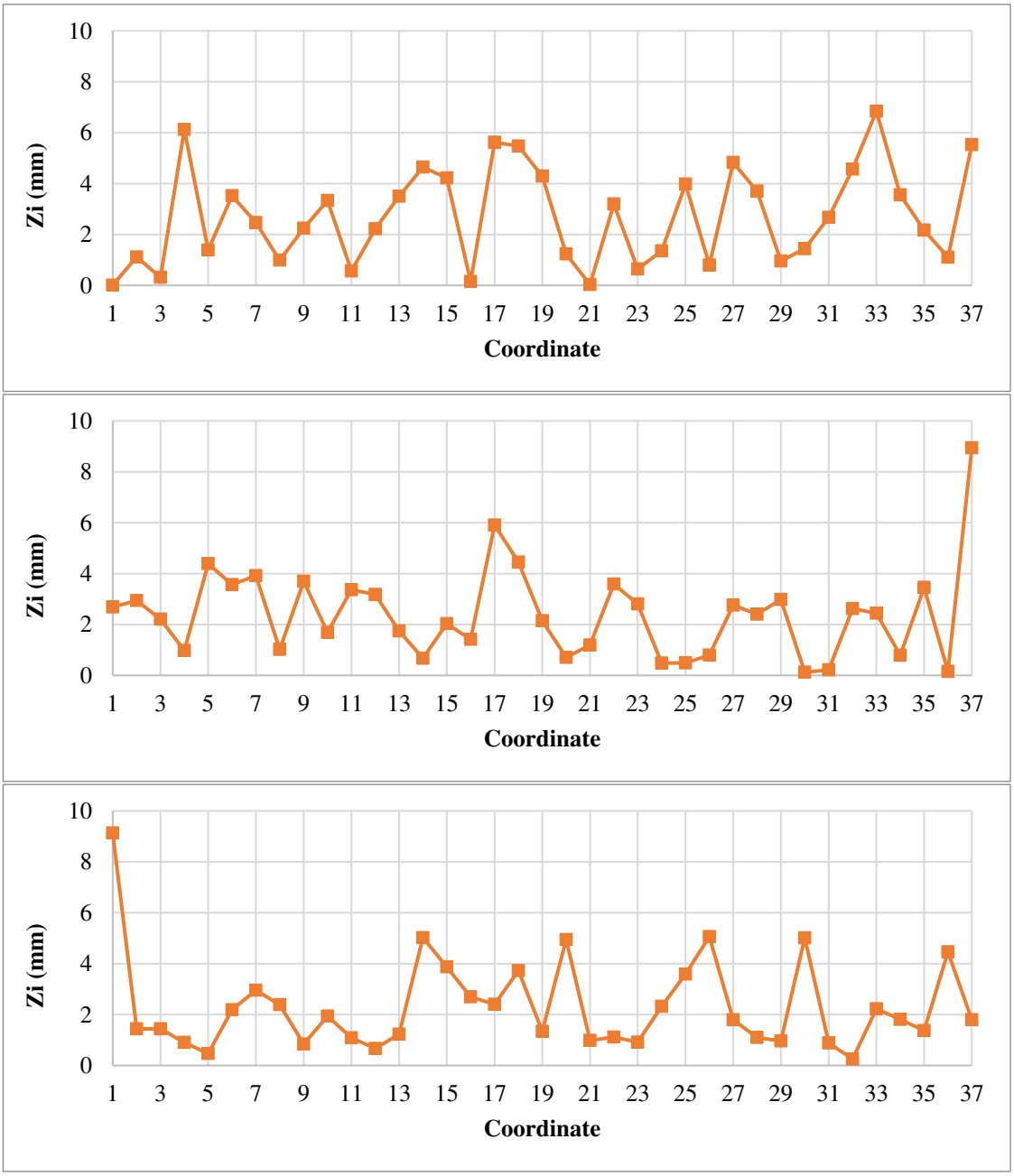


Figure 9.10 – Roughness profiles of the $R_S$-STANC specimen.

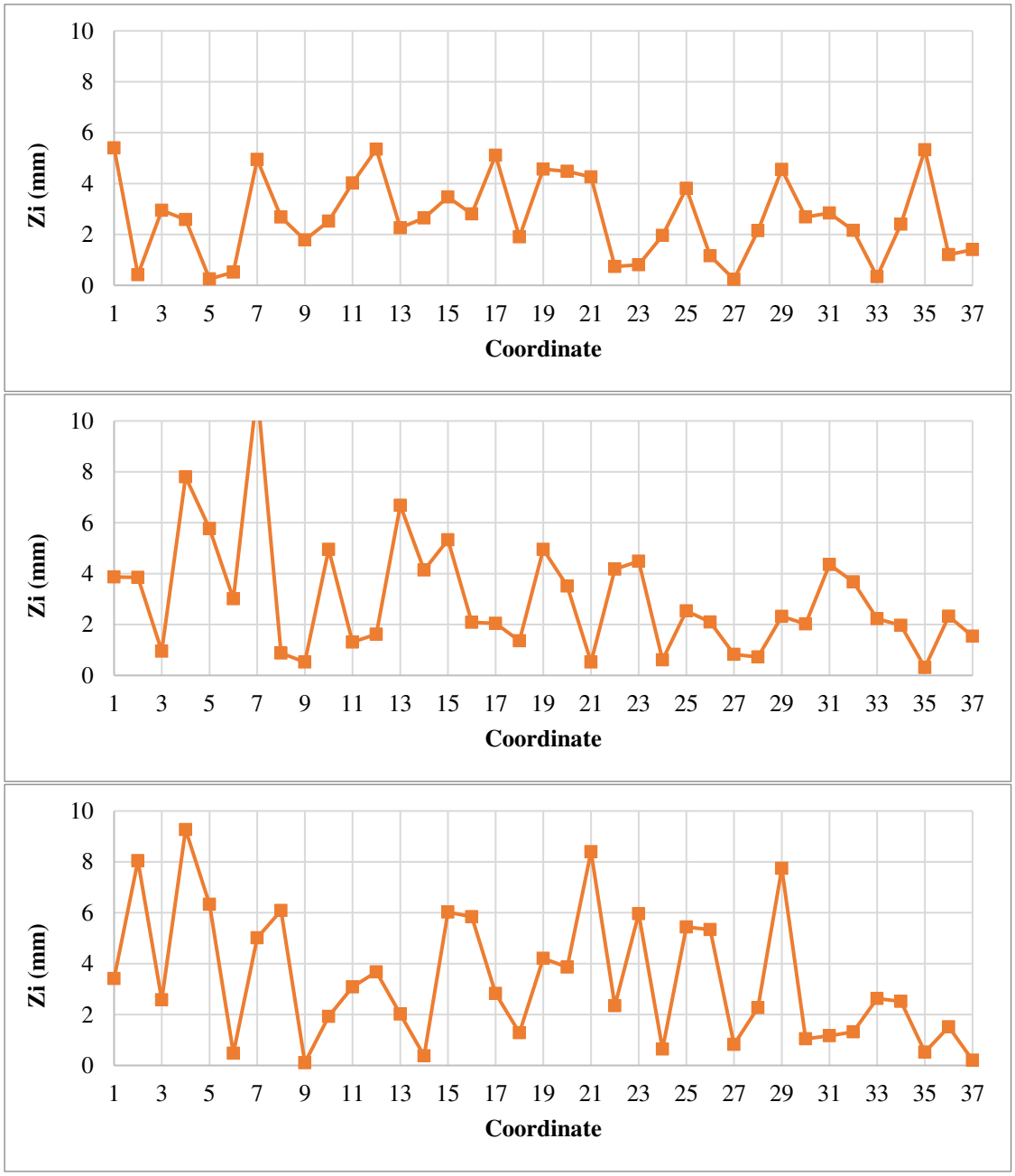


Figure 9.11 – Roughness profiles of the $R_S$-ANC-4 specimen.

Roughness of the first three sets of specimens - $R_S$-REF-1 to 3, $R_S$-ANC-1 to 3 and $R_S$-STC-1 to 3 – was analysed differently through mechanical profilometry on an equally spaced grid of point measurements with a manual calliper, as illustrated in Figure 9.12. Measurements and respective results are presented then in tables Table 3.8 to Table 9.9.

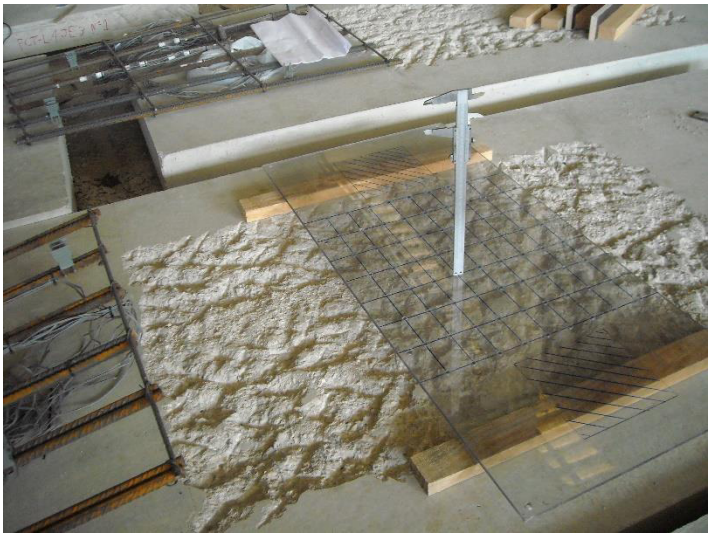

Figure 9.12 – Assessment of surface parameters with a manual calliper.

Table 9.1 – Surface characteristics after preparation of the $R_S$-REF-1 specimen.

| | **$R_S$-REF-1** | | | | | | | | | **AVG** | **Ra** | **Rt** |
|---|---|---|---|---|---|---|---|---|---|---|---|---|
| | 8.7 | 13.3 | 9.0 | 10.4 | 5.9 | 4.4 | 9.2 | 5.2 | 14.0 | 8.9 | 2.5 | 9.6 |
| | 11.0 | 13.9 | 4.0 | 10.3 | 3.2 | 12.3 | 7.5 | 10.6 | 9.0 | 9.1 | 2.8 | 10.7 |
| | 6.5 | 6.4 | 2.0 | 1.6 | 5.6 | 5.2 | 5.9 | 4.6 | 6.5 | 4.9 | 1.5 | 4.9 |
| | 4.6 | 1.5 | 1.3 | 2.9 | 8.7 | 3.8 | 6.0 | 7.0 | 6.3 | 4.7 | 2.1 | 7.4 |
| | 5.3 | 4.5 | 13.3 | 8.8 | 9.6 | 8.1 | 17.7 | 14.8 | 15.0 | 10.8 | 3.9 | 13.2 |
| | 9.4 | 8.5 | 11.6 | 14.0 | 14.7 | 4.4 | 6.0 | 3.6 | 11.1 | 9.3 | 3.2 | 11.1 |
| | 9.7 | 6.0 | 3.5 | 10.5 | 7.7 | 6.2 | 10.9 | 11.7 | 8.7 | 8.3 | 2.2 | 8.2 |
| | 7.0 | 3.7 | 3.8 | 7.3 | 8.0 | 6.5 | 19.0 | 12.5 | 9.6 | 8.6 | 3.4 | 15.3 |
| **AVG** | 7.8 | 7.2 | 6.1 | 8.2 | 7.9 | 6.4 | 10.3 | 8.8 | 10.0 | 8.1 | - | - |
| **Ra** | 1.9 | 3.5 | 3.9 | 3.2 | 2.3 | 2.0 | 4.2 | 3.7 | 2.5 | - | **2.9** | - |
| **Rt** | 6.4 | 12.4 | 12.0 | 12.4 | 11.5 | 8.5 | 13.1 | 11.2 | 8.7 | - | - | 10.4 |

Table 9.2 – Surface characteristics after preparation of the $R_S$-REF-2 specimen.

| | **$R_S$-REF-2** | | | | | | | | | **AVG** | **Ra** | **Rt** |
|---|---|---|---|---|---|---|---|---|---|---|---|---|
| | 20.9 | 15.9 | 10.6 | 10.8 | 16.7 | 5.0 | 10.5 | 12.0 | 16.4 | 13.2 | 3.8 | 15.9 |
| | 10.0 | 15.4 | 11.8 | 5.0 | 10.5 | 11.4 | 10.0 | 9.0 | 7.3 | 10.0 | 2.0 | 10.4 |
| | 8.8 | 9.4 | 9.7 | 9.4 | 7.1 | 13.6 | 7.8 | 8.3 | 12.9 | 9.7 | 1.6 | 6.5 |
| | 4.4 | 6.3 | 3.7 | 4.2 | 4.8 | 4.7 | 4.7 | 5.7 | 6.0 | 4.9 | 0.7 | 2.6 |
| | 3.2 | 4.5 | 6.7 | 5.7 | 6.6 | 14.0 | 9.0 | 10.3 | 12.0 | 8.0 | 3.0 | 10.8 |
| | 2.5 | 10.3 | 7.2 | 7.0 | 3.0 | 4.3 | 6.4 | 5.7 | 3.0 | 5.5 | 2.0 | 7.8 |
| | 2.0 | 7.2 | 12.6 | 3.8 | 10.0 | 2.7 | 7.7 | 12.9 | 4.0 | 7.0 | 3.4 | 10.9 |
| | 1.7 | 7.2 | 4.0 | 9.0 | 11.8 | 7.8 | 5.0 | 12.3 | 7.7 | 7.4 | 2.6 | 10.6 |
| **AVG** | 6.7 | 9.5 | 8.3 | 6.9 | 8.8 | 7.9 | 7.6 | 9.5 | 8.7 | 8.2 | - | - |
| **Ra** | 4.9 | 3.3 | 2.9 | 2.2 | 3.4 | 3.8 | 1.7 | 2.4 | 3.8 | - | **2.8** | - |
| **Rt** | 19.2 | 11.4 | 8.9 | 7.0 | 13.7 | 11.3 | 5.8 | 7.2 | 13.4 | - | - | 10.2 |

Table 9.3 – Surface characteristics after preparation of the $R_S$-REF-3 specimen.

| | $R_S$-REF-3 | | | | | | | | | AVG | Ra | Rt |
|---|---|---|---|---|---|---|---|---|---|---|---|---|
| | 4.8 | 3.3 | 7.6 | 8.3 | 5.0 | 8.1 | 7.1 | 9.0 | 6.3 | 6.6 | 1.6 | 5.7 |
| | 8.6 | 6.7 | 3.1 | 3.2 | 5.7 | 2.5 | 1.0 | 5.7 | 2.0 | 4.3 | 2.1 | 7.6 |
| | 5.3 | 1.9 | 7.3 | 2.8 | 6.2 | 2.7 | 12.7 | 12.6 | 0.0 | 5.7 | 3.5 | 12.7 |
| | 1.5 | 3.4 | 1.3 | 1.7 | 8.0 | 4.4 | 0.4 | 7.8 | 0.2 | 3.2 | 2.4 | 7.8 |
| | 9.2 | 3.6 | 1.2 | 12.8 | 1.0 | 9.5 | 7.2 | 0.5 | 0.7 | 5.1 | 4.1 | 12.3 |
| | 8.9 | 3.0 | 7.4 | 9.3 | 3.0 | 2.4 | 11.4 | 10.1 | 1.2 | 6.3 | 3.5 | 10.2 |
| | 6.4 | 8.4 | 4.0 | 5.7 | 3.8 | 9.0 | 7.2 | 9.0 | 9.4 | 7.0 | 1.8 | 5.6 |
| | 15.1 | 6.5 | 11.3 | 4.4 | 11.1 | 8.2 | 9.1 | 3.4 | 2.6 | 8.0 | 3.3 | 12.5 |
| **AVG** | 7.5 | 4.6 | 5.4 | 6.0 | 5.5 | 5.9 | 7.0 | 7.3 | 2.8 | 5.8 | - | - |
| **Ra** | 3.0 | 2.0 | 3.0 | 3.1 | 2.3 | 2.9 | 3.2 | 3.0 | 2.5 | - | **2.8** | - |
| **Rt** | 13.6 | 6.5 | 10.1 | 11.1 | 10.1 | 7.1 | 12.3 | 12.1 | 9.4 | - | - | 9.8 |

Table 9.4 – Surface characteristics after preparation of the $R_S$-ANC-1 specimen.

| | $R_S$-ANC-1 | | | | | | | | | AVG | Ra | Rt |
|---|---|---|---|---|---|---|---|---|---|---|---|---|
| | 8.6 | 15.0 | 3.0 | 4.2 | 2.7 | 4.4 | 12.8 | 5.9 | 11.2 | 7.5 | 3.9 | 12.3 |
| | 7.7 | 14.0 | 7.0 | 11.2 | 2.6 | 9.4 | 11.1 | 5.2 | 5.0 | 8.1 | 2.9 | 11.4 |
| | 10.2 | 9.5 | 9.4 | 11.1 | 6.4 | 7.7 | 9.9 | 11.0 | 5.5 | 9.0 | 1.6 | 5.6 |
| | 6.3 | 11.6 | 11.1 | 9.7 | 12.5 | 8.5 | 6.7 | 14.0 | 8.7 | 9.9 | 2.1 | 7.7 |
| | 0.0 | 12.2 | 4.7 | 1.2 | 3.1 | 2.3 | 5.3 | 1.9 | 4.7 | 3.9 | 2.5 | 12.2 |
| | 0.7 | 3.3 | 7.2 | 4.7 | 6.9 | 3.0 | 8.2 | 6.3 | 6.5 | 5.2 | 2.0 | 7.5 |
| | 1.0 | 9.3 | 3.2 | 0.3 | 3.3 | 5.0 | 3.8 | 4.0 | 16.6 | 5.2 | 3.5 | 16.3 |
| | 2.5 | 10.0 | 10.3 | 4.7 | 4.0 | 14.5 | 11.5 | 12.6 | 10.0 | 8.9 | 3.4 | 12.0 |
| **AVG** | 4.6 | 10.6 | 7.0 | 5.9 | 5.2 | 6.9 | 8.7 | 7.6 | 8.5 | 7.2 | - | - |
| **Ra** | 3.6 | 2.6 | 2.5 | 3.6 | 2.6 | 3.2 | 2.7 | 3.7 | 3.1 | - | **2.9** | - |
| **Rt** | 10.2 | 11.7 | 8.1 | 10.9 | 9.9 | 12.2 | 9.0 | 12.1 | 11.9 | - | - | 10.6 |

Table 9.5 – Surface characteristics after preparation of the $R_S$-ANC-2 specimen.

| | $R_S$-ANC-2 | | | | | | | | | AVG | Ra | Rt |
|---|---|---|---|---|---|---|---|---|---|---|---|---|
| | 16.3 | 4.0 | 7.1 | 11.8 | 4.0 | 9.5 | 2.2 | 2.7 | 6.0 | 7.1 | 3.7 | 14.1 |
| | 18.4 | 5.2 | 7.8 | 10.3 | 6.2 | 0.5 | -0.1 | 2.7 | 1.8 | 5.9 | 4.3 | 18.5 |
| | 12.0 | 7.0 | 11.8 | 1.6 | -0.2 | 2.1 | 1.6 | 4.0 | 0.3 | 4.5 | 3.9 | 12.2 |
| | 12.0 | 12.2 | 4.6 | 5.0 | 8.3 | 13.7 | 13.8 | 13.8 | 6.3 | 10.0 | 3.5 | 9.2 |
| | 8.7 | 9.4 | 10.2 | 7.2 | 4.6 | 3.4 | 3.0 | 8.0 | 4.8 | 6.6 | 2.3 | 7.2 |
| | 6.2 | 20.0 | 5.0 | 8.4 | 4.7 | 4.8 | 4.3 | 2.7 | 1.2 | 6.4 | 3.5 | 18.8 |
| | 11.2 | 10.5 | 4.3 | 9.0 | 10.0 | 3.8 | 2.7 | 3.3 | 4.4 | 6.6 | 3.2 | 8.5 |
| | 15.7 | 7.7 | 11.4 | 8.8 | 10.7 | 2.7 | 13.0 | 5.0 | 13.2 | 9.8 | 3.3 | 13.0 |
| **AVG** | 12.6 | 9.5 | 7.8 | 7.8 | 6.0 | 5.1 | 5.1 | 5.3 | 4.8 | 7.1 | - | - |
| **Ra** | 3.2 | 3.6 | 2.5 | 2.4 | 2.8 | 3.3 | 4.2 | 2.8 | 2.8 | - | **3.2** | - |
| **Rt** | 12.2 | 16.0 | 7.5 | 10.2 | 10.9 | 13.2 | 13.9 | 11.1 | 12.9 | - | - | 12.3 |

Table 9.6 – Surface characteristics after preparation of the $R_S$-ANC-3 specimen.

| | **$R_S$-ANC-3** | | | | | | | | | **AVG** | **Ra** | **Rt** |
|---|---|---|---|---|---|---|---|---|---|---|---|---|
| | 4.0 | 8.8 | 13.0 | 7.5 | 7.1 | 9.6 | 8.0 | 4.0 | 16.3 | 8.7 | 2.9 | 12.3 |
| | 11.3 | 16.2 | 7.1 | 14.9 | 8.4 | 4.0 | 7.9 | 10.0 | 11.7 | 10.2 | 3.0 | 12.2 |
| | 15.5 | 10.1 | 15.8 | 3.1 | 15.6 | 1.6 | 1.8 | 1.2 | 2.8 | 7.5 | 6.0 | 14.6 |
| | 10.0 | 2.5 | 19.0 | 3.0 | 5.9 | 8.3 | 2.2 | 15.9 | 6.0 | 8.1 | 4.6 | 16.8 |
| | 14.7 | 11.9 | 5.5 | 15.7 | 2.8 | 9.0 | 12.4 | 5.0 | 11.5 | 9.8 | 3.8 | 12.9 |
| | 4.0 | 13.7 | 3.8 | 8.4 | 4.0 | 12.1 | 8.0 | 6.6 | 3.6 | 7.1 | 3.0 | 10.1 |
| | 7.0 | 11.4 | 3.7 | 4.0 | 5.4 | 11.7 | 10.6 | 6.1 | 7.2 | 7.5 | 2.5 | 8.0 |
| | 4.3 | 10.8 | 11.7 | 4.0 | 13.5 | 16.0 | 16.8 | 9.0 | 8.0 | 10.5 | 3.7 | 12.8 |
| **AVG** | 8.9 | 10.7 | 10.0 | 7.6 | 7.8 | 9.0 | 8.5 | 7.2 | 8.4 | 8.7 | - | - |
| **Ra** | 4.0 | 2.7 | 4.9 | 4.1 | 3.5 | 3.3 | 3.6 | 3.3 | 3.6 | - | **3.7** | - |
| **Rt** | 11.5 | 13.7 | 15.3 | 12.7 | 12.8 | 14.4 | 15.0 | 14.7 | 13.5 | - | - | 13.1 |

Table 9.7 – Surface characteristics after preparation of the $R_S$-STC-1 specimen.

| | **$R_S$-STC-1** | | | | | | | | | **AVG** | **Ra** | **Rt** |
|---|---|---|---|---|---|---|---|---|---|---|---|---|
| | 8.7 | 13.3 | 9.0 | 10.4 | 5.9 | 4.4 | 9.2 | 5.2 | 14.0 | 8.9 | 2.5 | 9.6 |
| | 11.0 | 13.9 | 4.0 | 10.3 | 3.2 | 12.3 | 7.5 | 10.6 | 9.0 | 9.1 | 2.8 | 10.7 |
| | 6.5 | 6.4 | 2.0 | 1.6 | 5.6 | 5.2 | 5.9 | 4.6 | 6.5 | 4.9 | 1.5 | 4.9 |
| | 4.6 | 1.5 | 1.3 | 2.9 | 8.7 | 3.8 | 6.0 | 7.0 | 6.3 | 4.7 | 2.1 | 7.4 |
| | 5.3 | 4.5 | 13.3 | 8.8 | 9.6 | 8.1 | 17.7 | 14.8 | 15.0 | 10.8 | 3.9 | 13.2 |
| | 9.4 | 8.5 | 11.6 | 14.0 | 14.7 | 4.4 | 6.0 | 3.6 | 11.1 | 9.3 | 3.2 | 11.1 |
| | 9.7 | 6.0 | 3.5 | 10.5 | 7.7 | 6.2 | 10.9 | 11.7 | 8.7 | 8.3 | 2.2 | 8.2 |
| | 7.0 | 3.7 | 3.8 | 7.3 | 8.0 | 6.5 | 19.0 | 12.5 | 9.6 | 8.6 | 3.4 | 15.3 |
| **AVG** | 7.8 | 7.2 | 6.1 | 8.2 | 7.9 | 6.4 | 10.3 | 8.8 | 10.0 | 8.1 | - | - |
| **Ra** | 1.9 | 3.5 | 3.9 | 3.2 | 2.3 | 2.0 | 4.2 | 3.7 | 2.5 | - | **2.9** | - |
| **Rt** | 6.4 | 12.4 | 12.0 | 12.4 | 11.5 | 8.5 | 13.1 | 11.2 | 8.7 | - | - | 10.4 |

Table 9.8 – Surface characteristics after preparation of the $R_S$-STC-2 specimen.

| | **$R_S$-STC-2** | | | | | | | | | **AVG** | **Ra** | **Rt** |
|---|---|---|---|---|---|---|---|---|---|---|---|---|
| | 6.3 | 10.4 | 4.0 | 9.8 | 4.8 | 10.0 | 7.7 | 7.9 | 12.3 | 8.1 | 2.2 | 8.3 |
| | -0.3 | 8.8 | 8.3 | 0.0 | 1.2 | 9.4 | 9.0 | 9.3 | 4.0 | 5.5 | 3.8 | 9.7 |
| | 0.0 | 4.1 | 3.4 | 4.2 | 0.5 | 4.0 | 1.3 | 2.8 | 1.0 | 2.4 | 1.5 | 4.2 |
| | 3.8 | 0.1 | 2.4 | 1.9 | 3.8 | 4.0 | 1.2 | 2.8 | 1.2 | 2.4 | 1.1 | 3.9 |
| | 3.9 | 7.2 | -0.4 | 3.0 | 1.7 | 10.0 | -1.3 | 4.7 | -1.1 | 3.1 | 3.0 | 11.3 |
| | 0.0 | -0.3 | 10.7 | 6.9 | 7.0 | 1.0 | 11.7 | 7.2 | 5.7 | 5.5 | 3.5 | 12.0 |
| | 7.0 | 9.0 | 3.1 | 10.0 | 2.3 | 7.3 | 8.6 | 16.2 | 1.1 | 7.2 | 3.4 | 15.1 |
| | 6.5 | 10.6 | 8.6 | 12.5 | 5.5 | 5.4 | 6.3 | 5.0 | 8.3 | 7.6 | 2.1 | 7.5 |
| **AVG** | 3.4 | 6.2 | 5.0 | 6.0 | 3.4 | 6.4 | 5.6 | 7.0 | 4.1 | 5.2 | - | - |
| **Ra** | 2.6 | 3.7 | 3.1 | 3.8 | 1.9 | 2.8 | 3.9 | 3.2 | 3.5 | - | **2.9** | - |
| **Rt** | 7.3 | 10.9 | 11.1 | 12.5 | 6.5 | 9.0 | 13.0 | 13.4 | 13.4 | - | - | 9.9 |

Table 9.9 – Surface characteristics after preparation of the $R_S$-STC-3 specimen.

| | **$R_S$-STC-3** | | | | | | | | | **AVG** | **Ra** | **Rt** |
|---|---|---|---|---|---|---|---|---|---|---|---|---|
| | 4.5 | 3.6 | 7.4 | 4.7 | 10.6 | 7.7 | 10.5 | 10.4 | 12.0 | 7.9 | 2.6 | 8.4 |
| | 8.2 | 6.0 | 17.5 | 3.7 | 14.2 | 8.1 | 8.8 | 8.4 | 7.0 | 9.1 | 3.0 | 13.8 |
| | 11.7 | 9.0 | 3.0 | 5.2 | 4.3 | 5.0 | 4.5 | 8.4 | 14.6 | 7.3 | 3.2 | 11.6 |
| | 8.3 | 6.7 | 9.8 | 3.0 | 2.4 | 8.5 | 2.4 | 3.5 | 2.0 | 5.2 | 2.8 | 7.8 |
| | 12.0 | 9.0 | 13.6 | 3.3 | 15.6 | 9.8 | 3.7 | 8.7 | 10.1 | 9.5 | 3.0 | 12.3 |
| | 11.0 | 11.6 | 9.8 | 8.3 | 10.3 | 12.0 | 7.2 | 8.0 | 9.3 | 9.7 | 1.4 | 4.8 |
| | 18.5 | 15.5 | 9.5 | 7.0 | 5.7 | 12.0 | 11.2 | 11.7 | 10.3 | 11.3 | 2.8 | 12.8 |
| | 9.0 | 9.4 | 5.9 | 5.2 | 11.0 | 5.2 | 10.5 | 11.2 | 15.0 | 9.2 | 2.5 | 9.8 |
| **AVG** | 10.4 | 8.9 | 9.6 | 5.1 | 9.3 | 8.5 | 7.4 | 8.8 | 10.0 | 8.6 | - | - |
| **Ra** | 2.9 | 2.6 | 3.1 | 1.4 | 3.8 | 2.0 | 2.9 | 1.7 | 3.0 | - | **2.6** | - |
| **Rt** | 14.0 | 11.9 | 14.5 | 5.3 | 13.2 | 7.0 | 8.8 | 8.2 | 13.0 | - | - | 10.4 |

The resulting surface characteristics were calculated according to equations for the traced longitudinal profiles depicted on Figure 8.1 to Figure 9.11:

- (9.2) – average surface roughness $R_a$, where $n$ is the number of points measured, $y_i$ and $\bar{y}$ as stated before;

- (9.3) – total roughness $R_z$, where the highest peak-to-valley heights were measured over 5 equally spaced preconised lengths;

- (9.4) – peak-to-mean roughness $R_p$, where the peak heights $p_i$ are measured and evaluated according to the average depth of the roughness profile.

$$R_a = \frac{1}{l_m} . \int_0^{l_m} y(x)\, dx \approx \frac{1}{n} . \sum_{i=1}^{n} |y_i - \bar{y}| \tag{9.2}$$

$$R_z = \frac{1}{5} . \sum_{i=1}^{5} z_i \tag{9.3}$$

$$R_p = \frac{1}{n} . \sum_{i=1}^{n} |p_i - \bar{y}| \tag{9.4}$$

## 9.2. Roughness profiles of square specimens

The same procedure was performed on the square slab specimens, with the difference that roughness was characterised on both directions of the contact surface, as illustrated in the schematics of Figure 9.13. Such directions were identified according to the upper (in red) and lower (in blue) effective depths of flexural reinforcement.

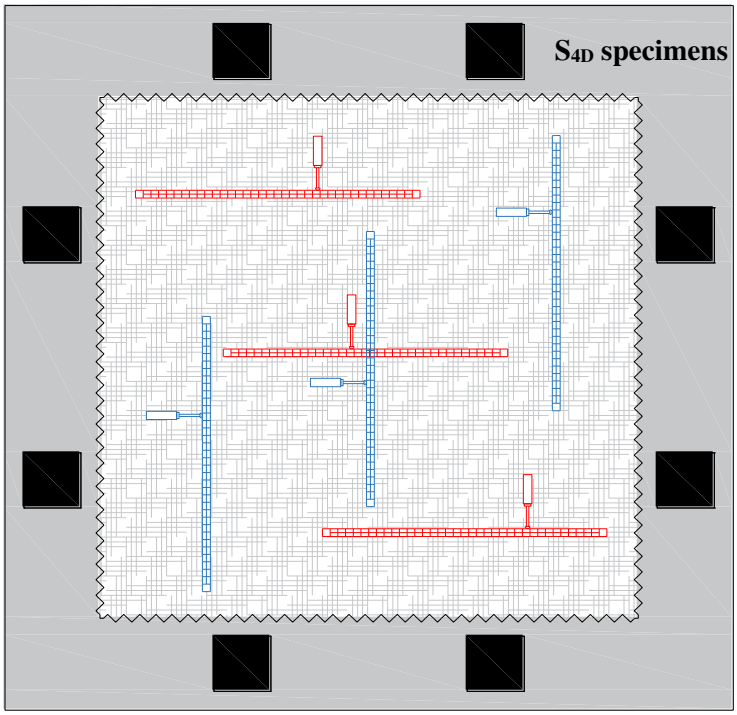


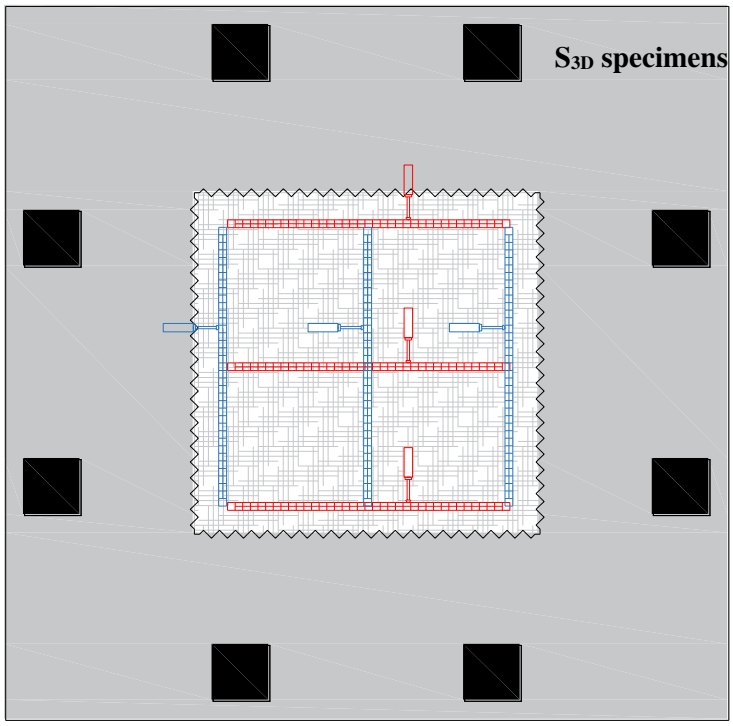

Figure 9.13 – Location of roughness assessment profiles on square specimens.

The resulting profiles were then traced considering the average of points measured, similarly to the method performed on rectangular specimens in the previous chapter and are presented on Figure 9.14 to Figure 9.17.

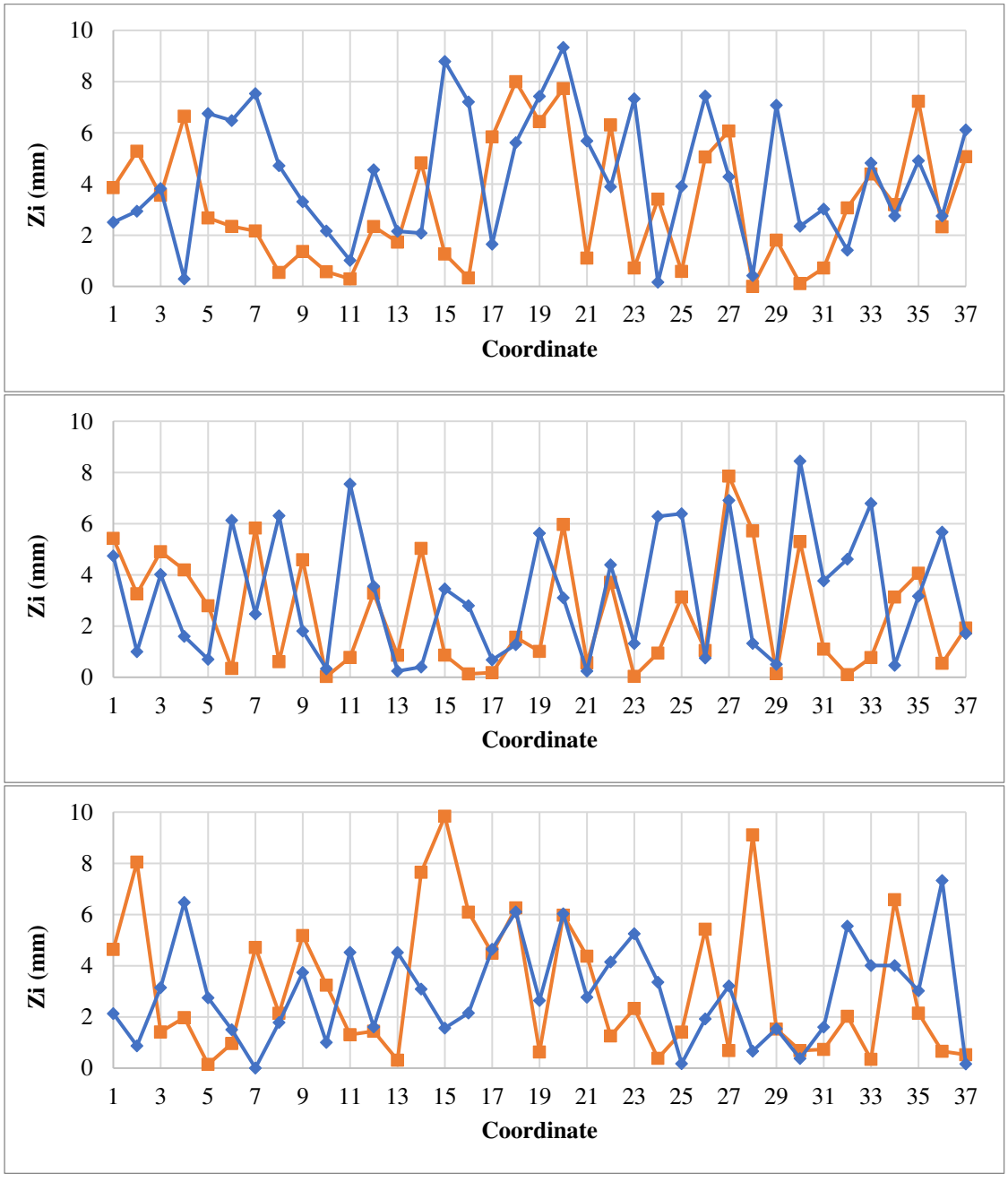


Figure 9.14 – Roughness profiles of the $S_{3D}$-ANC specimen:
(—) upper effective depth, (—) lower effective depth.

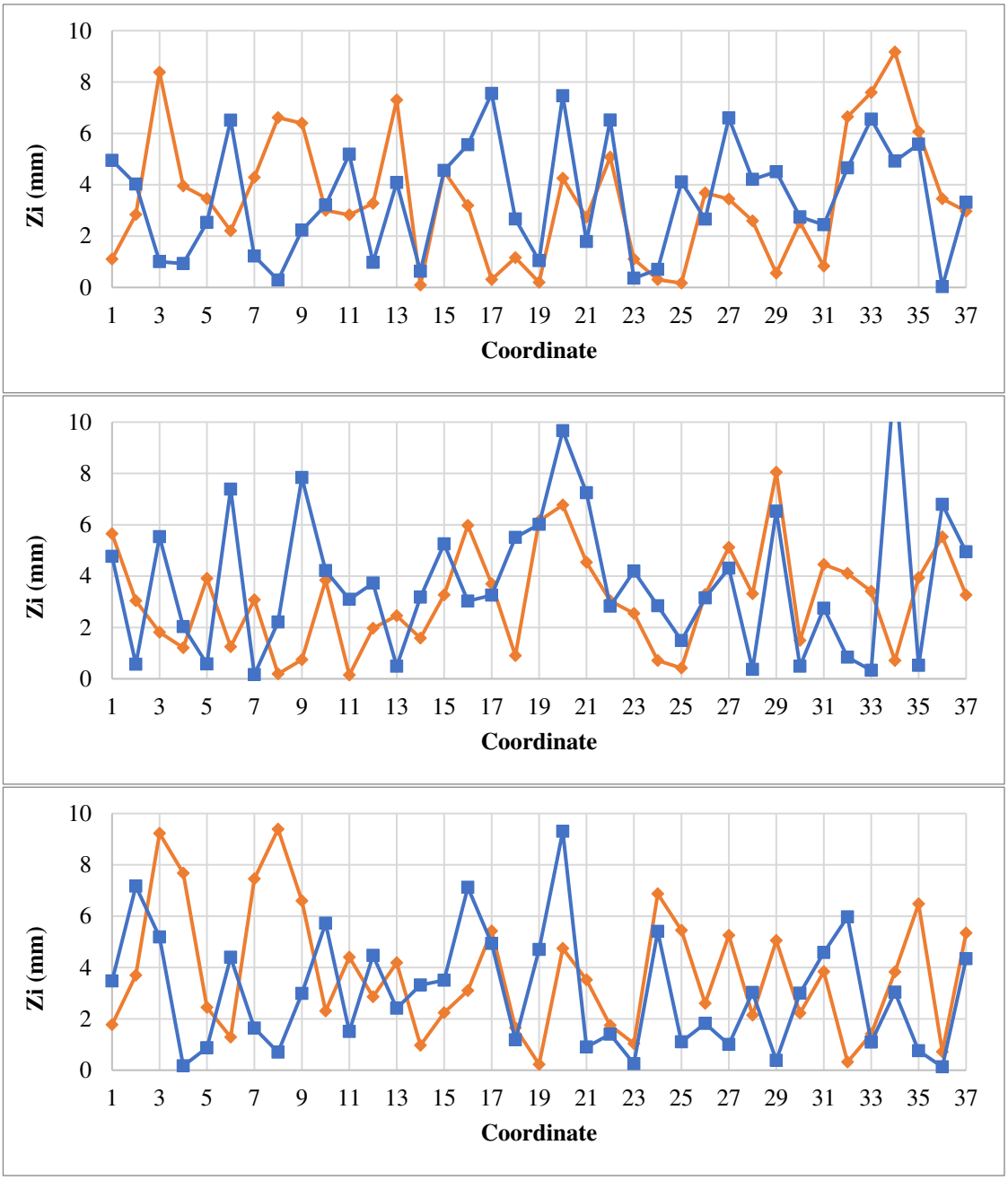


Figure 9.15 – Roughness profiles of the $S_{3D}$-STANC specimen:
(—) upper effective depth, (—) lower effective depth.

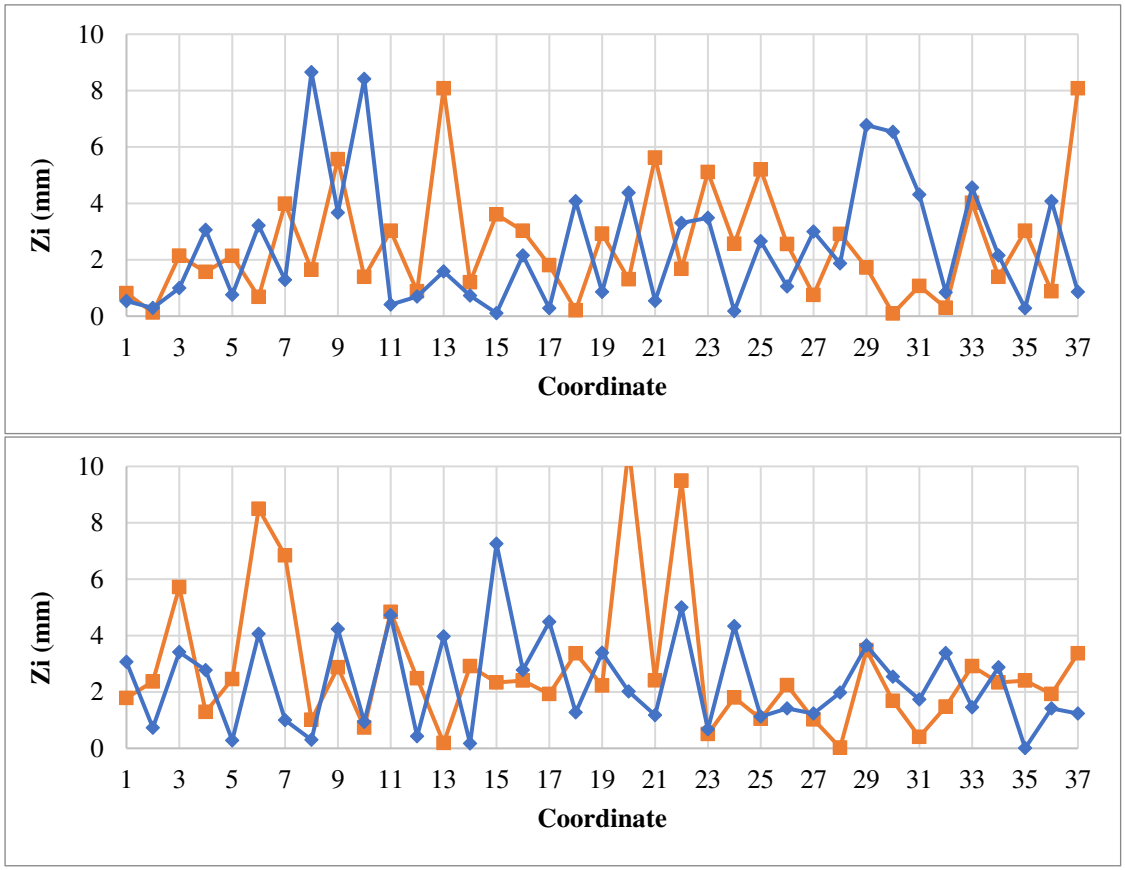


Figure 9.16 – Roughness profiles of the $S_{3D}$-STC specimen:
(—) upper effective depth, (—) lower effective depth.
(only two assessments were performed on each direction)

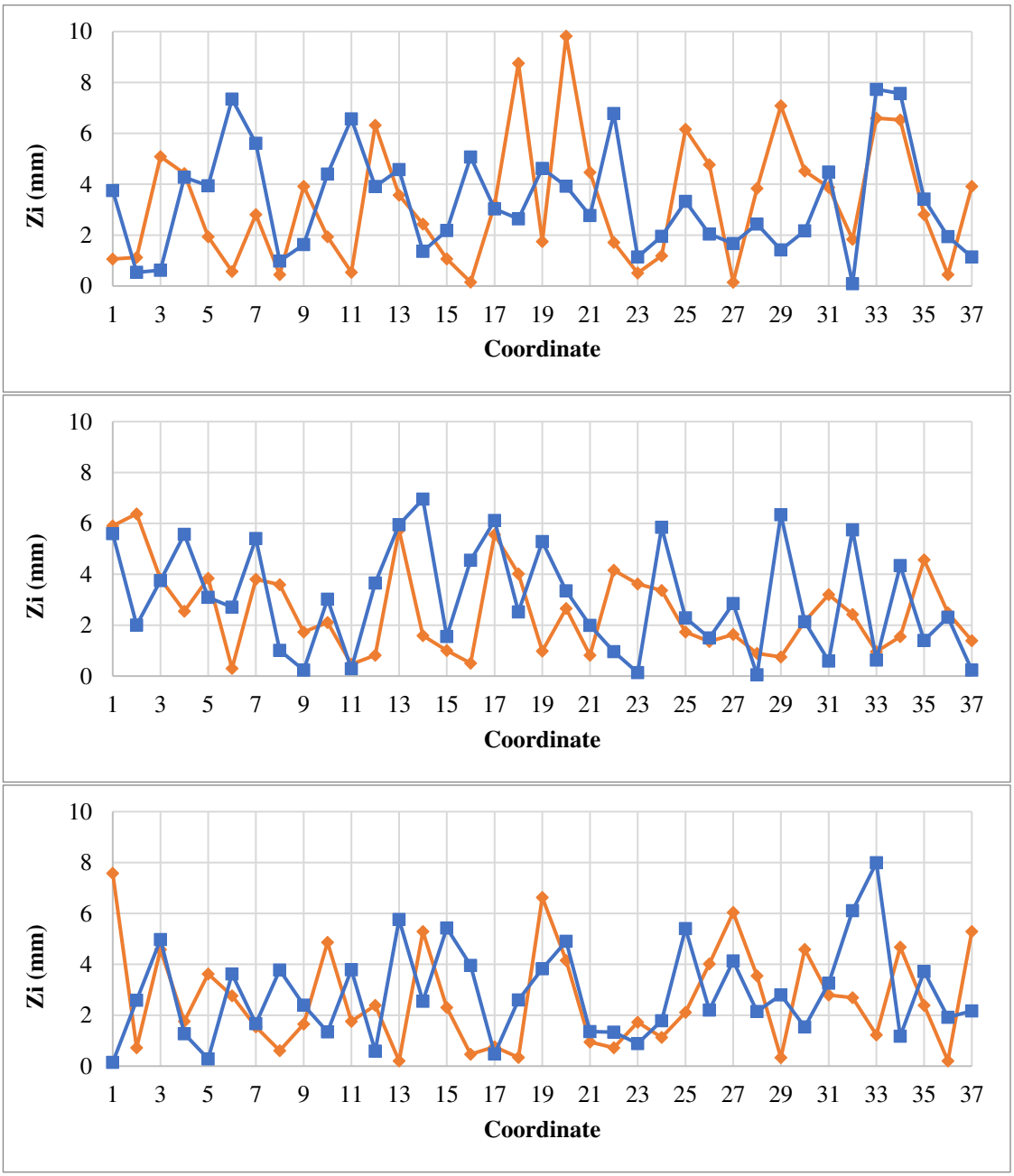


Figure 9.17 – Roughness profiles of the $S_{3D}$-REF specimen:
(—) upper effective depth, (—) lower effective depth.

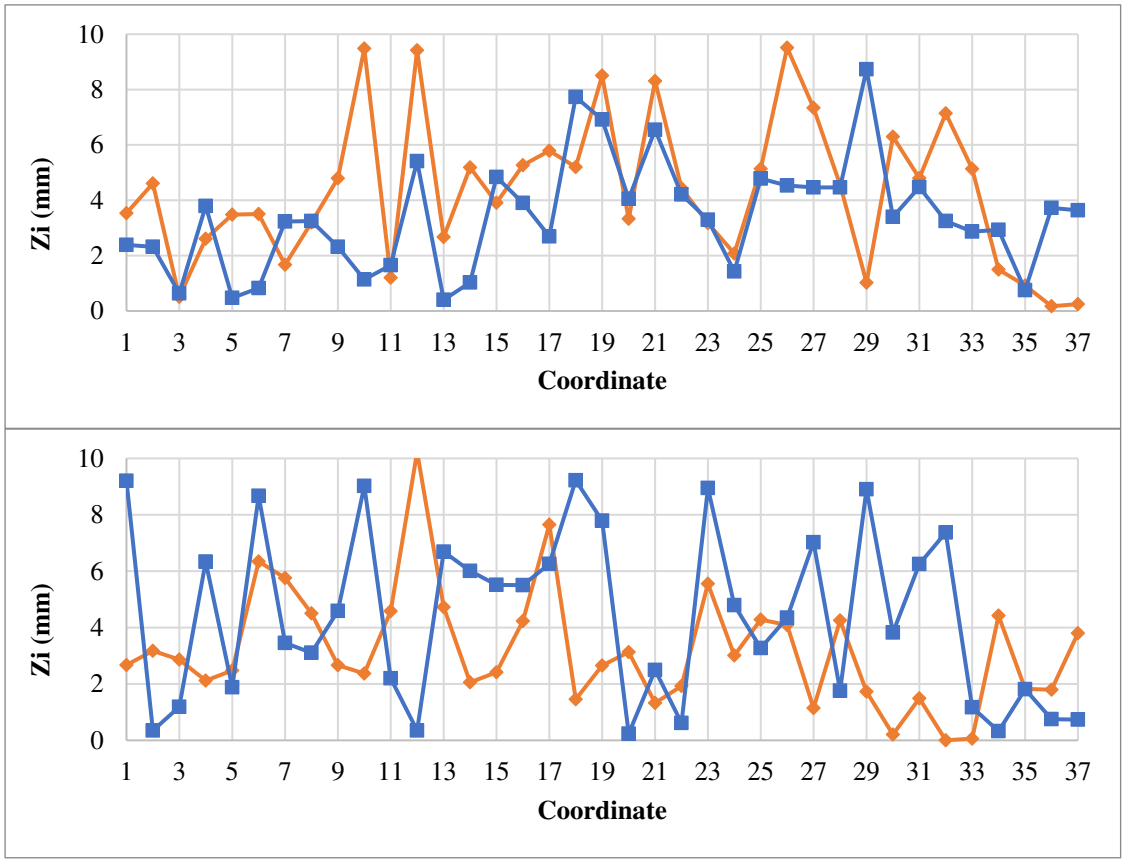


Figure 9.18 – Roughness profiles of the $S_{4D}$-ANC specimen:
(——) upper effective depth, (——) lower effective depth.
(only two assessments were performed on each direction)

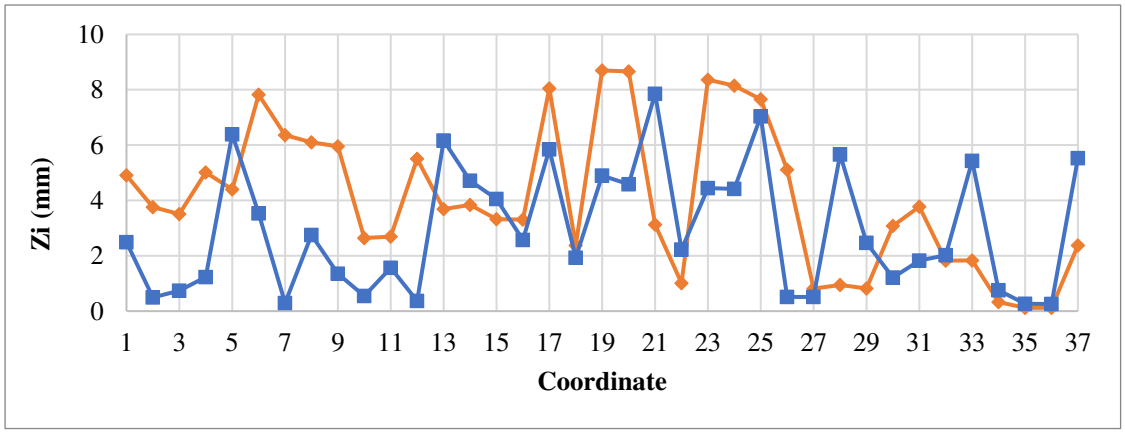

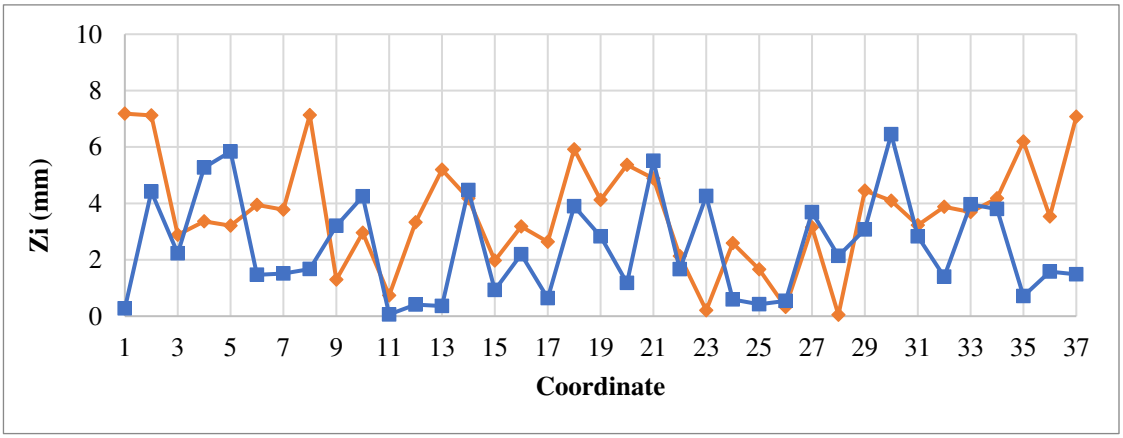


Figure 9.19 – Roughness profiles of the $S_{4D}$-STC specimen:
(—) upper effective depth, (—) lower effective depth.
(only two assessments were performed on each direction)

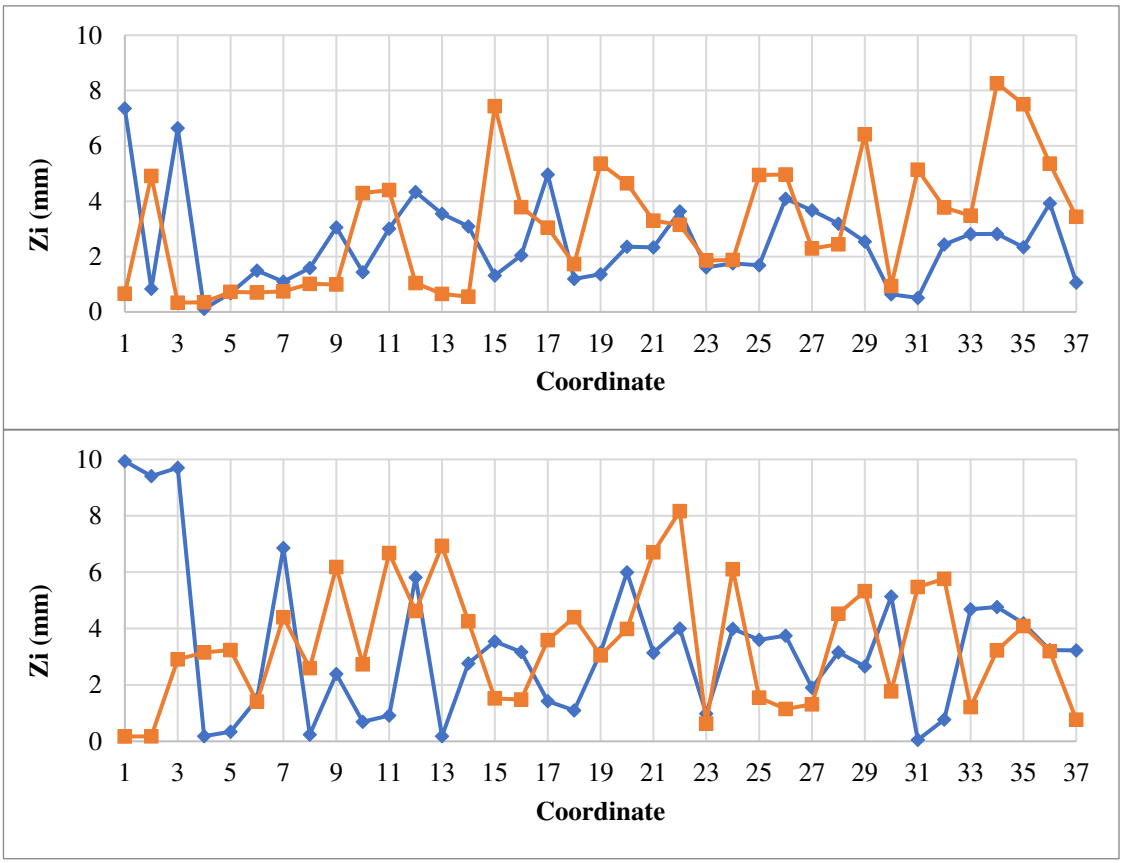


Figure 9.20 – Roughness profiles of the $S_{4D}$-STANC specimen:
(—) upper effective depth, (—) lower effective depth.
(only two assessments were performed on each direction)

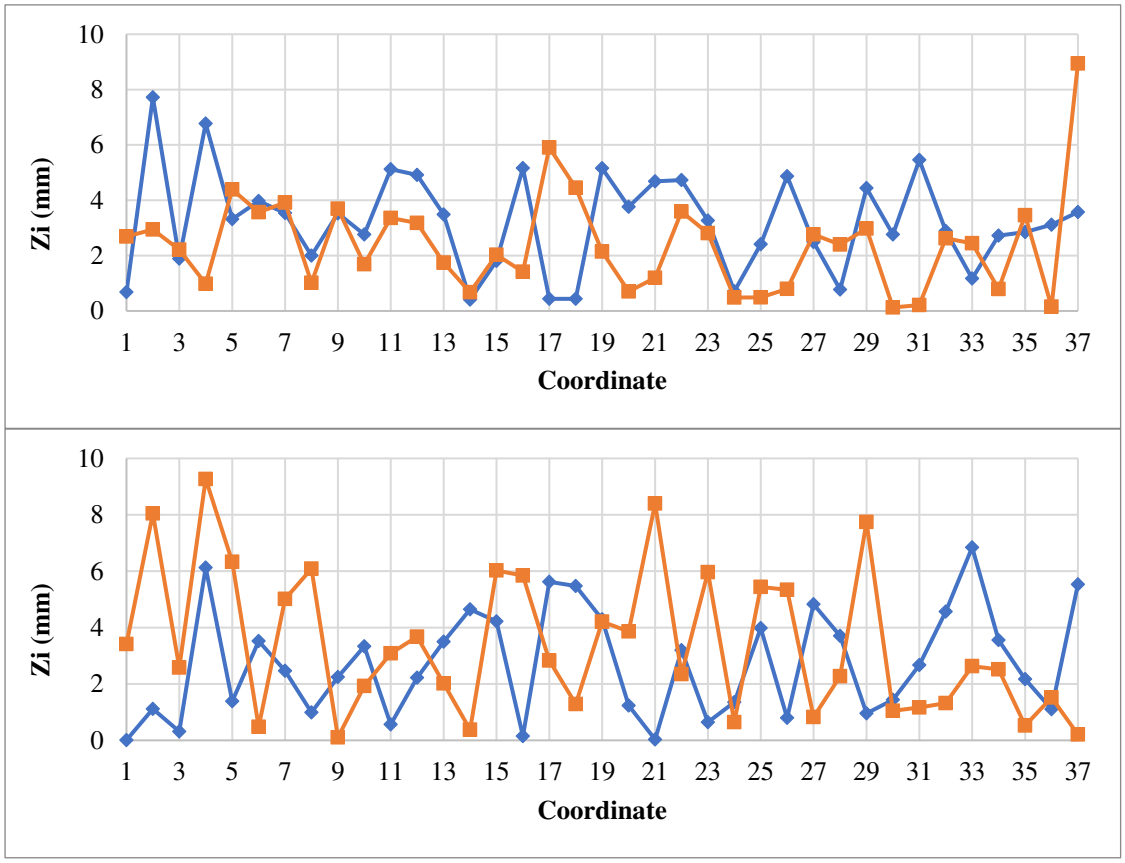


Figure 9.21 – Roughness profiles of the $S_{4D}$-STANC specimen:
(—) upper effective depth, (—) lower effective depth.
(only two assessments were performed on each direction)